Author:
Perkins, Rebecca

Title:
Post-Collisional Magmatism and Porphyry - Epithermal Style Mineralisation along the Maronia Magmatic Corridor, northeastern Greece

POST-COLLISIONAL MAGMATISM AND PORPHYRY – EPITHERMAL MINERALISATION ALONG THE MARONIA MAGMATIC CORRIDOR, NORTHEASTERN GREECE

Rebecca J. Perkins

Supervisors: F.J. Cooper, B. Tattitch, J. Naden & D.J. Condon

A dissertation submitted to the University of Bristol in accordance with the requirements for award of the degree of Doctor of Philosophy in the Faculty of Science

School of Earth Sciences

12th September 2018

Word Count:

42,986

Abstract

Porphyry copper deposits are not restricted to volcanic arcs alone and have been identified in extensional tectonic settings from across the world. Post-collisional crustal extension can result in areas of elevated heat flow generating small-volume, calc-alkaline to shoshonitic magmas, some of which are associated with exotic metal-bearing porphyry – epithermal systems. The Maronia Magmatic Corridor is a NE-trending belt of post-collisional Oligocene high-K calc-alkaline to shoshonitic plutons that intrude the northern Rhodope Core Complex in northeastern Greece. It is host to several documented occurrences of post-collisional porphyry – epithermal mineralisation associated with the intrusion of co-genetic evolved porphyritic dykes and stocks. By reconstructing the tectono-magmatic evolution of post-collisional magmatism along the Maronia Magmatic Corridor, this thesis aims to explore the processes governing porphyry – epithermal mineralisation in extensional tectonic settings.

Detailed petrology and whole-rock geochemistry of the host plutons provide evidence of plagioclase – pyroxene – amphibole controlled lower crustal fractionation to produce high-K calc-alkaline magmatism between 33–32 Ma, with a drier parental magma ($<$ 4.75 wt% H_2O) than is typically expected of subduction-related magmatism. I show that continued H_2O depletion of the metasomatised source mantle resulted in a 2.2 Myr hiatus in magmatism during which the source mantle was at sub-solidus conditions. The consequent transition to a shoshonitic trend was driven by lower crustal fractionation of an H_2O-poor ($<\sim$ 2 wt % H_2O) magma in the absence of olivine. Early high-K calc-alkaline magmatism has the physiochemical characteristics permissive for metal transport to the upper crust, whilst conventional fertility indicators suggest that the later phase of shoshonitic magmatism is insufficiently hydrous.

Pervasive, destructive alteration of the metal-bearing porphyritic intrusions from across the MMC means that conventional petrological and geochemical techniques have limited applicability in assessing the petrogenesis of the ore-bearing magmas. Instead, complimentary analyses of zircon trace element geochemistry, zircon-hosted melt inclusion chemistry and zircon U-Pb geochronology have been used for the first time to reconstruct the cryptic magmatic history of the metal-bearing intrusions. Signatures of both crustal- and mantle-derived inputs suggest hybridisation of magmas which can account for W enrichment in some the porphyry systems.

Finally, I document the exhumation history of the highly-telescoped Kassiteres porphyry – epithermal system in order to assess the influence of rapid exhumation on mineralising processes. I suggest that dilution and dispersal of the magmatic-hydrothermal fluids by sub-volcanic meteoric groundwater during syn-mineralisation exhumation of Kassiteres to the surface, resulted in the pre-mature transition from a porphyry to an epithermal environment and can account for the lack of preserved mineralisation at Kassiteres.

Author's Declaration

I declare that the work in this dissertation was carried out in accordance with the requirements of the University's Regulations and Code of Practice for Research Degree Programmes and that it has not been submitted for any other academic award. Except where indicated by specific reference in the text, the work is the candidate's own work. Work done in collaboration with, or with the assistance of, others, is indicated as such. Any views expressed in the dissertation are those of the author.

.....

Rebecca J. Perkins
The Author

12th September 2018

Acknowledgments

My PhD has been a challenging, but rewarding journey and I have been lucky enough to have had the support and advice of so many people. This thesis was funded by a NERC GW4+ DTP and British Geological Survey (BGS) CASE-funded scholarship with additional support from the Society of Economic Geologists (SEG) for travel to conferences and also from the SEG Hugh McKinstry Fund.

First and foremost, I would like to thank my supervisors, Frances Cooper, Dan Condon, Jon Naden and Brian Tattitch without whom this thesis would not have been possible. I am so grateful for all your support, enthusiasm and patience over the last four years, guiding me through my fieldwork in the hydrothermally altered terranes of northeastern Greece and the complex worlds of geochronology, thermochronology and petrology. Thank you for allowing me to pursue my own ideas but always being there to lend support, helping me to grow as a scientist.

This thesis has been made possible with analytical and scientific support from those at the NERC Isotope Geosciences Laboratory (NIGL) for U-Pb zircon geochronology and zircon trace element geochemistry analyses. In particular I would like to Simon Tapster whose help, advice and feedback have added greatly to this thesis. My thanks also go to the Inorganic Geochemical Facility at the British Geological Survey (BGS) for the whole rock geochemistry analyses and Claire Fleming at the BGS for assistance with clay spectroscopy. I am very grateful to Stuart Kearns and Ben Buse for their support and patience during many microprobe sessions. I also thank Byron Adams, Todd Ehlers (University of Tübingen), Mathjis van Soest (Univeristy of Arizona) and Ken Farley (California Institute of Technology) for analytical and modelling support of the (U-Th)/He thermochronology work.

I would like to thank the whole Bristol – BHP PCD group, I feel so privileged to have been a part of such an active research group who have contributed in so many ways to my work. I thank Dave Bertuch and the rest of the BHP North America Exploration team for the opportunity to work with the group during my internship. I also wish to say a huge thank you to Amy Gilmer, Marit van Zalinge, Laura Evenstar, Vladimir Matjuschkin and Cyril Chelle-Michou in Bristol who have really helped to shape my scientific thinking and supported me throughout. My thanks go to Katerina Gikka, Simon Dahlström and Ery Hughes for making my time in the field so much fun.

My PhD would not have been the same without my wonderful friends; we've been on a real rollercoaster throughout our PhDs but I wouldn't have it any other way. Ery, Ryan, Keri, Nicky, Neil, Luke, Serginio, Mike and so many more: thank you! You have made this an unforgettable four years. To everyone in the City of Bristol Women's squad, and the rest of the club, you have helped keep me sane throughout my PhD providing the best of distractions. Lucy and Tom, I couldn't have done this without you.

My final thanks are to my family, my parents, Russell and Alison, and my beautiful sister, Emma, for your unconditional love and support. To both of my Grandads, Bernard Perkins and Bernard Pike, who always encouraged me to pursue science, this thesis is for you.

Contents

List of Figures

List of Tables

Introduction

The Marmaritsa fault that cuts the southern margin of the Maronia pluton.

1.1 Thesis Outline

1.1.1 Rationale

Porphyry – epithermal mineral systems account for approximately 60 % of the global, annual Cu production, 20 % of the global, annual Au production and > 90 % of the global, annual Mo production. These systems are driven by magmatic–hydrothermal fluids that are exsolved from evolved, calc-alkaline magmas during decompression and crystallisation and interact with host wall-rock and meteoric waters to precipitate ore minerals. A wide range of mineralisation styles are associated with porphyry – epithermal systems including porphyry Cu-Au-Mo deposits (PCDs), Au-Ag-base metal high-, intermediate- and low-sulphidation epithermal deposits, Cu-Au-Fe skarns and Cu-base metal carbonate replacement deposits.

PCDs are typically associated with collisional tectonic settings where subduction-related volcanic arcs generate hydrous, highly fractionated calc-alkaline magmas favourable for mineralisation (e.g., Sillitoe 2010). It is in such convergent tectonic settings that world-class belts of PCDs have been found e.g., the Eocene-Oligocene porphyry belt of the Chilean Andes. However, PCDs are not restricted to volcanic arcs alone and have been identified in extensional tectonic settings, for example from across the Tethyan belt (e.g., Richards 2015). Post-collisional crustal extension can result in areas of elevated mantle heat flow generating small-volume, calc-alkaline to shoshonitic magmas, some of which are associated with exotic metal-bearing PCDs (Richards, 2009). These deposits are becoming increasingly important as they exhibit significant by-product metal endowments, including PGEs and semi-metals such as Te, which are in growing demand for a whole range of high technology and green energy applications. Therefore understanding if, and how, an extensional geodynamic setting influences magma petrogenesis and metal fertility, is of great importance to the future of mineral exploration.

In the northern Aegean, Cenozoic PCDs are associated with post-collisional crustal collapse following the two-continent collision of Africa with Eurasia, where extension, post-collisional magmatism, mineralisation and core complex exhumation are thought to be contemporaneous (e.g., Marchev et al. 2010; Rohrmeier et al. 2013; Marchev et al. 2013). The Maronia Magmatic Corridor in NE Greece defines a NE-trending belt of high-K calc-alkaline to shoshonitic plutons which is intruded by evolved porphyritic dykes and stocks and is host to porphyry, epithermal and carbonate-replacement mineralisation. These mineral systems have a striking semi-metal endowment, including previously documented Re & Te enrichment (e.g., Voudouris 2006; Voudouris et al. 2009, 2013b,a; Melfos and Voudouris 2017) and elevated W & Sn described in this thesis. Examples of post-collisional porphyry – epithermal mineralisation, the mineral deposits of the Maronia Magmatic Corridor provide ideal case studies for better understanding the processes governing mineralisation in extensional tectonic settings.

Detailed studies of the individual mineralised systems have been well-described in the literature (e.g., Melfos et al. 2002; Voudouris 2006; Voudouris et al. 2006, 2009, 2013a,b; Melfos and Voudouris 2017). It is not the intention of this thesis to reproduce detailed studies of the systems, rather it aims to provide magmatic and tectonic context to the existing studies. As a result, this thesis focuses on the petrogenesis of regional, host magmatism and metal-bearing porphyry intrusions and predominantly discusses the deep (3–5 km), magmatic porphyry phase of the mineralising system. Exhumation of the porphyry systems is also examined in this thesis and concentrates on the influence of unroofing of magmatic systems on porphyry mineralisation.

1.1.2 Aims

This thesis aims to answer a series of key research questions, these are:

1. How does the Maronia Magmatic Corridor relate to the Cenozoic tectonic extension in the northern Aegean, and how can we use our understanding of one to inform the other?
2. How does post-collisional magmatism along the Maronia Magmatic Corridor compare to volcanic arc-type magmatism; does it provide the necessary physiochemical conditions permissive for PCD mineralisation? This can be sub-divided into:
   (a) Regional host magmatism
   (b) Late-stage, metal-bearing porphyry magmatism
3. How do exhumation and mineralisation relate chronologically, and what influence does this have on the 'success' of deposit formation and preservation.

Each chapter addresses one of the aims, in part or in full, in order to develop a coherent thesis.

1.1.3 Thesis Structure

This thesis uses field observations combined with geochronological, geochemical and petrological analytical techniques to reconstruct the magmatic and tectonic history of the Maronia Magmatic Corridor. The Maronia Magmatic Corridor has been separated into three case study areas for the thesis: Maronia in the SW, Kassiteres in the centre and Leptokaria in the NE. Four science chapters are presented in addition to a final concluding chapter which synthesises the mineralisation history of the Maronia Magmatic Corridor and places the work in a wider geological context. Figure 1.1 outlines a schematic abstract of the thesis capturing the evolution of the Maronia Magmatic Corridor.

Firstly, ***Chapter 2*** presents petrology, geochemistry and geochronology of the host plutons to document the petrogenetic history of the Maronia Magmatic Corridor. Petrographic observations, whole-rock, major, minor and trace element geochemistry and high-precision isotope dilution thermal ionisation mass spectrometry (ID-TIMS) U-Pb zircon geochronology data are presented. The primary aim of the chapter is to use geochemical indicators to fingerprint the source of parental magmatism and provide a geochronological timeline of host magmatism on which to build the rest of the thesis. Petrology and geochemistry of the host intrusions identify two episodes of metasomatized-mantle derived magmatism which high-precision geochronology shows are separated by a 2.4 Myr temporal break in observed intrusions. Trace element geochemistry is used to identify the phases controlling fractionation of the two periods of magmatism. Comparison of the fractionating phase assemblage with existing experimental data, combined with fractional crystallisation modelling, constrains the H_2O content of the magmas and suggests evolving mantle melting conditions during petrogenesis of the Maronia Magmatic Corridor.

Chapter 3 is a detailed petrological study of the composition and texture of major and accessory minerals from the host plutons of the Maronia Magmatic Corridor with the aim to document the extensive parameters: temperature (T), pressure (P), and H_2O content, of the magmas during crystallisation. Electron-probe micro-analysis (EPMA) mineral chemistry data is used in this chapter. Geothermobarometry of plagioclase,

amphibole and pyroxene and accessory zircon and apatite from the host plutons record the T and P of crystallisation. Textural and compositional variations in phenocrysts from single samples record multiple periods of crystallisation consistent with current thinking of pulsed melt assembly during accumulation of magmatic bodies in the crust. Interpreting the emplacement history of the Maronia Magmatic Corridor within the geochronological framework established in Chapter 2, this chapter unpicks the P-T-H_2O-t evolution of the magmatic systems.

Chapter 4 focuses on the origin of the ore-bearing magmas using zircon-hosted melt inclusion EPMA major element chemistry, laser ablation inductively coupled plasma mass spectrometry (LA-ICP-MS) trace element zircon chemistry and U-Pb zircon geochronology data. Pervasive, destructive alteration of the metal-bearing porphyritic intrusions from across the Maronia Magmatic Corridor means that conventional petrological and geochemical techniques have limited applicability in assessing the generation of ore-bearing magmas. This chapter tackles this problem by using zircon as an archive of melt evolution. Integrated zircon trace element geochemistry and zircon-hosted melt inclusion petrology are used to reconstruct the composition of the ore-bearing magma and are integrated with high-spatial resolution

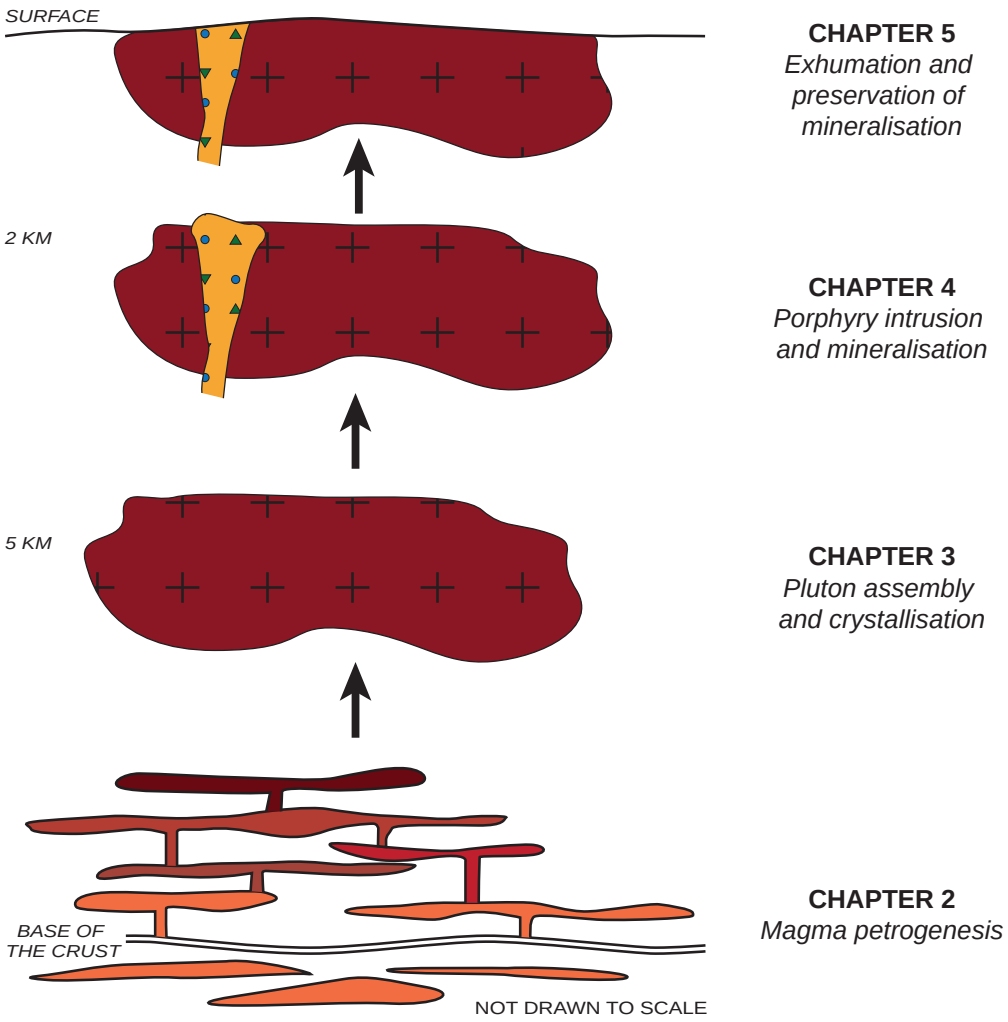

Figure 1.1: A graphical abstract of the thesis showing how this works tracks the evolution of the Maronia Magmatic Corridor from magma petrogenesis through pluton assembly and crystallisation, porphyry intrusion and mineralisation to exhumation and exposure at the surface

zircon geochronology to show convincing evidence of hybridisation of crustal- and mantle-derived inputs. Significantly, this chapter contains the first documented analyses of zircon-hosted melt inclusions from a magmatic mineralised system which allows for direct measurement of the ore-bearing magma. This chapter suggests that integrated zircon trace element and melt inclusion analyses are a promising avenue for further study of magma metal fertility.

Chapter 5 then considers the final stages of evolution of mineralised systems: exhumation from the shallow crust (2-5 km) to the surface focusing on the Kassiteres area. High-precision ID-TIMS U-Pb zircon geochronology, short-wave infra-red (SWIR) clay spectroscopy and field data are presented here in order to decipher the origin of extreme overprinting, or telescoping, of mineralisation in the Kassiteres porphyry – epithermal system. This chapter discusses current thinking about the role of exhumation syn-mineralisation, i.e. whilst the mineralising magmatic-hydrothermal fluid system is still active, and relates the extreme exhumation rates to the lack of preserved porphyry-style mineralisation at Kassiteres.

Exhumation of the Maronia and Leptokaria systems was also considered and (U-Th)/He thermochronology data, cooling ages of the intrusive units, was also collected from Leptokaria and Maronia systems. However, current understanding of the interplay between cooling on magma emplacement and cooling via advection of heat to the surface during exhumation is limited, and existing models of the geothermal structure of the crust do not account for this. Thermal modelling of conductive, magmatic cooling and advective, exhumation-related cooling is ongoing in order to convert the cooling paths of the intrusions to exhumation rates. This data does not form part of the thesis but is included for completeness in Appendix O.

Finally, ***Chapter 6*** concludes the thesis, synthesising the key scientific findings from each chapter and collating them to unravel the geological history of the Maronia Magmatic Corridor. The chapter places the thesis into the wider context of the mining industry, discussing the applicability of the techniques used to mineral exploration, and proposes future work along the Maronia Magmatic Corridor.

1.2 Porphyry Copper Deposits

PCDs are defined as tens to hundreds of cubic kilometres of hydrothermally altered rock that are genetically associated with the intrusion of small-volume, porphyritic dykes or stocks (e.g., Sillitoe 2010). The resultant porphyry Cu-Au-Mo-PGE mineralisation that makes up PCDs is typically low grade (0.5–1.5 wt.% Cu) and high tonnage with vein-hosted and disseminated sulphides the dominant hypogene mineralisation styles. The causative porphyritic intrusions emanate from equigranular, dioritic to granitic parental batholiths that extend at depth below the mineralising system (> 5–3 km). The link between PCDs and arc-volcanoes has long been recognised (e.g., Lowell and Guilbert 1970; Sillitoe 1972, 1973; Gustafson and Hunt 1975; Hunt 1977) through the spatial association of the systems with co-genetic volcanic rocks and similarities in morphology and timescales of magmatic activity (e.g., Dilles 1987). However, whether PCDs form in the roots of dome volcanoes or in blind intrusive complexes that do not reach the surface, is still a matter of debate in the community (e.g., Gilmer et al. 2017).

An array of satellite mineral deposits styles form above PCDs (between 2 km depth and the surface), such as high-, intermediate- and low-sulphidation epithermal deposits and carbonate-replacement deposits. These mineral systems are distal to the porphyry intrusion but are thought to derive a component of the mineralising hydrothermal fluid from the exsolved magmatic volatile phase related to the porphyry intrusion (e.g., Sillitoe 2010). PCDs are thought to represent the deeper magmatic roots of epithermal and carbonate replacement deposits, thus an understanding of the formation of PCDs feeds into genetic models of these mineralisation styles.

1.2.1 Distribution in Time and Space

PCDs are spatially associated with arc-magmatism above subduction zones in convergent tectonic settings (e.g., Seedorf 2005; Sillitoe 2010; Fig. 1.2). Magma generation in arc settings is driven by dehydration of the down-going slab and resultant metasomatism and melting of the overlying mantle wedge. Accumulation of melt sills occurs at the base of the crust forming a deep 'hot zone' at the base of the crust where partial

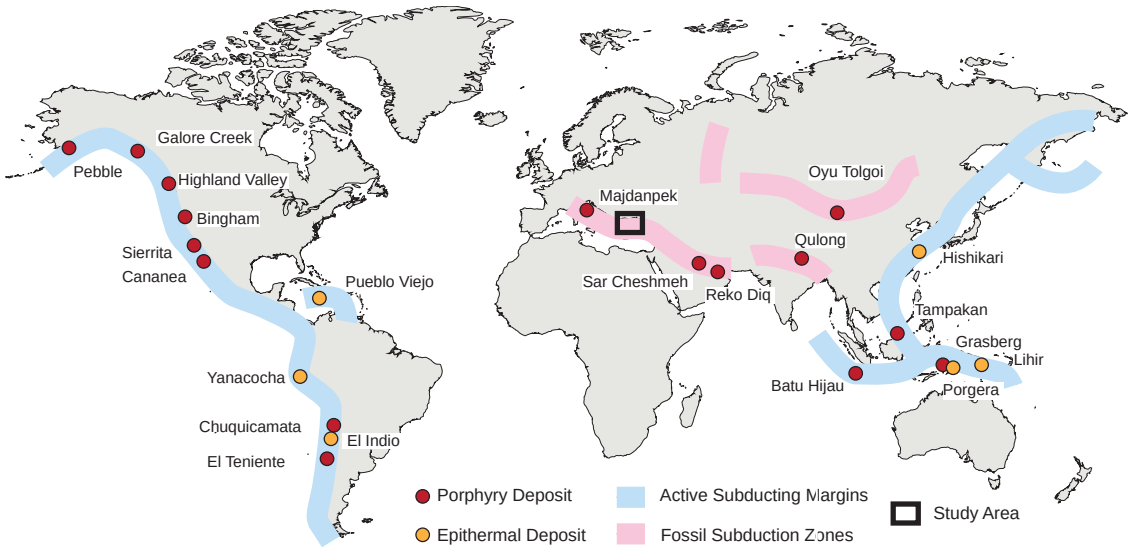

Figure 1.2: The global distribution of PCDs and associated epithermal systems; adapted from Richards (2013).

crystallisation of the magmas generates an incompatible- and volatile-rich residual liquid and latent heat of crystallisation results in melting and assimilation of lower crust material (e.g., Annen et al. 2006). Filtering of the magmas through further fractional crystallisation of olivine, pyroxene, amphibole ± garnet and late plagioclase as the melts rise through the trans-crustal mush systems gives arc-type magmas their characteristic fingerprint of high Sr/Y, La/Yb ratios, large ion lithophile element (LILE, e.g., K, Rb, Sr, Ba) enrichment and middle to heavy rare earth element (REE) depletion which is common across all porphyry-forming magmas (e.g., Chiaradia et al. 2012; Richards 2011a; Loucks 2014). Magmas generated in a post-subduction setting, be it during the transition to two-continent collision e.g., Tibet, or during post-collisional extension e.g., the Aegean, can still inherit the characteristics of arc-type magmatism by melting of subduction-modified lithospheric mantle leading to recognition of a class of post-subduction PCDs (e.g., Richards 2009).

Within magmatic arcs, PCDs typically lie along linear arrays, forming metallogeneic belts that trend sub-parallel to the subduction front (e.g., Sillitoe, 2010). Minimal overlapping of PCDs is observed, suggesting that mineralisation occurs in discrete metallogenic events, that migrate with the volcanic arc front. Lineaments of deposits within metallogenic belts typically follow strike-slip faults, for example: the Antofagasta–Calama lineament, Chile (e.g., Palacios et al. 2007) and the Ertsberg district (Grasberg), Indonesia (Sapiie and Cloos, 2004, 2013). In volcanic arcs, it is likely that local transpression along jogs in strike-slip fault systems provide a pathway for magmatism and create dynamic rock permeability through repetitive opening and sealing of complimentary fractures aiding fluid:wall-rock interaction (e.g., Cloos and Sapiie 2013).

Globally, PCDs are also clustered in time with Cenozoic systems the most abundant (e.g., Kesler and Wilkinson 2008). Rather than reflecting temporal changes in magmatic activity, this is likely a preservation artefact. As PCDs form in the upper 2–5 km of the crust they are particularly sensitive to exhumation with the decreasing abundance of known PCDs back through geological time reflecting erosion or burial of the deposits (Kesler and Wilkinson, 2008; Yanites and Kesler, 2015).

1.2.2 Features of Porphyry Copper Deposits

Over the last half century, a great deal of research has focused on detailed observations of PCDs with fundamental characteristics of alteration, veining and mineralisation common across all systems. The spatial association of shallow, high-sulphidation epithermal deposits overlying deeper, porphyry deposits suggest common processes controlling mineralisation. Whilst not all epithermal deposits are associated with porphyry deposits and vice versa, a co-genetic link between these deposits is suggested by shared textural and alteration features and similarities in fluid sources as identified by isotopic fingerprinting (e.g., Hedenquist and Lowenstern 1994) and has lead to continuum models of mineralisation (e.g., Sillitoe 2010).

PCDs form a cylindrical shape, typically centred on a series of pre-, syn- and post-mineral porphyritic dykes or stocks. The porphyry intrusions are generally andesitic to rhyolitic in composition with amphibole, biotite and plagioclase phenocrysts hosted in an aplitic (quartz + K-feldspar) matrix, although complete obliteration of primary magmatic textures during hydrothermal alteration is common (e.g., Sillitoe 2010). Diatremes and breccia pipes are found throughout PCDs formed during the release of magmatic overpressure. Irregularly-shaped bodies of igneous clasts in a hydrothermal cement, the breccia pipes and diatremes are highly permeable units and so are intensely altered and commonly host some of the highest ore grades (e.g., Sillitoe

1985; Turner 1999).

Alteration in PCDs generally forms a concentrically zoned shell outwards from the porphyry dyke or stock (e.g., Lowell and Guilbert 1970; Sillitoe 2010). Alteration is most intense in the centre of the shell and decreases in intensity laterally, with distance away from the causative intrusion. Magma chemistry exerts a strong control on the alteration style, a function of the availability of cations: Ca^+, Na^+, K^+ and H^+ (Sillitoe, 2010). The different alteration styles observed in porphyry – epithermal systems are outlined in Table 1.1 and annotated on a typical cross-section through a PCD in Figure 1.3 (taken from Sillitoe 2010). Veining is also highly distinctive of PCDs. First described by Gustafson and Hunt (1975) three generations of veins are found across all PCDs (Sillitoe, 2010): *(i)* a phase of monomineralic (actinolite, biotite, magnetite or K-feldspar), sulphide-free veining is associated with early, high-temperature alteration; *(ii)* a second phase of granular quartz + sulphide veining with no alteration halo is also associated with the high-temperature phase of the system; *(iii)* finally, a crystalline quartz + sulphide, and occasional sulphide-only, generation of veining typically have an alteration halo associated with the later, more acidic stage of alteration. Multiple cycles of veining are common, often repeatedly re-opening and re-sealing existing veins.

Lithocaps overlie most PCDs, and are associated with high-, intermediate- and low-sulphidation epithermal mineralisation, typically forming towards the end of the hydrothermal event. Several kilometres wide and up to a kilometre thick, lithocaps are the expression of intense acid alteration where magmatic-hydrothermal fluids interact with meteoric water and are an important feature across epithermal deposits (e.g., Sillitoe 1995; Hedenquist et al. 2000). Lithocaps form as acidic, magmatic fluids leach through the host rocks,

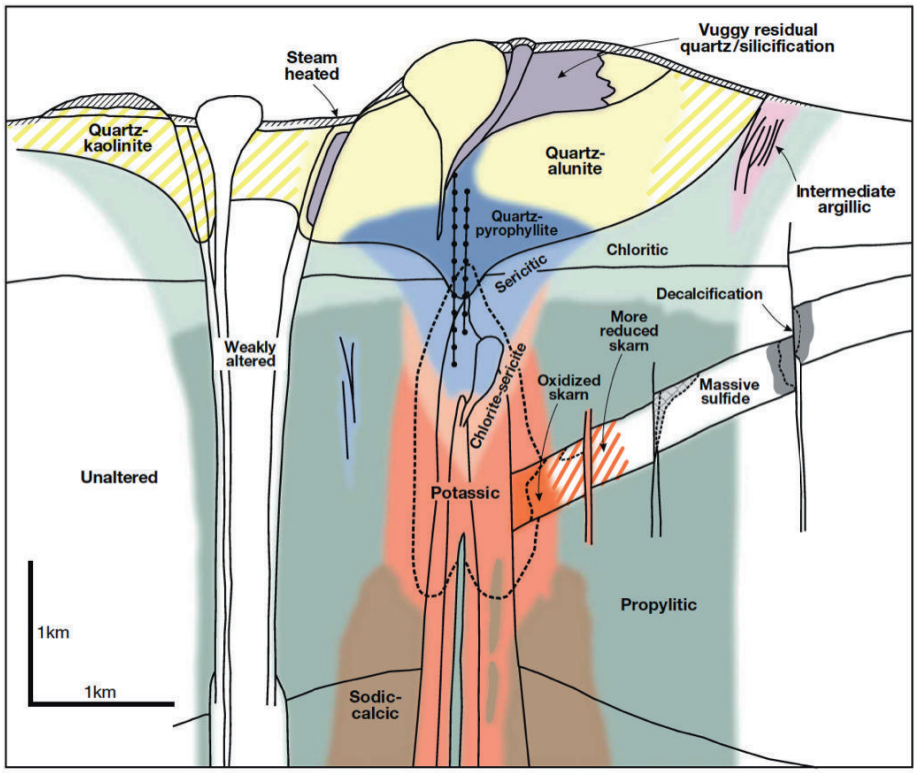

Figure 1.3: Alteration of PCDs has a distinctive, concentrically zoned pattern typically forming a shell centred on a porphyritic dyke- or stock-like intrusion. Overprinting of shallow alteration styles on top of deeper alteration is common as the rock package moves upwards through the cooling magmatic-hydrothermal fluid system; Figure 10 from Sillitoe (2010).

Table 1.1: Key characteristics of PCD alteration styles and their position in typical alteration shells; adapted from Sillitoe (2010). Descriptions of the vein styles *i-iii* are in the text.

Alteration style	Position in system	Key mineralogy	Characteristic sulphides	Vein Gen.	Ore potential
Sodic-calcic	Deep	Albite/oligoclase, actinolite, magnetite, epidote	Absent	*i*	Barren
Potassic	Core	Biotite, K-feldspar	Pyrite, chalcolpyrite $\pm$ bornite, $\pm$ chalcocite	*i, ii*	Major porphyry
Propylitic	Marginal, deep	Chlorite, epidote, albite	Pyrite	*ii*	Barren
Chlorite-serecite	Upper core	Chlorite, sericite, illite, haematite	Pyrite-chalcopyrite	*i*	Minor porphyry
Phyllic	Upper	Quartz, sericite, illite	Pyrite $\pm$ chalcopyrite	*iii*	Barren
Argillic (serecite/ quartz–pyrophyllite)	Above system	Quartz, alunite, sericite, illite, montmorillonite, kaolinite	Pyrite	*iii*	Major epithermal
Advanced argillic (quartz–alunite)	Well above system	Quartz, alunite, pyrophyllite, kaolinite, dickite	Pyrite	*iii*	Minor epithermal

dissolving most of the rock-forming minerals leaving residual vuggy quartz leach caps and precipitating fine-grained clays and alunite on cooling (e.g., Sillitoe 2010). Volcanic fumaroles, observed close to the vent of most active modern volcanoes, are thought to be modern day analogues of lithocaps providing further evidence of the link between porphyry – epithermal systems and dome volcanoes (e.g., Hedenquist et al. 2000).

1.2.3 Current Paradigms

Cline and Bodnar (1991) suggest that all calc-alkaline magmas generated from a metasomatised mantle source and fractionated through the crust have the potential to form PCDs. Therefore, optimisation and/or overprinting of later tectono-magmatic processes are thought to be imperative to mineralisation as not all calc-alkaline magmas do form PCDs (e.g., Richards 2003; Blundy et al. 2015).

Current paradigms of PCDs stem from models developed in the 1970s. These models identify the key components in the formation of PCDs to be: a shallowly emplaced, porphyritic intrusion in the cupola of a calc-alkaline batholith; an exsolved magmatic fluid phase which sequesters metals from the magma; and the collapse of the magmatic-hydrothermal fluid system during cooling driving sulphide precipitation and ore formation (e.g., Lowell and Guilbert 1970; Sillitoe 1973; Gustafson and Hunt 1975). These models attribute metal concentration, transport and distribution to a single, orthomagmatic fluid phase that is exsolved from a magma during first boiling (adiabatic decompression) and/or second boiling (crystallisation).

A simple mass balance argument can be made against the case of a single mineralising fluid; there is insufficient S in the volume of a 'typical' calc-alkaline magma associated with a PCDs to account for the S/Cu and S/Cl ratio of these systems (e.g., Hedenquist and Lowenstern 1994; Blundy et al. 2015). A similar mass balance problem is observed arc-volcanoes e.g., Soufrière Hills Volcano, where the flux of SO_2 out

of the vent during eruption is greater than can be supplied by degassing of the volume of magma erupted (e.g., Edmonds et al. 2010). In both cases, a source of excess SO_2 is required. Recent models have tried to account for the S anomaly associated with PCDs and they can be split into two main groups: *(i)* models that invoke an external volatile, S, source (e.g., Blundy et al. 2015; Nadeau et al. 2016), and *(ii)* models that invoke release of S trapped in sulphides and/or sulphates in the calc-alkaline magmas (e.g., Wilkinson 2013; Sun et al. 2015).

1.3 Post-Collisional Extension of Orogenic Systems

Post-collisional extension of orogenic systems is a well-documented phenomenon that occurs when mountain belts collapse due to gravitational instabilities developed in over-thickened crust (e.g., Pichon and Angelier 1979; Dewey 1988). Extended orogens are found throughout the geological record for example: the Palaeozoic Caledonide Belt in northern Europe (e.g., Gee et al. 2008), the Mesozoic Dabie Shan orogen in China (e.g., Xu et al. 2010), the Cenozoic Basin and Range Province in western U.S.A (e.g., Camp et al. 2015), and the Rhodope Massif in the northern Aegean, southern Bulgaria (e.g., Burg 2011). Trans-crustal fault structures develop in dissected orogens to accommodate large amounts of lateral extension and, along with preserved metamorphic terrains and post-collisional magmatism, are diagnostic features of extended terranes (e.g., Whitney et al. 2013).

1.3.1 Metamorphic Core Complexes

In extensional environments, strain localisation along one, or a few, interconnected faults can result in the ductile ascent of lower crustal material and the formation of metamorphic core complexes. Dome-shaped regions of medium- to high-grade metamorphic rocks, metamorphic core complexes are bound by low-angle normal faults, or detachment faults, and overlain by low-grade to unmetamorphosed, flat-lying to moderately tilted sedimentary units (e.g., Whitney et al. 2013; Platt et al. 2015). Metamorphic core complexes were first recognised in the North America Cordillera, forming as the result of Cenozoic Basin and Range horizontal extension and vertical thinning of the crust and have since been documented from across dissected orogenic terranes globally (e.g., Wernicke et al. 1987; Burg 2011; Whitney et al. 2013; Platt et al. 2015; Brun et al. 2016).

1.3.2 Post-Collisional Magmatism

Post-collisional magmatism is a near-ubiquitous feature across dissected orogens (e.g., Lister and Baldwin 1993), however, the relationship between magmatism and core complex unroofing during crustal thinning is unclear. Does magmatism facilitate core complex exhumation, providing a mechanism for strain localisation, facilitating slip along faults and promoting thermal weakening of the crust (e.g., Parsons and Thompson 1993)? Or, do trans-crustal extensional structures provide a pathway for magmatism (e.g., Jones et al. 1992)? Post-collisional magmatism can occur pre-, syn- or post-core complex exhumation suggesting considerable feedbacks between processes (e.g., Lister and Baldwin 1993; Baldwin et al. 2004; Whitney et al. 2013).

The conductive transfer of heat from upwelling of asthenospheric mantle beneath extended crust, can generate small volume, partial melts of both lithospheric and asthenospheric mantle during post-collisional extension (McKenzie and Bickle, 1988). Bi-modal magmatism is common in post-collisional settings

where melting of subduction-modified lithospheric mantle is followed by break-through magmatism with an asthenospheric mantle source (e.g., von Blanckenburg and Davies 1995). The geochemical signatures of magmatism can therefore be vital to interpreting the geodynamic evolution of a region. For example, in western Anatolia, a temporal evolution of magmatism from Eocene – Oligocene calc-alkaline magmatism with a metasomatised, lithospheric mantle affinity, to Miocene – Quaternary tholeiitic magmatism with an asthenospheric mantle source, is attributed to the change in the driving force for crustal extension from slab roll-back to slab break-off and mantle delamination (e.g., Dilek and Altunkaynak 2009; Ersoy et al. 2017).

1.3.3 Porphyry Copper Deposit Formation in Post-Collisonal Settings

PCD formation in post-collisional settings is co-genetic with asthenospheric mantle upwelling-induced, subduction-related magmatism (Fig. 1.4; e.g., Luhr 1997; Paquette et al. 2003). Post-collisional magmatism is typically short-lived, especially compared to Andean-type arcs, due to the transient nature of the heat source for melting, thus post-collisional magmas are typically small in volume resulting from low degrees of partial melting.

However, post-collisional magmatism can still inherit the high fO_2 and H_2O contents critical to metal transport (e.g., Richards 2009). Magmatism associated with mineralised deposits is typically moderately more alkaline in post-collisional systems and subtle variations in their trace element geochemistry suggest differences in magma petrogenesis (e.g., Richards 2009). Furthermore, post-collisional PCDs tend to be Au- and platinum element group (PGE)- rich and Mo-poor e.g., the Grasberg deposit in Indonesia (e.g., Macdonald and Arnold 1994; Richards 2013) and the Skouries deposit in Greece (e.g., Siron et al. 2016, 2018). Richards (2009) suggests that the more siderophile nature of Au over Cu results in Au enrichment of the subduction-modified lithosphere that is remobilised during post-collisional melting, whilst there is also greater potential for crustal contamination in extensional settings.

Trans-crustal structures developed during post-collisional extension have been suggested as pathways allowing rapid ascent of subduction-related fertile magmas into the upper crust, drawing upon the close spatial association of PCDs with fault systems (e.g., Richards et al. 1990; Marchev et al. 2005). However, the influence of rapid exhumation of the host terrane, e.g., a metamorphic core complex, in thinning lithosphere has not been well documented. Exhumation results in the advection of heat towards the surface, compressing crustal isotherms and generating steep geothermal gradients in the upper crust (e.g., Mancktelow and

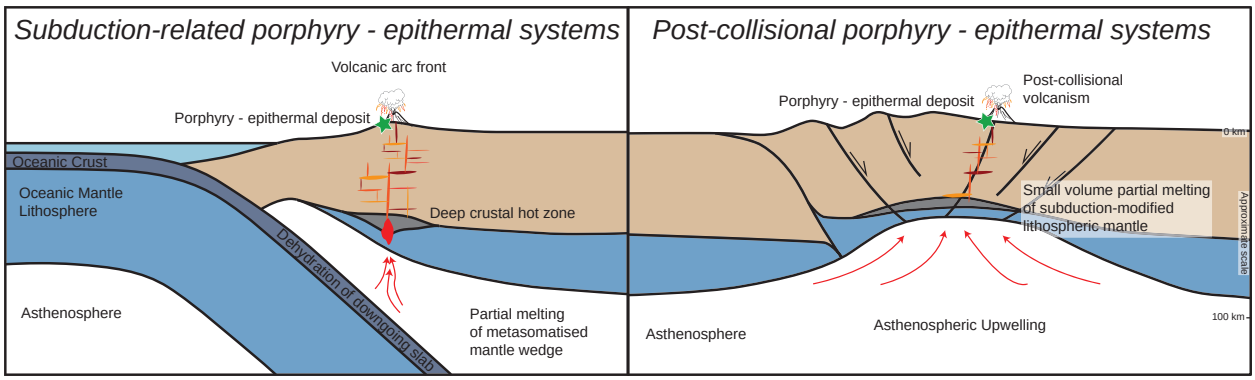

Figure 1.4: Magma petrogenesis leading to PCD formation in subduction-related (*left*) and post-collisional (*right*) tectonic settings; adapted from Richards (2009).

Grasemann 1997). Relatively quick exhumation of PCDs in volcanic-arcs has been suggested as one of the mechanisms by which to generate extreme telescoping of mineral deposits, where steep geothermal gradients out of the magmatic-hydrothermal system result in the development of a small but highly concentrated zone of mineralisation (e.g., McInnes et al. 2005a,b). This idea has yet to be explored in application to PCDs in extensional terranes.

1.3.4 Cenozoic Extension in the Aegean

In southeastern Europe, the Aegean is a well-studied example of a dissected orogen, where back-arc extension resulting from roll-back of the African slab has extended and thinned the crust. Metamorphic core complexes e.g., the Rhodope Massif and the Central Cyclades Core Complex, have been identified in the Cenozoic geological record across the Aegean (Fig. 1.5 e.g., Burg 2011; Brun et al. 2016). Preserved eclogites and blueschists lenses within the core complexes chronicle burial and buoyant exhumation of rocks along the subducting margin, whilst the metamorphic core complexes themselves record back-arc extension (e.g., Brun and Sokoutis 2010; Kydonakis et al. 2014). In the northern Aegean, the Rhodope Massif forms the hinterland to ongoing subduction along the Hellenic trench and can be split into two separate core complexes: *(i)* the northern Rhodope core complex (RCC) and *(ii)* the southern RCC (e.g., Burg 2011; Kydonakis et al. 2015a).

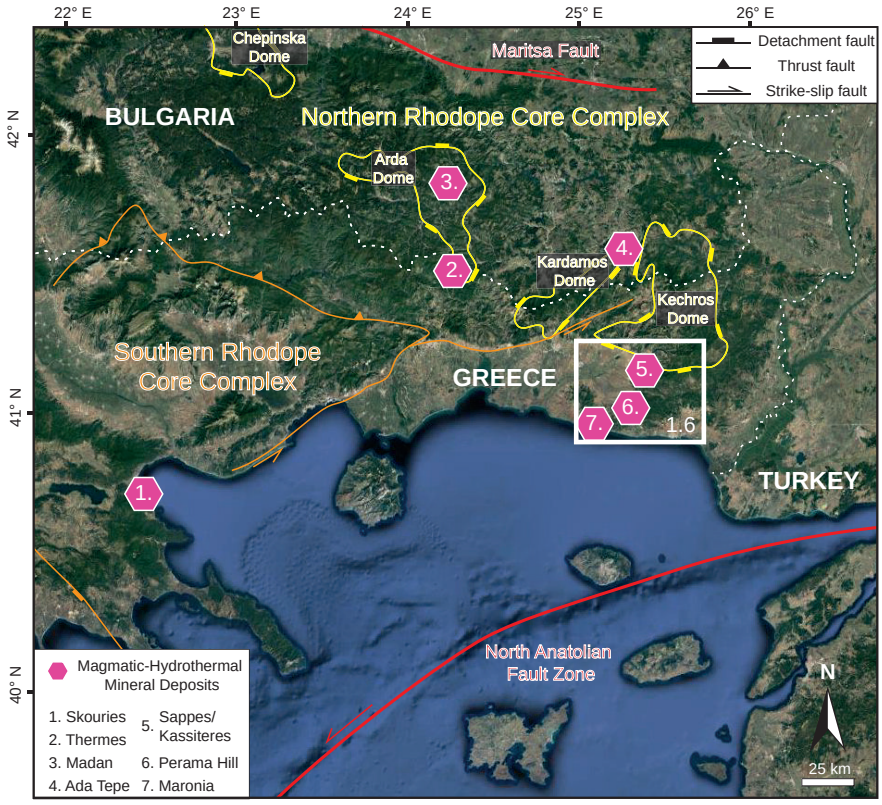

Figure 1.5: A Google Earth map of the northern and southern Rhodope core complexes, in yellow and orange respectively. The gneiss domes of the northern Rhodope Core Complex trend E-W along the Greek/Bulgarian border and are noticeable in the Google Earth image as areas of elevated relief and dense vegetation. The white box outlines the Maronia Magmatic Corridor and the area shown in Figure 1.6. Six magmatic-hydrothermal ore systems are known from the Rhodope core complexes including the Skouries Au-Cu-PGE porphyry system.

Exhumation of the core complexes began in the Eocene as back-arc extension, driven by slab roll-back, thinned the crust (e.g., Jolivet and Brun 2010; Ring et al. 2010; Brun et al. 2016). Brun et al. (2016) suggest a two-phase model of Cenozoic exhumation in the Aegean with localised extension in the Eocene – Oligocene restricted to the northern Aegean and later extension distributed across the Aegean from the Miocene onwards. They attribute the change in extension style to rapid trench retreat driven by accelerated convergence between the African and Eurasian plates. This thesis focuses only on the early, localised extension of the northern RCC in the Eocene and Oligocene.

Post-collisional magmatism punctuates across the northern and southern RCC and is reviewed in Chapter 2. Magmatic-hydrothermal mineral deposits are found across the Rhodope core complexes, associated with post-collisional, calc-alkaline to shoshonitic magmatism and volcanism; the deposit types range from porphyry – epithermal to carbonate-replacement and poly-metallic vein-hosted mineralisation (e.g., Marchev et al. 2013; Melfos and Voudouris 2017). The most notable porphyry – epithermal system in the region is the Skouries deposit with combined proven and probable reserves of 3.8 Moz Au (at 0.8 g/t) and 776 Mt (at 0.5 wt.%) and further PGE enrichment (e.g., Economou-Eliopoulos and Eliopoulos 2000; McFall 2016; Siron et al. 2016, 2018).

1.4 The Maronia Magmatic Corridor

The Maronia Magmatic Corridor (MMC) intrudes the southeastern margin of the northern RCC (Del Moro et al., 1988). A series of four small ($\sim$ 30 km diameter) gneiss domes aligned E – W, the northern RCC straddles the border between Greece and Bulgaria (Fig. 1.5). In Greece, the MMC is an 50 km long belt of Oligocene, calc-alkaline to shoshonitic equigranular intrusions that are associated with the basal detachment fault of the easternmost dome of the northern RCC, the Kechros – Biala-Reka dome, referred to as the Kechros dome from here onwards (Del Moro et al., 1988).

This project has split the MMC into three main case study areas (Figure 1.6): ***Leptokaria***: the northern most intrusions of the MMC (in blue) which are hosted across the hanging wall, fault zone and footwall of the Kechros dome; ***Kassiteres***: the central intrusion of the MMC (in green) which is hosted in the hanging wall of the Kechros dome; ***Maronia***: the southern most intrusion (in pink), separated from Kassiteres by the Petrota basin.

1.4.1 Field Observations

Fieldwork was conducted in three summer field seasons over 11 weeks, in September 2014, June 2015 and September 2016. The focus of the field work was to collect a representative sample suite of magmatism and mineralisation from across the MMC. Due to difficult field conditions, namely inaccessibility and dense scrub covering steep terrain, the spatial extent of magmatism in the region has been poorly constrained with discrepancies between geological maps and no sample localities (latitude-longitude or GPS co-ordinates) published with any of the work. A sampling campaign over the field seasons aimed to document the location of each of the intrusions, although field localities were biased to exposed outcrops in streams and on forest tracks (Fig. 1.7A). A secondary aim of the field work in the 2015 and 2016 field seasons, was to re-map the Kassiteres area, to closely constrain the relationships between magmatism, mineralisation and contemporaneous volcanism as the complex field relationships did not appear to be well captured in existing mapping.

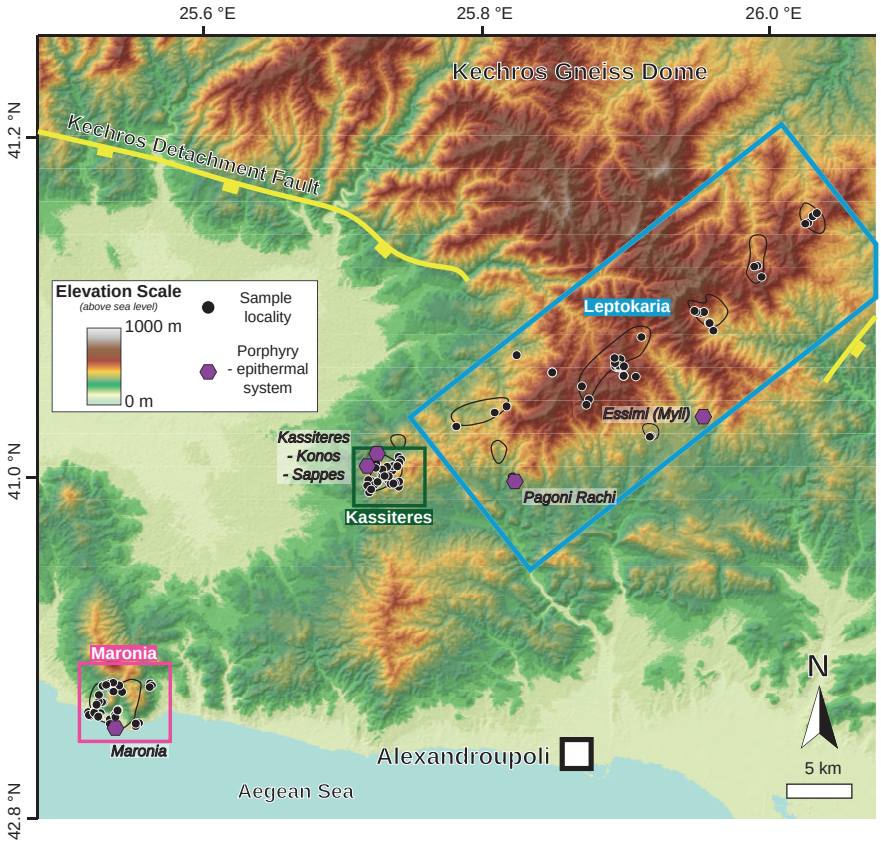

Figure 1.6: A map of the Maronia Magmatic Corridor showing the sample localities overlain on a digital elevation model (DEM). The three case study areas are outlined: *Maronia* in pink, *Kassiteres* in green and *Leptokaria* in blue; this colour scheme is maintained throughout the thesis. The Maronia Magmatic Corridor has a strong NE-trend and cuts the Kechros detachment fault with the Maronia and Kassiteres intrusions hosted in the hanging wall and some of the Leptokaria intrusions hosted in the footwall.

Figure 1.7: Field photographs from the Maronia Magmatic Corridor. **A**: View looking NW over the Leptokaria intrusion and the Kechros dome, dense vegetation and steep terrane make for difficult field conditions; **B**: Type (*ii*) quartz + pyrite + molybdenite vein from the Pagoni Rachi PCD; **C**: Breccia pipe from the Kassiteres porphyry – epithermal system with igneous clasts in a haematite matrix; **D**: Loose panels covering an ancient mine adit into the Maronia porphyry system.

A total of 188 samples were collected from the MMC, these samples cover the host intrusions, later porphyritic and aplitic cross-cutting dykes and stocks, vein associated with mineralisation, and the surrounding basement lithologies (Fig. 1.6; Table 1.2; full sample details are recorded in Appendix A). Extensive literature has documented mineralisation along the MMC (e.g., Melfos et al. 2002; Voudouris et al. 2006; Voudouris 2006; Voudouris et al. 2009, 2013a,b; Melfos and Voudouris 2017) and so the purpose of this thesis was to add petrological and tectonic context to the detailed studies of the porphyry and epithermal mineral deposits. Consequently, the thesis focuses on a subset of samples from the host plutons and cross-cutting porphyry intrusions, using an integrated approach of petrology, geochemistry, geochronology and structural geology to place the MMC in a regional petrological and tectonic framework.

1.4.2 Stratigraphy

Eocene – Oligocene unroofing of the northern RCC has exposed a wide cross-section of lithologies across the footwall and into the hanging wall of the individual gneiss domes. A simplified stratigraphy of the key units hosting the intrusion of the MMC is outlined below and shown graphically in Figure 1.8.

High-*T* amphibolite to granulite facies gneisses with lenses of *HP* to *UHP* eclogite make up the lowermost unit observed in the MMC, found in the footwall of the Kechros dome (e.g., Burg 2011). Along the Kechros detachment fault zone, anatectic leucogranites with a pegmatitic texture are commonly exposed, extending for up to 200 m. The Circum Rhodope Belt (CRB) tectonically overlies the gneisses in the Kechros dome, making up the hanging wall (e.g., Bonev and Stampfli 2003, 2011; Meinhold et al. 2010; Meinhold and Kostopoulos 2013). A basal ophiolite in the CRB is rarely preserved (Bonev et al., 2015) with the CRB predominantly consisting of Mesozoic, greenschist-facies metasedimentary units (e.g., Meinhold and Kostopoulos 2013).

Unconformably overlying the basement rocks of the Kechros gneiss dome and the CRB is an Eocene marine transgressive sequence of basal conglomerates transitioning to interbedded sandstones, carbonates and marls, deposited into the Thrace supra-detachment basin, formed in accommodation space created during exhumation of the Kechros dome (e.g., Kilias et al. 2013). In the Oligocene, the sediments of the Thrace basin became increasingly dominated by sub-aerial volcaniclastic units including pyroclastic deposits, small lava flows and block-and-ash flows (e.g., Christofides et al. 2004). Sedimentation has continued in the Thrace basin since the Miocene, dominanted by continental-derived sediments in normal-fault bound grabens (e.g., Kilias et al. 2013).

The intrusions of the MMC are hosted in the metamorphic basement (Kechros dome gneisses and CRB metasediments) and the overlying Eocene trangressive sedimentary series (Del Moro et al., 1988). Intrusive magmatism and sub-aerial volcanism along the MMC are contemporaneous, likely recording the same magmatic event (Christofides et al., 2004), with the Oligocene volcaniclastic units often onlapping onto the MMC plutons.

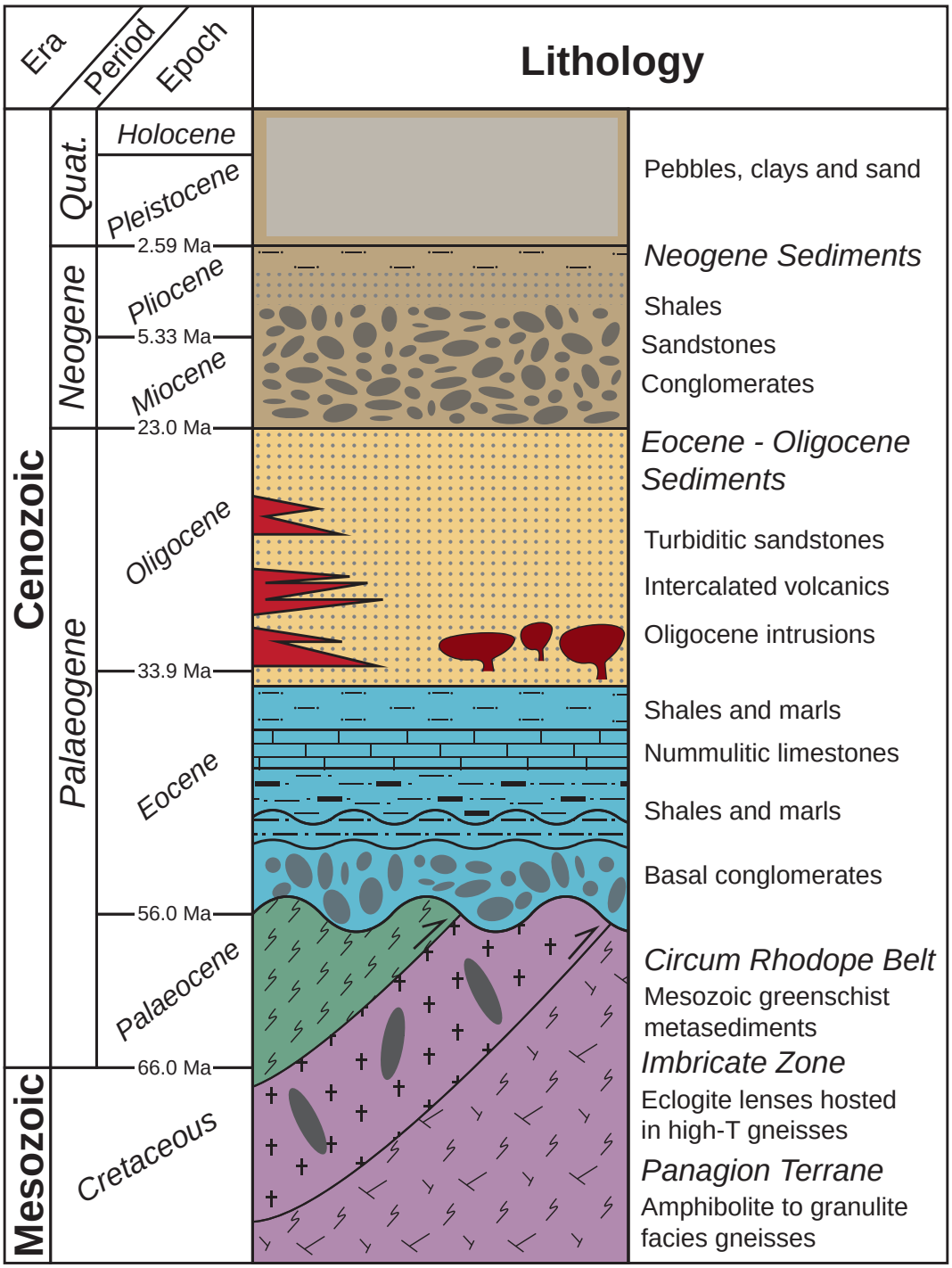

Figure 1.8: A simplified stratigraphy of the Maronia Magmatic Corridor adapted from Kilias et al. (2013) & Caracciolo et al. (2012).

Table 1.2: Abbreviated sample details as plotted on Figure 1.6, for full sample descriptions and GPS co-ordinates see Appendix A

Sample Type	Locality	*n*	Sample Numbers
			Intrusive Igneous Lithologies
Host intrusion	Maronia	28	RT14_003, RT14_005, RT14_006, MA15_001, MA15_002, MA15_004, MA15_006, MA15_007, MA15_008, MA15_010, MA15_011, MA15_012, MA15_013, MA15_014, MA15_015, MA15_016, MA15_017, MA15_019, MA15_020, MA15_021, MA15_022, MN16_005, MN16_007, MN16_008, MN16_012, MN16_014, MN16_015, MN16_018
	Kassiteres	18	RT14_027, RT14_028, KA15_002, KA15_004, KA15_008, KA15_009, KA15_013, KA15_016, KA15_017, KS16_002, KS16_004, KS16_005, KS16_006, KS16_010, KS16_011, KS16_020, FKA16_11, FKA16_13
	Leptokaria	27	RT14_009, RT14_010, RT14_014, RT14_015, RT14_017, RT14_018, RT14_019, RT14_020, RT14_022, RT14_023, RT14_024, RT14_025, LA15_011, LA15_020, LB15_003, LB15_004, LB15_006, LC15_002, LC15_003, LD15_002, LD15_003, PR15_008, LK16_001, LK16_003, LK16_004, LK16_011, LK16_012
Porphyritic dykes and stocks	Maronia	8	MA15_003, MN16_002, MN16_019, MN16_020, MN16_021, MN16_022, MN16_023, MN16_027
	Kassiteres	4	RT14_026, KA15_018, KA15_019, KO16_008
	Leptokaria	11	RT14_021, LA15_008, LA15_009, LK16_005, LK16_006, LK16_007, LK16_008, LK16_009, LK16_010, LK16_014, LK16_016
Aplitic dykes	Maronia	2	MN16_026, MN16_029
	Kassiteres	5	KA15_020, KS16_003, KS16_014, KS16_015, KS16_019
	Leptokaria	2	LK16_013, FLK16_15
			Mineralised Samples
Veins	Maronia	13	MA15_005, MN16_013, MN16_016, MN16_017, MN16_020, MN16_021, MN16_023, MN16_028, MN16_032, MN16_033, MN16_034, FMA16_45, FMA16_47
	Kassiteres	11	RT14_029, KN15_001, KN16_002, KN16_003, KS16_007, KS16_008, KS16_009, KS16_012, KO16_006, KS16_007, KO16_008
	Leptokaria	13	ES15_001, ES15_002, ES15_003, ES15_004, ES15_005, ES15_006, PR15_001, PR15_002, PR15_004, PR15_005, PR15_005, PR15_007, PR15_009
			Other Lithologies
Oligocene Volcaniclastics	Kassiteres & Leptokaria	11	RT14_008, RT14_012, RT14_013, KA15_001, KA15_003, KA15_005, KA15_006, KA15_010, PG16_001, PG16_002, PG16_003
Eocene Sediments	Kassiteres	1	KA15_011
Greenschist basement (CRB)	Maronia & Kassiteres	6	RT14_004, MA15_009, MN16_001, MN16_003, MN16_009, KS16_021
Gneiss (Kechros Dome)	Leptokaria	8	RT14_030, RT14_031, LA15_007, LA15_021, LA15_022, LB15_007, LC15_001, LD15_001
Miscellaneous samples		*20*	

Table 1.3: Mineral deposits of the Maronia Magmatic Corridor, after Melfos and Voudouris (2017). * indicates where the endowment is given as the highest metal concentrations reported in whole-rock assays, where reserves are unknown.

Host Intrusion	Porphyry System		Epithermal System		Reference(s)
	Name	Grade	Name	Grade	
Maronia	Maronia	0.5 wt.% Cu, 1 ppm Au, 0.8 wt.% Mo *	–	–	Melfos et al. (2002)
–	–	–	Perama Hill	3.13 ppm Au, 4 ppm Ag	Melfos and Voudouris (2017)
Kassiteres	Korfyes Hill	unknown	Sapana, Sta. Barbara, St. Nicolaus	unknown	Voudouris et al. (2006)
Kassiteres	Konos	unknown	Sappes	19.5 ppm Au, 9 ppm Ag, 0.4 wt.% Cu	Melfos and Voudouris (2017)
–	Pagoni Rachi	0.5 wt.% Cu, 5.1 ppm Au, 0.2 wt.% Mo *	St. Phillipos	Base metals and PGEs	Voudouris et al. (2013b)
–	Essimi (Myli)	unknown	–	–	Voudouris et al. (2013a)

1.4.3 Mineral Prospectivity

Multiple porphyry – epithermal systems have been documented from along the MMC with epithermal veining commonly overprinting deeper porphyry-style features (e.g., Melfos and Voudouris 2017). The Pagoni Rachi, Essimi (or Myli) porphyry – epithermal systems and the Perama Hill carbonate-replacement deposits lie off the main NE-trending lineament and are not associated with an equigranular intrusion of the MMC. Table 1.3 outlines the known mineral occurrences from MMC after Melfos and Voudouris (2017) and outlines the suggested links between known porphyry and epithermal systems.

Chapter 2

Post-collisional Cenozoic extension in the northern Aegean: The high-K to shoshonitic intrusive rocks of the Maronia Magmatic Corridor, northeastern Greece

Perkins, R.J., F.J. Cooper, D.J. Condon, B. Tattitch and J. Naden (2018), Post-collisional Cenozoic extension in the northern Aegean: The high-K to shoshonitic intrusive rocks of the Maronia Magmatic Corridor, northeastern Greece, *Lithosphere*, DOI:10.1130/L730.1.

Author contributions and declaration:

This chapter is currently in press having been accepted for publication in Lithosphere. The content of the chapter is identical to the manuscript, however, it has been formatted inline with the rest of the thesis to aid with consistent presentation. Field work was conducted by R. Perkins under the guidance of J. Naden and F. Cooper. The petrology and geochemical modelling presented in this chapter was conducted by R. Perkins and benefited from discussion with B. Tattitch and R. Loucks (Visiting Benjamin Meaker Professor). D. Condon conducted the ID-TIMS U-Pb zircon analyses on samples prepared by R. Perkins and processed the data at the NERC Isotope Geosciences Laboratory (NIGL); the interpretation of the U-Pb data was made by R. Perkins with advice from D. Condon. Whole-rock geochemistry sample preparation was done by R. Perkins and analyses were run by C. Gowring at the Inorganic Geochemical Facility at the British Geological Survey. The manuscript was written by R. Perkins with the supervision and guidance of all co-authors and has benefited from reviews by two anonymous reviewers and A. Kounov.

ABSTRACT

The Maronia Magmatic Corridor is a NE-trending belt of Oligocene plutons that intrudes the Kechros Dome of the northern Rhodope Core Complex in northeastern Greece. The post-collisional magmatism transitions from early high-K calc-alkaline magmatism in the NE to a younger, shoshonitic phase in the SW. We use a full suite of whole-rock geochemical analyses, including rare earth elements, to show a shared metasomatized mantle source of the magmatism. Evidence of plagioclase saturation from the onset of crystallisation and amphibole-pyroxene-controlled fractionation in the high-K calc-alkaline magmatism suggest a drier ($<$ 4.75 wt.% H_2O) parental magma than is typical of subduction-related magmatism. Continued H_2O depletion of the metasomatized source mantle resulted in the transition to a shoshonitic trend where deep crustal fractionation of an H_2O-poor ($<\sim$ 2 wt.% H_2O) magma in the absence of major olivine resulted in incompatible enrichment over a small range of SiO_2. High-precision U-Pb zircon geochronology is presented here for the first time to provide chronological markers for the transition in the magmatic evolution of the Kechros dome. A 2.2 Myr break in magmatism separates the intrusion of the shoshonitic Maronia pluton at 29.8 Ma from the emplacement of the rest of the high-K calc-alkaline Maronia Magmatic Corridor between 32.9 –32.0 Ma. The Maronia pluton is the hottest, driest, and youngest episode of post-collisional magmatism in the Kechros dome; we suggest that the emplacement of Maronia marks the cessation of magmatism in the northern Rhodope Core Complex as asthenospheric mantle upwelling migrated southward.

2.1 Introduction

Mountain-building events can generate thousands of kilometers of high elevation over periods of tens to hundreds of millions of years; the development of such high relief during orogenesis is supported by the development of a thick continental root (e.g., Dewey et al. 1993). In some orogens this crustal thickness is preserved long after collision, while in others post-collisional collapse of the orogen thins the crust and results in widespread extensional structures that dissect the region (e.g., Pichon and Angelier 1979; Dewey 1988; Wang et al. 2014). In extended orogens, strain localisation can drive the formation of trans-crustal normal detachment faults that transfer material from the ductile, lower crust to the surface and can aid the exhumation of metamorphic core complexes from $>$ 45 km depth (e.g., the North American Cordillera: Coney 1987; Wernicke et al. 1987; Camp et al. 2015; and the Aegean: Lister et al. 1984; Jolivet and Brun 2010; Burg 2011; Kydonakis et al. 2015b). Another feature of highly extended orogenic terranes is the ubiquitous presence of post-collisional magmatism. The conductive transfer of heat from upwelling hot, asthenospheric mantle beneath highly extended crust can generate small volume, partial melts which exploit crustal pathways developed during extensional deformation, leading to intrusive and extrusive post-collisional magmatism (e.g., McKenzie and Bickle 1988; von Blanckenburg and Davies 1995). Feedbacks between metamorphic core complex exhumation and magmatism are numerous, and include magmatic volatiles facilitating crustal deformation and crustal thinning, and resultant decompression and mantle upwelling, driving lithospheric melting (Teyssier and Whitney, 2002; Whitney et al., 2013; Platt et al., 2015). As a result, both metamorphic core complexes and post-collisional magmatic suites can be used to offer insights into the tectonic processes controlling crustal extension; here we focus on the petrogenesis of post-collisional magmatism.

In collisional orogenic belts, subduction-related calc-alkaline magmatism shows a trend of increasing K with maturity of the magmatic system (e.g., Lipman et al. 1972). The transition from high-K calc-alkaline to shoshonitic magmatism is common in post-collisional tectonic settings where the inherited metasomatized mantle wedge is depleted at the onset of magmatism (e.g., Aldanmaz et al. 2000; Seghedi et al. 2004). This high-K calc-alkaline to shoshonitic evolution in magma geochemistry is observed throughout the Aegean – for example, in the Eocene to middle-Miocene Biga orogenic rocks in NW Turkey and the Oligocene and Miocene magmatic rocks of NE and central Greece (e.g., Maronia, Samothraki, Lesbos and Limnos; Del Moro et al. 1988; Pe-Piper et al. 2009; Ersoy et al. 2017).

The generation of potassic melts is ascribed to be the result of anomalously hot mantle melting (Gill, 1981). Source mantle geochemistry is also widely considered to be key in the generation of potassic to ultra-potassic fractionation trends in subduction-related settings (e.g., Foley et al. 1987). However, the origin of a K-rich source mantle is debated; current hypotheses include, but are not limited to, *(i)* intense mantle metasomatism by K-rich fluids from the dehydrated, downgoing slab (e.g., Poli and Schmidt 2002; Condamine and Médard 2014); and *(ii)* contamination and physical mixing of mantle melts and lower crustal- or subducted sedimentary- melts (e.g., Beccaluva et al. 2013; Wang et al. 2017). In addition to source mantle geochemistry, conditions of magma generation and fractionation are also considered to be important in the production of potassic to ultra-potassic magmas (e.g., Peccerillo et al. 2013). Experimental and geochemical studies have shown that magmas generated at high pressures and temperatures, in the absence of abundant H_2O, can produce shoshonitic liquid lines of descent (LLDs) by stabilizing pyroxene and anorthite-rich plagioclase over olivine in the fractionating assemblage, and that the same magmas generated

under shallower or more fluid-rich conditions would fractionate a high-K calc-alkaline trend (Meen, 1987; Freise et al., 2009; Lanzo et al., 2016; Beermann et al., 2017). While all of these models require an elevated mantle geotherm to generate high-temperature mantle melts, the mechanism by which a shoshonitic fractionation trend is achieved has important implications for the conditions of magma petrogenesis.

The Hellenic Orogen (or Hellenides) is a 500-km-long mountain belt that stretches across the Aegean and is bound by the Balkanides in the north and the Hellenic trench, the point of present subduction of the African plate beneath Eurasia, in the south (Smith and Moores, 1974; Mountrakis, 2006). Resulting from closure of the Tethys Ocean and subsequent collision of the African and Eurasian plates, the Hellenic orogen is a well-studied example of post-collisional extension. Predominantly attributed to retreat of the Hellenic trench and roll-back of the African Slab, Hellenic extension is also thought to incorporate elements of lithospheric delamination and slab break-off beneath Anatolia to the east of the Aegean (Jolivet and Brun 2010; Ring et al. 2010; Burg 2011; Brun et al. 2016, and references therein). Terrane accretion and subduction of intermediate oceanic crust (the Vardar-Izmir and Pindos basins) during the Hellenic Orogen began in the late Cretaceous and continued into the Cenozoic (e.g., van Hinsbergen et al. 2005; Schmid et al. 2008). Post-collisional orogenic collapse of the Hellenides began in the late Mesozoic to Cenozoic, contemporaneous with continued north-dipping subduction further toward the south, and has been irregular both spatially and temporally ever since (e.g., Jolivet and Brun 2010; Ring et al. 2010).

A two-stage model for Aegean extension was developed to accommodate localised Palaeogene extension

Table 2.1: A compilation of literature geochronology of relevant geological events in the Kechros Dome and surrounding terranes of the northern Rhodope Core Complex, compiled from Bonev et al. (2015). TIMS – thermal ionisation mass spectrometry; LA-ICP-MS – laser ablation inductively coupled mass spectrometry; SHRIMP – secondary high-resolution ion microprobe; WR-GRT-CPX – whole-rock-garnet-clinopyroxene. CRB – Circum Rhodope Belt; IZ – imbricate zone.

Geological Event	Location	Age (Ma)	Method	Reference
CRB ophiolite gabbro crystallisation	Evros Ophiolite	176.4 ± 0.93	U-Pb zircon (LA-ICP-MS)	Bonev et al. (2015)
CRB protolith formation	Maronia-Makri Block	320–280 240	U-Pb SHRIMP	Meinhold et al. (2010)
IZ crustal melting	Kimi Complex	61.9 ± 1.9	U-Pb SHRIMP	Liati et al. (2002)
IZ metamorphic events	Kimi Complex	79 ± 3 73.5 ± 3.4 119 ± 3.5 115 160–170	U-Pb SHRIMP Sm-Nd WR-GRT-CPX U-Pb zircon SHRIMP	Bauer et al. (2007) Liati et al. (2002) Wawrzenitz and Mposkos (1997) Bauer et al. (2007)
IZ protolith formation	Kimi Complex	117.4 ± 1.9 150–160 288 ± 6	U-Pb SHRIMP U-Pb zircon (LA-ICP-MS)	Liati et al. (2002) Cornelius (2008)
	Soufli Complex	154 ± 1.5 160 ± 0.69	U-Pb zircon (LA-ICP-MS)	Bonev et al. (2015)
Panagion protolith formation	Kechros Dome	250–330 410–480 ~ 455 528–534	U-Pb zircon (LA-ICP-MS) U-Pb zircon (LA-ICP-MS)	Cornelius (2008) Bonev et al. (2013)

in NE Greece and distributed Neogene extension across the rest of the region (Jolivet and Brun 2010; Brun et al. 2016, and references therein). This paper focuses on localised tectonic extension in NE Greece where an early phase of trans-crustal extension accommodated exhumation of the northern Rhodope core complex (RCC) from mid- to lower- crustal levels (e.g., Burg 2011; Kydonakis et al. 2014). Later Neogene extension in the northern RCC was restricted to the upper crust and the formation of normal fault-bound sedimentary basins (e.g., Burchfiel et al. 2003; Kilias et al. 2013). The Maronia Magmatic Corridor (MMC), an 150-km-long NE-trending belt of post-collisional Oligocene calc-alkaline to shoshonitic plutons, intrudes the Kechros dome at the eastern margin of the northern RCC (Del Moro et al., 1988). In this paper, we present detailed field and petrographic observations and new whole-rock geochemistry, including a full suite of rare earth elements (REEs), of the MMC to better constrain the petrogenesis of the potassic post-collisional magmatism. We use field observations coupled with chemical abrasion-isotope dilution-thermal ionization mass spectrometry (CA-ID-TIMS) U-Pb zircon geochronology and whole-rock geochemistry of the plutons to constrain crystallisation to within tens of thousands of years, to investigate the temporal evolution of the MMC, and to discuss how geochemical changes in magma petrogenesis relate to the timing of Cenozoic post-collisional orogenic collapse in the northern RCC.

2.2 Geological Setting

The Rhodope Massif is located in the northern Aegean, straddling the border between northern Greece and southern Bulgaria (Fig. 2.1). The rocks of the Rhodope Massif have a long and complex tectonic history associated with terrane accretion during the Hellenic orogeny and subsequent core complex formation and exhumation (e.g., Ricou et al. 1998). A series of stacked nappes, the Rhodope Massif can be split into two tectonic domains, the northern RCC and the southern RCC, separated by the Nestos thrust (Fig. 2.1 A). The northern and southern RCC have a shared history during terrane accretion in the Mesozoic, but the evolution of the tectonic units diverged during Cenozoic exhumation (e.g., Kydonakis et al. 2014).

2.2.1 Convergent Orogenesis and Metamorphism

The Rhodope Massif has a broadly anticlinal structure and can be subdivided into three lithological units: *(i)* the lower Pangaion (or Thracia or Drama) terrane of ortho- and para-gneisses, exposed in the core of the fault-bound anticlinal domes (Krohe and Mposkos, 2002; Turpaud and Reischmann, 2010; Burg, 2011; Bonev et al., 2013); *(ii)* the overlying, upper Rhodope unit, a metaophiolite-gneiss-schist assemblage in the hanging wall of the Rhodope anticline (Krohe and Mposkos, 2002; Burg, 2011); and *(iii)* the highly deformed imbricate unit sandwiched along the Nestos suture zone between the upper and lower terranes (Bauer et al., 2007; Krenn et al., 2010). In the southern RCC the upper terrane is preserved in the hanging wall of the Kerdyllion fault (Fig. 2.1 A). In the northern RCC lower terrane gneiss domes dominate; in the east, the greenschist facies Mesozoic schist units of the Circum Rhodope Belt (CRB) are considered to be equivalents of the upper Rhodope terrane hanging wall (Bonev and Stampfli, 2008; Krenn et al., 2010; Meinhold et al., 2010; Bonev and Stampfli, 2011; Meinhold and Kostopoulos, 2013).

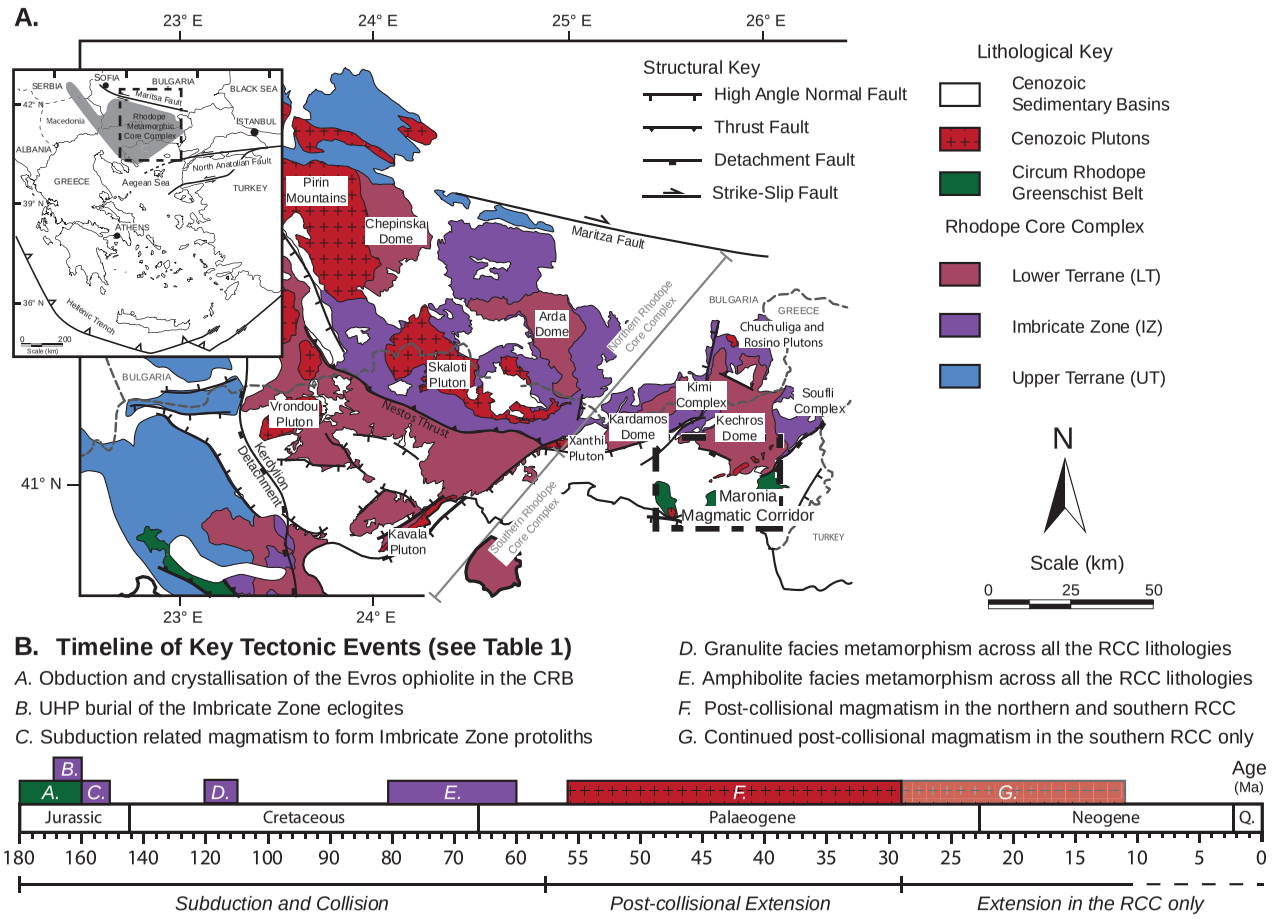

Figure 2.1: Geological map and geochronological timeline of the Rhodope Massif (inset grey-coloured area from Bonev et al. 2013); geological map modified from Burg (2011) & Kydonakis et al. (2014), and timeline complied from Burg (2011). The northern Rhodope Core Complex (RCC) is separated from the southern RCC by the Nestos Thrust, as marked by the gray line. Within the northern RCC, domes of lower plate gneiss were exhumed along multiple detachment and thrust faults, which are poorly mapped and not marked on the map. The exception is the Kechros Detachment, local to the Maronia Magmatic Corridor (the study area), and is marked where field and ASTER data suggest the presence of a significant trans-crustal structure. Four gneiss domes make up the northern RCC; from west to east they are the Chepinska, Arda, Kardamos – Kesebir and Kechros – Biala-Rika domes. The timeline summarizes the key tectonic events that affected the RCC from subduction through to continent collision and exhumation (using literature geochronology compiled in Table 2.1).

Considerable geochronological effort, in tandem with detailed microstructural and tectonic contextual study, has been put into unravelling the tectono-metamorphic evolution of the Rhodope Massif (synthesised in Fig. 2.1B; Table 2.1). Variscan-age rift-related igneous protoliths in the lower, Pangaion, and upper, Rhodope, terranes indicate a shared, European basement affinity of the tectonic units that make up the Rhodope Massif (Turpaud and Reischmann 2010; Burg 2011, and references therein). Jurassic – Cretaceous igneous protoliths in the imbricate unit record subduction-related magmatism on the Rhodopean margin, as the rift-basin that separated the Rhodope and Pangaion terranes in the early Mesozoic was closed (e.g., Schmid et al. 2008; Turpaud and Reischmann 2010; Burg 2011). This period of subduction is also recorded by diamond- and coesite-bearing ultra-high pressure (UHP) metamorphism, as lenses of the imbricate unit were buried along the Nestos suture zone between 180–160 Ma (Mposkos and Kostopoulos, 2001; Bauer et al., 2007; Krenn et al., 2010); this was co-incident with obduction of the Evros ophiolite onto the Rhodope terrane (Bonev et al., 2015). Greenschist facies metamorphism of the CRB was contemporaneous with the accretion of the Pangaion terrane and ophiolite obduction (Bonev et al., 2013, 2015). In the late Cretaceous, following the underthrusting of the Pangaion terrane beneath the Rhodope terrane, subduction of the Vardar-Izmir Ocean initiated to the south of the Rhodope Massif (e.g., van Hinsbergen et al. 2005; Schmid et al. 2008). Aegean extension initiated in the Rhodope Massif in the Cenozoic, during a transitional tectonic period from subduction-related convergence to subduction-related slab rollback and trans-crustal extension (Burchfiel et al., 2008).

2.2.2 Trans-Crustal Extension and Core Complex Exhumation

The Rhodope Massif was exhumed during late Cretaceous – Cenozoic trans-crustal extension driven by Aegean slab rollback (e.g., Jolivet and Brun 2010; Ring et al. 2010). Palaeocene – Oligocene localised extension formed a series of gneiss domes across the northern RCC and initiated exhumation along the Kerdyllion Detachment in the southern RCC (e.g., van Hinsbergen et al. 2008; Kydonakis et al. 2014, 2015b). Dehydration partial melting during core complex unroofing and exhumation is recorded in temporally sporadic Palaeocene – Eocene pegmatites and leucogranites across both the northern RCC and southern RCC (e.g., Del Moro et al. 1990; Mposkos and Wawrzenitz 1995; Wawrzenitz and Krohe 1998; Lips et al. 2000; Liati et al. 2002). Maastrichtian – Palaeocene to early Eocene sediments unconformably overlie the gneiss domes of the northern RCC indicating that these domes must have been exhumed, at least in part, before the early Eocene (Boyanov et al., 1982; Burg, 2011).

Exhumation in the northern RCC ceased abruptly in the Oligocene, likely with the onset of post-collisional volcanism across the northern RCC (e.g., Rohrmeier et al. 2013), and resulted in an E-trending belt of small ($\sim$ 30 km diameter), unconnected gneiss domes (Kydonakis et al., 2015a). This was contemporaneous with a change in extension style across the Aegean. Early Eocene – Oligocene extension was localised in the northern Aegean, restricted to the northern limit of the hinterland, the northern and southern RCC (Kydonakis et al., 2015b). From the mid-Miocene onward, extension was distributed across the Aegean with the formation of the Central Cyclades core complex further south and continued exhumation and SW-rotation of the southern RCC (van Hinsbergen et al., 2008; Kydonakis et al., 2014, 2015b). The change in extension style is attributed to an acceleration in trench retreat related to the increased rate of convergence between Africa and Eurasia and slab tearing beneath western Turkey in the mid-Miocene (e.g., Jolivet and Brun 2010; Jolivet et al. 2013; Brun et al. 2016).

Table 2.2: Compilation of existing geochronology data from the post-collisional intrusions of the Rhodope Massif from Burg (2011) supplemented by more recent geochronology. TIMS – thermal ionisation mass spectrometry; LA-ICP-MS – laser ablation-inductively coupled-mass spectrometry.

Intrusion	Emplacement Age (Ma)	Uncertainty (2σ)	Method	Reference
		Northern Rhodope Core Complex		
Rila	66.8 69.3	± 0.3 ± 0.3	U-Pb zircon (TIMS)	von Quadt and Peytcheva (2005)
Central Pirin/Spanchevo	37 56	± 2 ± 0.5	Rb-Sr whole-rock U-Pb zircon LA-ICP-MS	Zagorchev et al. (1987) Jahn-Awe et al. (2010)
Smiliyan	41.92 43.4	± 0.22 ± 1.41	U-Pb zircon (TIMS) U-Pb zircon	Rohrmeier et al. (2013) Ovtcharova et al. (2004)
Teshovo	32	± 0.02	U-Pb zircon (LA-ICP-MS)	Jahn-Awe et al. (2010)
Skaloti	42-44 49.99 55.93	 ± 0.88 ± 0.28	$^{40}Ar/^{39}Ar$ feldspar $^{40}Ar/^{39}Ar$ biotite U-Pb zircon (TIMS)	Soldatos et al. (2008)
Topolovo	52.54	± 0.19	U-Pb zircon (LA-ICP-MS)	Marchev et al. (2013)
Chuchuliga	68.94	± 0.40	U-Pb zircon (TIMS)	Marchev et al. (2006)
Rosino	68	± 1.5		
MMC	28.4 34.9	± 0.9 ± 1.5	Rb-Sr biotite	Del Moro et al. (1988)
Yugovo	42.29 42.3	± 0.08 ± 0.54	U-Pb zircon (TIMS)	Rohrmeier et al. (2013) Ovtcharova et al. (2004)
Drangovo	49.9	± 0.21	U-Pb zircon (LA-ICP-MS)	Marchev et al. (2013)
Dolno Dryanovo	55	± 0.5	U-Pb zircon (LA-ICP-MS)	Jahn-Awe et al. (2010)
		Southern Rhodope Core Complex		
Xanthi	27.1 27.9 30	± 0.4 ± 0.5 ± 1	K-Ar biotite K-Ar hornblende	Meyer (1968) Liati and Kreuzer (1990)
Vrondou	30	± 3	K-Ar biotite	Dürr et al. (1978)
Kavala	15.5 17.8 21.2	± 0.5 ± 0.8 ± 0.8	K-Ar biotite U-Pb titanite	Kokkinakis (1980) Dinter et al. (1995)
Ouranopolis	47	± 0.7	Ar-Ar muscovite	De Wet et al. (1989)
Stratoni	19.7 26.9 27.9 19.2 25.4	± 0.6 ± 2.0 ± 1.2 ± 0.2 ± 0.2	K-Ar biotite U-Pb (TIMS) U-Pb (LA-ICP-MS) 	Gilg and Frei (1994) Siron et al. (2016)
Skouries	20.6	± 0.5	U-Pb (LA-ICP-MS)	Siron et al. (2016)
Mesoropi	13.8 21.7	± 0.5 ± 0.5	$^{40}Ar/^{39}Ar$ biotite $^{40}Ar/^{39}Ar$ muscovite	Eleftheriadis et al. (2001)
Ierissos	53.6	± 6.2	U-Pb uranothorite (TIMS)	Frei (1996)
Strymon Valley	11.32 12.235	± 0.099 ± 0.026	U-Pb zircon (TIMS) U-Pb zircon (LA-ICP-MS)	Georgiev et al. (2013)
Samothraki	18 18.5	± 0.2 ± 0.2	Rb-Sr biotite	Christofides et al. (2000)

Post-subduction magmatism was contemporaneous with trans-crustal extension, punctuating across the Rhodope Massif from the middle Eocene (42 Ma, Smiliyan and Yugovo Plutons; Table 2.2; Rohrmeier et al. 2013) to the mid-Miocene (11.32 Ma, Strymon Valley volcanics; Table 2.2; Georgiev et al. 2013). Post-subduction magmatism is closely linked to extension, with trans-crustal structures providing pathways for magmas, evidenced by the spatial association of plutonic rocks and detachment fault systems (e.g., Jones

et al. 1992; Pe-Piper and Piper 2006; Fig. 2.1). This is noticeable in the distinction between the northern RCC and southern RCC, where magmatism, and concurrent volcanism, ceases in the late Oligocene in the northern RCC (e.g., Márton et al. 2010; Marchev et al. 2010) but continue into the Miocene in the southern RCC (Table 2.2; Georgiev et al. 2013).

Unconformably overlying the northern RCC metamorphic basement, syn-extensional sedimentation started in the mid-late Eocene as a transgressive sequence of conglomerates, limestones, sandstones, and marls filled the Thrace supra-detachment basin, formed in accommodation space to the SE of the exhuming northern RCC (Kilias et al., 2013). The switch from trans-crustal, ductile extension to upper-crustal, brittle extension in the northern RCC is recorded by the change in depositional environment from a supra-detachment basin in the Eocene–Oliogene, to a series of cross-cutting N- to NNE- trending fault-bound basins in the Oligocene-Miocene (Burchfiel et al., 2003, 2008; Kilias et al., 2013).

2.2.3 The Maronia Magmatic Corridor

The MMC is a NE-trending magmatic belt, comprising at least six Oligocene gabbroic to granodioritic intrusions (Fig. 2.2): the Tris Visses, Halasmata, Leptokaria, Kirki, Kassiteres, and Maronia plutons. The MMC is hosted in the easternmost dome of the northern RCC, the Kechros – Biala-Rika dome (from here on in referred to as the Kechros Dome). First described by Del Moro et al. (1988), the MMC plutons all intrude the northern RCC and associated lithologies, hosted either within the Kechros gneiss dome to the NE (Halasmata and Tris Visses), straddling the Kechros basal detachment in the center of the corridor (Leptokaria), or within the CRB greenschist basement to the SW (Kirki, Kassiteres, and Maronia; Fig. 2.2). Later Oligocene intercalated sedimentary and volcanic units onlap onto the MMC intrusions. Both the Kassiteres and Maronia plutons are cross-cut by younger porphyritic microgranite intrusions and host occurrences of porphyry – epithermal Au-Mo-Cu mineralisation (e.g., Melfos et al. 2002; Voudouris et al. 2006). Rb-Sr biotite–whole-rock isochron dating by Del Moro et al. (1988) suggests that the MMC plutons were emplaced between $\sim$ 32 and 28 Ma, younging progressively from NE to SW along the belt.

2.3 Methods

2.3.1 Field Geology and Petrology

Field observations, with particular focus on relationships between lithologies, were made over multiple summer field seasons in northeastern Greece. We have prepared our geological map, Figure 2.1, from existing geological maps of the area supplemented by our own field observations. The spatial extent of the plutons, in particular Kirki, Leptokaria, Halasmata, and Tris Visses, are poorly constrained due to difficult field conditions. The lack of exposure, steep topography, dense vegetation, and poor road access bias the outcrop localities of both this work and previous geological mapping by Del Moro et al. (1988), with most mapped outcrops found along small river channels. However, based on our field observations, we consider it more likely that the observed plutons represent small outcrops of a larger magmatic system interconnected at depth that is poorly exposed, and that additional outcrops could be found in more inaccessible areas.

A suite of 36 samples was collected from the MMC, representing each of the observed intrusive lithologies and alteration styles. At least eight samples were taken from each of the Maronia and Kassiteres plutons, and from across the Kirki–Leptokaria–Halasmata–Tris Visses outcrops to reflect changes in mineralogy between

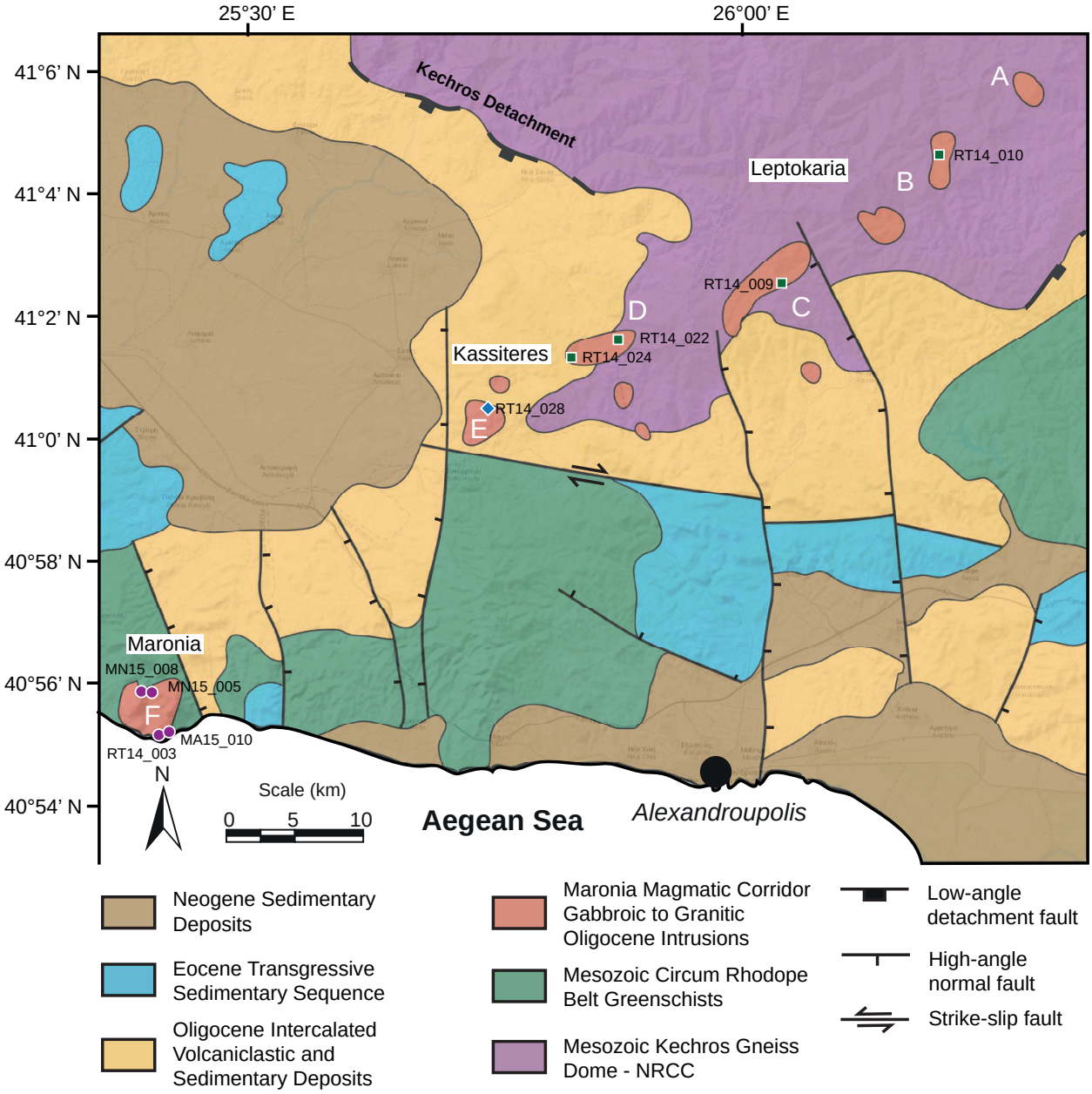

Figure 2.2: A geological map of the Maronia Magmatic Corridor and surrounding area drawn from field observations, interpretations of the digital elevation model (DEM), and adaption of the existing maps of Del Moro et al. (1988) & Bornovas and Rondogianni-Tsiabaou (1983). The white letters refer to the pluton names of Del Moro et al. (1988): A – Tris Visses; B – Halasmata; C – Leptokaria; D – Kirki; E – Kassiteres; F – Maronia. The symbols show the location of the named samples used for high-precision U-Pb geochronology: squares – Leptokaria; diamond – Kassiteres; and circles – Maronia. The Oligocene volcaniclastic and sedimentary units onlap onto the Kechros Dome, and the basal detachment is not exposed; field evidence of a trans-crustal extensional structure is observed in pegmatite dykes close to the margin of the dome and top to the SW microstructures (Kydonakis et al., 2014).

samples. Standard polished thin sections and epoxy mounts were prepared for a representative selection of samples from each pluton, and detailed petrographic observations were made under both transmitted and reflected light. Point counting of the least altered thin section(s) of each of the plutons was undertaken to obtain representative modal compositions of the samples. Scanning Electron Microscope (SEM) analysis was undertaken at the University of Bristol on a Hitachi S-3500 N instrument with 20 kV accelerating

voltage and a 15 mm working distance. Phase identification was performed using energy dispersive spectra (EDS) and back-scatter electron (BSE) imagery was used to establish key textural relationships.

2.3.2 Analytical Methods

Whole-rock Geochemistry

Powders of < 25 μm grain size were prepared at the University of Bristol and analysed in the Inorganic Geochemical Laboratories at the British Geological Survey (BGS), Keyworth. Powders were prepared for each of the igneous lithologies collected, with a total of 36 samples and eight repeats analysed. Weathered outer rims of individual samples were removed such that only the freshest material from the cores of the samples were used for analysis. Samples were then crushed and milled in a ball mill using an agate jar with 12 agate balls. Due to the large grain size ($>$1 mm) and relative heterogeneity of the samples, $>$1 kg of rock was used to ensure a homogenous powder was produced; a greater weight of sample was used for coarser-grained samples from the Maronia pluton. Samples were analysed following the UKAS Accreditation Schedule using wavelength dispersive–X-ray fluorescence spectrometry (WD–XRFS) on fused glass beads for major and minor element oxides, Na_2O_2 fusion inductively coupled plasma mass spectrometry (ICP-MS) for minor and trace element concentrations, and an aqua regia digest ICP-MS for Sc and Te.

New geochemical data presented in this study supplements previously published work by Del Moro et al. (1988) & Mavroudchiev et al. (1993) & Papadopoulou et al. (2004), presenting for the first time a complete suite of trace element and REE analyses for the entire magmatic belt. The results have been filtered by loss on ignition (LOI) values such that any results with LOI $>$2 wt.% have been omitted, removing any bias in the results from heavily clay-altered or hydrated samples.

U-Pb Zircon Geochronology

A subset of nine samples from the MMC sample suite were selected for high–precision U-Pb zircon geochronology (Maronia, n = 4; Kassiteres and Leptokaria n = 5). The MMC zircons have broadly similar euhedral morphologies with many inclusions of apatite, titanite, and melt. Zircons from Maronia were typically larger than those from Kassiteres and Leptokaria and were less abundant in the mineral separate. Inclusion- and defect-free crystals with well-preserved euhedral crystal faces were preferentially selected from the mineral separate for analysis (further details of sample preparation and zircon selection are included in Appendix B). The remaining zircon crystals were mounted in epoxy, polished, and imaged at the University of Bristol using a Centaur Cathodoluminescence (CL) detector on a Hitachi S-3500N Scanning Electron Microscope at 10 kV and 23 mm working distance. CL imagery of the zircons was used to investigate the internal morphology of the crystals, with particular focus on growth and resorption features in the zircons.

A total of 42 zircon crystals were analysed at the NERC Isotope Geosciences Laboratory (NIGL) using the CA-ID-TIMS technique. Three to seven individual zircon crystals from each sample were thermally annealed and chemically abraided to reduce Pb loss (Mattinson, 2005). Isotope dilution and mass spectrometry protocol followed the techniques and instrumentation described by Sahy et al. (2015), and further details are included in Appendix B.

2.4 Results

2.4.1 Field Geology and Petrology

We present primary field and petrographic observations of the MMC plutons. This work builds upon that of previous authors, in particular Del Moro et al. (1988), and focuses on the most voluminous intrusions along the belt: Maronia, Kassiteres, and Leptokaria (Fig. 2.2). Two additional, later phases of magmatism are found intruding each of the plutons: an array of aplitic dykes and small ($\sim$ 500 m^2), silicic porphyry intrusions. The felsic units are volumetrically insignificant compared to the host plutons and associated with post-pluton hydrothermal activity, including porphyry-style alteration and mineralisation in the area, leading to intense alteration of these rocks (e.g., Melfos and Voudouris 2016, and references therein). We consider the small-volume, evolved lithologies to be less important to the discussion on the changing geochemistry of the mantle magmatic system in the northern RCC, as they are highly fractionated and likely represent a mixed geochemical signature, reflecting both crustal and mantle melt sources.

The Leptokaria Complex

The Leptokaria, Kirki, Halasmata, and Tris Visses plutons were first described individually by Del Moro et al. (1988). However, in this paper, we group these plutons together on the basis of similar geochemistry and age, and we refer to them collectively as the Leptokaria complex, after the largest pluton in the group (Fig. 2.2).

The equigranular (0.2–1.0 mm) Leptokaria complex ranges from monzogabbro to granite in composition (Fig. 2.3A). A primary mineralogy of phenocrystic plagioclase + magnetite + hornblende + biotite assemblage is found in all samples of the Leptokaria pluton; clino- and ortho- pyroxene are present in the dioritic Leptokaria samples, while quartz + K-feldspar and accessory zircon + apatite are also present in the more evolved samples. Interstitial, granophyric quartz and K-feldspar intergrowths are found throughout the more evolved samples. Weak alteration, principally chlorite + epidote $\pm$ biotite $\pm$ orthoclase, is pervasive across Leptokaria, with breakdown of mafic phases and sericitisation of plagioclase. Small (0.5–1 cm-wide) veinlets of albite $\pm$ chlorite $\pm$ epidote are also common. Five of the Leptokaria samples have a cumulate-like texture with interlocking phenocrysts of plagioclase, amphibole (replacing relict clinopyroxene), and magnetite and the development of interstitial, poikilitic amphibole and plagioclase and visible plagioclase rims (Figs. 2.3B–C). These cumulate-like rocks likely characterise the mineral phases present during earliest magmatic crystallisation and differentiation. Alteration is continuous through the cumulate samples with chlorite-biotite-epidote alteration of mafic phases the most common break-down reaction observed.

The Leptokaria plutons are intruded into ortho- and para-gneisses of the Kechros Dome within the northern RCC. Around Leptokaria village, the pluton is hosted in a two-mica pegmatitic leucogranite, although the contact between the leucogranite and Leptokaria complex is not seen. Contacts between the plutons and the gneisses elsewhere in the Leptokaria Complex are undulose, with mixing of globules of gneiss in the pluton and vice-versa, this suggests that the host gneisses were not completely solid during magma emplacement and accumulation.

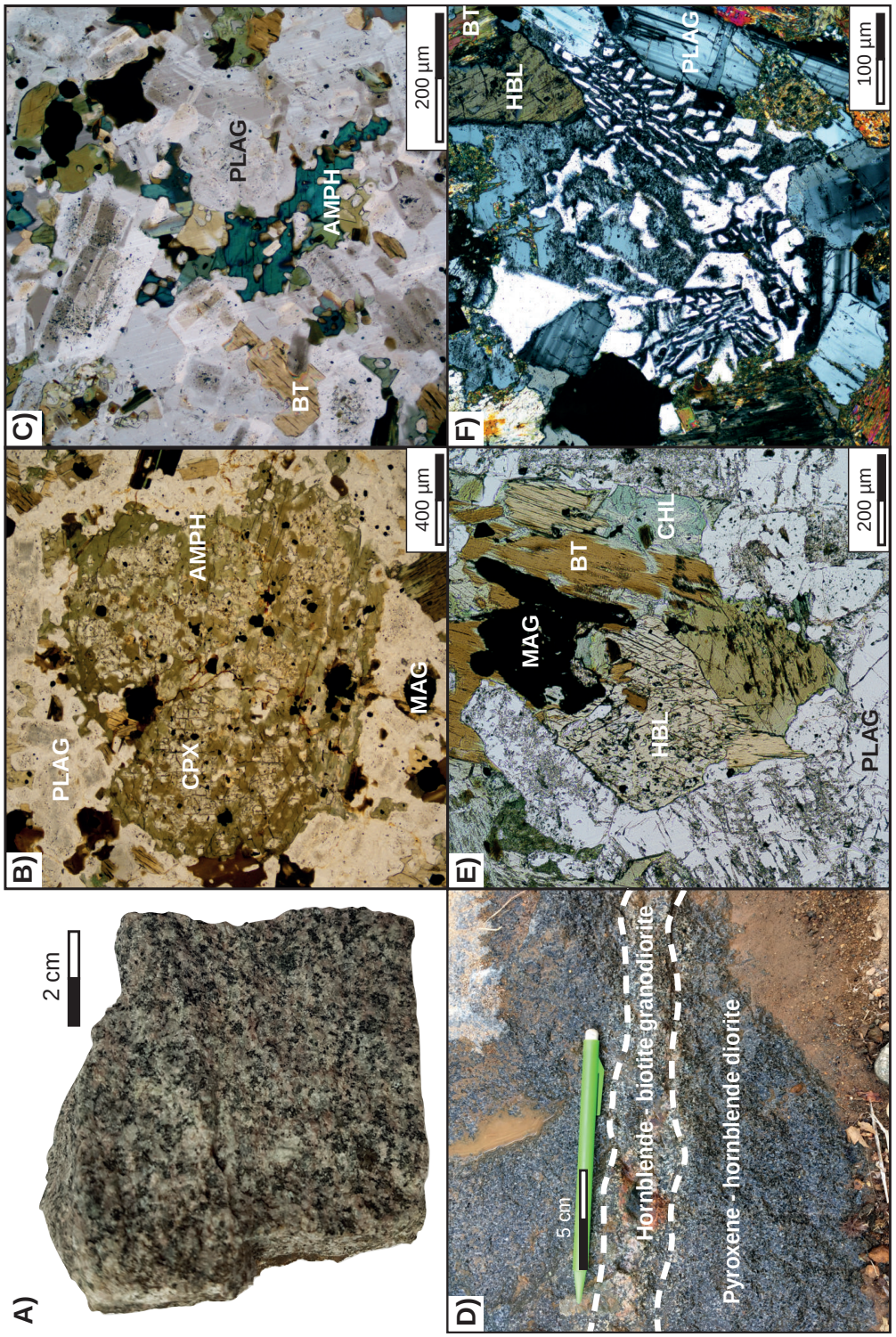

Figure 2.3: Representative field photos and photomicrographs of the Kassiteres and Leptokaria samples. PLAG – plagioclase; MAG – magnetite; AMPH – amphibole; CPX – clinopyroxene; BT – biotite; CHL – chlorite; HBL – hornblende. (A) A granitic sample from the Leptokaria suite. (B) Photomicrograph of the Leptokaria cumulate where a relict clinopyroxene phenocryst has been almost completely replaced by amphibole. (C) Photomicrograph of the interlocking plagioclase phenocrysts with clear rim growth surrounded by interstitial poikilitic amphibole. (D) Magma mixing of clinopyroxene–hornblende- and hornblende–biotite- rich end members of the Kassiteres intrusion. (E) A photomicrograph of the Kassiteres intrusion with primary hornblende + biotite + magnetite + plagioclase and minor chloritic alteration. (F) A photomicrograph of granophyric quartz-feldspar intergrowths from Kassiteres, also observed in the Leptokaria suite.

The Kassiteres Pluton

Kassiteres is a medium-grained (1–3 mm), clinopyroxene-hornblende diorite and is the next pluton moving SW along the MMC from Leptokaria (Fig. 2.2). The smallest of the named intrusions, Kassiteres has an aerial extent of $\sim$ 1.8 km^2. Kassiteres intrudes into metapelitic greenschists of the CRB basement and is unconformably overlain by Oligocene volcaniclastic units. The primary mineralogy of the Kassiteres diorite is clinopyroxene + hornblende + plagioclase + biotite + magnetite phenocrysts and interstitial K-feldspar + quartz with accessory apatite + titanite + zircon (Fig. 2.3E). Mixing of mafic, clinopyroxene-rich, and felsic, biotite-rich, end members are visible on the macroscopic scale, suggesting periodic injection of new melt into the crystallising magmatic system (Fig. 2.3D). Interstitial granophyric quartz-feldspar intergrowths suggest rapid cooling of interstitial melt during the later stages of pluton crystallisation (Fig. 2.3F).

The Kassiteres pluton is variably altered due to hydrothermal activity related to the later intrusion of a porphyritic stock and aplite dykes. Breakdown of clinopyroxene and hornblende to biotite, chlorite and plagioclase is characteristic of potassic alteration at Kassiteres, pervasive to varying degrees of intensity throughout the pluton. Advanced clay alteration is found in discrete fault zones within the diorite where the fault planes provide a pathway for enhanced fluid:wall-rock interaction. This alteration grades from silicified, advanced argillic alteration (silica + low-temperature clays) proximal to the fault plane, to argillic alteration (high-temperature clays) over 5 m from the fault. A diffuse gradation into potassically altered diorite occurs over a greater distance of 15–20 m from the faults.

The Maronia Pluton

Maronia is the southernmost pluton of the MMC, separated by $\sim$ 30 km from its nearest neighbour, Kassiteres. Outcropping as a stock with an area of $\sim$ 3.2 km^2, it is intruded into metapelites and marbles of the CRB. Three intrusive lithologies were recognised at Maronia by Papadopoulou et al. (2004): a voluminous monzonite – quartz monzonite unit (Fig. 2.4A), a minor gabbroic unit, and a minor porphyritic granitic unit. The gabbro is texturally and mineralogically indistinguishable from the monzonite–quartz monzonite unit in all but whole-rock geochemistry, while the granite porphyry shows sharp, cross-cutting contacts with the rest of the pluton (Fig. 2.4F). In this paper, we consider the gabbro–monzonite–quartz monzonite as a single unit (referred to herein as the monzonite unit) with subdivisions arising from varying phenocryst proportions.

The primary mineralogy of the monzonite is clinopyroxene + orthopyroxene + amphibole (tremolite-ferrosillite) + biotite + plagioclase + K-feldspar + apatite + magnetite + quartz $\pm$ rare olivine with accessory zircon. 1–2 cm diameter phenocrysts of primary plagioclase (50–80 % by area), clinopyroxene (5–15 %), and minor orthopyroxene (1–3 %) are surrounded by interstitial K-feldspar (up to 20 %; Fig. 2.4C). Primary biotite and amphibole phenocrysts in textural equilibrium with adjacent crystals are very rare and are more commonly found as secondary breakdown products of primary pyroxene phenocrysts (Fig. 2.4B). Evidence of post-magmatic hydrothermal alteration is visible in minor sericitization and uralization of plagioclase and pyroxene-amphibole phenocrysts respectively.

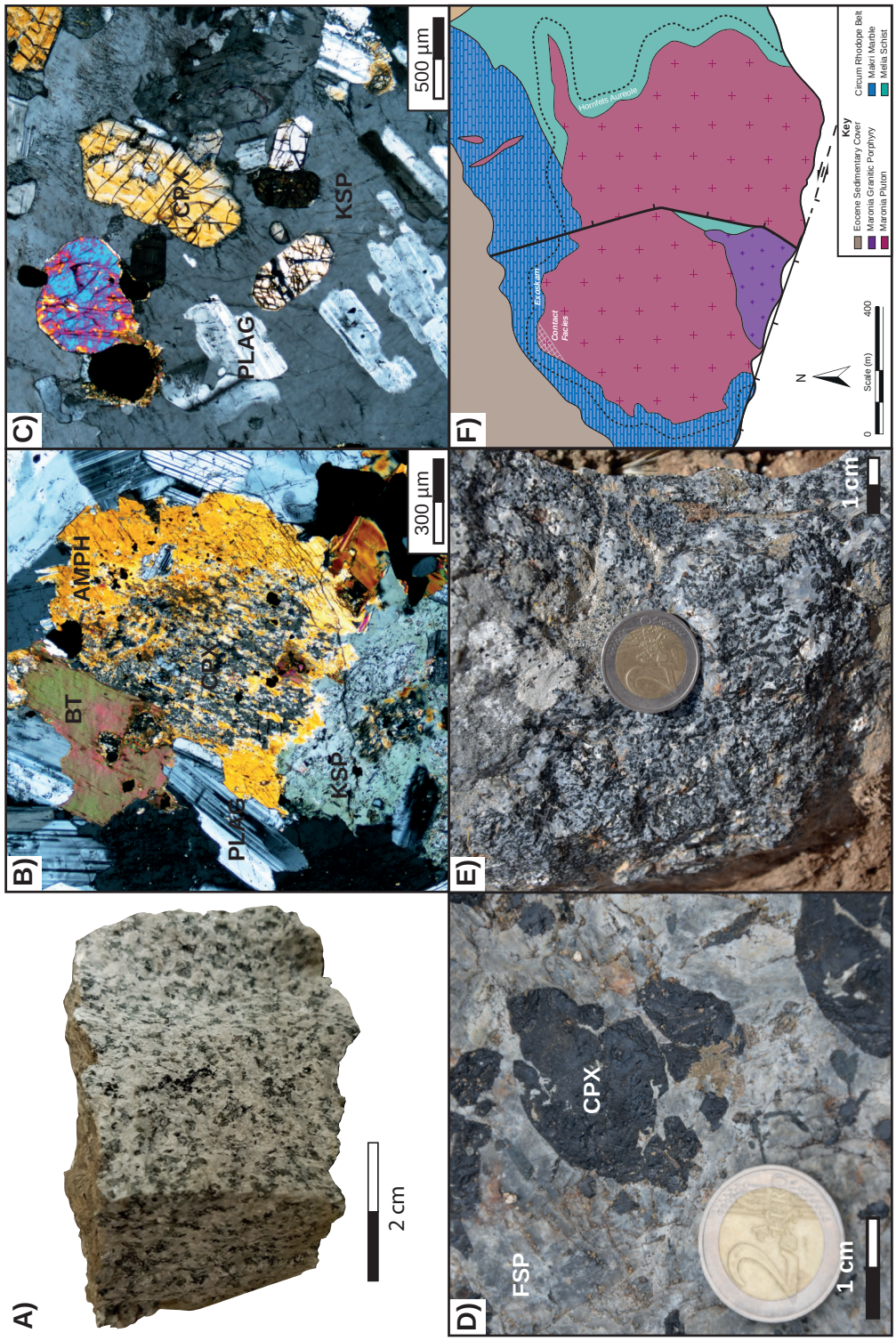

Figure 2.4: Field evidence from the Maronia pluton. AMPH– amphibole; BT– biotite; CPX– clinopyroxene; KSP– anorthite-albite; PLAG– orthoclase-albite. (A) Representative hand sample of the equigranular, coarse-grained (1–2 mm) Maronia monzonite. (B) Crossed-polar photomicrograph of a primary augite phenocryst with a breakdown rim of tremolite-ferrosilite amphibole. (C) The typical poikilitic texture of the monzonite with clinopyroxene and olivine adacrysts and oikocrystic anorthite. (D) Field photo of the Maronia contact facies with 2 cm phenocrysts of augite in K-feldspar phenocrysts up to 10 cm in diameter. (E) Endoskarn field photo. (F) Geological map of the Maronia pluton drawn from field observations and modified from Melfos et al. (2002).

Additional igneous facies are observed along the western margin of Maronia where the pluton intrudes CRB marbles. In addition to a thin ($\sim$ 1 m) endo-skarn boundary along the marble-monzonite contact (Katerinopoulou et al. 2009; Fig. 2.4 E), an orthocumulus facies is exposed in the northwest of the pluton extending for up to 10 m into the monzonite from endoskarn boundary (Fig. 2.4 D). Cumulus pyroxene adacrysts and intercumulus oikocrystic orthoclase-albite suggest that the western margin of the pluton exposes close to the base of the Maronia plutonic system. This orthocumulus facies is not observed on the eastern margin of Maronia where a $\sim$ 250-m-wide hornfels aureole extends into the host CRB metapelites.

The NNE- trending Ktismata Fault cuts the pluton separating the eastern and western portions of the intrusion (Melfos et al. 2002; Fig. 2.4F). Differing intrusive relationships between the western (deeper, orthocumulus facies) and eastern (shallow, baked aureole) margins of the pluton suggest an east-dipping normal fault. Minimal right-lateral displacement of $<$ 100 m is observed where the fault cuts the northern pluton margin, which can be accounted for by a minor oblique component of motion. An additional strike-slip fault, the Marmaritsa Fault, cuts the southern margin of the Maronia pluton subparallel to the coastline. This structure is part of a regional crustal trend, potentially related to the North Anatolian Fault Zone (Melfos et al., 2002). The brittle nature of the faulting, cutting Oligocene magmatic features within Maronia, suggest post-emplacement initiation of both structures.

2.4.2 Analytical Results

Whole-rock Geochemistry

The MMC samples vary in composition from 48 to 68 wt.% SiO_2 (Fig. 2.5; Table 2.3; Appendix C). The Maronia pluton has a more restricted SiO_2 compositional range (50–56 wt.% SiO_2), while the Kassiteres and Leptokaria samples cover the full range (48–68 wt.% SiO_2). Within the Leptokaria sample suite, a difference in SiO_2 content separates cumulate-like samples (48–53 wt.% SiO_2) from the intermediate to felsic plutonic samples (55–68 wt.% SiO_2), with all the Leptokaria samples falling on a linear fractionation trend. Samples from the MMC follow a high-K calc-alkaline differentiation trend; however, their similarity to 'typical' calc-alkaline magmatism is limited. As SiO_2 increases with differentiation, compatible elements, including MgO, $Fe_2O_3^T$, TiO_2, and CaO (Figs. 2.6B–E), decrease. A highly scattered, negative correlation between Al_2O_3 and SiO_2 is observed in all of the MMC samples (Fig. 2.6A). The incompatible elements, e.g., Na_2O, K_2O and Ba (Figs. 2.6F–G), show a positive correlation, increasing with SiO_2. Sr behaves as a compatible element in all the MMC samples with a steady decrease in Sr with fractionation (Fig. 2.6H). The MMC shows a spatial and geochemical migration from purely calc-alkaline magmatism in the Leptokaria samples in the north, to high-K calc-alkaline magmatism in the central Kassiteres samples, to shoshonitic magmatism in the southern Maronia pluton (Fig. 2.5A). In the Maronia samples, the absolute concentration of the incompatible elements is 1–1.5 times greater than in Kassiteres and Leptokaria samples, in line with shoshonitic magmatism (Figs. 2.6G–H).

Table 2.3: Abbreviated whole-rock geochemsitry results and modal phase compositions; full results in Appendix C. All oxides given in wt.%.

	Kassiteres							Leptokaria			
Sample ID	KA15_004	KA15_008	KA15_009	KA15_013	KA15_016	KA15_017	RT14_028	LA15_009	LA15_011	LB15_003	LB15_004
SiO_2	55.420	56.860	59.450	61.110	59.100	59.190	55.700	53.790	69.730	50.390	67.630
TiO_2	0.750	0.770	0.740	0.650	0.650	0.700	0.810	0.750	0.390	1.020	0.360
Al_2O_3	14.440	14.870	14.640	15.990	16.090	14.200	15.090	14.650	15.050	19.500	15.630
$Fe_2O_3^T$	7.820	7.380	6.720	6.090	6.670	6.190	7.480	6.850	2.990	8.590	3.580
Mn_3O_4	0.150	0.160	0.100	0.060	0.110	0.110	0.150	0.220	0.070	0.230	0.080
MgO	7.050	6.160	5.250	3.100	3.770	6.160	6.810	6.310	1.150	5.680	1.450
CaO	7.250	6.280	5.530	5.220	5.320	5.660	7.480	7.510	0.900	9.470	3.870
K_2O	2.270	2.630	2.740	2.780	3.070	3.190	2.590	2.030	5.560	0.550	2.830
P_2O_5	0.240	0.190	0.170	0.140	0.160	0.160	0.190	0.160	0.080	0.230	0.100
LOI	1.640	1.840	1.650	1.460	1.670	1.560	0.870	5.770	1.960	1.210	0.670
Total	99.560	99.650	99.800	99.780	99.620	99.790	99.990	99.900	100.020	99.940	99.690
Rb (ppm)	61	54	53	82	77	70	70	48	155	7	79
Sr (ppm)	346	292	298	317	314	259	359	371	258	590	298
Ba (ppm)	1247	889	783	702	769	793	1185	759	1249	227	685
Eu/Eu*	0.767	0.860	0.674	0.725	0.780	0.701	0.890	0.799	0.594	1.162	0.739
Dy/Yb	2.019	1.930	1.941	1.923	1.841	1.870	1.910	2.020	1.541	2.106	1.747
Plagioclase							43.1				
K-feldspar							12.7				
Quartz							9.0				
Amphibole							5.6				
Biotite							6.5				
Pyroxene							9.6				
Chlorite							10.5				
Fe-Ti Oxides							1.1				
Additional Phases							2.0				
Total							100.0				

Table 2.3: Continued...

Sample ID	LB15_ 006	LC15_ 002	LC15_ 003	LD15_ 002	LD15_ 003	Leptokaria RT14_ 009	RT14_ 010	RT14_ 015	RT14_ 017	RT14_ 022	RT14_ 024
SiO_2	62.380	60.380	64.730	53.200	52.970	60.240	67.340	53.600	48.270	58.900	56.140
TiO_2	0.620	0.730	0.500	0.840	0.760	0.730	0.400	0.840	1.130	0.710	0.630
Al_2O_3	17.630	17.370	15.970	18.030	19.260	16.390	15.370	18.150	20.640	15.690	13.630
$Fe_2O_3^T$	3.880	6.650	5.160	9.210	8.370	6.230	4.150	9.090	9.950	6.710	8.480
Mn_3O_4	0.110	0.170	0.120	0.190	0.180	0.100	0.100	0.180	0.170	0.160	0.140
MgO	2.580	2.730	2.190	4.580	4.130	3.370	1.550	4.540	4.280	3.950	6.600
CaO	5.610	5.050	4.300	8.430	8.850	5.910	2.860	7.980	10.740	3.820	6.900
Na_2O	4.890	3.120	3.280	2.860	2.980	3.720	2.990	2.810	2.510	3.010	2.620
K_2O	0.680	2.300	2.850	1.240	1.180	2.040	3.210	1.300	0.890	3.740	3.020
P_2O_5	0.160	0.170	0.120	0.110	0.150	0.160	0.090	0.120	0.130	0.150	0.190
LOI	1.180	1.300	0.800	0.910	0.810	1.140	1.550	1.270	0.940	2.220	1.320
Total	99.720	99.970	100.020	99.600	99.640	100.030	99.610	99.880	99.650	99.060	99.670
Rb (ppm)	19	56	76	34	28	43	71	38	19	103	80
Sr (ppm)	562	338	320	385	535	335	257	380	533	396	291
Ba (ppm)	200	670	809	379	404	736	990	418	248	999	618
Eu/Eu*	0.715	0.847	0.714	0.863	0.865	0.657	0.798	0.814	0.797	0.721	0.645
Dy/Yb	1.793	1.925	1.750	1.930	1.877	1.883	1.552	1.930	2.173	1.623	1.743
Plagioclase						33.8	45.6	66.7	64.0	67.6	32.4
K-feldspar						20.1	13.2	0.0	0.0	0.0	19.7
Quartz						24.7	26.5	0.0	5.7	1.4	9.3
Amphibole						6.4	1.4	22.4	17.0	0.0	15.2
Biotite						8.5	0.7	9.0	0.3	0.0	0.3
Pyroxene						3.6	0.0	0.0	4.4	2.1	7.3
Chlorite						1.3	11.1	0.0	2.5	21.9	14.4
Fe-Ti Oxides						1.3	1.4	2.0	6.0	7.0	1.4
Additional Phases						0.3	0.0	0.0	0.0	0.0	0.0
Total						100.0	100.0	100.0	100.0	100.0	100.0

Table 2.3: Continued...

Sample ID	Maronia										
	MA15_004	MA15_006	MA15_007	MA15_008	MA15_010	MA15_011	MA15_012	MA15_014	MA15_016	MA15_017	RT14_006
SiO_2	55.270	50.410	51.100	52.110	52.910	54.710	53.320	55.570	53.000	55.720	52.930
TiO_2	0.850	1.070	0.920	0.870	0.980	0.900	0.960	0.850	1.000	0.820	0.730
Al_2O_3	16.260	16.040	15.160	15.240	16.690	16.550	16.890	16.080	16.740	14.910	19.840
$Fe_2O_3^T$	7.350	9.990	9.350	8.760	9.160	8.240	8.770	7.570	8.790	7.400	6.140
Mn_3O_4	0.140	0.200	0.170	0.170	0.170	0.170	0.170	0.140	0.170	0.150	0.120
MgO	4.170	5.800	7.060	6.620	4.750	4.060	4.550	4.150	4.450	5.560	3.590
CaO	7.040	9.680	10.190	9.660	8.280	7.250	7.890	6.570	7.760	7.870	8.810
Na_2O	2.870	2.530	2.420	2.490	2.800	2.890	2.860	2.830	2.700	2.640	3.130
K_2O	4.290	2.710	2.220	2.750	3.070	3.500	3.240	4.680	4.020	4.350	3.050
P_2O_5	0.500	0.640	0.590	0.570	0.470	0.420	0.460	0.560	0.520	0.500	0.430
LOI	0.290	0.130	0.350	0.080	0.570	0.520	0.420	-0.040	0.210	0.110	0.930
Total	99.030	99.200	99.530	99.320	99.850	99.210	99.530	98.960	99.360	100.030	99.700
Rb (ppm)	168	107	92	96	123	127	135	208	150	178	134
Sr (ppm)	606	717	685	677	702	617	693	604	665	536	924
Ba (ppm)	1216	1208	746	960	994	813	1004	1293	1320	1178	727
Eu/Eu*	0.778	0.763	0.880	0.838	0.789	0.735	0.811	0.724	0.819	0.744	1.080
Dy/Yb	2.166	2.228	2.233	2.137	2.145	1.970	1.909	2.000	2.109	2.332	2.145
Plagioclase											33.8
K-feldspar											37.9
Quartz											0.2
Amphibole											10.0
Biotite											7.6
Pyroxene											3.6
Chlorite											4.2
Fe-Ti Oxides											2.4
Additional Phases											0.4
Total											100.0

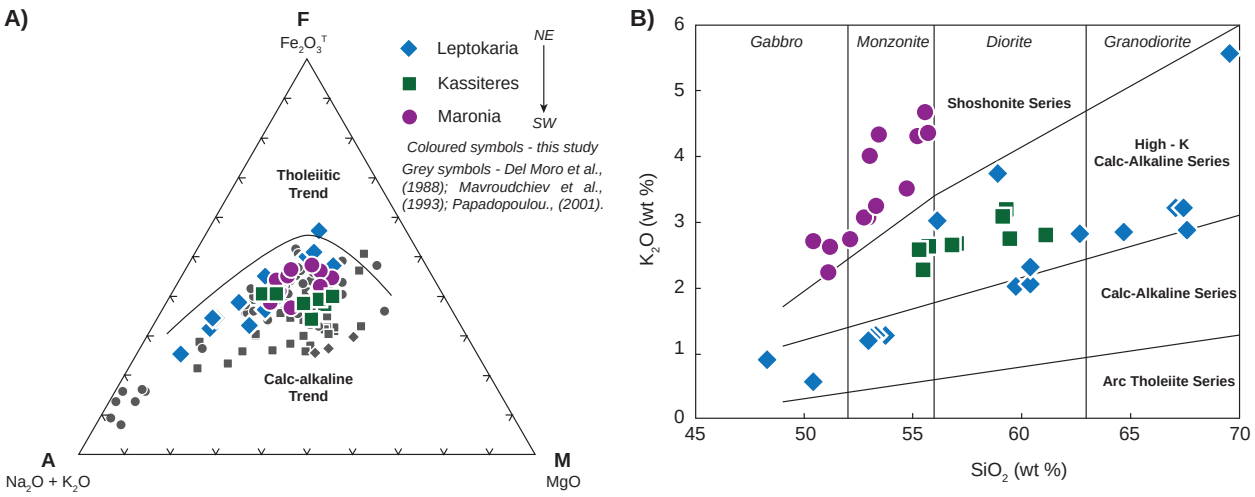

Figure 2.5: (A) AFM plot of the Maronia Magmatic Corridor (MMC) suite after Irvine and Baragar (1971); the samples plot on a calc-alkaline trend but vary to higher MgO fractions than would typically be expected. (B) A K_2O versus SiO_2 plot with rock-type classification after Peccerillo and Taylor (1976). The MMC samples range from 47–70 wt.% SiO_2(this study) with a more restricted range of compositions, 51–56 wt.% SiO_2 at Maronia. Samples of the Leptokaria cumulate can be distinguished from the main Leptokaria trend from 48 to 54 wt.% SiO_2 and have the lowest alkali component. The Maronia suite can be clearly distinguished from the Kassiteres and Leptokaria samples by elevated K_2O, falling along a shoshonitic trend, while the Kassiteres and Leptokaria are moderately potassic on a high-K calc-alkaline trend.

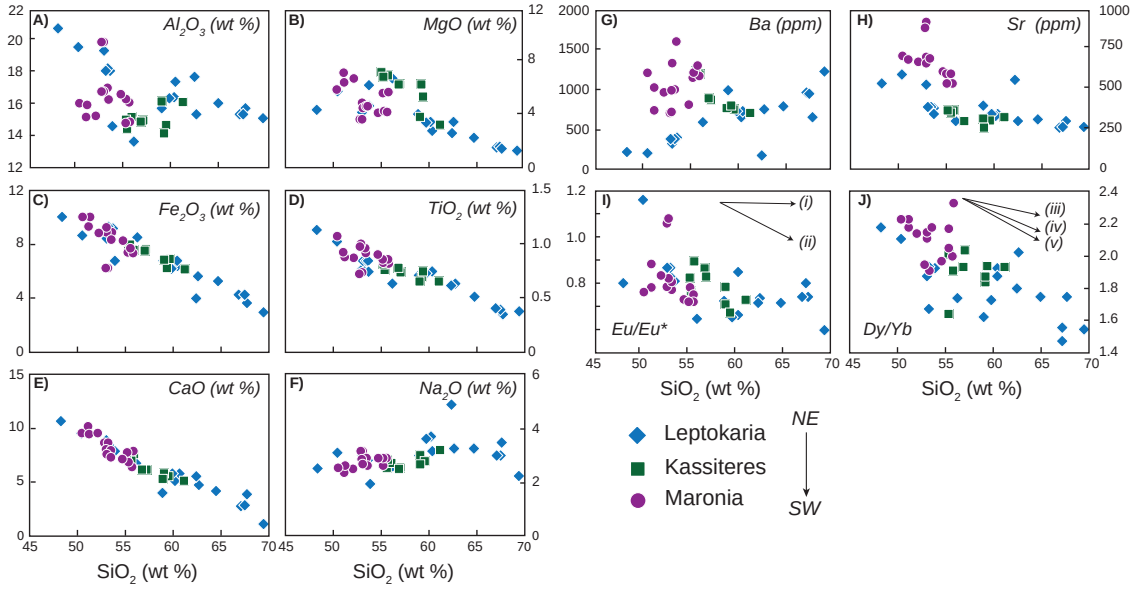

Figure 2.6: Element, oxide, or elemental ratio versus SiO_2 Harker plots; only data from this study is plotted for clarity of interpretation. (A-F) Major element versus SiO_2 plots show a liquid line of descent in each of the sample suites. (G-H) Ba/Sr versus SiO_2 plots show elevated concentrations of highly incompatible elements in the Maronia samples relative to Kassiteres and Leptokaria; in both magmatic suites Sr behaves as a compatible element. (I) Eu/Eu* vs. SiO2 shows a trend of decreasing Eu/Eu*, an increasingly negative Eu anomaly, with fractionation. The Leptokaria cumulate samples ($<$ 53 wt.% SiO_2) have a considerable, negative Eu anomaly ($<$ 0.9). The arrows show the expected fractionation trend of *(i)* oxidised (fO_2 = -7.27 log units) and *(ii)* reduced (fO_2 = -15.78 log units) end-members, assuming plagioclase as the main repository of Eu^{2+} in the melt and using the partition co-efficients of Wilke and Behrens (1999). J) Dy/Yb vs SiO_2 shows negative correlation showing fractionation of a middle REE–compatible phase, amphibole or pyroxene, during crystallisation. The arrows show the expected fractionation trend of *(iii)* clinopyroxene, *(iv)* clinopyroxene + amphibole and *(v)* amphibole using the partition co-efficients of Fujimaki et al. (1984).

Similar, saw-toothed trace element patterns are observed from all plutons along the MMC (Fig. 2.7A). The MMC samples are enriched in fluid mobile, large-ion lithophile elements (LILEs; e.g., Ba, Rb, Pb) and depleted in fluid immobile, high field-strength elements (HFSEs; e.g., Nb, Ta, Zr) compared to the primitive mantle, in a trace signature typical of a metasomatized, fertile mantle source (Elliott et al., 1997). The plutons are enriched in the light REEs relative the heavy REEs (Fig. 2.7B) and show decreasing Dy/Yb (middle REE to heavy REE fractionation) with differentiation (Fig. 2.6J). The mildly concave REE pattern is flatter than the highly convex, amphibole-controlled REE fractionation trend, and is most similar to that of a clinopyroxene-hornblende–controlled REE pattern (Pearce and Peate, 1995; Tatsumi, 1989; Davidson et al., 2013). A pronounced, negative Eu anomaly, which decreases with increasing SiO_2 is observed in all of the MMC samples (Fig. 2.6I).

U-Pb Zircon Geochronology

CL imaging revealed simple zoning patterns in most all of the zircons from the MMC (further descriptions are included in Appendix B). Oscillatory and sector zoning in the crystals reflect a simple magmatic history of the zircons with little evidence of zircon inheritance suggesting the zircons experienced a single period of crystallisation. Therefore, dissolution of full zircon crystals was justified to use the largest sample volume and reduce analytical uncertainty, offering the highest-precision dates. Two individual zircon analyses were excluded from our interpretations as high common Pb ($Pb_c > 2.5$ pg) was taken as an indicator of a low precision analysis (see Appendix E).

Our results were interpreted within a magmatic framework in which it is recognised that zircon crystallisation is protracted over time scales of 10^5–10^6 yr (e.g., von Quadt et al. 2011). The youngest statistically significant population of zircons was sought to represent the timing of the final stages of crystallisation. Our preferred age interpretations are presented in Table 2.4; alternative interpretations and a discussion of the sample discordance are included Appendix B. All ages reported are $^{206}Pb/^{238}U$ to minimize the influence of excess ^{207}Pb, the result of initial U/Pa disequilibrium, on our age interpretations (Crowley et al., 2007). Dates are reported in millions of years ago (Ma) to 2σ uncertainty.

The $^{206}Pb/^{238}U$ ages form two distinct groups (Fig. 2.8). We can interpret two geological windows in time for pluton emplacement and crystallisation, *(i)* intrusion of the Kassiteres and Leptokaria plutons over 0.9 Myrs (from 32.96 to 32.02 Ma); and 2.2 Myrs later, *(ii)* intrusion of the Maronia pluton over 0.2 Myrs (from 29.78 to 29.57 Ma). Antecrystic zircons, those crystallised prior to final pluton crystallisation either during an earlier phase of magmatism or deeper in the magmatic plumbing system, are recognised in the MMC analyses (e.g., z2 RT14_022; Appendix B). Zircons which that are much older that the interpreted ages of crystallisation (>5 Myrs) are interpreted as xenocrystic zircons, entrained from the wallrock during magma ascent (e.g., z2 RT14_024; Appendix B). The autocrystic zircons, those crystallised in situ in the magmatic system, show good clustering in seven of the nine samples from the MMC, allowing interpretation of a youngest population of zircons (Table 2.4). In Leptokaria samples RT14_022 and RT14_024, the youngest zircon is taken as a maximum age of crystallisation of the pluton, allowing the possibility of younger zircons in the sample.

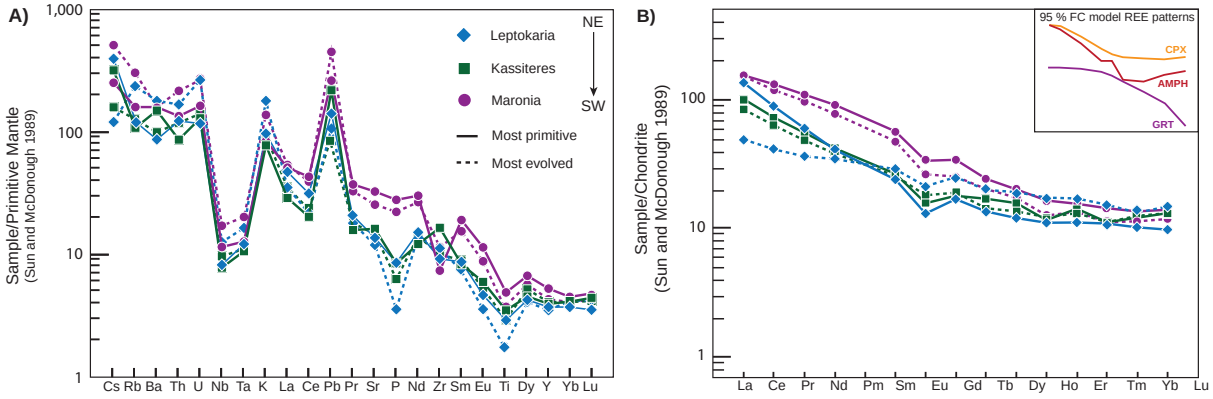

Figure 2.7: (A) Trace element spider plot; the irregular shape is typical of an enriched, metasomatic mantle signal. The Maronia Magmatic Corridor (MMC) shows elevated high field strength elements: Cs, Rb, Ba, Th, and U, and depleted large ion lithophile elements: Nb and Ta. Maronia shows elevated Sr, P, Nd, and Sm typical of a shoshonitic magma. (B) Rare earth element spider plot; the MMC shows a consistent negative Eu anomaly and moderately curved shape. Maronia is enriched in the light REEs (La to Sm) relative to Kassiteres and Leptokaria, which is again indicative of shoshonitic magmatism. The inset shows the modeled normalized REE shapes at 95 % fractional crystallisation for clinopyroxene (CPX), amphibole (AMPH), and garnet (GRT) for a source mineral composition of 70 % olivine, 30 % clinopyroxene or 70 % olivine, 25 % clinopyroxene, and 5 % amphibole/garnet after Davidson et al. (2013).

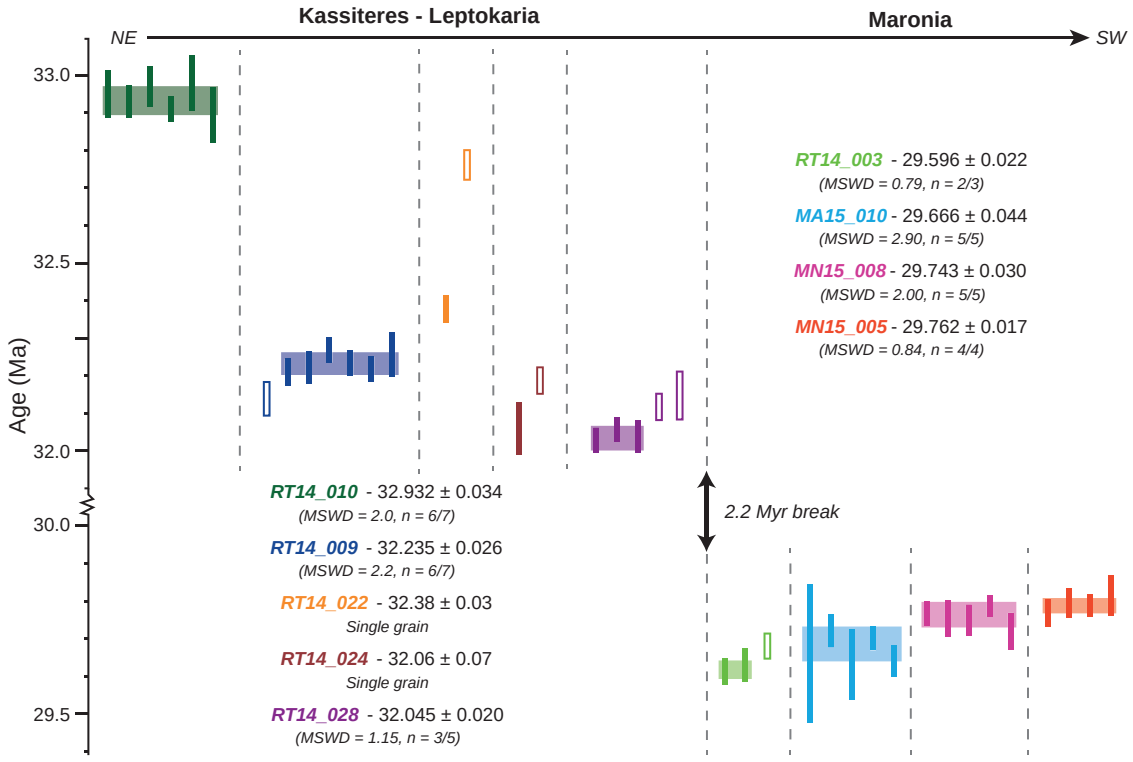

Figure 2.8: Geochronology dates for individual zircon crystals from Kassiteres–Leptokaria and Maronia. The solid bars represent analyses used to calculate the youngest single population from each sample and represent 2σ uncertainties; the open bars also represent 2σ uncertainties but are analyses that have been rejected from the youngest populations. There is a distinct temporal break between the age of crystallisation of Kassiteres–Leptokaria between 33 and 32 Ma and Maronia between 30 and 29.5 Ma. MSWD –mean square weighted deviation.

Table 2.4: Summary of the $^{206}Pb/^{238}U$ interpreted ages for the Maronia Magmatic Corridor. L–K – Kassiteres–Leptokaria magmatic suite, and M – Maronia pluton.

Sample ID	Intrusive Complex	$^{206}Pb/^{238}U$ date (Ma)	$\pm$ (x)	$\pm$ (y)	MSWD	n	Justification
RT14_010	L–K	32.932	0.034	0.052	2.00	6/6	Weighted mean (all)
RT14_009	L–K	32.235	0.026	0.047	2.20	6/7	Weighted mean (excluding high Pb_c)
RT14_022	L–K	32.38	0.03	0.049	-	-	Youngest date
RT14_024	L–K	32.06	0.07	0.080	-	-	Youngest date
RT14_028	L–K	32.045	0.020	0.044	1.15	3/5	Youngest three dates (weighted mean)
MN16_008	M	29.743	0.030	0.047	2.00	5/5	Weighted mean (all)
MN16_005	M	29.762	0.017	0.040	0.84	4/4	Weighted mean (all)
RT14_003	M	29.596	0.022	0.042	0.79	2/3	Youngest two dates (weighted mean)
MA15_010	M	29.666	0.044	0.060	2.90	5/5	Weighted mean (all)

x uncertainty – analytical only
y uncertainty –analytical + tracer calibration + ^{238}U decay constant

2.5 Discussion

Our geochemical and isotopic data strongly suggest heterogeneity between Maronia and the remainder of the MMC. Therefore, the petrogenesis of the Maronia pluton will be discussed separately to the Kassiteres–Leptokaria magmatic suite before the magmatism along the MMC as a whole is discussed in relation to the extensional tectonics in the Kechros dome.

2.5.1 Timescales of Magmatic Emplacement

Previous geochronological data from the MMC comprises nine Rb-Sr biotite–whole-rock pairs ranging from 34.9 $\pm$ 1.5 – 28.9 $\pm$ 1.5 Ma, which are interpreted to reflect an $\sim$8 Myr window of magmatism along the MMC, younging from NE to SW (Del Moro et al., 1988). However, the Rb-Sr geochronometer is highly susceptible to disturbance by hydrothermal overprinting (Jenkin et al., 2001), and at least three of the MMC plutons are associated with significant hydrothermal activity (Melfos and Voudouris 2017, and references therein). Our high-precision zircon CA-ID-TIMS U-Pb geochronological data show two tightly constrained magmatic windows: (*i*) 0.9 Myrs (from 32.045 $\pm$ 0.027 – 32.932 $\pm$ 0.039 Ma) for the Kassiteres–Leptokaria magmatic suite, and (*ii*) 0.2 Myrs (from 29.596 $\pm$ 0.027 – 29.762 $\pm$ 0.024) for the Maronia magmatic suite (Table 2.4; Fig. 2.8). These two discrete time periods are consistent with the distinct geochemical signature of Maronia compared to Kassiteres–Leptokaria.

Within the Kassiteres–Leptokaria magmatic suite, our data do not duplicate the younging of magmatic activity from NE to SW concluded by Del Moro et al. (1988). While the youngest and oldest samples, RT14_028 (32.045 $\pm$ 0.027 Ma) and RT14_010 (32.932 $\pm$ 0.039 Ma), respectively, do follow this SW-trend, the remaining three samples show ongoing crystallisation in the intervening time period, consistent with pulsed magma accumulation across the pluton. This agrees with our earlier interpretation that there is potential for the Leptokaria outcrops to be connected at depth by a large, mostly unexposed magmatic system. The inter-sample age range (0.887 $\pm$ 0.039 Myrs at Leptokaria and 0.166 $\pm$ 0.028 Myrs at Maronia) reflects the time scale of pluton cooling. As the larger intrusive body, the duration of cooling

of the Kassiteres–Leptokaria complex is nearly an order of magnitude greater than the Maronia pluton.

We emphasize that the high-precision U-Pb zircon geochronology presented in this paper shows a clear temporal break in exposed, intrusive magmatism in the MMC, reflecting two discrete magmatic periods. The first magmatic period produced the Kassiteres–Leptokaria magmatic suite and was followed, after an apparent 2.2 Myr break in recorded magmatism, by the Maronia plutonic complex.

2.5.2 Petrogenesis of the Kassiteres–Leptokaria Magmatic Suite

Equigranular, plutonic samples from the Kassiteres–Leptokaria magmatic suite record the first stage of post-collisional magmatism hosted in the southern Kechros dome. The high-K calc-alkaline magmatic suite has trace element geochemistry which that is consistent with a sub-continental lithospheric mantle source (e.g., Del Moro et al. 1988; Pe-Piper and Piper 2001). The presence of hornblende phenocrysts in textural equilibrium with surrounding mineral phases (Fig. 2.3E) indicates crystallisation of the magmatic suite at a depth of $>\sim$3 km (Lledo and Jenkins, 2007; Mutch et al., 2016). The intrusions show granophyric interstitial textures reflecting fast cooling of the last vestiges of melt during rapid final crystallisation.

The major and minor element geochemistry of the Kassiteres–Leptokaria suite, most notably the steadily depleting Al_2O_3 with fractionation, the consistently negative Eu anomaly, and the compatible behavior of Sr, suggest plagioclase was an important phase during magmatic differentiation. The presence of abundant plagioclase in the Leptokaria samples with a cumulate-like texture further supports the early appearance of plagioclase on the liquidus (Table 2.3). This is atypical of arc-type magmatism where partial mantle melts with elevated water contents suppress plagioclase saturation (Gaetani et al., 1993; Sisson and Grove, 1993). Decreasing Dy/Yb with fractionation (Fig. 2.6J) suggest clinopyroxene and/or amphibole are the predominant ferromagnesian phases controlling fractionation (Davidson et al., 2013). Amphibole is the most abundant phase in the cumulate-like samples (Table 2.3); however, relict subhedral clinopyroxene in the core of many of the amphibole phenocrysts (Fig. 2.3B) suggests clinopyroxene was a precursor to amphibole during fractionation. This can account for the more primitive REE pattern (Fig. 2.7B; Smith 2014).

Experimental studies on the effect of intensive parameters: temperature (T), pressure (P), H_2O content, and oxygen fugacity (fO_2), on phase equilibria are commonly used to investigate the physiochemical conditions of magma differentiation, crystallisation, and storage (e.g., Scaillet et al. 2016). Naney (1983) produced phase assemblage diagrams, at both 200 MPa ($\sim$ 6 km) and 800 MPa ($\sim$ 24 km), of fO_2 controlled granodiorite compositions as a function of T and H_2O content. The synthetic starting composition used by Naney (1983), 'R5 + 10MI', and the natural analogue hornblende, biotite, granodiorite R5 (Nockolds, 1954), are similar in composition to the Leptokaria tonalities which that make up the more evolved end member of Kassiteres–Leptokaria magmatism (Appendix C). Using the major fractionating assemblage of plagioclase + pyroxene + amphibole and the phase diagrams of Naney (1983), the T and H_2O field of lower crustal fractionation (at P = 800 MPa, 24 km) can be constrained to $880 < T < 980$ °C and $3 <$ H_2O content < 4.75 wt.% (Fig. 2.9). The drier nature of the magmas suggests that the fertile mantle source has been tapped by multiple different melting events during which H_2O has been mobilized, prior to the generation and emplacement of the Kassiteres–Leptokaria magmas between 32.9 and 32.0 Ma. We suggest that the elevated temperature necessary to melt a drier mantle wedge ($>$ 880 °C, Fig. 2.9) was provided by the accumulation of heat during prolonged (more than $\sim$10 Myr) asthenospheric upwelling and mantle

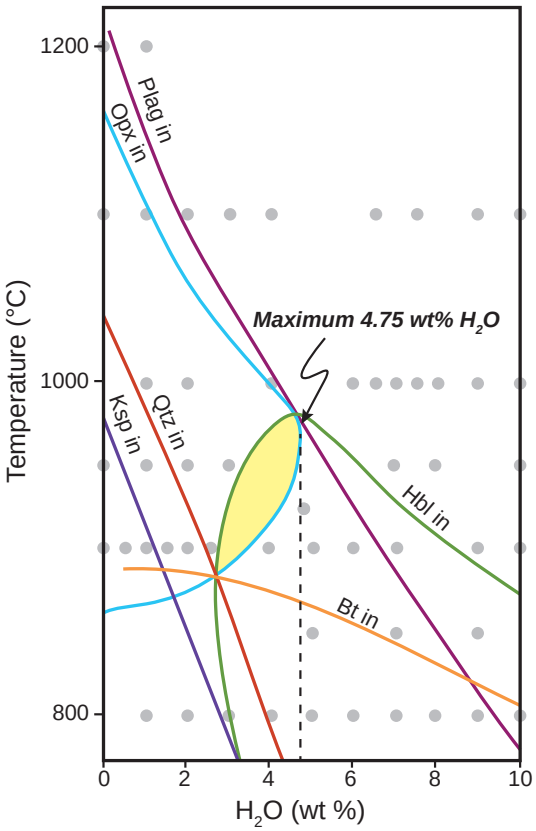

Figure 2.9:
Phase relations of synthetic granodiorite (R5 + 10M1) at 800 MPa (8 kbars, ∼ 24 km), expanded from Figure 4A in Naney (1983). The coloured lines indicate the stability field of each phase. Phase abbreviations: Plag – plagioclase; Opx – orthopyroxene; Hbl – hornblende; Qtz – quartz; Ksp – K-feldspar; Bt – biotite. Each grey circle indicates an experiment performed by Naney (1983). The synthetic granodiorite has a similar composition to samples RT14_010 and LB15_004, and the hornblende-biotite granodiorite sample it is based on is similar in composition to LC15_003. Our whole-rock geochemistry trace elements and REE rare earth element patterns indicate plagioclase and pyroxene are the primary minerals controlling deep crustal fractionation of the Kassiteres–Leptokaria suite. The yellow shaded area indicates the PLAG + OPX + HBL stability field for this composition and indicates a maximum water content of 4.75 wt.% H_2O.

melting in the northern Aegean, which began in the mid-Eocene (e.g., Rohrmeier et al. 2013).

2.5.3 Petrogenesis of the Maronia Pluton

Maronia shows a different petrogenetic evolution to Kassiteres–Leptokaria, coincident with a 2.2 Myr temporal, and a 30 km spatial, break in recorded magmatism. The Maronia monzonite has a shoshonitic affinity with significant enrichment in incompatible and volatile elements (e.g., P_2O_5, Pb, Sr, Rb; Figs. 2.5B, 2.6G,H). Geochemical and isotopic evidence advocate a heterogeneous, highly metasomatized source mantle as the foundation for the generation of ultra-potassic shoshonitic to lamproitic magmas (e.g., Foley et al. 1987; Beccaluva et al. 2013; Condamine and Médard 2014; Müller and Groves 2016). Sr isotopic data from the MMC reported by Del Moro et al. (1988) (in Table 4), show consistently enriched radiogenic ^{87}Sr across the Kassiteres–Leptokaria ($^{87}Sr/^{86}Sr$= 0.7057–0.7080) and Maronia ($^{87}Sr/^{86}Sr$= 0.7061–0.7076) magmatic suites. This is unlike the Sr isotopic data reported from the Eocene – Oligocene Biga orogenic volcanic rocks, NW Turkey, where the magmatic suite becomes increasingly radiogenic and potassic with time, which is interpreted to reflect an increasing crustal contribution (Ersoy et al., 2017). Consequently, we suggest that the MMC source mantle was enriched by a radiogenic source, likely crustal-derived metasomatic fluids prior to the start of high-K calc-alkaline magmatism at Kassiteres–Leptokaria. Therefore, processes involved in magma generation and fractionation were responsible for the evolution of a shoshonitic trend at Maronia. Further to this, experimental data for the contamination and mixing of mantle and sedimentary melts in the production of a K-rich starting melt generate evolved, peraluminous shoshonitic magmas (Wang et al., 2017), while the Maronia magmatic suite has a highly restricted SiO_2 (51–56 wt.% SiO_2) range and is metaluminous.

Melting of a phlogopite-rich veinlet in the highly metasomatized source mantle could be a potential source

of an anomalously K-rich melt from which to fractionate a shoshonitic trend (e.g., Condamine and Médard 2014). Such melts would inherit a diagnostic trace element pattern due to the compatible nature of LILEs (e.g., Rb and Ba) and incompatible nature of HFSEs (e.g., Zr and Y) in phlogopite (LaTourrette et al., 1995). However, the Maronia samples show a relative enrichment in Rb and Ba over the Kassiteres–Leptokaria suite and similar values of Zr and Y (Fig. 2.7A). Direct mantle melts would be expected to have a Mg# = 80 – 85 [Mg# = Mg/(Mg + Fe^{2+}) * 100; molar], which will decrease with fractionation (Herzberg et al., 2014). The Mg# of the Maronia shoshonites ranges from 49.4 < Mg # < 60.2 indicating that significant fractionation from direct lherzolitic or harzburgitic mantle would be required to produce the potassic fractionation trend observed at Maronia. Therefore, we favor the model of pyroxene + An-rich plagioclase + magnetite fractionation in the absence of major olivine in an H_2O-poor magma as a mechanism to produce a shoshonitic LLD (Meen, 1987; Freise et al., 2009; Lanzo et al., 2016; Beermann et al., 2017).

We have modelled fractional crystallisation by subtracting varying proportions of a proposed orthopyroxene + clinopyroxene + An-rich plagioclase + magnetite fractionating assemblage (Meen, 1987; Beermann et al., 2017) from the most primitive known sample from Maronia (MP 81; Mavroudchiev et al. 1993). Meen (1987) show experimentally that at low H_2O contents, the stability of pyroxenes is much greater than olivine and as such we do not include olivine in our fractionating assemblage, but consider it to be a minor phase in the generation of the LLD. As there are no K-bearing phases present, we assume K_2O to be completely incompatible during fractionation (Freise et al., 2009). Proportions of orthopyroxene + clinopyroxene + An-rich plagioclase + magnetite in the fractionating assemblage were varied until the petrological model best replicated whole-rock fractionation trends. The petrological model is in close agreement with the whole-rock data for the oxides with least variance e.g. MgO and CaO, and the fit is poorer where the oxides are more highly scattered e.g. Al_2O_3. K_2O is enriched in the petrological model over the observed fractionation trends, we attribute this to the model assumption that K is incompatible in the fractionating assemblage when it is likely that a small amount is accommodated in plagioclase. Further details of a comparison between the linear regression through the whole-rock dataset and the petrological model can be found in Appendix F.

The observed fractionation trend from the parent magma can be closely matched by a modelled fractionation assemblage of 15 % orthopyroxene (En 0.8), 25 % clinopyroxene (Di 0.8), 52 % plagioclase (An 75) and 8 % magnetite (Mag 0.7; Fig. 2.10A; Table 2.5). The close agreement between the modelled and observed LLDs suggests that fractionation of pyroxene + plagioclase (+ minor magnetite), which have higher silica content than olivine (OL ∼30 wt.% SiO_2; OPX ∼50 wt.% SiO_2; CPX ∼45 wt.% SiO_2; PLAG ∼50 wt.% SiO_2), can sufficiently enrich the residual magma in incompatible elements with small changes in melt SiO_2, to produce a shoshonitic LLD (Meen, 1987; Beermann et al., 2017). Using the predicted fractionating phase assemblage and estimated bulk partition coefficients (Table 2.6), the observed trace element fractionation trends can be reproduced and are shown in Figure 2.10B for Ba, Cr, Rb, Sr, Zr and Y.

A pyroxene + plagioclase + magnetite fractionating assemblage can be produced by an H_2O-poor (<2–3 wt.% H_2O) magma at high-T (950–1050 °C) and a range of pressures (200–1,000 MPa; Baker and Eggler 1987; Meen 1987; Beermann et al. 2017). This suggests that fractionation of the same parental mantle source region as Kassiteres–Leptokaria could produce a shoshonitic trend with a similar trace element signature as the Maronia pluton by losing H_2O. In a post-collisional setting, H_2O is a finite resource. Thus, if moderately wet magmas (<4.75 wt.% H_2O) were produced in the generation of the Kassiteres–Leptokaria

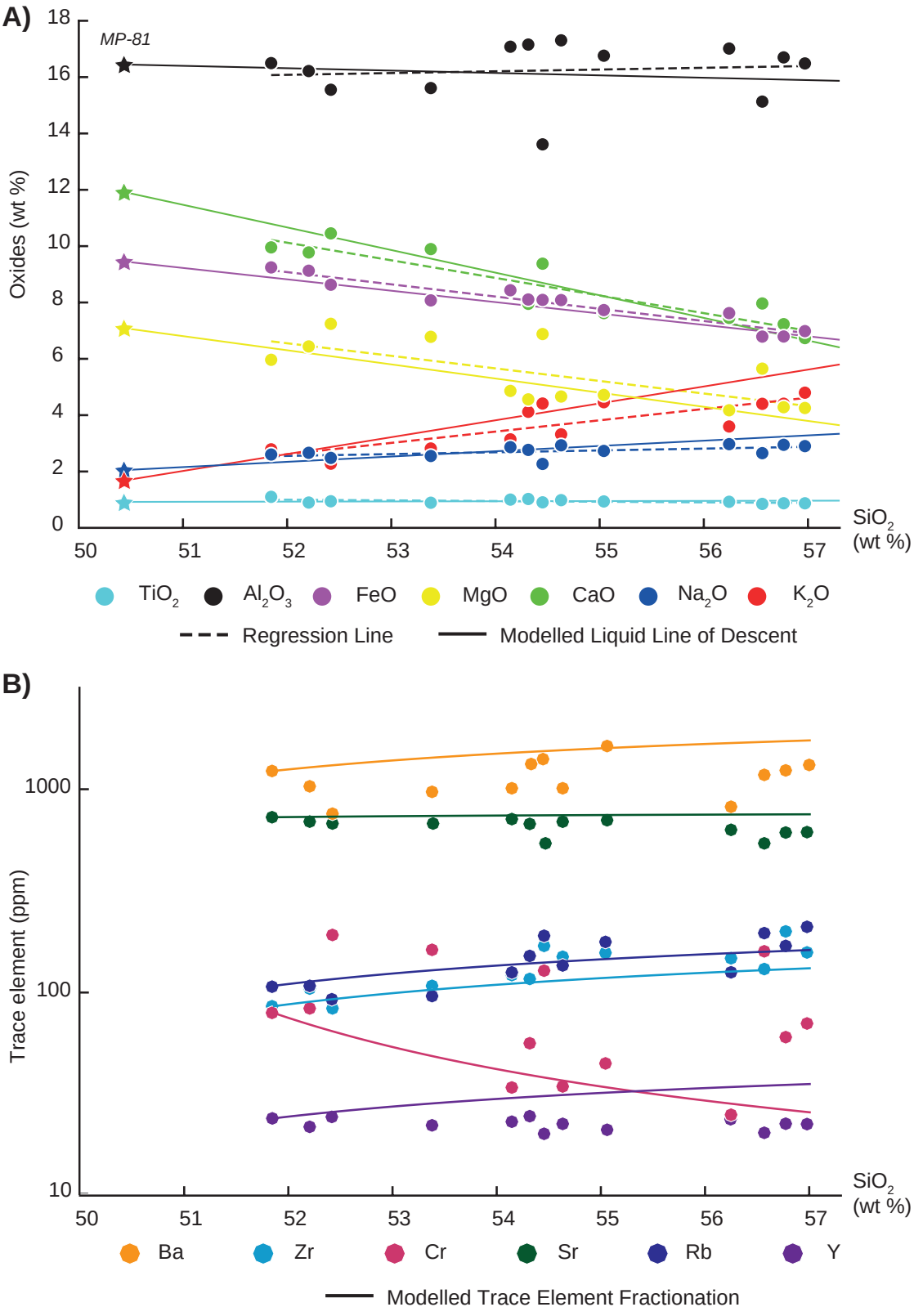

Figure 2.10: Modelled major (A) and trace element (B) distribution during clinopyroxene + orthopyroxene + plagioclase + magnetite fractionation in the absence of olivine (after Meen 1987). The distribution of Maronia samples can be closely reproduced by the model; see Table 2.5 for details of fractionating phase compositions and proportions, Table 2.6 for the partition coefficients for the trace element modelling, and Appendix F for details of the petrological modelling.

Table 2.5: Summary of the fractionation model. MP-81 was chosen as the starting composition as it had the most primitive mantle signature (a combination of low SiO_2, high Mg # and high Ni, Cr concentrations). The predicted liquid lines of descent can be found in Figure 2.10 plotted alongside the whole-rock analyses.

	SiO_2 wt.%	TiO_2 wt.%	Al_2O_3 wt.%	FeO wt.%	MgO wt.%	CaO wt.%	Na_2O wt.%	K_2O wt.%	Model Proportions
MP 81 *	49.28	0.90	16.08	9.25	6.94	11.67	2.00	1.63	-
Clinopyroxene	54.08	-	-	5.79	14.89	25.24	-	-	15%
Orthopyroxene	56.99	-	-	10.89	32.12	-	-	-	25%
Plagioclase	49.58	-	32.35	-	-	15.1125	2.955	-	52%
Magnetite	-	10.72	-	89.28	-	-	-	-	8%

Table 2.6: The trace element mineral:melt partition coefficients used for fractionation modelling.

	Sr (ppm)	Ba (ppm)	Cr (ppm)	Rb (ppm)	Zr (ppm)	Y (ppm)
Clinopyroxene	0.128 [a]	0.0007 [a]	3.8 [a]	0.011 [b]	0.123 [a]	0.47 [a]
Orthopyroxene	0.0012 [c]	0.004 [d]	7.8 [d]	0.004 [d]	0.032 [c]	0.095 [c]
Plagioclase	2 [e]	0.5 [e]	0.08 [e]	0.2 [e]	0.006 [e]	0.01 [e]

(*a*) Hart and Dunn (1993)
(*b*) McKenzie and O'nions (1991)
(*c*) Green et al. (2000)
(*d*) Adam and Green (2006)
(*e*) Bindeman et al. (1998)

magmatic suite driving the H_2O content of the parental source region down, the later Maronia magmas could be generated from an H_2O-poor ($<\sim$ 2 wt.%) source region in which pyroxene + plagioclase are stable instead of olivine. The generation of shoshonitic magmas at Maronia requires a change in mantle melting conditions between the intrusion of the Kassiteres–Leptokaria magmatic complex and intrusion of the Maronia pluton. We suggest that the temporal break (2.2 Myrs) in recorded magmatism in the MMC is the result of H_2O loss in the source mantle driving up the solidus temperature such that, between intrusion of Kassiteres–Leptokaria and Maronia, the source mantle was at sub-solidus conditions. We propose that prolonged heat conduction from the upwelling thermal anomaly beneath the Kechros dome in the intervening 2.2 Myrs is a potential source for the additional heat input required. Resultant melting of the H_2O-poor source mantle stabilized a pyroxene + plagioclase–dominated fractionating assemblage and generated a shoshonitic LLD at Maronia. A similar mechanism of restricted H_2O flux into a metasomatized mantle source is suggested for the generation of the shoshonitic volcanics in the Aeolian arc, Italy (e.g., Peccerillo et al. 2013; Beermann et al. 2017).

2.5.4 Summary of Magmatism and Extension in the Northern RCC

Post-collisional magmatism in the northern RCC began in the mid-Eocene, contemporaneous with a period of trans-crustal extension and core complex exhumation, and continued into the Oligocene (Table 2.2; e.g., Marchev et al. 2005; Rohrmeier et al. 2013). This phase of post-collisional extension is attributed to the collapse of thickened orogenic lithosphere induced by slab rollback of the N-ward subducting African plate (e.g., Jolivet and Brun 2010; Ring et al. 2010; Burg 2011; Kydonakis et al. 2015b). Eocene – Oligocene magmatism from across the northern RCC has a strong enriched metasomatic mantle signature, the result of asthenospheric mantle upwelling beneath thinned lithosphere remobilizing and re-melting the

sub-continental lithospheric mantle (e.g., Pe-Piper et al. 2009).

In the Kechros dome, Eocene crustal extension was accommodated by tectonic unroofing of the lower-crustal gneisses along the Kechros detachment fault, a trans-crustal structure that would be later exploited by post-collisional magmatism (Marchev et al., 2010; Márton et al., 2010). An Oligocene, high-K calc-alkaline magmatic event at 32.9–32.0 Ma in the southern Kechros dome resulted in the intrusion of the Kassiteres–Leptokaria magmatic suite, a high-K calc-alkaline series of intrusions with a strong subduction-related sub-continental lithospheric mantle signature. Following a 2.2 Myr break in magmatism, the intrusion of the shoshonitic Maronia pluton marks the last magmatic activity in the Kechros dome prior to tectonic change. The potassic intrusion, enriched in incompatible and volatile elements, marks an anomalously hot, short period of magmatism in the Kechros dome. Melting of a now H_2O-poor ($<\sim$ 2 wt.% H_2O) mantle source fractionated plagioclase + pyroxene to produce the Maronia intrusion and marked the culmination of asthenospheric heating of a mature, Cretaceous metasomatized lithospheric mantle. We suggest that the termination of magmatism in the Kechros dome following the intrusion of the Maronia pluton at 29.6 Ma, reflects the southward migration of the asthenospheric upwelling, switching off the heat source for mantle melting beneath the Kechros dome. We hypothesize that the asthenospheric upwelling migration is co-incident with initiation of SW-rotation of the southern RCC as described by van Hinsbergen et al. (2008) and others. The continuation of post-collisional magmatism in the southern RCC, such as the Miocene shoshonitic magmatism in Samothraki (e.g., Christofides et al. 2000) and Skouries (e.g., Siron et al. 2016) reflects the persistence of asthenospheric upwelling beneath the southern RCC and melting of the mature, H_2O-poor ($<\sim$ 2 wt.% H_2O) mantle wedge.

2.6 Conclusions

The MMC intrusions provide chronological markers and geochemical tracers that record the petrogenetic evolution of magmatism in the Kechros dome, northern RCC. Late Cretaceous to Oligocene extension of the northern Aegean resulted in asthenospheric mantle upwelling beneath the northern RCC, which provided a heat source for re-melting of the Cretaceous metasomatized mantle wedge. High-precision geochronology coupled with a full suite of whole-rock geochemical analyses, detailed field and petrographic observations, and petrological modeling demonstrate that:

1. The MMC does not represent a continuous magmatic period between 35 and 28 Ma (Del Moro et al., 1988) but two, temporally and geochemically distinct, magmatic complexes, the Kassiteres–Leptokaria magmatic suite and the Maronia plutonic complex. Intrusion of Kassiteres–Leptokaria was between 32.05 $\pm$ 0.02 and 32.93 $\pm$ 0.02 Ma, while magmatism at Maronia lasted from 29.60 $\pm$ 0.02 – 29.76 $\pm$ 0.02 Ma. In addition, it is recommended that the MMC zircon U-Pb data presented here are used in preference to Del Moro et al. (1988) to constrain the timing of magmatic activity in the MMC;

2. Extended hydrous ($3 <$ H_2O content $<$ 4.75 wt.%) partial mantle melting beneath the northern RCC allowed for the intrusion of batches of lithospheric mantle-source magma over an $\sim$900,000 year time scale at Kassiteres–Leptokaria;

3. The shoshonitic affinity of the Maronia samples reflects incompatible element enrichment produced by plagioclase + pyroxene–controlled mantle fractionation from a source mantle highly depleted in

H_2O($<\sim$ 2 wt.% H_2O); and therefore,

4. The temperature of mantle melting beneath the Kechros dome increased between intrusion of the Kassiteres–Leptokaria magmatic suite (at 32.9–32.0 Ma) and the Maronia pluton (29.8–29.6 Ma). Consequently, we suggest that the apparent 2.2 Myr break in recorded magmatism could be the result of a sub-solidus lithospheric mantle, and that heat accumulation in the intervening time period provided the heat required for the renewal of mantle melting.

Acknowledgments

This work was funded by a NERC GW4+ UK Doctoral Training Partnership Studentship (Grant: NEL0024341) and in part by the BGS University Funding Initiative (S276), which are gratefully acknowledged. Ben Buse and Stuart Kearns are thanked for their help with SEM analysis, and Dr. C. Gowing at the Inorganic Geochemical Facility at the British Geological Survey for the whole-rock geochemistry analyses. We would like to thank Katerina Gkika, Ery Hughes, and Simon Dahlström for assistance in the field, and the petrological modeling benefited greatly from discussions with Robert Loucks. D.J. Condon and J. Naden publish with the permission of the Executive Director, British Geological Survey (NERC). We thank Alexandre Kounov and two anonymous reviewers for their expert reviews, which have greatly improved the manuscript.

Chapter 3

A petrological study of the Maronia Magmatic Corridor, northeastern Greece: Constraining the intensive parameters during crystallisation

Author contributions and declaration:
This study was supervised by F. Cooper, B. Tattitch and J. Naden. All the mineral data presented in this chapter was collected by R. Perkins with the supervision and advice of S. Kearns on the microprobe and interpretation benefited from discussions with C. Chelle-Michou and A. Gilmer.

ABSTRACT

Constraining the intensive parameters (P, T, fO_2 and H_2O) of regional magmatism provides a first order assessment of the potential porphyry copper fertility of a magmatic terrane. Current paradigms of porphyry copper deposits suggest that the most fertile terranes result from oxidized, hydrous ($>$ 4 wt.% H_2O), calc-alkaline magmatism generated from partial melting of subduction-modified lithospheric mantle. In this study I assess the potential fertility of the Maronia Magmatic Corridor in northeastern Greece, a NE-trending belt of post-collisional, subduction-related high-K to shoshonitic intrusions. I use mineral chemistry of pyroxene, amphibole and plagioclase, in addition accessory mineral phase relationships, to constrain the P, T and H_2O content of the magmatism. Between 33 and 32 Ma, magmatism along the Maronia Magmatic Corridor was porphyry-fertile with $\sim$ 4.75 wt.% H_2O and final crystallisation occurred at the haplogranite solidus indicating the presence of an exsolved magmatic volatile phase. Remobilisation of an earlier, more hydrous phase of magmatism is suggested by antecrystic plagioclase and amphibole in textural disequilibrium with the host magmatism. The second intrusive magmatic period along the Maronia Magmatic Corridor occurred between 30 and 29.5 Ma and is less hydrous ($<\sim$ 2 wt.% H_2O). This suggests that, within our current understanding of the formation of porphyry copper deposits, the second period of magmatism along the MMC is less prospective for porphyry mineralisation.

3.1 Introduction

Metal-bearing porphyry intrusions are thought to emanate from evolved, hydrous magma-mush reservoirs stored in the upper crust, as is attested to by the close spatial relationship between porphyry-epithermal systems, shallow equigranular plutons and evolved volcanism (e.g., Dilles 1987; Sillitoe 2010). The abundance of porphyry – epithermal systems associated with regional, calc-alkaline magmatism in subduction or post-subduction settings suggests that the hydrous ($>$ 4 wt.% H_2O), oxidized (NNO $<$ fO_2 $<$ NNO + 2–4) magmas derived from partial melting of metasomatized mantle provide the ideal physiochemical conditions for the transport of metals and volatiles to the upper crust (e.g., Richards 2009; Sillitoe 2010). Consequently, constraining the extensive parameters of regional, host magmatism is of great importance for understanding the mineralising potential of a region (e.g., Chelle-Michou et al. 2015).

It has long been recognised that minerals archive the intensive conditions (P-T-fO_2-H_2O) of the magma from which they crystallise. As a result, a great deal of research has focused on understanding the phase relations of basaltic to granitic magmas in order to define conditions of melt evolution and storage in magmatic systems (e.g., Scaillet et al. 2016 and references therein). Quantitative constraints on phase relations can be provided by experimental studies and/or thermodynamic modelling. These are expensive and time intensive techniques and so the datasets are limited (e.g., Scaillet et al. 2016; Zhao et al. 2017). A simpler approach of detailed petrology, both mineral chemistry and textural phase relationships, can be used in tandem with existing experimental and thermodynamic literature to define regions of P-T-fO_2-H_2O space in which magma was stored (e.g., Chelle-Michou et al. 2015; van Zalinge et al. 2017).

Paradigms of magma storage and accumulation in the upper crust have shifted significantly in the last two decades, away from the classical view of large, predominantly molten magma chambers in the shallow crust, towards a series of inter-connected crystal mush lenses that accumulate over 100,000s yrs in short-lived pulses (100–1,000 yrs) of melt injection (e.g., Annen et al. 2006; Annen 2009; Menand et al. 2015). Variations in geochemistry and petrology across zones of plutons are thought to be both inherited from lower crustal fractionation and generated during magma emplacement (e.g., Coleman et al. 2004; Annen 2009). The different compositions reflect *xenocrystic*, phenocrysts entrained from crustal wall-rock, *antecrystic*, phenocrysts crystallised from the same batch of magma but at different conditions, and *autocrystic*, phenocrysts crystallised during pluton assembly and emplacement, crystal cargos and their complimentary residual melts. Consequently, resorption, zoning and magmatic breakdown of phenocrysts in plutons record the evolution of the melt as it transits through the crust and can be used to reconstruct the conditions of magma crystallisation during melt storage and emplacement.

In this chapter, I combine textural relationships between mineral phases with mineral chemistry to constrain the melt evolution of the Maronia Magmatic Corridor (MMC). I compare the mineral archive of crystallisation from three different systems in the MMC: *(i)* the Maronia pluton, a shoshonitic stock-like intrusion hosted in metasedimentary basement, *(ii)* the Kassiteres pluton, a high-K calc-alkaline intrusion hosted in the same metasedimentary basement, and *(iii)* the Leptokaria complex, a series of high-K calc-alkaline intrusions hosted in a core complex gneiss dome. Conditions of magma storage and pluton assembly are then related to the mineralising potential of the MMC through space and time. This builds upon the work presented in Chapter 2, detailing dehydration of the source mantle in the 2.2 Myr period between high-K calc-alkaline magmatism and shoshonitic magmatism.

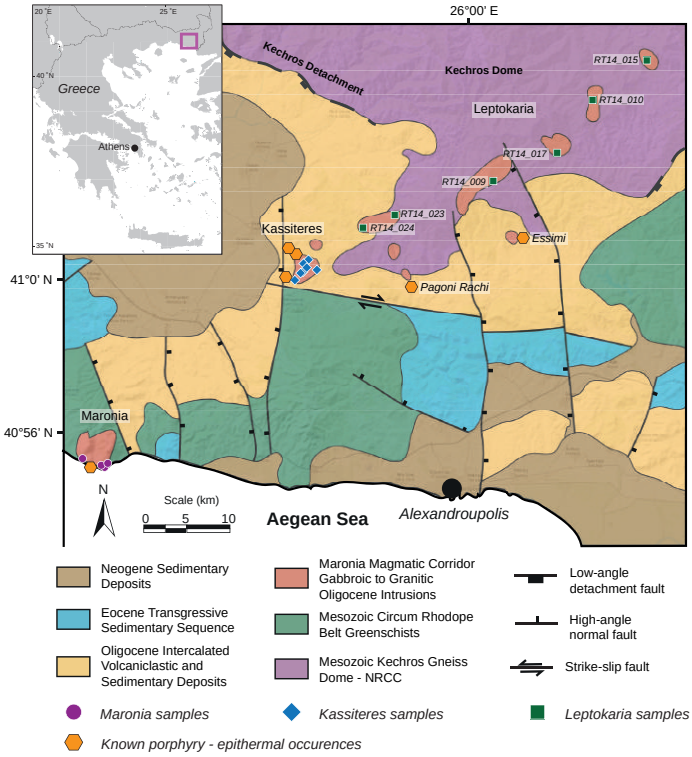

Figure 3.1: A geological map of the Maronia Magmatic Corridor, intruded along the southeastern margin of the Kechros dome (first presented in Chapter 2). Locations of each of the samples used in this chapter are marked on the map and samples numbers are given for the Leptokaria intrusions to show their spatial distribution. The known mineralised systems are labelled, notably they are all located in the hanging wall of the core complex.

3.2 The Maronia Magmatic Corridor

The MMC is a NE-trending belt of Oligocene, high-K calc-alkaline to shoshonitic plutons that intrudes the northern Rhodope Metamorphic Core Complex (RCC) in northeastern Greece (Fig. 3.1; Del Moro et al. 1988; Chapter 2). The northern RCC itself is an E-trending series of gneiss domes, exhumed from the lower crust during Eocene – Oligocene back-arc extension of the northern Aegean (e.g., Burg 2011; Kydonakis et al. 2015a). Post-collisional Oligocene magmatism punctuates across the northern RCC generated by extension-induced asthenospheric upwelling, heating subduction-modified lithospheric mantle (e.g., Pe-Piper et al. 2009; Chapter 2).

The MMC is situated at the southeastern margin of the eastern-most gneiss dome of the northern RCC, the Kechros dome and intrudes two different metamorphic basement lithologies: the granulite- to amphibolite-facies, ortho- and para-gneisses of the Kechros dome footwall, and the greenschist facies, metasedimentary units of the Circum Rhodope Belt (CRB) in the hanging wall of the Kechros dome (Fig. 3.1). Ten outcropping intrusions make up the MMC. They can be sub-divided on the basis of geochemistry into the shoshonitic Maronia pluton and the high-K calc-alkaline Kassiteres–Leptokaria intrusive complex (Chapter 2). This chapter further separates the Kassiteres–Leptokaria intrusive complex into the Kassiteres pluton and the Leptokaria complex; the Kassiteres pluton is solely hosted in the CRB in the hanging wall of the Kechros dome, whilst the Leptokaria intrusive complex intrudes the gneisses of the Kechros dome footwall.

Kassiteres

The dioritic to granodioritic Kassiteres pluton lies in the hanging wall of the Kechros dome, $\sim$ 2 km SW of the Kechros detachment, at the boundary between the CRB and overlying Eocene sediments (Fig. 3.1). It is overlain by Oligocene volcanic rocks including lava domes, ash-beds and pyroclastic flows (Voudouris et al., 2006). In Chapter 2, Kassiteres was discussed as part of the high-K calc-alkaline phase of magmatism

that intruded over an 900,000 year period between 32.0–32.9 Ma. In this chapter, Kassiteres is considered separately to the Leptokaria complex as it is the only intrusion hosted in the hanging wall of the Kechros dome, at a higher structural level in the crust.

Multi-centred, telescoped porphyry – epithermal mineralisation at Kassiteres is associated with the intrusion of a quartz-feldspar porphyry into the host Kassiteres pluton. Early, Cu-Mo-Au porphyry-style mineralisation is hosted in veinlets and vein stockworks (Voudouris et al., 2006; Melfos and Voudouris, 2017). Epithermal mineralisation is superimposed on pervasive alteration associated with the earlier phase of porphyry mineralisation, and is disseminated throughout the porphyry intrusion and overlying volcanic rocks (Voudouris et al., 2006). Two stages of epithermal veining are observed: early alunite + barite ± quartz veins host precious metal (Au, Ag) mineralisation associated with pyrite; later cross-cutting quartz + carbonate ± adularia veins are predominantly barren with minor base metal (Pb-Zn) associations (Voudouris et al., 2006; Voudouris, 2006; Melfos and Voudouris, 2017). At the time of writing (May, 2018), mineral exploration at Kassiteres is ongoing with land rights over most of the area owned by Eldorado Gold.

Leptokaria

Intruded into the Kechros dome footwall, the Leptokaria complex is a series of high-K calc-alkaline intrusions that were emplaced contemporaneously with the Kassiteres pluton between 32.0–32.8 Ma (Chapter 2). The Leptokaria complex is hosted in para- and ortho-gneisses in the core of the Kechros dome. Where the intrusions cut the Kechros detachment pegmatitic leucogranites are also found hosting magmatism. The Leptokaria intrusions range in composition from dioritic to granitic with cumulate textures preserved in some samples.

No porphyry or epithermal mineralisation has been identified hosted by the Leptokaria complex in the footwall of the Kechros dome, consistent with field observations made during this study. A $\sim$ 1 m-wide porphyritic dyke cuts the Leptokaria complex close to the sampling locality of RT14_009 (Fig. 1) with no mineralisation or veining observed. However, the Pagoni Rachi and Essimi (Myli) telescoped porphyry – epithermal systems are located off the magmatic lineament in the hanging wall of the Kechros dome and are not spatially associated with outcropping equigranular host magmatism. (Fig. 1; e.g., Melfos and Voudouris 2017). Sulphide-hosted Cu-Au-Mo mineralisation (pyrite + chalcopyrite + bornite + molybdenite) is disseminated throughout the causative porphyry intrusions and in quartz vein stockworks at both systems (Voudouris, 2006; Voudouris et al., 2009, 2013b,a). Pagoni Rachi is also host to the most Re-rich molybdenite – rheniite recorded from a porphyry – epithermal system (Voudouris et al., 2009, 2013b,a).

Maronia

The Maronia pluton is a gabbro – quartz monzonite hosted in the CRB, at the southwestern end of the MMC (Fig. 3.1). Emplaced over a 200,000 yr period between 29.8–29.6 Ma, the Maronia pluton marks the end of magmatism in the northern RCC (Chapter 2). A calcic endoskarn is observed in the contact aureole at the western margin of Maronia, where the pluton is hosted in a marble facies of the CRB (Katerinopoulou et al., 2009). The eastern margin of the Maronia pluton is in contact with pelitic schists units of the CRB with a minor hornfels aureole developed (Mposkos and Doryphoros, 1993).

A quartz-feldspar porphyry intrudes the Maronia pluton and hosts high-grade Cu-Mo-Au mineralisation (0.5 wt.% Cu, 0.8 wt.% Mo, 1 ppm Au) in vein-hosted and disseminated sulphides and sulphates (Melfos et al.,

2002). Mineralisation is restricted to the fault bound margins of the porphyry intrusion which entrain wedges of intensely mineralised schists from the CRB basement. Quartz-hosted fluid inclusions and sulphide S-isotope data indicate a magmatic-derived mineralising fluid between 280–460 °C and 0.15–0.5 kbars suggesting high-level mineralisation in the uppermost crust (Melfos et al., 2002).

3.3 Methods

3.3.1 Petrography

Thirty-one standard polished thin sections were prepared for from a representative selection of the MMC equigranular intrusive units (Appendix A). Petrographic observations of these samples were made under both transmitted and reflected light to identify a subset of the least-altered thin sections for further petrology. The subset, comprised of two thin sections from Maronia, two from Kassiteres and six from Leptokaria, covers each of the outcropping localities at Leptokaria; an additional nine polished epoxy mounts were made (three from Maronia and six from Kassiteres) to supplement the sample set from these locations. Scanning electron microscope (SEM) analysis was undertaken at the University of Bristol on a Hitachi S-3500 N instrument with 20 kV accelerating voltage and a 15 mm working distance. Phase identification was performed using energy dispersive spectra (EDS) and back-scatter electron (BSE) imagery was used to establish key textural relationships.

3.3.2 Electron Probe Microanalysis

Mineral chemistry of feldspars, amphiboles and pyroxene was determined by electron probe micro-analysis (EPMA) using wavelength dispersive spectroscopy (WDS) at the University of Bristol using a Cameca SX100. Operating conditions of 20 kV, 10 nA and a 5 μm beam diameter were used with counting times of 10–100 s. Na, K, Ca and Si were always measured first to minimise the effect of alkali migration on the analyses (full count times and calibration procedures can be found in Appendix G). Coupled amphibole – plagioclase and clinopyroxene – orthopyroxene analyses were taken at the rims of crystals in apparent textural equilibrium to ensure the compositions at the final stages of crystallisation were captured. Mineral analyses with either analysis totals < 98 wt.% or > 102 wt.% in plagioclase and pyroxene (where expected stochiometric totals are 100 wt.%) and < 95 wt.% or > 100 wt.% in amphibole (where expected stochiometric totals are 97–98 wt.%) were rejected as bad analyses.

3.4 Petrography

Petrographic textures of thin sections from across the MMC have been used to determine crystallisation histories of each of the intrusions. The main features of each locality are outlined below and in Table 3.1. Details of the modal composition of the samples and phase relationships can be found in Appendices D and H respectively.

3.4.1 Maronia

Maronia exhibits a poikilitic texture with phenocrysts of clinopyroxene, orthopyroxene, plagioclase and Fe-Ti oxides and less abundant primary biotite and accessory apatite $\pm$ zircon. K-feldspar is the dominant interstitial phase, often forming 1–3 cm oikocrysts encompassing chadacrysts of plagioclase and pyroxene;

Table 3.1: Key petrographic features of each of the Maronia Magmatic Corridor; the modal composition, phase relations and crystallisation sequence of each sample can be found in Appendices D and H. Acc. Min. – accessory minerals; Plag. – plagioclase; Px – clino- and ortho-pyroxene; Hbl – hornblende; Phen. – phenocrystic hornblende; Can. – cannibalistic and poikilitic hornblende; Ksp – K-feldspar; Qtz. – quartz; Bt. – biotite; Amph. – amphibole; Chl. – chlorite; Ap. – apatite; Zr. – zircon. The lighter shades indicate the presence of the minerals in only some of the samples from that locality; *n* = number of thin sections/epoxy mounts analysed.

	Composition	*Primary Phases*							*Secondary Phases*			*Acc. Min.*	
		Plag.	Px.	Bt.	Hbl. Pheno.	Hbl. Can.	Ksp	Qtz.	Amph.	Bt.	Chl.	Ap.	Zr.
Maronia *n* = 5	Gabbro to quartz monzonite												
Kassiteres *n* = 8	Diorite to granodiorite												
Leptokaria *n* = 6	Gabbro to tonalite												

minor interstitial quartz (< 5 % by area) is present in the more evolved samples. Co-crystallisation of clinopyroxene, orthopyroxene, plagioclase and Fe-Ti oxides is suggested by textural relationships. Inclusions of apatite in all of the major phenocryst phases suggests apatite saturation close to, or at, the liquidus. Zircon occurs only in interstitial quartz suggesting localised saturation of zircon during the final stages of melt crystallisation. Hydrothermal alteration is pervasive throughout the pluton although the primary magmatic features are still preserved; amphibole, biotite and chlorite are the common alteration products of the ferromagnesian phases whilst sericitisation of plagioclase and K-feldspar is ubiquitous. Minor hydrothermal alteration of plagioclase to calcite is also observed in samples close to the pluton – marble contact.

3.4.2 Kassiteres

Mineralogical textures at Kassiteres indicate co-crystallisation of major phenocrystic phases: clinopyroxene, orthopyroxene, hornblende, plagioclase and Fe-Ti oxides, whilst minor phases, K-feldspar, biotite and quartz crystallised later. Hornblende is present cannibalizing clinopyroxene and as 'poikilitic' and euhedral phenocrysts, although, not all clinopyroxene phenocrysts have hornblende overgrowths. Quartz and K-feldspar make up the interstitial phases with granophyric textures common. Unlike at Maronia, inclusions of apatite are found only in the later crystallising phases, quartz, K-feldspar and plagioclase, indicating the later apatite appearance of apatite on the solidus. Conversely, zircon is found as inclusions in plagioclase, K-feldspar and quartz demonstrating earlier saturation in zircon than at Maronia. Secondary alteration of pyroxene and hornblende to chlorite and sericitisation of plagioclase and K-feldspar is pervasive.

3.4.3 Leptokaria

At Leptokaria the phase relations are more complex. The major phenocryst phases are: clinopyroxene, hornblende, plagioclase, biotite and Fe-Ti oxides. Clinopyroxene is cannibalized by hornblende and is rarely found as well-preserved phenocrysts. Hornblende can be found in three distinct morphologies: *(i)* originally euhedral hornblende phenocrysts that have been resorbed (in RT14_010/RT14_017 only), *(ii)*

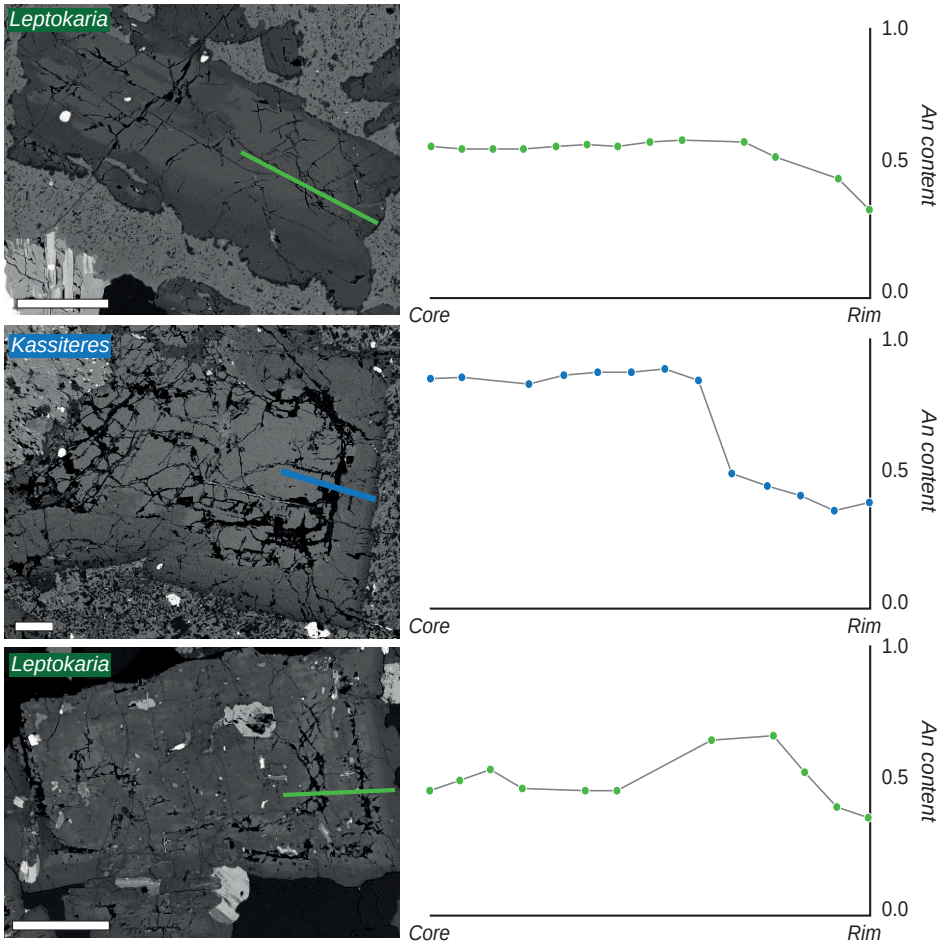

Figure 3.2: Back scattered electron (BSE) images and typical core – rim profiles of the three different plagioclase morphologies described from the Maronia Magmatic Corridor. An content = molar anorthite content of the plagioclase spot analysis. Each of the white scale bars represents 200 μm.

poikilitic hornblende forming along the boundary between plagioclase crystals and, *(iii)* euhedral hornblende phenocrysts that consume relict clinopyroxene. Plagioclase is the most abundant phenocrystic phase in all of the samples with the cores typically more altered than the rims. Biotite is present as a primary magmatic phase, included in plagioclase and hornblende, and also as a secondary breakdown product of the ferromagnesian minerals. Fe-Ti oxides are found included in all of the phenocrystic minerals. Quartz and K-feldspar are the major interstitial phases and granophyric intergrowths are much less prevalent than at Kassiteres and found only in samples RT14_009/RT14_023/RT14_024. Zircon and apatite are accessory minerals. Zircon is commonly present in quartz, K-feldspar and occasionally in plagioclase indicating zircon saturation late in the crystallisation history. Apatite has a range of hosts including quartz, K-feldspar (where present) and plagioclase and occasionally in poikilitic hornblende. Sericitisation of plagioclase and hydrothermal break down of clinopyroxene and hornblende to chlorite and biotite is common.

3.5 Mineral Chemistry

3.5.1 Plagioclase

Plagioclase is the most abundant phenocrystic phase in all the samples collected from the MMC. An contents vary widely across each of the intrusions from An_{98-04} at Leptokaria, An_{62-04} at Kassiteres and An_{75-10} at Maronia. Three distinct plagioclase populations are distinguished based upon compositional zonation (Fig. 3.2): *(i)* resorbed, originally euhedral phenocrysts with no internal textures but with decreasing anorthite content from $An_{(55-65)}$ in the core to $An_{(30-45)}$ at the rim and a minor 5–10 μm albitic boundary

layer found at the edge of some crystals; *(ii)* euhedral phenocrysts with high $An_{(85-60)}$ cores and lower $An_{(30-50)}$ rims; and *(iii)* euhedral phenocrysts with a core, intermediate zone and rim showing inverse zonation: the cores contain small, < 50 μm inclusions of Fe-oxides, clinopyroxene, amphibole and biotite but are compositionally homogenous between An_{55-60}; an intermediate zone of high $An_{(85-60)}$ and high relief, between 10–100 μm wide, separates the core from the simple, low $An_{(30-40)}$ rim. Plagioclases from Maronia are typically more enriched in Sr than Kassiteres or Leptokaria (500–1,500 ppm Sr at Maronia and 100–1,000 ppm Sr at Kassiteres and Leptokaria), in line with the elevated Sr and other incompatible elements in the shoshonitic pluton (Chapter 2). In all intrusions, the Sr content of the plagioclases closely follows the An zonation, decreasing with decreasing An content. There is a distinct population of plagioclase phenocrysts from Leptokaria with An > 80; these plagioclase crystals have Sr concentrations in the upper range of those observed at Leptokaria (500–1,000 ppm Sr) but fall off the main trend at Leptokaria where the more calcic plagioclases would be expected to have elevated Sr.

3.5.2 Amphibole

Amphibole occurs in all the intrusive units of the MMC. In the Kassiteres and Leptokaria samples, amphibole is present as primary euhedral phenocrysts, magmatic overgrowths around relict clinopyroxenes and as interstitial poikilitic growths (Fig. 3.3). At Maronia, amphibole is only present as a secondary breakdown product of primary clinopyroxene. Mineral chemistry of amphiboles from 15 samples were analysed by EPMA (1 from Maronia, 8 from Kassiteres and 6 from Leptokaria) with a total of 295 spot data collected. The ferric – ferrous iron content was calculated following the procedure of Holland and Blundy (1994) and cations were distributed between sites, normalising to 23 oxygens. All the amphiboles analysed are calcic (Ca per formula unit (pfu) > 0.79) and Mg-rich (Mg# $=$ Mg/Mg $+$ Fe^{2+} pfu > 0.79). Following the classification of (Leake et al., 1997), most amphiboles range from tremolite to magnesiohornblende in composition (Fig. 3.3).

Multiple populations of amphiboles can be distinguished using the Si and Al_{TOT} (pfu). Tremolites with Si > 7.5 and $Al_{TOT} < 0.5$ pfu are present in both the Kassiteres and Leptokaria samples with a greater proportion of tremolites found at Kassiteres. Higher Si, Ca and Mg# and lower K, Na and Fe (pfu) in the tremolites suggest that these are fluid-altered amphiboles. The tremolites are also typically pale-green in colour and non-pleochroic, suggestive of secondary alteration; this is in line with the greater prevalence of fluid-altered amphiboles at Kassiteres where potassic – propyllitic alteration is pervasive and more intense than across the Leptokaria intrusions. A population of intermediate-Al_{TOT} magnesiohornblendes ($0.5 <$ Al_{TOT} pfu < 0.9) with Si pfu from 7.5–7.3 are also present at both Kassiteres and Leptokaria. These hornblendes are more abundant at Leptokaria where the spread in Al_{TOT} is slightly larger (Fig. 3.3E). High-Al_{TOT} (Al_{TOT} pfu > 1.0) magnesiohornblendes and edenites are found at Leptokaria only in samples RT14_017 and RT14_010. The high-Al_{TOT} hornblendes are associated with the greatest frequency of tschmermak- and edenite-exchanges suggesting they record deeper crystallisation conditions. The high-Al_{TOT} hornblendes are typically euhedral with resorbed rims and are green-brown in colour with no pleochroism (Fig. 3.3C,D), whilst the intermediate-Al_{TOT} hornblendes are typically poikilitic or euhedral phenocrysts replacing clinopyroxene and exhibit green-dark green pleochroism (Fig. 3.3A,B). Decreasing Cl with decreasing Al_{TOT} is observed in the intermediate-Al_{TOT} magnesiohornblendes (from 2,500 to 1,000 ppm Cl). The high-Al_{TOT} hornblendes have consistent, lower Cl concentrations ($<$ 1,000 ppm) which do not vary with Al_{TOT}, whilst no trend is observed in the Cl concentration of the tremolites.

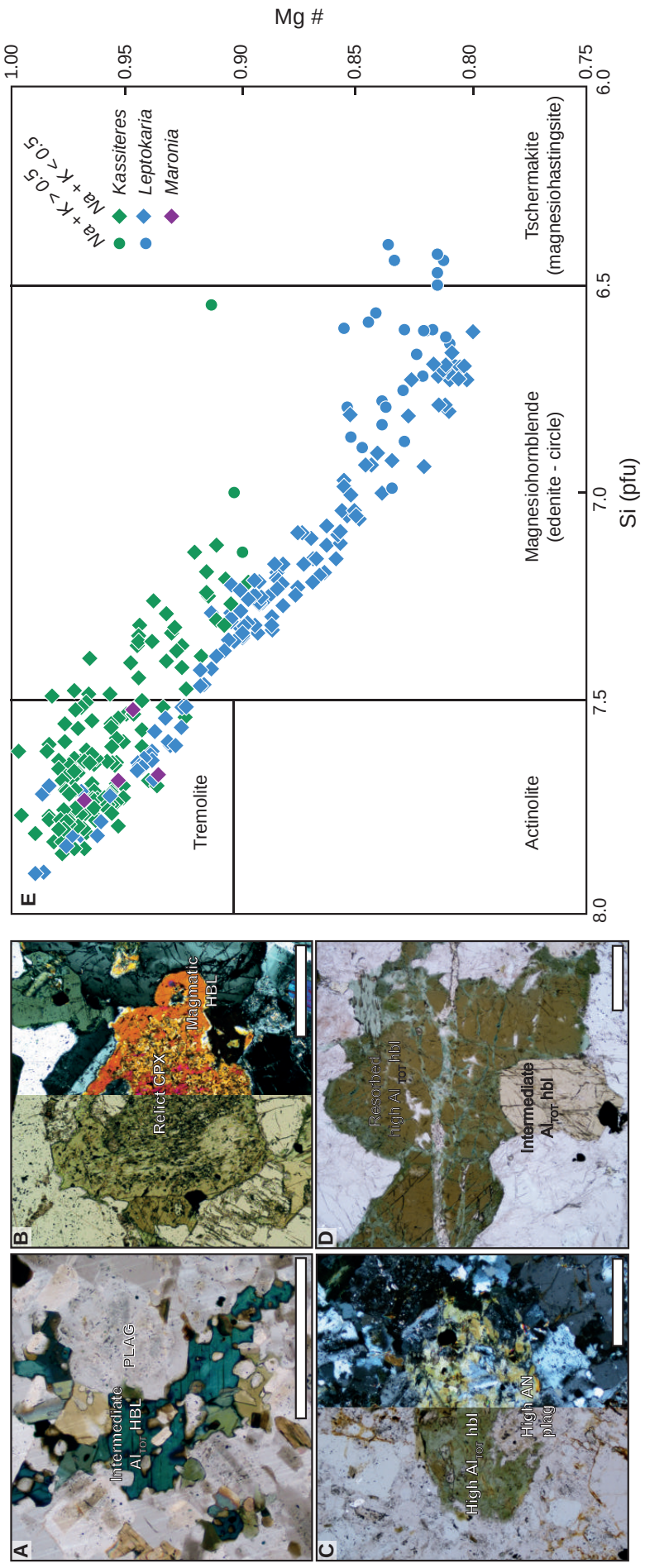

Figure 3.3: (A-D): Photomicrographs of typical Maronia Magmatic Corridor amphiboles. (A): Poikilitic intermediate-Al$_{TOT}$ magnesiohornblende with minor alteration to tremolite, recognisable by its pale colour and birefringence. (B): A euhedral intermediate-Al$_{TOT}$ magnesiohornblende (HBL) grown around a relict clinopyroxene (CPX) in a peritectic reaction. (C): High-Al$_{TOT}$ magnesiohornblende/edenite in equilibrium with high An plagioclase and is intensely altered by chlorite. (D): Originally euhedral high-Al$_{TOT}$ magnesiohornblende/edenite with resorption textures and overgrowth of an intermediate-Al$_{TOT}$ magnesiohornblende. (E): Amphibole classification after (Leake et al., 1997). Diamonds represent amphiboles with Na + K (per formula unit, pfu) < 0.5 whilst the circles are amphiboles with Na + K (pfu) > 0.5 that fall in the edenite or magnesiohastingsite regions. Three populations of amphibole can be distinguished based upon Si and Al$_{TOT}$ (pfu): high Si (> 7.5) and low-Al$_{TOT}$ (< 0.5) tremolites, intermediate Si (7.5–7.3) and intermediate-Al$_{TOT}$ (0.5–1.1) magnesiohornblendes and low Si (< 7.3) and high-Al$_{TOT}$ (> 1.0) magnesiohornblendes, edenites and magnesiohastingsites (see Table 3.2 for representative analyses of each group).

Table 3.2: Representative mineral chemistry of plagioclases, amphiboles and pyroxenes from the Maronia Magmatic Corrirdor. See Appendix G for full EPMA results used for geothermobarometry. CPX – clinopyroxene; OPX - orthopyroxene; Wo – woolastonite; En – enstatite.

	Plagioclases							*Amphiboles*						*Pyroxenes*	
	low	int.	low	int.	high	low	int	int	low	high	int.	low	low	OPX	CPX
	K	K	L	L	L	M	M	K	K	L	L	L	M	M	M
Major Element Oxides (wt.%)															
SiO_2	59.04	53.26	61.41	51.45	45.91	58.27	51.29	50.11	53.20	46.00	50.13	55.76	53.56	52.48	52.13
TiO_2								1.06	0.60	1.54	0.79	0.45	0.15	0.22	0.30
Al_2O_3	25.21	29.07	24.24	30.12	33.95	25.71	30.66	5.13	2.85	8.63	4.84	1.86	1.36	0.76	1.27
Cr_2O_3								0.04	0.06			0.04	0.04		
FeO	0.48	0.56	0.24	0.50	0.63	0.32	0.35	12.68	9.15	15.56	13.55	10.27	14.92	23.02	11.10
MgO				0.03	0.02	0.02	0.02	15.74	18.34	12.68	15.25	17.84	14.26	21.63	14.40
CaO	7.45	11.96	5.64	13.00	17.90	8.05	13.93	11.48	11.53	11.13	11.39	10.75	12.75	0.75	20.12
MnO								0.24	0.24	0.47	0.32	0.35	0.54	1.48	0.45
Na_2O	7.08	4.77	8.56	4.04	1.44	6.52	3.72	1.27	0.87	1.29	0.99	0.99	0.16	0.00	0.26
K_2O	0.37	0.27	0.40	0.19	0.03	0.40	0.08	0.47	0.24	0.36	0.47	0.16	0.06	0.01	0.00
TOTAL	99.67	99.96	100.52	99.41	99.99	99.39	100.16	98.55	97.73	98.05	97.91	98.53	97.79	100.35	100.04
Trace Elements (ppm)															
Sr	344	569	221	569	872	805	1038								
Cl								1930	1208	357	1618	586			
An content	0.36	0.57	0.26	0.63	0.87	0.40	0.67								
Si (p.f.u)								7.2	7.6	6.7	7.2	7.8	7.8		
Al (IV) site								0.20	0.11	0.32	0.19	0.05	0.06		
Na + K (pfu)								0.44	0.28	0.43	0.36	0.30	0.05		
Mg #								0.91	0.94	0.80	0.89	0.97	0.95	0.63	0.70
Wo content														2.95	40.91
En content														60.04	40.74

3.5.3 Pyroxene

Pyroxenes are present across the Maronia and Kassiteres sample suite and in the some of the Leptokaria samples (Fig. 3.4A-C). Exsolution textures in pyroxenes result from augite – pigeonite – hypersthene immiscibility. At Maronia, exsolved pyroxenes are limited to sample RT14_006, from the edge of the intrusion, where a single generation of exsolution lamellae are preserved in both augite and hypersthene indicating rapid cooling. Pyroxenes from Kassiteres and Leptokaria are most commonly found as relict cores in amphibole phenocrysts where pervasive alteration of the ferromagnesian phases often obscures identification of exsolution textures in the relict pyroxenes. Where pyroxene phenocrysts are preserved, a single generation of exsolution lamellae are observed in augite and hypersthene.

Pyroxene mineral chemistry focused on the Maronia intrusions where 186 analyses were taken from 3 samples. Mineral projection calculations followed the protocol of Lindsley (1983) in the distribution of ferric – ferrous iron. Pyroxenes from Maronia are dominated by Ca, Mg and Fe with minor substitution of Na ($<$ 0.4 wt.%), Mn ($<$ 0.9 wt.%) and Cr (below the detection limit, 0.02 wt.%). The pyroxenes are moderately magnesian, with higher Mg# in the clinopyroxenes (median Mg# $= 0.72$) than the orthopyroxenes (median Mg# $= 0.63$). The clinopyroxenes plot at the diopside – augite boundary with median $Wo_{43.2}$ (Fig. 3.4D). The dominance of Mg-rich clinopyroxenes relative to orthopyroxene in shoshonites has been noted before (e.g., Morrison 1980). This may be the result of increased Ca activity in the shoshonitic melt pushing clinopyroxene towards the Mg (diopside) end member in order to remain in equilibrium with co-crystallising orthopyroxene following the topography of the temperature-contoured pyroxene quadrilateral of Lindsley (1983) (Fig. 3.4D).

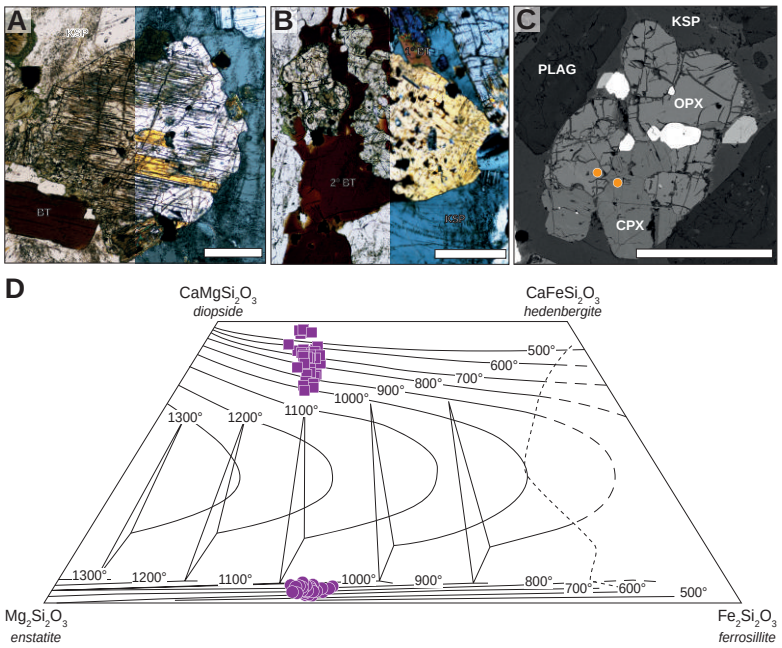

Figure 3.4: (A): Inverted pigeonite with a single phase of exsolution lamellae from Kassiteres. (B): Primary clinopyroxene from Maronia with a single phase of exsolution lamellae and secondary hydrothermal biotite overgrowth and alteration along cleavage planes. (C): A back scattered electron (BSE) image of apparent textural equilibrium between clinopyroxene (CPX) and orthopyroxene (OPX) from Maronia sample RT14_003. The orange circles indicate the typical textural relationship between paired analyses. (D): Mineral chemistry of pyroxenes from Maronia overlain on the isotherm contoured pyroxene quadrilateral of Lindsley (1983).

3.6 Intensive Parameters

Crystallisation of minerals records the intensive and extensive properties of a system at a particular instant in time. An understanding of the intensive parameters of a magma during crystallisation is vital to understand the petrogenesis of a magmatic system as solidus and liquidus phase relations are dependent upon pressure (P), temperature (T) and volatile content, amongst other intensive parameters. Geothermobarometry uses P- and T- dependant equilibrium cation-exchange between mineral phases to constrain the intensive parameters of an igneous system at crystallisation. Geothermobarometers can be calibrated by thermodynamic calculations, experimental data or a combination of the two, and are used to inform on the conditions of pluton assembly.

3.6.1 Temperature

In this chapter I will discuss two techniques used to estimate crystallisation temperatures: mineral equilibria thermometry and accessory mineral saturation thermometry. Mineral equilibria thermometers utilize chemical equilibria between mineral phases that have a large change in entropy (ΔS) over a small change in volume (ΔV) and so are highly sensitive to changes in temperature. The amphibole – plagioclase and two-pyroxene equilibrium cation-exchange thermometers are presented for the Kassiteres–Leptokaria and Maronia intrusions respectively. Accessory mineral saturation thermometers are used to assess the temperature of accessory mineral crystallisation using a range of experimentally determined solubility relationships and as such are powerful tools for constraining the thermal evolution of a magmatic system (e.g., Watson 1979; Watson and Harrison 1983; Harrison and Watson 1984; Pichavant et al. 1992; Tollari et al. 2006; Boehnke et al. 2013). Apatite and zircon are abundant accessory minerals in the MMC intrusions, and the use of both saturation thermometers, in tandem with detailed documentation of accessory mineral inclusion textures, are used to assess crystallisation temperatures.

Plagioclase – Amphibole Thermometry

The aluminium content of equilibrium plagioclase – amphibole pairs varies systemically with P, T and bulk composition (Hollister et al., 1987; Blundy and Holland, 1990). These relationships, together with the predominance of both minerals as a major crystallising phases in intermediate to evolved assemblages, make for an ideal geothermobarometer in dioritic to granitic systems (e.g., Mutch et al. 2016; Putirka 2016). In granitoid systems close to the solidus, there is little variance in the bulk composition meaning that substitution of Al into the amphibole lattice is dependent only on the intensive variables P and T (Hollister et al., 1987). There are two important plagioclase – amphibole substitutions: the T-dependent edenite substitution of Na between plagioclase and amphibole (Holland and Blundy, 1994), and the P-dependent tschermak substitution of Al between plagioclase and calcic amphibole – hornblende (Hollister et al., 1987). Blundy and Holland (1990) & Holland and Blundy (1994) calibrated two plagioclase – amphibole thermometers based upon the edenite exchange equilibria:

$$T^{A}_{plag} : \text{edenite} + 4\ \text{quartz} \longrightarrow \text{tremolite} + \text{anorthite}$$

$$T^{B}_{plag} : \text{edenite} + \text{albite} \longrightarrow \text{richterite} + \text{anorthite}$$

Crystallisation temperatures were calculated for Kassiteres and Leptokaria using both calibrations; Maronia was excluded from the plagioclase – amphibole thermometry calculations due to the absence of primary, magmatic amphibole. T^A_{plag} is applicable only to mineral assemblages with quartz, whilst T^B_{plag} is applicable to mineral assemblages without quartz. In quartz-absent systems T^A_{plag} should systematically over-estimate temperature whilst in quartz-bearing systems, T^A_{plag} and T^B_{plag} should overlap within error. If $T^B_{plag} > T^A_{plag}$, it indicates disequilibria between plagioclase and hornblende (Holland and Blundy, 1994); as a result, if estimates of $T^B_{plag} > T^A_{plag}$ then the paired analyses were discarded. I suggest that secondary alteration of plagioclase and/or amphibole results in compositional disequilibria between pairs in such situations. Of the remaining analyses, T^A_{plag} was used in final temperature estimates from samples where quartz is known to co-crystallise with plagioclase and amphibole (RT14_009/RT14_010/RT14_023/RT14_027/RT14_028 and KA15_013) and T^B_{plag} in samples where the presence of quartz is unknown (RT14_015/RT14_017). An uncertainty of $\pm$ 80 °C (2σ) is reported by Holland and Blundy (1994), combining analytical errors from EPMA with uncertainties associated with the thermometer calibrations, therefore, all individual T_{plag} estimates are reported with a 2σ uncertainty of $\pm$ 80 °C.

At Kassiteres, the plagioclase – amphibole thermometer predicts a consistent crystallisation temperature across the three samples with equilibrium pairs ranging from 925 to 604 °C. A mean square weighted deviation (MSWD) or reduced chi^2 test was performed on the data using 2σ uncertainty and assuming a unimodal normal distribution of temperature estimates, to estimate an error-weighted mean crystallisation temperature of 708 $\pm$ 17 °C (MSWD = 0.36, n = 23/24). At Leptokaria the plagioclase – amphibole thermometer predicts a wider range of temperatures from 1002 to 556 °C. A bimodal distribution of temperatures is visible in samples RT15_010 and RT14_017 which record high-T crystallisation ($>$ 800 °C) in addition to the low-T crystallisation recorded in the remaining Leptokaria samples. A mean low-T crystallisation temperature of 720 $\pm$ 13 °C (MSWD = 0.81, n = 38/38) and a mean high-T crystallisation temperature of 904 $\pm$ 14 °C (MSWD = 0.26, n = 34/34) were calculated. The high-T population is associated with a higher An content (mean An = 0.81) than the low-T population (mean An = 0.25). The weighted mean temperature estimates artificially collapse the uncertainties associated with the calibrations and so for comparison between thermometers, the average uncertainty of the calibration is added in quadrature to the MSWD uncertainty (Fig. 3.6).

Two-Pyroxene Thermometry

In the absence of primary magmatic amphibole in the Maronia samples, two-pyroxene thermometry was used to calculate the temperature of the monzodiorite pluton. Reviews of the two-pyroxene thermometer by Blundy and Cashman (2008) & Putirka (2008) showed that the T_{BKN} thermometer (of Brey and Köhler 1990) has the best reproducibility in predicting temperatures of experimental pyroxenes, although the uncertainty associated with the calibration was shown to be underestimated. T_{QUILF} (of Andersen et al. 1993) systematically overestimates experimental temperatures but a greater proportion of results fell within the predicted uncertainty. Temperature estimates using both calibrations are presented here for comparison. Further calibrations of the two-pyroxene thermometer by Putirka (2008) have not been used as the calibrations are most robust for Mg#$^{CPX} > 0.75$ whereas the samples from the Maronia have Mg#^{CPX} = 0.721 $\pm$ 0.029 (2σ).

Pressure estimates are required in the thermometry calculations, but a sensitivity analysis of the

thermometers showed that within the pressure range 1–5 kbar the temperatures calculated did not vary outside of the reported uncertainty. For all calculations, a pressure of 1.2 kbar as calculated for the Kasiteres pluton, the closest neighbour to Maronia along the MMC, was used. Chemical equilibrium between co-existing ortho- and clino-pyroxenes is an inherent assumption of two-pyroxene thermometry. In order to test if this is valid, Putirka (2008) suggest using Fe-Mg exchange equilibria between pairs using the formula:

$$K_D = \frac{X^{Fe}_{CPX}/X^{Mg}_{CPX}}{X^{Fe}_{OPX}/X^{Mg}_{OPX}} = 1.09 \pm 0.14$$

This is calibrated for pyroxenes richer in Mg than are found at Maronia (Mg# $>$ 0.75 in calibrant dataset, median Mg# = 0.72 at Maronia). I suggest that this check of exchange equilibria is invalid for a shoshonitic melt composition where the activity of Ca relative to Mg and Fe is greater than in a calc-alkaline composition. The temperature-contoured pyroxene quadrilateral of Lindsley (1983) suggests that the isotherms tend towards more magnesian compositions when Ca is more abundant, this would drive the K_D to lower values by decreasing $X^{Fe}_{CPX}/X^{Mg}_{CPX}$ and would result in apparent chemical disequilibria. I calculated an idealized clinopyroxene composition using a median orthopyroxene composition and assuming Ca + Mg + Fe (pfu) = 2 and found that the temperature predicted by T_{BKN} was within error of the median T_{BKN} for the analysed pyroxene pairs (ideal T_{BKN} = 848 $\pm$ 30 °C, median T_{BKN} = 820 $\pm$ 30 °C). Therefore, I have not used the chemical equilibria criteria to filter the pyroxene dataset but only calculate temperatures using paired rim analyses of co-existing clino- and ortho-pyroxene phenocrysts in textural equilibrium. In this study I use the pyroxene thermometry data in comparison with the Kassiteres and Leptokaria plagioclase – amphibole thermometry to determine the relative crystallisation temperatures of the systems. The idealized pyroxene thermometry suggests that the pyroxene thermometry results are valid in this comparison, as the uncertainty between the ideal and analytical thermometry calculations is smaller than the difference in calculated crystallisation temperature between the systems.

Both of the two-pyroxene thermometers predict high crystallisation temperatures at Maronia, within the range $752 < T_{BKN}$ (°C) < 893 and $874 < T_{QUILF}$ (°C) < 1064 (Fig. 5). A calibration uncertainty of $\pm$ 30 °C (2σ) is reported for T_{BKN} whilst an average uncertainty of $\pm$ 65 °C determined for T_{QUILF} calculations (Brey and Köhler, 1990; Andersen et al., 1993). A weighted mean analysis of the data suggests that a single population of crystallisation temperatures are recorded using both calibrations; weighted mean crystallisation temperatures of T_{BKN} = 820 $\pm$ 5 °C and T_{QUILF} = 923 $\pm$ 8 °C are calculated (in both datasets: MSWD = 1.1, n = 46/46). T_{QUILF} estimates consistently higher crystallisation temperatures than T_{BKN}, in agreement with the findings of (Blundy and Cashman, 2008). The pyroxene compositions were projected onto the graphical thermometer of Lindsley (1983) at both 0.001 kbar (1 atm) and 5 kbar for comparison. Whilst neither pressure is appropriate, both under- and over-estimating the expected depth of crystallisation ($\sim$ 1.2–1.5 kbar as calculated along the rest of the MMC), the temperature contours do not vary significantly within the level of precision with which the crystallisation temperatures are interpreted. The graphical thermometer closely agrees with the empirical thermometer calculations with pyroxene pairs falling between the 750–1100 °C isotherms (Fig. 3.4D).

Zircon Saturation Thermometry

Zircon is an ubiquitous mineral across the MMC intrusions. In the Kassiteres and Leptokaria samples, the zircons are typically euhedral with well-preserved crystal faces; simple oscillatory zoning in most of the

zircons from the equigranular intrusions suggest a single phase of crystallisation. At Maronia, the zircons have a more complex external morphology. In addition to being a less abundant accessory phase, zircons from the Maronia samples are generally larger crystals (up to 250 μm) and have undulose crystal faces in $\sim$ 75% of the zircons observed suggesting the zircons experienced multiple cycles of saturation and crystallisation followed by undersaturation and resorption. Further evidence of this is observed in the CL images which show resorption surfaces within the Maronia zircons. Inclusions of melt, rutile and apatite are common in zircons from all of the MMC samples. In thin section, zircon crystals are typically found as inclusions in quartz $\pm$ K-feldspar $\pm$ plagioclase rims indicating co-crystallisation with interstitial minerals. Zircon saturation is commonly reached towards the end of crystallisation as incompatible Zr builds up in the residual liquid; consequently, zircon saturation temperatures are frequently used as a proxy for the temperature of the final stages of crystallisation (Hanchar and Watson, 2003).

I use the zircon saturation model of Boehnke et al. (2013) which builds upon the earlier work by Watson (1979) & Watson and Harrison (1983) to calculate zircon saturation temperatures. As zircon saturation is dependent on composition, the model requires calculation of an M factor ($M = \frac{(Na+K+2Ca)}{(Al*Si)}$ molar) using the whole-rock composition. The saturation model of Boehnke et al. (2013) is calibrated for calc-alkaline magmas when M $<$ 2; MMC samples where M $>$ 2 were excluded as they fall outside the calibration range. As a result, no estimates of zircon saturation temperatures were made from Maronia and only from two samples from Kassiteres and six samples from Leptokaria. A more recent study of zircon saturation by Gervasoni et al. (2016) extends the calibration of the zircon saturation model to peraluminous and peralkaline melts, however, potassic compositions were not used in the calibrant dataset for the model so it has not been used in this work. Estimates of Zr concentration in the melt are obtained from whole-rock analyses and an assumed ideal zircon stoichiometry ($ZrSiO_4$) was used to calculate the concentration of Zr in zircon (assuming 10,000 ppm Hf, Zr = 490,186 ppm). Errors are propagated through the model following Boehnke et al. (2013) and using reproducibility of repeat analyses as a measure of analytical error on the whole-rock analyses (whole-rock reproducibility is given in Appendix C). An average uncertainty of $\pm$ 28 °C is reported at the 2σ confidence level.

Zircon saturation temperatures range from 602 to 725 °C (Fig. 3.5). Saturation temperatures increase with increasing SiO_2 in the melt suggesting that zircon appears on the solidus earlier, with a higher fraction of melt remaining and greater temperatures, in more evolved systems. This agrees with the observation of more abundant zircon in the granitic samples.

Apatite Saturation Thermometry

Apatite is found in all samples from the MMC and is most abundant at Maronia. Apatites from Kassiteres and Leptokaria are typically sub-rounded crystals with cloudy interiors with the equant to sub-equant crystals suggesting near-equilibrium crystallisation (Wyllie et al., 1962). At Maronia the apatites are also equant to sub-equant but the crystals are larger (200–300 μm long axis at Maronia, 100–150 μm long axis at Kassiteres and Leptokaria) with well-preserved crystal faces and terminations and clear interiors. Apatites are often found as inclusions in plagioclase, quartz, K-feldspar and pyroxene (Maronia only) indicating apatite saturation was reached during crystallisation of these phases. Inclusions of apatite in zircon suggest that apatite appeared on the solidus before zircon.

The solubility of apatite in silicate melt has been the subject of much research which has found solubility

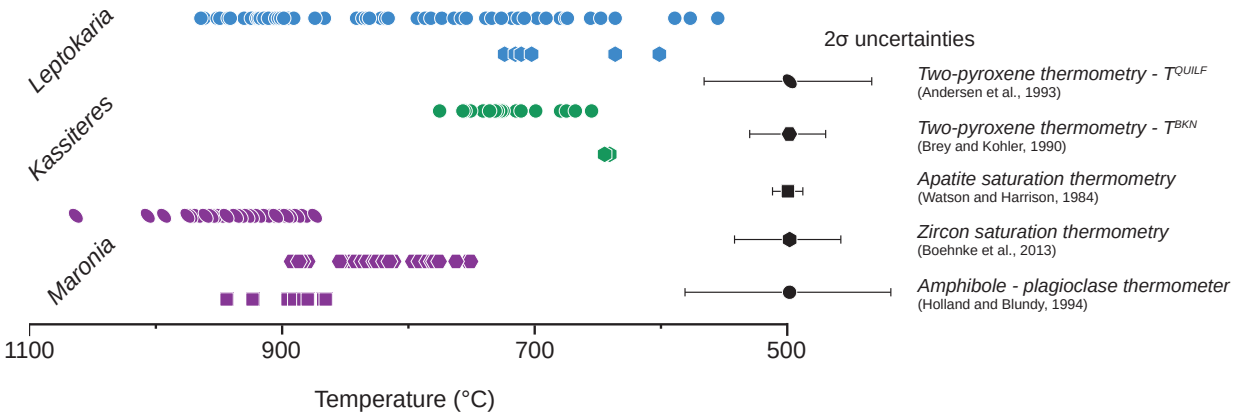

Figure 3.5: Thermometry results from the Maronia Magmatic Corridor with typical uncertainties on each thermometer given. Overall, the thermometers predict higher crystallisation temperatures at Maronia with two-pyroxene and apatite saturation thermometry predicting the crystallisation of liquidus minerals, at 850–900 °C. At Kassiteres, amphibole– plagioclase and zircon saturation thermometry predict solidus crystallisation temperatures of $\sim$ 700 °C. A bimodal temperature distribution is observed in the Leptokaria amphibole – plagioclase thermometry results with a high-T population ($\sim$ 900 °C) calculated from the high-An plagioclase and high-Al_{TOT} amphiboles. The low-T population agrees with solidus crystallisation at $\sim$ 720 °Cin agreement with the zircon saturation thermometry and slightly hotter than, although within error of, the Kassiteres results.

to increase with increasing T and melt CaO content and, decreasing melt polymerization and SiO_2 content (e.g., Harrison and Watson 1984; Pichavant et al. 1992; Wolf and London 1994; London et al. 1999; Tollari et al. 2006). Harrison and Watson (1984) calibrated an apatite saturation model for typical crustal conditions (750–1300 °C, 0–10 wt.% H_2O at 1–8 kbar) across an SiO_2 range from 45 to 75 wt.% reporting that P and H_2O content are not significant, independent controls on apatite solubility.

The calibration curves are plotted with P_2O_5 from 0.039–5.0 wt.% in the melt. In the MMC, 0.09 $<$ wt.% P_2O_5 $<$ 0.64 with the high P_2O_5concentrations ($>$ 0.4 wt.% P_2O_5) found in the incompatible-rich shoshonitic samples from Maronia. As with models of zircon saturation, melt compositions in equilibrium with crystallising apatite are required to estimate apatite saturation temperatures. However, as apatite saturation models have a greater dependence upon composition than the zircon saturation models, knowledge of the melt composition is more important. Piccoli and Candela (2002) suggested that unless apatite is an early crystallising phase, whole-rock compositions will estimate inaccurate apatite saturation temperatures and they advise against using apatite saturation thermometry except in rocks where this might be true (e.g., minimum felsic melts). In order to account for this, I only calculate apatite saturation temperatures for the Maronia samples where elevated P_2O_5 and phase relationships suggests apatite saturation from the onset of crystallisation. At Maronia, estimates of apatite saturation temperature range from 866 to 945 °C (Fig. 3.5). Errors associated with the reproducibility of the whole-rock analyses were propagated through the solubility calculations although no uncertainties are reported with the calibration so a 2σ uncertainty of $\pm$ 12 °C is an underestimation.

3.6.2 Pressure

Geobarometry utilizes mineral equilibria reactions that have large ΔV between products and reactants to predict crystallisation pressures. In magmatic systems, inappropriate mineral assemblages and high compositional variance of minerals present, hinder geobarometry (Anderson et al., 2008). Al exchange

between calcic amphibole (hornblende) and plagioclase is a *P*-dependent equilibrium cation-exchange that is associated with a large ΔV and a small ΔS and is commonly used as a geobarometer in igneous petrology (e.g., Mutch et al. 2016; Putirka 2016). The Al-in-hornblende barometer is applied to both the Kassiteres and Leptokaria samples, however, the lack of primary magmatic amphibole in the H_2O-poor Maronia monzonite means that the barometer cannot be applied. Calibrations of a two-pyroxene barometer have been presented by Nimis and Ulmer (1998) & Nimis (1999) & Putirka (2008) but are calibrated for Mg-rich, calc-alkaline systems. As Maronia is a shoshonitic intrusion with low-Mg# and high CaO, the barometers have not been applied here as there are no existing calibrations for appropriate compositions.

Al-in-Hornblende Barometry

The *P*-dependent Tschermak exchange has a complex set of equilibria requirements and has thus been the subject of multiple studies spanning decades (e.g., Hammarstrom and Zen 1986; Hollister et al. 1987; Johnson and Rutherford 1989; Schmidt 1992; Ague 1997). It can be described by two reactions:

$$\text{Tremolite} + \text{Phlogopite} + 2\,\text{Albite} + 2\,\text{Anorthite} \longrightarrow 2\,\text{Pargasite} + 6\,\text{Quartz} + \text{Orthoclase}$$
$$\text{Phlogopite} + 2\,\text{Quartz} + 2\,\text{Anorthite} \longrightarrow \text{Tschermakite} + \text{Orthoclase}$$

Different approaches of theoretical thermodynamics, experimentally-determined calibrations and field-based calibrations were used by these authors to produce an array of calibrations; the variation between calibrations is attributed to differences in starting or natural mineral assemblages and experimental methods. The most recent experimental study by Mutch et al. (2016) reconciles the differences between calibrations by using a tightly constrained phase assemblage in order to assume a low-variance system and has been used to calculate the pressure estimates presented here.

The following criteria were adopted by Mutch et al. (2016) in order to assume a low-variance, 11 component, 10 phase system with three degrees of freedom: *(i)* the presence of eight phases in textural equilibrium: amphibole, biotite, plagioclase, K-feldspar, quartz, magnetite, ilmenite (or titanite), apatite; and, *(ii)* the implicit presence of additional melt and vapour phases which are assumed to have been present during crystallisation. Hornblende – plagioclase analyses were only used for thermobarometry in samples where all eight phases were visible in textural equilibrium within the same thin section. The paired analyses were screened using predicted plagioclase – amphibole crystallisation temperatures such that only analyses where $T^A_{plag} > T^B_{plag}$ and T^A_{plag} was within 75 °C of the haplogranite solidus (parameterized by Mutch et al. 2016 based on the experimental work of Holtz and Johannes 1994) were used to predict the depth of emplacement. A regression through the valid data points for each sample was used to calculate the best-fit intersection with the haplogranite solidus to estimate a final depth of emplacement (Fig. 3.6). Uncertainties at the 2σ confidence level were calculated by adding the standard deviation of the data point scatter to the calibration uncertainty in quadrature.

Using the criteria outlined above, depths were estimated for two samples from Kassiteres (RT14_028 and KA15_013) and two samples from Leptokaria (RT14_010 and RT14_023). At Kassiteres, sample KA15_013 gave a *P* of 1.20 ± 0.5 kbar (n = 3) and RT14_028 of 1.18 ± 0.5 kbar (n = 12), whilst at Leptokaria, RT14_010 gave a *P* of 1.39 ± 0.5 kbar (n = 10) and RT14_023 of 1.43 ± 0.5 kbar (n = 16). Assuming an average upper crustal density of 2750 g/cm^3, this equates to an emplacement depth of 4.4 ± 1.9 km for Kassiteres and 5.3 ± 1.9 km for Leptokaria.

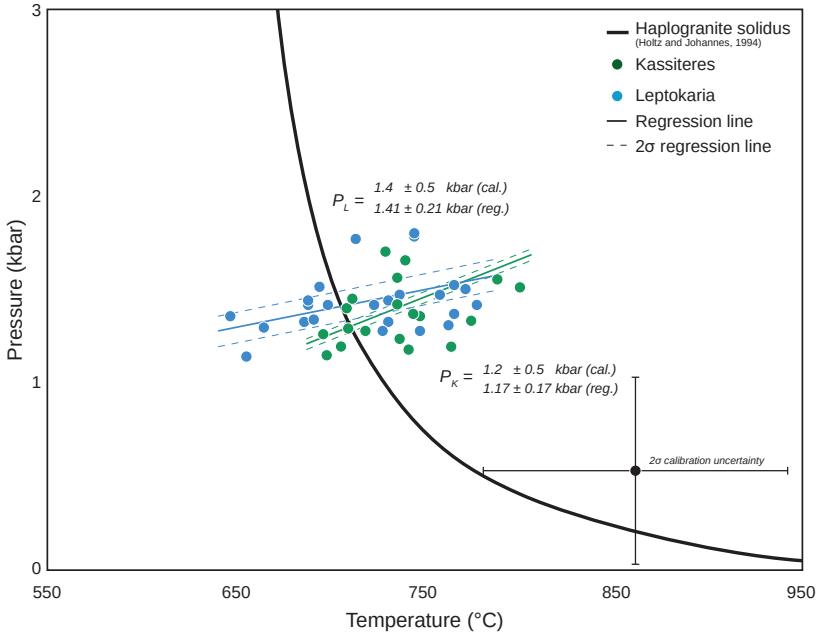

Figure 3.6: Barometry results from Kassiteres and Leptokaria. Individual paired hornblende – plagioclase analyses are compared with the H_2O-saturated granite solidus (Holtz and Johannes, 1994). Linear regressions through the data are plotted and P estimates are given with calibration uncertainties (cal.), for comparison with other barometers and conversion to depth, and regression uncertaintites (reg.), for comparision between Kassiteres and Leptokaria. Assuming an average crustal density of 2750 g/cm^3 the depth estimates for Kassiteres is 4.4 $\pm$ 1.9 km and for Leptokaria is 5.3 $\pm$ 1.9km.

Table 3.3: Compilation of the thermometry and barometry results from the Maronia Magmatic Corridor. T given in °C and P given in kbar.

	Amph. – Plag.				Two-Pyroxene				Zircon Sat.		Apatite Sat.		Al-in-hbl	
	High-T	±	Low-T	±	T_{BKN}	±	T_{QUILF}	±	T	±	T	±	P	±
Kassiteres			708	80					646	42			1.2	0.5
Leptokaria	904	80	720	80					683	42			1.4	0.5
Maronia					820	30	923	66			897	12		

3.6.3 Water Content

The water content of a magma is critical to understanding liquidus – solidus phase relations and depths of magma degassing. It is of increased importance when considering porphyry-forming magmas where exsolution of an aqueous Cl-rich fluid phase is thought to be responsible for the concentration and transport of metals (e.g., Sillitoe 2010; Wilkinson 2013; Blundy et al. 2015; Chelle-Michou and Chiaradia 2017). In Chapter 2 the water content of the Kassiteres-Leptokaria and Maronia igneous complexes was estimated to be 2 $<$ H_2O wt.% $<$ 4.75 and $<$ 2 H_2O wt.% respectively, using experimentally determined phase relationships from the literature (Naney, 1983; Baker and Eggler, 1987; Meen, 1987). The crystallisation P and T estimates from Kassiteres and Leptokaria trend towards the haplogranite solidus indicating that during final crystallisation, the magma was H_2O-saturated and an exsolved magmatic volatile phase was present (Fig. 3.6). The presence of primary fluid inclusions in interstitial quartz from Kassiteres and Leptokaria provides further evidence of this and suggest the magmatic volatile phase was saline. Two types of fluid inclusion are found in close spatial proximity *(i)* a population of inclusions with daughter salt crystals typical of a high-density brine; and *(ii)* a population of inclusions with a large, moving vapour bubble indicative of a low-density, low-salinity phase.

3.7 Assembly of the Maronia Magmatic Corridor

3.7.1 Magma Storage and Crystallisation

Evidence of incremental pluton assembly, with discrete pulses of melt injection, is found across the MMC. The dominant mineral phase in the MMC, plagioclase has three distinct morphologies and bimodal compositions (Figs. 3.2, 3.7). Liquidus plagioclase compositions are affected by three factors: melt composition, P and T which act to drive plagioclase compositions to lower An contents with melt evolution, decompression and cooling (Blundy et al., 2006). A low $An_{(25-40)}$ rim composition is consistent across all of the plagioclase phenocrysts, reflecting crystallisation from the same melt composition at similar P-T conditions during the later stages of crystallisation. High $An_{(>60)}$ plagioclase cores likely reflect crystallisation from a less evolved melt, deeper and/or at greater temperatures in the magmatic plumbing system. Inverse zoning in some plagioclase phenocrysts records the same An content as the high $An_{(>60)}$ plagioclase cores in intermediate zones in the phenocrysts, suggesting a cyclicity in the composition of plagioclase in equilibrium with co-existing magma. This is likely driven by recharge of the melt towards less evolved compositions or greater temperatures by injection of a less evolved melt into the system during incremental pluton assembly (e.g., Couch et al. 2001; Annen et al. 2006).

Phase relations in the MMC can be inferred from the textural relationships between ferromagnesian minerals. Clino- and ortho-pyroxene are present in the less evolved samples from Leptokaria, Kassiteres and Maronia. The euhedral habit of pyroxenes from across the MMC indicate the early appearance of pyroxene

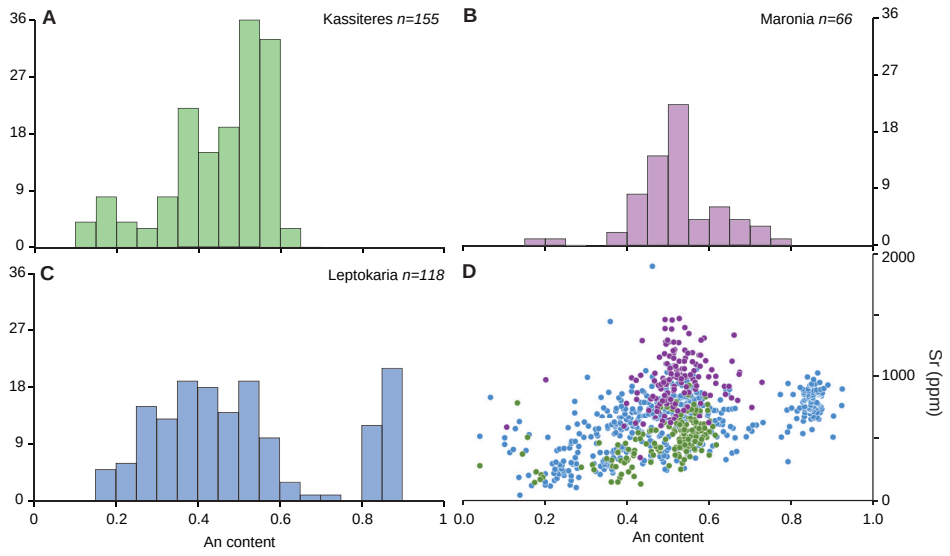

Figure 3.7: Plagioclase populations from the Maronia Magmatic Corridor. (A): A bimodal distribution of An (molar anorthite) content plagioclases are observed at Kassiteres with the intermediate An plagioclases forming the core of the phenocrysts and the low-An plagioclases found at the rim. (B): A bimodal distribution of An content is also found Maronia, although the An content is typically higher, buffered by the early saturation of K-feldspar in the shoshonitic magma. (C): Three populations of plagioclase are observed at Leptokaria; intermediate- and low- An populations are the same as those observed at Kassiteres with a high-An population of plagioclases (An $>$ 80) only observed in samples RT14_010 and RT14_017, in association with high-Al_{TOT} hornblendes. (D): Sr concentrations in plagioclase steadily decrease with An content. Elevated Sr concentrations in plagioclases at Maronia are consistent with the incompatible-rich shoshonitic composition of the pluton. The high-An population of plagioclases from Leptokaria fall off the overall trend with lower Sr concentrations than would be expected.

on the liquidus. A single phase of fine-grained exsolution lamellae are observed in augite and hypersthene from Kassiteres, Leptokaria and the margin of Maronia, preserving the cooling of the magmatic system through the augite – hypersthene immiscibility gap.

Multiple phases of amphibole growth are observed in the Kassiteres and Leptokaria intrusions reflecting different hydrothermal and magmatic processes. A low-Al_{TOT} population of tremolites record the hydrothermal alteration of primary intermediate-Al_{TOT} hornblendes at both Kassiteres and Leptokaria (Fig. 3.3A). The intermediate-Al_{TOT} hornblendes are either poikilitic or euhedral phenocrysts replacing relict clinopyroxene (Fig 3.3A,B). A peritectic reaction between clinopyroxene and hornblende has been recorded in dioritic to granitic systems (e.g., Naney 1983; Prouteau and Scaillet 2003). This, in addition the poikilitic texture of the remaining hornblendes, suggests that hornblende appears on the liquidus after appreciable crystallisation of pyroxene and plagioclase (Fig. 3.9; e.g., Naney 1983; Prouteau and Scaillet 2003). The Cl content of amphibole mimics that of the melt from which it crystalises meaning that decreasing Cl with Al_{TOT}, a proxy for fractionation, reflects decreasing Cl in the melt (Sato et al., 2005; Zhang et al., 2012; Giesting and Filiberto, 2014; Chelle-Michou and Chiaradia, 2017). The presence of a magmatic volatile phase during crystallisation would deplete the melt in Cl and could account for the observed trend B in Figure 3.8C. The steeper gradient of Cl loss at Leptokaria, trend B*(i)*, could reflect the higher Cl fluid-melt partition coefficient ($D_{Cl}^{(fluid/melt)}$) at elevated *P* (e.g., Webster 1997), consistent with the greater crystallisation pressures recorded at Leptokaria. At Maronia, only tremolite, a hydrothermal breakdown product of pyroxene, is present as the shoshonitic magma was too dry ($\sim$ 2 wt.% H_2O, Chapter 2) to stabilize primary amphibole (e.g., Naney 1983; Meen 1987; Beermann et al. 2017).

3.7.2 A Deeper Magmatic Signal

Samples RT14_010 and RT14_017 from Leptokaria record a deeper magmatic signal than the rest of the MMC; the evidence for this is two-fold. Firstly, a discrete population of calcic plagioclases (An $>$ 80) is only found in these samples. The An-rich plagioclases fall off the MMC trend of steadily decreasing Sr with An (Fig 3.7D) and, where in textural equilibrium with amphibole, record high-*T* crystallisation at 904 $\pm$ 80 °C. Secondly, a population of high-Al_{TOT} hornblendes (and edenites) are also only found in these samples in textural equilibrium with the calcic plagioclases (Fig. 3.3C,D). The high-Al_{TOT} hornblendes are characterised by elevated Al in the IV-fold co-ordination site (*P*-dependent tschermak exchange) and elevated alkalis (Na + K in the T-dependent edenite exchange), suggesting crystallisation deeper in the magmatic system (Fig. 3.8; Holland and Blundy 1994; Mutch et al. 2016). Barometry estimates of the plagioclase – hornblende pairs were not made as there is no evidence validating the required buffering assemblage. However, comparison of the high-Al_{TOT} hornblendes with experimental Al_{TOT} in hornblende data (complied by van Zalinge et al. 2017 from Johnson and Rutherford 1989; Schmidt 1992; Scaillet and Evans 1999; Prouteau and Scaillet 2003; Cadoux et al. 2014; Riker et al. 2015; Mutch et al. 2016) suggest that crystallisation of the high-Al_{TOT} hornblendes occurred at $>$ 2 kbar ($>\sim$ 7 km).

Rims of low $An_{(25-40)}$ plagioclase and intermediate-Al_{TOT} hornblende are common in the An-rich plagioclase and high-Al_{TOT} hornblende, suggesting magmatic overgrowth at low-*T* near-solidus conditions. Resorption boundaries in the calcic plagioclases and aluminous hornblendes indicate that the minerals were not stable in the magma prior to magmatic overgrowth which I interpret to reflect a xenocrystic or antecrystic origin of the phenocrysts. The resorption textures can be explained by super-heating of the magma upon

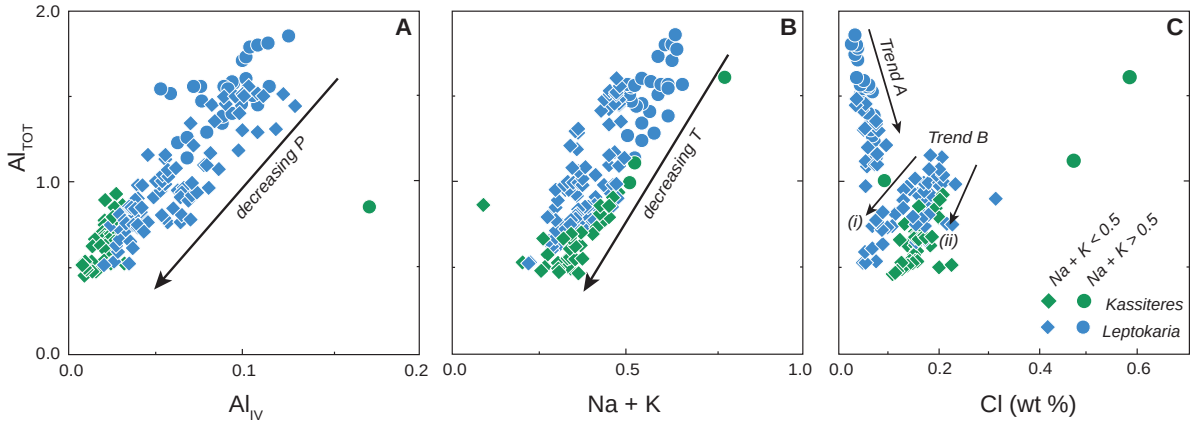

Figure 3.8: Mineral chemistry of the intermediate-Al_{TOT} and high-Al_{TOT} hornblendes from Kassiteres and Leptokaria. A: Al_{TOT} vs. Al_{IV} describes the Tschermak substitution between hornblende and plagioclase, the decreasing Al_{TOT} and Al_{IV} corresponds to decreasing pressure of crystallisation. B: Al_{TOT} vs Na + K describes the edenite substitution between hornblende and plagioclase which decreases in magnitude with decreasing *T*. In both plots (A) and (B) the high-Al_{TOT} population of hornblendes from Leptokaria indicate crystallisation at higher *T* and *P* indicating greater depths in the magmatic plumbing system. (C): Trend A shows that the high-Al_{TOT} hornblendes from Leptokaria increase in Cl concentration with crystallisation. Trend B: shows the intermediate-Al_{TOT} hornblendes from both Leptokaria and Kassiteres are offset from trend A and show decreasing Cl with crystallisation. The Leptokaria hornblendes show a steeper slope of Cl depletion – Trend B*(i)*, than the Kassiteres hornblendes – Trend B*(ii)*.

near-adiabatic ascent from deeper in the magmatic plumbing system into the shallow crust (Prouteau and Scaillet, 2003; Annen et al., 2006).

The notable absence of relict clinopyroxene in the euhedral high-Al_{TOT} hornblendes suggests that crystallisation of the high-Al_{TOT} hornblendes occurred earlier in the crystallisation history than is recorded by the poikilitic and cannibalizing textures observed in the intermediate-Al_{TOT} hornblendes. This requires a change in phase relations between periods of hornblende growth, in part driven by the change in *P* and *T* of crystallisation, but may also reflect changes in the melt composition. Sisson and Grove (1993) presented experimental evidence that An-rich plagioclases (An $>$ 90) can only crystallise from H_2O-rich calc-alkaline magmas, whilst Laumonier et al. (2017) used starting compositions similar to the intermediate diorites from Leptokaria to show that at P $>$ 500 MPa and T $\sim$ 900 °C, a magmatic H_2O content of $>$ 8 wt.% is required to produce An $>$ 80. Whilst the experimental conditions do not exactly match those inferred for Leptokaria, the observed range of An_{80-95} in the An-rich plagioclases is more calcic than could be crystallised from the Kassiteres-Leptokaria parent magma with 2–4.75 wt.% H_2O, even at greater *P*-*T*, requiring a more hydrous melt composition.

Furthermore, trace elements Sr in the high-An plagioclase and Cl in the high-Al_{TOT} hornblende, corroborate the need for a different *P* or H_2O content of the parental melt as the high-An plagioclases and high-Al_{TOT} hornblendes fall off the co-genetic trend (Fig. 3.7D, 3.8C). Increasing Cl with Al_{TOT} in the hornblendes shows that Cl behaves like an incompatible element during crystallisation of the high-Al_{TOT} hornblende, suggesting that the parental magmas are fluid undersaturated, allowing for elevated dissolved magmatic H_2O at high degrees of melt fraction (Chelle-Michou and Chiaradia, 2017). A xenocrystic or antecrystic origin of the high-An plagioclases and high-Al_{TOT} hornblendes is thus inferred. I suggest entrainment of these phenocrysts from a more hydrous phase of calc-alkaline magmatism deeper within the plumbing

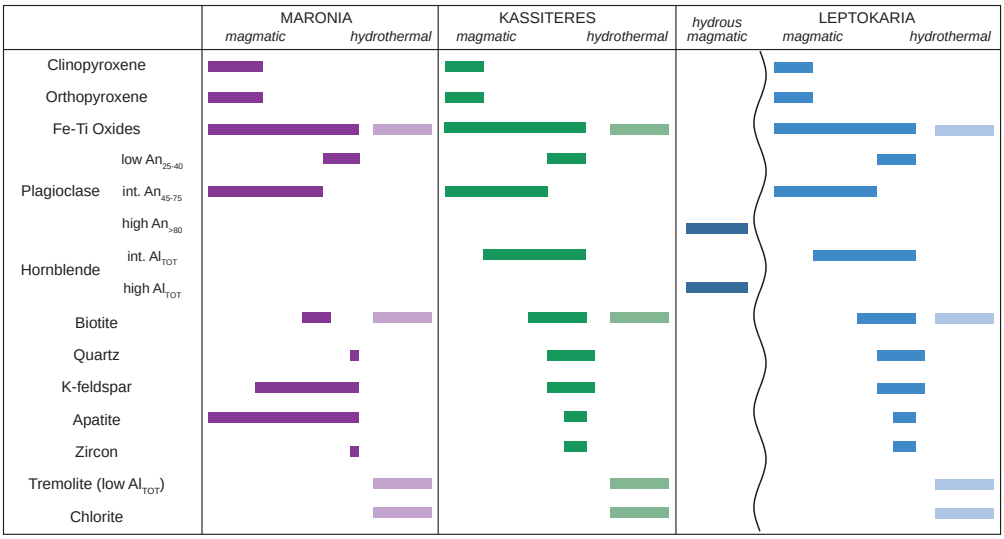

Figure 3.9: A crystallisation sequence from each of the case study areas showing both the magmatic and hydrothermal phases of crystallisation. At Maronia, the notable features are the early saturation of apatite and K-feldspar and the absence of intermediate- or high-Al_{TOT} hornblendes. The later stage of magmatic crystallisation at Kassiteres and Leptokaria is the same. The delayed appearance of intermediate-Al_{TOT} hornblende on the liquidus is indicated by the peritectic consumption of pyroxenes and the poikilitic texture of hornblende. Granophyric textures indicate that quartz and feldspar were the latest crystallising phases. At Leptokaria, an earlier hydrous phase of magmatism (discussed in the main text) crystallises high-An plagioclase and high-Al_{TOT} hornblendes that are entrained as xenocrysts. Hydrothermal alteration across the Maronia Magmatic Corridor has the same propyllitic mineral assemblage: Fe-Ti oxides + biotite + tremolite + chlorite.

system, perhaps from remobilising an existing cumulate package residual from previous subduction-related magmatism.

3.7.3 Temporal and Spatial Evolution of Magmatism

The MMC records two periods of post-collisional mantle melting, magma fractionation and storage, and pluton assembly (Fig. 3.10). In the early Oligocene (32–31 Ma), moderately hydrous ($2 < H_2O$ wt.% < 4.75), calc-alkaline magmatism was generated by extension-induced partial melting of subduction-modified mantle, producing a zoned intrusive complex, Kassiteres–Leptokaria, which ranges from dioritic to granitic in composition (Chapter 2). Pyroxene, plagioclase and Fe-Ti oxides are the liquidus phases at Kassiteres–Leptokaria with hornblende, K-feldspar and quartz appearing later in the crystallisation sequence. Al-in-hornblende barometry indicates crystallisation of the complex at a depth of $\sim$ 4.4–5.3 km (Fig. 3.6), whilst plagioclase – amphibole and zircon saturation thermometry predict near-solidus temperatures of $\sim$ 650 – 750 °C (Fig. 3.5).

After a $\sim$ 2.2 Myr break in recorded magmatism, the Maronia pluton was emplaced in the late Oligocene (29.6–30.0 Ma; Chapter 2). Fractional crystallisation modelling of the shoshonitic composition at Maronia presented in Chapter 2 suggests a drier ($<\sim$ 2 wt.% H_2O), incompatible-rich parent magma, likely generated at elevated temperatures compared to earlier high-K calc-alkaline magmatism (e.g., Meen 1987; Beermann et al. 2017). The different mineral assemblage at Maronia, particularly the lack of primary magmatic amphibole, made estimating the extensive parameters at crystallisation more complex. Liquidus temperatures were estimated between $\sim$ 750–1,000 °C using two-pyroxene and apatite saturation thermometry (Fig. 3.5) but no emplacement depth estimates were possible. These T estimates are

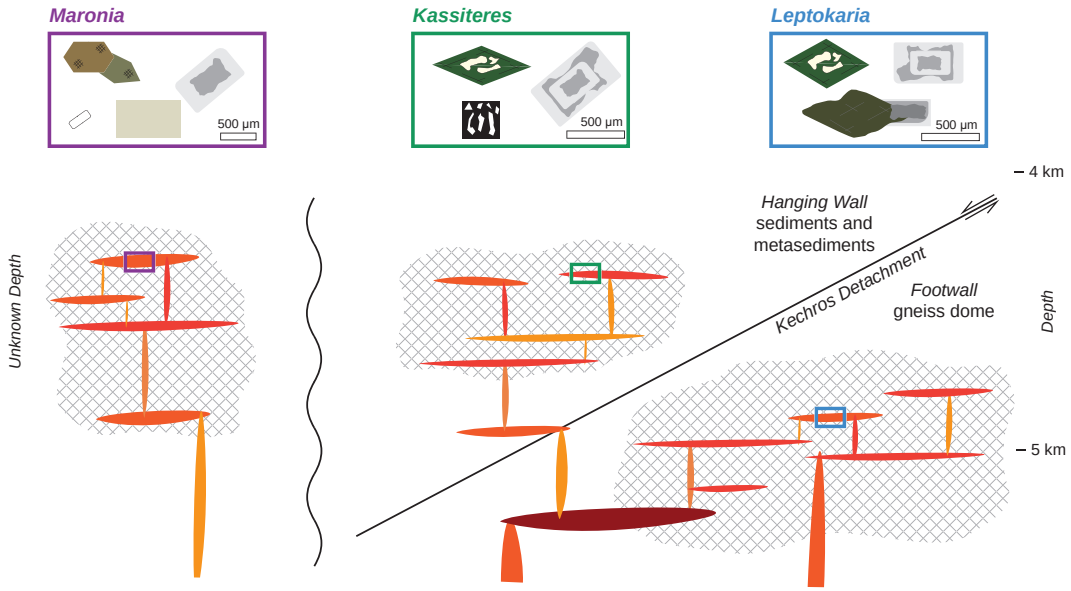

Figure 3.10: A schematic model of magma assembly and crystallisation along the Maronia Magmatic Corridor. The grey hashed areas indicate volumes of crystal mush which are replenished by dykes and sills of melt. The coloured squares contain schematic diagrams of the most important mineralogical textures. Leptokaria: intermediate-Al_{TOT} hornblendes replace relict pyroxenes, plagioclase phenocrysts exhibit normal and inverse zoning, whilst xenocrystic high-An plagioclases and high-Al_{TOT} hornblendes show resorption textures. Kassiteres: the same intermediate-Al_{TOT} hornblendes and zoned plagioclase phenocrysts as at Leptokaria are observed in addition to abundant, well-developed quartz-feldspar granophyric intergrowths. Maronia: zoned plagioclase phenocrysts are buffered to higher An contents by the early appearance of K-feldspar on the liquidus. Clino- and orthopyroxene are the primary ferromagnesian phases in textural equilibrium whilst the incompatible-rich shoshonitic magma saturates with apatite at, or close to, the liquidus.

corroborated by mineral chemistry of the contact endoskarn at the western margin of the Maronia intrusion, which predicts peak metamorphic temperatures of $\sim$ 900 °C (Katerinopoulou et al., 2009). Liquidus temperature estimates at Maronia are expectedly higher than the solidus temperatures estimates from Kassiteres–Leptokaria; however, direct comparison between liquidus and solidus temperatures is inappropriate.

Textural and mineralogical differences between the Kassiteres pluton and the Leptokaria complex record subtle qualitative variations between magmatism in the footwall vs. hanging wall of the Kechros dome (Fig. 3.10). Whilst *P* estimates from the Kassiteres pluton are within calibration uncertainty of the Leptokaria complex (1.2 $\pm$ 0.5 kbar and 1.4 $\pm$ 0.5 kbar respectively), intra-barometer comparison of the regression lines with 2σ uncertainties yield distinct *P* estimates (1.19 $\pm$ 0.17 kbar and 1.41 $\pm$ 0.21 kbar for Kassiteres and Leptokaria respectively). Thus, direction comparison of the geobarometry results suggest that the Kassiteres pluton was emplaced at shallower depths than Leptokaria. This is supported by the intrusion of the Kassiteres pluton into the hanging wall of the Kechros dome at structurally higher levels in the crust than the Leptokaria complex hosted in the footwall of the Kechros dome. The Kassiteres pluton also has plentiful, granophyric intergrowths of quartz and K-feldspar, a texture indicative of rapid cooling beyond the eutectic (Schreyer, 1983). Granophyric intergrowths are observed in the Leptokaria complex from intrusions along the Kechros detachment, but they are less common and not as well developed as at Kassiteres, and are completely absent from intrusions hosted entirely in the Kechros gneiss dome. This implies that cooling is more rapid in the hanging wall of the Kechros dome. Additionally, the high-An plagioclase and high-

Al_{TOT} hornblende xenocrysts that document an early phase of more hydrous magmatism are only observed in intrusions hosted entirely in the footwall of the Kechros dome. This could reflect exposure of deeper levels of the magmatic system in footwall of the Kechros dome where unroofing of the core complex has exhumed deeper parts of the magmatic plumbing system.

3.7.4 Potential for Mineralisation

The high-K calc-alkaline phase of magmatism that formed the Kassiteres-Leptokaria complex falls within the permissible range of H_2O content, *P* and *T* for forming porphyry – epithermal systems (Richards, 2011a, 2013). This is consistent with the presence of porphyry – epithermal systems associated with the Kassiteres pluton. No mineralisation is known to be associated with the Leptokaria complex, although Pagoni Rachi and Essimi porphyry – epithermal systems could be the upper reaches of the system, separated from the parent intrusions by movement along the Kechros detachment fault. Additionally, difficult field conditions in the Leptokaria complex, especially in the NE, could have hindered attempts to locate mineralisation. At Maronia, the host magmatism is too dry for the current paradigms of porphyry – epithermal mineralisation. Mineralisation at Maronia is high grade and spatially restricted to fault zones, and as such the overall tonnage of mineralisation and the extent to mineralisation extends away from the fault zones, is unknown (Melfos et al., 2002). It could represent highly inefficient metal transport and precipitation resulting in high-grade but low-tonnage mineralisation. The Maronia intrusion represents an interesting avenue for further study of how a 'dry', potassic magma can generate high-grade porphyry-style mineralisation?

3.8 Conclusions

Mineral chemistry of the post-collisional, high-K calc-alkaline to shoshonitic magmatism of the MMC has been used to infer the conditions of magma storage and crystallisation. From this, a model of the extensive parameters of the magma during emplacement of the intrusions has been developed. The high-K calc-alkaline Kassiteres–Leptokaria intrusions were emplaced in the shallow crust (< 5.5 km) at H_2O-saturated conditions. Normal and inverse zoning of plagioclase indicates rejuvenation of the magmatic system by repeated injection of melt during pluton assembly. A signal of earlier, hydrous magmatism is recorded in xenocrysts of calcic plagioclase and aluminous hornblende from some of the Leptokaria intrusions, which document crystallisation at greater depths and elevated temperatures. Evidence of a saline magmatic volatile phase is observed in the Kassiteres–Leptokaria complex suggesting that the high-K calc-alkaline magmatism had mineralising potential with the addition of a metal-bearing phase of magmatism. Estimating the depth and temperature of emplacement of the shoshonitic Maronia intrusion was more complex, as the influence of alkalis on phase relations and mineral exchange equilibria is less well constrained. High liquidus temperatures (> 850 °C) are in line with the fractional crystallisation modelling presented in Chapter 2, which suggests that the shoshonitic generation of magmatism was derived from drier source mantle. Low magmatic H_2O contents at Maronia ($<\sim 2$ wt.% H_2O) suggest that the shoshonitic phase of magmatism has a lower potential for mineralisation, which is in contrast with the observed high-grade copper and molybdenum porphyry-style veining. Detailed petrology of each of the case study intrusions along the MMC provides important petrological context to existing studies of porphyry – epithermal style mineralisation from along the MMC.

Chapter 4

Reconstructing cryptic melt hybridisation using zircon geochemistry, melt inclusion petrology and geochronology in highly-altered porphyry systems from along the Maronia Magmatic Corridor, NE Greece

Author contributions and declaration:

All analyses presented in this chapter were made by R. Perkins. B. Tattitch helped with melt inclusion homogenisation and B. Buse provided advice and supervision for the EPMA at the University of Bristol. S. Tapster supervised and provided advice for the zircon trace element and zircon U-Pb LA-ICP-MS analyses that were conducted at NIGL. Useful discussions were had with C. Chelle-Michou on the melt inclusion petrology and zircon trace element geochemistry. S. Tapster and B. Tattitch provided feedback on the manuscript which is aimed for submission to EPSL in the near future.

ABSTRACT

Determining the petrogenesis of metal-bearing porphyritic intrusions in porphyry Cu-Au-Mo-PGE systems is complex as the original magmatic textures and mineralogy are frequently obliterated by pervasive hydrothermal alteration during mineralisation. As a result, regional magmatism is commonly used as a proxy. Zircon, a geologically robust mineral ubiquitous across evolved calc-alkaline magmas, offers a solution to this problem, allowing for direct determination of the geochemistry of the metal-bearing porphyry magmas. Zircon records the evolution of the porphyry magma during crystallisation over tens to hundreds of thousands of years, through its zonation and in the trace element substitution into the lattice, but also through trapped melt inclusions. This study is the first application of zircon-hosted melt inclusion analysis to magmatic mineral systems and demonstrates the fidelity of the melt inclusion record in relation to the geochemistry of the metal-bearing porphyry magma. Zircon-hosted melt inclusions chemistry is applied to a case study area along the Maronia Magmatic Corridor in northeastern Greece. In tandem with zircon trace element geochemistry and U-Pb geochronology, the zircon-hosted melt inclusions record hybridisation of crustal- and mantle-derived magmas along the Maronia Magmatic Corridor. Two different compositions of crustal melt are identified in two different porphyry systems, Kassiteres and Essimi, in addition to a mantle-only end-member of shared magmatism in a porphyry dyke from Leptokaria. Crustal mixing is identified as a key control on the metallogenesis of the porphyry systems, introducing Sn and W into the Kassiteres porphyry magma. Further work on zircon-hosted melt inclusions is suggested, *(i)* to expand understanding of the petrogenesis of porphyry intrusions by direct sampling of the melt composition and, *(ii)* to ascertain whether crustal mixing is a previously unidentified but important control on porphyry Cu-Au-Mo-PGE metallogeny.

4.1 Introduction

Porphyry Cu-Au-Mo-PGE systems are a globally important source of base and precious metals (e.g., Sillitoe 2010). As a result, decades of research have generated multiple models of magmatic mineralisation, centred on fundamental observations common across porphyry systems (Sillitoe, 1973; Hedenquist and Lowenstern, 1994; Sillitoe, 2010; Richards, 2013; Wilkinson, 2013; Blundy et al., 2015; Nadeau et al., 2016). These models have several ideas in common: *(i)* requisite, regional calc-alkaline magmatism produces highly fractionated, hydrous magmas; *(ii)* oxidised conditions are necessary to allow for the transport of sufficient S, Cl and metals to the upper crust within the magma; *(iii)* a shallow, exsolved hydrothermal fluid phase is responsible for extracting metals from the magma; and *(iv)* a mechanism of fixing the metals into the observed reduced, sulphide-hosted hypogene mineralisation is required. Important field studies, focused on large-scale trends in regional magmatism (e.g., Sillitoe 1997; Wilkinson and Kesler 2007; Richards 2015) and small-scale observations of mineralisation in specific systems (e.g., Lowell and Guilbert 1970; Gilmer et al. 2017), have championed attempts to quantify regional magma geochemistry and mechanisms of sulphide mineralisation. However, constraining metal transport in the magma and the subsequent concentration of those metals in the fluid phase has proved more complex.

Destructive hydrothermal alteration of the causative intrusions in porphyry systems, means that conventional petrological techniques have limited applicability in assessing the petrogenesis of metal-bearing magmas as most all primary magmatic textures and minerals are obliterated. As a result, traditional studies of the petrogenesis of porphyry systems have used host equigranular intrusions as a proxy for magmatism (e.g., Dilles 1987) rather than studying the mineralising intrusions themselves. In the last decade, the use of zircon geochemistry to combat this problem has proliferated. A geochemically durable mineral, zircon remains robust throughout hydrothermal alteration meaning that zircon trace element geochemistry is unaffected by destructive hydrothermal alteration. Consequently, zircon chemistry of porphyry intrusions offers valuable insights into the petrogenesis of the mineralising magmatic systems and provide a unique solution to this problem (e.g., Chelle-Michou et al. 2014; Tapster et al. 2016; Tapster 2016; Buret et al. 2016, 2017; Lee et al. 2017). In this study we expand the utility of zircon analyses using the petrology of zircon-hosted melt inclusions (MIs), trapped aliquots of silicate melt, to reconstruct the major and metal geochemistry of highly-altered porphyry intrusions.

4.1.1 Zircon Chemistry in Porphyry Systems

Zircon ($ZrSiO_4$) is an accessory mineral ubiquitous across evolved, calc-alkaline magmatic systems and has long been established as a rigid geo- and thermo- chronometer (e.g., Scherer et al. 2007). It can be used to constrain the temperature-time (T-t) evolution of a magmatic system from crystallisation (with a closure temperature of 900 °C to the U-Pb decay chains, e.g., Tapster 2016), through to cooling and exhumation in the upper crust (with a closure temperature of $\sim$ 250 °C via fission track chronometry and $\sim$ 190 °C via (U-Th)/He chronometry; e.g., Fayon et al. 2017). The solubility of zircon in silicate melts has been well-constrained experimentally and zircon saturation is frequently used as a magmatic thermometer (e.g., Watson 1979; Watson and Harrison 1983; Boehnke et al. 2013). Zircons incorporate significant quantities of trace elements, in particular the tri-valent REEs and tetra-valent U and Th, in substitutions dependent upon intensive parameters such as T, P and fO_2 (Cherniak et al., 1997; Ballard et al., 2002; Ferry and Watson, 2007). The slow diffusion of cations through the zircon lattice preserves variations in zircon chemistry,

recording the compositional evolution of the melt during crystallisation, making zircon an ideal mineral to investigate the conditions of magma petrogenesis (Cherniak and Watson, 2003).

Most importantly, the zircon lattice is robust during the majority of intense hydrothermal events and retaining its geological information through high- and low- *T* hydrothermal alteration. Consequently, zircon chemistry is an ideal method to see through intense hydrothermal alteration in order to study the petrogenesis of metal-bearing magmas whose magmatic history would otherwise be lost (Chelle-Michou et al., 2014; Tapster et al., 2016; Buret et al., 2016, 2017). Zircon chemistry, integrated with petrochemical modelling, has been used to make inferences about the petrogenesis of metal-bearing magmas. These inferences include but are not limited to: *(i)* rapid, small volume magma recharge during porphyry emplacement (Tapster et al., 2016); *(ii)* hydrous, oxidised metal-bearing magmas generated following hornblende – magnetite – titanite fractionation in the lower crust (e.g., Lee et al. 2017; Loader et al. 2017); and *(iii)* supply of sufficient volatiles for mineralisation (primarily S and Cl) by a late, mafic magmatic input into the porphyry system (e.g., Buret et al. 2016). Additionally, arc-scale detrital zircon studies using fertility indexes as described by the literature (e.g., Lu et al. 2016), have been used to define fertile domains to direct mineral exploration teams.

4.1.2 Melt Inclusion Analyses in Porphyry Systems

Significant petrological work has long been dedicated to using melt inclusions (MIs), aliquots of melt trapped during crystallisation, to study the geochemistry of magmatic systems where analysis of the bulk rock is unavailable or unrepresentative e.g., from phenocrysts in volcanic pumice and scoria (Blundy and Cashman, 2008). In typical volcanic suites, igneous petrologists use MIs trapped in primary magmatic phenocryst phases such as quartz, plagioclase, amphibole and pyroxene to study magmatic differentiation, crystal fractionation and magma degassing (e.g., Donovan et al. 2018; Grocke et al. 2018; Hartley et al. 2018). However, studies of MIs in porphyry systems are rare. Student and Bodnar (2004) suggest that this is due to difficulties recognising MIs in highly altered porphyry intrusions where the inclusions tend to be crystalline in nature and frequently show alteration to clay minerals. Current MI studies of porphyry systems have been focussed on a small number of deposits where intact phenocrysts host melt inclusions, such as at Bajo de la Alumbrera (Harris et al., 2003; Halter et al., 2005; Heinrich et al., 2005) and Bingham Canyon (Zhang and Audétat, 2017). These studies used analyses of quartz-, plagioclase-, amphibole- and pyroxene-hosted MIs to constrain the volatile and metal budget of ore-forming magmas, concluding that ore-forming magmas are not unusually metal-rich in comparison to arc magmas (Halter et al., 2005; Heinrich et al., 2005; Zhang and Audétat, 2017). Heinrich et al. (2005) was one of the first studies to document the spatial and temporal evolution of ore-forming magmas tracking silicate and sulphide melts and brine and vapour fluid phases in a combined study of melt and fluid inclusions.

In this study, we aim to broaden the scope of MI studies of porphyry systems by analysing zircon-hosted MIs. Early work on zircon-hosted MIs was reviewed by Thomas (2003) who concluded that the geochemistry of MIs reflects that of the parent melt from which it was trapped and suggest an abundance of scientific opportunity through further study of zircon-hosted MIs. Of particular note, Thomas (2003) suggest that zircon-hosted MIs offer a unique opportunity to study the time-integrated evolution of melt chemistry in zircons which host melt inclusions in multiple domains. However, to the best of our knowledge, this study is the first reported analyses of zircon-hosted MIs in mineralised porphyry Cu-Au-Mo systems where other

potential MI host phenocrysts have been destroyed by intense hydrothermal alteration. We suggest that the physical and chemical durability of zircons through high- and low-temperature hydrothermal alteration, intrinsic to porphyry systems, means that zircon provides ideal armouring for MIs post-entrapment. Furthermore, zircon is a ubiquitous phase in intermediate to evolved calc-alkaline magmas and is thus present with reasonable abundance in the metal-bearing intrusions of porphyry systems. Consequently, zircon-hosted MIs should be plentiful and well-preserved across variably altered magmatic mineral deposits, widening the applicability of MI studies in intensely altered systems.

Here we present an integrated study of zircon U-Pb geochronology, zircon geochemistry and zircon-hosted MI petrology of the Oligocene Kassiteres and Essimi porphyry systems in northeastern Greece. Our data set includes, to the best of our knowledge, the first published analyses of zircon-hosted MIs from porphyry systems. We use high-spatial resolution U-Pb geochronology to evaluate the degree of inheritance in the zircon populations from the three porphyry systems. We show compelling evidence in the zircon-hosted MI geochemistry for mixing of crustal- and mantle-derived melts in the generation of the metal-bearing magmas. Finally, we use zircon trace element geochemistry, including the first well constrained analyses of W and Sn in zircon from mineralising intrusions, to account for the curious W-Sn enrichment of these nominally Cu-Au-Mo porphyry – epithermal systems.

4.2 Geological Setting

The Kassiteres, Essimi and Leptokaria porphyry stocks intrude the post-collisional plutons of the Maronia Magmatic Corridor (MMC) located at the southern margin of the Kechros – Biala Rika dome in northeastern Greece (Fig. 4.1). The Kechros – Biala-Rika dome is the eastern-most gneiss dome of the northern Rhodope core complex (RCC). A series of stacked nappes accreted during the Mesozoic, the northern RCC gneiss domes are characterised by three distinct metamorphic lithologies: *(i)* high-T ortho- and para-gneisses of the core complex footwall (Turpaud and Reischmann, 2010; Burg, 2011); *(ii)* greenschist-facies metasedimentary and meta-ophiolitic units of the Circum Rhodope Belt in the hanging wall of the core complex (Bonev and Stampfli, 2008; Meinhold et al., 2010; Bonev and Stampfli, 2011; Meinhold and Kostopoulos, 2013); and *(iii)* the eclogite-bearing imbricate unit sandwiched along the Nestos suture zone between the footwall and hanging wall (Mposkos and Kostopoulos, 2001; Bauer et al., 2007; Krenn et al., 2010). An Eocene transgressive sedimentary unit and an intercalated volcano-sedimentary sequence unconformably overlie the hanging wall of the Kechros dome in the Thrace supra-detachment basin (Burchfiel et al., 2008; Kilias et al., 2013, 2015). The onset of northern Aegean post-collisional magmatism in the middle Eocene was contemporaneous with core complex exhumation in the northern RCC (Rohrmeier et al., 2013). Post-collisional magmatism continued into the Oligocene e.g., the MMC, and has a geochemical signature indicative of a sub-continental lithospheric mantle source, thought to be relict from Mesozoic subduction (e.g., Pe-Piper et al. 2009; Chapter 2).

The Kassiteres porphyry is a small intrusion (150 m by 500 m diameter) that intrudes the 32.045 $\pm$ 0.020 Ma Kassiteres dioritic – granodioritic pluton (Voudouris et al. 2006; Chapter 2). Hosted in the hanging wall of the Kechros dome at the unconformity between the CRB metamorphic basement and the Eocene sedimentary sequence, the Kassiteres pluton and porphyry are overlain by onlapping Oligocene, intercalated volcaniclastic and sedimentary deposits (Fig. 4.1). The Essimi and Leptokaria porphyries are $\sim$ 20 km to the East of Kassiteres, separated from one another by the Kechros detachment fault. The Essimi porphyry

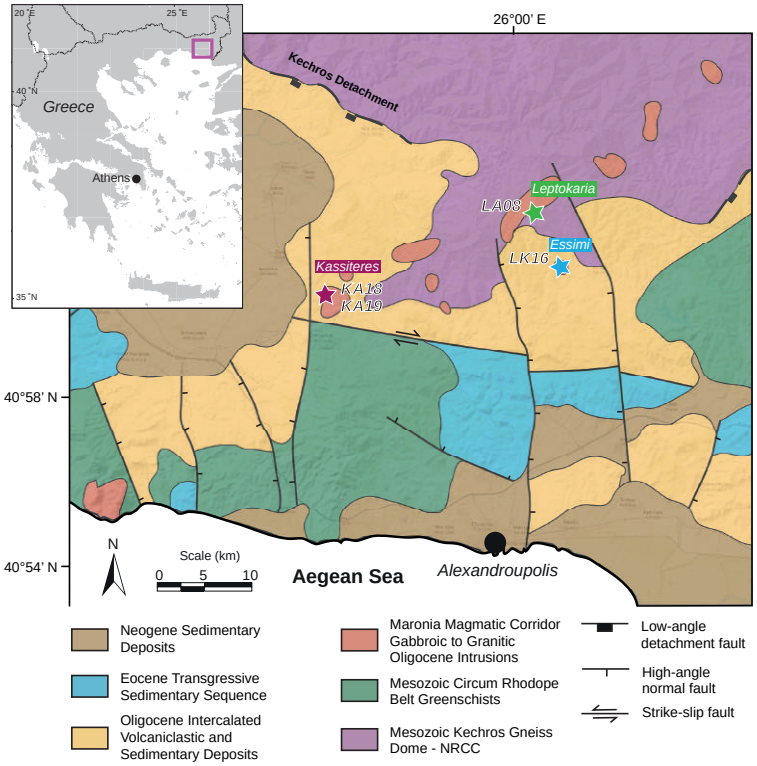

Figure 4.1: A geological map of the study area, first presented in Chapter 2. Three porphyry systems are used as case studies: Kassiteres (KA15_018, KA15_019), Essimi (LK16_016) and Leptokaria (LA15_008). Both Kassiteres and Essimi are associated with porphyry-style quartz + sulphide veining whilst no mineralisation is recorded from Leptokaria (Melfos and Voudouris, 2017). The Kassiteres and Essimi systems are hosted in the Circum Rhodope Belt (CRB) greenschist metasedimentary basement in the hanging wall of the Kechros dome, whilst the Leptokaria porphyry is hosted in the ortho- and para-gneisses of footwall. Both the Kassiteres and Leptokaria porphyry intrude into the eponymous host equigranular dioritic to granodioritic intrusions of the Maronia Magmatic Corridor (MMC), described in Chapter 2 and 3, whilst the Essimi porphyry is not associated with any MMC magmatism and falls off the NE-trend of the MMC lineament.

stock does not have any visible field contact with an MMC pluton and is hosted in the intercalated Oligocene volcaniclastic and sedimentary unit of the Kechros dome hanging wall, $\sim$ 3 km to the South of the Kechros detachment. North of the Kechros detachment, the Leptokaria porphyry dyke cuts the across the Leptokaria granodioritic to granitic pluton (32.235 $\pm$ 0.026 Ma; Chapter 2) into the orthogneisses of the Kechros dome footwall.

4.3 Samples and Approach

Four samples from the porphyry stocks of the MMC were selected for detailed zircon analyses to establish the petrogenetic history of the metal-bearing magmas. Pervasive, destructive alteration is intrinsic to magmatic-hydrothermal systems; the samples selected for analysis typify this with little to no original magmatic textures or primary mineral assemblage remaining (Fig. 4.2A). Below we describe the petrogenetic history of these intrusions as established using conventional petrological techniques.

At Kassiteres, two samples (KA15_018 and KA15_019) from two different alteration zones in the same porphyry intrusion were selected for analysis to compare the robustness of zircon analyses through differing degrees of acid alteration. KA15_018 is from the argillic zone of the Kassiteres alteration system. Relict feldspar phenocryst habits (from 0.5 cm to 3 cm long axis) infilled by clays (montmorillonite + illite) in a micro-granular grey, friable matrix and secondary glassy quartz eyes are the only intact features remaining. KA15_019 has been subject to similar degrees of destructive alteration. From the phyllic zone, the matrix of KA15_019 has been intensely silicified such that even the plagioclase phenocryst habits are no longer preserved and a high-T clay assemblage of muscovite + illite dominates. The whole-rock geochemistry of these samples do not represent the bulk chemistry of the metal-bearing magma due to such intense alteration. This is especially obvious in the highly mobile alkali elements (Fig. 4.2B), where samples KA15_018 and KA15_019 have low CaO and Na_2O, approaching or below the detection limit. KA15_018 is also depleted

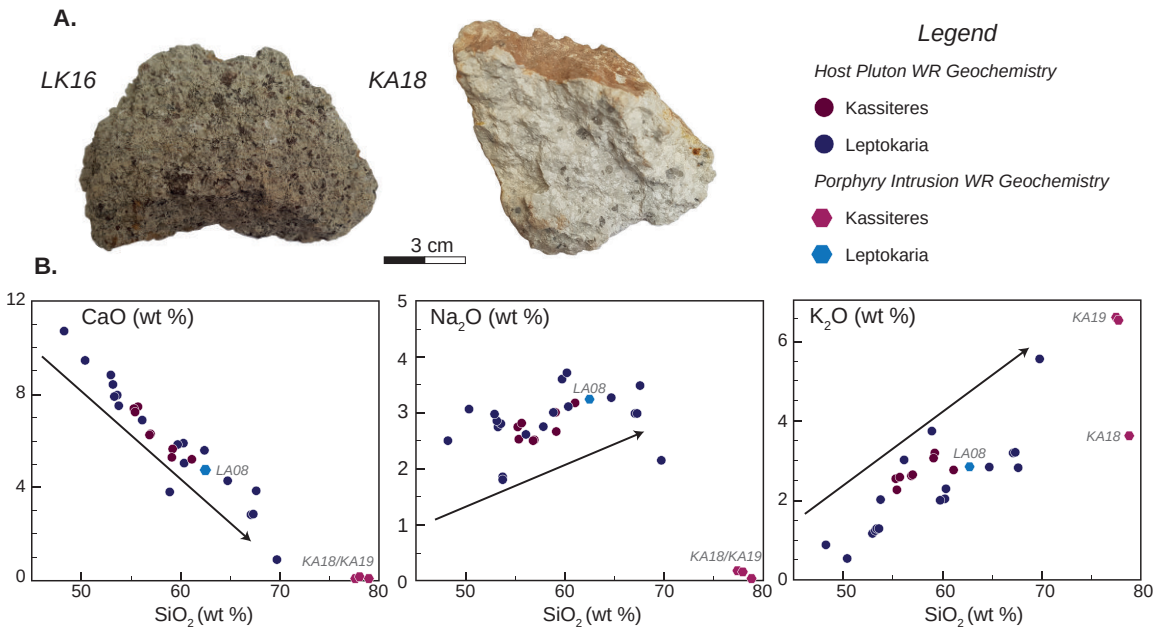

Figure 4.2: (A): The porphyry hand samples from each of the intrusions are destructively altered by pervasive hydrothermal alteration. (B): As a result the whole-rock geochemistry of the intrusions is unrepresentative of the original magma composition. This is most notable in the alkali elements CaO, $Na_2O$and K_2Owhich fall off the regional fractionation trend defined by the host pluton whole-rock geochemistry (Chapter 2).

in K_2O; fortuitously, sample KA15_019 does fall on the K_2O regional fractionation trend which we suggest is the result of the high-*T*, K-bearing clays present in KA15_019 but not KA15_018.

Single samples from Leptokaria and Essimi were selected to compare with the Kassiteres system. LA15_008 is from a porphyry dyke that cuts the equigranular, granodioritic Leptokaria pluton and is not associated with any known mineralisation. A phenocrystic assemblage of amphibole needles ($\sim$ 0.2 cm diameter) and relict feldspar habits ($\sim$ 0.5 cm diameter) in a silicified, green matrix are the remaining igneous features characterising the porphyritic texture of the sample. LK16_016 is from the Essimi porphyry stock, located $\sim$ 500 m west of a porphyry vein stockwork (quartz + pyrite + chalcopyrite + sphalerite) which makes up the Essimi porphyry occurrence (Melfos and Voudouris, 2016). Sample LK16_016 is the least altered porphyry intrusion studied with phenocrysts of amphibole, feldspar and quartz (from 0.1 to 1.5 cm diameter) hosted in a granular grey matrix. LK16_016 is more phenocryst rich (80 %) than the LA15_008 (30 %) based on the abundance of intact phenocrysts and relict crystal habits. The presence of amphibole phenocrysts in both LA15_008 and LK16_016 suggest a hydrous magma ($>$ 3 wt.% H_2O) with an early phase of phenocryst crystallisation occurring at $>$ 0.8 kbar ($\sim$ 2.5 km depth; e.g. Lledo and Jenkins 2007). We do not have any whole-rock analyses of sample LK16_016; however, the Leptokaria porphyry sample (LA15_008) does fall on the regional magmatic trend suggesting a genetic link with the post-collisional magmatism of the plutons into which it intrudes (Fig. 4.2B).

This study compares the magma chemistry of the three case study porphyry intrusions. The Leptokaria dyke (LA15_008) acts as a control; it is genetically associated with the regional post-collisional magmatism and is not connected with any known mineralisation. It thus provides a framework with which to compare the Kassiteres (KA15_018/KA15_019) and Essimi (LK16_016) porphyries and unpick which processes may have controlled the endowment of the metal-bearing porphyry intrusions.

4.4 Methods

4.4.1 Zircon Characterisation

Zircon mineral separates were obtained using conventional heavy mineral separation techniques: over 2kg of rock from each sample was crushed, sieved, rinsed and density separated at the University of Bristol. Zircon crystals were hand-picked from the mineral separates and then annealed in vacuum-sealed quartz tubes for between 72–100 hours at 1000–1050 °C. The zircons were then bulk mounted in epoxy and hand polished to expose the centre cross-section of as many melt inclusions within the crystals as possible. Scanning Electron Microscope (SEM) analyses were undertaken at the University of Bristol on a Hitachi S-3500 N instrument with 20 kV accelerating voltage and a 15 mm working distance. Reflected light and back-scattered electron (BSE) imagery was used to distinguish homogenised melt inclusions and cathodoluminscence (CL) imagery to characterise the internal morphology of the zircons prior to analysis. Zircons containing inclusions with obvious exotic crystals e.g., sulphides or oxides, were mounted without being homogenised for SEM energy dispersive spectrometry (EDS) compositional analysis of the daughter phases.

4.4.2 Whole-Rock Geochemistry

Powders of < 25 μm grain size were prepared at the University of Bristol and analysed in the Inorganic Geochemical Laboratories at the British Geological Survey (BGS), Keyworth. Powders were prepared for samples KA15_018, KA15_019 and LA15_008. Weathered outer rims of individual samples were removed such that only the freshest material from the cores of the samples were used for analysis. Samples were then crushed and milled in a ball mill using an agate jar. Due to the large grain size (> 1 mm) and relative heterogeneity of the samples, > 2 kg of rock was used to ensure a homogenous powder was produced. Samples were analysed following the UKAS Accreditation Schedule using WD-XRFS on fused glass beads for major and minor element oxides, Na_2O_2 fusion ICP-MS for minor and trace element concentrations, and an aqua regia digest ICP-MS for Sc and Te. The geochemistry of the porphyry samples presented here is supplemented by geochemistry of the host intrusions from Chapter 2.

4.4.3 U-Pb Zircon Geochronology

High-spatial resolution laser ablation geochronology was undertaken to constrain intra-zircon age relationships between core and rim zones identified in CL imagery of samples KA15_018, LK16_016 and LA15_008. KA15_019 was not analysed as KA15_018 and KA15_019 sample the same porphyry intrusion in different alteration zones such that the zircon age populations of both samples should be the same. All zircons analysed by U-Pb geochronology were annealed during melt inclusion homogenisation at 1000–1050 °C for 72–100 hours. Laser ablation high resolution multi-collector inductively coupled plasma mass spectrometry (LA-HR-MC-ICP-MS) was conducted at the NERC isotope geosciences laboratory (NIGL) using a Nu Plasma multi collector laser. Operating conditions for the ablation were 10 Hz frequency, 1.4-1.6 J/cm^2 fluence, 40 % output on a 20 μm spot with a 30 s dwell time and a 15 s laser warm-up period between ablations. 91500 zircon was used as a primary reference material and GJ1 zircon and Mud Tank zircon reference materials were used as secondary and tertiary validations following community driven data reduction protocols of Horstwood et al. (2016). Ablation spot locations were selected based on the internal morphology of the zircon observed in the CL imagery; for each zircon crystal, spots from both the rim and

core of the crystal were analysed. Additional ablations of zircons whose core analysis gave a $^{206}Pb/^{238}U$ age > 35 Ma were taken to determine the domain-by-domain age of the crystal. Data has been filtered according to $^{206}Pb/^{238}U$–$^{207}Pb/^{235}U$ discordance as calculated by the $^{206}Pb/^{238}U$age / $^{207}Pb/^{235}U$ age ratio (C). Analyses where the discordance is greater than 5 % ($0.95 > C > 1.05$) have been rejected on the basis of common Pb contamination or mixing of age domains.

4.4.4 Zircon-Hosted Melt Inclusion Analyses

Zircons from the four samples studied were plentiful with abundant inclusions of apatite, feldspar and oxides in addition to melt. Zircons with MIs, crystalline or glassy, were hand-picked from the mineral separates for annealing and subsequent analysis.

Homogenisation

All zircons picked were annealed and then quenched in order to re-homogenise the enclosed crystalline MIs. Heating experiments were conducted on five zircons from samples KA15_018 and LK16_016 on a high temperature heating stage (Linkam 1400XY) linked to a petrographic microscope prior to bulk zircon annealing to determine an appropriate annealing temperature. The zircons were heated to 700 °C and then step-heated in 50 °C increments to 900 °C and then 10 °C increments to 1200 °C. Homogenisation of enclosed MIs was reached between 950–1000 °C whilst microlite growth was observed in melt embayments or MIs where a hairline fracture intersected the inclusion providing a pathway for interaction between the melt and the ambient environment. A temperature of between 1000–1050 °C was chosen for bulk annealing in order to ensure that the enclosed crystalline melt inclusions were held at super-liquidus temperatures for re-homogenisation. Zircons were annealed in vacuum-sealed fused-quartz tubes to minimise any diffusive gradients into the crystals. The fused-quartz tubes were suspended by nickel wire in a cold-seal furnace for between 72 to 100 hours. At the end of heating, the fused-quartz tubes were quenched in a bucket of water, cooling to below $\sim$ 600 °C in less than five seconds and were cool to the touch after less than one minute. Silicate melts are thought to pass through the glass transition at $\sim$ 500 °C (Deubener et al., 2003) which the zircons cooled through within the first minute of leaving the furnace, thus quenching the melt inclusions to glass. The fused-quartz tubes were broken and rinsed with ethanol to ensure all zircons were collected.

Major Element Chemistry

Melt inclusion major element chemistry was obtained by electron probe micro-analysis (EPMA) on a JEOL JXA 8530F Hyperprobe at the School of Earth Sciences, University of Bristol; full analytical detail can be found in Appendix J. A time dependant intensity (TDI) correction was used on the mobile elements Na, K, Al and Si and H_2O was included in the matrix correction to obtain a H_2O-by-difference estimate of the melts. Data was filtered to exclude any analyses with > 1 wt.% $\sim ZrO_2$ (zircon present in the analytical volume), > 9 wt.% H_2O (indication of a bad analysis) or $K_2O/Na_2O < 0.5$ (indication of alkali mobility and potential hydrothermal alteration). A total of 148 analyses of inclusions in zircons were made, of these 80 were rejected (35 clay altered inclusions, 12 bad analyses and 33 with ZrO_2 contamination) using the filters above. Host (ZrO_2) contamination was the most significant analytical challenge owing to the small diameter of the melt inclusions (5–20 μm). The remaining analyses are split between all four samples: KA15_018 = 13, KA15_019 = 7, LA15_008 = 9 and LK16_016 = 39.

4.4.5 Laser Ablation Trace Element Analyses

LA-ICP-MS was conducted on both the zircon crystals. Analyses were conducted at NIGL by single collector sector field laser ablation inductively coupled plasma mass spectrometry (SC-SF-LA-ICP-MS) using a Nu Instruments Attom HR single collector inductively coupled plasma mass spectrometer in linkscan (or linked-scan) mode. Laser ablation was conducted using a 'large-format' New-Wave research cell. For zircon trace element geochemistry, the ablation parameters were refined between analytical sessions. Initial conditions were a 4 J/cm^2 fluence, a 10 Hz frequency, 15 s dwell time and 10 s wash out period, and a 20 μm spot size. In order to reduce the ablation volume, a smaller spot size and lower fluence were used in the second session with conditions: 2.4 J/cm^2 fluence, a 10 Hz frequency, 15 s dwell time and 15 s wash out period, and a 10 μm spot size. NIST-610 was used as the primary standard materials in analyses of the zircons and data was validated against NIST-612. The matrix-matched 91500 and GJ1 zircons (GeoReM preferred values in Wiedenbeck et al. 2004; Jochum et al. 2005) were used as secondary standards during the zircon analyses. Samples were run by typical sample standard bracketing with 30–35 zircon analyses between 3–4 runs of each reference material. The zircons were analysed for: ^{24}Mg, ^{27}Al, ^{44}Ca, ^{45}Sc, ^{49}Ti, ^{51}V, ^{63}Cu, ^{77}Se, ^{88}Sr, ^{89}Y, ^{93}Nb, ^{96}Zr, ^{100}Mo, ^{105}Pd, ^{120}Sn, ^{121}Sb, ^{125}Te, ^{139}La, ^{140}Ce, ^{141}Pr, ^{146}Nd, ^{149}Sm, ^{153}Eu, ^{157}Gd, ^{159}Tb, ^{163}Dy, ^{166}Er, ^{172}Yb, ^{175}Lu, ^{177}Hf, ^{181}Ta, ^{182}W, ^{185}Re, ^{195}Pt, ^{197}Au, ^{206}Pb, ^{209}Bi, ^{232}Th and ^{238}U counts, and normalised to 32.5 wt.% SiO_2 (^{29}Si) in zircon. All zircon trace element data was reduced using the Iolite software.

4.5 Results

4.5.1 Zircon Morphology: Internal Textures and Melt Inclusions

CL images of all zircons analysed provide a database of the different internal morphologies of crystals from each sample; a representative selection of CL images are shown in Figure 4.3. Zircons from all samples are multi-faceted with well-preserved crystal terminations and an outer zone with strong oscillatory zonation and sector zoning; these outer domains likely represent the final zircon growth during crystal emplacement as they are common across all crystals in all samples. MIs are visible in the CL images from all samples as dark (no CL emission) spots which typically truncate or warp oscillatory zoning. The Leptokaria porphyry dyke, LA15_008, has the simplest zircon population with > 95 % of zircons equant crystals showing a single period of growth with simple oscillatory and sector zoning. Occasional (< 5 %) simple cores with constant CL emission were also observed. LK16_016, the Essimi porphyry stock, has a more complex population of zircons. Elongate, prismatic zircons, characterised by oscillatory and sector zoning suggesting a single phase of zircon growth, make up ~ 30 % of the zircon population of LK16_016. The remaining 70 % of zircons show evidence of multiple phases of rim overgrowth on zircon cores with resorption textures and cross-cutting oscillatory zoning the dominant features of the zircons. Three styles of zircon growth are observed in the intermediate domains and cores of crystals: *(i)* elongate cores with planar zoning abruptly terminated by oscillatory overgrowth, *(ii)* equant domains with sector zoning only, and *(iii)* domains, commonly cores, with incoherent CL patterns. KA15_018 and KA15_019 have zircon morphologies similar to LK16_016. A small population, < 20 %, of the zircons from KA15_018 and KA15_019 are elongate, prismatic zircons which typically host narrow but long (50–100 μm), undulose (or 'wormy') melt inclusions. Over 80 % of zircons from KA15_018 and KA15_019 show multi-domain zircon growth with styles the same as LK16_016, with additional domains of constant CL emission lacking any zonation present in KA15_018 and KA15_019.

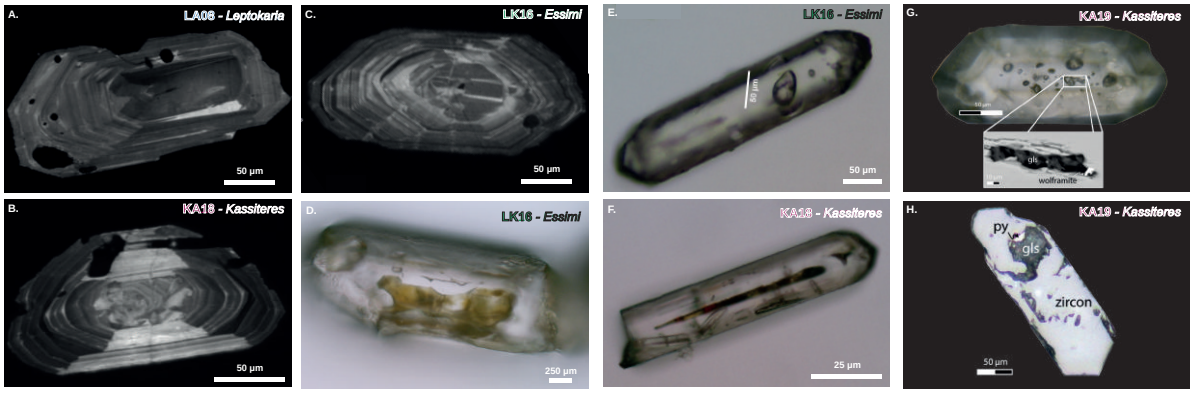

Figure 4.3: Images of zircon and zircon-hosted melt inclusion morphology from the Maronia Magmatic Corridor porphyries. (A): A cathodoluminscence (CL) image of an equant zircon typical of the zircon population from LA15_008; the zircon shows simple oscillatory zoning. (B): A CL image of a zircon with a xenocrystic core, exhibiting incoherent CL patterns, from Kassiteres porphyry sample KA15_018. (C): A CL image of a zircon with a xenocrystic core from Essimi sample LK16_016, the core shows parallel planar twins whilst the rim has simple oscillatory zoning. All of the CL image of the zircons show fine resorption boundaries in the oscillatory zoned domains. (D): A large, glassy inclusion from Essimi porphyry sample LK16_016. (E): A small, equant inclusion with microlite daughter crystal prior to homogenisation, from Essimi sample LK16_016. (F): A wormy inclusion along the centre of a zircon from Kassiteres sample KA15_018. (G): An image of a melt inclusion rich zircon crystal from Kassiteres sample KA15_019; the back scattered electron (BSE) inset shows a wolframite sibling crystal that was co-entrapped during formation of the melt inclusion. (H): A reflected light image of a melt inclusion from Kassiteres sample KA15_019 with a pyrite co-entrapment crystal.

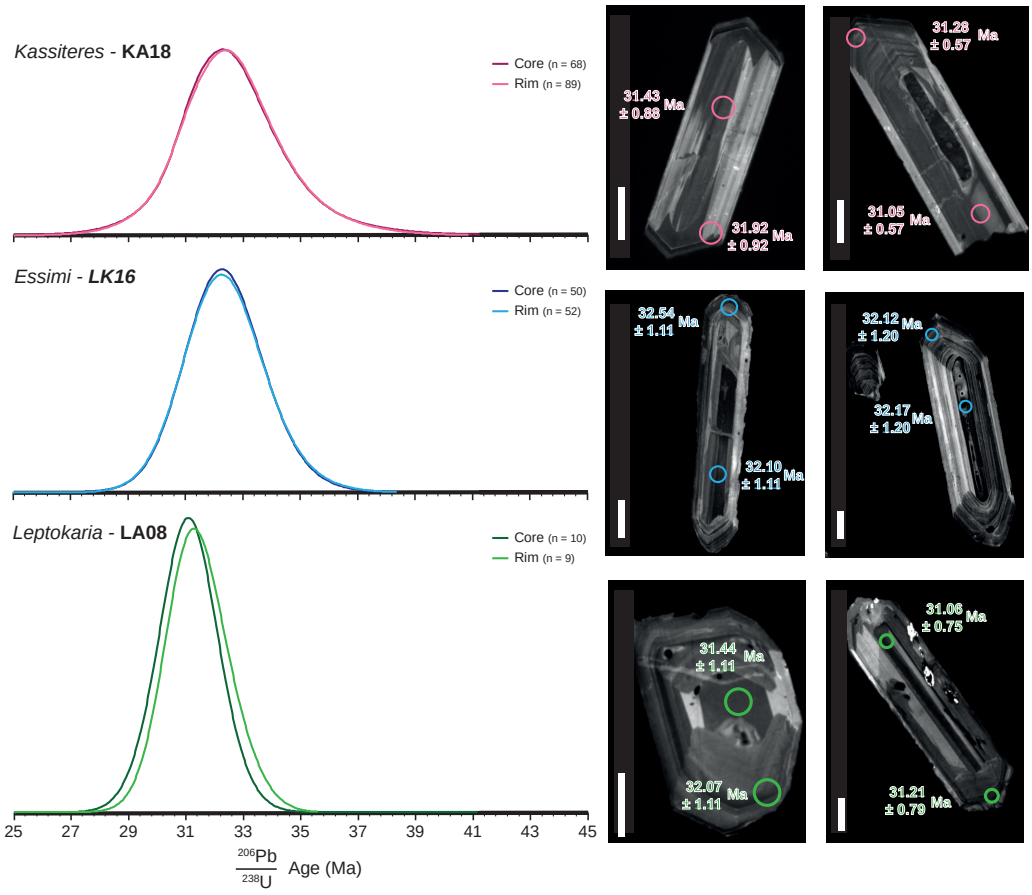

Figure 4.4: Probability density plots of the core and rim ages of the Oligocene zircon population from the Maronia Magmatic Corridor porphyries. Rim and core zircon ages overlap in many of the zircons from all three of the porphyries even where textural features in the cathodoluminescence (CL) images suggest resorption of the zircon between crystallisation of the core and rim. White bars on the CL images are 50 μm.

MIs were observed in $>$ 90 % of zircons from all four samples. The MIs can be grouped into three distinct categories based upon reflected light observations of unhomogenised inclusions (Fig. 4.3): *(i)* small, equant inclusions (10–20 μm) with trapped volatile bubbles; these inclusions typically appear glassy in reflected light but when exposed and observed in BSE the inclusions are microcrystalline with quartz, feldspar and Fe-oxides the most abundant phases. *(ii)* large glassy inclusions (up to 50 μm) that typically follow a planar surface within the zircon and consequently do not continue to any depth (2–5 μm). *(iii)* irregularly shaped inclusions, often 'wormy' through the centre of the crystals, that contain abundant microlites easily observable in reflected light microscopy; these inclusions are commonly intersected by fractures or incompletely enclosed by the zircon crystal. Upon heating, inclusions of types *(i)* and *(ii)* re-melted and quenched to form homogenous glasses suitable for analysis, whilst inclusions of type *(iii)* nucleated further crystals suggesting that they might form by exploiting pre-existing fractures in the zircons. Daughter crystals were distinguished from microlite crystals in some inclusions on the basis of size (large: 2–5 μm diameter). Fe-Ti-oxides and Ca- and REE-phosphates were the most common daughter crystals in all samples whilst wolframite (Fe,Mn)WO_4 and Fe-sulphide crystals were observed in inclusions from KA15_018 and KA15_019 only (Fig. 4.3).

4.5.2 Analytical Results

U-Pb Zircon Geochronology

The data shows clear zircon age populations in all three samples. Dominant age populations around 31–32 Ma are observed in all of the samples and both KA15_018 and LK16_016 also have xenocrystic cores with Palaeozoic to Mesozoic ages. In all samples, resorption textures are observed in zircons where the zircon core and rim analyses give the same age within error (Fig. 4.4). This indicates that at the resolution of the analyses there is no systematic time difference between core and rim growth in these zircons, thus the texturally complex internal morphology of these zircons was developed over time periods smaller than the 100s kyrs uncertainty on the U-Pb geochronology. The age of final emplacement age of LA15_008 has been calculated by taking the weighted average of the rim population of concordant ($0.95 \leq C2 \geq 1.05$) analyses to sample the youngest possible zircon population. All weighted mean ages presented have been calculated using the random, analytical uncertainty before the systematic uncertainty was propagated through the final weighted mean to avoid artificial reduction (Horstwood et al., 2016). A weighted mean age of 31.21 $\pm$ 0.22 Ma (MSWD = 0.91, n = 19) is calculated for the Leptokaria porphyry dyke sample LA15_008.

Xenocrystic zircon cores are present in KA15_018 and LK16_016 whilst LA15_008 does not sample any zircons older than 33 Ma. KA15_018 has zircon core populations that cluster in the Jurassic, Triassic – Permian and a small outlying population in the Silurian – Cambrian (Fig. 4.5A). Conversely, LK16_016 does not sample a Jurassic population of xenocrystic cores but has significant populations of Triassic – Permian and Silurian – Cambrian zircon cores which overlap with those observed in KA15_018 although the Silurian – Cambrian cores are much more prevalent in LK16_016 (Fig. 4.5B). A single xenocrystic core from LK16_016 is from the Proterozoic. The full set of U-Pb geochronology data are given in Appendix I.

Zircon-Hosted Melt Inclusions Major Element Chemistry

EPMA major element geochemistry shows two clear populations of melt inclusions: an abundant, high-Si population between 69–78 wt.% SiO_2 (Table 4.1) and a less common, low-Si population between 47–63

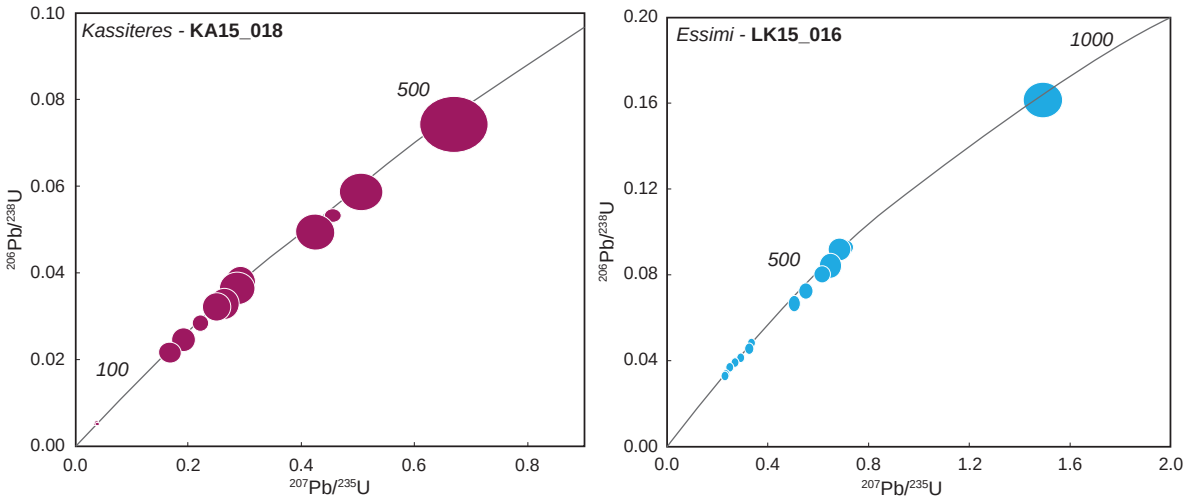

Figure 4.5: Concordia plots of the inherited xenocrystic population of zircons from the Kassiteres and Essimi porphyries; no inheritance was observed in the Leptokaria porphyry sample LA15_008. The Concordia curves are annotated with ages in Ma indicating concordant $^{206}Pb/^{238}U$ and $^{207}Pb/^{235}U$ analyses. The Kassiteres and Essimi porphyries have broadly similar xenocrystic populations between 150–300 Ma and 400–550 Ma. At Essimi, a single zircon analyses samples the Proterozoic at $\sim$ 950 Ma.

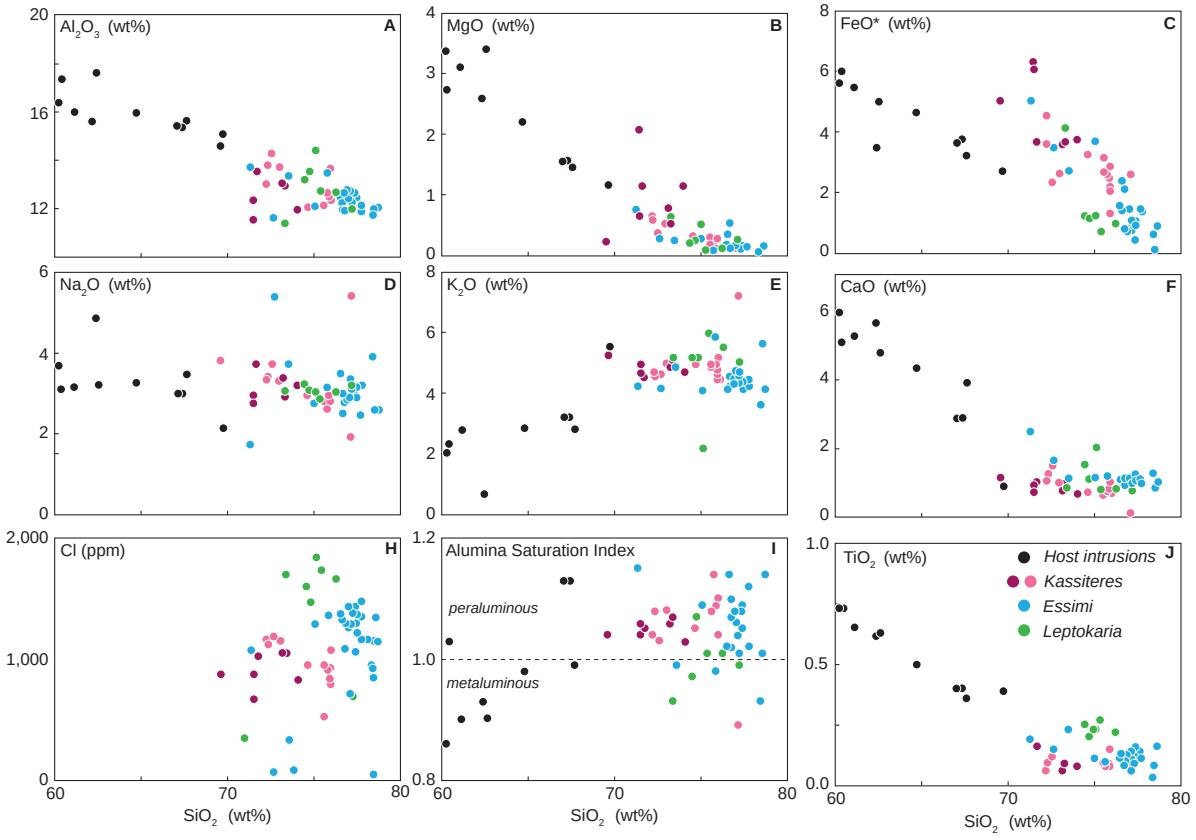

Figure 4.6: (A–J): Major element chemistry of the porphyry zircon-hosted melt inclusions compared with the regional Maronia Magmatic Corridor (MMC) liquid line of descent. Two shades of pink in the Kassiteres analyses represent the two different Kassiteres samples KA15_018 and KA15_019 and is consistent throughout the rest of the plots. The zircon-hosted melt inclusions fall on a co-genetic trend with the MMC. (I): The Kassiteres and Essimi zircon-hosted melt inclusions are peraluminous whilst the MMC host intrusion and Leptokaria porphyry melt inclusions are on the metaluminous – peraluminous boundary.

wt.% SiO_2. The low-Si analyses are further characterised by high Al_2O_3 (> 20 wt.%) and elevated alkalis. The low-Si analyses were always taken from melt inclusions intersected by hairline fractures or touching an external crystal face (style *(iii)* MIs), and as such we suggest that the melts were altered by magmatic-hydrothermal fluids during acid alteration and are consequently not sampling a low-Si melt composition. The analyses are stochiometrically similar to clays with varying proportions of smectite, kaolinite and illite between analyses (Appendix J).

The zircon-hosted MIs from the porphyry samples fall on a fractionation trend consistent with the regional magmatism and their plutonic hosts (Fig 4.6). The MIs from the Essimi and Leptokaria samples (LK16_016 and LA15_008) are more evolved than the Kassiteres samples (KA15_018 and KA15_019) with mean SiO_2 values of 75.78 wt.% SiO_2 and 71.78 wt.% SiO_2 respectively. Al_2O_3, TiO_2, FeO, MgO and CaO behave as compatible elements throughout, decreasing with fractionation (increasing SiO_2), whilst K_2O behaves as an incompatible element throughout. The porphyry MIs are peraluminous a mean aluminium saturation index (ASI $\frac{Na+K+Ca}{Al}$ molar) = 1.06 at Kassiteres, mean ASI = 1.03 at Essimi and mean ASI = 1.01 at Leptokaria, whilst the host plutons are metaluminous (mean ASI = 0.78 host plutons). This suggests an aluminous component to the porphyry magmas that is most significant at Kassiteres (Fig. 4.6). An apparent inflexion maximum in Na_2O occurs between the porphyry MIs and the host intrusion whole-rock with Na_2O behaving as a compatible element in the MIs. In combination with the flattening of the Al_2O_3 and CaO trends, this suggests Na- and Si-rich, Ca- and Al-poor albite is more prevalent than anorthite in the porphyry magmas compared to host intrusions. The porphyry MIs are enriched in TiO_2 and FeO over the regional magmatic trend suggesting assimilation of a Ti-Fe rich phase in the porphyry melts. H_2O, as measured by the H_2O-by-difference technique during EPMA, is highly scattered ranging from 0–7.5 wt.% H_2O in the inclusions (Table 4.1). The Cl data presented are amongst the first direct Cl measurements of a metal-bearing melt from an magmatic mineralising system; the data range from 200–1900 ppm Cl. Cl behaves incompatibly, increasing with fractionation, and a difference in Cl between the elevated LK16_016 and LA15_008 MIs and the lower KA15_018 and KA15_019 MIs is distinguished (Fig. 4.6).

Table 4.1: Major element chemistry of the zircon-hosted melt inclusions as measured by EPMA. Oxides are anhydrous normalised (wt.%) and Cl (ppm).

	Kassiteres						Essimi			Leptokaria		
	KA18 (n = 13)			KA19 (n = 7)			LK16 (n = 39)			LA08 (n = 19)		
	Average	Max.	Min.	Average	Max.	Min.	Average	Max.	Min.	Average	Max.	Min.
SiO_2	74.81	77.11	72.25	72.12	74.04	69.58	78.07	85.22	71.31	75.75	81.94	70.91
TiO_2	0.07	0.15	0.00	0.06	0.16	0.00	0.10	0.23	0.00	0.15	0.27	0.00
Al_2O_3	12.67	14.29	9.95	12.86	14.64	11.55	12.08	13.73	7.22	13.67	19.84	11.03
FeO	2.71	4.55	1.29	4.56	6.31	3.54	1.02	5.03	0.00	1.11	2.41	0.36
MgO	0.31	0.63	0.10	0.93	2.08	0.22	0.16	0.75	0.00	0.43	1.79	0.08
MnO	0.04	0.09	0.00	0.06	0.10	0.04	0.05	0.11	0.00	0.03	0.09	0.00
CaO	0.85	1.47	0.10	0.89	1.15	0.67	1.20	2.47	0.40	1.08	2.02	0.22
Na_2O	2.98	3.74	1.94	3.25	3.79	2.77	3.80	6.24	1.74	3.29	4.22	2.86
K_2O	4.99	7.24	4.45	4.87	5.26	4.52	3.09	5.86	0.11	3.86	6.02	0.59
Cl	924	1200	286	922	1062	680	994	1480	0	1178	1851	0
H_2O	3.65	7.85	1.28	1.17	2.97	0.24	2.34	7.16	0.00	3.36	8.55	0.00
ZrO_2	0.47	1.00	0.20	0.32	0.46	0.22	0.33	1.02	0.00	0.51	1.03	0.00

Zircon Trace Element Geochemistry

The zircon trace element signatures of both Kassiteres samples (KA15_018 from the argillic alteration zone and KA15_019 from the phyllic alteration) are indistinguishable. Intra-zircon variability, that is the difference in chemistry between the core and rim of a single zircon crystal, in the zircon trace element geochemistry was minimal showing no detectable trends; however, clear differences are observed between the Kassiteres, Essimi (LK16_016) and Leptokaria (LA15_008) samples.

Distinct populations of Hf are observed between localities; Leptokaria is has the lowest Hf concentration, Essimi intermediate and Kassiteres has the most elevated Hf (Fig 4.7). Overall, the REE trace element patterns from all of the samples show increasing concentrations from the light REEs (LREEs) to the heavy REEs (HREEs) consistent with the increased compatibility of the REE as a function of decreasing ionic radius from La to Yb (Figs. 4.8A-C). The magnitude of the Ce anomaly, using Ce_N/Nd_N as a proxy, is greater in Essimi sample LK16_016, than in either the Leptokaria or Kassiteres samples (Fig. 4.8D). All the samples have a distinct, negative Eu anomaly (Eu/Eu* < 1) indicating the presence of divalent Eu which is less compatible in zircon than the trivalent REE cations. The porphyry samples show overlapping degrees of middle REE (MREE) to HREE fractionation as indicated by the Gd_N/Lu_N ratio (Fig. 4.8F). The magnitude of the negative Eu anomaly is smaller at Essimi than Kassiteres and Leptokaria indicating less abundant Eu^{2+} in the Essimi melt (Fig. 4.8E).

All the zircons studied show elevated Ta/Nb ratios (> 0.2) compared to the Ta/Nb ratio of the continental crust (0.08–0.1; Barth et al., 2000) and depleted mantle (0.07–0.06; Hofmann and Jochum 1996), and are compatible with the highly variable Ta/Nb ratios observed in granites from a variety of tectonic settings (0.04–>0.5; Green 1995). The Essimi and Leptokaria zircons show close overlap with a mean Ta/Nb = 0.47 $\pm$ 0.13 (2σ scatter) whereas the Kassiteres zircons show much greater variability with a mean Ta/Nb = 0.31 $\pm$ 0.14 (Fig. 4.9A). The lower Ta/Nb at Kassiteres is the result of elevated Nb concentrations, of up to an order of magnitude, in the Kassiteres zircons. The low Ta/Nb Kassiteres zircons are also enriched in U/Yb, W and Sn (Fig. 4.9B-D). U is highly incompatible element that is enriched in the crust whilst Yb is compatible in mantle minerals and thus enriched in mantle melts; the U/Yb ratio is an indicator of crustal contamination with elevated U/Yb indicating an increasingly large crustal component in the melt (Gardiner et al., 2017). The U/Yb ratio and the concentration of incompatible metal Sn, correlate strongly with Nb at Kassiteres, whilst incompatible metal W also shows a relationship with increasing Nb.

The Kassiteres zircons have W concentrations up to thousands of ppm (max. 1590 $\pm$ 150 ppm W). Whilst there is wolframite present as a sibling crystal in some of the MIs, the ablation profiles and probe mapping suggest the W measured is bound in the zircon lattice. Sn in the Kassiteres zircons is typically between 0.5 and 1.0 ppm with a max. concentration of 3.25 $\pm$ 0.62 ppm. U/Yb, W and Sn in the Essimi and Leptokaria zircons are much lower (max. 42 $\pm$ 8 ppm W and 0.62 $\pm$ 0.42 ppm Sn) and show little correlation with Nb concentration and Ta/Nb ratio. We considered the possibility of that elevated Sn and W values may result from mass interferences from the zircon matrix on ^{182}W and ^{120}Sn. Although no reference values exist for our zircon validation materials GJ-1 and 91500, the much lower measured concentrations of W and Sn measured within the zircon validation materials than our sample set (GJ1: W = 0.23 ppm and Sn = 0.68 ppm; and 91500: W = 0.63 ppm and Sn = 0.15 ppm) indicate that the elevated W and Sn within Kassiteres, Essimi and Leptokaria zircons result from real counts of these elements rather than interferences.

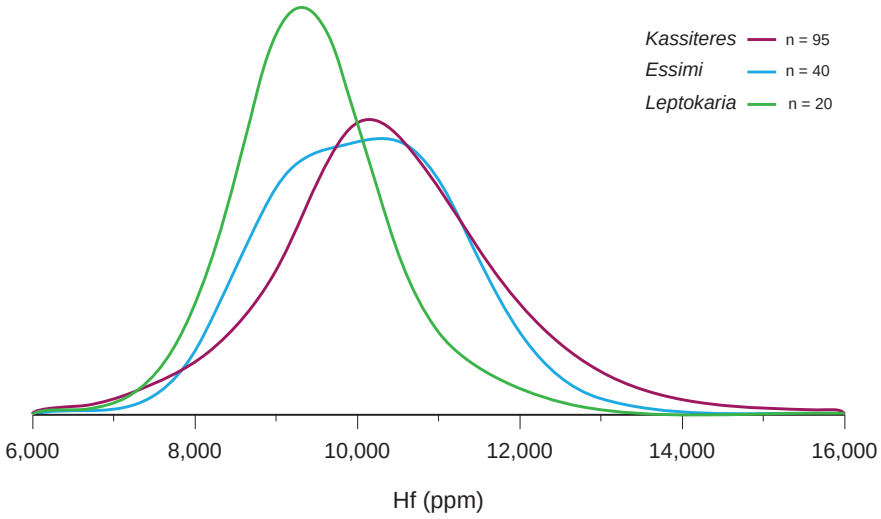

Figure 4.7: Probability density plots (PDPs) of the Hf concentration of the Kassiteres, Essimi and Leptokaria porphyries. The Kassiteres and Essimi zircons have greater concentrations of Hf than the Leptokaria zircons.

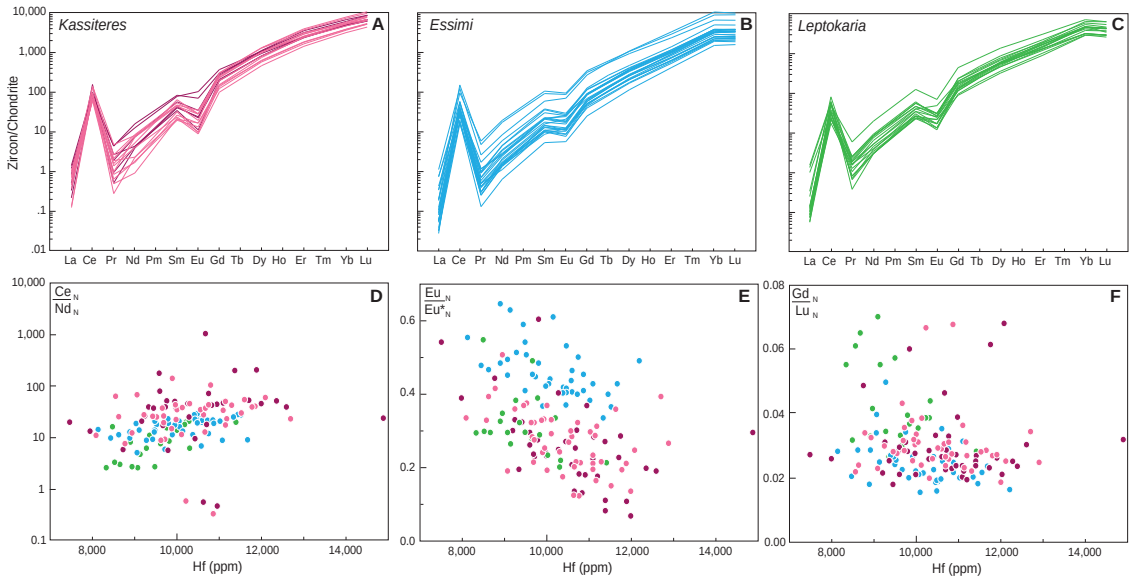

Figure 4.8: Rare earth element (REE) zircon geochemistry from the Maronia Magmatic Corridor (MMC) porphyry intrusions. (A–C): The overall REE trend is similar across the all of the porphyries. Fractionation of Yb from Lu is observed at Essimi and Leptokaria samples compared to Kassiteres, however, comparison of the secondary standard date between analytical sessions shows uncertainty in the Yb concentrations and this could be an analytical artefact. As a result, we do not interpret any trends in the data using Yb. (D): The Ce anomaly, using Ce_N/Nd_N as a proxy, is an indicator of melt oxidation and shows reduced melt concentrations (elevated Ce_N/Nd_N) at Kassiteres and Essimi over Leptokaria. (E): Sub-parallel trends in Eu/Eu* with Hf, an indicator of magmatic differentiation, show decreasing Eu/Eu* with crystallisation, likely reflecting saturation in plagioclase. Elevated intial Eu/Eu* is recorded at Essimi over Kassiteres and Leptokaria. (F): Gd_N/Lu_N is an indicator of MREE/HREE fractionation and shows overlapping values across the MMC, suggesting that the REE fractionation signature is common to all of the porphyry magmas.

Table 4.2: Average zircon trace element concentrations and ratios. Rare earth elements chondrite normalised after Sun and McDonough (1989); A.R.E. – average relative (%) error at 2σ confidence level

Element	Kassiteres								Essimi				Leptokaria			
	KA18 (n = 42)				KA19 (n = 50)				LK16 (n = 20)				LA08 (n = 41)			
	Average	Max.	Min.	A.R.E.	Average	Max.	Min.	A.R.E	Average	Max.	Min.	A.R.E.	Average	Max.	Min.	A.R.E.
Y	2120	3690	211	9	2066	4930	1030	8	1754	3640	948	7	1095	3750	411	7
Nb	9.9	26.7	0.0	34.8	8.9	33.8	0.0	34.8	5.0	14.6	1.5	7.9	3.8	9.2	1.6	8.9
Sn	0.3	1.2	0.0	104.3	0.4	3.3	0.0	58.1	0.3	0.7	0.0	32.0	0.1	0.3	0.0	29.7
Hf	10605	14900	7480	9	10451	12900	8100	8	9472	11410	8330	7	10121	12200	8130	7
Ta	3.1	6.6	0.3	19.9	2.8	9.1	0.6	18.4	2.2	6.6	0.6	10.9	1.8	3.9	0.7	10.4
W	13.4	225.0	0.0	23.2	127.3	1590.0	0.0	42.3	1.0	8.2	0.0	59.3	2.0	42.3	0.0	60.0
Pb	29.0	73.9	11.6	11.6	28.4	102.0	8.6	11.4	14.1	28.1	4.5	10.3	12.3	32.3	3.4	9.9
Th	640	2060	9	11	669	2290	146	10	492	1170	157	8	467	3060	94	9
U	1270	3300	219	9	1202	4280	345	9	716	1440	224	8	607	1782	189	8
La/N	0.2	1.9	0.0	60.0	0.2	1.6	0.0	103.1	0.3	1.5	0.0	60.2	0.1	1.2	0.0	59.2
Ce/N	67.5	153.9	0.7	11.6	66.2	135.1	6.1	10.3	40.2	80.2	16.3	7.6	41.7	152.9	14.8	8.1
Pr/N	0.6	4.4	0.0	114.3	0.8	4.6	0.0	90.3	1.6	5.9	0.4	28.1	0.9	6.0	0.1	31.9
Nd/N	2.7	15.6	0.0	79.8	3.3	19.1	0.0	52.7	5.9	19.5	2.9	15.5	3.3	19.8	0.7	17.9
Sm/N	28.9	96.1	0.0	39.1	30.8	121.6	10.7	32.0	40.8	123.5	22.6	12.4	21.8	107.2	5.5	15.0
Eu/N	17.8	101.7	0.3	52.9	17.0	37.9	4.8	36.0	25.6	69.1	11.9	12.0	20.5	95.5	5.8	13.4
Gd/N	159	365	24	17	163	594	70	15	167	436	88	10	88	346	25	11
Dy/N	652	1106	84	11	650	1843	323	11	603	1346	317	8	335	1083	116	8
Er/N	1985	3486	138	10	1876	4048	937	10	1581	3033	894	7	1008	3305	421	8
Yb/N	4053	7412	258	10	3866	7376	2076	10	4333	7012	2594	8	3308	10282	1494	8
Lu/N	5470	9173	346	10	5284	10039	2744	9	3928	6220	2232	7	3332	9646	1567	7
Ce/Nd (N)	74.2	1076.5	0.4	76.6	32.3	143.2	0.3	51.6	16.8	30.0	4.9	20.0	8.9	20.4	2.5	17.6
Eu (N)/Eu*	0.2	0.6	0.0	68.3	0.3	0.5	0.0	50.9	0.3	0.5	0.2	19.9	0.5	0.6	0.3	23.0
Gd/Lu (N)	0.030	0.068	0.018	19.6	0.030	0.067	0.019	17.5	0.025	0.049	0.016	13.0	0.043	0.070	0.026	12.2
U/Yb	2.2	19.1	0.4	13.5	1.8	3.7	0.3	13.4	1.0	1.8	0.5	11.8	1.1	1.8	0.5	11.2
Ta/Nb	0.3	0.5	0.2	45.0	0.3	0.5	0.2	39.9	0.4	0.7	0.4	13.7	0.5	0.6	0.3	13.8

4.6 Utility of Zircon-Hosted Melt Inclusion Analysis

4.6.1 The Ability of Zircon-Hosted Melt Inclusions to Record Parent Magma Chemistry

Major Element Chemistry

The geochemistry of MIs is assumed to be representative of the composition of the magma outside the crystal at the time of trapping and are thus important repositories of petrogenetic information in systems where whole-rock analyses are unrepresentative and/or unavailable e.g., volcanic eruptive products. MIs and whole-rock analyses record two different sets of geochemical information, both of which can be used to reconstruct the composition of the original melt. MIs sample the instantaneous composition of the melt at the time of trapping whilst whole-rock geochemical analyses integrate the composition of the phenocryst assemblage of the rock. MIs have an additional advantage in that a suite of co-genetic MIs will give a range of compositions, sampling melt throughout crystallisation of the host mineral and MIs will thus record a part of the liquid line of descent (LLD), mapping the geochemical evolution of the magma (e.g., Blundy and Cashman 2005). A wide body of work has been devoted to testing the ability of MIs to represent the magma chemistry of the melts from which they crystallise, concluding that this is a valid assumption if the effects of boundary layers and post-entrapment modification are minimal, discussed below in relation to zircon-hosted MIs (Roedder, 1979; Qin et al., 1992; Thomas, 2003; Danyushevsky et al., 2000, 2004; Baker, 2008).

MIs are trapped in defects in the crystal lattice, embayments, that form as the result of disruption to the planar crystal-melt interface. Rapid crystal growth and/or nucleation of smaller crystals or volatile bubbles on phenocrysts surfaces are among the mechanisms invoked to explain embayment formation (e.g., Roedder 1979). Boundary layers of incompatible-rich melt have been shown to form in rapidly crystallising systems where the region of melt immediately adjacent to a crystal interface which is in disequilibrium with the surrounding melt reservoir (e.g., Kent 2008). For most MI hosts, this means that boundary layers are significant when considering slowly diffusing trace elements that are highly incompatible or highly compatible in the host mineral, and thus artificially enriched or depleted, in the melt immediately surrounding the crystal. In an evolved hydrous melt, Zr diffuses through the melt slowly and is the limiting element in zircon growth (e.g., Hofmann et al. 2009). The trace element ions of interest, the REEs and volatile species, are more mobile than Zr in evolved melts and thus will remain in diffusive equilibrium with the melt reservoir during rapid zircon growth (Watson and Harrison, 1983; Baker, 2008). Furthermore, Thomas (2003) studied the effect of boundary layers in zircon-hosted MIs in additional to MIs hosted in plagioclase, quartz and allanite from the same magma, and found no systematic fractionation of the REEs between MIs hosted in different phases. Consequently, we reason that the negligible influence of boundary layers effects on the major, trace and volatile components in the zircon-melt system, means that zircon is an ideal host for finding MIs that are representative of bulk magma compositions.

Post-entrapment modification of MIs is another potential pitfall where the composition of MIs could be unrepresentative of the bulk composition of the melt from which it was trapped. Our analyses of zircon-hosted melt inclusions showed a bimodal population of high-Si rhyolite glasses and low-Si, high-Al clay-altered inclusions. The altered analyses were easy to identify owing to their anomalous enrichment in immobile Al and comparative loss of the mobile alkali cations (K, Na and Ca) and Si. The presence of rhyolitic inclusions in zircons from highly altered samples suggests that pristine zircons effectively armour against hydrothermal alteration. This could be the result of volume restrictions in inclusions in rigid

zircon which limited clay formation or, more likely, the result of geologically slow diffusion rates through zircon preventing cation exchange between the melt inclusions and hydrothermal fluids (e.g., Cherniak and Watson 2003). However, the clay-altered inclusions show that zircon is not an infallible MI host and that hydrothermal alteration of inclusions occurs where the inclusions are incompletely encased by zircon or are cut by hairline fractures. Post-entrapment modification is a widely observed problem in MIs from a variety of hosts (Créon et al., 2018); zircon, with geologically slow ionic diffusion rates and high resistance to hydrothermal alteration, withstands post-entrapment modification of major melt chemistry to a much greater extent than other MI host minerals.

Volatile Chemistry

Zircon-hosted MIs from porphyry intrusions have the potential for direct analysis of volatile components in mineralising magmas; this is an exciting and prosperous avenue to explore further through MI petrology of porphyry systems. Diffusive re-equilibration of volatiles in MIs post-entrapment has been found to have a significant impact on MI composition in a variety of host minerals, both during the geological history of the MIs and during cooling experiments (e.g., Danyushevsky et al. 2002). Significant work on both experimental and natural samples has studied the ability of plagioclase- and olivine-hosted MIs to record initial volatile concentrations. Traditionally is has been assumed that the strength of host minerals during decompression protects MIs from volatile loss on ascent and cooling (e.g., Sobolev and Danyushevsky 1994; Danyushevsky et al. 2002); however, more recent work has shown that H_2O re-equilibration in olivine occurs within hours to days in basaltic systems due to the rapid diffusive exchange of H^+ (e.g., Gaetani et al. 2012), and that few primary magmatic signals are recorded in the H_2O and CO_2 analyses of plagioclase-hosted MIs (Neave et al., 2017, 2018). Cl typically has a lower diffusion coefficient than H_2O, CO_2 or any of their cations, and has been shown to correlate with slow diffusing incompatible trace elements leading to the conclusion that Cl concentrations in plagioclase-hosted MIs typically record dissolved magmatic concentrations of Cl (e.g., Neave et al. 2017). In general, the predicted diffusion rate of ionic species through zircon is slower than estimates for plagioclase and olivine (Cherniak and Watson, 2003; Cherniak et al., 2009), therefore, we suggest that re-equilibration of volatile species in zircon-hosted MIs is less significant that other MI host minerals. However, further study of H^+ OH^- and CO_2 diffusion through zircon is required for the interpretation of H_2O and CO_2 concentrations in zircon-hosted MIs.

4.6.2 Crystal Phases in Zircon-Hosted Melt Inclusions

Crystals in MIs are common (Fig. 4.3) and can form two ways: *(i)* crystallisation of the melt post-entrapment (daughter crystals), and *(ii)* co-entrapment of a small crystal on the surface of the host phenocryst (sibling crystals). Microlites and nanolites are common daughter crystals and many homogenisation experiments, including this study, have heated and quenched the MI host crystals from super-liquidus temperatures in order to re-homogenise the MIs prior to analysis (e.g., Nielsen et al. 1997; Michaud et al. 2000; Thomas 2003). However, MI heating and quenching would also affect sibling crystals and could result in the homogenisation of the crystals into the melt to give an artificial and unrepresentative melt inclusion composition. Sibling crystals, often Fe-sulphides, Fe-oxides and apatite, are typically sufficiently large that they are visible during crystal picking and thus can be avoided in the selection of crystals for homogenisation. Simple mass balance calculations show that accidental homogenisation of a pyrite crystal making up 5 % by volume of a rhyolite melt inclusion would add an excess 5.5 wt.% FeO to the

homogenised melt and 5 wt.% S, not an analyte in our EPMA, would be accounted for as H_2O-by-difference (assuming a density of 5 g/cm^3 pyrite, 2.5 g/cm^3 rhyolite). Careful screening of EPMA data of MIs is thus required and where a correlation between elevated FeO and H_2O-by-difference occurs, the possibility of re-homogenisation of a sibling crystal should be considered. Additionally, S and P could also be added to the EPMA analyte list as an additional check for accidental re-homogenisation of sulphide and apatite sibling crystals.

Overall, zircon-hosted MIs offer a window into the composition of the parental melt. As outlined above, the minimal impact of boundary layer effects and easily recognisable post-entrapment modification, make zircon an ideal host for MIs. Zircon-hosted MIs are of great value to the study of magmatic-hydrothermal mineral deposits. Specifically, the chemical robustness of zircon during hydrothermal alteration which obliterates the primary magmatic mineral assemblage which could otherwise preserve MIs, means zircon-hosted MIs are a unique repository of the chemistry of ore-forming magmas. With careful selection of MIs and screening of results as discussed above, zircon-hosted MIs are a powerful tool for studying the petrogenesis of magmatic mineral deposits going forward.

4.7 Complex Mixing Signals along the MMC and their Influence on Metallogenesis

4.7.1 Porphyry Melt Composition

The rhyolitic MIs fall on a fractionation trend shared with the regional host magmatism and host plutons suggesting a common, parental magma source between them (Fig. 4.6). In general, the MIs are more evolved than the host plutons. This is expected for two reasons: *(i)* the relict mineralogy of the porphyry intrusions suggests an evolved, rhyolitic quartz + feldspar ± hornblende mineral assemblage and, *(ii)* zircon saturates late in the crystallisation sequence of a magma so the melts trapped in zircon-hosted inclusions will sample the later, more evolved stages of residual melt. Elevated SiO_2 in the Essimi and Leptokaria MIs suggest a more evolved melt than is sampled in the MIs from Kassiteres. Both the Kassiteres and Essimi porphyries are more aluminous that the host intrusions (mean ASI = 1.06 Kassiteres; mean ASI = 1.03 Essimi; mean ASI = 0.78 host intrusions), suggesting mixing of an aluminous, crustal component in the porphyry magmas. Leptokaria is the least aluminous porphyry (mean ASI = 1.01) and falls on a co-genetic trend with the host intrusions suggesting no aluminous mixing component in the Leptokaria porphyry melt. Elevated FeO is observed in the Kassiteres and Essimi porphyries over the regional magmatic trend suggesting that it was also supplied during mixing. Cl in MIs ranges from 63–1851 ppm Cl and is within the permissible range of dissolved Cl contents in subduction-related melts (e.g., Webster et al. 2018), providing further evidence of a component of post-collisional magmatism derived from subduction-modified lithospheric mantle in the porphyry magmas.

4.7.2 Trace Element Budget of the Porphyry Magmas

The zircon trace element geochemistry of the porphyry samples is distinct from each of the localities: Kassiteres, Essimi and Leptokaria. Zircon trace element chemistry records subtle changes in the trace element budget of a melt, resulting from initial melt composition, melt mixing and melt evolution during crystallisation; it is overprinted by the complex, T-dependent zircon/melt partition coefficients of the trace elements (e.g., Cherniak et al. 1997). Here we use the trace element chemistry of the zircons to unpick the mixing components identified in the zircon-hosted MI chemistry.

The Kassiteres zircons have the highest average Hf concentration ([Hf]; Fig. 4.7). Hf is a highly incompatible element in major rock forming minerals with a mineral/melt (andesite) partition coefficient less than one ($D^{Hf} < 1$) in amphibole, clinopyroxene, olivine, plagioclase and magnetite (Luhr and Carmichael, 1980). It is thus an indicator of magmatic differentiation, increasing in concentration in the melt during crystallisation. Without prior knowledge, the elevated [Hf] at Kassiteres could indicate the Kassiteres melt was more evolved than Essimi and Leptokaria. However, the evidence from the major element geochemistry of the zircon-hosted MIs shows elevated SiO_2 at Essimi and Leptokaria relative to Kassiteres. As an incompatible element, Hf is also enriched in the crust, and greater [Hf] in zircon has been used as an indicator of a crustal component to magmatism (Burnham and Berry, 2017). This is in keeping with the ASI of the zircon-hosted MIs which showed the greatest degree of crustal mixing at Kassiteres. The Leptokaria porphyry, which has the lowest [Hf], also has the lowest ASI and Essimi is intermediate in both indicators. This could reflect a crustal component to the magmas at Kassiteres, a lesser degree of crustal mixing at Essimi and a predominantly mantle-derived melt at Leptokaria. We will go on to test this hypothesis using the rest of the zircon trace element data.

Rare Earth Elements

The REE patterns of the porphyry zircons provide further evidence of the trace element budgets of each of the parental magmas. Similar trends in the REE patterns are observed between the systems. Using the Hf in zircon as a fractionation index identifies overlapping fractionation trends in Gd/Lu (MREEs/HREEs) from all of the systems indicating a shared source of the overall REE element signature of the magmas (Fig. 4.8F). However, subtle differences are observed in both the Ce and Eu concentrations between systems. Given the difficulty measuring absolute concentrations of La in zircon due to its low abundance, we refrain assigning absolute values to the Ce anomaly, but instead use the Ce_N/Nd_N ratio as a proxy for oxidation (Chelle-Michou et al., 2014; Lu et al., 2016). Larger magnitude Ce anomalies are observed at Kassiteres and Essimi over Leptokaria and indicate a more oxidised initial melt composition (Fig. 4.8D). The zircon trace elements show sub-parallel Eu/Eu* fractionation trends with decreasing Eu/Eu* during fractionation reflecting plagioclase crystallisation (Fig. 4.8E). At Essimi, the fractionation trend, whilst sub-parallel to that at Leptokaria and Kassiteres, starts from a higher initial Eu/Eu*. If the Eu anomalies are taken as an indicator of oxidation state, this would suggest that the Essimi magma was more oxidised than Kassiteres or Leptokaria, which one might attribute to magmatic degassing (Dilles et al., 2015). However, the Ce anomaly is greater at Kassiteres and Essimi than Leptokaria indicating that oxidation state is a less likely cause of the Eu anomaly and it more likely reflects different starting magma compositions. Given the crustal mixing noted in the zircon-hosted MIs from Essimi, this suggests that the crustal mixing component at Essimi was Eu-rich.

Our results suggest that the REE budget of the magmas was predominantly controlled by the mantle-derived magma component with trends overlapping in all systems. Elevated Ce anomalies at Kassiteres and Essimi may indicate that crustal mixing in these systems may have resulted in a more oxidised melt. This is contrary to the Ce_N/Nd_N signal observed in the zircon trace element compilation of Lu et al. (2016), where the crustal-derived granites show lower Ce_N/Nd_N than their mantle-derived counterparts. The crustal-derived melts appear to differ in composition between the Kassiteres and Essimi samples, with an elevated Eu/Eu* signal in the Essimi crustal component.

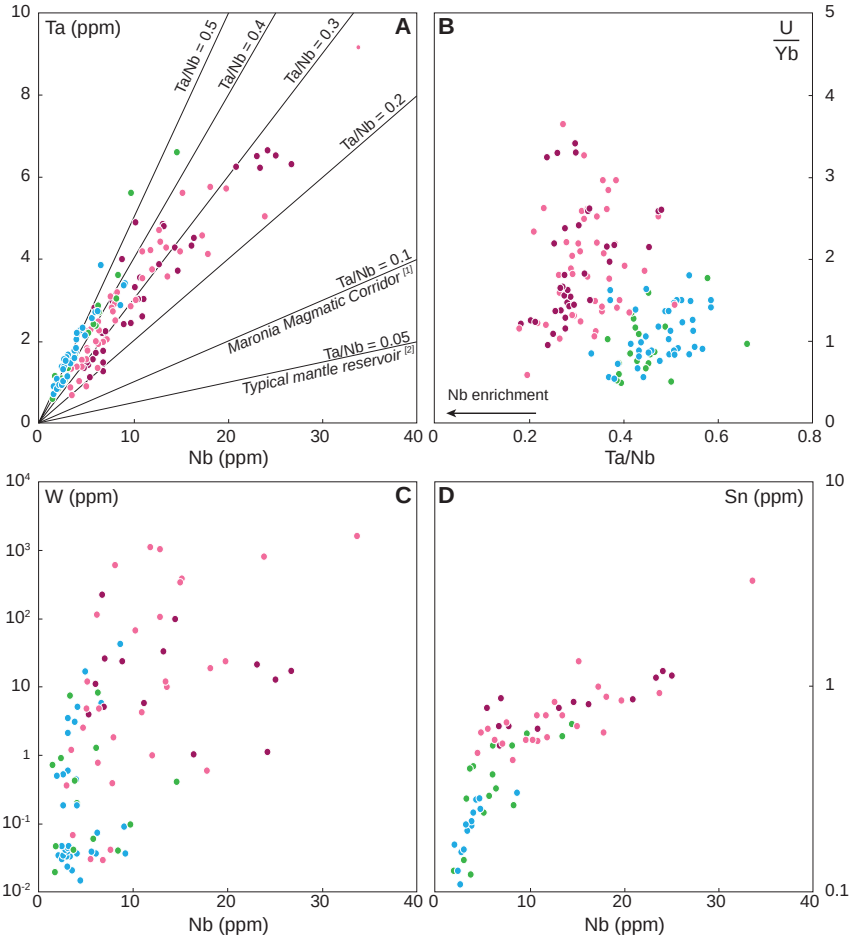

Figure 4.9:
Trace element concentrations in the porphyry zircon from the Maronia Magmatic Corridor (MMC). (A): The MMC porphyries have elevated concentrations of Ta and Kassiteres also shows elevated Nb. (B–D): Enrichment in Nb shows positive relationship with increasing U/Yb (an indicator of crustal contamination), W and Sn, suggesting that the enrichment in these elements is the result of crustal mixing. *[1]* values for the equigranular host plutons of the MMC from Chapter 2; *[2]* typical mantle reservoir values from Green (1995)

High Field Strength Elements

The high field strength elements (HFSEs) Nb, Ta and U show clear differences between the Kassiteres and Essimi – Leptokaria magmas. The porphyry zircons from all three localities show overlapping Ta (0.5–7 ppm), however, the Kassiteres zircons are elevated in Nb relative to the Essimi and Leptokaria zircons (0–10 ppm Nb Essimi and Leptokaria; 3–30 ppm Nb Kassiteres). This leads to higher Ta/Nb ratios at Essimi and Leptokaria (Ta/Nb = 0.5–0.4) than Kassiteres (Ta/Nb = $\sim$ 0.3). Zircon fractionates Ta from Nb, preferentially partitioning Ta, with zircon/melt partition coefficients D^{Ta} = 2.9 and D^{Nb} = 1.6 (Nardi et al., 2013). Accounting for the fractionation of Ta from Nb during zircon crystallisation gives Ta/Nb ratios of 0.17–0.27 in the model MMC porphyry magmas, an order of magnitude greater than the Ta/Nb values observed from the host intrusions of the MMC (Ta/Nb = 0.02–0.09; Chapter 2). The lower Ta/Nb at Kassiteres over Essimi and Leptokaria is the result of excess Nb enrichment rather than depletion of Ta (Fig. 4.9A). Correlation between excess Nb at Kassiteres and elevated U/Yb (an indicator of crustal contamination), suggest that the crustal mixing component at Kassiteres was elevated in Nb.

Ta and Nb are frequently referred to as 'geochemical twins' owing to their similar charge and ionic radius, consequently Ta and Nb should not be fractionated from one another during magmatic fractionation (Goldschmidt, 1937). However, variable Ta/Nb ratios throughout the igneous rock record suggest fractionation Nb from Ta during crust formation leaving crustal rocks enriched in Ta (e.g., Stepanov and Hermann 2013). Many mechanisms of fractionating Ta and Nb have been suggested and include, but are not limited to: *(i)* fractional crystallisation (e.g., Stepanov et al. 2014); *(ii)* hydrothermal alteration (e.g., Dostal

et al. 2015; Ballouard et al. 2016); *(iii)* crustal contamination (e.g., Acosta-Vigil et al. 2014; Stepanov et al. 2014); and *(iv)* titanite fractionation (Stepanov and Hermann, 2013; Loader et al., 2017). Elevated absolute concentrations of Ta and Nb in addition to high Ta/Nb ratios are characteristic of highly evolved mantle-derived magmas and crustal melts (e.g., Romer and Kroner 2016; Simons et al. 2017).

In the assumed scenario where the porphyry magmas were derived from the same parental mantle source as the MMC host plutons, we do not envisage that fractional crystallisation alone can account for the Ta enrichment in the MMC porphyry magma without unreasonable degrees of crystal fractionation or and unlikely fractionating assemblage, in agreement with Ballouard et al. (2016). The consistent [Ta] across the Essimi, Leptokaria and Kassiteres zircons suggest that Ta/Nb fractionation was imparted on the mantle-derived magmas and excess Nb was added to the Kassiteres system during later-stage crustal mixing. Both Nb^{4+} and Ta^{4+} variably substitute for Ti^{4+} in Ti-bearing phases such as micas, amphiboles and Fe-Ti-oxides during crystallisation, therefore, Nb and Ta can be fractionated from one another by substitution into these phases dependent upon which cation is preferentially partitioned (Green and Pearson, 1987). In amphibole and ilmenite $D^{Ta} \sim D^{Nb}$, in titanite and rutile $D^{Ta} > D^{Nb}$ whilst in micas $D^{Ta} < D^{Nb}$ (e.g., Stepanov and Hermann 2013; Ballouard et al. 2016). Thus, the most probable means to generate the observed features in the generation of the MMC porphyry magmas is by mixing magmas with a source enriched in Ta, yet with little excess Nb, perhaps the result of assimilating a Ta-rich melt generated by the melting or dissolution of a Ta-rich phase e.g., rutile, titanite (Green et al., 2000). Elevated $TiO_2$and FeO in the porphyry melt inclusions suggest an additional Ti-Fe source in the porphyry magmas consistent with assimilating a titanite-bearing melt. An alternative explanation for the enrichment in Ta could be presence of an orthomagmatic fluid which redistributed the more incompatible Ta (e.g., Dostal et al. 2015). An additional source of Nb, which correlates closely with U, is required in the Kassiteres porphyry magmas. Micas, phengite and biotite, are the primary sinks of Nb over Ta (Bachmann, 2004; Stepanov and Hermann, 2013). We propose that mixing with crustal melts at Kassiteres melted biotite and/or phengite, and suggest this as the source of elevated Nb at Kassiteres in contrast to the the Essimi and Leptokaria porphyry magmas.

To conclude, the zircon trace element geochemistry suggests that the Leptokaria porphyry is a good approximation of the mantle-derived mixing end member, and indicates two different compositions of crustal mixing components at Kassiteres and Essimi. All of the MMC porphyries share the same REE fractionation trend and show the same degree of enrichment in Ta which suggests that these features were derived from the predominantly mantle-sourced magma. The crustal component of magmatism at Essimi is Eu rich and generates an elevated Eu/Eu* starting anomaly, amphibole or titanite are some of the possibilities. At Kassiteres, elevated Nb shows a relationship with increasing U/Yb indicating that it is derived from the same crustal mixing source. Micas are the one of the few minerals that preferentially partition Nb over Ta, as such we suggest a mica-rich source of crustal mixing at Kassiteres.

Sn and W in the Kassiteres, Essimi and Leptokaria Porphyries

In this study we have presented systematic analyses of W and Sn from zircons and zircon-hosted MIs, sampling the metal-bearing porphyry intrusions of the magmatic mineral systems. High concentrations of W and Sn ($>$10 ppm and $>$ 1 ppm within zircon respectively) from the Kassiteres system indicate enrichment in these metals in the magmas over the Essimi and Leptokaria magmas. Elevated W and Sn shows a positive relationship with Nb in the Kassiteres porphyry zircons suggesting a common source of these elements.

Melting of micas biotite and/or phengite are suggested as a source of excess Nb in the Kassiteres system, as they preferentially partition Nb from Ta (Bachmann, 2004; Stepanov and Hermann, 2013); the micas are also the primary mineral hosts of W and Sn in the crust (Romer and Kroner, 2016; Simons et al., 2017). A crustal source of W from melting of a mica-rich crustal source is in line with presence of wolframite in the zircon inclusions, as wolframite solubility is lower in flux-rich systems such as crustal melts (Che et al., 2013). Given the presence of magmatic wolframite from either autocrystic or xenocrystic domains of zircon, we would expect the peraluminous Oligocene magmas to be enriched in W. Flat ablation traces show steady counts of W and Sn, consistent with metal distribution throughout the zircon crystal. Ablation of microscopic inclusions of wolframite and cassiterite which would give peaks and troughs in ablation counts and should be visible in BSE imagery of the zircons. Ablation of probable wolframite inclusions was also observed and these analyses removed from the dataset.

Tungsten has two valence states, W^{4+} and W^{6+}; the presence of W^{4+} would require unrealistic, extremely reducing conditions so we have only considered the incorporation of W^{6+}. The mechanism for substitution of W^{6+} and Sn^{4+} into the zircon lattice is unclear. W^{6+} in 4-fold coordination has a similar ionic radius to Si^{4+}; exchange of tungstate – silicate tetrahedra is a possibility but would require a charge balance (WO_4^{2-} and SiO_4^{4-}). Sn^{4+} has a smaller ionic radius than Zr^{4+} in 8-fold co-ordination (Sn^{4+} = 0.81 $\AA$, Zr^{4+} = 0.98 $\AA$ and so simple cation substitution could occur. Taking the maximum [Sn] and [W] in the host plutons (W = 3.3 ppm and Sn = 5.0 ppm; Chapter 2), a simple modelling of fractional crystallisation assuming W and Sn are perfectly incompatible (i.e. $D^{crystal/melt} = 0$) in any crystal assemblage, can enrich the magma to just 50 ppm W or Sn at $>$ 80 % crystallisation. Magmatic differentiation assuming W and Sn are perfectly incompatible can account for the concentrations of W and Sn observed in the Essimi and Leptokaria zircons and some of Kassiteres analyses. However, concentrations of $>$ 100 ppm W observed at Kassiteres required mixing with a W-rich source, consistent with a biotite or phengite melt as suggested by the Ta/Nb ratios.

4.7.3 Zircon Crystallisation in the MMC Porphyries

U-Pb geochronology of the Kassiteres and Essimi zircons show that these porphyry stocks inherited a Mesozoic population of zircons that is not present in the Leptokaria porphyry dyke (Fig. 4.3); this supports the morphological characterisation of the Leptokaria zircons that suggested that simple oscillatory and sector zoning in these zircons without internal features of resorption recorded a single episode of crystallisation. The Leptokaria porphyry dyke gives an emplacement age of 31.33 $\pm$ 0.32 Ma (MSWD = 0.94, n = 9) which is consistent with intrusion of the dyke cutting the Leptokaria granodioritic intrusion (32.235 $\pm$ 0.026 Ma, U-Pb zircon CA-ID-TIMS, Chapter 2).

Similarly, the Kassiteres porphyry stock cuts the Kassiteres granodiorite intrusion. However, the age of the youngest population of zircon rims (32.16 $\pm$ 0.26 Ma, MSWD = 0.77, n = 25) overlaps with the emplacement age of the Kassiteres granodiorite suggesting penecontemporaneous emplacement (Kassiteres granodiorite: 32.045 $\pm$ 0.020 Ma, U-Pb zircon CA-ID-TIMS, Chapter 2). Zircon petrography suggests that there is a resorption zone in the outer rims that occurs at a finer scale than the 25 um ablation spot, which suggests that a bias towards older growth zones that occur on the timescale of the magmatic system (e.g., Tapster 2016). Selecting a population of dates that arise only from zircons whose internal morphology is similar to those from LA15_008 and which we interpret to be representative of a single crystallisation event, yields an interpreted emplacement age of 31.46 $\pm$ 0.34 Ma (MSWD = 1.6, n = 10). This age is resolvable as younger

than emplacement age of the host pluton and overlaps with the crystallisation age of the Leptokaria dyke, LA15_008. Using a comparable evaluation of the emplacement of the Essimi stock, yields a weighted mean age of the rim populations of 32.19 ± 0.24 Ma (MWSD = 0.28, n = 41) and a weighted mean age from 'simple internal morphology' zircons of 32.01 ± 0.35 Ma (MSWD = 0.33, n = 11) which we take as the best representation of final crystallisation and emplacement of the porphyry intrusion.

Within the Kassiteres and Essimi Oligocene zircon populations, textural variations in the internal morphology of the zircon crystals, including resorption fronts, yielded equivalent dates across zircon core – rim domains (Fig. 4.4). This indicates that formation of these internal morphologies occurred within timescales shorter than the resolution of the U-Pb geochronology, i.e. less than 100s kyrs, likely the result of short-lived thermal-rejuvenation of the magmatic system during emplacement (e.g., Tapster et al. 2016).

Both the Essimi and Kassiteres porphyries have a population of Mesozoic-Palaeozoic inherited cores (Fig 4.5), suggesting introduction of older xenocrystic zircons, likely through mixing of the primary mantle-derived magma with crustal melts as indicated by the geochemical evidence. Due to additional bias that may be introduced by zircon dissolution during the lifetime of the magmatic system and analytical sampling, the zircon inheritance record should not be treated in the same way as a true detrital data zircon U-Pb data set, where the frequency/magnitude of a population can be used to infer relative contributions of sources. Instead, we use this data set to identify if a source of a particular age is present or not. The xenocrystic zircon populations are similar between the Kassiteres and Essimi porphyry intrusions, with a broad peak in the Permo-Triassic (Fig. 4.9). Within the nuances of the xenocrystic record, the Kassiteres porphyry has a

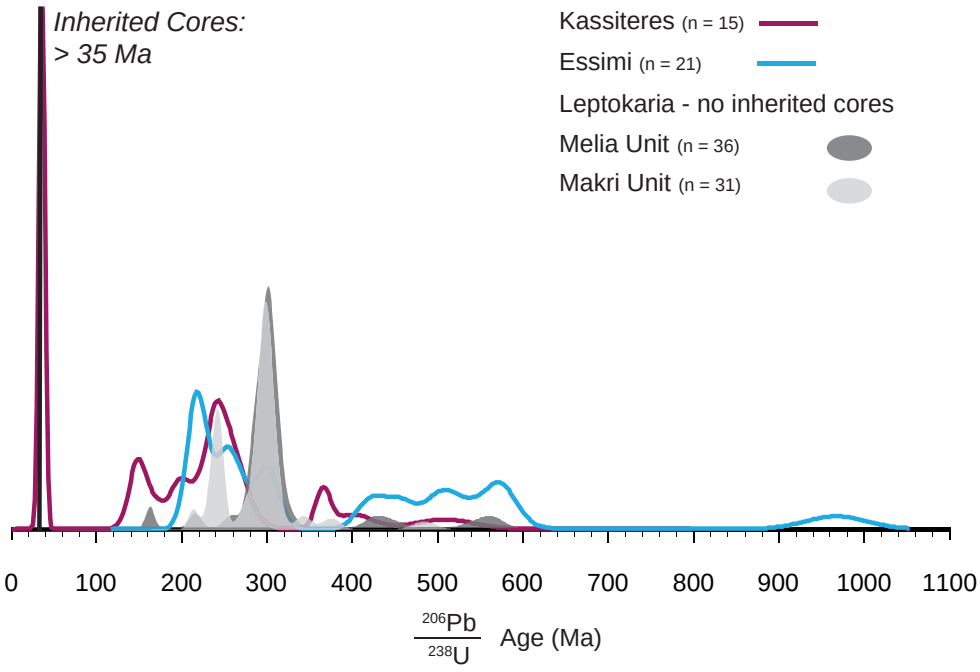

Figure 4.10: Comparison of the inherited xenocrystic population of zircons from the Kassiteres and Essimi porphyry intrusions with the detrital zircon population from the local hanging wall basement, the Circum Rhodope Belt (detrital zircon data from Meinhold et al. 2010). The xenocrystic zircon population of the porphyries should not be treated as a detrital data set owing to sampling bias and zircon preservation bias during resorption, rather it should be treated as an analogue indicator as to whether an age population is present. Broadly similar peaks in age indicate that the xenocrystic zircon population of the Kassiteres and Essimi porphyries is consistent with local basement.

zircon population centred on $\sim$ 140 Ma in the Jurassic that is not observed in the Essimi porphyry. A $\sim$ 300 Ma Permo-Carboniferous peak is observed at Essimi but not Kassiteres. The oldest zircon population at Kassiteres peaks as $\sim$ 360 Ma in the late Devonian with a small tail back into the Ordovician. Essimi samples two older zircon populations than Kassiteres, one broad peak in the Cambrian to Silurian and a small tail in the Proterozoic.

The distribution of zircon core ages from both Essimi and Kassiteres overlaps with the detrital zircon record of the CRB metasediments, the Makri and Melia units, which host the magmatic systems (Fig 4.9; Meinhold et al. 2010; Meinhold and Kostopoulos 2013). The Melia unit of the CRB outcrops to the east of Essimi whilst the spatial extent of the CRB to the South of Kassiteres has been poorly mapped with the Makri unit known to outcrop at the coast (Bonev and Stampfli, 2003, 2011; Meinhold et al., 2010; Meinhold and Kostopoulos, 2013). Meinhold et al. (2010) suggest thart the Melia unit tectonically overlies the Makri unit, with tectonic imbrication of Melia wedges in the Marki unit. No systematic preference for one lithology of the CRB metasediments is observed, but the broad agreement in ages suggests that the xenocrystic population of the Kassiteres and Essimi zircons is consistent with the basement zircon population. This implies that the inheritance signature is derived local to emplacement rather than on ascent through the deep crustal plumbing system.

The xenocrystic zircon ages provide direct evidence of the contribution of crustal material to Kassiteres and Essmi porphyries. No unique correlations can be made fingerprinting basement units as the source of crustal material at either Kassiteres or Leptokaria, but the xenocrystic zircon populations suggest that either: *(i)* the metasedimentary CRB shares a parental source of detrital material with the crustal component of magmatism at Kassiteres and Leptokaria; or *(ii)* the CRB was the direct source of the crustal melt at Kassiteres and Leptokaria. The absence of an inherited population of zircons from Leptokaria does not rule out mixing of a crustal component, as zircon xenocrysts may have been entirely resorbed into the mixed melt prior to zircon saturation. However, we suggest that it is more likely that the lack of xenocrystic zircons at Leptokaria reflects minimal crustal contribution to magmatism, in line with the zircon trace element geochemistry and melt inclusion petrology.

4.7.4 A Genetic Model for the Petrogenesis of Porphyry Magmatism along the MMC

The similarities and differences between the Kassiteres, Leptokaria and Essimi porphyries are summarised in Table 4.3. Zircon trace element and zircon-hosted MI geochemistry provide evidence of mixed crustal and mantle signatures in the Essimi and Kassiteres porphyries and suggest that the Leptokaria porphyry provides an end-member of mantle-derived magmatism with minimal crustal mixing. The zircon-hosted MIs fall on a fractionation trend consistent with a shared LLD with the MMC host magmatism; however, the more aluminous nature of the MIs from Kassiteres, and to a lesser degree Essimi, indicate mixing of crustal-derived melt into the porphyry magmas in these systems (Fig. 4.6). We consider that the less aluminous Leptokaria zircon-hosted MIs indicate a predominantly mantle-derived signature to magmatism in the Leptokaria porphyry. This is supported by elevated Hf concentrations in the Kassiteres and Essimi porphyries indicating a greater degree of crustal mixing (Fig. 4.7). Shared LREE to MREE to HREE fractionation trends in the zircon trace element geochemistry from the Kassiteres, Essimi and Leptokaria suggest that this fingerprints the shared mantle-derived geochemistry (Fig. 4.8). Elevated Ce/Nd at Kassiteres and Essimi suggest a more oxidised starting melt composition in these porphyry systems over

Table 4.3: Comparative characteristics of the Kassiteres, Essimi and Leptokaria porphyry intrusions

Characteristic	Kassiteres	Essimi	Leptokaria
	U-Pb Geochronology		
Oligocene zircon population			
Jurassic – Cretaceous zircon population			
Permo – Triassic zircon population			
Devonian – Cambrian zircon population			
Proterozoic zircon population			
	Melt Inclusion Chemistry		
SiO_2	Low (71.78 wt.%)	High (75.78 wt.%)	
Alumina Saturation Index	High (av. 1.06)	Int. (av. 1.03)	Low (av. 1.01)
Elevated above MMC fractionation trend	K_2O, FeO	FeO, TiO_2	
	Zircon Trace Element Geochemistry		
Hf	High (10,250 ppm)	Int. (10,000 pm)	Low (9,000 ppm)
Eu/Eu*	Low (< 0.4)	High (> 0.4)	Low (< 0.4)
Ta/Nb	Low (0.31 ± 0.14)	High (0.47 ± 0.13)	
U/Yb	High (> 1.5)	Low (< 1.5)	
W	High (> 1 ppm)	Low (< 1 ppm)	
Sn	High (> 0.5 ppm)	Low (< 0.5 ppm)	

the Leptokaria system.

The U-Pb geochronology is consistent with the trace element geochemistry. Inheritance of Mesozoic and Palaeozoic xenocrystic zircon cores is observed in the Essimi and Kassiteres porphyries only, consistent with mixing of crustal melts in these systems and a dominantly mantle-derived signature in the Leptokaria porphyry. Autocrystic and antecrystic zircon rims and cores in the MMC porphyries show resorption features that developed within the temporal resolution of the U-Pb geochronology and no core –rim variations in geochemistry. This indicates that Oligocene porphyry magmatism along the MMC was mixed in the Kassiteres and Essimi porphyries prior to saturation of zircon, and likely indicates significant resorption of the inherited zircon population as observed in the sub-hedral shape of the xenocrystic zircon cores. Pulsed intrusion of magmas into the porphyry system at each locality is likely, providing the thermal instabilities to generate resorption textures on timescales of $<$ 100s kyrs and as little as a few kyrs (e.g., Tapster et al. 2016).

Two different compositions of crustal mixing components are fingerprinted in the Eu anomaly of the Essimi system and the HFSE and metal endowment of the Kassiteres porphyry. Sub-parallel fractionation trends in Eu/Eu* across the MMC porphyries are inherited from the start of zircon crystallisation, and indicate a more Eu-rich magma composition at Essimi, likely derived from mixing of Eu-rich crustal melt, perhaps an amphibole or titanite dominated source (Luhr and Carmichael, 1980). Fractionation of Nb from Ta is common across the MMC porphyries with elevated concentrations of Ta common in all the systems implying that this was inherited from the shared mantle-derived component of magmatism (Fig. 4.9). At Kassiteres, elevated Nb, U, W and Sn reveal a mica-rich crustal component enriching only the Kassiteres porphyry magma in these elements.

We propose two possible, end-member explanations to generate the differing compositions of crustal melts at Kassiteres and Essimi: *(i)* compositional differences in two different crustal melt sources, such as

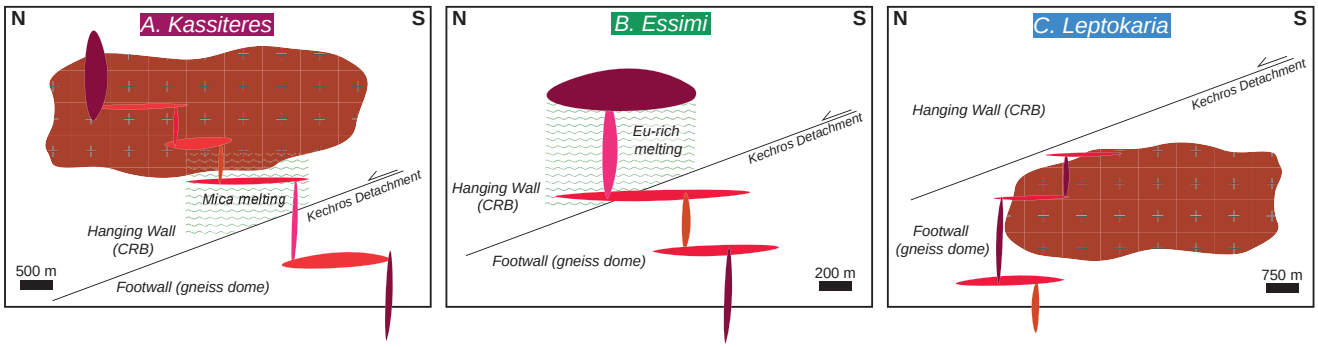

Figure 4.11: A schematic model of porphyry petrogenesis at each of the case study systems, depth scale unknown. (A): At Kassiteres, the regional mantle-derived melts are mixed with a crustal-derived, mica rich source and is emplaced in the hanging wall of the Kechros dome. (B): At Essimi, the porphyry is similarly hosted in the hanging wall of the Kechros dome but the crustal component to mixing was Eu-rich, perhaps an amphibole dominant source. (C): The Leptokaria porphyry intrudes the Leptokaria complex in the Kechros gneiss dome and does not experience significant crustal mixing as noted by the zircon geochemistry and the lack of inherited zircon xenocrysts.

lithological variations in the melt host, and *(ii)* low- vs. high-temperature melting in the Essimi and Kassiteres systems respectively resulting in compositional differences in the crustal melts produced from a shared crustal source. U-Pb geochronology shows a Palaeozoic – Mesozoic inheritance signal in both the Kassiteres and Essimi zircons that is absent from the Leptokaria sample. This is coincident with intrusion of the Kassiteres and Essimi porphyry stocks into the CRB sediments of the hanging wall of the Kechros dome whilst the Leptokaria porphyry dyke is hosted in the gneissic footwall (Fig. 4.1, 4.11). The xenocrystic zircon population from the Kassiteres and Essimi populations broadly overlap with the detrital zircon populations of the CRB from two different lithological units, the Melia and Makri units, although no systematic preference for one system over another is observed (Fig. 4.10). We suggest that the crustal-derived component of magmatism in the Kassiteres and Essimi porphyry suites is the result of local basement melting and mixing in the hanging wall whereas no crustal signature is observed where the Leptokaria porphyry intrudes the gneissic footwall of the Kechros dome (Fig. 4.11).

4.8 Conclusions

Our discussion above outlines the potential power of zircon-hosted MI analyses in studying acid altered mineralised systems in addition to the possible pitfalls. We conclude that zircon-hosted MIs are a repository of vital petrological information in systems where other sources of information have been lost by destructive acid alteration. The analysis of zircon-hosted MIs has allowed direct measurement of the major element chemistry of late-stage porphyry melts for comparison with unaltered, regional magmatism. Combined with U-Pb geochronology and zircon trace element, MI analyses provide a unique insight into the temporal and petrogenetic evolution of magmatic systems. When applied to the MMC, significant crustal contamination was identified by the aluminous MIs, the metal enrichment of the zircons and MIs, and the inherited zircon populations. The xenocrystic age domains in the Kassiteres and Essimi zircon populations suggest that the local greenschist basement could have been the source of the crustal-derived melts. Interestingly, the Leptokaria porphyry, the only system not to cut through the local greenschist basement, does not show any evidence of xenocrystic inheritance. A dominantly mantle-derived signature of magmatism in the Leptokaria porphyry is consistent with the absence of zircon xenocrysts in the sample, suggesting that the Leptokaria

porphyry is a less-mixed end-member of porphyry magmatism along the MMC. Mixing of a mica-rich crustal source at Kassiteres is identified by the Ta/Nb ratios of the zircons and is suggested as a source of W and Sn metal enrichment in the Kassiteres system.

The case study from the MMC is the first application of zircon-hosted MI geochemistry to magmatic mineral deposits. Combined with zircon trace element geochemistry and U-Pb zircon geochronology, the case-study shows cryptic evidence of crustal- and mantle-derived melt hybridisation. This would have been unrecognisable with conventional petrological techniques as the original magmatic mineral assemblage and petrographic textures were destroyed by pervasive alteration, intrinsic to magmatic mineral systems. Wider application of zircon-hosted MI analysis, integrated with zircon U-Pb geochronology and trace element geochemistry, to additional magmatic mineralised systems would identify whether this crustal hybridisation and overprinting of porphyry and S-type mineralisation has previously gone unnoticed in magmatic mineral systems. The integrated study of zircon trace element geochemistry, zircon-hosted MI petrology and high-spatial resolution U-Pb zircon geochronology presented here is a novel approach to the study of highly-altered porphyry intrusions. It is allows direct measurement of preserved aliquots of metal-bearing magma and as a result is a powerful tool that combines existing analytical protocol in a unified workflow of zircon analyses. Application of this technique to other mineralised porphyry systems would provide insights into the petrogenesis of metal-bearing magmas that could be used to inform current paradigms of porphyry copper deposit formation.

Chapter 5

Rapid exhumation leading to failed porphyry mineralisation of the Kassiteres system, the Maronia Magmatic Corridor, northeastern Greece

Author contributions and declaration:

This study was supervised by F. Cooper. B. Tattitch and J. Naden provided useful discussion in the field. U-Pb zircon geochronology was analysed by D. Condon from zircon separates prepared by R. Perkins; interpretations of the U-Pb geochronology data were made by R. Perkins with the advice of D. Condon. Useful discussion was had with R. Moritz (University of Geneva) about the alunite $^{40}Ar/^{39}Ar$ data from Kassiteres reported by Ortelli et al. (2009, 2010).

ABSTRACT

Rapid cooling ($>$ 400 °C/Myr) of mineralising magmatic-hydrothermal systems is commonly invoked as a mechanism for the generation of economic porphyry Cu-Au mineral deposits. In exhuming terranes, rapid cooling can result from the advection of heat and elevation of geothermal gradients developed during tectonic uplift and/or surface erosion, and can trap magmatic-hydrothermal systems within regions of compressed isotherms. This can generate telescoping of the mineralising systems, whereby deep Cu-Au porphyry mineralisation is overprinted by shallower Au-Ag epithermal mineralisation resulting in a zone of high-grade, concentrated metal enrichment. Kassiteres, a Cenozoic post-collisional porphyry – epithermal system in the Thrace basin in northeastern Greece, is a prime example of telescoping, where high- and low-T alteration and mineralisation are juxtaposed. In spite of this, Kassiteres is a poorly mineralised porphyry system with only minor Cu-Au porphyry-style veining, overprinted by multiple occurrences of high-sulphidation epithermal Au-Ag mineralisation, the dominant mineralisation style in the system. In order to investigate the controls on mineralisation at Kassiteres and the reasons why only minor porphyry mineralisation is observed, I combine Al-in-hornblende geobarometry and high-precision U-Pb zircon geochronology with existing $^{40}Ar/^{39}Ar$ geochronology of magmatic steam-heated alunite to constrain the exhumation history of the system. My results show that the dioritic-granodioritic Kassiteres pluton, host to mineralisation, was emplaced in the upper crust (4.4 $\pm$ 1.9 km) in the Oligocene (32.02 $\pm$ 0.04 Ma) and reached the surface by $\sim$ 31 Ma during the final stages of advanced argillic alteration and steam-heated lithocap formation. This gives a miniumum estimated exhumation rate of 5.2 $\pm$ 3.0 km/Myr, in line with existing estimates of Cenozoic exhumation in the northern Aegean. I suggest that rapid exhumation of the Kassiteres system may have hindered porphyry mineralisation as dilution and dispersal of the magmatic-hydrothermal fluids by sub-volcanic meteoric water resulted in the pre-mature transition from a porphyry to an epithermal environment. This can account for the lack of preserved porphyry-style mineralisation at Kassiteres.

5.1 Introduction

Porphyry – epithermal systems host nearly 75 % of the world's known Cu reserves along with considerable volumes of precious metal mineralisation (Sillitoe, 2010). Consequently, a considerable body of work has studied the controls on mineralisation with an aim to identify key geological processes that lead to significant metal enrichment. Porphyry Cu $\pm$ Au $\pm$ Mo deposits (PCDs) typically form in the shallow crust (1-3 km; Seedorf 2005) in a concentrically zoned shell of mineralisation centred around a porphyritic intrusion. The porphyry intrusions typically emanate from a multi-phase, equigranular host pluton, intruded at greater depth (e.g., Sillitoe 2010). A magmatic volatile phase (MVP), exsolved from the evolved porphyry intrusion, forms the mineralising magmatic-hydrothermal fluid which, upon cooling and interaction with the host rocks, precipitates hypogene mineralisation (e.g., Burnham 1979; Candela 1989; Sillitoe 2010). Epithermal Au $\pm$ Ag $\pm$ PGEs $\pm$ base metals deposits are classically viewed as the upper continuation of PCDs in the uppermost crust where the MVPs interact with meteoric water and the atmosphere, precipitating metals in the upper 500 m of the crust (e.g., Arribas et al. 1995). A genetic link between porphyry – epithermal systems and volcanoes has become increasingly important in recent models of mineralisation, borne out of the close spatial association of porphyry – epithermal and volcanic systems and the similarity in morphology between well-exposed PCDs and the internal architecture of volcanoes (e.g., Sillitoe 1973; Dilles 1987; Blundy et al. 2015; Nadeau et al. 2016).

PCDs and their associated epithermal deposits are most frequently found within volcanic arcs, where subduction-related processes generate hydrous, highly fractionated calc-alkaline magmas favourable for mineralisation (Hedenquist and Lowenstern, 1994; Sillitoe, 2010). However, PCDs are not restricted to collisional tectonic regimes. Post-collisional crustal extension can result in areas of elevated heat flow generating small-volume, calc-alkaline to shoshonitic magmas, some of which are associated with exotic metal-bearing porphyry – epithermal systems (e.g., Richards 2009, 2011b). Whilst the major and minor element geochemistry of subduction-related and post-collisional porphyries is somewhat similar, the largest difference between systems is their tectonic evolution (Richards, 2009). The tectonic evolution of PCDs from emplacement between 1–5 km (average 2 km; Seedorf 2005) depth in the crust and current exposure at, or near, the surface is poorly constrained in most PCDs with the influence of exhumation rates on mineralisation an additional unknown. Is exhumation monotonic from emplacement to the surface; is rapid exhumation preferable to generate favourable mineralising conditions resulting in the formation of a giant ore deposits; and what is the influence of stepped-wise exhumation on mineralisation?

Exhumation is a complex process resulting from the interplay between surface erosion and tectonic uplift that results in the movement of rocks towards the Earth's surface. At high exhumation rates, it can also be a mechanism for advecting heat upwards through the crust, generating elevated geothermal gradients and compressing isotherms in the shallow crust (Benfield, 1949; Stüwe et al., 1994; Mancktelow and Grasemann, 1997). As temperature is one of the key controls on the solubility of metals in MVPs (e.g., Williams-Jones and Migdisov 2014), it follows that advection of heat during exhumation should play an important role in mineralising processes (McInnes et al., 2005b). When exsolved from the parent magma, the MVP undergoes two stages of evolution: *(i)* phase separation during decompression and/or cooling (to $\sim$ 500 °C) from a supercritical fluid to a dense, saline brine which remains trapped in the hydrothermal system and is concentrated in metals, and a less dense, vapour phase which is degassed to the surface (e.g., Blundy et al. 2015; Nadeau et al. 2016); and *(ii)* dilution of the brine phase during cooling, mineralisation and mixing

with meteoric waters (e.g., Taylor 1997; Harris and Golding 2002). Stage *(i)* is associated with the primary phase of porphyry-style mineralisation and high-T alteration of the host rock, whilst stage *(ii)* follows and is associated with pervasive low-T alteration of the surrounding lithologies and the primary phase of epithermal mineralisation.

In an exhuming terrane, the resultant elevated geothermal gradient and compressed isotherms will confine the magmatic-hydrothermal system and generate steep temperature gradients out of the system. This concentrates fluid:wall-rock interaction and forms a concentrated shell of high-grade mineralisation. Conversely, in a static terrane with a lower geothermal gradient, the temperature gradient out of the magmatic-hydrothermal system will be smaller and mineralisation will develop over a more diffuse zone at lower grades (McInnes et al., 2005b,a). Studies on the cooling rates of some giant ore deposits support this relationship, with the best endowed PCDs also experiencing the most rapid cooling (McInnes et al., 2005b,a). For example, comparative thermal modelling of two Indonesian PCDs, Grasberg, one of the world's richest porphyry ore bodies (Van Nort, 1991; Macdonald and Arnold, 1994) and Ciemas, a sub-economic porphyry occurrence (McInnes et al., 2005a), shows that the giant Grasberg deposit experienced hydrothermal cooling over a duration of 15 kyrs, whilst the Ciemas deposit cooled much more slowly over 1,040 kyrs (McInnes et al., 2005b,a). Furthermore, exhumation of rocks through the magmatic-hydrothermal fluid regime can lead to overprinting, or telescoping, of systems if the rocks that experience deep, high-T porphyry-style alteration and mineralisation are brought to shallower levels at the same rate as cooling and rise of the magmatic-hydrothermal system (e.g., Sillitoe 1994, 2010). However, it is important to note that if post-mineralisation exhumation of porphyry – epithermal systems is too rapid, a deposit can reach the surface and be lost to erosion (Wilkinson and Kesler, 2007). It is, therefore, also important that exhumation slows down post-mineralisation, such that the deposit remains in-tact but is within the near-surface environment for exploration and economic metal extraction (Kesler and Wilkinson, 2008). The exhumation of PCDs is typically $<\sim$ 1.4 km/Myr, averaged over the lifetime of the deposits from emplacement at 2 km depth to exposure at the surface at present (Yanites and Kesler, 2015).

In this chapter I investigate the role of exhumation on mineralisation in the Kassiteres porphyry – epithermal system in NE Greece. By combining petrology, geobarometry and high-precision geochronology on intrusive and extrusive rocks, I establish that the Kassiteres system was exhumed at $>\sim$ 5 km/Myr, in line with existing estimates of exhumation in the northern Rhodope Core Complex (Peytcheva et al., 2004; Márton et al., 2010). This estimated exhumation rate is extremely rapid when compared with the average exhumation rate of PCDs globally ($<\sim$ 1.4 km/Myr; Yanites and Kesler 2015), although it represents a discrete tectonic interval in the Oligocene rather than the lifetime of the Kassiteres system. I suggest that rapid exhumation at Kassiteres ($>$ 5 km/Myr) disrupted the deep porphyry mineralising magmatic-hydrothermal system, forcing it to transition prematurely to a sub-volcanic epithermal system as the MVP was diluted by interaction with meteoric waters and dispersed through the highly permeable overlying volcanics. I envisage that this mechanism could account for the pervasive, telescoped nature of alteration, restricted porphyry-style mineralisation and overprinting epithermal mineralisation found at Kassiteres, suggesting that rapid exhumation is not always favourable for PCD formation.

5.2 Tectonic Setting

The Kassiteres porphyry – epithermal system is hosted by high-K calc-alkaline magmatism of the Maronia Magmatic Corridor (MMC) in northeastern Greece (Fig. 5.1; Voudouris et al. 2006). The MMC is made up of at least ten Oligocene post-collisional plutons that intrude the footwall and hanging wall of the Kechros dome in northern Rhodope Core Complex (RCC) along a northeasterly trend (Del Moro et al., 1988).

The northern RCC comprises a series of stacked nappes accreted during Mesozoic convergence in the Hellenic orogen (e.g., Burg 2011). It was subsequently exhumed from lower crustal levels during post-collisional extension in the early Cenozoic (e.g., Burg et al. 1996; Ricou et al. 1998; Burg 2011; Kydonakis et al. 2015a). The footwall of the northern RCC is exposed in an E-trending series of detachment fault-bound gneiss domes, the eastern-most of which, the Kechros – Biala-Rika dome (from here on in referred to as the Kechros dome), is $\sim$ 2 km NE of Kassiteres. The hanging wall of the Kechros dome, the Circum Rhodope Belt (CRB), is also exposed in the Thrace basin (Bonev and Stampfli, 2003, 2011). A stack of allochthonous Mesozoic schists and meta-ophiolites characterise the CRB that was unroofed during the tectonic-driven extensional exhumation of the northern RCC in the early Cenozoic (Bonev and Stampfli, 2003; Meinhold et al., 2010; Bonev and Stampfli, 2011; Meinhold and Kostopoulos, 2013; Bonev et al., 2015). $^{40}Ar/^{39}Ar$ dating of white micas from granite mylonites and augengneisses from the Kechros dome date extension-related mylonization and exhumation of the Kechros dome to the late Eocene to early Oligocene, between 42 and 35 Ma (Wawrzenitz and Mposkos, 1997; Lips et al., 2000; Marchev et al., 2003; Bonev et al., 2013). Elsewhere in the northern RCC, Peytcheva et al. (2004) constrained exhumation of the Arda dome gneisses to the West of the Kechros dome, to between 38 and 35 Ma with an estimated exhumation rate of 3–5 km/Myr.

Post-collisional magmatism is common across the northern RCC, including the MMC, and is related to Cenozoic back-arc extension of the Aegean, when asthenospheric mantle upwelling generated small-volume partial melts of the Mesozoic subduction-modified lithospheric mantle (e.g., Pe-Piper et al. 2009; Chapter 2). In the early Oligocene, a period of post-collisional magmatism in the northern RCC was contemporaneous with a phase of metallogeny, with porphyry – epithermal mineralisation developed along the MMC in Greece to the south (e.g., Melfos and Voudouris 2017), and the formation of a series of sediment-hosted epithermal Au-base metal deposits to the north in Bulgaria (e.g., Marchev et al. 2003, 2005, 2006, 2010). In Bulgaria, rapid post-mineralisation exhumation of the hanging wall of the northern RCC was documented between 33–30 Ma by Márton et al. (2010) which is thought to have promoted mineralisation.

In the southern hanging wall of the Kechros dome, the Eocene Thrace supra-detachment basin developed in accommodation space created by extensional crustal subsidence (Kilias et al., 2013, 2015). Sedimentation in the Thrace basin was syn-extensional, coeval with Eocene – Oligocene exhumation of the northern RCC as shed sediment infilled the basin (Kilias et al., 2013, 2015). In the Oligocene, the infill of the Thrace basin was intercalated with extrusive, sub-aerial volcanism with volcaniclastic deposits becoming increasingly dominant with time (Christofides et al., 2004). The Thrace supra-detachment basin experienced two important deformational events in the early Cenozoic: *(i)* Eocene – Oligocene, E-trending, N-dipping, high-angle normal faulting complimentary to detachment controlled exhumation of the northern RCC; and, *(ii)* Oligocene – Miocene high-angle strike-slip faulting in conjugate NNE-trending, sinistral and WNW-trending, dextral fault sets which commonly exploit previous normal fault structures (Kilias et al., 2013). Kassiteres is nestled in an isolated portion of the Thrace basin. Locally to Kassiteres, the Thrace basin

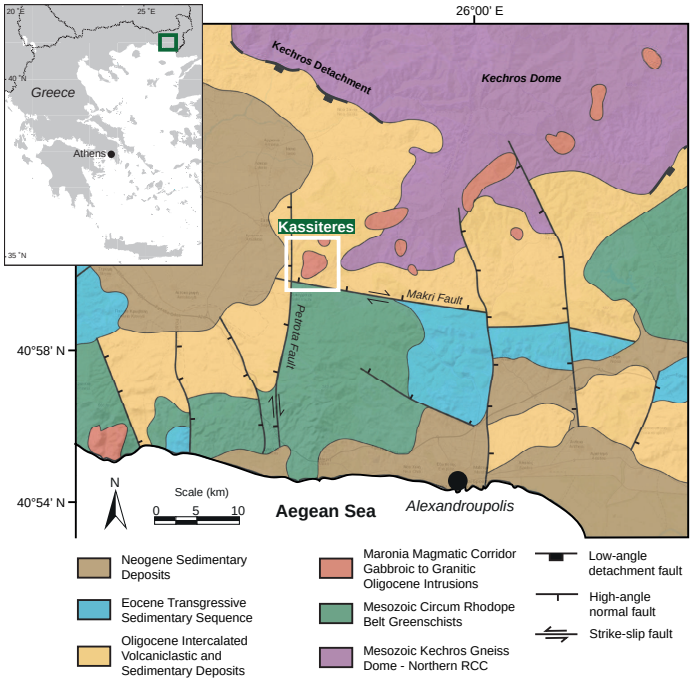

Figure 5.1: A geological map of the Maronia Magmatic Corridor, intruded along the southern portion of the Kechros dome (first presented in Chapter 2). The Kassiteres system is located in the hanging wall of the Kechros dome, $\sim$ 2 km southwest of the Kechros dome and lies at the intersection of the Makri and Petrota faults. Annotated on the faults are the sense of motion indicators after Kilias et al. (2013). Initial motion on the Makri fault was Eocene N-dipping dip-slip which transitioned to dextral strike-slip motion in the Oligocene. The Petrota fault initiated in the Oligocene with a sinistral strike-slip sense of motion with a minor W-dipping component. In the late Oligocene – Miocene, motion on the Petrota fault was predominantly W-dipping normal motion.

is bound to the north the by metamorphic basement of the Kechros gneiss dome, and to the south by the metasediments of the Makri block of the Circum Rhodope Belt (CRB). A high-angle, W-dipping normal fault separates the rest of the Thrace basin in the West (Fig. 5.1).

Kassiteres is an example of a highly telescoped porphyry – epithermal mineralised system (Voudouris et al., 2006). It lies in the centre of the MMC, $\sim$ 2 km to the SW of the Kechros detachment, and is hosted by CRB metasediments of the Kechros dome hanging wall (Fig. 5.2). The Kassiteres porphyry – epithermal system is co-genetic with the emplacement of a quartz-feldspar porphyry intrusion (150 m by 500 m), hosted in the equigranular, dioritic to granodioritic pluton. The Kassiteres porphyry – epithermal system comprises at least three mineral prospects (Voudouris et al., 2006), including the Korfyes Hill porphyry-showings (occurences of mineralisation with unknown economic value), and the Santa Barbara and Sapana epithermal prospects. The Sappes – Konos porphyry – epithermal system is $\sim$ 1500 m north of Kassiteres and at lower elevation, $\sim$ 500 m; it comprises of the Konos porphyry occurrence and the Sappes epithermal Au-Ag-Te system, which includes the Viper and St Demetrios deposits (owned by Eldorado Gold, May 2018). In this study we consider only the Kassiteres system which is directly hosted by the Kassiteres diorite-granodiorite pluton but agree with Voudouris et al. (2006) & Ortelli et al. (2009, 2010) who suggest a co-genetic magmatic plumbing system feeding both the Kassiteres and Sappes-Konos systems.

At Kassiteres, early Cu-Mo porphyry veining is overprinted by later Ag-Au-base metal epithermal mineralisation (Voudouris, 2006; Voudouris et al., 2006; Melfos and Voudouris, 2017). Porphyry-style mineralisation in the Kassiteres system is characterised by disseminated and vein-hosted sulphides (pyrite + chalcopyrite + molybdenite) with local vein stockworks developed; it is overprinted by pervasive argillic alteration except where the veins cut the Kassiteres pluton (Voudouris et al., 2006). Porphyry veining at Kassiteres is overprinted by epithermal mineralisation. Early alunite + barite + chalcedony veins are host to Au-Ag tellurides, native Au and molybdenite, and are cross-cut by quartz + carbonate $\pm$ adularia veins which are commonly barren (Voudouris et al., 2006; Melfos and Voudouris, 2016, 2017). Hydrothermal alteration is pervasive throughout Kassiteres, with steam-heated quartz-alunite lithocaps developing in close

spatial proximity to haematite-rich breccia pipes (Voudouris, 2014).

5.3 New Analysis of the Kassiteres System

5.3.1 Field Observations

The Kassiteres area was mapped and sampled over three field seasons (Fig. 5.2, Appendix N). Key contextual relationships between lithologies, including relative timings, were established in the field, and a suite of 19 samples representative of each lithology were collected for further analysis (Table 5.1).

There are six key lithologies at Kassiteres (Fig. 5.2). The greenschist metasedimentary basement of the CRB (Makri block) and the overlying Eocene transgressive, sedimentary units host the Oligocene igneous units of interest to this study. The earliest of these is the Kassiteres host pluton, an equigranular intrusive pluton made up of two facies of magmatism: a pyroxene-hornblende diorite and a hornblende-biotite granodiorite. The Kassiteres pluton hosts a small (150 m by 500 m), highly altered quartz-feldspar porphyry intrusion (Voudouris et al., 2006) and is cut by a series of aplitic dykes. Unconformably overlying both the Kassiteres pluton and porphyry is a volcaniclastic unit made up of small-volume pyroclastic deposits interbedded with volcaniclastic-rich sandstones and host to clasts of the Kassiteres pluton (Fig. 5.4A-B). A series of quartz-alunite-serecite-adularia lithocaps, associated with steam-heated alteration blankets that typically overlie porphyry-epithermal systems (Fig. 5.4C; Sillitoe 2010; Hedenquist and Taran 2013), cut all of the units and is the youngest outcropping lithology at Kassiteres (Voudouris et al., 2006; Ortelli et al., 2009, 2010; Voudouris, 2014).

Table 5.1: Details of the samples analysed from Kassiteres. [1] samples of host pluton with detailed petrology; [2] samples of remaining lithologies chosen for petrographic analyses; [3] samples analysed by infrared spectroscopy to identify the clay assemblage; * samples selected for U-Pb zircon geochronology (ID-TIMS). plag – plagioclase; hbl – hornblende; cpx – clinopyroxene; opx – orthopyroxene; bt – biotite; kfsp – K-feldspar; qtz – quartz; mag – Fe-Ti oxides

Sample number	Locality (WGS 84) Long.	Lat.	Lithology (major phase assemblage)
RT14_027 [1]	40.998943 N	25.738683 E	Diorite – plag + hbl + cpx + opx + bt + kfsp + qtz + mag
RT14_028 *,[1]	41.004680 N	25.745895 E	Granodiorite – plag + hbl + bt + cpx + kfsp + qtz + mag
KA15_008 [1]	40.999342 N	25.743087 E	Diorite – plag + cpx + opx + hbl + kfsp + qtx + mag
KA15_013 [1]	40.995719 N	25.747641 E	Granodiorite – plag + hbl + bt + kfsp + qtz + mag
KA15_016 [1]	40.992889 N	25.730730 E	Diorite – plag + cpx + opx + hbl + kfsp + qtx + mag
KA15_017 [1]	40.996062 N	25.735367 E	Granodiorite – plag + hbl + bt + kfsp + qtz + mag
KS16_006A [1]	40.996010 N	25.733270 E	Diorite – plag + cpx + opx + hbl + kfsp + qtx + mag
KS16_006C [1]	40.996010 N	25.733270 E	Granodiorite – plag + hbl + bt + kfsp + qtz + mag
KA15_018 *,[3]	41.006028 N	25.734220 E	Quartz-feldspar porphyry – glassy qtz eyes + relict fsp habits altered to sericite + clay matrix
KA15_019 *,[2,3]	41.006028 N	25.733729 E	Quartz-feldspar porphyry – glassy qtz eyes + relict fsp habits altered to sericite + clay matrix
KA15_005 *,[3]	41.004306 N	25.741843 E	Volcaniclastic unit – pyroclastic facies, crystal poor
KA15_010 *,[2,3]	40.994007 N	25.727996 E	Volcaniclastic unit – pyroclastic facies with crystal rich lenses, adjacent to erosive contact with pluton
KA15_007 [3]	40.999085 N	25.743087 E	Diorite – plag + cpx + opx + hbl + kfsp + qtx + mag
KA15_012 [3]	40.994486 N	25.733171 E	Granodiorite – plag + hbl + bt + kfsp + qtz + mag + cpx
KA15_014 [3]	40.994486 N	25.733171 E	Diorite – plag + cpx + opx + hbl + kfsp + qtx + mag
KA15_001 [3]	41.009893 N	25.750232 E	Volcaniclastic unit – fine-grained, clastic facies
KA15_003 [3]	41.006940 N	25.750649 E	Volcaniclastic unit – fine-grained, clastic facies
KA15_006 [3]	41.002879 N	25.739777 E	Volcaniclastic unit – fine-grained, clastic facies
KA15_015 [3]	40.993176 N	25.729258 E	Volcaniclastic unit – pyroclastic facies, crystal rich lense

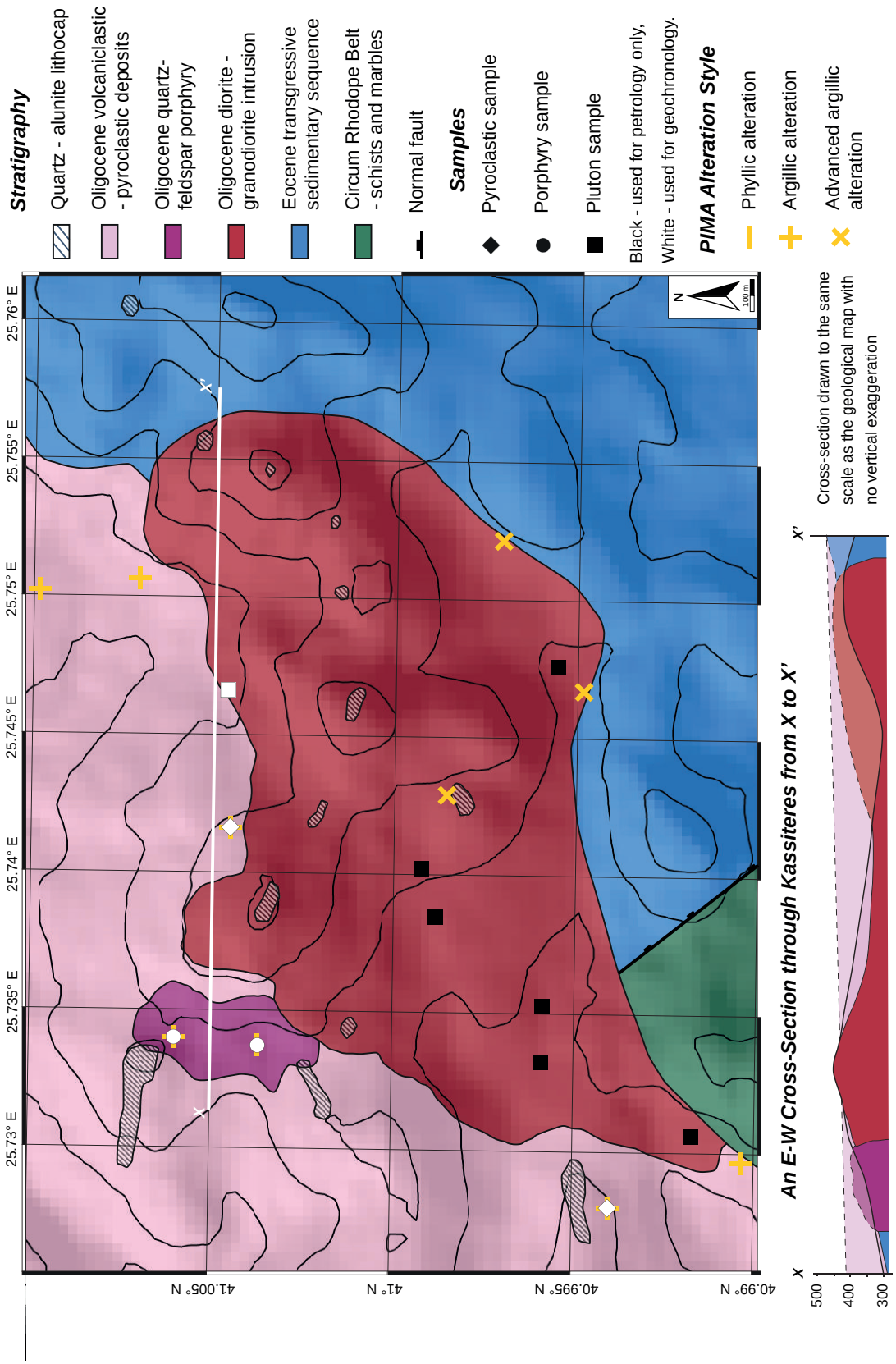

Figure 5.2: A geological map of the Kassiteres system drawn from field observations. Figure 5.3 explains the field contacts through a series of schematic cross-sections.

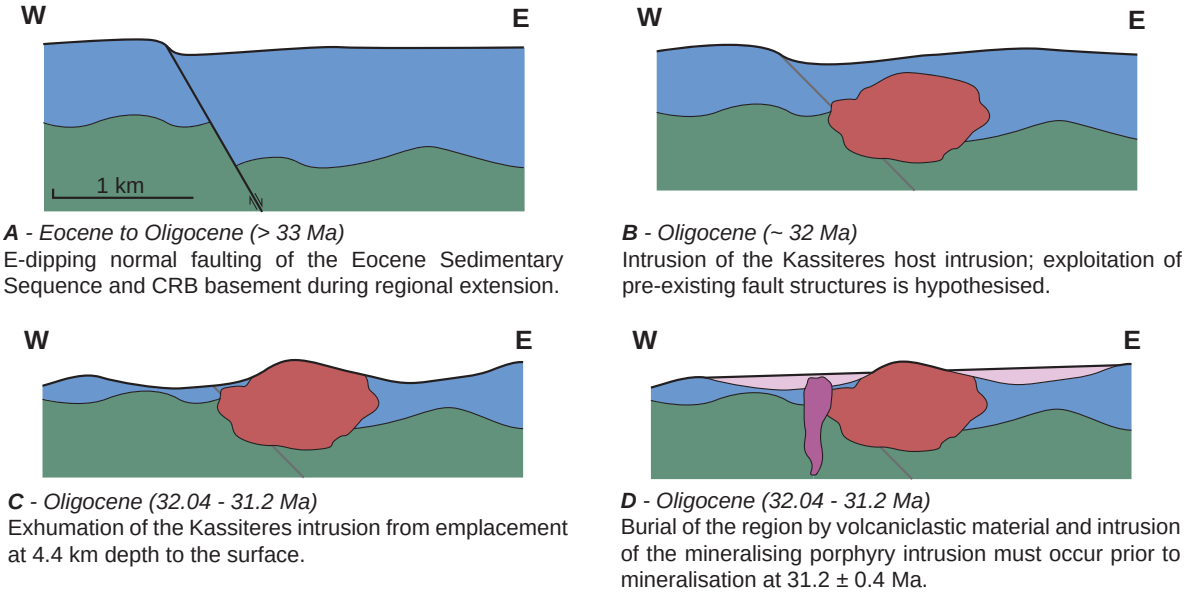

***A** - Eocene to Oligocene (> 33 Ma)*
E-dipping normal faulting of the Eocene Sedimentary Sequence and CRB basement during regional extension.

***B** - Oligocene (~ 32 Ma)*
Intrusion of the Kassiteres host intrusion; exploitation of pre-existing fault structures is hypothesised.

***C** - Oligocene (32.04 - 31.2 Ma)*
Exhumation of the Kassiteres intrusion from emplacement at 4.4 km depth to the surface.

***D** - Oligocene (32.04 - 31.2 Ma)*
Burial of the region by volcaniclastic material and intrusion of the mineralising porphyry intrusion must occur prior to mineralisation at 31.2 ± 0.4 Ma.

Figure 5.3: A set of schematic cross sections through Kassiteres with geological time. The Kassiteres intrusion is hosted along a normal fault at the unconformity between the Eocene sedimentary sequence and the Circum Rhodope Belt Basement. Exhumation of the Kassiteres intrusion occurred prior to deposition of the Oligocene volcaniclastic unit, as indicated by the erosive field contacts observed. The intrusion of the Kassiteres porphyry was contemporaneous with volcanism and likely cross-cuts the earlier portions of the volcaniclastic unit and is buried by later material.

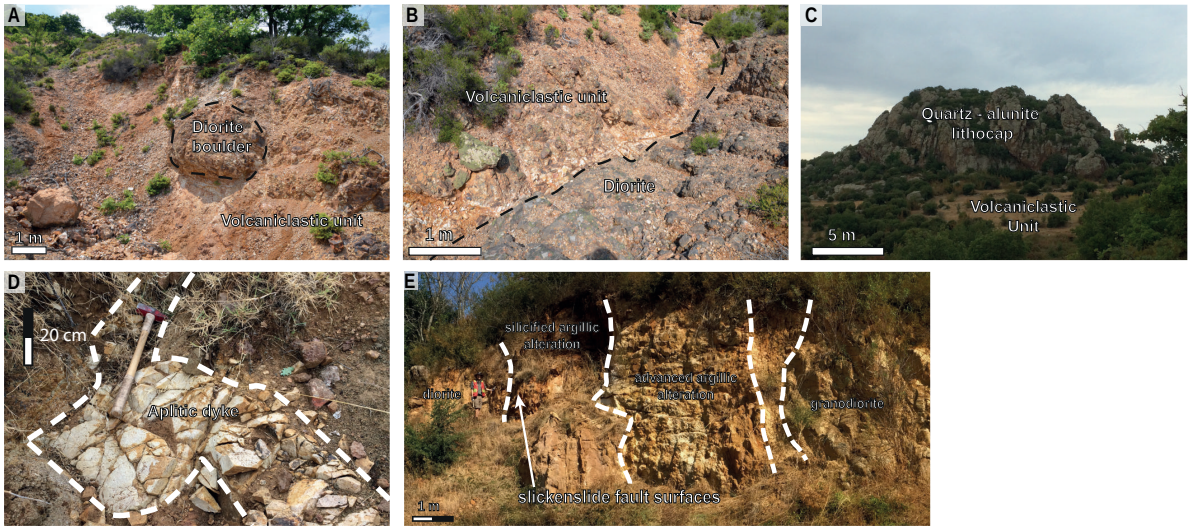

Figure 5.4: Field photographs of the key field observations from Kassiteres. (A): A diorite boulder entrained in the pyroclastic facies of the Kassiteres volcaniclastic unit, photograph taken at sample locality KA15_010. (B): The erosive contact between the pyroclastic facies and the host pluton, photograph taken at sample locality 1, Appendix N. (C): The advanced argillic, quartz-alunite lithocaps are the youngest geological feature at Kassiteres, overlying the volcaniclastic unit, photograph taken from sample locality KA15_019. (D): An aplitic dyke cross-cuts the Kassiteres intrusion, photograph taken at sample locality KS16_003. (E): A fault surface in the Kassiteres intrusion showing the gradation from the most intense advanced argillic alteration along the fault surface through argillic alteration into potassic altered diorite over < 5 m from the structure; photograph taken at sample locality KA15_017.

5.3.2 Petrology

Methods

Standard polished thin sections and epoxy mounts were prepared for eight samples of the Kassiteres host pluton (Table 5.1). Detailed petrographic observations were made under both transmitted and reflected light. Scanning electron microscope (SEM) analysis of these samples was undertaken at the University of Bristol on a Hitachi S-3500 N instrument with 20 kV accelerating voltage and a 15 mm working distance. Phase identification was performed using energy dispersive spectra (EDS) and back-scatter electron (BSE) imagery was used to establish key textural relationships.

The equigranular diorite and granodiorite phases of the Kassiteres host pluton can be distinguished based upon the modal abundances of the major minerals (hornblende + clinopyroxene + biotite + plagioclase + K-feldspar + quartz + magnetite + ilmenite + apatite + zircon ± orthopyroxene). The more evolved hornblende-biotite granodiorite cuts the pyroxene-hornblende diorite with the contact between the units diffuse, suggesting phenocryst exchange between the units and pulsed magma accumulation during pluton assembly (Fig. 5.4D). Granophyric quartz-feldspar textures, indicative of rapid cooling, are observed in both the diorite and granodiorite (Chapters 2 and 3). Ferromagnesian phases from the Kassiteres host pluton show varying degrees of potassic and propylitic alteration, although in-tact phenocrysts with minimal alteration were identified for mineral chemistry in all samples studied (Chapters 2 and 3).

Geobarometry

Geobarometry was conducted on pairs of euhedral hornblende and plagioclase phenocrysts in textural equilibrium. Mineral chemistry was measured by electron probe micro-analysis (EPMA) using wavelength dispersive spectroscopy (WDS) at the University of Bristol, using a Cameca SX100 on thin sections (RT14_027/RT14_028) and polished epoxy mounts (KA15_008/KA15_013/KA15_016/KA15_017). For hornblende, operating conditions of 20 kV, 10 nA and a 5 μm diameter beam were used with counting times of 10 s (Na, K, Si), 30 s (Ca, Fe, Al, Mg), 40s (Ti, Cr), 60 s (Mn) and 100 s (F, Cl). For plagioclase dual conditions of 20 kV, 10 nA and a 5μm diameter beam and counting times of 10 s (Na, K, Si, Al, Ca) and 20 kV, 100 nA and 5 μm beam and counting times of 30 s (Mg, Sr, Fe) on two spectrometers each (Mg and Sr only) were used. Estimates of temperature and pressure were made using the amphibole – plagioclase geothermometer (Holland and Blundy, 1994) and Al-in-hornblende geobarometer (Mutch et al. 2016 calibration). The results were first presented in Chapter 3 and are further interpreted in the context of exhumation at the Kassiteres system here (full results are given in Appendix G).

Samples RT14_028 and KA15_013 gave predicted temperatures within the range of the haplogranite solidus (680–750 °C). A regression through the valid data points for each sample was used to calculate the best-fit intersection with the haplogranite solidus to estimate a final depth of emplacement. Uncertainties were calculated by adding the standard deviation of the data point scatter to the calibration uncertainty in quadrature and are reported to a 2σ confidence level. KA15_013 gave a P estimate of 1.2 ± 0.5 kbar (n = 3) and RT14_028 an estimate of 1.2 ± 0.5 kbar (n = 12). Assuming an average upper crustal density of 2750 g/cm^3, RT14_028 approximates a depth of emplacement for the Kassiteres host pluton of 4.4 ± 1.9 km (Fig. 5.6).

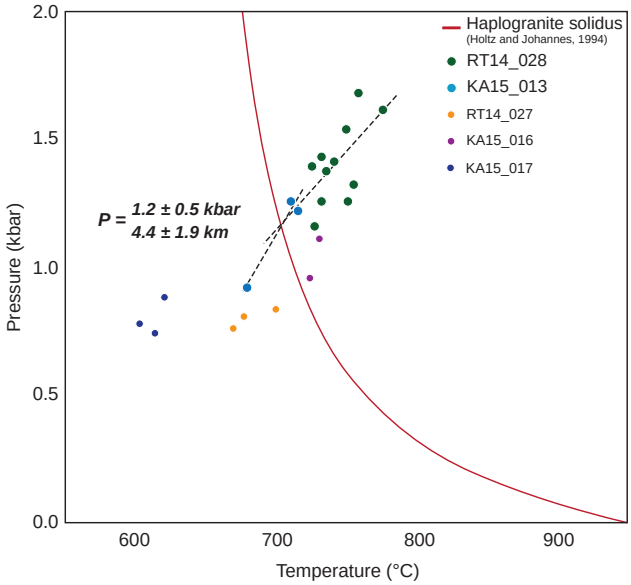

Figure 5.5: Geothermobarometry of the Kassiteres host pluton first presented in Chapter 3. Intensive parameters of crystallisation (P and T) were calculated using the calibrations of Holland and Blundy (1994) & Mutch et al. (2016) respectively.

5.3.3 Alteration Mapping

Methods

Clay minerals (the kaolinite-, smectite- and illite-groups) form from the alteration of primary rock-forming minerals during interactions between fluids and rocks e.g., in hydrothermal alteration and during weathering. In porphyry – epithermal systems the T, P, pH and degree of wall-rock interaction with the fluids changes as a function of distance from the fluid source, resulting in concentric zoning of alteration, with each alteration zone characterised by a distinct clay assemblage (e.g., Sillitoe 2010). Alteration is most intense in the upper core of the alteration shell where the wall-rock has experienced the most protracted interaction with hydrothermal fluids (Fig. 5.5; e.g., Sillitoe 2010). Accordingly, the alteration zone, and thus the distance from the fluid source, can be estimated by identification of the clay assemblage (e.g., Lowell and Guilbert 1970). Due to the secondary nature of the clay minerals, they accommodate a wide variety of cation substitutions and thus have a highly variable mineral chemistry and stoichiometry. As a result, clay minerals are typically analysed by short-wave infrared reflectance (SWIR) spectroscopy where the clay minerals can be identified by absorption signals characteristic to specific bonds (*-OH, -H_2O, -AlOH, -FeOH, -MgOH*) rather than by mineral chemistry as is typical of microprobe techniques (Thompson, 1999). I used SWIR spectroscopy to characterise the clay mineral assemblage of highly-altered samples and define alteration zones in the Kassiteres system.

Powders of < 25 μm grain size were prepared at the University of Bristol for each of the 11 destructively-altered igneous lithologies collected. Samples were crushed and milled in a ball mill using an agate jar with 12 agate balls. Due to the large grain size (> 1 mm) and relative heterogeneity of the samples, > 1 kg of rock was used to ensure a homogenous powder was produced. Powders were analysed using a portable infrared mineral analyser (PIMA) at the British Geological Survey (BGS), Keyworth. Up to four SWIR spectra were taken from each sample and interpretations (clay identification) were made using the cleanest spectrum from each sample (Appendix L).

Results

Pervasive potassic (secondary biotite, quartz and K-feldspar) and propylitic (chlorite, epidote and secondary albite) alteration and serecitisation of plagioclase was observed throughout the host pluton both in the field and with petrographic observations. Destructive alteration was restricted to distinct fault zones within the host pluton but pervasive throughout the quartz-feldspar porphyry intrusion and overlying volcaniclastic lithologies. Three styles of destructive alteration were observed at Kassiteres (Fig. 5.5): *(i)* a phyllic assemblage of muscovite + illite with a single absorption peak at 1410 nm and a shallow peak at 1900 nm; *(ii)* an argillic assemblage of monmorillonite + illite with a broad double peak from 1400–1450 nm and a strong peak at 1900 nm; and *(iii)* an advanced argillic alteration assemblage of illite + kaolinite + halloysite with a narrow triple peak from 1380–1420 nm, a strong peak at 1900 nm and a strong double peak from 2150–2210 nm. Only one sample, KA15_019 from the Kassiteres porphyry, was characterized by phyllic alteration. Argillic alteration was pervasive throughout the remaining samples of the Kassiteres porphyry and overlying volcaniclastics. The most intense advanced argillic alteration was restricted to faults zones in the Kassiteres pluton, immediately adjacent to the quartz-alunite lithocaps.

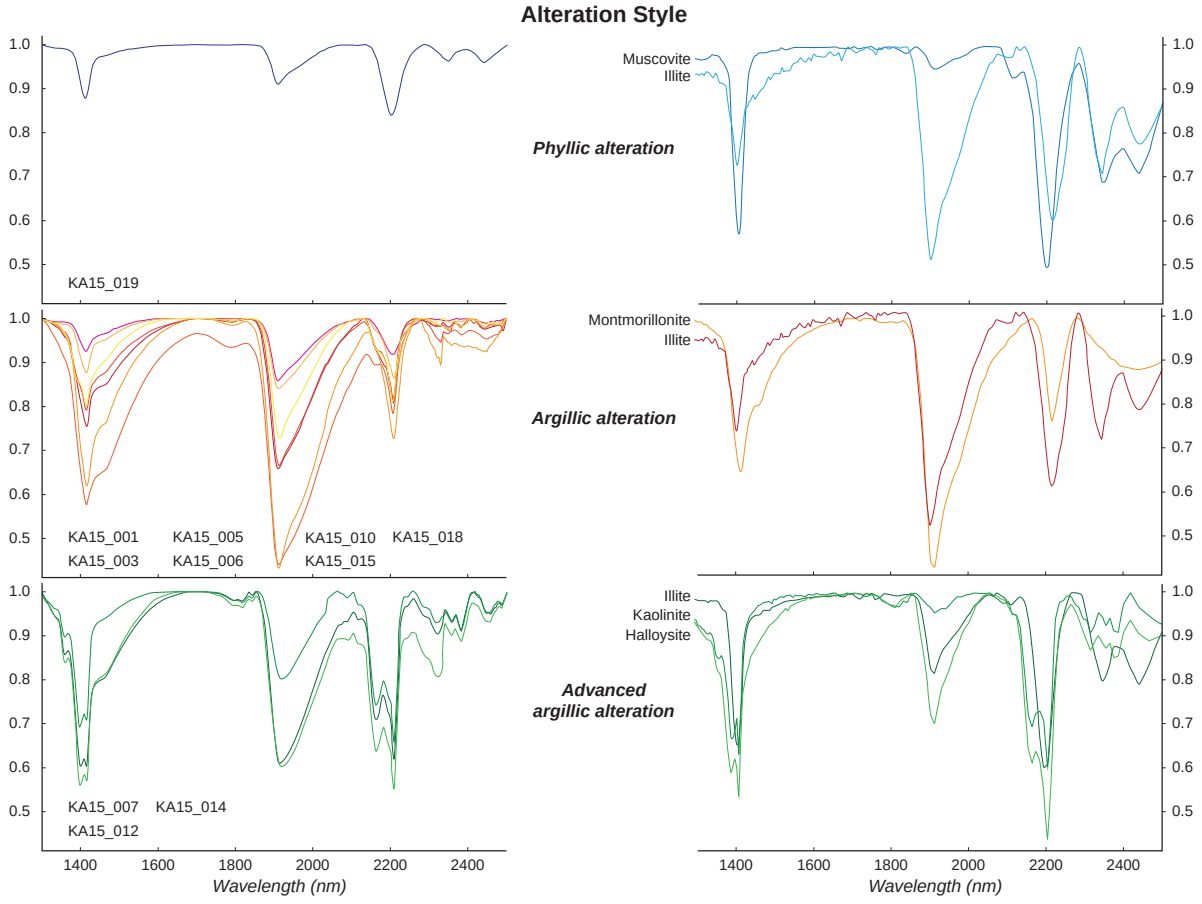

Figure 5.6: Short-wave infrared (SWIR) spectra from the Kassiteres system. In the panel on the right are the spectra from different alteration zones from Kassiteres, on the left are the USGS spectra for the clay assemblages from each alteration zone. Sample KA15_019 from the phyllic alteration zone is from the porphyry intrusion. Samples from the argillic alteration zone are from the overlying volcaniclastic units with the exception of KA15_018 which is from the porphyry intrusion. Samples KA15_007/KA15_012/KA15_014 are from fault zones in the Kassiteres host pluton, where the faults provided fluid pathways for mixing of the MVP and meteoric water and increased fluid:wall-rock interaction resulting in the most intense, and destructive advanced argillic alteration.

5.3.4 U-Pb Zircon Geochronology

Methods

The relative chronology of lithologies from Kassiteres was established in the field and a subset of five samples were selected for U-Pb geochronology to place absolute dates on the geological events. All U-Pb zircon geochronology presented was analysed using the chemical abrasion isotope dilution thermal ionization mass spectrometry (CA-ID-TIMS) technique (Mattinson, 2005; Condon et al., 2015; McLean et al., 2015) in order to give the highest analytical precision ($\leq$ 0.1% at 2σ; Schaltegger et al. 2015). Such high-precision geochronology provides the temporal resolution necessary to resolve the timing of zircon crystallisation in each igneous lithology. Over 3 kg of rock was collected for each sample to provide sufficient material for zircon mineral separation. Samples were crushed, sieved, rinsed and density separated following standard procedures at the University of Bristol. Individual zircon crystals were picked from the 50–250 μm size fraction (20–100 for each sample). Half of the zircons from each sample were selected for analysis whilst the other half were mounted in epoxy resin and polished for SEM characterisation at the University of Bristol using a Centaur Cathodoluminescence (CL) detector on a Hitachi S-3500N SEM at 10 kV and 23 mm working distance.

Isotope dilution geochronology integrates the isotopic ratio across the sample dissolved and thus has no spatial resolution between age domains across the volume of zircon analysed, typically a single crystal. Consequently, CL imagery of the zircons was used to characterise the internal zircon morphology of the mounted crystals prior to dissolution. A criterion of simple magmatic oscillatory zonation without evidence of zircon resorption or inheritance of an earlier zircon core observed in the CL imagery (e.g., Samperton et al. 2015), was developed to elect whether full crystal- or partial crystal- dissolution was appropriate. Samples KA15_005 and KA15_010 were selected from the pyroclastic facies of the Kassiteres volcaniclastic unit; sample KA15_005 is a crystal poor end-member of the pyroclastic deposit, whilst KA15_010 is a crystal-rich sample of the pyroclastic deposit from the outcrop in erosive contact with the Kassiteres pluton. Zircons from the volcaniclastic unit were euhedral with no evidence of resorption or inheritance and were selected for full crystal dissolution. Five zircon crystals were analysed from both KA15_005 and KA15_010. Porphyry samples KA15_018 and KA15_019 were selected for geochronology. CL imagery of the epoxy mounted zircons showed an inherited zircon core in $>$ 50 % of the crystals and evidence of zircon resorption in $>$ 80 % (an example of a porphyry zircon is shown in Fig. 5.7A). Following thermal annealing, the zircons selected for analysis (from KA15_018/KA15_019) were mounted in epoxy resin, polished and CL imaged to establish the internal morphology of each of the crystals. Zircon crystals with large outer growth zones were then fractured with a scalpel prior to analysis to isolate the outer most domains with simple magmatic zonation for dilution: $n = 2$ for KA15_018 and $n = 3$ for KA15_019. Annealed zircon crystals (KA15_005/KA15_010) and zircon fragments (KA15_018/KA15_019) were chemically abraided prior to dissolution to reduce Pb loss (Mattinson, 2005). Isotope dilution and mass spectrometry followed the protocol described in Sahy et al. (2015) and outlined in Appendix B.

Results

Five full zircon crystals were analysed from each of the pyroclastic samples; three of these analyses rejected due to elevated common lead (Pbc $>$ 3 pg; Appendix E). The remaining eight analyses (n = 4, KA15_010

and n = 3, KA15_005) show a period of protracted crystallisation between 32.32 ± 0.08 and 32.12 ± 0.13 Ma (Fig. 5.7B). As emplacement of a pyroclastic unit is a discrete event in time following which no more zircon crystallisation can occur, the youngest zircon age, or statistically significant population of ages, can be taken as the maximum age of eruption, i.e. the eruption could not occur earlier than this time as the crystallisation of zircon would be unlikely post-eruption and cooling. Our data suggest that the maximum age of eruption is 32.12 ± 0.06 Ma (KA15_018, n = 1, single crystal).

A total of seven fractured outer domains of zircon crystals were analysed for the porphyry samples (n = 4, KA15_018 and n = 3 KA15_019). Two analyses from sample KA15_018 are interpreted to record antecrystic zircon crystallisation deeper in the magmatic plumbing system in the Eocene (40.46 ± 0.02 and 40.75 ± 0.02 Ma). The remaining five analyses show an 800,000 yr period of crystallisation in the porphyry intrusion between 32.82 ± 0.05 and 32.04 ± 0.03 Ma. In an intrusive magmatic framework, as zircon saturation is reached towards the end of crystallisation, autocrystic zircon U-Pb dates are interpreted to reflect the final stages of crystallisation of the intrusion during emplacement (e.g., Watson 1979). Typically, the youngest statistically significant population of zircons from an intrusive igneous sample is interpreted to be the age of emplacement (von Quadt et al., 2011). Our data suggest a final emplacement age of the Kassiteres porphyry at 32.04 ± 0.06 Ma (KA15_010, n = 1, single crystal).

Table 5.2: Summary of the $^{206}Pb/^{238}U$ interpreted ages from Kassiteres. QF – quartz-feldspar; PF – pyroclastic facies.

Sample Name	Lithology	$^{206}Pb/^{238}U$ date (Ma)	± (x)	± (y)	MSWD	n	Justification
RT14_028	Host pluton	32.05	0.02	0.04	1.15	3/5	Youngest three dates (weighted mean)
KA15_018	QF porphyry	32.04	0.06	0.07	-	-	Youngest date
KA15_019	QF porphyry	32.17	0.02	0.04	0.21	2/3	Youngest two dates (weighted mean)
KA15_005	Volcaniclastic unit (PF)	32.16	0.04	0.06	0.32	3/5	Youngest three dates (weighted mean)
KA15_010	Volcaniclastic unit (PF)	32.12	0.06	0.07	-	-	Youngest date

x uncertainty – analytical only
y uncertainty – analytical + tracer calibration + ^{238}U decay constant

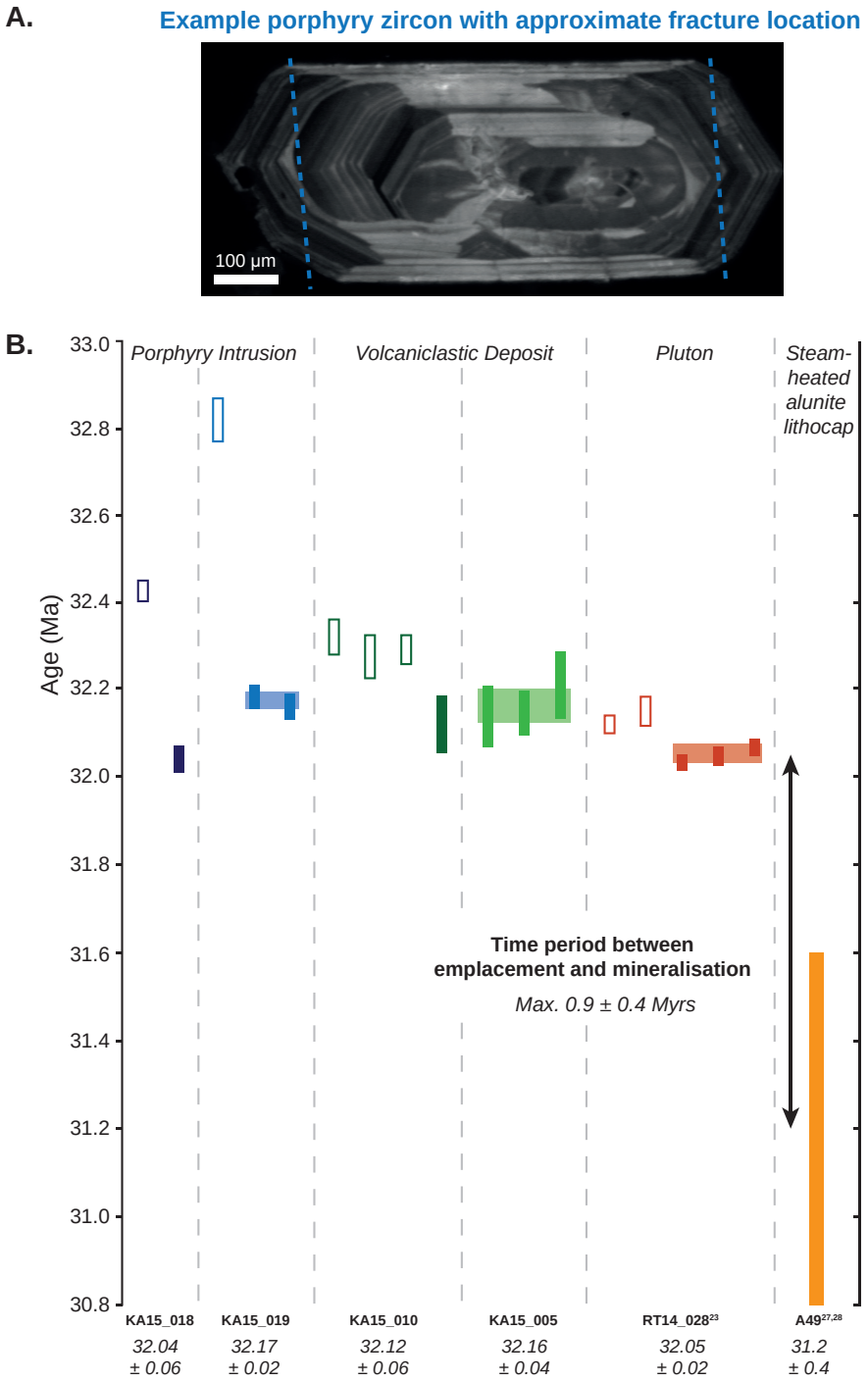

Figure 5.7: (A): Cathodoluminscence (CL) imaging of zircons from each unit showed simple magmatic zonation in the Kassiteres granodiorite and volcaniclastic units, but more complex zircon core inheritance and resorption in the quartz-feldspar porphyry. Zircons from the quartz-feldspar porphyry were fractured (along the lines drawn) prior to U-Pb analysis in order to isolate the oldest age domain. (B): Intrusion and autocrystic zircon crystallisation in the Kassiteres pluton is dated to 32.05 $\pm$ 0.02 Ma; high-precision U-Pb geochronology from the Kassiteres quartz-feldspar porphyry and overlying volcaniclastic unit show zircon crystallisation earlier than the emplacement of the intrusion. As our field relationship show that the quartz-feldspar porphyry intruded the Kassiteres pluton and the volcaniclastics overlie all intrusive units, we interpret the crystallisation ages as antecrystic, recording zircon crystallisation from the magma in transit prior to final porphyry and volcaniclastic emplacement. The $^{40}Ar/^{39}Ar$ age of steam-heated alunite from Sapana (Ortelli et al., 2009, 2010) indicates a minimum age of mineralisation and a timescale of $<$ 900,000 yrs for exhumation of the system prior to the interaction between the magmatic-hydrothermal system and the palaeosurface.

5.4 Discussion

5.4.1 A Temporal Framework of Magmatism

The field relationships at Kassiteres show a clear timeline of magmatic events in the Oligocene: intrusion of the host diorite-granodiorite pluton followed by intrusion of the small (150 m by 500 m), quartz-feldspar porphyry and then eruption of the pyroclastic facies of the volcaniclastic unit. These field relationships allow constraints to be placed upon exhumation of the Kassiteres system: Kassiteres must have been exhumed from the depth at which the host pluton was emplaced to the surface in the period between final pluton emplacement (approximated by final crystallisation) and eruption of the overlying pyroclastic facies.

U-Pb zircon geochronology was used to place absolute constraints on the Oligocene magmatic events at Kassiteres; using the relative chronological framework developed through field observations, I aimed to bracket pluton exhumation using the emplacement age of the host pluton and eruption age of the volcaniclastic unit. However, based upon my field observations, the zircon crystallisation ages from the quartz-feldspar porphyry and the pyroclastic facies of the volcaniclastic unit cannot be interpreted as emplacement/eruption ages of these lithologies, as the zircon U-Pb ages of the porphyry and pyroclastic are older than the zircon U-Pb crystallisation age of the host pluton. I consider that the zircon dates in the pyroclastic samples reflect two possible scenarios: *(i)* the pyroclastic zircons are antecrystic and crystallised during magma ascent and storage prior to eruption; or *(ii)* the pyroclastic zircons are xenocrystic and were entrained from the surrounding magmatic wall-rock during magma ascent and eruption. Similarly, I interpret the porphyry zircons as antecrystic, reflecting a protracted 800,000 yr period of magma storage and crystallisation prior to porphyry intrusion into the Kassiteres pluton. High-spatial resolution U-Pb zircon geochronology presented in Chapter 4 provides two lines of evidence to support this: *(i)* an interpreted final crystallisation age of the Kassiteres porphyry at 31.46 $\pm$ 0.34 Ma is younger than crystallisation of the Kassiteres intrusion; and *(ii)* resorption features in the Kassiteres porphyry zircons have equivalent crystallisation ages (within error) indicating thermal fluctuations in the magma storage system over timescales less than hundreds of thousands of yrs, the temporal resolution of the analysis. Final emplacement of the Kassiteres pluton occurred at 32.05 $\pm$ 0.02 Ma (Chapter 2), intrusion of the small, quartz-feldspar porphyry at 31.46 $\pm$ 0.34 Ma and eruption and emplacement of the pyroclastic facies of the volcaniclastic unit must have followed.

5.4.2 Estimating Exhumation at Kassiteres

Porphyry – epithermal style mineralisation is the youngest event recorded at Kassiteres overprinting all intrusive and extrusive igneous lithologies (Voudouris et al., 2006; Ortelli et al., 2009, 2010). Therefore, the age of the hydrothermal event provides a minimum estimation of the depositional age of the volcaniclastic deposits. Furthermore, it provides an estimated time-window for the exhumation at Kassiteres between host pluton emplacement and at-surface mineralisation. $^{40}Ar/^{39}Ar$ dates of magmatic steam-heated alunites from the Sapana and Santa Barbara lithocaps and adularia from milky quartz-calcite veins cutting the Kassiteres intrusion, date pervasive alteration of the Kassiteres system to between 31.9 $\pm$ 0.6 Ma and 31.2 $\pm$ 0.4 Ma (Ortelli et al., 2009, 2010). I consider the youngest steam-heated alunite $^{40}Ar/^{39}Ar$ age of the Santa Barbara lithocap as dating the youngest possible at-surface hydrothermal event at Kassiteres. It therefore provides a minimum age (31.2 $\pm$ 0.4 Ma) of deposition of the volcaniclastic unit which hosts pervasive argillic

alteration from this, or an earlier, at-surface hydrothermal event. I can thus conclude that exhumation of the host pluton from emplacement at 4.4 $\pm$ 1.9 km and 32.05 $\pm$ 0.04 Ma to the surface prior to volcaniclastic deposition and pyroclastic eruption occurred before 31.2 $\pm$ 0.4 Ma. Assuming a constant rate of exhumation, a normally distributed uncertainty on the exhumation time window, and a truncated normal distribution at $<$ 1.9 km (0.5 kbar), the lower limit of amphibole stability (Mutch et al., 2016), on the depth of emplacement, a Monte Carlo error propagation protocol was implemented with 10^6 simulations to estimate the exhumation rate. I calculate a minimum exhumation rate of 5.2 $\pm$ 3.0 km/Myr at Kassiteres; full details of the Monte Carlo simulation are included in Appendix M.

5.4.3 Magmatism and Rapid Exhumation at Kassiteres

In the Eocene, Kassiteres was part of the Thrace basin, a depositional centre for sediments shedding off the bounding metamorphic terranes (Fig. 5.1; Kilias et al. 2013, 2015). Oligocene, post-collisional magmatism at Kassiteres exploited the existing fault structures as lithospheric mantle melts migrated upwards through the crust (Fig. 5.8A; Christofides et al. 2004). The Kassiteres dioritic to granodioritic intrusion is part of the larger Maronia Magmatic Corridor (MMC), a NE-trending belt of post-collisional high-K calc-alkaline intrusions that was emplaced in the Oligocene along the SW margin of the Kechros dome (Fig. 5.1; Chapter 2). The subsequent transition from hypabyssal to sub-volcanic depths occured as a result of exhumation of Kassiteres. The intrusion of the small, ore-bearing porphyry intrusion likely occurred at a depth of $<$ 2 km in the crust, although the destructive nature of alteration of the Kassiteres porphyry prevents estimation of the intrusion using thermobarometry. Evolved magmatism at Kassiteres then breached the surface, with volcaniclastic deposits overlying the Kassiteres pluton and porphyry (Fig. 5.8A).

In classical porphyry systems rapid exhumation is attributed to high denudation rates and/or sector collapse of the volcanic overburden (e.g., Sillitoe 1994). Sector collapse is common in arc volcanoes when gravitational instability in the volcanic cone results in excavation of a horseshoe-shaped collapse feature, several hundred meters in depth (e.g., Siebert 1984; Grosse et al. 2009). However, this study has shown that the Kassiteres system was exhumed from a depth of 4.4 $\pm$ 1.9 km in an 0.9 $\pm$ 0.4 Myr time period, corresponding to an exhumation rate 5.2 $\pm$ 3.0 km/Myr; it is unlikely that this can be accounted for solely by sector collapse. In the Oligocene, the northern RCC experienced a temperate climate, suggesting that surface erosion alone cannot account for the exhumation of the Kassiteres systems and that tectonic uplift must have played an important role (Márton et al., 2010).

Kilias et al. (2013) suggested that the Thrace basin was affected by two sequential deformational events that could have affected exhumation at Kassiteres. Firstly, Eocene – Oligocene trans-crustal extension formed the S-dipping, Kechros detachment fault at the northern margin of the basin and a complimentary set of E-trending, N-dipping high-angle normal faults, including the Makri fault, developed in the hanging wall across the Thrace basin (Burg, 2011; Bonev et al., 2013; Kilias et al., 2013, 2015). Active from the mid-Eocene to the Oligocene, these faults accommodated exhumation of the lower-crustal Kechros dome along the Kechros detachment (e.g., Burg 2011; Kilias et al. 2013). In the Oligocene to Miocene, extension was then accommodated in the upper crust, with the formation of N- to NNE-trending sinistral strike-slip faults with a minor W-dipping dip-slip motion (e.g., the Petrota fault) and reactivated the E-trending high-angle normal faults (e.g., the Makri fault) with a dextral-sense strike-slip motion (Kilias et al., 2013). Kassiteres sits at the intersection of the Makri and Petrota faults, where N-ward motion in the footwall, east of the

Petrota fault and W-ward motion in the hanging wall, north of the Makri fault, generates localised extension facilitating exhumation of Kassiteres around 32 Ma. This is in agreement with Márton et al. (2010) who propose rapid uplift in the northern hanging wall of the Kechros and Kardamos domes in Bulgaria between 30–33 Ma associated with sediment-hosted epithermal-Au mineralisation. This suggests similar tectonic events across the northern and southern hanging walls of the Kechros domes in the Oligocene.

5.4.4 Mineralisation at Kassiteres

Kassiteres is an excellent example of a telescoped porphyry – epithermal system. The gradation from high-T, neutral pH phyllic alteration in the core of the mineralising porphyry intrusion to pervasive argillic alteration in the overlying volcaniclastics and propyllitic alteration in the host pluton reflects cooling of the MVP as it migrates away from the source porphyry. High-T potassic alteration in the host pluton marks initial interaction between the MVP and the wall-rock. Low-T, neutral-pH propyllitic alteration, that typically forms the outermost shell of distal alteration as the MVP cools and disperses without interaction with meteoric water (Sillitoe, 2010), overprints potassic alteration in the Kassiteres host pluton. Low-T, low pH argillic alteration is typically found in the upper portion of the porphyry – epithermal alteration pattern as the cooling magmatic-hydrothermal system interacts with circulating meteoric waters (e.g., Taylor 1997; Harris and Golding 2002; Sillitoe 2010). At Kassiteres, porphyry-style potassic and propyllitic alteration and quartz + pyrite $\pm$ molybdenite veining is restricted to the dioritic-granodioritic host pluton, but these veins are scarce with porphyry-style veining concentrated close to the breccia pipes and lithocap of the Korfyes Hill occurence at the northern margin of the host pluton (Voudouris et al., 2006). The Sapana and Santa Barbara Au-Ag-Te epithermal occurences are hosted by the overlying volcaniclastic units, spatially close to the porphyry intrusion in the west of the system and are associated with the pervasive, argillic phase of alteration (Voudouris et al., 2006).

The juxtaposition of alteration and mineralisation styles at Kassiteres suggests mixing of hot, saline magmatic brines (the MVP) and cool, meteoric water diluted the mineralising system occasioning the transition from stage *(i)*, high-T alteration and porphyry-Cu deposition, to stage *(ii)*, low-T alteration and epithermal-Au deposition (Fig. 5.8B). A similar mechanism has been suggested for the Porgera epithermal Au-Ag-Te system, which is also thought to record the porphyry to epithermal transition, where isotope ratios in fluid inclusions document a strong meteoric water component to the mineralising fluid (Handley and Bradshaw, 1986; Richards et al., 1990; Richards, 1992; Richards and Kerrich, 1993). Mixing of meteoric water with the MVP is thought to be important in generating a moderate salinity, metalliferous mineralising fluid at Porgera, and Richards (1992) & Richards and Kerrich (1993) suggest that the meteoric waters may have remobilized earlier hypogene sulphides disseminated during porphyry-style mineralisation. At Kassiteres, a strong lithological control on alteration style suggests that the host pluton acted as an impermeable barrier to meteoric water thus preserving high-T potassic and low-T, neutral pH propylitic alteration and porphyry-style veining only in the host pluton.

Ore-minerals and metals precipitate out of solution as the result of changes to the physiochemistry (P, T, $fO_2$and pH) of the magmatic-hydrothermal fluid. At Porgera, mineral precipitation is thought to have been induced by flash cooling and depressurizing events, induced by fault-related activity (Richards, 1992; Richards and Kerrich, 1993; Peterson and Mavrogenes, 2014). At Kassiteres the pervasive nature of argillic alteration throughout the overlying volcaniclastics, suggests the magmatic-hydrothermal system was poorly

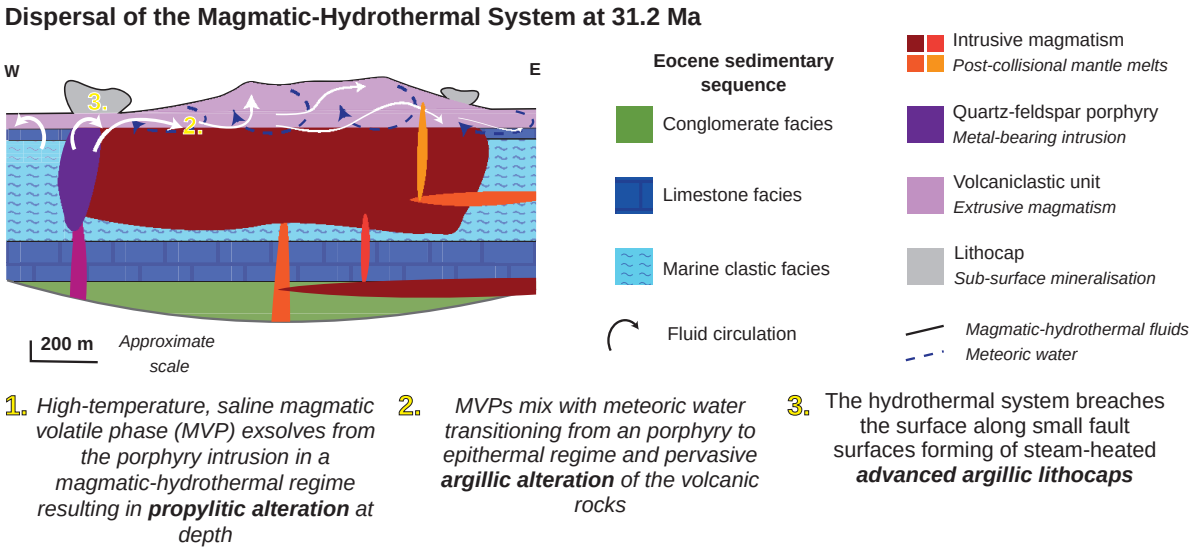

Figure 5.8: Circulation of meteoric waters in the highly permeable volcanic rocks interacted with the magmatic-hydrothermal fluids and resulted in cooling and dispersal of the hydrothermal regime and pervasive argillic alteration of the volcaniclastic unit and porphyry intrusion. Advanced argillic steam-heated lithocaps formed where the fluids vented to the surface along shear zones in the host pluton.

confined and able to interact with a large volume of wall-rock. Therefore, I suggest that dilution and decompression of the metalliferous fluids by the ingress of meteoric water through the highly permeable volcaniclastic rocks overlying the system at Kassiteres, resulted in disseminated mineralisation. Disperal of the magmatic-hydrothermal fluids by meteoric water in highly permeable wall-rock at Kassiteres, rather than in catastrophic faulting and fracturing events as at Porgera, could account for the difference in grade between the systems. This would suggest that the overlying lithologies are important for confining the magmatic-hydrothermal systems and suggest that permeable capping lithologies such as poorly welded pyroclastic deposits and volcaniclastic sediments are detrimental to the concentration of metals in magmatic-hydrothermal systems. Additional evidence of this can be found in the advanced argillic alteration at Kassiteres, which is restricted to shear zones in the dioritic-granodioritic pluton where faults provided pathways to vent magmatic-hydrothermal fluids to the surface. Limited interaction with groundwater along these shear zones and associated breccia pipes results in the MVP reaching the surface, forming steam-heated, quartz-alunite lithocaps (Hedenquist and Taran, 2013).

5.4.5 The Influence of Exhumation on Mineralisation

Elevated exhumation rates and geothermal gradients can last many millions of years (e.g., Mancktelow and Grasemann 1997), whilst the circulation of metal-rich mineralising fluids in magmatic-hydrothermal systems is relatively short-lived, typically lasting only tens to hundreds of thousands of years (e.g., McInnes et al. 2005b; von Quadt et al. 2011; Buret et al. 2016). Consequently, when comparing exhumation rates with the lifetime of mineralising systems, we are considering processes that operate over different timescales. Exhumation rates of between 0.5–1.4 km/Myr typically reported for PCDs consider the evolution of PCDs from emplacement to the surface (Kesler and Wilkinson, 2008; Yanites and Kesler, 2015), and will not effectively capture catastrophic events that might accommodate a phase of sub-surface exhumation on the timescales of hydrothermal systems, e.g., overlying volcanic sector collapse (Sillitoe, 1994). Considering

the earlier example of the Grasberg and Ciemas deposits in Indonesia, the difference in cooling timescales (between 500–300 °C in 0.015 Myr at Grasberg and 1.040 Myr at Ciemas) is not captured by the average exhumation rate of the systems 0.38 km/Myr and 0.35 km/Myr for the Grasberg and Ciemas deposits respectively (McInnes et al., 2005a). Whilst mineralisation in an exhuming terrane can be favourable for the formation of PCDs by inducing strong thermal gradients between the magmatic-hydrothermal system and the wall-rock (e.g., Ok Tedi, Papua New Guinea; McInnes et al. 2005b; Dongen et al. 2010), the systems must stall in the upper 1–2 km of the crust in order to preserve the magmatic-hydrothermal system and prevent the pre-mature dilution and dispersal of the MVPs by meteoric water as observed at Kassiteres, or erosion of the mineralised system (e.g., Yanites and Kesler 2015).

However, at Kassiteres, exhumation of the host equigranular pluton from 4.4 $\pm$ 1.9 km depth is recorded within 0.9 $\pm$ 0.4 Myrs, on the same timescale as porphyry intrusion and porphyry – epithermal mineralisation. Tectonic-driven rapid exhumation of the Porgera magmatic system within the lifetime of the hydrothermal system is thought to be responsible for rapid transition from a porphyry to an epithermal regime (Richards, 1992). The short-lived porphyry-stage of mineralisation ceased prematurely when the ingress of groundwater dominated the system and mineralisation occurred in discrete faulting events (Richards, 1992; Richards and Kerrich, 1993; Peterson and Mavrogenes, 2014). I envisage a similar scenario at Kassiteres where mixing with meteoric water occasioned the transition from a porphyry to an epithermal mineralising system and can account for the poorly preserved porphyry-style mineralisation. An additional lithological control on mineralisation is also proposed where the permeable nature of the overburden at Kassiteres allowed for the dispersal of the hydrothermal system. This was the result of exhumation of the Kassiteres magmatic system to the surface and the deposition of a volcaniclastic unit capping the hydrothermal system, driving circulation of meteoric groundwater.

5.5 Conclusions

This chapter has shown that whilst elevated rates of exhumation aide the concentration of mineralisation in many giant porphyry ore bodies, the Kassiteres system was exhumed too rapidly (a minimum estimated rate of exhumation of 5.2 $\pm$ 3.0 km/Myr) to allow a porphyry-style magmatic-hydrothermal system to fully develop. A similar mechanism is suggested for the porphyry to epithermal transition recorded at the Porgera deposit in Papua New Guinea (Handley and Bradshaw, 1986; Richards, 1992). An additional lithological control during mineralisation at Kassiteres is proposed, where exhumation of the magmatic system to the surface, resulted in the contemporaneous eruption of pyroclastic material which created a permeable overburden for the effective dispersal of the magmatic-hydrothermal system by the circulation of meteoric groundwater. Resultant features of highly-telescoped mineralisation and alteration at Kassiteres include: *(i)* well-developed, potassic and overprinting propylitic alteration of the host dioritic-granodioritic pluton; *(ii)* restricted preserved porphyry-style mineralisation within shear zones in the impermeable host pluton; *(iii)* pervasive argillic alteration of the overlying volcanic rocks; and, *(iv)* small-volume, Au-telluride epithermal mineralisation and veining.

Chapter 6

Conclusions

The view looking northeast across the Leptokaria complex and Kechros dome from Leptokaria village

6.1 Summary

Cenozoic back-arc extension of the northern Aegean was driven by roll-back of the Hellenic slab and resulted in the exhumation of a series of core complex gneiss domes along the northern limit of the back-arc, forming the Rhodope Massif in northern Greece and southern Bulgaria (e.g., Burg 2011; Kydonakis et al. 2015a; Brun et al. 2016). Asthenospheric upwelling beneath the extended lithosphere of the Rhodope Massif provided a heat source for re-melting of the subduction-modified lithospheric mantle and generated contemporaneous post-collisional magmatism. The Rhodope Massif can be split into two discrete core complexes, the northern Rhodope core complex (RCC) and the southern RCC, defined by the duration of exhumation (Kydonakis et al., 2015a,b). Exhumation of both the northern and southern RCC began in the Eocene with the onset of Hellenic slab roll-back (e.g., Burg 2011; Kydonakis et al. 2014, 2015a). In the northern RCC, core complex exhumation and post-collisional magmatism ceased in the Oligocene whilst post-collisional extension, exhumation and magmatism continued into the Miocene in the southern RCC (e.g., Burg 2011; Kydonakis et al. 2015a,b).

The Maronia Magmatic Corridor (MMC) is an Oligocene belt of high-K calc-alkaline to shoshonitic plutons that intrude the Kechros dome of the northern RCC in northeastern Greece (Del Moro et al., 1988). Magmatism along the MMC is post-collisional and intrudes towards the end of the exhumation of the Kechros dome. The MMC plutons are host to four porphyry – epithermal systems with Cu-Au-Mo-Te-W(?) mineralisation of varying grades and economic potential (e.g., Melfos and Voudouris 2017). This thesis has combined petrological, geochemical and geochronological analyses with field observations to reconstruct the evolution of the MMC. The results are schematically outlined in Figure 6.1. This thesis provides petrological context to the MMC, which is interpreted within the tectonic framework of the northern Aegean (***Chapters 2 & 5***) and related to the potential for porphyry – epithermal mineralisation along the MMC (***Chapters 3, 4 & 5***).

A representative sample suite, collected over three field seasons, captures the intrusive units from across the MMC. ***Chapter 2*** focuses on the petrogenetic evolution of the MMC using petrographic observations, whole-rock geochemical analyses and high-precision isotope dilution thermal ionisation mass spectrometry (ID-TIMS) U-Pb zircon geochronology (Fig. 6.2A,D). The MMC does not represent a continuous magmatic period, as suggested by Del Moro et al. (1988) but two, temporally and compositionally distinct magmatic complexes. The Kassiteres–Leptokaria complex was intruded in a 900,000 yr window between 32.9 - 32.0 Ma; it is a high-K calc-alkaline suite of plutons that show trace element patterns consistent with plagioclase + pyroxene + amphibole controlled fractionation. Comparison with the phase diagram of Naney, (1983; Fig. 4) shows that for compositions similar to the tonalites of the Kassiteres–Leptokaria complex, lower crustal fractionation (at 8 kbar, $\sim$ 24 km depth) of a plagioclase + pyroxene + amphibole assemblage requires a magma with $3 < H_2O$ wt. % < 4.75.

Maronia is an incompatible-rich shoshonitic pluton separated by 30 km from the rest of the MMC to the NE. Fractional crystallisation modelling suggests that pyroxene and plagioclase were the dominant phases during lower crustal fractionation, enriching the residual melt in incompatible alkalis over small changes in SiO_2 and generating a shoshonitic liquid line of descent (Meen, 1987). This requires an H_2O-poor magma ($<\sim 2$ wt. % H_2O) with melting occuring at elevated temperatures (Baker and Eggler, 1987). A similar mechanism is discussed by Freise et al. (2009); Lanzo et al. (2016) & Beermann et al. (2017) for the generation of Pleistocene ultra-potassic magmatism in the Aeolian Islands. Emplacement of the Maronia pluton occurred

2.2 Myr after intrusion of the Kassiteres–Leptokaria complex. Experimental petrology results suggest that the apparent break in magmatism is a consequence of sub-solidus conditions, the result of dehydration during melting to produce the Kassiteres–Leptokaria complex. The intervening 2.2 Myrs allowed for the accumulation of heat allowing for the renewal in melting.

Magmatism in the Kechros dome, and across the northern RCC ceased following the intrusion of the Maronia pluton. Two scenarios can be envisaged to explain this, although they are not mutually exclusive: *(i)* further dehydration of the mantle during petrogenesis of the Maronia magmas drove the solidus temperature in the lithospheric mantle even higher *T*s and insufficient heat was accumulated to rejuvenate melting; *(ii)* the asthenospheric mantle upwelling migrated southwards, co-incident with the end of trans-crustal extension in the northern RCC, as a result there was no heat source to drive mantle melting beneath the Kechros dome and across the northern RCC (e.g., Burg 2011). A combination of both ideas is most likely, meaning that intrusion of Maronia at 29.6 Ma provides a time marker for the end of extension in the northern RCC. Magmatism in the southern RCC continued into the Miocene, for example the Samothraki and Aspro Lakkos (Kassandra) intrusions, with continued, now SW-vergent rotational, exhumation of the southern RCC (Christofides et al., 2000; Kydonakis et al., 2014, 2015b; Siron et al., 2016, 2018). This suggests that migration of asthenospheric upwelling from beneath the northern RCC facilitated rotational exhumation of the southern RCC, and generated continued magmatism, of a shoshonitic composition, in the southern RCC.

Chapter 3 then considers the transit of the post-collisional melts through the crust, and constrains the extensive conditions of the systems during magma crystallisation using electron probe micro-analysis (EPMA) of mineral chemistry (Fig. 6.2A,D). The Kassiteres–Leptokaria complex was emplaced in the upper crust at depths of between 4–6 km. Zoning in plagioclase crystals and a wide spread in zircon crystallisation

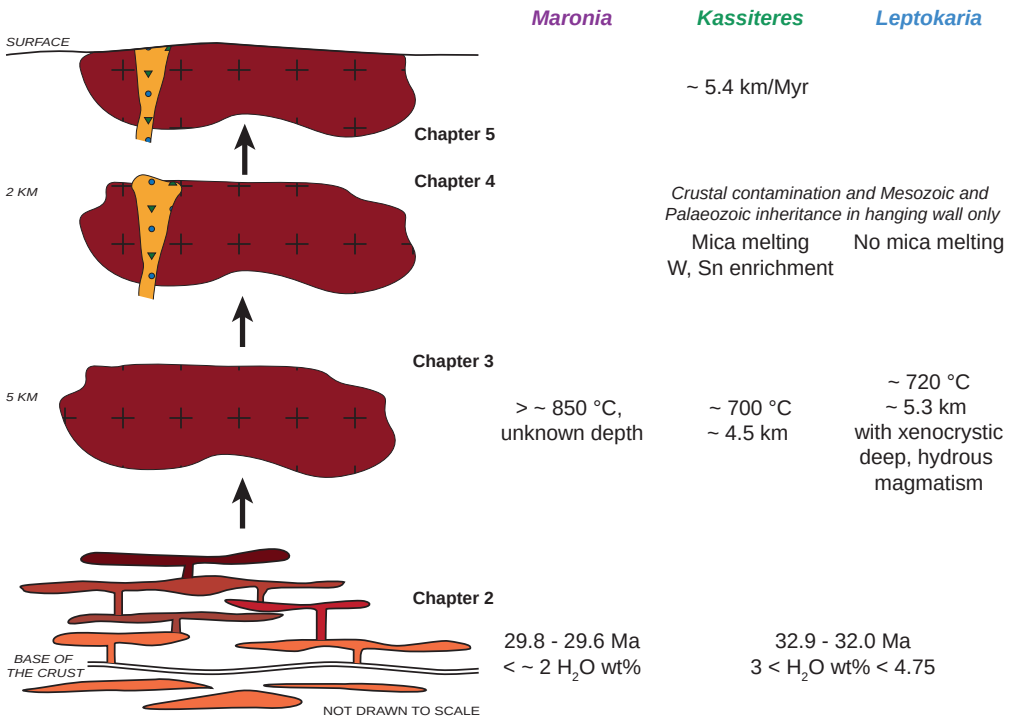

Figure 6.1: A graphical summary of the thesis. This work tracks the evolution of the Maronia Magmatic Corridor from magma petrogenesis, through pluton assembly and crystallisation, porphyry intrusion and mineralisation to exhumation and exposure at the surface.

ages (Chapter 2), evidence multiple periods of magma injection into a crystal mush reservoir in the upper crust, in line with current thinking on pluton assembly (e.g., Annen et al. 2006; Samperton et al. 2015). Paired estimates of *T* and *P* from the Kassiteres–Leptokaria complex fall within error of the haplogranite solidus, as defined by Holtz and Johannes (1994). This, in addition to decreasing Cl concentrations with *P* in amphibole and the presence of multi-phase primary magmatic fluid inclusions in quartz, suggests the presence of an exsolved, magmatic volatile phase during final emplacement of the intrusions.

The Kassiteres pluton is the only intrusion from the Kassiteres–Leptokaria complex which is hosted in the hanging wall of the Kechros dome. *T* and *P* estimates of the Kassiteres pluton suggest shallower and cooler emplacement conditions in the hanging wall. In the Leptokaria plutons, xenocrystic high-Al_{TOT} amphiboles and high-An plagioclases record crystallisation from an earlier, hydrous magma at greater *T* and *P* in the magmatic system. This signal is restricted to two samples from the MMC, RT14_010 and RT14_017. Of interesting note, sample RT14_010 also has the oldest zircon crystallisation age, 32.932 ± 0.034 Ma (Chapter 2). Both low-Al_{TOT} and high-Al_{TOT} amphiboles are found in this sample. Thermobarometry of the low-Al_{TOT} amphiboles in equilibrium with low-An plagioclases give crystallisation *T* and *P* of 680–780 °C and 1.4 ± 0.5 kbar (5.3 ± 1.9 km). Petrographically, zircon is only observed included in interstitial quartz and K-feldspar from this sample, suggesting near-solidus zircon saturation during final crystallisation at upper crustal temperatures and pressures; thus the crystallisation age for RT14_010 dates emplacement of the magma in the upper crust. The older age of RT14_010 suggests that it could record one of the earlier injections of melt into the upper crust which could explain entrainment of xenocrystic cargo during ascent. If this is the case, RT14_017, with a cumulate like-texture, is likely also an early phase of magmatism.

Constraining the extensive parameters of crystallisation of the Maronia pluton was more difficult. The influence of elevated alkalis, importantly K, on phase relations is not well known and most thermobarometers are not calibrated for such compositions. The *P* (depth) of crystallisation is unknown, although higher crystallisation *T* estimates are consistent with the generation of shoshonitic magmatism from a drier source mantle, as suggested by the two-pyroxene- and apatite saturation- thermometers in ***Chapter 2***.

The petrogenesis of the metal-bearing magmas that produce the metal-bearing porphyry intrusions is considered in ***Chapter 4*** (Fig. 6.2B). The work focuses on porphyry intrusions from the Kassiteres–Leptokaria complex using case studies of known porphyry – epithermal systems at Kassiteres and Essimi and a porphyry dyke intrusion at Leptokaria with no observed mineralisation. Destructive alteration of the porphyry intrusions from Kassiteres and Essimi means that traditional petrological techniques have limited applicability to these samples. Instead the work uses zircons as repositories of invaluable geochemical data. An integrated approach of laser ablation inductively coupled plasma mass spectrometry (LA-ICP-MS) zircon trace element geochemistry, high spatial-resolution LA-ICP-MS U-Pb zircon geochronology and EPMA melt inclusion petrology were used to unravel the petrogenesis of the fertile magmas. This pioneering study is, to the best of my knowledge, the first documentation of the geochemistry of zircon-hosted melt inclusions from magmatic mineral systems.

Geochemical signatures of mixing are observed in the porphyry intrusions from across the MMC. The peraluminous melt inclusions record the composition of the mixed magma, which, combined with the zircon trace element geochemistry and geochronology, fingerprint mixing of a crustal melt with a mantle-derived magma. Two different compositions of crustal melt are identified between the Kassiteres and Essimi porphyries with: *(i)* high-Ta, -Nb, and -W, and *(ii)* high-Eu signatures respectively. The Leptokaria porphyry

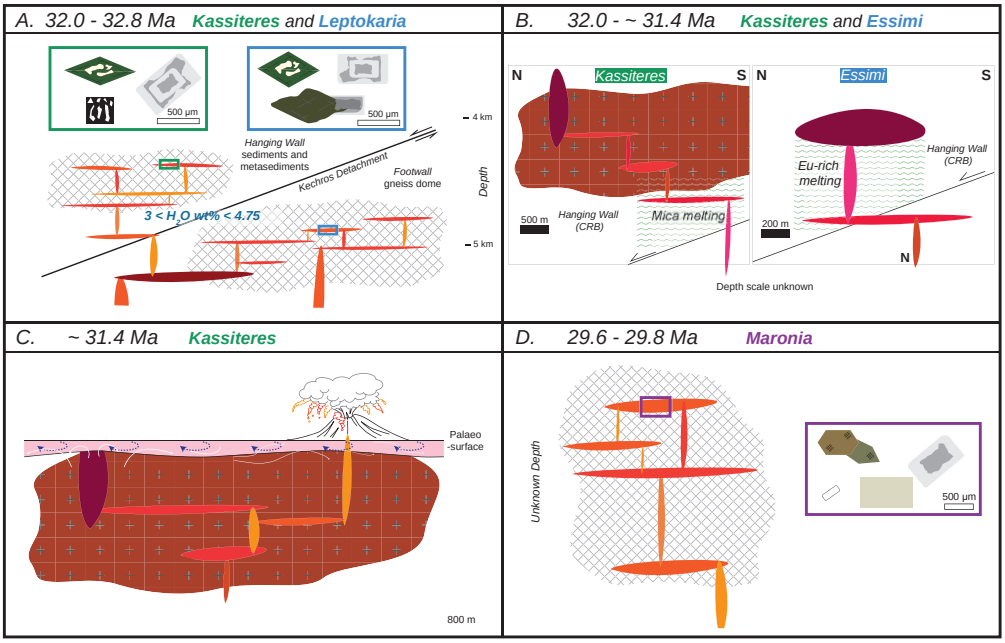

Figure 6.2: A cartoon illustrating the evolution of the Maronia Magmatic Corridor. **A**: petrogenesis of the Kassiteres–Leptokaria complex (*Chapter 2 & 3*). **B**: intrusion of mantle-derived magmas and mixing with a crustal component resulted in the formation of porphyry systems at Kassiteres and Essimi. The Leptokaria porphyry intrusion is not shown in this figure but represents a less mixed, predominantly mantle-derived end-member of the porphyry phase of magmatism (*Chapter 4*). **C**: the Kassiteres system is exhumed to the surface syn-mineralisation with rapid dispersal of dilute fluids due to ingress of meteoric water. This resulted in a breached porphyry system (*Chapter 5*). **D**: petrogenesis of the dry, shoshonitic Maronia pluton (*Chapter 2 & 3*).

has a dominantly mantle-derived composition which suggests it represents the shared end-member mixing component of porphyry magmatism along the MMC. Small-volume crustal melts with an Eu-rich signature are the expected crustal-component at Essimi. Melting of a mica-rich crustal lithology is the suggested mixing component with magmatism at Kassiteres and the source of W, Sn enrichment.

Finally, ***Chapter 5*** discusses the role of exhumation on porphyry – epithermal mineralisation at Kassiteres (Fig. 6.2C). Kassiteres is a telescoped porphyry – epithermal system with overprinting alteration and veining; multiple small-volume Au-Ag-Te epithermal systems are known from Kassiteres, whilst deeper, porphyry style mineralisation is poorly preserved in the equigranular host intrusion. Field relationships are used to develop a timeline of magmatic events, from hypabyssal pluton emplacement and crystallisation at 32.045 $\pm$ 0.020 Ma, through sub-volcanic porphyry intrusion, exhumation to the surface and burial by a pyroclastic deposit, and the final stages of epithermal mineralisation at 31.2 $\pm$ 0.4 Ma. An 0.9 $\pm$ 0.4 Myr window between pluton emplacement and at-surface mineralisation, allows exhumation of Kassiteres from a depth of 4.4 $\pm$ 1.9 km to the surface, at a rate of 5.5 $\pm$ 4.4 km/Myr.

Typical long-term exhumation rates of porphyry – epithermal systems are $<\sim$ 1.4 km/Myr (Yanites and Kesler, 2015). At Kassiteres, rapid exhumation within the lifetime of the mineralising system is thought to have had a detrimental influence on mineralisation. As the magmatic-hydrothermal fluid system moved up towards the surface it interacted with meteoric groundwater very early on in the lifetime of the system and, as a result, the meteoric waters diluted the hydrothermal system and efficiently dispersed the fluids through permeable wall-rock. At Kassiteres, the overlying volcaniclastic units provide this permeability. The porphyry – epithermal transition is also observed at the Porgera deposit in Papua New Guinea, where

the ingress of meteoric waters driven by exhumation of the system is thought to trigger the change in fluid regime (e.g., Handley and Bradshaw 1986; Richards et al. 1990; Richards 1992; Richards and Kerrich 1993). However, the key difference between the systems is that the epithermal fluid system at Porgera is fault-controlled so any permeability is transient (e.g., Richards et al. 1990; Peterson and Mavrogenes 2014). I suggest that the permeable wall-rock at Kassiteres, the overlying volcaniclastic unit that formed as magmatism breached the surface during syn-mineralisation exhumation, hindered the epithermal system, allowing dispersal of the magmatic-hydrothermal system. Consequently, I attribute the lack of preserved porphyry-style mineralisation and the abundance of low-grade epithermal systems at Kassiteres to rapid exhumation, where premature dilution and dispersal of the MVPs resulted in a breached porphyry – epithermal system.

6.2 Implications for Mineralisation

Current models of porphyry copper deposit (PCD) formation require regional, hydrous calc-alkaline magmatism in order to generate a fertile magma (e.g., Sillitoe 2010; Wilkinson 2013; Blundy et al. 2015; Nadeau et al. 2016). The oxidized nature of calc-alkaline magmatism is thought to delay early sulphide saturation which would sequester metals out of the melt (e.g., Mungall 2002; Matjuschkin et al. 2016), whilst the hydrous magmas exsolve a saline MVP at depth which concentrates metals prior to mineralisation (Hedenquist and Lowenstern, 1994). This work has not estimated the fO_2 of the magmatism from along the MMC; however, the presence of magnetite in the calc-alkaline intrusions, suggests moderately oxidized conditions with $fO_2 >$ NNO -1 (Scaillet et al., 2016). H_2O in the Kassiteres-Leptokaria magmas (3–4.75 wt. %) is less that is typical of arc-type magmatism, but is within the lower limit of the threshold water contents thought to produce fertile upper-crustal magmas ($>$ 4 wt. % H_2O; e.g., Richards 2009). The Maronia intrusion has considerably lower H_2O ($\sim$ 2 wt. %; Chapter 2) than would be expected to produce a metal-fertile magma. Therefore, it is puzzling that the Maronia porphyry system hosts the highest Cu and Mo grades reported from the MMC (Melfos and Voudouris, 2017). Mineralisation at Maronia is concentrated in highly localised zone of veining and sulphide enrichment that are restricted to fault zones (Melfos et al., 2002). Without understanding how mineralisation persists into the intrusions away from outcrop and at depth, the extent of mineralisation (tonnage) is hard to constrain.

An interesting empirical relationship can be drawn between the restriction of mineralised systems to the hanging wall of the Kechros dome, and the textures indicative of rapid cooling in the Kassiteres intrusion, again hosted in the hanging wall. McInnes et al. (2005b) use thermal modelling of magmatic systems to show that rapid cooling generates steep isotherms outwards from the intrusions into the country rock which can aid the concentration of mineralisation, forming high-grade ore shells. This mechanism could explain the presence of porphyry systems in the hanging wall of the Kechros dome where cooler ambient temperatures and/or elevated exhumation rates might generate steep thermal gradients out of the system which would favour mineralisation. Preservation bias is another means to concentrate mineralised systems in the hanging wall of a core complex (Kesler and Wilkinson, 2008; Yanites and Kesler, 2015). The footwall of the core complex has been unroofed from greater depths to expose deeper structural levels in the crust, and any shallow mineralised systems might simply have been eroded during unroofing. Alternatively, given the poor exposure of outcrop in the Leptokaria complex and the lack of knowledge of the subsurface geology from geophysical surveys or drill cores, there is the possibility that mineralisation in the Leptokaria complex has not yet been discovered.

Chapter 4 described W and Sn enrichment of the porphyry intrusion at Kassiteres, the result of mixing between mantle and crustal melts. Current models of mineralisation at Kassiteres focus on the endowment of the porphyry- and epithermal-systems in Au, Cu, Mo, Ag and the semi-metal Te. The Kassiteres system is named after the eponymous village which is built upon the pluton; Kassiteres is a derivation of 'tin', 'kassiteros' in Greek. A search for the history of the Kassiteres village does not reveal the source of the name, but perhaps it was related to tin enrichment in the area. In any case, expanding the metals of interest to W and Sn could increase the reserve estimates for the Kassiteres deposit and increase the economic potential of the area.

6.3 Comparison of the MMC Mineral Deposits with other Porphyry – Epithermal Systems

6.3.1 The Kassandra District, Greece

The Oligocene – Miocene Kassandra mining district in northern Greece is hosted in the southern RCC and thus makes an excellent comparator with the MMC in the northern RCC (Melfos and Voudouris, 2017). Post-collisional intrusion-related porphyry (Skouries) and carbonate replacement (Olympias) mineralisation is found in the district and contains over 12 Moz Au (Siron et al., 2018). Three periods of post-collisional magmatism are observed associated with two metallogenic events (Gilg and Frei, 1994; Hahn et al., 2012; Siron et al., 2016). Eocene intrusion of the calc-alkaline subduction-related Ierissos is dated to 53.6 $\pm$ 6.2 Ma (Gilg and Frei, 1994; Frei, 1996) and primed the crust. Magmatism then transitioned to late Oligocene high-K calc-alkaline intrusion of monzogabbro to granodiorite stocks between 25–27 Ma (Tsikara, Stratoni, Fisoka), which are attributed as the causative intrusions of the carbonate-replacement deposit (Siron et al., 2016). Finally, intrusion of the shoshonitic quartz monzonite porphyry stock, Skouries, occured in the early Miocene, $\sim$ 19–20 Ma and is genetically associated with porphyry mineralisation (Siron et al., 2016).

The similarities between the Kassandra district and the MMC are striking. In both regions magmatism is hosted variably across the hanging wall and footwall of the core complexes and follows a NE-trend suggesting a regional preference along this orientation, perhaps exploiting a pre-existing structure (Siron et al., 2018). The temporal transition from high-K to shoshonitic magmatism is observed both in the MMC and the Kassandra district. In the MMC this transition occurs over a $\sim$ 3.5 Myr period from 33–29.5 Ma and is spread out spatially over a distance of $\sim$ 100 km; at Kassandra the magmatism is temporally protracted over a 7 Myr period between 27 and 20 Ma but is spatially overlapping within 3 km (Siron et al., 2016, 2018). PCDs are typically found towards the end of the lifetime of a magmatic arc, which has led recent studies to suggest 'pre-heating' of the magmatic system aides the formation of PCDs (Richards et al., 2012). Perhaps this is true of the Skouries system where spatially overlapping magmatism led to the formation of the porphyry Au-Cu Skouries ore-body. In contrast along the MMC, the later, shoshonitic phase of magmatism does not overlap the earlier Kassiteres–Leptokaria suite but is geologically separated by the Petrota basin. The shoshonitic magmatism at Kassandra is thought to be the causative phase of magmatism for porphyry mineralisation; if the shoshonitic magmatism was generated by pyroxene- not olivine-controlled fractionation, as at Maronia, it suggests that H_2O content was not the limiting factor for porphyry mineralisation. Further comparison of the geochemistry of the two shoshonitic phases of magmatism, Skouries and Maronia in the Kassandra district and the MMC respectively, would have interesting implications for current models of the role of H_2O in PCD formation.

6.3.2 Porgera, Papua New Guinea

A post-subduction generation of Miocene porphyry – epithermal systems in the Circum-Pacific are typically Au-rich and Cu-poor (Sillitoe, 1997). Mineralisation in these systems is associated with a volatile-rich, mafic phase of alkalic magmatism induced by back-arc extension in the transitional period between subduction-related convergence and terrane accretion (e.g., Sillitoe 1997; Richards 2011b). Remelting of Au-rich mantle cumulates, residual from previous subduction-related magmatism, has been suggested as a mechanism by which to generate the Au-rich and comparatively Cu-poor systems observed, owing to the more siderophile nature of Au which is more compatible than Cu in silicate minerals (e.g., Sillitoe 1997; Richards 2009, 2011b). Rapid exhumation and cooling of post-subduction porphyry – epithermal systems in the Circum-Pacific is thought to aid the concentration of Au in the exsolved MVP, with host lithology permeability playing an important role in the concentration of high-grade mineralisation (Sillitoe, 1997).

Within the post-subduction Circum-Pacific systems, the Porgera epithermal Au deposit is of marked similarity with the Kassiteres system of the MMC. A telescoped system with low-T epithermal mineralisation overprinting deeper porphyry-style veining, the Porgera deposit is thought to capture the porphyry to epithermal transition (Handley and Bradshaw, 1986; Richards, 1992). The two stages of mineralisation are found at Porgera and very closely resemble those observed at Kassiteres: *(i)* high-T quartz veining, phyllic alteration and disseminated sulphides the result of saline (7–12, 31–58 wt. % NaCl equiv.) fluids with a mantle isotopic signatures; and *(ii)* low-T hydrothermal brecciation with native-Au and Au-Ag tellurides precipitated from a dilute (3–10 wt. % NaCl equiv.) fluid with a uniform, mixed mantle/meteoric- isotopic composition (Richards et al., 1990; Richards, 1992; Richards and Kerrich, 1993). However, the host magmatism between the two systems is geochemically very distinct. Porgera is associated with a volatile-rich, ultra-alkalic phase of porphyritic magmatism with a limited SiO_2 content ($<$ 55 wt. % SiO_2) and REE pattern indicative of a garnet-lherzolite source mantle (Richards et al., 1990). In contrast, the Kassiteres porphyry intrusion is dacitic to rhyolitic ($>$ 65 wt. % SiO_2), mildly alkaline and at the lower limit of H_2O contents permissible for porphyry – epithermal mineralisation (Chapter 2–4). This suggests that contrary to the suggestion of Richards, 1990, mafic magmatism in not crucial for the formation of Au-rich post-subduction mineralisation.

Shallow exsolution of a MVP in the extending post-subduction terranes would generate a less saline fluid than if MVP exsolution occured deeper (e.g., Webster 1997), and as Au transport is less dependant on the salinity of the MVP, this could be a mechanism by which to generate an Au-rich, comparatively Cu-poor, magmatic-hydrothermal fluid. Epithermal mineralisation at Porgera is thought to have occurred at 1-2 km depth in the upper crust (Richards et al., 1990), similar to suggested subsurface mineralisation at Kassiteres (Chapter 5), and could account for the absence of Cu mineralisation in both of the systems. The source of Te to form Au-Ag telluride complexes in both deposits is unknown, but the contrasting compositions of causative magmas between the two systems suggest that perhaps it is the similarity in tectonic environment or involvement of meteoric fluid that facilitated Te concentration in the mineralising fluid. Overall, the Kassiteres and Porgera deposits make an interesting comparison, and further examination of the differences and similarities between the two systems would make for an insightful study into the porphyry – epithermal transition and the role of syn-mineralisation exhumation. In particular, a fluid inclusion study to compare the isotopic composition of the different stages of mineralisation at Kassiteres with the existing work at Porgera, could provide compelling evidence of the link between magmatic-hydrothermal systems, meteoric

groundwater and the transition from a porphyry to an epithermal fluid regime.

6.4 Future Work

This thesis has provided petrological context to existing studies of mineralisation along the MMC. It has also opened many avenues for further research, which are discussed below.

6.4.1 The Maronia Magmatic Corridor

Exhumation

The tectonic evolution of the mineralising systems from the MMC through the crust syn- and post-mineralisation, is an interesting area of future research that would aide exploration attempts in northeastern Greece. ***Chapters 2 & 3*** lay the groundwork for such a study by constraining the *P-T-*H_2O-fO_2-*t* conditions of the MMC during host intrusion emplacement. Additionally, as discussed in ***Chapter 5***, the telescoped alteration and lack of preserved porphyry-style mineralisation at Kassiteres is hypothesised to be the result of rapid exhumation ($> 5.5 \pm 4.4$ km/Myr) of the system. The extent of mineralisation at the other telescoped porphyry systems in the MMC, Pagoni Rachi and Essimi, is not well known. Estimating the exhumation rate of the Pagoni Rachi and Essimi systems, in addition to constraining the degree of mineralisation, would be an excellent test of this hypothesis in different systems from a similar tectonic environment. Thermochronology (zircon and apatite (U-Th)/He) data have been collected from the MMC (Appendix O) which suggest faster cooling rates in the hanging wall and centre of the footwall of the core complex and slower cooling rates along the detachment. Modelling cooling rates and exhumation paths using these data would provide the foundations for a study of the exhumation rates across the MMC and would provide insights into the role of syn- to post-mineralisation exhumation on the formation of porphyry systems and the transition to an epithermal mineralising regime.

Maronia

There is ample scope for further study of the Maronia pluton. As discussed in ***Chapters 2 & 3***, the extensive parameters of the Maronia pluton are less well constrained than for the Kassiteres–Leptokaria intrusive complex. Whilst experimental studies of shoshonitic magmas have been conducted, they are less common in the literature, a reflection of their relative scarcity in the geological record compared with calc-alkaline magmatism. No experimental studies with similar starting compositions to the Maronia monzonites were found in the literature, as the existing studies are too aluminous ($Al_2O_3 > 17$ wt. %), magnesian (MgO > 6 wt. %) and alkali-poor to predict relevant phase relationships. Consequently, a logical starting point for further study of the Maronia pluton would be to constrain phase relationships in an appropriate melt composition for varying P, T, fO_2 and H_2O content, using either crystallisation experiments or thermodynamic modelling (e.g., MELTS; Ghiorso and Sack 1995).

Furthermore, skarn metasomatism is found along the western margin of the Maronia pluton, where it intrudes a marble unit of the Circum Rhodope Belt metasediments. Katerinopoulou et al. (2009) described Cr-rich garnets from the exoskarn but the influence of the calc-silicate host lithology on phase relationship and crystallisation of the shoshonitic magmatism is unknown. The presence of a 'contact facies' of albite and orthoclase oikocrysts (up to 20 cm in diameter) with chadacrysts of clinopyroxene (up to 3 cm in diameter)

is observed along the western, marble-hosted margin of the Maronia pluton. This indicates that excess Ca derived from the host marbles is accommodated in monoclinic pyroxenes rather than plagioclase. Exploring the nature of this contact further would compliment a petrological study of shoshonitic phase relations at Maronia.

Porphyry-style mineralisation at Maronia is unexpectedly high-grade given the suggested H_2O-poor source magma composition (***Chapter 3***). Further characterisation of the porphyry melt composition at Maronia using the methodology developed in ***Chapter 4*** would give insight into the ability of shoshonitic magmatism to generate metal-fertile magmas, particularly the efficiency of metal extraction in H_2O-poor systems. A previously un-mapped porphyry intrusion was observed at the eastern margin of the Maronia pluton at the end of the last field season. Mapping and sampling of this porphyry intrusion, and any potential mineralisation associated with it, should be an important component of any future study of mineralisation at Maronia.

6.4.2 Zircon-Hosted Melt Inclusion Analysis

Chapter 4 presented a successful, new application of melt inclusion analyses. Therefore, there is potential to apply melt inclusion petrology to zircon-hosted melt inclusions from a wide range of magmatic mineral deposits. Study of the major element and metal chemistry of causative intrusions in magmatic mineral deposits, such as porphyry systems, is hindered by pervasive alteration, which destroys the original geochemistry of the samples. Building a database of zircon-hosted melt inclusion analyses from deposits globally, will help inform on the physiochemical properties of fertile magmas. Furthermore, zircon-hosted melt inclusion analysis has application in exploration. Lu et al. (2016) developed a series of zircon trace element discriminant plots, that are used to identify potentially fertile, magmatic terranes. This approach has been applied with success to detrital zircon studies in industry, and has become a widely used exploration tool. Modifying the analytical procedure of samples used in these studies to include homogenisation and melt inclusions electron probe micro-analysis (EPMA), would be simple and provide a qualifying dataset to compliment the zircon trace element analyses.

Further development of the zircon-hosted melt inclusion technique, could unlock important information about the volatile content of fertile magmas. Secondary ionisation mass spectrometry (SIMS) has been widely used in studies of melt inclusions hosted in olivine and plagioclase in volcanic and plutonic systems (e.g., Neave et al. 2017, 2018; Hartley et al. 2018). Zircon-hosted melt inclusions are typically at the lower limit ($\sim$ 20–30 μm) of inclusions that can be analysed by SIMS making it an analytical challenge to recover H_2O and CO_2 concentrations. Additionally, the degree to which post-entrapment modification of zircon-hosted melt inclusions alters the volatile content of the inclusions, by diffusive re-equilibration or leakage, is poorly understood. As discussed in ***Chapter 4***, zircon is a geologically robust mineral, with experimentally-determined extremely slow cation diffusion rates preserving oscillatory zoning down to the < 5 μm scale (Cherniak and Watson, 2003). However, the diffusion of H^+, OH^- and other anions through zircon is unknown. This is an important area of research if zircon-hosted melt inclusions are to be used to determine the volatile budget of fertile intrusions in magmatic mineral deposits.

6.5 Synthesis

This thesis has combined petrology, geochemistry and geochronology with field observations in order to reconstruct the magmatic and tectonic evolution of the Maronia Magmatic Corridor (MMC) in northeastern Greece. A NE-trending belt of high-K to shoshonitic intrusions, the MMC was intruded into the Kechros dome of the northern Rhodope Core Complex during Oligocene trans-crustal extension and post-collisional magmatism. The MMC is host to at least four porphyry – epithermal systems, which are examples of these mineral deposits in a post-collisional tectonic setting. Existing work along the MMC focused on the style of mineralisation at each of these deposits, characterising the metal-sulphide assemblage of the deposits and evaluating the fluid chemistry of the mineralising magmatic volatile phase (e.g., Melfos et al. 2002; Voudouris 2006; Voudouris et al. 2006, 2009, 2013a,b). This thesis builds upon this work by constraining the petrogenesis of the causative magmatism and tracking the temporal and spatial evolution of the systems within the regional tectonic framework.

A two-pronged approach was used to investigate the magmatism associated with the porphyry copper systems along the MMC. Firstly, petrogenesis of the regional magmatism was studied using unaltered samples collected from the equigranular host plutons. Secondly, direct analyses of original melt from the causative porphyry intrusions were made using zircon-hosted melt inclusions, zircon trace element geochemistry and U-Pb zircon geochronology. By studying both the regional and causative magmatism associated with porphyry mineralisation, this thesis offers insights into:

i the terrane-scale evolution of the MMC, concluding that magmatism between 33–32 Ma was of the right physio-chemical composition, if only just sufficiently hydrous, to transport metals into the upper crust. Elsewhere in the northern RCC, asthenospheric mantle-melting of the subduction-modified lithospheric mantle will likely be of the same composition, permissive for porphyry magmatism and could prove a fruitful region for further exploration.

ii the deposits-scale evolution of the Kassiteres, Essimi and Leptokaria porphyry systems, indicating that crustal mixing played an important role in the metallogenesis in these systems. Additionally, this thesis demonstrates the utility of zircon-hosted melt inclusions as a well-armoured repository of petrological information in highly altered porphyry systems and suggests that it has potential utility as an exploration tool, for example, in studying the evolution of specific mineralised systems and in detrital studies to identify target terranes.

Finally, the thesis studied the influence of syn-mineralisation exhumation on the Kassiteres porphyry – epithermal system. Unroofing of the host intrusions was shown to have an important influence on the mineralising system, where shallow intrusion of the causative porphyry during exhumation generates a dilute magmatic-hydrothermal fluid system which is easily dispersed by circulating meteoric waters. This produces telescoped alteration, poorly perserved porphyry-style veining and mineralisation with multiple, small-volume high- sulphidation epithermal systems with main source of economic mineralisation. By placing the post-collisional porphyry – epithermal systems in petrologic and tectonic context, this thesis suggests that mineralisation along the Maronia Magmatic Corridor is under-explored and has potential for previously unconsidered metal endowments.

References

Acosta-Vigil, A., Rubatto, D., Bartoli, O., Cesare, B., Meli, S., Pedrera, A., Azor, A., Tajčmanová, L., 2014. Age of anatexis in the crustal footwall of the Ronda peridotites, S Spain. Lithos 210-211, 147–167.

Adam, J., Green, T., 2006. Trace element partitioning between mica-and amphibole-bearing garnet lherzolite and hydrous basanitic melt: 1. Experimental results and the investigation of controls on partitioning behaviour. Contributions to Mineralogy and Petrology 152 (1), 1–17.

Ague, J. J., 1997. Thermodynamic calculation of emplacement pressuresfor batholithic rocks, California: Implications for thealuminum-in-hornblende barometer. Geology 25 (6), 563–566.

Aldanmaz, E., Pearce, J. A., Thirlwall, M. F., Mitchell, J. G., 2000. Petrogenetic evolution of late Cenozoic, post-collision volcanism in western Anatolia, Turkey. Journal of Volcanology and Geothermal Research 102 (1), 67–95.

Andersen, D. J., Lindsley, D. H., Davidson, P. M., 1993. QUILF: A pascal program to assess equilibria among FeMgMnTi oxides, pyroxenes, olivine, and quartz. Computers and Geosciences 19 (9), 1333–1350.

Anderson, J. L., Barth, A. P., Wooden, J. L., Mazdab, F., 2008. Thermometers and Thermobarometers in Granitic Systems. Reviews in Mineralogy and Geochemistry 69 (1), 121–142.

Annen, C., 2009. From plutons to magma chambers: Thermal constraints on the accumulation of eruptible silicic magma in the upper crust. Earth and Planetary Science Letters 284 (3-4), 409–416.

Annen, C., Blundy, J. D., Sparks, R. S., 2006. The genesis of intermediate and silicic magmas in deep crustal hot zones. Journal of Petrology 47 (3), 505–539.

Arribas, A., Hedenquist, J. W., Itaya, T., Okada, T., Concepcion, R. A., Garcia, J. S., 1995. Contemporaneous formation of adjacent porphyry and epithermal Cu-Au deposits over 300 ka in northern Luzon, Philippines. Geology 23 (4), 337–340.

Bachmann, O., 2004. On the Origin of Crystal-poor Rhyolites: Extracted from Batholithic Crystal Mushes. Journal of Petrology 45 (8), 1565–1582.

Baker, D. R., 2008. The fidelity of melt inclusions as records of melt composition. Contributions to Mineralogy and Petrology 156 (3), 377–395.

Baker, D. R., Eggler, D. H., 1987. Compositions of anhydrous and hydrous melts coexisting with plagioclase, augite, and olivine or low-Ca pyroxene from 1 atm to 8 kbar; application to the Aleutian volcanic center of Atka. American Mineralogist 72 (1-2), 12–28.

Baldwin, S. L., Monteleone, B. B., Webb, L. E., Fitzgerald, P. G., Grove, M., Hill, E. J., 2004. Pliocene eclogite exhumation at plate tectonic rates in eastern Papua New Guinea. Nature 431 (7006), 263–267.

Ballard, J. R., Palin, M. J., Campbell, I. H., 2002. Relative oxidation states of magmas inferred from Ce (IV)/Ce (III) in zircon: application to porphyry copper deposits of northern Chile. Contributions to Mineralogy and Petrology 144 (3), 347–364.

Ballouard, C., Poujol, M., Boulvais, P., Branquet, Y., Tartèse, R., Vigneresse, J. L., 2016. Nb-Ta fractionation in peraluminous granites: A marker of the magmatic-hydrothermal transition. Geology 44 (3), 231–234.

Bauer, C., Rubatto, D., Krenn, K., Proyer, A., Hoinkes, G., 2007. A zircon study from the Rhodope metamorphic complex, N-Greece: Time record of a multistage evolution. Lithos 99 (3-4), 207–228.

Beccaluva, L., Bianchini, G., Mameli, P., Natali, C., 2013. Miocene shoshonite volcanism in Sardinia: Implications for magma sources and geodynamic evolution of the central-western Mediterranean. Lithos 180-181, 128–137.

Beermann, O., Holtz, F., Duesterhoeft, E., 2017. Magma storage conditions and differentiation of the mafic Lower Pollara volcanics, Salina Island, Aeolian Islands, Italy: implications for the formation conditions of shoshonites and potassic rocks. Contributions to Mineralogy and Petrology 172 (5), 37.

Benfield, A. E., 1949. The effect of uplift and denudation on underground temperatures. Journal of Applied Physics 20 (1), 66–70.

Bindeman, I. N., Davis, A. M., Drake, M. J., 1998. Ion microprobe study of plagioclase-basalt partition experiments at natural concentration levels of trace elements. Geochimica et Cosmochimica Acta 62 (7), 1175–1193.

Blundy, J., Cashman, K., 2005. Rapid decompression-driven crystallization recorded by melt inclusions from Mount St. Helens volcano. Geology 33 (10), 793–796.

Blundy, J., Cashman, K., 2008. Petrologic reconstruction of magmatic system variables and processes. Reviews in Mineralogy and Geochemistry 69 (1), 179–239.

Blundy, J., Cashman, K., Humphreys, M., 2006. Magma heating by decompression-driven crystallization beneath andesite volcanoes. Nature 443 (7107), 76–80.

Blundy, J., Mavrogenes, J., Tattitch, B., Sparks, S., Gilmer, A., 2015. Generation of porphyry copper deposits by gas-brine reaction in volcanic arcs. Nature Geoscience 8 (3), 235–240.

Blundy, J. D., Holland, T. J. B., 1990. Calcic amphibole equilibria and a new amphibole-plagioclase geothermometer. Contributions to mineralogy and petrology 104 (2), 208–224.

Boehnke, P., Watson, E. B., Trail, D., Harrison, T. M., Schmitt, A. K., 2013. Zircon saturation re-revisited. Chemical Geology 351, 324–334.

Bonev, N., Marchev, P., Moritz, R., Collings, D., 2015. Jurassic subduction zone tectonics of the Rhodope Massif in the Thrace region (NE Greece) as revealed by new U-Pb and 40Ar/39Ar geochronology of the Evros ophiolite and high-grade basement rocks. Gondwana Research 27 (2), 760–775.

Bonev, N., Ovtcharova-Schaltegger, M., Moritz, R., Marchev, P., Ulianov, A., 2013. Peri-Gondwanan Ordovician crustal fragments in the high-grade basement of the Eastern Rhodope Massif, Bulgaria: evidence from U-Pb LA-ICP-MS zircon geochronology and geochemistry. Geodinamica Acta 26 (3-4), 207–229.

Bonev, N., Stampfli, G., 2008. Petrology, geochemistry and geodynamic implications of Jurassic island arc magmatism as revealed by mafic volcanic rocks in the Mesozoic low-grade sequence, eastern Rhodope, Bulgaria. Lithos 100 (1-4), 210–233.

Bonev, N., Stampfli, G., 2011. Alpine tectonic evolution of a Jurassic subduction-accretionary complex: Deformation, kinematics and 40Ar/39Ar age constraints on the Mesozoic low-grade schists of the Circum-Rhodope Belt in the eastern Rhodope-Thrace region, Bulgaria-Greece. Journal of Geodynamics 52 (2), 143–167.

Bonev, N. G., Stampfli, G. M., 2003. New structural and petrologic data on Mesozoic schists in the Rhodope (Bulgaria): geodynamic implications. Comptes Rendus Geoscience 335 (8), 691–699.

Bornovas, J., Rondogianni-Tsiabaou, T., 1983. Geological Map of Greece (1:50,000), 2nd Edition. Institute of Geology and Mining Exploration, Athens, Greece.

Boyanov, I., Ruseva, M., Dimitrova, E., 1982. First find of Upper Cretaceous foraminifers in East Rhodopes. Geologica Balcanica 12 (4), 20.

Braun, J., 2003. Pecube: A new finite-element code to solve the 3D heat transport equation including the effects of a time-varying, finite amplitude surface topography. Computers & Geosciences 29 (6), 787–794.

Braun, J., 2005. Quantitative constraints on the rate of landform evolution derived from low-temperature thermochronology. Reviews in Mineralogy and Geochemistry 58 (1), 351–374.

Brey, G. P., Köhler, T., 1990. Geothermobarometry in 4-phase lherzolites .2. New thermobarometers, and practical assessment of existing thermobarometers. Journal of Petrology 31 (6), 1353–1378.

Brun, J.-P., Faccenna, C., Gueydan, F., Sokoutis, D., Philippon, M., Kydonakis, K., Gorini, C., 2016. The two-stage Aegean extension, from localized to distributed, a result of slab rollback acceleration. Canadian journal of earth sciences 1157 (February), 1142–1157.

Brun, J.-P., Sokoutis, D., 2010. 45 my of Aegean crust and mantle flow driven by trench retreat. Geology 38 (9), 815–818.

Burchfiel, B. C., Nakov, R., Dumurdzanov, N., Papanikolaou, D., Tzankov, T., Serafimovski, T., King, R. R. W., Kotzev, V., Todosov, A., Nurce, B., 2008. Evolution and dynamics of the Cenozoic tectonics of the South Balkan extensional system. Geosphere 4 (6), 919–938.

Burchfiel, B. C., Nakov, R., Tzankov, T., 2003. Evidence from the Mesta half-graben, SW Bulgaria, for the Late Eocene beginning of Aegean extension in the Central Balkan Peninsula. Tectonophysics 375 (1), 61–76.

Buret, Y., von Quadt, A., Heinrich, C., Selby, D., Wälle, M., Peytcheva, I., 2016. From a long-lived upper-crustal magma chamber to rapid porphyry copper emplacement: Reading the geochemistry of zircon crystals at Bajo de la Alumbrera (NW Argentina). Earth and Planetary Science Letters 450, 120–131.

Buret, Y., Wotzlaw, J. F., Roozen, S., Guillong, M., von Quadt, A., Heinrich, C. A., 2017. Zircon petrochronological evidence for a plutonic-volcanic connection in porphyry copper deposits. Geology 45 (7), 623–626.

Burg, J.-P., 2011. Rhodope : From Mesozoic convergence to Cenozoic extension . Review of petro-structural data in the geochronological frame Rhodope : From Mesozoic convergence to Cenozoic extension . Review of petro-structural data in the geochronological frame. Journal of the Virtual Explorer 39, 1–44.

Burg, J.-P., Ricou, L.-E., Ivano, Z., Godfriaux, I., Dimov, D., Klain, L., 1996. Syn-metamorphic nappe complex in the Rhodope Massif. Structure and kinematics. Terra Nova 8 (1), 6–15.

Burnham, A. D., Berry, A. J., 2017. Formation of Hadean granites by melting of igneous crust. Nature Geoscience 10 (6), 457–461.

Burnham, C. W., 1979. Magmas and hydrothermal fluids. Geochemistry of Hydrothermal Ore Deposits., 71–136.

Cadoux, A., Scaillet, B., Druitt, T. H., Deloule, E., 2014. Magma storage conditions of large Plinian eruptions of Santorini Volcano (Greece). Journal of Petrology 55 (6), 1129–1171.

Camp, V. E., Pierce, K. L., Morgan, L. A., 2015. Yellowstone plume trigger for Basin and Range extension, and coeval emplacement of the Nevada–Columbia Basin magmatic belt. Geosphere 11 (2), 203–225.

Candela, P. A., 1989. Felsic magmas, volatiles, and metallogenesis. Ore deposition associated with magmas, 223–233.

Caracciolo, L., Orlando, A., Critelli, S., Kolios, N., Manetti, P., Marchev, P., 2012. the Tertiary Thrace Basins of Se Bulgaria and Ne Greece : a Review of Petrological and. Acta Vulcanologica 25 (1/2), 21–42.

Carslaw, H. S., Jaeger, J. C., 1959. Conduction of heat in solids. Oxford: Clarendon Press, 1959, 2nd ed.

Che, X. D., Linnen, R. L., Wang, R. C., Aseri, A., Thibault, Y., 2013. Tungsten solubility in evolved granitic melts: An evaluation of magmatic wolframite. Geochimica et Cosmochimica Acta 106, 84–98.

Chelle-Michou, C., Chiaradia, M., 2017. Amphibole and apatite insights into the evolution and mass balance of Cl and S in magmas associated with porphyry copper deposits. Contributions to Mineralogy and Petrology 172 (11-12), 1–26.

Chelle-Michou, C., Chiaradia, M., Béguelin, P., Ulianov, A., 2015. Petrological evolution of the magmatic suite associated with the Coroccohuayco Cu(-Au-Fe) porphyry-skarn deposit, Peru. Journal of Petrology 56 (9), 1829–1862.

Chelle-Michou, C., Chiaradia, M., Ovtcharova, M., Ulianov, A., Wotzlaw, J.-F., 2014. Zircon petrochronology reveals the temporal link between porphyry systems and the magmatic evolution of their hidden plutonic roots (the Eocene Coroccohuayco deposit, Peru). Lithos 198, 129–140.

Cherniak, D. J., Hanchar, J. M., Watson, E. B., 1997. Rare-earth diffusion in zircon. Chemical Geology 134 (4), 289–301.

Cherniak, D. J., Watson, E. B., 2003. Diffusion in zircon. Reviews in mineralogy and geochemistry 53 (1), 113–143.

Cherniak, D. J., Watson, E. B., Thomas, J. B., 2009. Diffusion of helium in zircon and apatite. Chemical Geology 268 (1-2), 155–166.

Chiaradia, M., Ulianov, A., Kouzmanov, K., Beate, B., 2012. Why large porphyry Cu deposits like high Sr/Y magmas? Scientific reports 2, 685.

Christofides, G., Eleftheriadis, G., Esson, J., Soldatos, T., Koroneos, A., Brocker, M., 2000. The evolution of the Samothraki granitic pluton (N. Aegean sea, Greece): geochronology, chemical and isotopic constraints for AFC modelling. In: Proceedings of the Third International Conference on the Geology of the Eastern Mediterranean. pp. 193–209.

Christofides, G., Peckskay, Z., Eleftheriadis, G., Soldatos, T., Koroneos, A., 2004. The Tertiary Evros Volcanic Rocks (Thrace, Northeastern Greece): Petrology and K/Ar Geochronology. Geologica Carpathica 55 (5), 397–409.

Cline, J., Bodnar, R. J., 1991. Can Economic Porphyry Copper Mineralisation be Generated by a Typical Calc-Alkaline Melt? In: Copper Mineralization from Calc-Alkaline Melts. Vol. 96. pp. 8113–8126.

Cloos, M., Sapiie, B., 2013. Porphyry copper deposits: strike–slip faulting and throttling cupolas. International Geology Review 55 (1), 43–65.

Coleman, D. S., Gray, W., Glazner, A. F., 2004. Rethinking the emplacement and evolution of zoned plutons: Geochronologic evidence for incremental assembly of the Tuolumne Intrusive Suite, California. Geology 32 (5), 433–436.

Condamine, P., Médard, E., 2014. Experimental melting of phlogopite-bearing mantle at 1 GPa: Implications for potassic magmatism. Earth and Planetary Science Letters 397, 80–92.

Condon, D. J., Schoene, B., McLean, N. M., Bowring, S. A., Parrish, R. R., 2015. Metrology and traceability of U–Pb isotope dilution geochronology (EARTHTIME Tracer Calibration Part I). Geochimica et Cosmochimica Acta 164, 464–480.

Coney, P. J., 1987. The regional tectonic setting and possible causes of Cenozoic extension in the North American Cordillera. Geological Society, London, Special Publications 28 (1), 177–186.

Cornelius, N. K., 2008. UHP metamorphic rocks of the Eastern Rhodope Massif , NE Greece : new constraints from petrology , geochemistry and zircon ages. Ph.D. thesis, Johannes Gutenberg-Universitat Mainz.

Couch, S., Sparks, R. S. J., Carroll, M. R., 2001. Mineral disequilibrium in lavas explained by convective self-mixing in open magma chambers. Nature 411 (6841), 1037–1039.

Créon, L., Levresse, G., Remusat, L., Bureau, H., Carrasco-Núñez, G., 2018. New method for initial composition determination of crystallized silicate melt inclusions. Chemical Geology 483 (March), 162–173.

Crowley, J. L., Schoene, B., Bowring, S. A., 2007. U-Pb dating of zircon in the Bishop Tuff at the millennial scale. Geology 35 (12), 1123–1126.

Danyushevsky, L. V., Della-Pasqua, F. N., Sokolov, S., 2000. Re-equilibration of melt inclusions trapped by magnesian olivine phenocrysts from subduction-related magmas: Petrological implications. Contributions to Mineralogy and Petrology 138 (1), 68–83.

Danyushevsky, L. V., Leslie, R. A. J., Crawford, A. J., Durance, P., 2004. Melt inclusions in primitive olivine phenocrysts: The role of localized reaction processes in the origin of anomalous compositions. Journal of Petrology 45 (12), 2531–2553.

Danyushevsky, L. V., McNeill, A. W., Sobolev, A. V., 2002. Experimental and petrological studies of melt inclusions in phenocrysts from mantle-derived magmas: an overview of techniques, advantages and complications. Chemical Geology 183 (1-4), 5–24.

Davidson, J., Turner, S., Plank, T., 2013. Dy/Dy*: Variations arising from mantle sources and petrogenetic processes. Journal of Petrology 54 (3), 525–537.

De Wet, A. P., Miller, J. A., Bickle, M. J., Chapman, H. J., 1989. Geology and geochronology of the Arnea, Sithonia and Ouranopolis intrusions, Chalkidiki peninsula, northern Greece. Tectonophysics 161 (1-2), 65–79.

Del Moro, A., Innocenti, F., Kyriakopoulos, C., Manetti, P., Papadopoulos, P., 1988. Tertiary granitoids from Thrace (Northern Greece): Sr isotopic and petrochemical data. Neues Jahrbuch f{ü}r Mineralogie Abhandlungen 159 (2), 113–115.

Del Moro, A., Kyriakopoulos, K., Pezzino, A., Atzori, P., Giudice, A. L., 1990. The metamorphic complex associated to the Kavala plutonites: An Rb-Sr geochronological, petrological and structural study. Geol. Rhodop 2, 143–152.

Deubener, J., Muller, R., Behrens, H., Heide, G., 2003. Water and the glass transition temperature of silicate melts. Journal of Non-Crystaline Solids 330, 268–273.

Dewey, J. F., 1988. Extensional collapse of orogens. Tectonics 7 (6), 1123–1139.

Dewey, J. F., Ryan, P. D., Andersen, T. B., 1993. Orogenic uplift and collapse, crustal thickness, fabrics and metamorphic phase changes: the role of eclogites. Geological Society, London, Special Publications 76 (1), 325–343.

Dilek, Y., Altunkaynak, S., 2009. Geochemical and temporal evolution of Cenozoic magmatism in western Turkey: mantle response to collision, slab break-off, and lithospheric tearing in an orogenic belt. Geological Society, London, Special Publications 311 (1), 213–233.

Dilles, J. H., 1987. Petrology of the Yerington batholit, Nevada: Evidence for evolution of porphyry copper ore fluids. Economic Geology 82-7,1750-, 1750–1789.

Dilles, J. H., Kent, A. J. R., Wooden, J. L., Tosdal, R. M., Koleszar, A., Lee, R. G., Farmer, L. P., 2015. Zircon compositional evidence for sulfur-degassing from ore-forming arc magmas. Economic Geology 110 (1), 241–251.

Dinter, D. A., Macfarlane, A., Hames, W., Isachsen, C., Bowring, S., Royden, L., 1995. U-Pb and 40 Ar/ 39 Ar geochronology of the Symvolon granodiorite: Implications for the thermal and structural evolution of the Rhodope metamorphic core complex, northeastern Greece. Tectonics 14 (4), 886–908.

Dodson, M. H., 1973. Closure temperature in cooling geochronological and petrological systems. Contributions to Mineralogy and Petrology 40 (3), 259–274.

Dongen, M. V., Weinberg, R. F., Tomkins, A. G., Armstrong, R. A., Woodhead, J. D., 2010. Lithos Recycling of Proterozoic crust in Pleistocene juvenile magma and rapid formation of the Ok Tedi porphyry Cu Au deposit , Papua New Guinea. LITHOS 114 (3-4), 282–292.

Donovan, A., Blundy, J., Oppenheimer, C., Buisman, I., 2018. The 2011 eruption of Nabro volcano, Eritrea: perspectives on magmatic processes from melt inclusions. Contributions to Mineralogy and Petrology 173 (1), 1.

Dostal, J., Kontak, D. J., Gerel, O., Gregory Shellnutt, J., Fayek, M., 2015. Cretaceous ongonites (topaz-bearing albite-rich microleucogranites) from Ongon Khairkhan, Central Mongolia: Products of extreme magmatic fractionation and pervasive metasomatic fluid: Rock interaction. Lithos 236-237, 173–189.

Dürr, S., Altherr, R., Keller, J., Okrusch, M., Seidel, E., 1978. The median Aegean crystalline belt: stratigraphy, structure, metamorphism, magmatism. Alps, Apennines, Hellenides 38, 455–476.

Economou-Eliopoulos, M., Eliopoulos, D. G., 2000. Palladium, platinum and gold concentration in porphyry copper systems of Greece and their genetic significance. Ore Geology Reviews 16 (1-2), 59–70.

Edmonds, M., Aiuppa, A., Humphreys, M., Moretti, R., Giudice, G., Martin, R. S., Herd, R. A., Christopher, T., 2010. Excess volatiles supplied by mingling of mafic magma at an andesite arc volcano. Geochemistry, Geophysics, Geosystems 11 (4), 1–16.

Ehlers, T. A., 2005. Crustal thermal processes and the interpretation of thermochronometer data. Reviews in Mineralogy and Geochemistry 58 (1), 315–350.

Ehlers, T. A., Chaudhri, T., Kumar, S., Fuller, C. W., Willett, S. D., Ketcham, R. A., Brandon, M. T., Belton, D. X., Kohn, B. P., Gleadow, A. J. W., Others, 2005. Computational tools for low-temperature thermochronometer interpretation. Reviews in Mineralogy and Geochemistry 58 (1), 589–622.

Eleftheriadis, G., Frank, W., Petrakakis, K., 2001. 40Ar/39Ar dating and cooling history of the Pangeon granitoids, Rhodope Massif (eastern Macedonia, Greece). Bull. Geol. Soc. Greece 34 (3), 911–916.

Ersoy, E. Y., Palmer, M. R., Genç, C., Prelević, D., Akal, C., Uysal, I., 2017. Chemo-probe into the mantle origin of the NW Anatolia Eocene to Miocene volcanic rocks: Implications for the role of, crustal accretion, subduction, slab roll-back and slab break-off processes in genesis of post-collisional magmatism. Lithos 288, 55–71.

Fayon, A. K., Tikoff, B., Kahn, M., Gaschnig, R. M., 2017. Cooling and exhumation of the southern Idaho batholith. Lithosphere 9 (2), 299–314.

Ferry, J. M., Watson, E. B., 2007. New thermodynamic models and revised calibrations for the Ti-in-zircon and Zr-in-rutile thermometers. Contributions to Mineralogy and Petrology 154 (4), 429–437.

Foley, S., Venturelli, G., Green, D. H., Toscani, L., 1987. The ultrapotassic rocks: characteristics, classification, and constraints for petrogenetic models. Earth-Science Reviews 24 (2), 81–134.

Frei, R., 1996. The extent of inter-mineral isotope equilibrium: a systematic bulk U-Pb and Pb step leaching (PbSL) isotope study of individual minerals from the Tertiary granite of Ierissos (northern Greece). European Journal of Mineralogy, 1175–1190.

Freise, M., Holtz, F., Nowak, M., Scoates, J. S., Strauss, H., 2009. Differentiation and crystallization conditions of basalts from the Kerguelen large igneous province: an experimental study. Contributions to Mineralogy and Petrology 158 (4), 505.

Fu, F. Q., McInnes, B. I. A., Evans, N. J., Davies, P. J., 2010. Numerical modeling of magmatic–hydrothermal systems constrained by U–Th–Pb–He time–temperature histories. Journal of Geochemical Exploration 106 (1-3), 90–109.

Fujimaki, H., Tatsumoto, M., Aoki, K.-i., 1984. Partition coefficients of hf, zr, and ree between phenocrysts and groundmasses. Journal of Geophysical Research: Solid Earth 89 (S02), B662–B672.

Gaetani, G. A., Grove, T. L., Bryan, W. B., 1993. The influence of water on the petrogenesis of subduction-related igneous rocks. Nature 365 (6444), 332–334.

Gaetani, G. A., O'Leary, J. A., Shimizu, N., Bucholz, C. E., Newville, M., 2012. Rapid reequilibration of H_2O and oxygen fugacity in olivine-hosted melt inclusions. Geology 40 (10), 915–918.

Gardiner, N. J., Hawkesworth, C. J., Robb, L. J., Whitehouse, M. J., Roberts, N. M., Kirkland, C. L., Evans, N. J., 2017. Contrasting Granite Metallogeny through the Zircon Record: A Case Study from Myanmar. Scientific Reports 7 (1), 1–8.

Gee, D. G., Fossen, H., Henriksen, N., Higgins, A. K., 2008. From the early Paleozoic platforms of Baltica and Laurentia to the Caledonide Orogen of Scandinavia and Greenland. Episodes 31 (1), 44–51.

Georgiev, S., Marchev, P., Peytcheva, I., von Quadt, A., Peitcheva, I., von Quadt, A., Vaselli, O., 2013. Miocene extensional magmatic activity along Strymon valley and Doyran region , Bulgaria , Greece and the former Yugoslav Republic of Macedonia. Acta Vulcanologica 25, 153–168.

Gervasoni, F., Klemme, S., Rocha-Júnior, E. R., Berndt, J., 2016. Zircon saturation in silicate melts: a new and improved model for aluminous and alkaline melts. Contributions to Mineralogy and Petrology 171 (3), 1–12.

Ghiorso, M. S., Sack, R. O., 1995. Chemical mass transfer in magmatic processes IV. A revised and internally consistent thermodynamic model for the interpolation and extrapolation of liquid-solid equilibria in magmatic systems at elevated temperatures and pressures. Contributions to Mineralogy and Petrology 119 (2-3), 197–212.

Giesting, P. A., Filiberto, J., 2014. Quantitative models linking igneous amphibole composition with magma Cl and OH content. American Mineralogist 99 (4), 852.

Gilg, H. A., Frei, R., 1994. Chronology of magmatism and mineralization in the Kassandra mining area, Greece: The potentials and limitations of dating hydrothermal illites. Geochimica et Cosmochimica Acta 58 (9), 2107–2122.

Gill, J. B., 1981. The Plate Tectonic Connection. In: Orogenic Andesites and Plate Tectonics. Springer, pp. 13–43.

Gilmer, A. K., Sparks, R. S. J., Rust, A. C., Tapster, S., Webb, A. D., Barfod, D. N., 2017. Geology of the Don Manuel igneous complex, central Chile: Implications for igneous processes in porphyry copper systems. Geological Society of America Bulletin, B31524—-1.

Goldschmidt, V. M., 1937. The principles of distribution of chemical elements in minerals and rocks. The seventh Hugo Müller Lecture, delivered before the Chemical Society on March 17th, 1937. Journal of the Chemical Society (Resumed), 655–673.

Green, T. H., 1995. Significance of Nb/Ta as an indicator of geochemical processes in the crust-mantle system. Chemical Geology 120 (3-4), 347–359.

Green, T. H., Blundy, J. D., Adam, J., Yaxley, G. M., 2000. SIMS determination of trace element partition coefficients between garnet, clinopyroxene and hydrous basaltic liquids at 2–7.5 GPa and 1080–1200 C. Lithos 53 (3), 165–187.

Green, T. H., Pearson, N. J., 1987. An experimental study of Nb and Ta partitioning between Ti-rich minerals and silicate liquids at high pressure and temperature. Geochimica et Cosmochimica Acta 51 (1), 55–62.

Grocke, S. B., de Silva, S. L., Wallace, P. J., Cottrell, E., Schmitt, A. K., 2018. Catastrophic Caldera-Forming (CCF) Monotonous Silicic Magma Reservoirs: Constraints from Volatiles in Melt Inclusions from the 3.49 Ma Tara Supereruption, Guacha II Caldera, SW Bolivia. Journal of Petrology.

Grosse, P., van Wyk de Vries, B., Petrinovic, I. A., Euillades, P. A., Alvarado, G. E., 2009. Morphometry and evolution of arc volcanoes. Geology 37 (7), 651–654.

Gustafson, L. B., Hunt, J. P., 1975. The porphyry copper deposit at El Salvador, Chile. Economic Geology 70 (5), 857–912.

Hahn, A., Naden, J., Treloar, P. J., Kilias, S. P., Rankin, A. H., Forward, P., 2012. A new time framefor the mineralisation in the Kassandra mine district, N Greece: deposit formation during metamorphic core complex exhumation. Journal of Earth Sciences 96, 1079–1099.

Halter, W. E., Heinrich, C. A., Pettke, T., 2005. Magma evolution and the formation of porphyry Cu-Au ore fluids: Evidence from silicate and sulfide melt inclusions. Mineralium Deposita 39 (8), 845–863.

Hammarstrom, J. M., Zen, E.-a., 1986. Aluminum in hornblende; an empirical igneous geobarometer. American Mineralogist 71 (11-12), 1297–1313.

Hanchar, J. M., Watson, E. B., 2003. Zircon Saturation Thermometry. Reviews in Mineralogy and Geochemistry 53 (1), 89–112.

Handley, G., Bradshaw, P., 1986. The Porgera gold deposit, Papua New Guinea. In: Proceedings in Gold, 86. pp. 416 – 424.

Harris, A., Golding, S., 2002. New evidence of magmatic-fluid related phyllic alteration: Implications for the genesis of porphyry Cu deposits. Geology 30 (4), 335–338.

Harris, A. C., Kamenetsky, V. S., White, N. C., van Achterbergh, E., Ryan, C. G., 2003. Melt inclusions in veins: linking magmas and porphyry Cu deposits. Science 302 (5653), 2109–2111.

Harrison, T. M., Watson, E. B., 1984. The behavior of apatite during crustal anatexis: Equilibrium and kinetic considerations. Geochimica et Cosmochimica Acta 48 (7), 1467–1477.

Harrison, T. M., Zeitler, P. K., 2005. Fundamentals of noble gas thermochronometry. Reviews in Mineralogy and Geochemistry 58 (1), 123–149.

Hart, S. R., Dunn, T., 1993. Experimental cpx/melt partitioning of 24 trace elements. Contributions to Mineralogy and Petrology 113 (1), 1–8.

Hartley, M. E., Bali, E., Maclennan, J., Neave, D. A., Halldórsson, S. A., 2018. Melt inclusion constraints on petrogenesis of the 2014–2015 Holuhraun eruption, Iceland. Contributions to Mineralogy and Petrology 173 (2), 10.

Hedenquist, J. W., Arribas, A., Gonzalez-Urien, E., Others, 2000. Exploration for epithermal gold deposits. Reviews in Economic Geology 13 (2), 45–77.

Hedenquist, J. W., Lowenstern, J. B., 1994. The role of magmas in the formation of hydrothermal ore deposits. Nature 370 (6490), 519–527.

Hedenquist, J. W., Taran, Y. A., 2013. Modeling the formation of advanced argillic lithocaps: volcanic vapor condensation above porphyry intrusions. Economic Geology 108 (7), 1523–1540.

Heinrich, C. A., Halter, W., Landtwing, M. R., Pettke, T., 2005. The formation of economic porphyry copper (-gold) deposits: Constraints from microanalysis of fluid and melt inclusions. Geological Society Special Publication 248, 247–263.

Herzberg, C., Cabral, R. A., Jackson, M. G., Vidito, C., Day, J. M. D., Hauri, E. H., 2014. Phantom Archean crust in Mangaia hotspot lavas and the meaning of heterogeneous mantle. Earth and Planetary Science Letters 396, 97–106.

Hofmann, A. E., Valley, J. W., Watson, E. B., Cavosie, A. J., Eiler, J. M., 2009. Sub-micron scale distributions of trace elements in zircon. Contributions to Mineralogy and Petrology 158 (3), 317–335.

Hofmann, A. W., Jochum, K. P., 1996. Source characteristics derived from very incompatible trace elements in Mauna Loa and

Mauna Kea basalts, Hawaii Scientific Drilling Project. Journal of Geophysical Research: Solid Earth 101 (B5), 11831–11839.

Holland, T., Blundy, J., 1994. Non-ideal interactions in calcic amphiboles and their bearing on amphibole-plagioclase thermometry. Contributions to Mineralogy and Petrology 116 (4), 433–447.

Hollister, L. S., Grissom, G. C., Peters, E. K., Stowell, H. H., Sisson, V. B., 1987. Confirmation of the empirical correlation of Al in hornblende with pressure of solidification of calc-alkaline plutons. American Mineralogist 72 (3-4), 231–239.

Holtz, F., Johannes, W., 1994. Maximum and minimum water contents of granitic melts: implications for chemical and physical properties of ascending magmas. Lithos 32 (1-2), 149–159.

Horstwood, M. S., Košler, J., Gehrels, G., Jackson, S. E., McLean, N. M., Paton, C., Pearson, N. J., Sircombe, K., Sylvester, P., Vermeesch, P., Bowring, J. F., Condon, D. J., Schoene, B., 2016. Community-Derived Standards for LA-ICP-MS U-(Th-)Pb Geochronology Uncertainty Propagation, Age Interpretation and Data Reporting. Geostandards and Geoanalytical Research 40 (3), 311–332.

Hunt, J. P., 1977. Porphyry copper deposits. Geological Society, London, Special Publications 7 (1), 98.

Irvine, T. N. J., Baragar, W., 1971. A guide to the chemical classification of the common volcanic rocks. Canadian journal of earth sciences 8 (5), 523–548.

Jaffey, A. H., Flynn, K. F., Glendenin, L. E., Bentley, W. C. T., Essling, A. M., 1971. Precision measurement of half-lives and specific activities of U 235 and U 238. Physical Review C 4 (5), 1889.

Jahn-Awe, S., Froitzheim, N., Nagel, T. J., Frei, D., Georgiev, N., Pleuger, J., 2010. Structural and geochronological evidence for Paleogene thrusting in the western Rhodopes, SW Bulgaria: Elements for a new tectonic model of the Rhodope Metamorphic Province. Tectonics 29 (3).

Jenkin, G. R. T., Ellam, R. M., Rogers, G., Stuart, F. M., 2001. An investigation of closure temperature of the biotite Rb-Sr system: The importance of cation exchange. Geochimica et Cosmochimica Acta 65 (7), 1141–1160.

Jochum, K. P., Nohl, U., Herwig, K., Lammel, E., Stoll, B., Hofmann, A. W., 2005. GeoReM: a new geochemical database for reference materials and isotopic standards. Geostandards and Geoanalytical Research 29 (3), 333–338.

Johnson, M. C., Rutherford, M. J., 1989. Experimental calibration of the aluminum-in-hornblende geobarometer with application to Long Valley caldera (California) volcanic rocks. Geology 17 (9), 837–841.

Jolivet, L., Brun, J. P., 2010. Cenozoic geodynamic evolution of the Aegean. International Journal of Earth Sciences 99 (1), 109–138.

Jolivet, L., Faccenna, C., Huet, B., Labrousse, L., Le Pourhiet, L., Lacombe, O., Lecomte, E., Burov, E., Denele, Y., Brun, J.-P., Others, 2013. Aegean tectonics: Strain localisation, slab tearing and trench retreat. Tectonophysics 597, 1–33.

Jones, C. E., Tarney, J., Baker, J. H., Gerouki, F., 1992. Tertiary granitoids of Rhodope, northern Greece: Magmatism related to extensional collapse of the Hellenic Orogen? Tectonophysics 210 (3-4), 295–314.

Katerinopoulou, A., Katerinopoulos, A., Voudouris, P., Bieniok, A., Musso, M., Amthauer, G., 2009. A multi-analytical study of the crystal structure of unusual Ti–Zr–Cr-rich Andradite from the Maronia skarn, Rhodope massif, western Thrace, Greece. Mineralogy and Petrology 95 (1-2), 113.

Kent, A. J. R., 2008. Melt inclusions in basaltic and related volcanic rocks. Reviews in Mineralogy and Geochemistry 69 (1), 273–331.

Kesler, S. E., Wilkinson, B. H., 2008. Earth's copper resources estimated from tectonic diffusion of porphyry copper deposits. Geology 36 (3), 255–258.

Kilias, A., Falalakis, G., Sfeikos, A., Papadimitriou, E., Vamvaka, A., Gkarlaouni, C., 2013. The Thrace basin in the Rhodope province of NE Greece - A tertiary supradetachment basin and its geodynamic implications. Tectonophysics 595-596, 90–105.

Kilias, A. D., Vamvaka, A., Falalakis, G., Sfeikos, A., Papadimitriou, E., Gkarlaouni, C. H., Karakostas, B., 2015. The Mesohellenic Trough and the paleogene Thrace basin on the Rhodope massif, their structural evolution and geotectonic significance in the Hellenides. J. Geol. and Geosc 4 (2), 198.

Kokkinakis, A., 1980. Altersbeziehungen zwischen Metamorphosen, mechanischen Deformationen und Intrusionen am Suedrand des Rhodope-Massivs (Makedonien, Griechenland). Geologische Rundschau 69 (3), 726–744.

Krenn, K., Bauer, C., Proyer, A., Klötzli, U., Hoinkes, G., 2010. Tectonometamorphic evolution of the Rhodope orogen. Tectonics 29 (4), 1–25.

Krohe, A., Mposkos, E., 2002. Multiple generations of extensional detachments in the Rhodope Mountains (northern Greece): evidence of episodic exhumation of high-pressure rocks. Geological Society, London, Special Publications 204 (1), 151–178.

Kydonakis, K., Brun, J.-P., Sokoutis, D., 2015a. North Aegean core complexes, the gravity spreading of a thrust wedge. Journal of Geophysical Research: Solid Earth 120 (1), 595–616.

Kydonakis, K., Brun, J. P., Sokoutis, D., Gueydan, F., 2015b. Kinematics of Cretaceous subduction and exhumation in the western Rhodope (Chalkidiki block). Tectonophysics 665, 218–235.

Kydonakis, K., Gallagher, K., Brun, J. P., Jolivet, M., Gueydan, F., Kostopoulos, D., 2014. Upper Cretaceous exhumation of the western Rhodope Metamorphic Province (Chalkidiki Peninsula, northern Greece). Tectonics 33 (6), 1113–1132.

Lanzo, G., Di Carlo, I., Pichavant, M., Rotolo, S. G., Scaillet, B., 2016. Origin of primitive ultra-calcic arc melts at crustal conditionsExperimental evidence on the La Sommata basalt, Vulcano, Aeolian Islands. Journal of Volcanology and Geothermal Research 321, 85–101.

LaTourrette, T., Hervig, R. L., Holloway, J. R., 1995. Trace element partitioning between amphibole, phlogopite, and basanite melt. Earth and Planetary Science Letters 135 (1-4), 13–30.

Laumonier, M., Gaillard, F., Muir, D., Blundy, J., Unsworth, M., 2017. Giant magmatic water reservoirs at mid-crustal depth inferred from electrical conductivity and the growth of the continental crust. Earth and Planetary Science Letters 457 (October), 173–180.

Leake, B. E., Woolley, A. R., Arps, C. E. S., Birch, W. D., Gilbert, M. C., Grice, J. D., Hawthorne, F. C., Kato, A., Kisch, H. J., Krivovichev, V. G., Others, 1997. Report. Nomenclature of amphiboles: report of the subcommittee on amphiboles of the international mineralogical association commission on new minerals and mineral names. Mineralogical magazine 61 (2), 295–321.

Lee, R. G., Dilles, J. H., Tosdal, R. M., Wooden, J. L., Mazdab, F. K., 2017. Magmatic evolution of granodiorite intrusions at the El Salvador porphyry copper deposit, Chile, based on trace element composition and U/Pb age of zircons. Economic Geology 112 (2), 245–273.

Liati, A., Gebauer, D., Wysoczanski, R., 2002. UPb SHRIMP-dating of zircon domains from UHP garnet-rich mafic rocks and late pegmatoids in the Rhodope zone (N Greece); evidence for Early Cretaceous crystallization and Late Cretaceous metamorphism. Chemical Geology 184 (3-4), 281–299.

Liati, A., Kreuzer, H., 1990. K-Ar dating of metamorphic and magmatic rocks from the Xanthi and Drama areas, Greek part of the Rhodope zone. Eur J Mineral 2 (Bh 1), 161.

Lindsley, D. H., 1983. Pyroxene thermometry. American Mineralogist 68 (5-6), 477–493.

Lipman, P. W., Prostka, H. J., Christiansen, R. L., 1972. Cenozoic volcanism and plate-tectonic evolution of the Western United States. I. Early and middle Cenozoic. Philosophical Transactions of the Royal Society A: Mathematical, Physical and Engineering Sciences 271 (1213), 217–248.

Lips, A. L. W., White, S. H., Wijbrans, J. R., 2000. Middle-late Alpine thermotectonic evolution of the southern Rhodope Massif, Greece. Geodinamica Acta 13 (5), 281–292.

Lister, G. S., Baldwin, S. L., 1993. Plutonism and the origin of metamorphic core complexes. Geology 21 (7), 607–610.

Lister, G. S., Banga, G., Feenstra, A., 1984. Metamorphic core complexes of Cordilleran type in the Cyclades, Aegean Sea, Greece. Geology 12 (4), 221–225.

Lledo, H. L., Jenkins, D. M., 2007. Experimental investigation of the upper thermal stability of Mg-rich actinolite; implications for Kiruna-type iron deposits. Journal of Petrology 49 (2), 225–238.

Loader, M. A., Wilkinson, J. J., Armstrong, R. N., 2017. The effect of titanite crystallisation on Eu and Ce anomalies in zircon and its implications for the assessment of porphyry Cu deposit fertility. Earth and Planetary Science Letters 472, 107–119.

London, D., Wolf, M. B., Morgan VI, G. B., Garrido, M. G., 1999. Experimental silicate-phosphate equilibria in peraluminous granitic magmas, with a case study of the Alburquerque batholith at Tres Arroyos, Badajoz, Spain. Journal of Petrology 40 (1), 215–240.

Loucks, R. R., 2014. Distinctive composition of copper-ore-forming arcmagmas. Australian Journal of Earth Sciences 61 (1), 5–16.

Lowell, J. D., Guilbert, J. M., 1970. Lateral and vertical alteration-mineralization zoning in porphyry ore deposits. Economic Geology 65 (4), 373–408.

Lu, Y.-J., Loucks, R. R., Fiorentini, M., Mccuaig, T. C., Evans, N. J., Yang, Z.-M., Hou, Z.-Q., Kirkland, C. L., Parra-Avila, L. A., Kobussen, A., Al, L., 2016. Zircon Compositions as a Pathfinder for Porphyry Cu $\pm$ Mo $\pm$ Au Deposits. Economic Geology Special Publication 19 (May), 329–347.

Luhr, J. F., 1997. Extensional tectonics and the diverse primitive volcanic rocks in the western Mexican Volcanic Belt. The Canadian Mineralogist 35 (2), 473–500.

Luhr, J. F., Carmichael, I. S. E., 1980. The Colima Volcanic complex, Mexico. Contributions to Mineralogy and Petrology 71 (4), 343–372.

Macdonald, G. D., Arnold, L. C., 1994. Geological and Geochemical Zoning of the Grasberg Igneous Complex, Irian-Jaya, Indonesia. Journal of Geochemical Exploration 50 (1-3), 143–178.

Mancktelow, N. S., Grasemann, B., 1997. Time-dependent effects of heat advection and topography on cooling histories during erosion. Tectonophysics 270 (3-4), 167–195.

Marchev, P., Georgiev, S., Raicheva, R., Peytcheva, I., von Quadt, A., Ovtcharova, M., Bonev, N., 2013. Adakitic magmatism in post-collisional setting: An example from the Early-Middle Eocene Magmatic Belt in Southern Bulgaria and Northern Greece. Lithos 180-181, 159–180.

Marchev, P., Kaiser-Rohrmeier, M., Heinrich, C., Ovtcharova, M., von Quadt, A., Raicheva, R., 2005. 2: Hydrothermal ore deposits related to post-orogenic extensional magmatism and core complex formation: The Rhodope Massif of Bulgaria and Greece. Ore Geology Reviews 27 (1-4), 53–89.

Marchev, P., Kibarov, P., Spikings, R. A., Ovtcharova, M., Marton, I., Moritz, R., 2010. 40Ar/39Ar and U-Pb geochronology of the Iran Tepe volcanic complex, Eastern Rhodopes. Geologica Balcanica 39 (3), 3–12.

Marchev, P., Peytcheva, I., Ovtcharova, M., 2006. The age and origin of the Chuchuliga and Rozino granites , Eastern Rhodopes. Geosciences, 102–105.

Marchev, P., Singer, B., Andrew, C., Hasson, S., Moritz, R., Bonev, N., 2003. Characteristics and preliminary 40Ar/39Ar and 87Sr/86Sr data of the Upper Eocene sedimentary-hosted low-sulfidation gold deposits Ada Tepe and Rosino, SE Bulgaria: possible relation with core complex formation. Mineral exploration and sustainable development. Millpress, Rotterdam, 1193–1196.

Márton, I., Moritz, R., Spikings, R., 2010. Application of low-temperature thermochronology to hydrothermal ore deposits: Formation, preservation and exhumation of epithermal gold systems from the Eastern Rhodopes, Bulgaria. Tectonophysics 483 (3-4), 240–254.

Matjuschkin, V., Blundy, J. D., Brooker, R. A., 2016. The effect of pressure on sulphur speciation in mid- to deep-crustal arc magmas and implications for the formation of porphyry copper deposits. Contributions to Mineralogy and Petrology 171 (7), 1–25.

Mattinson, J. M., 2005. Zircon U–Pb chemical abrasion (CA-TIMS) method: combined annealing and multi-step partial dissolution analysis for improved precision and accuracy of zircon ages. Chemical Geology 220 (1), 47–66.

Mavroudchiev, B., Nedyalkov, R., Eleftheriadis, G., Soldatos, T., Christofides, G., 1993. Tertiary plutonic rocks from East Rhodope in Bulgaria and Greece. Bulletin of the Geological Society of Greece 27 (2), 643–660.

McFall, K. A., 2016. Critical metals in porphyry copper deposits. Ph.D. thesis, University of Southampton.

McInnes, B., Evans, N., Fu, F., Garwin, S., Belousova, E., Griffin, W. L., Bertens, A., Sukarna, D., Permanadewi, S., Andrew, R. L., Deckart, K., 2005a. Thermal history analysis of selected chilean, indonesian and iranian porphyry Cu-Mo-Au deposits. In: Super porphyry copper & gold deposits: a global perspective. PGC Publishing, Adelaide, pp. 1–16.

McInnes, B., Fu, F., 2006. 4DTHERM: Constraining thermal and exhumation histories of magmatic-hydrothermal systems using UPb and (UTh)/He data. Geochimica et Cosmochimica Acta 70 (18), A412.

McInnes, B. I. A., Evans, N. J., Fu, F. Q., Garwin, S., 2005b. Application of Thermochronology to Hydrothermal Ore Deposits. Reviews in Mineralogy and Geochemistry 58 (1), 467–498.

McKenzie, D., Bickle, M. J., 1988. The volume and composition of melt generated by extension of the lithosphere. Journal of Petrology 29 (3), 625–679.

McKenzie, D., O'nions, R. K., 1991. Partial melt distributions from inversion of rare earth element concentrations. Journal of Petrology 32 (5), 1021–1091.

McLean, N. M., Condon, D. J., Schoene, B., Bowring, S. A., 2015. Evaluating uncertainties in the calibration of isotopic reference materials and multi-element isotopic tracers (EARTHTIME Tracer Calibration Part II). Geochimica et Cosmochimica Acta 164, 481–501.

Meen, J. K., 1987. Formation of shoshonites from calcalkaline basalt magmas: geochemical and experimental constraints from the type locality. Contributions to Mineralogy and Petrology 97 (3), 333–351.

Meinhold, G., Kostopoulos, D. K., 2013. The Circum-Rhodope Belt, northern Greece: Age, provenance, and tectonic setting. Tectonophysics 595-596, 55–68.

Meinhold, G., Reischmann, T., Kostopoulos, D., Frei, D., Larionov, A. N., 2010. Mineral chemical and geochronological constraints on the age and provenance of the eastern Circum-Rhodope Belt low-grade metasedimentary rocks, NE Greece. Sedimentary Geology 229 (4), 207–223.

Melfos, V., Vavelidis, M., Christofides, G., Seidel, E., 2002. Origin and evolution of the Tertiary Maronia porphyry copper-molybdenum deposit, Thrace, Greece. Mineralium Deposita 37 (6-7), 648–668.

Melfos, V., Voudouris, P., 2016. Fluid evolution in Tertiary magmatic-hydrothermal ore systems at the Rhodope metallogenic province, NE Greece. A review. Geologia Croatica 69 (1), 157–167.

Melfos, V., Voudouris, P., 2017. Cenozoic metallogeny of Greece and potential for precious, critical and rare metals exploration. Ore Geology Reviews 89, 1030–1057.

Menand, T., Annen, C., Blanquat, M. D. S., 2015. Rates of magma transfer in the crust: Insights into magma reservoir recharge and pluton growth. Geology 43 (3), 199–202.

Meyer, W., 1968. Alterstellung des Plutonismus im Südteil der Rila-Rhodope-Masse (Nordgriechenland). Geologica et Palaeontologica 2, 173–192.

Michaud, V., Clocchiatti, R., Sbrana, S., 2000. The Minoan and post-Minoan eruptions, Santorini (Greece), in the light of melt inclusions: Chlorine and sulphur behaviour. Journal of Volcanology and Geothermal Research 99 (1-4), 195–214.

Morrison, G. W., 1980. Characteristics and tectonic setting of the shoshonite rock association. Lithos 13, 97–108.

Mountrakis, D., 2006. Tertiary and Quaternary tectonics of Greece. Geological Society of America Special Papers 409, 125–136.

Mposkos, E., Doryphoros, K., 1993. High temperature skarns in the Maronia area (NE Greece). Bulletin of the Geological Society of Greece 28 (2), 23.

Mposkos, E., Wawrzenitz, N., 1995. Metapegmatites and pegmatites bracketing the time of high P-metamorphism in polymetamorphic rocks of the E-Rhodope, N. Greece: petrological and geochronological constraints. Geol. Soc. Greece Spec. Publ 4 (2), 602–608.

Mposkos, E. D., Kostopoulos, D. K., 2001. Diamond, former coesite and supersilicic garnet in metasedimentary rocks from the

Greek Rhodope: a new ultrahigh-pressure metamorphic province established. Earth and Planetary Science Letters 192 (4), 497–506.

Müller, D., Groves, D. I., 2016. Primary Enrichment of Precious Metals in Potassic Igneous Rocks. In: Potassic Igneous Rocks and Associated Gold-Copper Mineralization. Springer, pp. 77–96.

Mungall, J. E., 2002. Roasting the mantle: Slab melting and the genesis of major Au and Au-rich Cu deposits. Geology 30 (10), 915–918.

Mutch, E. J., Blundy, J. D., Tattitch, B. C., Cooper, F. J., Brooker, R. A., 2016. An Experimental Study of Amphibole Stability in Low Pressure Granitic Magmas and a Revised Al-in-Hornblende Geobarometer. Contributions to Mineralogy and Petrology 171 (10), 85.

Nadeau, O., Stix, J., Williams-Jones, A. E., 2016. Links between arc volcanoes and porphyry-epithermal ore deposits. Geology 44 (1), 11–14.

Naney, M. T., 1983. Phase equilibria of rock-forming ferromagnesian silicates in granitic systems.

Nardi, L. V. S., Formoso, M. L. L., Müller, I. F., Fontana, E., Jarvis, K., Lamarão, C., 2013. Zircon/rock partition coefficients of REEs, Y, Th, U, Nb, and Ta in granitic rocks: Uses for provenance and mineral exploration purposes. Chemical Geology 335, 1–7.

Neave, D. A., Hartley, M. E., Maclennan, J., Edmonds, M., Thordarson, T., 2017. Volatile and light lithophile elements in high-anorthite plagioclase-hosted melt inclusions from Iceland. Geochimica et Cosmochimica Acta 205, 100–118.

Neave, D. A., Shorttle, O., Oeser, M., Weyer, S., Kobayashi, K., 2018. Mantle-derived trace element variability in olivines and their melt inclusions. Earth and Planetary Science Letters 483, 90–104.

Nielsen, T. F., Solovova, I. P., Veksler, I. V., 1997. Parental melts of melilitolite and origin of alkaline carbonatite: Evidence from crystallised melt inclusions, Gardiner complex. Contributions to Mineralogy and Petrology 126 (4), 331–344.

Nimis, P., 1999. Clinopyroxene geobarometry of magmatic rocks. Part 2. Structural geobarometers for basic to acid, tholeiitic and mildly alkaline magmatic systems. Contributions to Mineralogy and Petrology 135 (1), 62–74.

Nimis, P., Ulmer, P., 1998. Clinopyroxene geobarometry of magmatic rocks Part 1: An expanded structural geobarometer for anhydrous and hydrous, basic and ultrabasic systems. Contributions to Mineralogy and Petrology 133 (1-2), 122–135.

Nockolds, S. R., 1954. Average chemical compositions of some igneous rocks. Geological Society of America Bulletin 65 (10), 1007–1032.

Ortelli, M., Moritz, R., Voudouris, P., Cosca, M., Spangenberg, J., 2010. Tertiary Porphyry and Epithermal Association of the Sapes-Kassiteres District, Eastern Rhodopes, Greece. In: SEG 2010: The Challenge of Finding New Mineral Resources: Global Metallogeny, Innovative Exploration, and New Discoveries. Keystone.

Ortelli, M., Moritz, R., Voudouris, P., Spangenberg, J., 2009. Tertiary porphyry and epithermal association of the Sapes-Kassiteres district, Eastern Rhodopes, Greece. In: Proceedings of the 10th biennial SGA meeting, Townsville, Australia. pp. 536–538.

Ovtcharova, M., Quadt, A. V., Cherneva, Z., Sarov, S., Heinrich, C., Peytcheva, I., 2004. U-Pb dating of zircon and monazite from granitoids and migmatites in the core and eastern periphery of the Central Rhodopean Dome, Bulgaria. Geochimica et cosmochimica acta 68 (11), A664–A664.

Palacios, C., Ramírez, L. E., Townley, B., Solari, M., Guerra, N., 2007. The role of the Antofagasta-Calama Lineament in ore deposit deformation in the Andes of northern Chile. Mineralium Deposita 42 (3), 301–308.

Papadopoulou, L., Christofides, G., Koroneos, A., Bröcker, M., Soldatos, T., Eleftheriadis, G., 2004. Evolution and original of the Maronia pluton, Thrace, Greece. Bulletin of the Geological Society of Greece 36.

Paquette, J.-L., Ménot, R.-P., Pin, C., Orsini, J.-B., 2003. Episodic and short-lived granitic pulses in a post-collisional setting: evidence from precise U–Pb zircon dating through a crustal cross-section in Corsica. Chemical Geology 198 (1-2), 1–20.

Parsons, T., Thompson, G. A., 1993. Does magmatism influence low-angle normal faulting? Geology 21 (3), 247–250.

Pe-Piper, G., Piper, D. J. W., 2001. Late Cenozoic, post-collisional Aegean igneous rocks: Nd, Pb and Sr isotopic constraints on petrogenetic and tectonic models. Geological Magazine 138 (6), 653–668.

Pe-Piper, G., Piper, D. J. W., 2006. Unique features of the Cenozoic igneous rocks of Greece. Geological Society of America Special Papers 409, 259–282.

Pe-Piper, G., Piper, D. J. W., Koukouvelas, I., Dolansky, L. M., Kokkalas, S., 2009. Postorogenic shoshonitic rocks and their origin by melting underplated basalts: The miocene of Limnos, Greece. Bulletin of the Geological Society of America 121 (1-2), 39–54.

Pearce, J. A., Peate, D. W., 1995. Tectonic implications of the composition of volcanic arc magmas. Annual Review of Earth and Planetary Sciences 23 (1), 251–285.

Peccerillo, A., De Astis, G., Faraone, D., Forni, F., Frezzotti, M. L., 2013. Compositional variations of magmas in the Aeolian arc: implications for petrogenesis and geodynamics. Geological Society, London, Memoirs 37 (1), 491–510.

Peccerillo, A., Taylor, S. R., 1976. Geochemistry of Eocene calc-alkaline volcanic rocks from the Kastamonu area, northern Turkey. Contributions to mineralogy and petrology 58 (1), 63–81.

Peterson, E. C., Mavrogenes, J. A., 2014. Linking high-grade gold mineralization to earthquake-induced fault-valve processes in the Porgera gold deposit, Papua New Guinea. Geology 42 (5), 383–386.

Peytcheva, I., von Quadt, A., Ovtcharova, M., Handler, R., Neubauer, F., Salnikova, E., Kostitsyn, Y., Sarov, S., Kolcheva, K., 2004. Metagranitoids from the eastern part of the Central Rhodopean Dome (Bulgaria): U/Pb, Rb/Sr and 40Ar/39Ar timing of emplacement and exhumation and isotope-geochemical features. Mineralogy and Petrology 82 (1-2), 1–31.

Piccoli, P. M., Candela, P. A., 2002. Apatite in Igneous Systems. Reviews in Mineralogy and Geochemistry 48 (1), 255–292.

Pichavant, M., Montel, J. M., Richard, L. R., 1992. Apatite solubility in peraluminous liquids: Experimental data and an extension of the Harrison-Watson model. Geochimica et Cosmochimica Acta 56 (10), 3855–3861.

Pichon, X. L., Angelier, J., 1979. The hellenic arc and trench system: A key to the neotectonic evolution of the eastern mediterranean area. Tectonophysics 60 (1-2), 1–42.

Platt, J. P., Behr, W. M., Cooper, F. J., 2015. Metamorphic core complexes: windows into the mechanics and rheology of the crust. Journal of the Geological Society 172 (1), 9–27.

Poli, S., Schmidt, M. W., 2002. Petrology of subducted slabs. Annual Review of Earth and Planetary Sciences 30 (1), 207–235.

Prouteau, G., Scaillet, B., 2003. Experimental Constraints on the Origin of the 1991 Pinatubo Dacite. Journal of Petrology 44 (12), 2203–2241.

Putirka, K., 2016. Amphibole thermometers and barometers for igneous systems and some implications for eruption mechanisms of felsic magmas at arc volcanoes. American Mineralogist 101 (4), 841–858.

Putirka, K. D., 2008. Thermometers and Barometers for Volcanic Systems. Reviews in Mineralogy and Geochemistry 69 (1), 61–120.

Qin, Z., Lu, F., Anderson, A. T., 1992. Diffusive reequilibration of melt and fluid inclusions. American Mineralogist 77 (5-6), 565–576.

Richards, J. P., 1992. Magmatic-epithermal transitions in alkalic systems: Porgera gold deposit, Papua New Guinea. Geology 20 (6), 547–550.

Richards, J. P., 2003. Tectono-magmatic precursors for porphyry Cu-(Mo-Au) deposit formation. Economic Geology 98 (8), 1515–1533.

Richards, J. P., 2009. Postsubduction porphyry Cu-Au and epithermal Au deposits: Products of remelting of subduction-modified lithosphere. Geology 37 (3), 247–250.

Richards, J. P., 2011a. High Sr/Y arc magmas and porphyry Cu–Mo–Au deposits: just add water. Economic Geology 106 (7), 1075–1081.

Richards, J. P., 2011b. Magmatic to hydrothermal metal fluxes in convergent and collided margins. Ore Geology Reviews 40 (1), 1–26.

Richards, J. P., 2013. Giant ore deposits formed by optimal alignments and combinations of geological processes. Nature Geoscience 6 (11), 911–916.

Richards, J. P., 2015. Tectonic, magmatic, and metallogenic evolution of the Tethyan orogen: From subduction to collision. Ore Geology Reviews 70, 323–345.

Richards, J. P., Chappell, B. W., McCulloch, M. T., 1990. Intraplate-type magmatism in a continent-island-arc collision zone: Porgera intrusive complex, Papua New Guinea. Geology 18 (10), 958–961.

Richards, J. P., Kerrich, R., 1993. The Porgera gold mine, Papua New Guinea: magmatic hydrothermal to epithermal evolution of an alkalic-type precious metal deposit. Economic Geology 88 (5), 1017–1052.

Richards, J. P., Spell, T., Rameh, E., Razique, A., Fletcher, T., 2012. High Sr/Y magmas reflect arc maturity, high magmatic water content, and porphyry Cu Mo Au potential: Examples from the tethyan arcs of central and eastern iran and Western Pakistan. Economic Geology 107 (2), 295–332.

Ricou, L. E., Burg, J. P., Godfriaux, I., Ivanov, Z., 1998. Rhodope and Vardar: the metamorphic and the olistostromic paired belts related to the Cretaceous subduction under Europe. Geodinamica Acta 11 (6), 285–309.

Riker, J. M., Blundy, J. D., Rust, A. C., Botcharnikov, R. E., Humphreys, M. C., 2015. Experimental phase equilibria of a Mount St. Helens rhyodacite: a framework for interpreting crystallization paths in degassing silicic magmas. Contributions to Mineralogy and Petrology 170 (1), 1–22.

Ring, U., Glodny, J., Will, T., Thomson, S., 2010. The Hellenic subduction system: high-pressure metamorphism, exhumation, normal faulting, and large-scale extension. Annual Review of Earth and Planetary Sciences 38, 45–76.

Roedder, E., 1979. Origin and significance of magmatic inclusions. Bull. Mineral. 102, 487–510.

Rohrmeier, M. K., von Quadt, A., Driesner, T., Heinrich, C. a., Handler, R., Ovtcharova, M., Ivanov, Z., Petrov, P., Sarov, S., Peytcheva, I., 2013. Post-Orogenic Extension and Hydrothermal Ore Formation: High-Precision Geochronology of the Central Rhodopian Metamorphic Core Complex (Bulgaria-Greece). Economic Geology 108 (4), 691–718.

Romer, R. L., Kroner, U., 2016. Phanerozoic tin and tungsten mineralization-Tectonic controls on the distribution of enriched protoliths and heat sources for crustal melting. Gondwana Research 31, 60–95.

Sahy, D., Condon, D. J., Terry, D. O., Fischer, A. U., Kuiper, K. F., 2015. Synchronizing terrestrial and marine records of environmental change across the Eocene-Oligocene transition. Earth and Planetary Science Letters 427, 171–182.

Samperton, K. M., Schoene, B., Cottle, J. M., Brenhin Keller, C., Crowley, J. L., Schmitz, M. D., 2015. Magma emplacement, differentiation and cooling in the middle crust: Integrated zircon geochronological-geochemical constraints from the Bergell Intrusion, Central Alps. Chemical Geology 417, 322–340.

Sapiie, B., Cloos, M., 2004. Strike-slip faulting in the core of the Central Range of west New Guinea: Ertsberg Mining District, Indonesia. Bulletin of the Geological Society of America 116 (3-4), 277–293.

Sapiie, B., Cloos, M., 2013. Strike-slip faulting and veining in the Grasberg giant porphyry Cu-Au deposit, Ertsberg (Gunung Bijih) mining district, Papua, Indonesia. International Geology Review 55 (1), 1–42.

Sato, H., Holtz, F., Behrens, H., Botcharnikov, R., Nakada, S., 2005. Experimental petrology of the 1991-1995 Unzen dacite, Japan. Part II: Cl/OH partitioning between hornblende and melt and its implications for the origin of oscillatory zoning of hornblende phenocrysts. Journal of Petrology 46 (2), 339–354.

Scaillet, B., Evans, B. W., 1999. The 15 June 1991 eruption of Mount Pinatubo. I. Phase equilibria and pre-eruption P–T–f O2–f H2O conditions of the dacite magma. Journal of Petrology 40 (3), 381–411.

Scaillet, B., Holtz, F., Pichavant, M., 2016. Experimental constraints on the formation of silicic magmas. Elements 12 (2), 109–114.

Schaltegger, U., Schmitt, A. K., Horstwood, M. S. A., 2015. U–Th–Pb zircon geochronology by ID-TIMS, SIMS, and laser ablation ICP-MS: Recipes, interpretations, and opportunities. Chemical Geology 402, 89–110.

Scherer, E. E., Whitehouse, M. J., Munker, C., 2007. Zircon as a monitor of crustal growth. Elements 3 (1), 19–24.

Schmid, S. M., Bernoulli, D., Fügenschuh, B., Matenco, L., Schefer, S., Schuster, R., Tischler, M., Ustaszewski, K., 2008. The Alpine-Carpathian-Dinaridic orogenic system: correlation and evolution of tectonic units. Swiss Journal of Geosciences 101 (1), 139–183.

Schmidt, M. W., 1992. Amphibole composition in tonalite as a function of pressure: an experimental calibration of the Al-in-hornblende barometer. Contributions to mineralogy and petrology 110 (2-3), 304–310.

Schmitz, M. D., Schoene, B., 2007. Derivation of isotope ratios, errors, and error correlations for U-Pb geochronology using 205Pb-235U-(233U)-spiked isotope dilution thermal ionization mass spectrometric data. Geochemistry, Geophysics, Geosystems 8 (8).

Schreyer, W., 1983. Metamorphism and fluid inclusions in the basement of the Vredefort Dome, South Africa: guidelines to the origin of the structure. Journal of Petrology 24 (1), 26–47.

Seedorf, E., 2005. Porphyry deposits: Characteristics and origin of hypogene features. Econ. Geol. 100, 251–298.

Seghedi, I., Downes, H., Szakács, A., Mason, P. R. D., Thirlwall, M. F., Rocsu, E., Pécskay, Z., Márton, E., Panaiotu, C., 2004. Neogene–Quaternary magmatism and geodynamics in the Carpathian–Pannonian region: a synthesis. Lithos 72 (3), 117–146.

Siebert, L., 1984. Large volcanic debris avalanches: characteristics of source areas, deposits, and associated eruptions. Journal of volcanology and geothermal research 22 (3-4), 163–197.

Sillitoe, R. H., 1972. A plate tectonic model for the origin of porphyry copper deposits. Economic geology 67 (2), 184–197.

Sillitoe, R. H., 1973. The tops and bottoms of porphyry copper deposits. Economic Geology 68 (6), 799–815.

Sillitoe, R. H., 1985. Ore-related breccias in volcanoplutonic arcs. Economic Geology 80 (6), 1467–1514.

Sillitoe, R. H., 1994. Erosion and collapse of volcanoes: Causes of telescoping in intrusion-centered ore deposits. Geology 22 (10), 945–948.

Sillitoe, R. H., 1995. Exploration of porphyry copper lithocaps. In: Pacrim Congress 1995. The Australasian Institute of Mining and Metallurgy, pp. 527–532.

Sillitoe, R. H., 1997. Characteristics and controls of the largest porphyry copper-gold and epithermal gold deposits in the circum-Pacific region. Australian Journal of Earth Sciences 44 (3), 373–388.

Sillitoe, R. H., 2010. Porphyry Copper Systems. Economic Geology 105, 3–41.

Simons, B., Andersen, J. C., Shail, R. K., Jenner, F. E., 2017. Fractionation of Li, Be, Ga, Nb, Ta, In, Sn, Sb, W and Bi in the peraluminous Early Permian Variscan granites of the Cornubian Batholith: Precursor processes to magmatic-hydrothermal mineralisation. Lithos 278-281, 491–512.

Siron, C. R., Rhys, D., Thompson, J. F., Baker, T., Veligrakis, T., Camacho, A., Dalampiras, L., 2018. Structural controls on porphyry Au-Cu and Au-rich polymetallic Carbonate-hosted replacement deposits of the Kassandra mining District, Northern Greece. Economic Geology 113 (2), 309–345.

Siron, C. R., Thompson, J. F. H., Baker, T., Friedman, R., Tsitsanis, P., Russell, S., Randall, S., Mortensen, J., 2016. Magmatic and metallogenic framework of Au-Cu porphyry and polymetallic carbonate-hosted replacement deposits of the Kassandra mining district, Northern Greece. Society of Economic Geologists, Special Publication 19, 29–55.

Sisson, T. W., Grove, T. L., 1993. Experimental investigations of the role of H2O in calc-alkaline differentiation and subduction zone magmatism. Contributions to Mineralogy and Petrology 113 (2), 143–166.

Smith, A. G., Moores, E. M., 1974. Hellenides. Geological Society, London, Special Publications 4 (1), 159–185.

Smith, D. J., 2014. Clinopyroxene precursors to amphibole sponge in arc crust. Nature Communications 5, 1–6.

Sobolev, A. V., Danyushevsky, L. V., 1994. Petrology and geochemistry of boninites from the north termination of the Tonga Trench: constraints on the generation conditions of primary high-Ca boninite magmas. Journal of Petrology 35 (5), 1183–1211.

Soldatos, T., Koroneos, A., Kamenov, B. K., Peytcheva, I., von Quadt, A., Christofides, G., Zheng, X., Sang, H., 2008. New U-Pb

and Ar-Ar mineral ages for the Barutin-Buynovo-Elatia-Skaloti-Paranesti batholith (Bulgaria and Greece): refinement of its debatable age. Geochem Mineral Petrol 46, 85–102.

Stepanov, A., Mavrogenes, J. A., Meffre, S., Davidson, P., 2014. The key role of mica during igneous concentration of tantalum. Contributions to Mineralogy and Petrology 167 (6), 1–8.

Stepanov, A. S., Hermann, J., 2013. Fractionation of Nb and Ta by biotite and phengite: Implications for the "missing Nb paradox". Geology 41 (3), 303–306.

Student, J. J., Bodnar, R. J., 2004. Silicate melt inclusions in porphyry copper deposits: Identification and homogenization behavior. Canadian Mineralogist 42 (5), 1583–1599.

Stüwe, K., White, L., Brown, R., 1994. The influence of eroding topography on steady-state isotherms. Application to fission track analysis. Earth and Planetary Science Letters 124 (1-4), 63–74.

Sun, S.-S., McDonough, W.-S., 1989. Chemical and isotopic systematics of oceanic basalts: implications for mantle composition and processes. Geological Society, London, Special Publications 42 (1), 313–345.

Sun, W., fang Huang, R., Li, H., bin Hu, Y., chan Zhang, C., jun Sun, S., peng Zhang, L., Ding, X., ying Li, C., Zartman, R. E., xing Ling, M., 2015. Porphyry deposits and oxidized magmas. Ore Geology Reviews 65 (P1), 97–131.

Tapster, S., 2016. A zircon perspective on magma dynamics leading to porphyry copper deposit formation 7453.

Tapster, S., Condon, D. J., Naden, J., Noble, S. R., Petterson, M. G., Roberts, N. M. W., Saunders, A. D., Smith, D. J., 2016. Rapid thermal rejuvenation of high-crystallinity magma linked to porphyry copper deposit formation; evidence from the Koloula Porphyry Prospect, Solomon Islands. Earth and Planetary Science Letters 442, 206–217.

Tatsumi, Y., 1989. Migration of fluid phases and genesis of basalt magmas in subduction zones. Journal of Geophysical Research: Solid Earth 94 (B4), 4697–4707.

Taylor, H. P., 1997. Oxygen and hydrogen isotope relationships in hydrothermal mineral deposits. Geochemistry of hydrothermal ore deposits 3, 229–302.

Teyssier, C., Whitney, D. L., 2002. Gneiss domes and orogeny. Geology 30 (12), 1139–1142.

Thomas, J. B., 2003. Melt Inclusions in Zircon. Reviews in Mineralogy and Geochemistry 53 (1), 63–87.

Thompson, A. J. B., 1999. Alteration mapping in exploration: Application of short wave infrared (SWIR) spectroscopy. Econ. Geol. Newsl. 30, 13.

Tollari, N., Toplis, M. J., Barnes, S. J., 2006. Predicting phosphate saturation in silicate magmas: An experimental study of the effects of melt composition and temperature. Geochimica et Cosmochimica Acta 70 (6), 1518–1536.

Turner, S. J., 1999. Settings and styles of high-sulphidation gold deposits in the Cajamarca region, northern Peru. In: Pacrim. Vol. 99. pp. 461–468.

Turpaud, P., Reischmann, T., 2010. Characterisation of igneous terranes by zircon dating: implications for UHP occurrences and suture identification in the Central Rhodope, northern Greece. International Journal of Earth Sciences 99 (3), 567–591.

van Hinsbergen, D. J. J., Dupont-Nivet, G., Nakov, R., Oud, K., Panaiotu, C., 2008. No significant post-Eocene rotation of the Moesian Platform and Rhodope (Bulgaria): Implications for the kinematic evolution of the Carpathian and Aegean arcs. Earth and Planetary Science Letters 273 (3-4), 345–358.

van Hinsbergen, D. J. J., Hafkenscheid, E., Spakman, W., Meulenkamp, J. E., Wortel, R., 2005. Nappe stacking resulting from subduction of oceanic and continental lithosphere below Greece. Geology 33 (4), 325.

Van Nort, S. D., 1991. Geology and mineralization of the Grasberg porphyry copper-gold deposit, Irian Jaya, Indonesia. Mining Eng., 300–303.

van Zalinge, M. E., Sparks, R. S., Blundy, J. D., 2017. Petrogenesis of the large-volume cardones ignimbrite, Chile; development and destabilization of a complex magma-mush system. Journal of Petrology 58 (10), 1975–2006.

von Blanckenburg, F., Davies, J. H., 1995. Slab breakoff: A model for syncollisional magmatism and tectonics in the Alps. Tectonics

14 (1), 120–131.

von Quadt, A., Erni, M., Martinek, K., Moll, M., Peytcheva, I., Heinrich, C. A., 2011. Zircon crystallization and the lifetimes of ore-forming magmatic-hydrothermal systems. Geology 39 (8), 731–734.

von Quadt, A., Peytcheva, I., 2005. The southern extension of the Srednogorie-type Upper Cretaceous magmatism in Rila-Western Rhodopes: Constraints from isotope geochronological and geochemical data. In: Proceedings of the Bulgarian Geological Society Annual Conference (80th Anniversary). pp. 113–116.

Voudouris, P., 2006. A comparative mineralogical study of Te-rich magmatic-hydrothermal systems in northeastern Greece. Mineralogy and Petrology 87 (3-4), 241–275.

Voudouris, P., Melfos, V., Spry, P. G., Bindi, L., Moritz, R., Ortelli, M., Kartal, T., 2013a. Extremely Re-Rich Molybdenite from Porphyry Cu-Mo-Au Prospects in Northeastern Greece: Mode of Occurrence, Causes of Enrichment, and Implications for Gold Exploration. Minerals 3 (2), 165–191.

Voudouris, P., Tarkian, M., Arikas, K., 2006. Mineralogy of telluride-bearing epithermal ores in the Kassiteres-Sappes area, western Thrace, Greece. Mineralogy and Petrology 87 (1-2), 31–52.

Voudouris, P. C., 2014. Hydrothermal corundum, topaz, diaspore and alunite supergroup minerals in the advanced argillic alteration lithocap of the Kassiteres-Sapes porphyry-epithermal system, western Thrace, Greece. Neues Jahrbuch für Mineralogie-Abhandlungen: Journal of Mineralogy and Geochemistry 191 (2), 117–136.

Voudouris, P. C., Melfos, V., Spry, P. G., Bindi, L., Kartal, T., Arikas, K., Moritz, R., Ortelli, M., 2009. Rhemium-Rich Molybdenite and Rhenite in the Pagoni Rachi Mo-Cu-Te-Ag-Au Prospect, Northern Greece: Implications for the Re Geochemistry of Porphyry-Style Cu-Mo and Mo Mineralisation. The Canadian Mineralogist 47 (5), 1013–1036.

Voudouris, P. C., Melfos, V., Spry, P. G., Kartal, T., Schleicher, H., Moritz, R., Ortelli, M., 2013b. The Pagoni Rachi/Kirki Cu-MoReAu deposit, northern Greece: Mineralogical and fluid inclusion constraints on the evolution of a telescoped porphyry-epithermal system. Canadian Mineralogist 51 (2), 253–284.

Wang, M., Song, S., Niu, Y., Su, L., 2014. Post-collisional magmatism: Consequences of UHPM terrane exhumation and orogen collapse, N. Qaidam UHPM belt, NW China. Lithos 210-211, 181–198.

Wang, Y., Foley, S. F., Prelević, D., 2017. Potassium-rich magmatism from a phlogopite-free source. Geology 45 (5), 467–470.

Watson, E. B., 1979. Zircon saturation in felsic liquids: experimental results and applications to trace element geochemistry. Contributions to Mineralogy and Petrology 70 (4), 407–419.

Watson, E. B., Harrison, T. M., 1983. Zircon saturation revisited: temperature and composition effects in a variety of crustal magma types. Earth and Planetary Science Letters 64 (2), 295–304.

Wawrzenitz, N., Krohe, A., 1998. Exhumation and doming of the Thasos metamorphic core complex (S Rhodope, Greece): structural and geochronological constraints. Tectonophysics 285 (3), 301–332.

Wawrzenitz, N., Mposkos, E., 1997. First evidence for Lower Cretaceous HP/HT-metamorphism in the eastern Rhodope, North Aegean region, North-east Greece. European Journal of Mineralogy, 659–664.

Webster, J. D., 1997. Exsolution of magmatic volatile phases from Cl-enriched mineralizing granitic magmas and implications for ore metal transport. Geochimica et Cosmochimica Acta 61 (5), 1017–1029.

Webster, J. D., Baker, D. R., Aiuppa, A., 2018. Halogens in Mafic and Intermediate-Silica Content Magmas. Springer International Publishing, Cham, pp. 307–430.

Wernicke, B. P., England, P. C., Sonder, L. J., Christiansen, R. L., 1987. Tectonomagmatic evolution of Cenozoic extension in the North American Cordillera. Geological Society, London, Special Publications 28 (1), 203–221.

Whitney, D. L., Teyssier, C., Rey, P., Roger Buck, W., 2013. Continental and oceanic core complexes. Bulletin of the Geological Society of America 125 (3-4), 273–298.

Wiedenbeck, M., Hanchar, J. M., Peck, W. H., Sylvester, P., Valley, J., Whitehouse, M., Kronz, A., Morishita, Y., Nasdala, L., Fiebig, J., Others, 2004. Further characterisation of the 91500 zircon crystal. Geostandards and Geoanalytical Research 28 (1),

9–39.

Wilke, M., Behrens, H., 1999. The dependence of the partitioning of iron and europium between plagioclase and hydrous tonalitic melt on oxygen fugacity. Contributions to Mineralogy and Petrology 137 (1-2), 102–114.

Wilkinson, B. H., Kesler, S. E., 2007. Tectonism and exhumation in convergent margin orogens: Insights from ore deposits. The Journal of Geology 115 (6), 611–627.

Wilkinson, J. J., 2013. Triggers for the formation of porphyry ore deposits in magmatic arcs. Nature Geoscience 6 (11), 917–925.

Williams-Jones, A. E., Migdisov, A., 2014. Experimental Constraints on the Transport and Deposition of Metals in Ore-Forming Hydrothermal Systems. Economic Geology Special Publication (18), 77–95.

Wolf, M. B., London, D., 1994. Apatite dissolution into peraluminous haplogranitic melts: An experimental study of solubilities and mechanisms. Geochimica et Cosmochimica Acta 58 (19), 4127–4145.

Wyllie, P. J., Cox, K. G., Biggar, G., 1962. The Habit of Apatite in Synthetic Systems and Igneous Rocks. Journal of Petrology 3 (2), 238–243.

Xu, W.-C., Zhang, H.-F., Guo, L., Yuan, H.-L., 2010. Miocene high Sr/Y magmatism, south Tibet: product of partial melting of subducted Indian continental crust and its tectonic implication. Lithos 114 (3), 293–306.

Yanites, B. J., Kesler, S. E., 2015. A climate signal in exhumation patterns revealed by porphyry copper deposits. Nature Geoscience 8 (6), 462–465.

Zagorchev, I., Moorbath, S., Lilov, P., 1987. Radiogeochronological data on the Alpine igneous activity in the western part of the Rhodope Massif. Geologica Balcanica 17 (2), 59–71.

Zhang, C., Holtz, F., Ma, C., Wolff, P. E., Li, X., 2012. Tracing the evolution and distribution of F and Cl in plutonic systems from volatile-bearing minerals: A case study from the Liujiawa pluton (Dabie orogen, China). Contributions to Mineralogy and Petrology 164 (5), 859–879.

Zhang, D., Audétat, A., 2017. What Caused the Formation of the Giant Bingham Canyon Porphyry Cu-Mo-Au Deposit? Insights from Melt Inclusions and Magmatic Sulfides. Economic Geology 112 (2), 221–244.

Zhao, K., Xu, X., Erdmann, S., 2017. Crystallization conditions of peraluminous charnockites: constraints from mineral thermometry and thermodynamic modelling. Contributions to Mineralogy and Petrology 172 (5), 1–19.

Appendices

Appendix A

Sample Inventory

This appendix contains the sample ID, GPS locality (WGS84) and rock type of all samples collected across the three field seasons.

Table A1: Sample inventory.

Table A1: Sample localities. Latitude ° N, longitude ° E in decimal degrees. TS – thin section or polished epoxy mount prepared for sample.

Sample ID	Latitude, N	Longitude, E	Location	Description	TS
September 2014					
RT14_006	40.87	25.54	Maronia	Monzonite	X
RT14_003	40.86	25.57	Maronia	Monzonite	X
RT14_007	40.87	25.53	Maronia	Massive magnetite	X
RT14_004	40.87	25.55	Maronia	Schists	X
RT14_005	40.87	25.55	Maronia	Monzonite	X
RT14_011	40.91	25.64	Perama Hill	Sandstone	X
RT14_012	40.91	25.64	Perama Hill	Sandstone	X
RT14_013	40.91	25.64	Perama Hill	Lava dome	X
RT14_001	40.93	25.61	Perama Hill	Silica lithocap	X
RT14_002	40.93	25.61	Perama Hill	Mangnese lithocap	X
RT14_027	41.00	25.74	Kassiteres	Granodiorite	X
RT14_029	41.00	25.75	Kassiteres	Aplite	X
RT14_028	41.00	25.75	Kassiteres	Diorite	X
RT14_018	41.01	25.82	Leptokaria	Quartz-feldspar porphyry	X
RT14_019	41.01	25.82	Leptokaria	Diorite	X
RT14_021	41.02	25.82	Leptokaria	Granodiorite	X
RT14_026	41.02	25.76	Leptokaria	Tonalite	X
RT14_024	41.03	25.79	Leptokaria	Diorite	X
RT14_025	41.03	25.79	Leptokaria	Gabbro	X
RT14_022	41.03	25.82	Leptokaria	Granodiorite	X
RT14_023	41.04	25.83	Leptokaria	Granodiorite	X
RT14_008	41.05	25.89	Leptokaria	Volcanics - andesite	X
RT14_030	41.06	25.86	Leptokaria	Pegmatitic granite	X
RT14_031	41.06	25.86	Leptokaria	Amphibolite	X
RT14_009	41.06	25.91	Leptokaria	Granite	X
RT14_020	41.07	25.82	Leptokaria	Porphyry intrusion	X
RT14_017	41.09	25.97	Leptokaria	Quartz monzonite	X
RT14_010	41.12	26.00	Leptokaria	Tonalite	X
RT14_015	41.14	26.04	Leptokaria	Diorite	X
RT14_016	41.14	26.04	Leptokaria	Biotite vein	X
RT14_014	41.14	26.05	Leptokaria	Diorite	X
June 2015					
KA15_001	41.01	25.75	Kassiteres	Volcaniclastic deposit	
KA15_002	41.01	25.75	Kassiteres	Diorite	
KA15_003	41.01	25.75	Kassiteres	Volcaniclastic deposit	
KA15_004	41.00	25.75	Kassiteres	Diorite	
KA15_005	41.00	25.74	Kassiteres	Volcaniclastic deposit	
KA15_006	41.00	25.74	Kassiteres	Diorite	
KA15_007	41.00	25.74	Kassiteres	Highly-altered diorite	
KA15_008	41.00	25.74	Kassiteres	Diorite	X
KA15_009	40.99	25.73	Kassiteres	Diorite	
KA15_010	40.99	25.73	Kassiteres	Volcaniclastic deposit	
KA15_011	40.99	25.75	Kassiteres	Diorite	
KA15_012	41.00	25.75	Kassiteres	Highly-altered diorite	
KA15_013	41.00	25.75	Kassiteres	Diorite	X
KA15_014	41.00	25.75	Kassiteres	Highly-altered diorite	
KA15_015	40.99	25.73	Kassiteres	Volcaniclastic deposit	
KA15_016	40.99	25.73	Kassiteres	Diorite	X
KA15_017	41.00	25.74	Kassiteres	Diorite	X
KA15_018	41.01	25.73	Kassiteres	Quartz-feldspar porphyry	
KA15_019	41.00	25.73	Kassiteres	Quartz-feldspar porphyry	
KA15_020	41.00	25.75	Kassiteres	Aplite	
LA15_001	41.07	25.91	Leptokaria	Gneiss	
LA15_002	41.06	25.91	Leptokaria	Porphyry in core complex	
LA15_007	41.07	25.83	Leptokaria	Porphyry intrsion	
LA15_008	41.06	25.90	Leptokaria	Pegmatitic granite	
LA15_009	41.07	25.90	Leptokaria	Granodiorite	
LA15_010	41.06	25.92	Leptokaria	Granodiorite	
LA15_011	41.08	25.92	Leptokaria	Pegmatitic granite	

Table A1 continued...

Sample ID	Latitude, N	Longitude, E	Location	Description	TS
LA15_020	41.06	25.91	Leptokaria	Porphyry in core complex	
LA15_021	41.06	25.91	Leptokaria	Tonalite	
LA15_022	41.06	25.91	Leptokaria	Granodiorite	
LB15_001	41.09	25.97	Leptokaria	Mafic enclave	
LB15_002	41.09	25.96	Leptokaria	Tonalite	
LB15_003	41.09	25.96	Leptokaria	Tonalite	
LB15_004	41.09	25.97	Leptokaria	Granite	
LB15_006	41.09	25.97	Leptokaria	Granite	
LB15_007	41.08	25.98	Leptokaria	Gneiss	
LC15_001	41.11	26.01	Leptokaria	Gneiss	
LC15_002	41.12	26.01	Leptokaria	Tonalite	
LC15_003	41.12	26.00	Leptokaria	Diorite	
LD15_001	41.14	26.04	Leptokaria	Gneiss	
LD15_002	41.14	26.05	Leptokaria	Gabbro	
LD15_003	41.15	26.05	Leptokaria	Quartz monzonite	
MA14_004	40.87	25.55	Maronia	Monzonite	
MA15_001	40.87	25.53	Maronia	Skarn	
MA15_002	40.87	25.53	Maronia	Skarn	
MA15_003	40.87	25.55	Maronia	Monzonite	
MA15_005	40.86	25.55	Maronia	Quartz vein	
MA15_006	40.87	25.55	Maronia	Monzonite	
MA15_007	40.87	25.55	Maronia	Monzonite	
MA15_008	40.87	25.55	Maronia	Monzonite	
MA15_009	40.86	25.57	Maronia	Hornfels	
MA15_010	40.86	25.56	Maronia	Monzonite	X
MA15_011	40.86	25.56	Maronia	Monzonite	X
MA15_012	40.86	25.56	Maronia	Monzonite	
MA15_013	40.87	25.54	Maronia	Monzonite	
MA15_014	40.87	25.54	Maronia	Monzonite	
MA15_015	40.87	25.54	Maronia	Monzonite	
MA15_016	40.87	25.54	Maronia	Monzonite	
MA15_017	40.87	25.54	Maronia	Monzonite	
MA15_018	40.87	25.54	Maronia	Pegmatitic granite	
MA15_019	40.88	25.54	Maronia	Cumulate	
MA15_020	40.88	25.54	Maronia	Monzonite	
MA15_021	40.88	25.54	Maronia	Cumulate	X
MA15_022	40.88	25.54	Maronia	Skarn	
ES15_001	41.01	25.97	Essimi	Quartz-sulphide vein	
ES15_003	41.01	25.97	Essimi	Quartz-sulphide vein	
ES15_004	41.01	25.97	Essimi	Quartz-sulphide vein	
KN15_001	41.02	25.75	Konos	Quartz-sulphide vein	
KN15_002	41.02	25.75	Konos	Quartz-sulphide vein	
PR15_001	40.99	25.84	Pagoni Rachi	Diorite	
PR15_002	41.00	25.84	Pagoni Rachi	Quartz-sulphide vein	
PR15_004	41.00	25.83	Pagoni Rachi	Quartz-sulphide vein	
PR15_005	41.00	25.83	Pagoni Rachi	Quartz-sulphide vein	
PR15_006	41.00	25.83	Pagoni Rachi	Quartz-sulphide vein	
ES15_002	41.01	25.97	Essimi	Sandstone	
ES15_005	41.01	25.97	Essimi	Quartz-sulphide vein	
ES15_006	41.01	25.97	Essimi	Quartz-sulphide vein	
KN15_003	41.02	25.75	Konos	Quartz-feldspar porphyry	
PR15_007	41.00	25.83	Pagoni Rachi	Volcaniclastic deposit	
PR15_008	41.00	25.83	Pagoni Rachi	Diorite	
PR15_009	40.99	25.83	Pagoni Rachi	Volcaniclastic deposit	
September 2016					
KS16_001	41.00	25.74	Kassiteres	Diorite	
KS16_002	41.00	25.74	Kassiteres	Diorite	
KS16_003	41.00	25.74	Kassiteres	Aplite	
KS16_004	41.00	25.74	Kassiteres	Diorite	
KS16_018	41.00	25.74	Kassiteres	Diorite	
KS16_005	41.00	25.73	Kassiteres	Diorite	

Table A1 continued...

Sample ID	Latitude, N	Longitude, E	Location	Description	TS
KS16_006	41.00	25.73	Kassiteres	Diorite	
KS16_007	41.00	25.74	Kassiteres	Quartz-feldspar porphyry	
KS16_008	41.00	25.74	Kassiteres	Quartz-feldspar porphyry	
KS16_009	41.00	25.74	Kassiteres	Quartz-feldspar porphyry	
KS16_010	41.00	25.75	Kassiteres	Diorite	
KS16_011	41.00	25.75	Kassiteres	Diorite	
KS16_012	41.00	25.74	Kassiteres	Diorite	
KS16_014	41.00	25.74	Kassiteres	Aplite	
KS16_015	41.00	25.74	Kassiteres	Aplite	
KS16_016	41.00	25.74	Kassiteres	Schists	
KS16_018	41.00	25.74	Kassiteres	Aplite	
KS16_019	41.00	25.74	Kassiteres	Diorite	
KS16_020	41.00	25.73	Kassiteres	Volcaniclastic deposit	
KS16_021	41.00	25.73	Kassiteres	Schists	
LK16_001	41.04	25.89	Leptokaria	Tonalite	
LK16_002	41.04	25.88	Leptokaria	Quartz-feldspar porphyry	
LK16_003	41.05	25.88	Leptokaria	Diorite	
LK16_004	41.06	25.91	Leptokaria	Diorite	
LK16_005	41.06	25.91	Leptokaria	Quartz-feldspar porphyry	
LK16_006	41.06	25.91	Leptokaria	Quartz-feldspar porphyry	
LK16_007	41.06	25.90	Leptokaria	Quartz-feldspar porphyry	
LK16_008	41.02	25.93	Leptokaria	Quartz-feldspar porphyry	
LK16_016	41.02	25.93	Leptokaria	Quartz-feldspar porphyry	
LK16_009	41.06	25.91	Leptokaria	Quartz-feldspar porphyry	
LK16_010	41.06	25.91	Leptokaria	Quartz-feldspar porphyry	
LK16_011	41.06	25.91	Leptokaria	Granodiorite	
LK16_012	41.06	25.91	Leptokaria	Granodiorite	
LK16_013	41.06	25.91	Leptokaria	Aplite	
LK16_014	41.06	25.91	Leptokaria	Quartz-feldspar porphyry	
LK16_016	41.02	25.93	Leptokaria	Quartz-feldspar porphyry	
MN16_001	40.88	25.57	Maronia	Schists	
MN16_002	40.88	25.58	Maronia	Quartz-feldspar porphyry	
MN16_003	40.88	25.57	Maronia	Schists	
MN16_005	40.88	25.55	Maronia	Diorite	
MN16_006	40.88	25.55	Maronia	Marble	
MN16_007	40.88	25.55	Maronia	Skarn	
MN16_008	40.88	25.55	Maronia	Diorite	
MN16_009	40.88	25.55	Maronia	Marble	
MN16_010	40.88	25.55	Maronia	Marble	
MN16_011	40.88	25.55	Maronia	Marble	
MN16_012	40.88	25.55	Maronia	Cumulate	
MN16_013	40.88	25.55	Maronia	Marble	
MN16_014	40.88	25.54	Maronia	Cumulate	
MN16_015	40.88	25.54	Maronia	Cumulate	
MN16_016	40.87	25.53	Maronia	Marble	
MN16_017	40.87	25.53	Maronia	Marble	
MN16_018	40.87	25.53	Maronia	Marble	
MN16_019	40.86	25.55	Maronia	Quartz-feldspar porphyry	
MN16_020	40.86	25.55	Maronia	Quartz-feldspar porphyry	
MN16_021	40.86	25.55	Maronia	Quartz-feldspar porphyry	
MN16_022	40.86	25.55	Maronia	Quartz-feldspar porphyry	
MN16_026	40.86	25.55	Maronia	Diorite	
MN16_027	40.86	25.55	Maronia	Quartz-feldspar porphyry	
MN16_028	40.86	25.55	Maronia	Quartz-feldspar porphyry	

Appendix B

Supplementary Material for Chapter 2

This appendix contains the supplementary material published alongside Chapter 2.

Table B1: Sample locations.
Table B2: Preferred interpretations of ID-TIMS data.

Figure B1: Cathodoluminscence images of the MMC zircons.
Figure B2: Concordia plots of ID-TIMS data reported in Chapter 2.
Figure B3: Th-correction sensitivity testing.
Figure B4: Initial $^{238}U/^{235}U$ sensitivity testing.

Sample Descriptions

Table B1: Locations (WGS84) and descriptions of each of the samples used in this study. [1] denotes samples used for geochronology, [2] samples with thin sections selected for point counting and [3] samples that do not have a whole rock analysis.

Sample ID	Location		Project	Notes (mineralogy, major phases)
	Latitude	Longitude		
KA15_004	41.005°N	25.749°E	Kassiteres	Diorite – plagioclase + clinopyroxene + hornblende + magnetite
KA15_008	40.999°N	25.740°E	Kassiteres	Diorite – plagioclase + hornblende + clinopyroxene + K-feldspar + quartz + magnetite
KA15_009	40.994°N	25.733°E	Kassiteres	Granodiorite – plagioclase + hornblende + K-feldspar + quartz + magnetite
KA15_013	40.996°N	25.748°E	Kassiteres	Granodiorite – plagioclase + hornblende + K-feldspar + quartz + magnetite
KA15_016	40.992°N	25.731°E	Kassiteres	Granodiorite – plagioclase + hornblende + K-feldspar + quartz + magnetite
KA15_017	40.996°N	25.735°E	Kassiteres	Granodiorite – plagioclase + hornblende + K-feldspar + quartz + magnetite
RT14_028[1,2]	41.005°N	25.746°E	Kassiteres	Diorite – plagioclase + hornblende + clinopyroxene + K-feldspar + quartz + magnetite
RT14_026[2]	41.021°N	25.761°E	Kassiteres	Granodiorite – plagioclase + K-feldspar + hornblende + quartz + magnetite with intense chloritisation
RT14_022[1,2]	41.035°N	25.819°E	Leptokaria	Granodiorite with propylitic alteration – plagioclase + clinopyroxene + amphibole + quartz + K-feldspar + magnetite
RT14_024[1,2]	41.027°N	25.791°E	Leptokaria	Diorite with propylitic alteration – plagioclase + clinopyroxene + chlorite + biotite + magnetite
RT14_025[3]	41.027°N	25.791°E	Leptokaria	Gabbro – intensely propylitically altered (chlorite + epidote) – relict clinopyroxene + plagioclase + magnetite
LA15_009	41.066°N	25.904°E	Leptokaria	Granodiorite – plagioclase + hornblende + clinopyroxene + quartz + magnetite
LA15_011	41.077°N	25.924°E	Leptokaria	Granite – K-feldspar + plagioclase + quartz + hornblende + biotite + clinopyroxene + magnetite
RT14_009[1,2]	41.060°N	25.911°E	Leptokaria	Granite – k-feldspar + plagioclase + quartz + hornblende + biotite + clinopyroxene + magnetite
LB15_003	41.092°N	25.961°E	Leptokaria	Tonalite – Plagioclase + quartz + hornblende + magnetite
LB15_004	41.086°N	25.972°E	Leptokaria	Granite with epidote veining – K-feldspar + quartz + plagioclase + hornblende + biotite + magnetite
LB15_006	41.085°N	25.972°E	Leptokaria	Granite with epidote veining – K-feldspar + plagioclase + quartz + hornblende + magnetite
RT14_017[2]	41.091°N	25.966°E	Leptokaria	Quartz-monzonite cumulate with epidote veining – hornblende + plagioclase + quartz + K-feldspar + magnetite
LC15_002	41.117°N	26.004°E	Leptokaria	Tonalite porphyry – plagioclase + hornblende + quartz phenocrysts
LC15_003	41.117°N	26.004°E	Leptokaria	Diorite – plagioclase + hornblende + clinopyroxene + biotite + quartz + magnetite
RT14_010[1,2]	41.117°N	26.001°E	Leptokaria	Tonalite with minor chlorite alteration – plagioclase + quartz + K-feldspar + hornblende + chlorite + magnetite
LD15_002	41.146°N	26.049°E	Leptokaria	Gabbro – clinopyroxene + orthopyroxene + hornblende + plagioclase + magnetite
LD15_003	41.146°N	26.049°E	Leptokaria	Quartz monzonite with epidote veining – K-feldspar + plagioclase + clinopyroxene + quartz + magnetite
RT15_015[2]	41.141°N	26.042°E	Leptokaria	Diorite with minor chlorite alteration – plagioclase + biotite + hornblende + magnetite
MA15_004	40.866°N	25.549°E	Maronia	Monzonite – plagioclase + clinopyroxene + orthopyroxene + biotite + K-feldspar + magnetite + quartz + secondary amphibole

Table B1 continued...

Sample ID	Location Latitude	Longitude	Project	Notes (mineralogy, major phases)
MA15_006	40.869°N	25.552°E	Maronia	Monzonite – plagioclase + clinopyroxene + orthopyroxene + biotite + K-feldspar + magnetite + quartz + secondary amphibole
MA15_007	40.869°N	25.552°E	Maronia	Monzonite – plagioclase + clinopyroxene + orthopyroxene + biotite + K-feldspar + magnetite + quartz + secondary amphibole
MA15_008	40.869°N	25.551°E	Maronia	Monzonite – plagioclase + clinopyroxene + orthopyroxene + biotite + K-feldspar + magnetite + quartz + secondary amphibole
MA15_010[1]	40.861°N	25.565°E	Maronia	Monzonite – plagioclase + clinopyroxene + orthopyroxene + biotite + K-feldspar + magnetite + quartz + secondary amphibole
MA15_011	40.860°N	25.565°E	Maronia	Monzonite – plagioclase + clinopyroxene + orthopyroxene + biotite + K-feldspar + magnetite + quartz + secondary amphibole
MA15_012	40.862°N	25.564°E	Maronia	Monzonite – plagioclase + clinopyroxene + orthopyroxene + biotite + K-feldspar + magnetite + quartz + secondary amphibole
MA15_014	40.873°N	25.540°E	Maronia	Monzonite – plagioclase + clinopyroxene + orthopyroxene + biotite + K-feldspar + magnetite + quartz + secondary amphibole
MA15_015	40.873°N	25.538°E	Maronia	Monzonite – plagioclase + clinopyroxene + orthopyroxene + biotite + K-feldspar + magnetite + quartz + secondary amphibole
MA15_016	40.872°N	25.536°E	Maronia	Monzonite – plagioclase + clinopyroxene + orthopyroxene + biotite + K-feldspar + magnetite + quartz + secondary amphibole
MA15_017	40.865°N	25.538°E	Maronia	Monzonite – plagioclase + clinopyroxene + orthopyroxene + biotite + K-feldspar + magnetite + quartz + secondary amphibole
MA15_020	40.877°N	25.538°E	Maronia	Monzonite – plagioclase + clinopyroxene + orthopyroxene + biotite + K-feldspar + magnetite + quartz + secondary amphibole
RT14_003[1,2]	40.862°N	25.565°E	Maronia	Monzonite – plagioclase + clinopyroxene + orthopyroxene + biotite + K-feldspar + magnetite + quartz + secondary amphibole
RT14_006[2]	40.867°N	25.539°E	Maronia	Monzonite – plagioclase + clinopyroxene + orthopyroxene + biotite + K-feldspar + magnetite + quartz + secondary amphibole
MN16_008[1,3]	40.879°N	25.547°E	Maronia	Monzonite – plagioclase + clinopyroxene + orthopyroxene + biotite + K-feldspar + magnetite + quartz + secondary amphibole
MN16_005[1,3]	40.879°N	25.554°E	Maronia	Monzonite – plagioclase + clinopyroxene + orthopyroxene + biotite + K-feldspar + magnetite + quartz + secondary amphibole

U-Pb Geochronology

This section of the supplementary material covers a detailed outline of sample selection, analytical procedure and data interpretation of the CA-ID-TIMS (Chemical Abrasion Isotope Dilution Thermal Ionisation Mass Spectrometry) U-Pb in zircon geochronology.

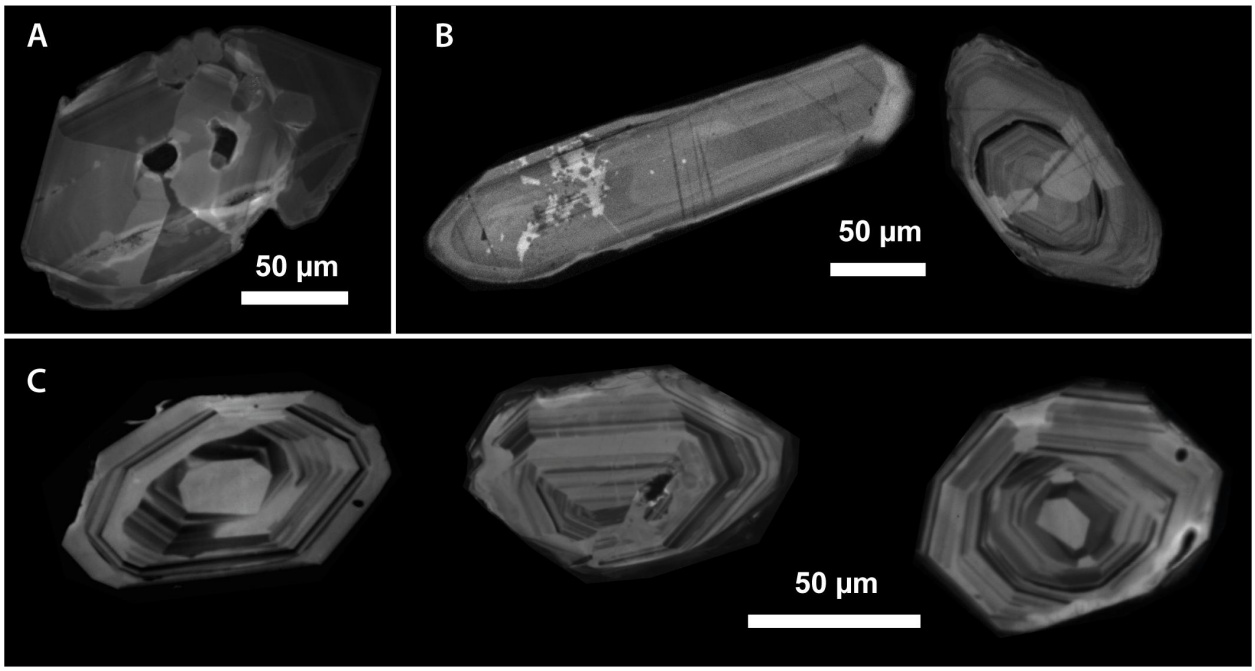

Figure B1: Representative cathodoluminescence (CL) images of zircons from the MMC. Zircons range in size from 250 to 75 μm, are typically euhedral and show simple oscillatory and sector zoning with little evidence of magmatic resorption or inheritance in all samples. (A) Maronia: Zircons have abundant inclusions of apatite or melt. (B) Kassiteres: Zircons commonly show evidence of hydrothermal fluid activity e.g. the mottled white texture in the left zircon. (C) Leptokaria: Zircons are typically very simple.

Dating Methods

Cathodoluminescence Imagery and Crystal Selection

A total of nine samples were collected from the Maronia Magmatic Corridor (MMC) for geochronology in this study, five from the Kassiteres–Leptokaria magmatic suite and four from the Maronia plutonic complex. Over 3 kg of rock was collected for each sample to provide sufficient material for zircon mineral separation. Samples were crushed, sieved, rinsed and density separated following standard procedures at the University of Bristol. Individual zircon crystals were picked from the 50–250 μm size fraction (20–50 for each sample).

After crystal selection, the remaining zircons were mounted in epoxy resin and polished for scanning electron microscope (SEM) work. Cathodoluminscence (CL) imaging revealed simple zoning patterns in most all of the zircons from the MMC pluton samples (Fig. B1). Oscillatory and sector zoning in the zircon crystals reflect a single zircon crystallisation event in each of the plutons with no evidence of zircon resorption or inheritance reflecting multiple period of crystallisation.

Chemistry, Mass Spectrometry and Corrections

Zircons selected for analysis were chemically abraded following a modified procedure from Mattinson, (2005) to remove damaged parts of the crystal that were likely to have experienced open-system behaviour. Firstly, the zircons were thermally annealed at 900 °C for 60 hours in quartz crucibles before being individually selected, photographed and loaded into FEP Teflon beakers. Single zircon crystals, or fragments, were selected for dissolution using transmitted light microscopy. Zircons were selected based

upon their external morphology and observation of internal feature (i.e., visible cores).

Zircons were then refluxed in 4 M HNO_3 on a hotplate at 120 °C for $>$ 2 hours, followed by ultrasonic cleaning for at least 20 minutes. The zircon crystals were rinsed with acetone and 4 M HNO_3 and loaded into individual 300 μl FEP Teflon microcapsules and leached in 29 M HF inside a Parr vessel (a self-sealing stainless-steel jacket) for 12 hours at 180 °C. The zircons were rinsed with 4 M HNO_3 and refluxed in 6 M HCl at 120 °C for 2-5 hours, before a final rinsing with 4 M HNO_3 several times.

The leached zircons and all total procedural blanks were spiked with mixed ^{205}Pb–^{233}U–^{235}U (ET535) EARTHTIME tracer solution and dissolved in ∼150 μl 29 M HF and trace HNO_3 in a Parr vessel at 220 °C for at least 60 hours. Complete dissolution was checked by visual inspection of some larger crystals and assumed for smaller grains, following standard protocol for dissolution at NIGL. The solutions were dried down as fluorides and re-dissolved in 3 M HCl in a Parr vessel overnight at 180 °C. U and Pb fractions were isolated by a HCl-based anion exchange procedure using Bio-Rad AG-1 resin in Teflon columns. Pb and U fractions were then recombined and dried down with 10 μl of H_3PO_4. The dried samples were then loaded onto zone-refined Re filaments in a silica gel matrix to enhance ionisation (after Gerstenberger & Haase, 1997).

Isotope ratios were measured on a Thermo-Electron Triton thermal ionisation mass spectrometer (TIMS). Pb was measured in dynamic mode on a MassCom secondary electron multiplier; Pb mass bias corrections were made using a fractionation factor of 0.14 $\pm$ 0.02 %/amu (1 σ) for samples spiked using ET535. Dead-time and linearity of the secondary electron multiplier were monitored using repeated analyses of the standards NBS 982, NBS 981 and U 500. U oxide (UO_2) was measured, and corrected for isobaric interferences using a ^{18}O/^{16}O value of 0.00205 (IUPAC value and measured in-house at NIGL). U was measured in dynamic mode and a mass bias fractionation correction calculated in real-time using the ^{233}U–^{235}U ratio of the ET535 tracer solutions (Condon et al., 2015). Corrections for the addition of Pb and U during the procedure (i.e., laboratory contamination) were made using the long-term measured isotopic composition and variability of blanks using an amount that is based upon contemporary total procedural blanks. The U/Pb ratio for each analyses was determined via isotope dilution principles and the ET535 mixed ^{205}Pb–^{233}U–^{235}U tracer (Condon et al., 2015; McLean et al., 2015). A ^{238}U/^{235}U value of 137.818 (Hiess et al., 2012) was assumed and used in the data reduction algorithm.

U-Pb Data, Corrections and Assessment

Once the radiogenic isotopic compositions (^{206}Pb/^{238}U and ^{207}Pb/^{235}U) have been determined for a given analysis/zircon a number of factors must be considered prior to geochronological interpretation (i.e., age assignment).

Initial ^{230}Th disequilibrium. Due to the slightly larger ionic radius of Th the intermediate daughter ^{230}Th is excluded during zircon crystallisation such that a correction is required to account for ^{230}Th disequilibrium and resulting in deficit ^{206}Pb (e.g. Schrer 1984; Parrish 1990). This disequilibrium correction requires *a priori* knowledge of the Th/U of the magma coexisting with the crystal during growth. A sensitivity analysis of the choice of Th/U ratio in the Th-correction shows an inverse exponential relationship between the magnitude of the Th-correction and Th/U ratio that plateaus between Th/U = 3-4 (Figure B1). It is not possible to account for the excess ^{207}Pb by the Th-correction alone. The whole rock Th/U ratio of the full MMC suite varies between 3 and 5.5. A value of Th/U = 3.5 was selected for the Th-correction in this study.

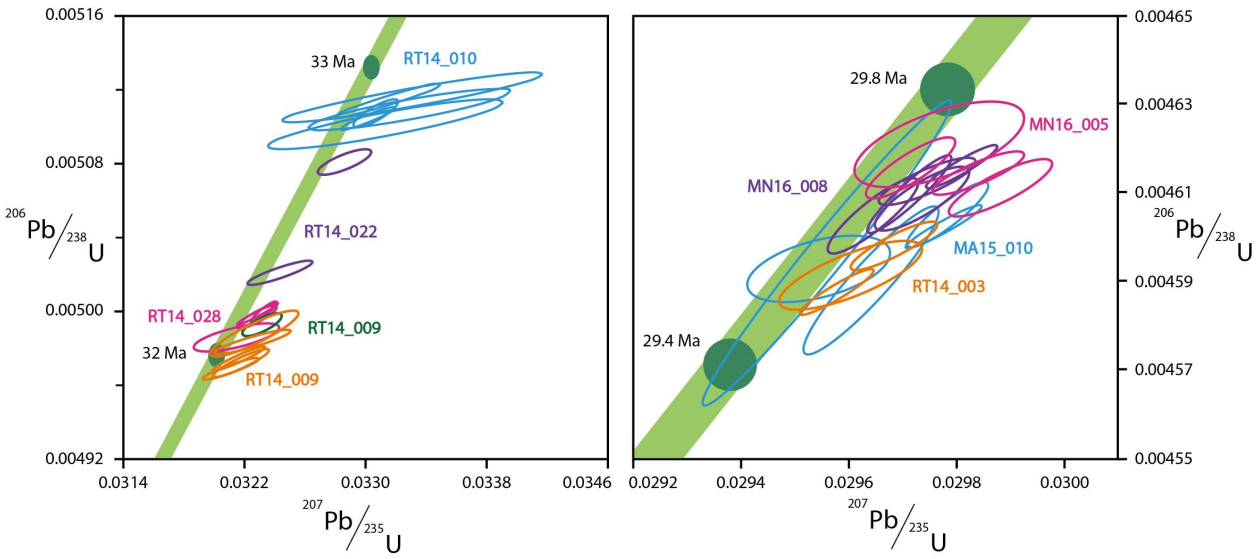

Figure B2: Concordia plot of the Kassiteres–Leptokaria samples (left) and the Maronia samples (right). Note the horizontal translation of the data points off Concordia with excess ^{207}Pb.

Concordance of U-Pb system. Once this correction has been applied it is noticeable that in general the U-Pb are discordant with ^{207}Pb/^{235}U dates $>$ ^{206}Pb/^{238}U dates (Figure B1). The U-Pb analyses from the MMC plot off Concordia in some, if not all analyses, from 8 out of 9 samples. The discordance could reflect either excess ^{207}Pb and/or lost ^{235}U or inheritance. In the case of inheritance of an older zircon core, the data would plot on a chord intersecting Concordia an older age (e.g. the xenocrystic zircons from RT14_025). However, the deviation from Concordia of most all data is a horizontal translation of the analyses interpreted as autocrystic youngest zircons. We consider what could be causing this.

An initial ^{238}U/^{235}Uratio is also assumed in Concordia. A value of ^{238}U/^{235}U= 137.818 $\pm$ 0.045, representative of 'bulk Earth', is commonly used in U-Pb calculations (Hiess et al., 2012). A sensitivity analysis of the ^{238}U/^{235}U within the measured terrestrial range 137.772–137.908 (Hiess et al., 2012) found that the initial assumed ^{238}U/^{235}U cannot account for excess ^{207}Pb observed in the discordant data (Figure B2). The 'bulk Earth' value of ^{238}U/^{235}U = 137.818 $\pm$ 0.045 has been used in this study.

We do not consider that the laboratory procedure introduced a systematic or random bias into the analyses as the data were collected in numerous sessions of column chemistry and mass spectrometer analysis over a number of years at NIGL. The high Pb*/Pbc ratios indicate this is not a likely cause of the discordance, and a sensitivity analyses confirms this (i.e., a non-terrestrial Pbc composition would be required). Furthermore, such discordance is not observed in other similar age zircons made following the same laboratory protocol conducted at NIGL and with lower Pb*/Pbc (Sahy et al., 2015).

Previous work has encountered similar ^{207}Pb excess which cannot be accounted for by assumptions in the data reduction or by laboratory procedure (e.g. Crowley et al., 2007). The discordance has been attributed to initial Pa/U disequilibrium from the partitioning of excess Pa into the zircon, which is significant only in very reduced or young (Cenozoic) systems (e.g. Schmitt 2007). Crowley et al., (2007) attribute the 52,000 yr bias between their ^{206}Pb/^{238}U and ^{207}Pb/^{235}U dates of the Bishop Tuff to Pa/U disequilibrium and suggest that similar variations could be observed in rocks $<$ 10 Ma. We suggest that Pa/U disequilibrium is accountable for the average 23,000 yr difference between ^{206}Pb/^{238}U and ^{207}Pb/^{235}U dates. To conclude,

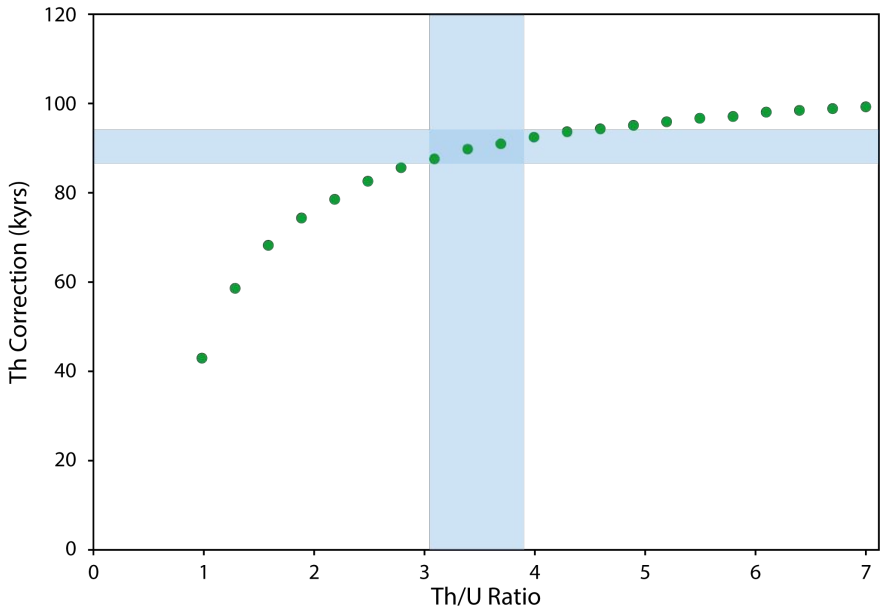

Figure B3: A sensitivity test of the magnitude of the Th-correction with varying Th/U ratio. In order to match the discordance observed in the data a large Th-correction is needed to account for excess ^{207}Pb compared to ^{206}Pb. There is an inverse exponential relationship between Th/U ratio and the magnitude of the Th-correction which plateaus at a Th-correction of 90 kyrs when Th/U $>$ 3. Therefore, the discordance in the data ($>$ 100,000 kyrs for each sample) cannot be accounted for solely by changing the Th/U ratio.

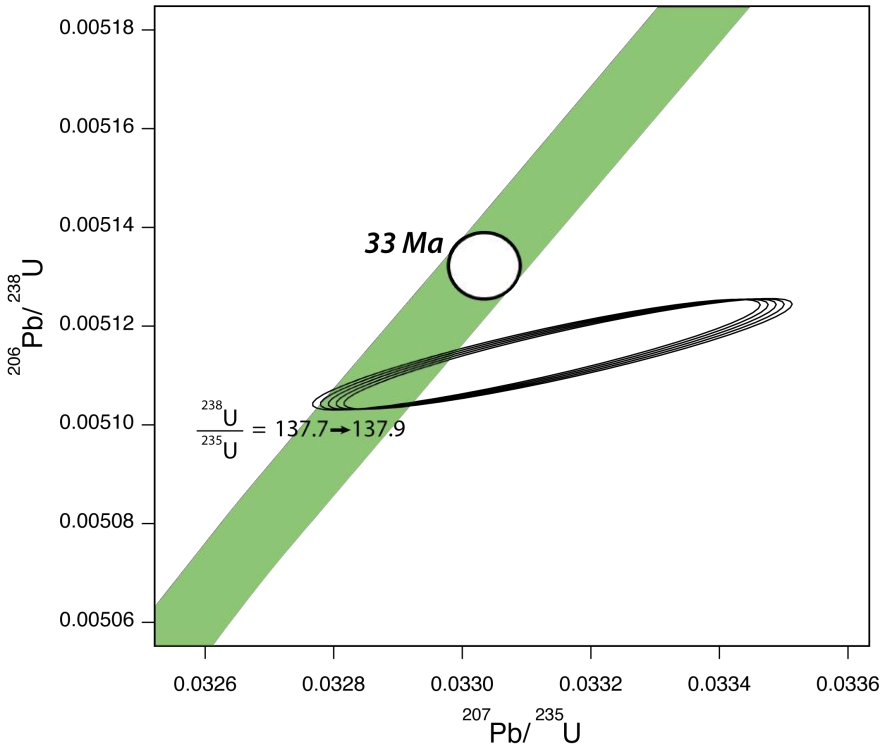

Figure B4: Sensitivity test of the ^{238}U/^{235}U ratio and the concordance of the ^{207}Pb/^{235}U and ^{206}Pb/^{238}U ages, a concordant analysis would lie on the green Concordia line (with decay constant uncertainty). Increasing the ^{206}Pb/^{238}Uratio used can horizontally shift the data points away from Concordia affecting only the ^{207}Pb/^{235}U age. However, the magnitude of this shift is small and cannot account for the discordance seen in our dataset.

we believe that this discordance between the $^{207}Pb/^{235}U$ and $^{206}Pb/^{238}U$ is real and proceed to interpret the (^{230}Th corrected) $^{206}Pb/^{238}U$ dates as being geologically meaningful as they are unaffected by the ^{207}Pb from Pa disequilibrium.

Zircon U-Pb Data Interpretation

Date – the calculated time since closure of a system in a single analysis.

Age – the geological interpretation of a collection of dates from a single sample and represents the final interpretation of the timing of a geological event.

U-Pb in zircon is a long-lived radiogenic isotopic geochronometer that is used across geological disciplines to constrain the timing of geological events. In plutonic systems, the U-Pb system is used to date crystallisation of zircon from the magma as the closure temperature of the isotopic systems is $\sim$ 900 °C, well above the zircon saturation temperature of most evolved magmatic systems. In order to constrain the final stages of pluton crystallisation, the time of emplacement, the youngest zircon from the system would ideally be dated. In the absence of dating all of the zircons from a single plutonic system to constrain emplacement, the youngest analysis or cluster of analyses (i.e. $^{206}Pb/^{238}U$ dates), is frequently interpreted as the crystallisation age of the magmatic system. Older dates from the same sample are interpreted as antecrystic, reflecting the lifespan of the magmatic system with crystallisation occurring over a period of 10,000s to 100,000s yrs prior to final emplacement (e.g. von Quadt et al., 2011). If the youngest, single, zircon date is used to interpret the pluton emplacement with a 95 % confidence level then in 1 out of 20 scenarios the actual age of zircon will fall outside of the given value. In order to combat this, populations of zircons are used and rely on the reproducibility of analyses to reduce the uncertainty associated with data interpretation.

Below we outline the multiple interpretations of the analyses of each sample from this study and show that to the degree the data is interpreted in this study, the choice of interpretation makes little difference for most samples. In general, our approach is to derive a sample age based upon a weighted mean (Th-corrected) $^{206}Pb/^{238}U$ date derived from the youngest coherent population. This allows for ages to be based upon reproduced $^{206}Pb/^{238}U$ and not a single analysis. The coherence of a dataset was decided based upon the MSWD (mean square weighted deviation – a chi–squared statistical test; Wendt & Carl 1991) where values exceeding that expected for the given sample size indicate excess scatter and the likely presence of pre-eruptive zircon.

The Kassiteres–Leptokaria Magmatic Suite

Five samples were selected for U-Pb geochronology from the Kassiteres–Leptokaria Magmatic Suite to represent intra-system variability in crystallisation ages and estimate the lifespan of magmatic system. Autocrystic zircon analyses, those interpreted to reflect the final stages of crystallisation, range in age from 32.03 to 32.98 Ma suggested pulsed magma accumulation and crystallisation in the Kassiteres – Leptokaria system over a period of at least 1 Myrs.

Analyses of RT14_009 range between 32.10 and 32.30 Ma ($^{206}Pb/^{238}U$ dates, n = 7). There are three interpretations of these analyses: *(i)* the samples represent a single population with an interpreted geological age of 32.225 $\pm$ 0.036 (MSWD = 5.2, n = 7), however, the MSWD is too high (if n = 7, MSWD $<$ 2.26

at 22σ confidence levels) to represent a statistically significant population indicating over-dispersion of the data; *(ii)* the youngest analysis represents a maximum age of final crystallisation of the intrusion of 32.14 $\pm$ 0.04 Ma; *(iii)* as all the analyses overlap within error, our favoured approach is to exclude the outlying youngest analysis and interpret a geological age of 32.235 $\pm$ 0.026 Ma (MSWD = 2.2, n = 6).

Analyses of RT14_010 range between 32.82 and 33.05 Ma ($^{206}Pb/^{238}U$ dates, n = 6). Our favoured interpretation of these analyses is that the data represent a single population of zircons with an interpreted $^{206}Pb/^{238}U$ geological age of 32.932 $\pm$ 0.034 Ma (MSWD = 2.9, n = 6); the MSWD is fractionally too high indicating mild over-dispersion of the data (if n = 6, MSWD $<$ 2.41 at 2σ confidence levels). An alternative approach would be to reject the older two analyses as an antecrystic zircons and interpret a youngest population with a geological age of 32.917 $\pm$ 0.021 Ma (MSWD = 0.87, n = 4).

Analyses of RT14_022 range between 36.05 and 32.35 Ma ($^{206}Pb/^{238}U$ dates, n = 3). The anomalously old date calculated for one of these zircon analyses (35.94 $\pm$ 0.11 Ma) suggests an xenocrystic origin of the single zircon reflecting transport and entrainment of crystals from greater crustal depths in the magmatic system during magma emplacement, a process well documented in complex plutonic systems (e.g. Samperton et al., 2015). The intermediate analysis is likely from an antecrystic zircon whilst the youngest zircon represents a maximum age of final pluton crystallisation at 32.38 $\pm$ 0.03 Ma.

A total of four analyses were made of RT14_025, all the analyses lie off Concordia with excess ^{207}Pb. Two highly discordant dates are significantly older at 97.99 $\pm$ 0.09 and 48.45 $\pm$ 0.06 Ma, thus are interpreted to be xenocrystic zircons inherited from a much earlier phase of crystallisation in the magmatic system. The youngest analysis is likely an autocrystic zircon and can thus be interpreted as a maximum age of final crystallisation at 32.06 $\pm$ 0.07 Ma.

Analyses of RT14_028 range between 32.00 and 32.21 Ma ($^{206}Pb/^{238}U$ dates, n = 5). One interpretation of these analyses would be that the data represent a single population of zircons with an interpreted $^{206}Pb/^{238}U$ geological age of 32.069 $\pm$ 0.054 (MSWD = 5.4, n = 5), however the MSWD indicates over-dispersion of the data, i.e. they do not represent a statistically significant population (if n = 5, MSWD $<$ 2.63 at 2σ confidence levels). We interpret a youngest population of zircons as representative of pluton emplacement with a geological age of 32.045 $\pm$ 0.020 Ma (MSWD = 1.15, n = 3).

The Maronia Plutonic Complex

Four samples of the Maronia monzonite were dated and show a strong clustering of autocrystic zircon ages ranging from 29.52 to 29.84 Ma ($^{206}Pb/^{238}U$ dates, n = 17).

Analyses of RT14_003 range between 29.69 and 29.56 Ma ($^{206}Pb/^{238}U$ dates, n = 3). An interpretation of these analyses would be that the data represent a single population of zircons with an interpreted $^{206}Pb/^{238}U$ geological age of 29.619 $\pm$ 0.093 (MSWD = 5.8, n = 3), however the MSWD indicates over-dispersion of the data (if n = 3, MSWD $<$ 3.83 at 2σ confidence levels). Our favoured approach is to reject the oldest analysis as antecrystic and interpret the youngest two analyses as representative of pluton emplacement with a geological age of 29.619 $\pm$ 0.093 Ma (MSWD = 0.79, n = 2).

Analyses of MA15_010 range between 29.52 and 29.74 Ma ($^{206}Pb/^{238}U$ dates, n = 5). Our interpretation of these analyses is that the data represent a single population of zircons with an interpreted $^{206}Pb/^{238}U$ geological age of 29.666 $\pm$ 0.044 Ma (MSWD = 2.9, n = 5); however the MSWD is slightly high indicating

mild over-dispersion of the data (if n = 5, MSWD $<$ 2.63 at 2σ confidence levels). An alternative approach would be reject the two oldest analyses as antecrystic and interpret the remaining three analyses as representative of pluton emplacement with a geological age of 29.617 $\pm$ 0.035 Ma (MSWD = 0.044, n = 3). Both of these interpretations overlap within uncertainty and reflect the robustness of age assignment to variable selection of data for age calculation. Our preferred age is based upon the youngest three $^{206}Pb/^{238}U$ dates.

Analyses of MN16_008 range between 29.66 and 29.80 Ma ($^{206}Pb/^{238}U$ dates, n = 5). Our interpretation of these analyses is that the data represent a single population of zircons with an interpreted $^{206}Pb/^{238}U$ geological age of 29.743 $\pm$ 0.030 Ma (MSWD = 2.0, n = 5). An alternative approach is to select the younger analyses as a zircon crystal population representing of final pluton crystallisation with a geological age of 29.720 $\pm$ 0.024 Ma (MSWD = 0.64, n = 3).

Analyses of MN16_005 range between 29.71 and 29.84 Ma ($^{206}Pb/^{238}U$ dates, n = 4) and are concordant within error. These analyses can be interpreted as a single population cluster with a geological age of 29.762 $\pm$ 0.017 Ma (MSWD = 0.84, n = 4).

Preferred Interpretations

Table B2: Our preferred interpretations of the geological age. Uncertainties: x – analytical uncertainty in the measurements for comparison with other U-Pb data measured within the EARTHTIME framework; y – total uncertainty for comparison of the ages with ages from other isotope systems.

Sample ID	Geological Age (Ma)	*x uncertainty*	*y uncertainty*	Preferred Interpretation
RT14_010	32.932	$\pm$ 0.034	$\pm$ 0.039	Weighted mean of single population
RT14_009	32.235	$\pm$ 0.026	$\pm$ 0.031	Youngest population of zircons (n = 6, n = 7)
RT14_025	32.06	$\pm$ 0.07	$\pm$ 0.07	Youngest single zircon age
RT14_022	32.38	$\pm$ 0.03	$\pm$ 0.03	Youngest single zircon age
RT14_028	32.045	$\pm$ 0.020	$\pm$ 0.027	Youngest population of zircons (n = 3, n = 5)
MN16_008	29.72	$\pm$ 0.024	$\pm$ 0.034	Weighted mean of single population
MN16_005	29.762	$\pm$ 0.017	$\pm$ 0.034	Weighted mean of single population
RT14_003	29.596	$\pm$ 0.022	$\pm$ 0.027	Youngest population of zircons (n = 2, n = 3)
MA15_010	29.616	$\pm$ 0.035	$\pm$ 0.047	Weighted mean of single population

Comparison between Rb-Sr and U-Pb ages

Comparing Rb-Sr and U-Pb ages introduces two additional levels of uncertainty than when comparing ages in the same isotopic system: 1) the uncertainty in our analytical understanding of each system (e.g. the decay constant) and, 2) the uncertainty in the geological interpretation of the ages. The first is an uncertainty associated with turning the measured isotope ratios in a date and can be accounted for in the uncertainty reported with an age. In Table B2, the U-Pb zircon ages are reported with two levels of uncertainty where x – analytical uncertainty in the measurement and can be used for comparison within this dataset and other U-Pb data measured within the EARTHTIME (Condon et al., 2015; McLean et al., 2015); and y – total uncertainty in the measurement including the EARTHTIME tracer uncertainty and the decay constant uncertainty and can be compared with other decay systems e.g. Rb-Sr biotite geochronology.

The uncertainty in the geological interpretation of ages between isotopic systems is more difficult to quantify. The U-Pb isotope system has a closure temperature of $\sim$ 900 °C which is greater than the zircon saturation

temperature of most intermediate to felsic magma systems (800–750 °C), consequently, the U-Pb isotope system in zircon is widely interpreted as closed from crystallisation and thus dates zircon crystallisation. In most magmatic systems, an additional interpretation that the youngest autocrystic age of a sample represents final crystallisation of the pluton is made. In contrast, the closure temperature of the Rb-Sr isotope system in biotite is more difficult to constrain and is quoted between 300–400 °C depending on the cooling rate (e.g. Jenkin et al., 2001). This means that a Rb-Sr age dates the timing of magmatic cooling rather than magmatic crystallisation. Consequently, the U-Pb and Rb-Sr isotope systems are dating two different geological events which makes Rb-Sr and U-Pb ages incomparable beyond the logical conclusion that the cooling (Rb-Sr) age of a system should be younger than the crystallisation (U-Pb) age of that same system. The Rb-Sr biotite ages presented by Del Moro et al., (1988) are remarkably close to the U-Pb zircon ages presented in this study despite much greater uncertainty in the age including the uncertainty in geological interpretation which is not accounted for in the published errors.

Appendix C

Whole Rock Geochemistry Data from the Maronia Magmatic Corridor

This appendix contains all of the whole rock geochemistry results for the Maronia Magmatic Corridor. Samples were analysed following the UKAS Accreditation Schedule using wavelength dispersive-X-ray fluorescence spectrometry (WD-XRFS) on fused glass beads for major and minor element oxides, Na_2O_2 fusion inductively coupled plasma-mass spectrometry (ICP-MS) for minor and trace element concentrations, and an aqua regia digest ICP-MS for Sc and Te.

Table C1: Full whole rock geochemistry data.

Table C2: % difference between repeat analyses, average % difference and estimated 2σ uncertainty (relative).

Table C1: Oxides reported as wt% and elements reported as ppm.

Sample	System	SiO_2	TiO_2	Al_2O_3	Fe_2O_2'	Mn_3O_4	MgO	CaO	Na_2O	K_2O	P_2O_5	F	Cl	LOI	Total	Sc	V	Cr	Co
KA15-002	Kassiteres	58.88	0.69	15.45	5.13	0.10	4.88	7.78	4.34	0.59	0.16	<0.1	<0.1	2.02	100.15	3.75	174	107	12.7
KA15-004	Kassiteres	55.42	0.75	14.44	7.82	0.15	7.05	7.25	2.53	2.27	0.24	<0.1	<0.1	1.64	99.84	1.97	217	225	30.0
KA15-005	Kassiteres	63.60	0.71	22.14	1.20	0.01	0.44	2.18	3.10	0.79	0.01	<0.1	<0.1	5.48	99.69	9.70	73	19	3.3
KA15-008	Kassiteres	56.86	0.77	14.87	7.38	0.16	6.16	6.28	2.51	2.63	0.19	<0.1	<0.1	1.84	99.89	4.43	192	240	35.8
KA15-008	Kassiteres	56.97	0.74	14.90	7.40	0.16	6.23	6.30	2.52	2.65	0.19	<0.1	<0.1	1.74	100.05	4.17	189	233	34.8
KA15-009	Kassiteres	59.45	0.74	14.64	6.72	0.10	5.25	5.53	2.81	2.74	0.17	<0.1	<0.1	1.65	99.99	3.70	157	199	22.0
KA15-019	Kassiteres	77.66	0.24	12.17	0.30	0.02	0.42	0.05	0.17	6.61	0.02	<0.1	<0.1	1.49	99.34	0.46	18	6	0.5
KA15-010	Kassiteres	69.72	0.48	15.59	1.30	0.02	0.35	0.19	0.67	8.67	0.12	<0.1	<0.1	2.22	99.48	3.92	91	8	0.8
KA15-013	Kassiteres	61.11	0.65	15.99	6.09	0.06	3.10	5.22	3.18	2.78	0.14	<0.1	<0.1	1.46	99.92	2.41	159	32	19.7
KA15-016	Kassiteres	59.10	0.65	16.09	6.67	0.11	3.77	5.32	3.01	3.07	0.16	<0.1	<0.1	1.67	99.80	7.46	186	79	18.2
KA15-017	Kassiteres	59.19	0.70	14.20	6.19	0.11	6.16	5.66	2.67	3.19	0.16	<0.1	<0.1	1.56	100.02	3.11	191	258	27.3
KA15-018	Kassiteres	78.81	0.25	13.15	0.40	0.02	0.51	0.05	<0.05	3.62	0.02	<0.1	<0.1	2.33	99.20	0.36	25	7	0.3
KA15-019	Kassiteres	77.80	0.25	12.08	0.30	0.02	0.41	0.05	0.16	6.56	0.02	<0.1	<0.1	1.53	99.37	0.45	19	6	0.4
KA15-020	Kassiteres	70.65	0.24	15.09	1.67	0.04	0.84	0.86	6.13	2.54	0.09	<0.1	<0.1	0.90	99.15	1.71	42	9	4.5
RT14-028	Kassiteres	55.70	0.81	15.09	7.48	0.15	6.81	7.48	2.82	2.59	0.19	<0.1	<0.1	0.87	100.31	2.85	199	234	30.1
RT14-028	Kassiteres	55.30	0.80	14.96	7.37	0.15	6.76	7.39	2.75	2.55	0.19	<0.1	<0.1	0.99	99.51	3.22	199	223	28.4
LA15-008	Leptokaria	62.58	0.63	15.32	5.53	0.12	3.39	4.76	3.25	2.81	0.15	<0.1	<0.1	1.23	99.91	4.04	151	72	17.3
LA15-009	Leptokaria	53.79	0.75	14.65	6.85	0.22	6.31	7.51	1.86	2.03	0.16	<0.1	<0.1	5.77	100.12	13.67	189	276	29.4
LA15-009	Leptokaria	53.80	0.74	14.64	6.85	0.22	6.35	7.51	1.81	2.02	0.16	<0.1	<0.1	5.66	99.98	14.53	176	271	27.3
LA15-010	Leptokaria	72.35	0.13	14.08	1.81	0.07	2.76	2.08	4.55	0.26	0.10	<0.1	<0.1	1.69	99.97	0.35	13	5	9.0
LA15-011	Leptokaria	69.73	0.39	15.05	2.99	0.07	1.15	0.90	2.14	5.56	0.08	<0.1	<0.1	1.96	100.22	3.41	61	10	5.5
LA15-020	Leptokaria	63.44	0.67	15.44	4.86	0.21	5.43	2.53	2.61	1.35	0.13	<0.1	<0.1	3.45	100.34	7.60	113	136	22.8
LA15-021	Leptokaria	74.20	0.11	15.22	0.46	0.03	0.48	2.79	5.00	0.31	<0.01	<0.1	<0.1	0.88	99.54	0.48	6	0	1.0
LB15-003	Leptokaria	50.39	1.02	19.50	8.59	0.23	5.68	9.47	3.07	0.55	0.23	<0.1	<0.1	1.21	100.09	6.59	276	27	29.0
LB15-004	Leptokaria	67.63	0.36	15.63	3.58	0.08	1.45	3.87	3.49	2.83	0.10	<0.1	<0.1	0.67	99.82	2.72	71	6	6.5
LB15-005	Leptokaria	69.39	0.31	14.97	3.08	0.06	1.21	3.61	3.50	2.74	0.08	<0.1	<0.1	0.93	100.02	3.01	65	6	5.9
LB15-006	Leptokaria	62.38	0.62	17.63	3.88	0.11	2.58	5.61	4.89	0.68	0.16	<0.1	<0.1	1.18	99.84	2.45	146	5	8.2
LB15-007	Leptokaria	53.92	0.83	17.49	8.84	0.17	4.70	8.13	3.02	0.97	0.14	<0.1	<0.1	1.62	99.95	8.11	252	15	23.2
LC15-002	Leptokaria	60.38	0.73	17.37	6.65	0.17	2.73	5.05	3.12	2.30	0.17	<0.1	<0.1	1.30	100.12	8.43	161	8	16.6
LC15-003	Leptokaria	64.73	0.50	15.97	5.16	0.12	2.19	4.30	3.28	2.85	0.12	<0.1	<0.1	0.80	100.16	4.99	121	6	12.0
LD15-002	Leptokaria	53.20	0.84	18.03	9.21	0.19	4.58	8.43	2.86	1.24	0.11	<0.1	<0.1	0.91	99.77	11.24	306	22	28.4
LD15-003	Leptokaria	52.97	0.76	19.26	8.37	0.18	4.13	8.85	2.98	1.18	0.15	<0.1	<0.1	0.81	99.79	5.20	235	9	23.1
RT14-009	Leptokaria	60.24	0.73	16.39	6.23	0.10	3.37	5.91	3.72	2.04	0.16	<0.1	<0.1	1.14	100.20	2.66	148	28	14.6
RT14-009	Leptokaria	59.75	0.72	16.29	6.18	0.11	3.34	5.86	3.61	2.01	0.16	<0.1	<0.1	1.14	99.35	2.71	158	30	14.8
RT14-010	Leptokaria	67.34	0.40	15.37	4.15	0.10	1.55	2.86	2.99	3.21	0.09	<0.1	<0.1	1.55	99.76	4.23	80	8	7.2
RT14-010	Leptokaria	67.10	0.40	15.39	4.05	0.09	1.54	2.85	2.99	3.21	0.09	<0.1	<0.1	1.67	99.52	4.38	79	10	7.0

Table C1 continued...

Sample	System	SiO_2	TiO_2	Al_2O_3	$Fe_2O_2^t$	Mn_3O_4	MgO	CaO	Na_2O	K_2O	P_2O_5	F	Cl	LOI	Total	Sc	V	Cr	Co
RT14-015	Leptokaria	53.60	0.84	18.15	9.09	0.18	4.54	7.98	2.81	1.30	0.12	<0.1	<0.1	1.27	100.02	5.74	290	18	23.9
RT14-015	Leptokaria	53.34	0.83	18.09	9.00	0.18	4.52	7.92	2.75	1.29	0.12	<0.1	<0.1	1.37	99.56	6.08	281	21	22.2
RT14-017	Leptokaria	48.27	1.13	20.64	9.95	0.17	4.28	10.74	2.51	0.89	0.13	<0.1	<0.1	0.94	99.80	15.89	302	6	24.6
RT14-022	Leptokaria	58.90	0.71	15.69	6.71	0.16	3.95	3.82	3.01	3.74	0.15	<0.1	<0.1	2.22	99.26	8.48	174	72	19.4
RT14-024	Leptokaria	56.14	0.63	13.63	8.48	0.14	6.60	6.90	2.62	3.02	0.19	<0.1	<0.1	1.32	99.85	3.27	188	233	30.1
MA15_015	Maronia	51.16	0.88	15.89	9.94	0.18	6.31	9.58	2.61	2.62	0.61	<0.1	<0.1	0.17	100.24	6.41	272	83	35.7
MA15_022	Maronia	52.52	0.87	13.08	8.70	0.16	6.62	9.03	2.19	4.22	0.56	<0.1	<0.1	1.73	100.01	5.78	234	130	33.8
MA15-001	Maronia	42.16	0.66	12.28	8.97	0.20	1.14	27.59	0.95	1.44	0.02	<0.1	<0.1	4.10	99.58	3.36	48	24	6.2
MA15-003	Maronia	74.78	0.25	13.97	1.31	0.02	0.17	0.15	2.14	5.29	0.05	<0.1	<0.1	1.26	99.47	0.60	25	14	0.3
MA15-004E	Maronia	50.41	1.19	15.56	6.97	0.21	7.78	12.83	2.61	1.74	0.19	<0.1	<0.1	0.35	100.06	5.57	278	192	29.9
MA15-004H	Maronia	55.27	0.85	16.26	7.35	0.14	4.17	7.04	2.87	4.29	0.50	<0.1	<0.1	0.29	99.31	6.63	197	60	23.1
MA15-006	Maronia	50.41	1.07	16.04	9.99	0.20	5.80	9.68	2.53	2.71	0.64	<0.1	<0.1	0.13	99.50	5.43	272	79	32.9
MA15-007	Maronia	51.10	0.92	15.16	9.35	0.17	7.06	10.19	2.42	2.22	0.59	<0.1	<0.1	0.35	99.79	6.44	256	193	33.8
MA15-008	Maronia	52.11	0.87	15.24	8.76	0.17	6.62	9.66	2.49	2.75	0.57	<0.1	<0.1	0.08	99.60	4.92	242	163	32.8
MA15-010	Maronia	52.91	0.98	16.69	9.16	0.17	4.75	8.28	2.80	3.07	0.47	<0.1	<0.1	0.57	100.11	3.17	249	34	29.4
MA15-011	Maronia	54.71	0.90	16.55	8.24	0.17	4.06	7.25	2.89	3.50	0.42	<0.1	<0.1	0.52	99.47	3.44	172	25	25.0
MA15-012	Maronia	53.32	0.96	16.89	8.77	0.17	4.55	7.89	2.86	3.24	0.46	<0.1	<0.1	0.42	99.80	4.93	249	35	28.2
MA15-014	Maronia	55.57	0.85	16.08	7.57	0.14	4.15	6.57	2.83	4.68	0.56	<0.1	<0.1	-0.04	99.27	6.35	196	70	24.9
MA15-016	Maronia	53.00	1.00	16.74	8.79	0.17	4.45	7.76	2.70	4.02	0.52	<0.1	<0.1	0.21	99.66	5.09	244	56	28.9
MA15-017	Maronia	55.72	0.82	14.91	7.40	0.15	5.56	7.87	2.64	4.35	0.50	<0.1	<0.1	0.11	100.34	3.46	182	158	26.8
MA15-017	Maronia	55.25	0.83	14.78	7.37	0.15	5.52	7.78	2.59	4.30	0.50	<0.1	<0.1	0.05	99.43	3.23	191	158	26.8
MA15-018	Maronia	53.39	0.93	15.91	8.09	0.15	5.11	7.57	2.73	3.77	0.44	<0.1	<0.1	1.51	99.87	3.97	236	84	24.6
MA15-020	Maronia	53.43	0.91	16.27	8.34	0.16	4.58	7.40	2.65	4.33	0.60	<0.1	<0.1	0.25	99.25	7.61	234	44	28.7
MA15-022	Maronia	52.32	0.87	13.08	8.64	0.17	6.61	9.01	2.18	4.24	0.55	<0.1	<0.1	1.86	99.86	7.08	231	127	33.3
MA15-023	Maronia	50.15	0.84	7.74	8.49	0.18	7.25	17.45	1.47	3.72	1.41	<0.1	<0.1	1.12	99.97	6.81	249	58	29.1
RT14-006	Maronia	52.93	0.73	19.84	6.14	0.12	3.59	8.81	3.13	3.05	0.43	<0.1	<0.1	0.93	99.96	2.97	149	68	21.3
RT14-006	Maronia	52.83	0.72	19.80	6.14	0.12	3.59	8.76	3.13	3.03	0.43	<0.1	<0.1	1.01	99.82	2.42	156	74	19.7
PR15-007	Pagoni Rachi	58.05	0.57	16.14	4.90	0.15	3.76	4.52	2.82	1.26	0.09	<0.1	<0.1	5.84	99.19	8.27	150	7	8.1
PR15-008	Pagoni Rachi	61.65	0.46	16.36	5.83	0.04	2.91	2.59	4.87	1.09	0.12	<0.1	<0.1	3.61	99.59	5.47	118	8	6.2
PR15-009	Pagoni Rachi	74.10	0.61	16.70	0.48	<0.01	0.36	0.07	0.78	2.73	0.16	<0.1	<0.1	3.26	99.35	2.10	136	6	0.3
PR15-009	Pagoni Rachi	73.96	0.60	16.55	0.47	<0.01	0.39	0.09	0.77	2.70	0.16	<0.1	<0.1	3.44	99.23	2.24	127	6	0.3
ES15-002	Essimi	67.03	0.44	16.11	4.64	0.02	0.63	0.09	0.11	4.68	0.02	<0.1	<0.1	4.64	99.41	0.48	116	8	10.8
ES15-006	Essimi	66.34	0.50	18.04	3.49	0.01	0.59	0.34	0.38	4.50	0.07	<0.1	<0.1	4.91	99.27	0.91	114	8	9.7
KN15-003	Konos	72.11	0.45	13.63	4.97	<0.01	0.19	0.03	0.30	1.18	0.02	<0.1	<0.1	6.24	99.18	0.66	92	7	11.2
KN15-003	Konos	71.93	0.45	13.80	5.07	<0.01	0.19	0.02	0.28	1.18	0.02	<0.1	<0.1	6.38	99.39	0.66	93	5	10.9

Table C1 continued...

Sample	Ni	Cu	Zn	As	Rb	Sr	Y	Zr	Nb	Mo	Sn	Sb	Te	Cs	Ba	La	Ce	Pr	Nd	Sm	Eu	Tb
KA15-002	35	14.0	41	3.4	7	376	17.8	116	6.7	0.0	2.6	0.42	0.00	0.0	285	19.8	40	4.46	16.6	3.86	1.02	0.58
KA15-004	107	83.6	40	1.3	61	346	21.0	55	6.3	0.5	2.0	0.26	0.07	2.4	1247	21.6	42	5.26	21.8	4.55	1.11	0.67
KA15-005	4	26.5	47	12.9	17	188	1.66	61	3.5	2.1	2.6	0.21	0.05	0.5	71	2.9	5	0.46	1.5	0.25	0.25	0.04
KA15-008	95	205	39	3.4	54	292	17.4	108	6.8	0.4	1.9	0.18	0.09	0.8	889	21.8	42	4.92	19.6	3.67	0.98	0.55
KA15-008	92	202	46	3.1	51	293	16.4	104	6.5	0.5	1.6	0.24	0.05	0.9	882	21.4	40	4.74	18.5	3.86	0.97	0.54
KA15-009	87	7.0	26	2.1	53	298	20.0	88	7.6	0.0	1.1	0.26	0.08	0.4	783	18.0	36	4.69	19.4	4.34	0.90	0.64
KA15-019	3	3.9	13	0.8	173	79	15.1	116	10.2	0.4	3.0	0.10	0.07	1.4	1702	30.6	54	5.81	19.6	3.50	0.62	0.43
KA15-010	0	4.8	13	412	335	87	25.5	104	7.4	1.2	1.1	12.0	0.00	12.3	1144	23.2	43	4.86	18.3	3.89	0.98	0.89
KA15-013	21	15.1	10	1.7	82	317	19.3	110	7.0	0.4	1.8	0.07	0.05	1.2	702	24.1	44	5.28	19.7	4.09	0.92	0.63
KA15-016	35	14.2	81	2.9	77	314	20.1	134	6.2	0.9	2.3	0.36	0.00	1.7	769	23.0	44	5.30	20.0	4.38	1.04	0.66
KA15-017	107	58.5	34	3.7	70	259	17.5	114	7.6	0.7	2.7	0.24	0.00	1.3	793	19.8	38	4.73	18.5	3.95	0.85	0.58
KA15-018	0	40.9	0	1.2	126	14	11.2	120	10.1	1.5	3.2	0.76	0.18	2.6	302	38.8	67	6.97	22.7	3.13	0.39	0.31
KA15-019	0	4.6	20	0.5	176	80	15.2	115	10.5	0.4	2.8	0.10	0.06	1.4	1761	31.9	57	6.07	20.0	3.41	0.69	0.45
KA15-020	12	72.9	47	4.0	65	254	6.0	108	4.7	0.3	0.6	0.20	0.19	0.5	663	33.9	56	5.66	17.6	1.99	0.58	0.20
RT14-028	99	119	61	2.9	70	359	18.0	152	5.4	1.1	1.4	0.19	0.00	2.7	1185	20.0	40	4.66	19.2	4.07	1.13	0.61
RT14-028	94	116	58	2.6	73	354	18.5	194	5.8	1.0	1.7	0.18	0.00	2.5	1148	20.0	38	4.56	17.9	3.89	1.04	0.54
LA15-008	31	42.9	62	1.2	68	304	19.5	95	6.8	0.6	1.9	0.15	0.00	1.7	769	24.5	44	5.34	19.6	4.38	0.97	0.61
LA15-009	102	31.2	76	0.4	48	371	23.8	121	7.0	0.5	1.6	0.67	0.00	0.6	759	21.9	38	4.85	18.2	3.96	1.02	0.60
LA15-009	94	29.3	72	0.6	44	351	23.0	115	6.6	0.4	1.7	0.54	0.00	0.4	725	19.9	35	4.51	17.5	3.61	0.90	0.58
LA15-010	98	27.6	82	0.6	5	484	3.88	129	0.8	0.0	0.0	0.07	0.00	0.5	111	4.0	5	1.12	4.0	0.93	0.36	0.16
LA15-011	5	7.0	39	0.7	155	258	16.6	135	9.1	0.3	2.2	0.39	0.00	1.0	1249	24.5	40	5.10	19.3	3.46	0.62	0.51
LA15-020	54	3.2	71	1.0	48	369	23.6	157	9.2	0.4	1.7	0.26	0.00	0.4	915	29.3	55	6.82	25.9	4.99	0.91	0.75
LA15-021	4	1.9	20	0.3	5	606	2.55	54	0.0	0.0	0.6	0.00	0.00	0.0	102	2.5	6	0.64	2.4	0.65	0.34	0.10
LB15-003	10	17.1	108	0.6	7	590	17.4	51	5.1	0.4	1.0	0.07	0.05	0.0	227	15.5	32	4.15	19.4	3.86	1.45	0.59
LB15-004	4	4.0	28	0.3	79	298	16.8	72	6.9	0.0	1.5	0.04	0.06	0.8	685	27.9	52	5.62	20.4	3.90	0.85	0.54
LB15-005	3	3.3	15	0.7	70	314	14.3	70	6.4	1.4	1.4	0.00	0.00	0.7	875	26.2	45	4.78	17.3	2.73	0.76	0.43
LB15-006	3	2.0	19	1.0	19	562	22.0	72	7.1	1.3	3.1	0.14	0.00	0.5	200	26.7	52	6.17	22.8	4.68	1.01	0.67
LB15-007	8	2.7	57	0.5	22	375	17.6	71	4.4	0.0	2.1	0.09	0.00	0.0	311	17.5	36	4.25	16.6	3.08	1.04	0.52
LC15-002	5	55.9	71	0.4	56	338	21.7	113	7.6	0.6	2.0	0.00	0.00	1.5	670	25.0	46	5.74	20.8	4.57	1.19	0.67
LC15-003	4	6.3	38	0.4	76	320	21.7	103	6.8	0.3	1.9	0.00	0.00	0.5	809	26.0	47	5.48	19.6	4.02	0.90	0.61
LD15-002	12	117	81	0.6	34	385	18.6	66	3.3	0.7	1.2	0.30	0.06	1.9	379	13.4	27	3.45	14.2	3.37	0.95	0.55
LD15-003	12	26.7	86	0.8	28	535	19.2	62	4.0	0.4	1.0	0.12	0.00	0.5	404	15.2	33	4.10	17.7	3.83	1.07	0.60
RT14-009	15	5.6	22	0.3	43	335	22.0	89	8.5	0.3	2.5	0.13	0.00	0.4	736	23.9	46	5.64	22.2	5.13	1.02	0.66
RT14-009	15	5.9	25	0.6	48	337	22.8	144	8.9	0.0	2.6	0.10	0.00	0.4	740	25.0	47	5.88	21.2	4.55	0.97	0.69
RT14-010	6	6.1	46	0.6	71	257	13.4	92	6.1	0.4	1.5	0.13	0.00	1.2	990	25.6	47	5.08	18.5	3.19	0.77	0.46
RT14-010	5	5.5	37	0.3	81	258	14.5	99	6.4	0.0	1.6	0.09	0.00	1.4	995	30.3	52	5.53	20.2	3.27	0.75	0.42

Table C1 continued...

Sample	Ni	Cu	Zn	As	Rb	Sr	Y	Zr	Nb	Mo	Sn	Sb	Te	Cs	Ba	La	Ce	Pr	Nd	Sm	Eu	Tb
RT14-015	13	22.7	80	0.5	38	380	19.9	73	3.6	0.6	1.2	0.30	0.00	1.8	418	14.3	28	3.60	15.0	3.65	0.96	0.62
RT14-015	12	22.9	75	0.5	40	384	20.5	74	3.9	0.3	1.3	0.21	0.00	1.8	407	14.5	27	3.60	14.4	3.46	0.98	0.58
RT14-017	5	22.0	82	0.0	19	533	23.6	65	4.0	0.0	1.3	0.05	0.00	0.0	248	11.5	25	3.44	16.1	4.39	1.24	0.75
RT14-022	29	32.7	58	2.3	103	396	19.7	142	7.3	0.4	1.9	0.73	0.00	3.2	999	22.2	41	5.06	20.3	3.89	0.94	0.59
RT14-024	99	51.0	28	1.6	80	291	17.1	104	5.9	2.1	2.9	0.35	0.00	3.2	618	32.8	56	5.78	20.2	3.85	0.78	0.52
MA15_015	40	69.1	74	1.4	106	689	22.0	103	8.9	1.6	4.8	0.17	0.00	2.6	1029	40.2	82	10.4	40.1	7.98	1.77	0.83
MA15_022	53	108	80	0.5	186	519	21.4	198	15.0	1.2	4.5	0.24	0.00	6.4	1363	41.3	82	10.4	40.5	7.72	1.68	0.80
MA15-001	10	73.7	23	21.1	53	165	19.5	205	4.6	0.3	5.8	2.07	0.10	0.6	261	9.0	29	4.69	22.4	5.19	1.00	0.63
MA15-003	0	45.0	12	1.6	186	152	11.1	101	10.5	19.3	4.8	1.24	0.05	3.4	617	24.5	42	4.43	14.9	2.49	0.51	0.31
MA15-004E	86	65.6	102	0.6	102	329	18.0	94	6.7	0.7	2.8	0.05	0.00	2.8	639	10.0	22	2.72	12.0	2.87	0.92	0.51
MA15-004H	24	32.7	70	1.0	168	606	22.5	198	12.6	2.9	5.1	0.06	0.11	2.8	1216	40.0	80	10.0	40.4	7.51	1.70	0.82
MA15-006	38	76.6	90	1.2	107	717	24.0	85	8.4	1.3	3.5	0.04	0.00	2.1	1208	36.7	79	10.4	42.0	8.69	1.95	0.91
MA15-007	65	69.7	84	1.2	92	685	24.6	81	6.4	0.9	3.5	0.26	0.00	2.7	746	33.3	68	9.24	39.9	7.86	2.09	0.89
MA15-008	56	58.2	95	0.8	96	677	22.1	107	5.6	0.7	2.7	0.16	0.00	2.1	960	31.7	67	8.80	37.9	7.53	1.89	0.84
MA15-010	25	92.6	73	2.0	123	702	23.3	122	10.4	2.4	3.7	0.16	0.08	4.1	994	37.9	76	9.49	38.5	7.22	1.70	0.80
MA15-011	23	74.8	71	2.0	127	617	23.2	146	12.7	0.8	4.0	0.26	0.09	4.9	813	40.1	78	9.61	38.0	6.96	1.51	0.78
MA15-012	26	78.9	83	2.1	135	693	22.4	150	10.7	0.9	3.7	0.11	0.00	3.1	1004	36.8	74	9.19	35.7	7.21	1.71	0.80
MA15-014	31	73.8	69	2.5	208	604	22.7	156	14.5	2.0	5.2	1.82	0.00	4.8	1293	46.4	91	11.0	41.5	7.85	1.62	0.80
MA15-016	27	77.5	83	1.8	150	665	24.4	116	11.8	1.6	4.2	0.14	0.00	3.1	1320	39.9	83	10.6	42.7	8.14	1.95	0.87
MA15-017	51	52.5	65	1.0	178	536	20.3	97	10.8	1.6	4.1	0.08	0.05	3.9	1178	36.5	73	9.23	36.2	7.36	1.51	0.75
MA15-017	51	52.1	64	1.5	194	534	20.1	131	12.4	1.6	4.4	0.11	0.00	4.0	1161	36.7	73	9.19	36.9	7.00	1.49	0.73
MA15-018	35	37.3	61	16.3	133	605	22.4	131	9.6	0.8	3.6	1.22	0.47	2.1	1115	35.8	71	9.00	37.1	7.49	1.68	0.80
MA15-020	29	91.0	133	1.7	174	694	21.1	156	11.7	1.7	4.0	0.16	0.00	3.3	1594	44.3	89	10.9	44.6	7.84	1.74	0.78
MA15-022	53	106	70	1.0	190	527	20.4	169	14.3	1.2	4.4	0.23	0.05	6.7	1383	40.9	82	10.4	41.4	7.75	1.66	0.83
MA15-023	19	23.5	63	2.2	162	193	32.3	245	9.3	2.1	5.3	0.12	0.00	3.9	446	76.3	160	19.9	78.0	13.9	2.11	1.26
RT14-006	32	85.1	54	2.6	134	924	17.2	103	11.2	0.6	3.4	0.68	0.05	4.9	727	36.7	69	8.70	33.3	5.88	1.75	0.63
RT14-006	32	77.8	58	2.4	140	893	17.5	132	11.9	0.6	3.3	0.62	0.08	5.3	714	35.7	69	8.48	32.5	5.50	1.71	0.57
PR15-007	6	160	53	5.6	43	153	16.4	87	5.0	1.4	1.8	0.12	0.05	10.5	176	20.5	38	4.35	16.5	2.93	0.87	0.49
PR15-008	4	58.3	29	1.4	38	276	14.8	93	5.6	2.0	1.8	0.10	0.00	8.0	200	18.4	35	3.99	15.3	3.34	0.78	0.45
PR15-009	0	2.8	0	0.9	65	73	19.2	100	7.4	0.3	2.4	0.24	0.05	1.1	621	28.2	54	6.45	26.1	5.49	1.37	0.66
PR15-009	0	3.5	13	0.6	68	72	17.9	108	7.4	0.3	2.8	0.12	0.00	1.1	571	25.9	50	6.14	24.2	4.79	1.21	0.57
ES15-002	7	14.0	66	68.9	122	100	12.3	65	5.7	7.1	4.6	3.65	0.00	2.3	6308	15.6	30	3.44	12.3	2.57	0.59	0.36
ES15-006	6	5.2	0	2.7	129	21	7.42	81	6.5	1.0	4.4	4.24	0.08	3.5	749	11.9	22	2.37	8.5	1.43	0.27	0.18
KN15-003	5	166	36	47.7	36	18	14.3	74	6.8	2.7	5.1	3.95	0.25	0.0	218	22.9	44	4.92	18.4	2.87	0.64	0.40
KN15-003	4	157	38	45.3	35	17	14.6	75	6.5	3.4	4.9	3.13	0.37	0.0	212	24.2	46	4.98	18.3	2.82	0.63	0.39

Table C1 continued...

Sample	Gd	Dy	Ho	Er	Tm	Yb	Lu	Hf	Ta	W	Pb	Bi	Th	U
KA15-002	3.32	3.60	0.63	2.13	0.28	1.97	0.28	3.5	0.50	0.0	8.3	0.06	9.9	3.15
KA15-004	4.30	4.18	0.77	2.32	0.30	2.07	0.30	1.8	0.53	0.8	10.0	0.06	6.7	2.20
KA15-005	0.27	0.29	0.07	0.26	0.00	0.33	0.00	2.0	0.26	1.4	10.6	0.26	0.9	1.93
KA15-008	3.31	3.59	0.62	2.12	0.26	1.86	0.27	3.1	0.50	1.0	12.6	0.09	9.2	2.23
KA15-008	3.31	3.51	0.60	2.00	0.26	1.73	0.26	2.7	0.40	1.0	12.1	0.10	8.9	2.18
KA15-009	3.84	3.92	0.71	2.37	0.30	2.02	0.31	2.6	0.51	0.0	6.1	0.06	8.4	1.47
KA15-019	2.54	2.80	0.52	1.81	0.24	1.89	0.26	3.3	0.84	2.3	6.4	0.37	7.2	3.12
KA15-010	4.73	6.04	1.05	3.44	0.39	2.36	0.34	3.1	0.65	2.9	20.3	0.09	11.8	4.58
KA15-013	3.68	4.00	0.66	2.38	0.29	2.08	0.33	3.0	0.45	0.8	6.0	0.04	10.1	3.01
KA15-016	3.79	3.83	0.74	2.51	0.32	2.08	0.31	3.7	0.39	1.2	9.9	0.05	9.9	2.59
KA15-017	3.48	3.46	0.61	2.21	0.28	1.85	0.28	3.2	0.57	1.1	12.2	0.05	11.5	2.18
KA15-018	1.84	1.95	0.42	1.40	0.24	1.69	0.31	4.0	1.00	2.6	8.1	0.70	8.5	3.49
KA15-019	2.72	2.95	0.52	1.85	0.26	1.86	0.28	3.5	0.91	2.6	6.3	0.36	7.3	3.22
KA15-020	1.50	1.12	0.21	0.69	0.10	0.67	0.13	3.5	0.50	0.8	22.0	0.30	16.7	3.72
RT14-028	3.70	3.82	0.66	2.22	0.32	2.00	0.31	4.0	0.30	1.0	16.9	0.16	9.0	2.84
RT14-028	3.83	3.42	0.69	2.11	0.28	2.09	0.33	5.3	0.45	1.0	16.9	0.16	7.5	2.81
LA15-008	3.69	3.85	0.66	2.21	0.27	1.90	0.29	2.6	0.44	2.5	19.2	0.15	12.1	3.98
LA15-009	3.85	4.02	0.73	2.44	0.29	1.99	0.29	3.0	0.41	1.7	6.5	0.18	8.9	3.50
LA15-009	3.84	3.69	0.70	2.27	0.28	2.02	0.28	3.0	0.35	1.7	6.3	0.25	8.7	3.36
LA15-010	0.82	0.79	0.18	0.45	0.08	0.41	0.09	3.2	0.00	0.6	32.1	0.03	0.1	0.88
LA15-011	2.94	3.19	0.58	2.04	0.28	2.07	0.32	4.0	0.70	1.3	7.6	0.22	14.5	5.80
LA15-020	4.46	4.77	0.85	2.91	0.39	2.64	0.37	4.5	0.64	3.7	3.0	0.27	13.9	4.53
LA15-021	0.68	0.61	0.10	0.27	0.00	0.29	0.00	2.0	0.00	0.0	7.2	0.02	0.7	0.68
LB15-003	3.77	3.96	0.64	2.21	0.27	1.88	0.26	1.3	0.19	1.1	7.8	0.09	2.9	0.59
LB15-004	3.17	3.25	0.62	2.10	0.28	1.86	0.29	2.1	0.58	1.2	13.2	0.03	13.2	2.56
LB15-005	2.60	2.69	0.47	1.66	0.22	1.66	0.26	2.1	0.60	1.1	12.7	0.03	15.9	4.74
LB15-006	3.99	4.34	0.79	2.61	0.34	2.42	0.35	2.2	0.39	3.2	5.3	0.08	10.0	2.24
LB15-007	3.14	3.50	0.60	2.14	0.27	1.86	0.28	1.9	0.15	0.0	6.8	0.07	4.8	1.12
LC15-002	4.04	4.35	0.77	2.62	0.35	2.26	0.36	3.1	0.42	2.2	32.8	0.15	9.0	2.97
LC15-003	3.69	3.99	0.72	2.39	0.32	2.28	0.34	3.0	0.52	1.0	13.2	0.07	10.5	2.94
LD15-002	3.36	3.84	0.68	2.25	0.29	1.99	0.29	1.8	0.08	0.8	9.2	0.10	3.7	0.94
LD15-003	3.73	4.11	0.72	2.38	0.31	2.19	0.34	1.6	0.09	0.0	10.7	0.06	3.9	1.24
RT14-009	4.39	4.50	0.79	2.73	0.35	2.39	0.36	2.7	0.48	0.8	7.6	0.08	12.8	3.64
RT14-009	4.55	4.36	0.87	2.64	0.35	2.52	0.40	4.4	0.66	0.9	7.9	0.07	13.0	3.89
RT14-010	2.73	2.70	0.54	1.69	0.24	1.74	0.28	2.6	0.40	1.9	14.6	0.10	14.0	3.08
RT14-010	2.93	2.62	0.54	1.65	0.25	1.78	0.26	3.4	0.55	0.8	14.6	0.06	14.3	2.87

Table C1 continued...

Sample	Gd	Dy	Ho	Er	Tm	Yb	Lu	Hf	Ta	W	Pb	Bi	Th	U
RT14-015	3.56	4.11	0.70	2.54	0.31	2.13	0.30	1.9	0.11	3.3	8.8	0.13	4.2	0.96
RT14-015	3.80	3.72	0.77	2.25	0.33	2.23	0.32	2.3	0.28	0.0	9.1	0.13	4.8	0.93
RT14-017	5.16	4.89	0.98	2.84	0.39	2.25	0.38	2.3	0.28	0.8	6.3	0.09	2.8	0.89
RT14-022	4.08	3.70	0.72	2.21	0.31	2.28	0.36	4.4	0.59	0.9	7.1	0.06	10.8	3.50
RT14-024	3.55	3.19	0.65	1.90	0.29	1.83	0.26	3.4	0.51	1.2	10.6	0.06	10.9	2.55
MA15_015	6.02	4.72	0.82	2.52	0.32	2.17	0.31	3.3	0.46	1.0	23.9	0.08	19.2	6.11
MA15_022	5.93	4.61	0.76	2.33	0.32	2.13	0.33	6.4	1.03	1.3	28.0	0.12	35.6	10.3
MA15-001	4.09	3.75	0.68	2.23	0.31	2.14	0.31	6.1	0.78	2.5	13.0	3.10	13.4	1.72
MA15-003	1.98	2.04	0.38	1.41	0.20	1.39	0.21	3.0	0.89	5.7	80.4	0.36	12.1	2.91
MA15-004E	3.20	3.57	0.70	2.23	0.31	2.11	0.31	2.4	0.44	0.6	14.3	0.11	2.9	2.58
MA15-004H	5.94	4.96	0.85	2.55	0.33	2.29	0.33	6.1	0.78	1.1	31.0	0.09	19.1	5.67
MA15-006	7.02	5.17	0.93	2.59	0.37	2.32	0.36	3.1	0.51	0.7	19.8	0.08	11.5	3.54
MA15-007	6.70	5.07	0.88	2.65	0.34	2.27	0.33	2.8	0.41	0.9	18.5	0.12	9.8	3.13
MA15-008	6.32	4.68	0.85	2.41	0.32	2.19	0.32	3.5	0.37	0.0	25.3	0.10	8.5	2.62
MA15-010	6.01	4.74	0.89	2.62	0.36	2.21	0.38	4.1	0.71	1.7	27.3	0.08	19.7	5.40
MA15-011	5.67	4.65	0.84	2.68	0.34	2.36	0.36	4.7	0.95	2.2	32.2	0.23	28.6	8.99
MA15-012	5.77	4.62	0.86	2.47	0.34	2.42	0.36	4.8	0.71	1.6	27.0	0.10	18.4	5.66
MA15-014	5.96	4.60	0.78	2.42	0.34	2.30	0.35	5.0	0.98	1.7	37.8	0.11	30.2	9.83
MA15-016	6.51	5.04	0.86	2.54	0.36	2.39	0.34	4.0	0.76	1.0	27.5	0.12	16.6	5.21
MA15-017	5.23	4.43	0.71	2.25	0.29	1.90	0.30	3.0	0.59	3.8	31.8	0.15	17.8	5.68
MA15-017	5.65	4.35	0.76	2.21	0.32	2.13	0.31	4.5	0.87	1.0	31.9	0.17	18.5	5.86
MA15-018	6.04	4.80	0.84	2.52	0.33	2.22	0.34	4.1	0.64	1.7	26.9	0.57	11.7	3.96
MA15-020	5.97	4.45	0.81	2.38	0.32	2.04	0.30	5.0	0.73	1.0	32.2	0.14	18.1	5.68
MA15-022	5.99	4.33	0.78	2.20	0.31	2.03	0.29	5.9	0.98	1.3	28.0	0.09	36.7	9.01
MA15-023	10.12	6.92	1.23	3.49	0.49	3.18	0.47	9.0	0.68	0.9	20.9	0.07	35.6	10.5
RT14-006	4.17	3.56	0.64	2.09	0.25	1.66	0.21	3.0	0.61	1.4	35.7	0.15	22.8	6.67
RT14-006	4.40	3.40	0.66	1.94	0.27	1.74	0.26	4.2	0.80	1.4	36.3	0.13	21.8	6.12
PR15-007	3.19	3.23	0.61	1.88	0.28	1.89	0.29	2.6	0.44	1.0	6.2	0.18	5.9	2.12
PR15-008	2.86	2.74	0.57	1.78	0.26	1.89	0.30	2.9	0.50	1.1	6.9	0.18	6.2	2.29
PR15-009	4.22	4.05	0.70	2.37	0.32	2.13	0.34	2.7	0.52	1.5	2.6	1.26	9.7	3.39
PR15-009	4.27	3.68	0.71	2.15	0.29	2.09	0.32	3.5	0.66	1.6	2.5	1.24	8.9	3.22
ES15-002	2.20	2.30	0.42	1.46	0.20	1.39	0.21	2.3	0.67	6.4	10.9	0.21	5.6	2.00
ES15-006	1.03	1.30	0.24	1.02	0.15	1.18	0.18	2.5	0.71	2.3	7.5	0.65	5.2	2.78
KN15-003	2.22	2.82	0.51	1.90	0.24	1.83	0.28	2.2	0.55	2.7	17.9	8.21	10.6	4.44
KN15-003	2.33	2.74	0.49	1.82	0.24	1.84	0.28	2.2	0.46	2.9	18.2	6.66	11.2	4.38

Table C2: Estimated uncertainties and repeat analyses, oxides reported as wt% and elements reported as ppm.

Sample	SiO_2	TiO_2	Al_2O_3	$Fe_2O_2^t$	Mn_3O_4	MgO	CaO	Na_2O	K_2O	P_2O_5	F	Cl	LOI	Total	Sc	V	Cr	Co
The relative difference between repeats																		
KA15_008	0.05	0.99	0.05	0.07	0.00	0.28	0.08	0.10	0.19	0.00	0.00	0.00	1.40	0.04	1.49	0.39	0.78	0.76
KA15_009	0.05	1.02	0.19	0.00	0.00	0.60	0.00	1.52	0.19	0.00	0.00	0.00	0.66	0.01	0.60	1.50	0.07	3.64
KN15_003	0.06	0.00	0.31	0.50		0.00	10.00	1.72	0.00	0.00	0.00	0.00	0.55	0.05	0.04	0.30	5.85	0.66
LA15_009	0.00	0.34	0.02	0.00	0.00	0.16	0.00	0.68	0.12	0.00	0.00	0.00	0.48	0.03	1.52	1.81	0.45	1.86
MA15_017	0.21	0.30	0.22	0.10	0.00	0.18	0.29	0.48	0.29	0.00	0.00	0.00	18.75	0.23	1.75	1.27	0.04	0.06
PR15_009	0.05	0.41	0.23	0.53		2.00	6.25	0.32	0.28	0.00	0.00	0.00	1.34	0.03	1.62	1.72	2.39	1.68
RT14_006	0.05	0.34	0.05	0.00	0.00	0.00	0.14	0.00	0.16	0.00	0.00	0.00	2.06	0.04	5.15	1.09	2.12	1.92
RT14_009	0.20	0.34	0.15	0.20	2.38	0.22	0.21	0.75	0.37	0.00	0.00	0.00	0.00	0.21	0.50	1.67	2.43	0.48
RT14_010	0.09	0.00	0.03	0.61	2.63	0.16	0.09	0.00	0.00	0.00	0.00	0.00	1.86	0.06	0.89	0.34	4.04	0.65
RT14_015	0.12	0.30	0.08	0.25	0.00	0.11	0.19	0.54	0.19	0.00	0.00	0.00	1.89	0.12	1.47	0.75	2.93	1.83
RT14_028	0.18	0.31	0.22	0.37	0.00	0.18	0.30	0.63	0.39	0.00	0.00	0.00	3.23	0.20	3.12	0.01	1.20	1.43
Average relative difference between repeats																		
	0.10	0.40	0.14	0.24	0.56	0.35	1.60	0.61	0.20	0.00	0.00	0.00	2.93	0.09	1.65	0.99	2.03	1.36
2 σ scatter between repeats, used as estimated uncertainty (relative)																		
	0.14	0.66	0.20	0.46	2.21	1.14	6.67	1.13	0.26	0.00	0.00	0.00	10.65	0.16	2.84	1.31	3.59	1.99

Table C2 continued...

Sample	Ni	Cu	Zn	As	Rb	Sr	Y	Zr	Nb	Mo	Sn	Sb	Te	Cs	Ba	La	Ce	Pr	Nd	Sm
The relative difference between repeats																				
KA15_008	0.75	0.36	4.44	2.54	1.79	0.09	1.46	1.15	1.06	4.52	3.96	6.96	13.55	1.72	0.20	0.44	1.26	0.94	1.38	1.25
KA15_009	50.00	3.76	10.63	11.07	0.34	0.40	0.09	0.35	0.83	1.15	1.85	0.38	5.62	0.42	0.85	1.04	1.47	1.09	0.42	0.67
KN15_003	7.49	1.50	1.55	1.29	0.77	0.88	0.50	0.45	1.29	5.67	0.95	5.80	9.61	0.00	0.65	1.41	1.02	0.33	0.18	0.47
LA15_009	1.99	1.51	1.28	11.13	2.05	1.41	0.83	1.43	1.48	2.01	1.48	5.23	0.00	7.44	1.13	2.39	1.68	1.84	0.92	2.31
MA15_017	0.01	0.17	0.42	9.15	2.16	0.09	0.24	7.54	3.45	0.02	1.94	6.91	50.00	0.70	0.36	0.14	0.12	0.09	0.53	1.23
PR15_009	0.00	5.26	50.00	9.32	0.97	0.40	1.75	1.79	0.20	1.75	4.21	17.40	50.00	1.65	2.13	2.11	2.01	1.23	1.89	3.42
RT14_006	0.22	2.23	1.89	1.87	1.20	0.85	0.40	6.13	1.42	0.59	0.78	2.12	11.35	2.34	0.44	0.67	0.09	0.65	0.65	1.64
RT14_009	0.17	1.12	3.33	20.69	2.44	0.17	0.85	11.88	1.18	50.00	1.37	5.17	0.00	2.61	0.12	1.08	0.32	1.03	1.13	3.01
RT14_010	2.28	2.59	5.58	14.00	3.43	0.13	1.95	1.92	1.08	50.00	2.00	8.46	0.00	2.36	0.13	4.21	2.78	2.11	2.08	0.65
RT14_015	1.64	0.13	1.34	1.79	1.17	0.26	0.68	0.62	1.75	12.57	1.18	8.27	0.00	0.51	0.68	0.36	1.19	0.05	1.11	1.30
RT14_028	1.37	0.49	1.05	2.73	1.10	0.35	0.55	6.01	1.58	1.48	5.97	2.42	0.00	2.13	0.78	0.09	1.04	0.55	1.78	1.16
Average relative difference between repeats																				
	6.59	1.74	7.41	7.78	1.58	0.46	0.85	3.57	1.39	11.80	2.33	6.28	23.36	2.19	0.68	1.27	1.18	0.90	1.10	1.55
2 σ scatter between repeats, used as estimated uncertainty (relative)																				
	30.81	3.25	28.86	12.61	1.77	0.84	1.23	7.55	1.60	38.42	3.30	9.01	41.60	4.03	1.16	2.47	1.64	1.33	1.27	1.93

Table C2 continued...

Sample	Eu	Tb	Gd	Dy	Ho	Er	Tm	Yb	Lu	Hf	Ta	W	Pb	Bi	Th	U
The relative difference between repeats																
KA15_008	0.24	0.68	0.02	0.56	0.86	1.43	0.36	1.86	1.06	3.42	5.17	1.08	0.95	2.25	0.61	0.53
KA15_009	2.74	1.08	1.68	1.30	0.23	0.57	1.27	0.38	1.72	1.34	1.98	2.98	0.22	0.64	0.39	0.80
KN15_003	0.41	0.66	1.22	0.75	0.97	0.99	0.42	0.20	0.72	0.01	4.19	0.93	0.39	5.19	1.43	0.34
LA15_009	2.89	0.76	0.06	2.15	0.84	1.77	0.30	0.35	0.41	0.01	4.05	0.90	0.94	8.16	0.42	1.03
MA15_017	0.26	0.63	1.92	0.48	1.64	0.54	2.97	2.76	0.87	9.99	9.73	29.26	0.12	2.29	0.98	0.80
PR15_009	3.19	3.70	0.32	2.36	0.27	2.42	2.28	0.52	1.87	6.22	5.94	0.41	1.30	0.41	2.11	1.33
RT14_006	0.67	2.67	1.31	1.09	0.76	1.95	1.76	1.07	4.97	8.26	6.66	0.80	0.39	1.97	1.14	2.17
RT14_009	1.28	0.97	0.89	0.80	2.22	0.76	0.09	1.30	2.52	12.17	8.11	2.08	0.80	4.92	0.43	1.63
RT14_010	0.43	2.11	1.82	0.74	0.06	0.54	0.28	0.53	1.52	6.35	8.12	20.77	0.11	13.12	0.63	1.80
RT14_015	0.32	1.78	1.64	2.54	2.24	3.03	1.83	1.19	1.77	5.29	22.36	50.00	0.71	1.72	3.78	0.72
RT14_028	2.00	2.69	0.83	2.78	0.86	1.25	3.40	1.19	1.79	6.79	10.11	0.40	0.06	0.26	4.60	0.27
Average relative difference between repeats																
	1.31	1.61	1.06	1.42	0.99	1.38	1.36	1.03	1.75	5.44	7.86	9.96	0.54	3.72	1.50	1.04
2 σ scatter between repeats, used as estimated uncertainty (relative)																
	2.35	2.10	1.40	1.74	1.49	1.66	2.35	1.54	2.46	7.92	10.84	32.94	0.83	7.89	2.87	1.24

Appendix D

Modal Compositions

This appendix contains the modal compositions of the least altered thin sections from the Maronia Magmatic Corridor.

Table D1: Point counting data from $>$ 1,000 points across the least altered thin sections.

Table D1: Modal point counting results from the Maronia Magmatic Corridor.

Sample	Pluton	Plagioclase	K-feldspar	Quartz	Amphibole	Biotite	Pyroxene	Chlorite	Fe-Ti Oxides	Additional Phases	*Total*
RT14_003	Maronia	45.1	23.4	0.7	4.3	10.6	7.2	5.8	2.5	0.4	100.0
RT14_006	Maronia	33.8	37.9	0.2	10.0	7.6	3.6	4.2	2.4	0.4	100.0
RT14_028	Kassiteres	43.1	12.7	9.0	5.6	6.5	9.6	10.5	1.1	2.0	100.0
RT14_009	Leptokaria	33.8	20.1	24.7	6.4	8.5	3.6	1.3	1.3	0.3	100.0
RT14_010	Leptokaria	45.6	13.2	26.5	1.4	0.7	0.0	11.1	1.4	0.0	100.0
RT14_024	Leptokaria	32.4	19.7	9.3	15.2	0.3	7.3	14.4	1.4	0.0	100.0
RT14_017	Leptokaria	64.0	0.0	5.7	17.0	0.3	4.4	2.5	6.0	0.0	100.0
RT14_010	Leptokaria	47.5	21.0	17.4	2.7	0.4	0.0	8.5	2.3	0.2	100.0
RT14_015	Leptokaria	66.7	0.0	0.0	22.4	9.0	0.0	0.0	2.0	0.0	100.0
RT14_022	Leptokaria	67.6	0.0	1.4	0.0	0.0	2.1	21.9	7.0	0.0	100.0
RT14_026	Leptokaria	25.6	25.2	11.5	14.9	0.4	0.8	19.3	2.2	0.0	100.0

Appendix E

High-Precision U-Pb Zircon Geochronology

This appendix contains the high-precision chemical abrasion isotope dilution thermal ionisation mass spectrometry (CA-ID-TIMS) U-Pb zircon geochronology data presented in Chapters 2 and 5.

(a) z1, z2 etc. are labels for fractions composed of single zircon grains or fragments; all fractions annealed and chemically abraded after Mattinson (2005).
(b) Nominal fraction weights estimated from photomicrographic grain dimensions, adjusted for partial dissolution during chemical abrasion.
(c) Nominal U and total Pb concentrations subject to uncertainty in photomicrographic estimation of weight and partial dissolution during chemical abrasion.
(d) Model Th/U ratio calculated from radiogenic $^{208Pb}/^{206}$Pb ratio and ^{207}Pb$/^{235}$U age.
(e) Pb* and Pb$_c$ represent radiogenic and common Pb, respectively; mol % ^{206}Pb* with respect to radiogenic, blank and initial common Pb.
(f) Measured ratio corrected for spike and fractionation only. Daly analyses, based on analysis of NBS-981 and NBS-982.
(g) Corrected for fractionation, spike, and common Pb; up to 1 pg of common Pb was assumed to be procedural blank: ^{206}Pb$/^{204}$Pb = 18.60 0.80%; ^{207}Pb$/^{204}$Pb = 15.69 0.32%; ^{208}Pb$/^{204}$Pb = 38.51 $\pm$ 0.74% (all uncertainties 1 σ). Excess over blank was assigned to initial common Pb.
(h) Errors are 2 σ, propagated using the algorithms of Schmitz and Schoene (2007); Crowley et al. (2007).
(i) Calculations are based on the decay constants of Jaffey et al. (1971). ^{206}Pb$/^{238}$U and ^{207}Pb$/^{206}$Pb ages corrected for initial disequilibrium in ^{230}Th$/^{238}$U using Th/U$_{magma}$ = 3.

Table E1: CA-ID-TIMS data presented in Chapter 2.
Table E2: CA-ID-TIMS data presented in Chapter 5.

Figures E1–4: Concordia plots of ID-TIMS data from Kassiteres samples KA15_005, KA15_010, KA15_018, KA15_019 and RT14_028.

Table E1: CA-ID-TIMS data presented in Chapter 2

Zircon analysis	Th/U	$^{206}Pb^*$ x10^{-13} mol	mol% $^{206}Pb^*$	Pb^*/Pb_c	Pb_c (pg)	$^{206}Pb/^{204}Pb$	$^{208}Pb/^{206}Pb$	$^{207}Pb/^{206}Pb$	% error	$^{207}Pb/^{235}U$	% error
(a)	(d)	(e)	(e)	(e)	(e)	(f)	(g)	(g)	(h)	(g)	(h)
Leptokaria											
RT14_010											
z6	0.797	0.22	95.28	7	0.89	390	0.26	0.05	1.58	0.03	1.91
z3	0.784	0.95	99.22	41	0.61	2357	0.25	0.05	0.34	0.03	0.45
z2	0.653	1.51	98.89	28	1.40	1663	0.21	0.05	0.27	0.03	0.36
z5	0.425	0.23	98.41	18	0.30	1143	0.14	0.05	1.28	0.03	1.63
z1	0.603	0.49	97.96	15	0.84	902	0.19	0.05	0.69	0.03	0.86
z4	0.668	0.17	97.82	14	0.32	835	0.22	0.05	1.66	0.03	2.10
RT14_022											
z3	0.57	0.81	98.76	24	0.84	1478	0.18	0.05	0.42	0.03	0.54
z1	0.62	1.53	98.29	18	2.19	1085	0.20	0.05	0.36	0.03	0.44
z2	0.46	0.53	84.73	2	7.77	122	0.15	0.05	2.57	0.04	2.75
RT14_024											
z7	0.49	1.97	99.37	48	1.03	2939	0.16	0.05	0.22	0.03	0.36
z1	0.74	2.27	99.03	33	1.84	1902	0.24	0.05	0.26	0.03	0.34
z2	0.27	3.49	99.63	79	1.06	5032	0.11	0.06	0.13	0.06	0.23
z3	0.22	7.49	99.84	172	1.01	11326	0.07	0.05	0.09	0.11	0.18
RT14_009											
z4	0.872	0.88	96.70	10	2.48	563	0.28	0.05	0.64	0.03	0.72
z2	0.999	1.13	99.11	38	0.84	2063	0.32	0.05	0.24	0.03	0.33
z1	1.009	1.36	99.40	56	0.68	3037	0.32	0.05	0.25	0.03	0.34
z4	0.972	0.47	99.39	55	0.24	2965	0.31	0.05	0.47	0.03	0.59
z3	0.654	2.60	99.55	69	0.98	4058	0.21	0.05	0.14	0.03	0.22
z5	1.060	0.28	98.58	24	0.34	1282	0.34	0.05	0.87	0.03	1.03
z6	0.866	0.75	99.43	58	0.36	3196	0.28	0.05	0.29	0.03	0.39
Kassiteres											
RT14_028											
z2	1.01	0.99	98.40	21	1.34	1152	0.33	0.05	0.37	0.03	0.48
z1	1.16	0.94	99.04	37	0.75	1913	0.37	0.05	0.37	0.03	0.48
z3	1.03	1.03	99.16	41	0.72	2189	0.33	0.05	0.34	0.03	0.44
z4	1.22	0.64	98.70	27	0.69	1413	0.39	0.05	0.51	0.03	0.65
z5	1.11	0.56	98.53	24	0.69	1249	0.36	0.05	0.57	0.03	0.74

Table E1 continued...

Zircon analysis	Th/U	$^{206}Pb^*$ x10^{-13} mol	mol% $^{206}Pb^*$	Pb^*/Pb_c	Pb_c (pg)	$^{206}Pb/^{204}Pb$	$^{208}Pb/^{206}Pb$	$^{207}Pb/^{206}Pb$	% error	$^{207}Pb/^{235}U$	% error
(a)	(d)	(e)	(e)	(e)	(e)	(f)	(g)	(g)	(h)	(g)	(h)
					Maronia						
RT14_003											
z1	0.80	8.16	99.70	110	2.00	6223	0.26	0.05	0.11	0.03	0.19
z8	0.86	1.18	99.15	38	0.84	2153	0.28	0.05	0.28	0.03	0.37
z3	0.77	2.61	99.57	75	0.92	4304	0.25	0.05	0.14	0.03	0.22
MA15_010											
z4	0.51	4.93	99.82	167	0.74	10170	0.16	0.05	0.13	0.03	0.35
z2	0.86	1.45	99.57	76	0.52	4233	0.28	0.05	0.33	0.03	0.37
z3	0.80	3.10	99.48	62	1.34	3542	0.26	0.05	0.12	0.03	0.64
z5	0.87	2.29	99.45	60	1.05	3326	0.28	0.05	0.11	0.03	0.19
z1	0.70	5.12	99.70	107	1.26	6194	0.23	0.05	0.11	0.03	0.21
MN16_008											
z2	0.83	2.72	99.63	89	0.83	4973	0.27	0.05	0.12	0.03	0.23
z1	0.72	3.06	99.34	48	1.69	2785	0.23	0.05	0.16	0.03	0.24
z3	0.78	6.75	99.87	247	0.73	14006	0.25	0.05	0.09	0.03	0.21
z4	0.92	2.75	98.82	28	2.70	1577	0.30	0.05	0.18	0.03	0.25
z5	0.94	2.25	99.82	182	0.35	9855	0.30	0.05	0.10	0.03	0.18
MN16_005											
z4	0.69	1.44	98.51	21	1.79	1245	0.22	0.05	0.18	0.03	0.26
z5	0.80	1.03	99.25	43	0.65	2428	0.26	0.05	0.17	0.03	0.24
z2	0.86	1.09	99.50	65	0.46	3617	0.28	0.05	0.14	0.03	0.23
z1	1.23	0.77	98.44	23	1.01	1183	0.40	0.05	0.36	0.03	0.44

Table E1 continued...

	$^{206}Pb/^{238}U$	% error	correlation coefficient	$^{207}Pb/^{206}Pb$		$^{207}Pb/^{235}U$		$^{206}Pb/^{238}U$	
(a)	(g)	(h)		(i)	(h)	(i)	(h)	(i)	(h)
				Leptokaria					
RT14_010									
z6	0.01	0.22	0.88	48.12	37.59	33.09	0.62	32.89	0.07
z3	0.01	0.10	0.94	38.66	8.24	32.98	0.15	32.91	0.03
z2	0.01	0.12	0.83	40.47	6.52	33.03	0.12	32.93	0.04
z5	0.01	0.17	0.87	55.01	30.51	33.25	0.53	32.95	0.06
z1	0.01	0.14	0.96	42.82	16.58	33.11	0.28	32.97	0.05
z4	0.01	0.22	0.93	53.86	39.63	33.27	0.69	32.98	0.07
RT14_022									
z3	0.01	0.10	0.89	34.93	10.15	32.41	0.17	32.38	0.03
z1	0.01	0.11	0.78	37.72	8.72	32.83	0.14	32.76	0.03
z2	0.01	0.30	0.63	65.66	61.10	36.38	0.98	35.94	0.11
RT14_024									
z7	0.00	0.21	0.82	40.13	5.31	32.17	0.11	32.06	0.07
z1	0.00	0.11	0.76	39.93	6.32	32.29	0.11	32.19	0.03
z2	0.01	0.13	0.87	614.57	2.89	61.78	0.14	48.45	0.06
z3	0.02	0.10	0.96	229.26	2.13	103.37	0.18	97.99	0.09
RT14_009									
z4	0.00	0.13	0.696	31.11	15.21	32.13	0.23	32.14	0.04
z2	0.00	0.10	0.867	35.62	5.85	32.26	0.10	32.21	0.03
z1	0.00	0.09	0.968	35.32	6.03	32.26	0.11	32.22	0.03
z4	0.00	0.12	0.984	37.35	11.34	32.29	0.19	32.22	0.04
z3	0.00	0.09	0.907	37.43	3.34	32.31	0.07	32.24	0.03
z5	0.01	0.17	0.979	36.74	20.78	32.32	0.33	32.26	0.05
z6	0.01	0.10	0.997	38.77	7.03	32.36	0.12	32.27	0.03
				Kassiteres					
RT14_028									
z2	0.00	0.10	0.92	36.44	8.94	32.09	0.15	32.03	0.03
z1	0.00	0.12	0.91	40.41	8.85	32.15	0.15	32.04	0.04
z3	0.00	0.11	0.95	38.11	8.03	32.14	0.14	32.06	0.03
z4	0.00	0.11	0.90	40.64	12.25	32.23	0.21	32.12	0.03
z5	0.00	0.20	0.88	39.41	13.51	32.24	0.23	32.15	0.06

Table E1 continued...

	$^{206}Pb/^{238}U$	% error	correlation coefficient	$^{207}Pb/^{206}Pb$		$^{207}Pb/^{235}U$		$^{206}Pb/^{238}U$	
(a)	(g)	(h)		(i)	(h)	(i)	(h)	(i)	(h)
				Maronia					
RT14_003									
z1	0.00	0.09	0.93	30.11	2.62	29.60	0.06	29.59	0.03
z8	0.00	0.14	0.75	30.43	6.64	29.62	0.11	29.61	0.04
z3	0.00	0.10	0.88	33.30	3.43	29.70	0.06	29.66	0.03
MA15_010									
z4	0.00	0.30	0.93	33.51	3.06	29.66	0.10	29.61	0.09
z2	0.00	0.13	0.47	25.19	7.85	29.56	0.11	29.62	0.04
z3	0.00	0.61	0.98	24.43	2.96	29.58	0.19	29.64	0.18
z5	0.00	0.09	0.95	39.14	2.71	29.79	0.06	29.68	0.03
z1	0.00	0.13	0.90	37.81	2.60	29.80	0.06	29.70	0.04
MN16_008									
z2	0.00	0.15	0.88	26.80	2.91	29.66	0.07	29.70	0.04
z1	0.00	0.13	0.82	31.85	3.73	29.75	0.07	29.73	0.04
z3	0.00	0.16	0.93	29.65	2.13	29.73	0.06	29.73	0.05
z4	0.00	0.10	0.84	31.06	4.20	29.76	0.07	29.75	0.03
z5	0.00	0.09	0.93	34.68	2.50	29.83	0.05	29.77	0.03
MN16_005									
z4	0.00	0.12	0.84	42.28	4.21	29.90	0.08	29.74	0.03
z5	0.00	0.09	0.84	37.52	4.01	29.86	0.07	29.76	0.03
z2	0.00	0.12	0.85	26.83	3.42	29.73	0.07	29.77	0.04
z1	0.00	0.17	0.61	29.32	8.57	29.78	0.13	29.79	0.05

Table E2: CA-ID-TIMS data presented in Chapter 5

Zircon analysis	Th/U	$^{206}Pb^*$ x10^{-13} mol	mol% $^{206}Pb^*$	Pb^*/Pb_c	Pb_c (pg)	$^{206}Pb/^{204}Pb$	$^{208}Pb/^{206}Pb$	$^{207}Pb/^{206}Pb$	% error	$^{207}Pb/^{235}U$	% error
(a)	(d)	(e)	(e)	(e)	(e)	(f)	(g)	(g)	(h)	(g)	(h)
Porphyry Intrusion											
KA15_018											
z17a	0.409	0.32	97.38%	11	0.71	694	0.13	0.05	1.88	0.03	2.00
z19a	0.469	0.36	96.32%	8	1.13	494	0.15	0.05	2.72	0.03	2.89
z15a	0.548	0.98	99.48 %	59	0.42	3527	0.18	0.05	0.39	0.04	0.44
z17c	0.442	0.69	99.33 %	44	0.39	2725	0.15	0.05	0.46	0.04	0.51
KA15_019											
z8a	0.633	0.42	94.02%	5	2.21	304	0.20	0.05	4.44	0.03	4.71
z17a	0.587	0.23	97.06%	10	0.59	618	0.19	0.05	2.12	0.03	2.25
z17c	0.655	0.16	97.17%	11	0.39	643	0.21	0.05	2.05	0.03	2.19
Volcaniclastic Deposit											
KA15_010											
z1	0.736	0.59	95.48%	7	2.30	403	0.23	0.05	3.36	0.03	3.58
z2	0.752	0.18	94.09%	5	0.91	308	0.24	0.05	4.39	0.03	4.66
z3	0.649	0.31	81.20%	1	5.90	97	0.20	0.05	16.50	0.03	17.45
z4	0.608	0.22	96.43%	8	0.68	510	0.20	0.05	2.62	0.03	2.78
z5	0.706	0.70	95.60%	7	2.68	414	0.23	0.05	3.21	0.03	3.41
KA15_005											
z1	5.578	0.16	91.42%	8	1.24	212	1.81	0.05	6.50	0.03	6.89
z2	3.730	0.36	74.69%	2	10.15	72	1.25	0.05	22.44	0.03	23.81
z3	3.239	0.16	95.13%	10	0.67	374	1.03	0.05	3.77	0.03	3.98
z4	0.959	0.09	59.84%	1	5.28	45	0.33	0.05	42.42	0.09	45.15
z5	2.128	0.13	90.56%	4	1.17	193	0.69	0.05	7.29	0.03	7.72

Table E2 continued...

	$^{206}Pb/^{238}U$	% error	correlation coefficient	$^{207}Pb/^{206}Pb$		$^{207}Pb/^{235}U$		$^{206}Pb/^{238}U$	
(a)	(g)	(h)		(i)	(h)	(i)	(h)	(i)	(h)
				Porphyry Intrusion					
KA15_018									
z17a	0.01	0.15	0.81	42.04	44.91	32.55	0.64	32.43	0.05
z19a	0.00	0.19	0.89	17.61	65.27	31.85	0.91	32.04	0.06
z15a	0.01	0.10	0.588	115.85	9.23	41.74	0.18	40.46	0.04
z17c	0.01	0.09	0.662	99.56	10.76	41.75	0.21	40.75	0.04
KA15_019									
z8a	0.01	0.29	0.92	28.82	106.33	32.77	1.52	32.82	0.09
z17a	0.00	0.17	0.81	39.99	50.68	32.29	0.72	32.18	0.05
z17c	0.00	0.17	0.78	37.15	49.13	32.22	0.69	32.16	0.06
				Volcaniclastic Deposit					
KA15_010									
z1	0.00	0.40	0.58	10.58	80.77	31.84	1.12	32.12	0.13
z2	0.01	0.29	0.91	30.82	105.19	32.25	1.48	32.27	0.09
z3	0.01	1.02	0.94	-23.81	399.12	31.54	5.42	32.27	0.33
z4	0.01	0.19	0.85	29.89	62.62	32.26	0.88	32.29	0.06
z5	0.01	0.24	0.84	33.39	76.82	32.33	1.08	32.32	0.08
KA15_005									
z1	0.01	0.42	0.93	65.68	154.89	32.58	2.21	32.14	0.14
z2	0.00	1.45	0.95	129.14	527.95	33.24	7.79	31.93	0.46
z3	0.00	0.30	0.73	5.88	90.70	31.80	1.25	32.14	0.10
z4	0.01	2.89	0.95	251.54	975.51	89.14	38.53	83.19	2.39
z5	0.01	0.47	0.92	42.07	174.16	32.34	2.46	32.21	0.15

Concordia plots of the Kassiteres CA-ID-TIMS U-Pb data

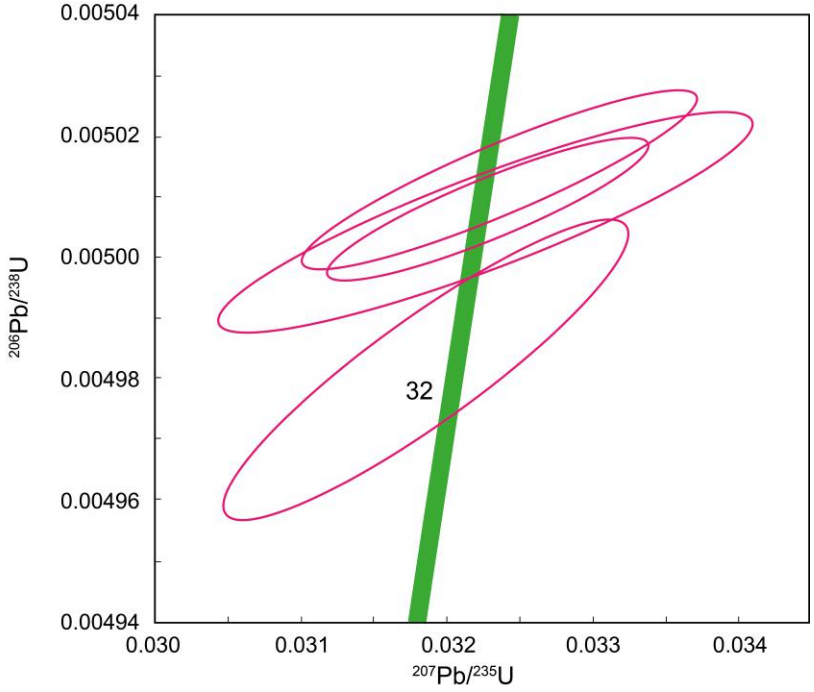

Figure E1: KA15_010 – crystal rich pyroclastic sample overlapping Concordia.

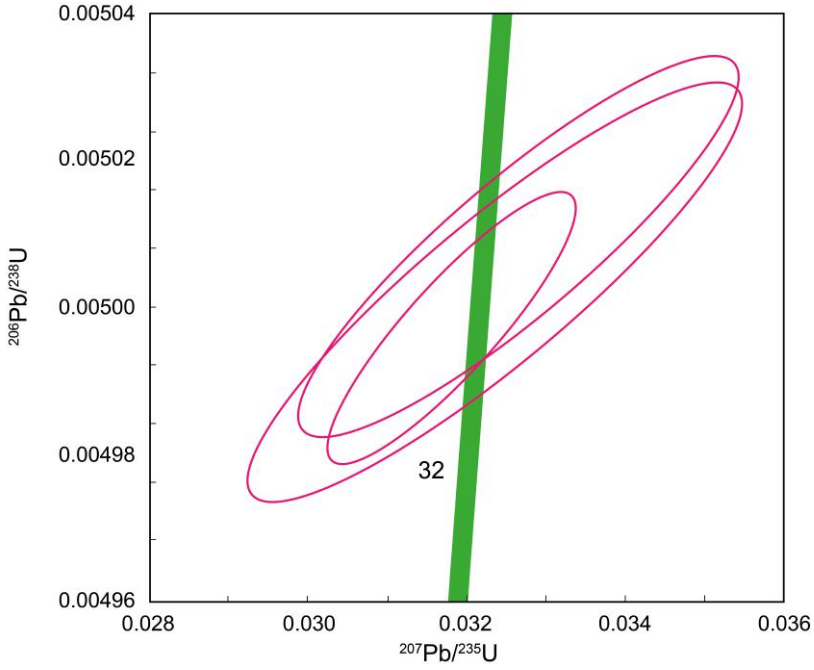

Figure E2: KA15_005 – crystal poor pyroclastic sample overlapping Concordia.

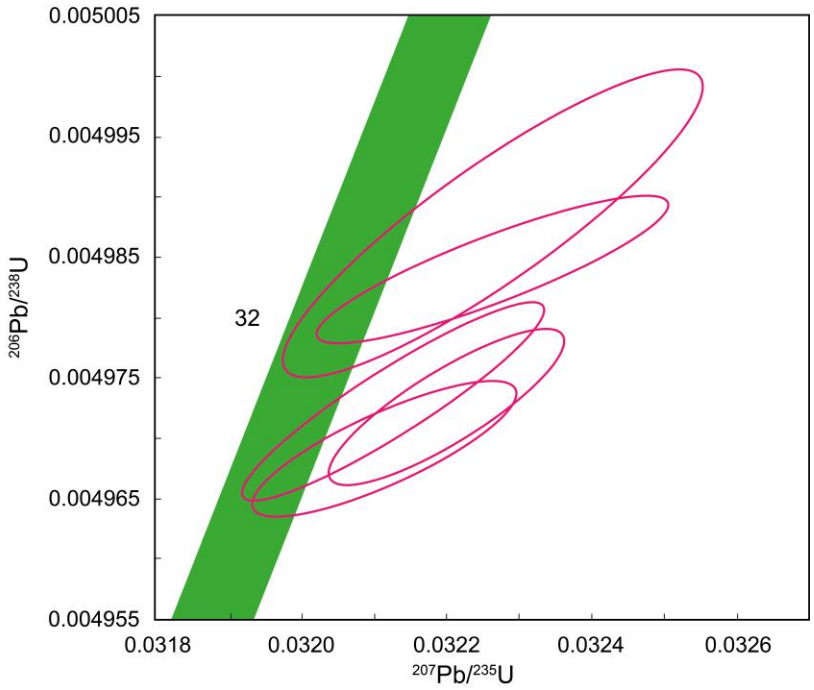

Figure E3: RT14_028 – equigranular host intrusion displaced from Concordia by initial ^{230}Pa disequilibrium.

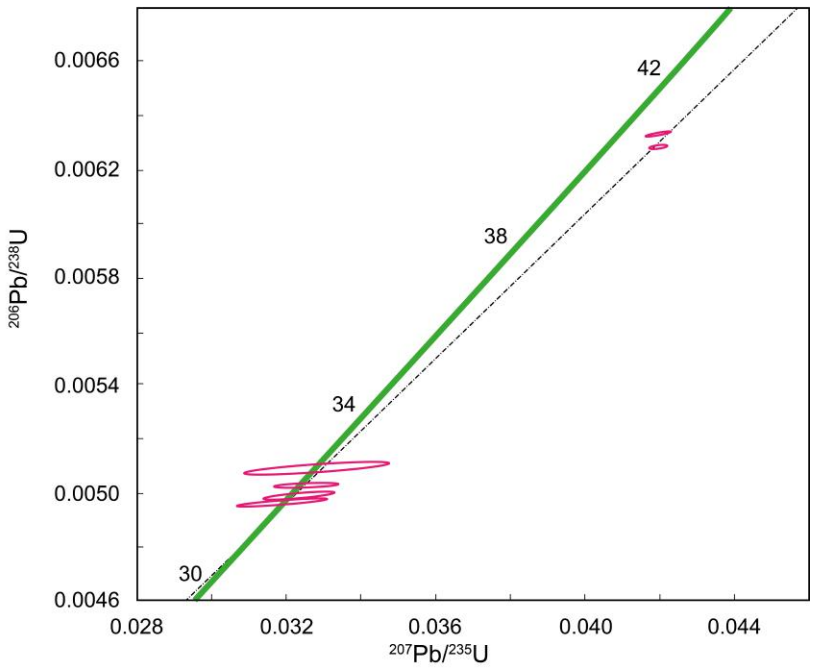

Figure E4: Porphyry zircon tips (both KA15_019 and KA15_018), the autocrystic tips overlap Concordia whilst some of the crystal tips contain inherited domains with a calculated intercept at ca. 331 Ma.

Appendix F

Petrological Modelling

This appendix contains the MATLAB codes used for the petrological modelling presented in Chapter 2 and a comparison of the least-squared linear regression models and petrological models.

Table F1: Summary of the least-squares linear regression through the whole-rock, major element geochemical data.

Figure F1: Comparison of the whole-rock, least-square linear regression and the petrological modelling.

MATLAB Code

```
%MAJOR ELEMENT MODELLING
F_step = 0.01;
F_max = 0.75; %maximum amount of melt crystallisation

%MELT COMPOSITION
melt = [49.28 0.9 16.08 9.25 6.94 11.67 2.00 1.63]; %MP81 from Mavroudchiev the lowest
%K2O sample that follows the LLD
total = sum(melt); %normalise
melt = melt / total * 100;

%CRYSTAL COMPOSITION
hedenbergite = [48.44 0 0 28.96 0 22.6 0 0]; %hedebergite CaFeSi2O6
diopside = [55.49 0 0 0 18.61 25.90 0 0]; %diopside CaMgSi2O6
ferrosillite = [45.54 0 0 54.46 0 0 0 0]; %ferrosillite FeSiO3
enstatite = [59.85 0 0 0 40.15 0 0 0]; %enstatite MgSiO3
anorthite = [43.19 0 36.65 0 0 20.15 0 0]; %anorthite CaAl2Si2O8
albite = [68.74 0 19.44 0 0 0 11.82 0]; %albite NaAlSi3O8
magnetite = [0 0 0 100 0 0 0 0]; %magnetite Fe3O4
ulvospinel = [0 35.73 0 64.28 0 0 0 0]; %ulvospinel TiFe204
crystal1 = (0.8 * enstatite) + (0.2 * ferrosillite);
crystal2 = (0.2 * hedenbergite) + (0.8 * diopside);
crystal3 = (0.75 * anorthite) + (0.25 * albite);
crystal4 = (0.7 * magnetite) + (0.3 * ulvospinel);
Fcrystal1 = 0.15; %percentage crystal 1
Fcrystal2 = 0.25; %percentage crystal 2
Fcrystal3 = 0.52;
Fcrystal4 = 0.08;
crystal = (Fcrystal1 * crystal1) + (Fcrystal2 * crystal2) + (Fcrystal3 * crystal3)
        + (Fcrystal4 * crystal4);
%in order: SiO2, TiO2, Al2O3, FeO, MgO, CaO, Na2O, K2O - in wt%

%PERCENTAGE CRYSTAL CRYSTALLISED
F = [0:F_step:F_max];

%CALCULATE RESIDUAL MELT COMPOSITION
for j = 1:length(F)
    for i = 1:length(melt)
        rmelta(i,1) = melt(i) - (F_step * crystal(i));
        rmelta(i,j+1) = rmelta(i,j) - (F_step * crystal(i));
    end
    total = sum(rmelta);
    rmelt(:,j) = rmelta(:,j) / total(j) * 100;
end

%plot crystallisation model LLDs
figure
% scatter(F,rmelta(1,:))
plot(rmelt(1,:),rmelt(8,:),'r')
hold on
plot(rmelt(1,:),rmelt(7,:),'b')
plot(rmelt(1,:),rmelt(6,:),'g')
```

```
plot(rmelt(1,:),rmelt(4,:),'m')
plot(rmelt(1,:),rmelt(5,:),'y')
plot(rmelt(1,:),rmelt(3,:),'k')
plot(rmelt(1,:),rmelt(2,:),'c')
legend('K2O','Na2O','CaO','FeO','MgO','Al2O3','TiO2')

%import WR chemistry results
data = xlsread('Maronia.xlsx');
a = [3 4 5 7 9 10 11 12];
majors = data(:,a);
total = sum(majors,2);
for i = 1:length(total)
    majors(i,:) = majors(i,:) / total(i) * 100;
end

scatter(majors(:,1),majors(:,8),'r')
scatter(majors(:,1),majors(:,7),'b')
scatter(majors(:,1),majors(:,6),'g')
scatter(majors(:,1),majors(:,4),'m')
scatter(majors(:,1),majors(:,5),'y')
scatter(majors(:,1),majors(:,3),'k')
scatter(majors(:,1),majors(:,2),'c')

%find the row of the matrix with the SiO2 closest to MA15_006 (most primitive of the
%samples for which starting trace element concentrations are known (SiO2 = 50.41 wt %).
[c n] = min(abs(rmelt(1,:)-majors(1,1)));
F(n)

%TRACE ELEMENT MODELLING
Fr = 1 - [0:F_step:((F_step*length(rmelt(1,n:end)))-F_step)];
CO = [717 1208 79 107 85 24]; % initial concentration of the trace element
%in order Sr, Ba, Cr, Rb

%MINERAL FRACTIONS
Fplag = 0.45;
Fopx = 0.35;
Fcpx = 0.2;
Fmin = [Fplag Fopx Fcpx];

%PARTITION COEFFICIENTS (see Table 2.6)
Dplag = [2 0.5 0.08 0.2 0.006 0.01];
Dopx = [0.0012 0.0036 7.78 0.0038 0.032 0.095];
Dcpx = [0.128 0.0007 3.8 0.011 0.123 0.467];
%In order: Sr, Ba, Cr, Rb, Zr, Y

%BULK PARTITION COEFFICIENTS
DSrB = (Dplag(1) * Fmin(1)) + (Dopx(1) * Fmin(2)) + (Dcpx(1) * Fmin(3));
DBaB = (Dplag(2) * Fmin(1)) + (Dopx(2) * Fmin(2)) + (Dcpx(2) * Fmin(3));
DCrB = (Dplag(3) * Fmin(1)) + (Dopx(3) * Fmin(2)) + (Dcpx(3) * Fmin(3));
DRbB = (Dplag(4) * Fmin(1)) + (Dopx(4) * Fmin(2)) + (Dcpx(4) * Fmin(3));
DZrB = (Dplag(5) * Fmin(1)) + (Dopx(5) * Fmin(2)) + (Dcpx(5) * Fmin(3));
DYB = (Dplag(6) * Fmin(1)) + (Dopx(6) * Fmin(2)) + (Dcpx(6) * Fmin(3));
D = [DSrB DBaB DCrB DRbB DZrB DYB];
```

```
for j = 1:length(D)
    for i = 1:length(Fr)
        ClC0(i,j) = Fr(i) ^ (D(j) - 1); %liquid composition
        CrcC0(i,j) = (1 - Fr(i)^D(j))/(1 - Fr(i)); % residue composition
    end
end

%plot liquid composition
semilogy(Fr,ClC0)
ylabel('Cl/C0')
xlabel('F')
title('Rayleigh Fractionation - Concentration in Residual Liquid')
legend('Sr','Ba','Cr','Rb','Zr','Y')

%plot residue composition
figure
semilogy(Fr,CrcC0)
ylabel('Crc/C0')
xlabel('F')
title('Rayleigh Fractionation - Concentration in Cumulate')
legend('Sr','Ba','Cr','Rb','Zr','Y')

%PLOT THE PREDICTED TRACE ELEMENT COMPOSITION VS SIO2

for j = 1:length(D)
    for i = 1:length(Fr)
        Cl(i,j) = CO(j) * ClC0(i,j);
    end
end

figure
plot(rmelt(1,n:end), log10(Cl(:,3)),'g')
hold on
plot(rmelt(1,n:end), log10(Cl(:,2)),'k')
plot(rmelt(1,n:end), log10(Cl(:,1)),'m')
plot(rmelt(1,n:end), log10(Cl(:,4)),'b')
plot(rmelt(1,n:end), log10(Cl(:,5)),'r')
plot(rmelt(1,n:end), log10(Cl(:,6)),'c')
xlabel('SiO2 wt % - calculated in fractional crystallisation model')
ylabel('Trace element (ppm)')

%IMPORT AND PLOT GEOCHEMICAL DATA

dataRb = data(:,19);
dataSr = data(:,20);
dataCr = data(:,24);
dataBa = data(:,21);
dataZr = data(:,28);
dataY = data(:,27);

scatter(majors(:,1),log10(dataSr),'m','filled','c')
scatter(majors(:,1),log10(dataBa),'k','filled','c')
```

```
scatter(majors(:,1),log10(dataCr),'g','filled','c')
scatter(majors(:,1),log10(dataRb),'b','filled','c')
scatter(majors(:,1),log10(dataZr),'r','filled','c')
scatter(majors(:,1),log10(dataY),'c','filled','c')
legend('Cr','Ba','Sr','Rb','Zr','Y','Sr','Ba','Cr','Rb','Zr','Y')
```

Model Comparison

A least-squared linear regression was carried out on the major element whole-rock data from Maronia to compare the observed fractionation trends with the fractionation trends predicted by the petrological modelling. This assumes that the observed fractionation trends are linear with no inflection points; whilst this is an over-simplification of the natural systems, it is an appropriate first-order approximation of the data.

The petrological model agrees with the direction of observed fractionation trends for K_2O, Na_2O, CaO, FeO and MgO whilst the slope of the models overlap within 2 σ uncertainty (Figure F1). Closest agreement between the petrological model and linear regression is observed in the whole-rock datasets with the highest R-squared value, i.e. the datasets with the least scatter; the closest fit is with CaO. The Al_2O_3 whole-rock data is highly scattered with an adjusted R-squared value of -0.079 indicating that a linear fit is a poor approximation of the data. The petrological model of Al_2O_3 predicts a fractionation trend within the scatter of the 2σ uncertainty envelope. $TiO_2$is the only variable where the petrological model disagrees with the least-squares linear regression. Variance in the TiO_2 whole-rock dataset is minimal with $0.85 < TiO_2$wt.% < 1.1 and petrological modelling of TiO_2 is highly dependent upon the chemistry of the Fe-Ti-oxide phase magnetite.

Table F1: Compilation of the R-squared and adjusted R-squared values from the least-squared linear regression models. The adjusted R-squared values account for the number of values within the dataset.

Element	Linear Regression with SiO_2	
	R^2	Adjusted R^2
TiO_2	0.316	0.254
Al_2O_3	0.011	-0.079
MgO	0.488	0.442
FeO	0.912	0.904
CaO	0.819	0.802
Na_2O	0.293	0.228
K_2O	0.693	0.665

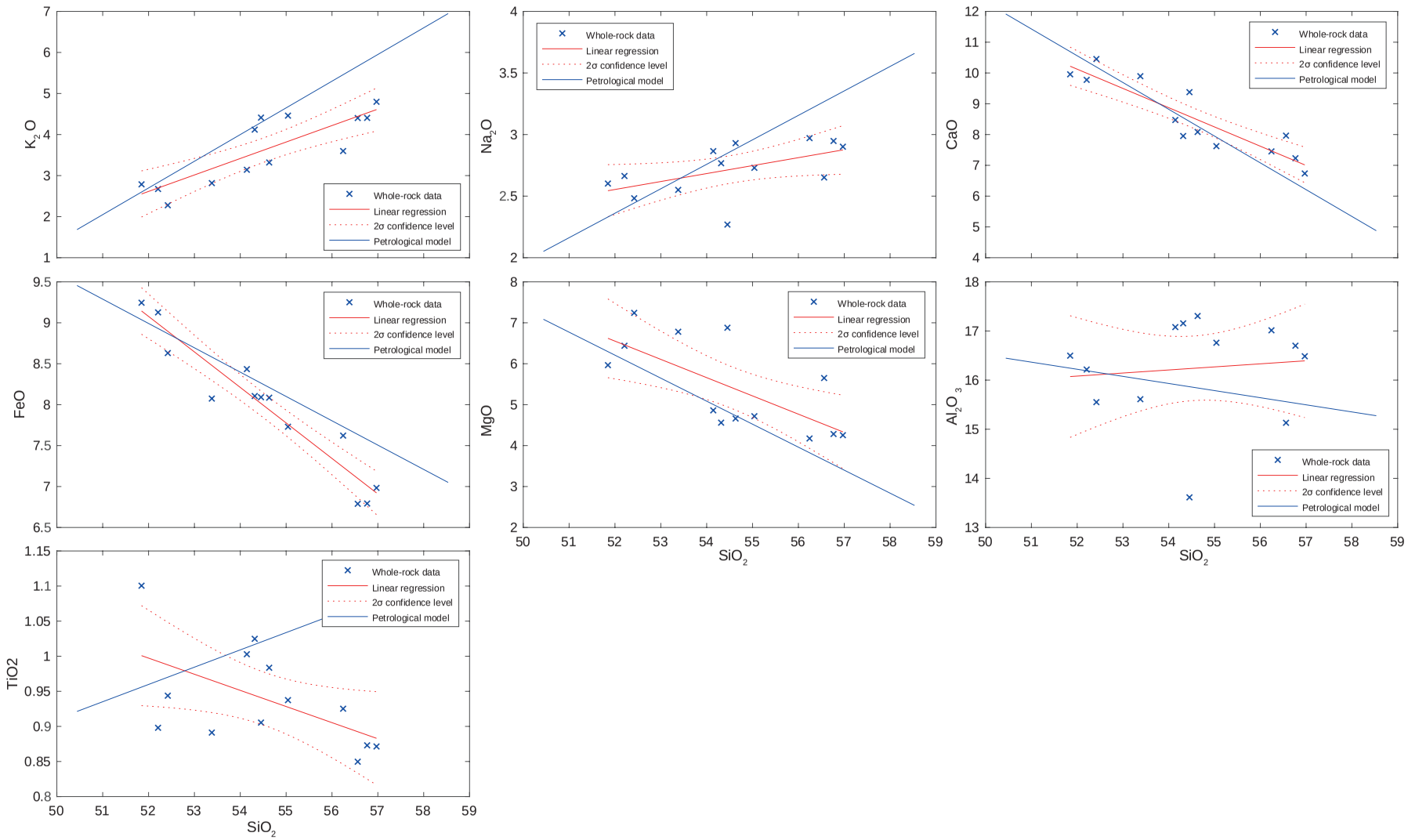

Figure F1: Comparison of least-squared linear regression trends through whole-rock data with predicted petrological modelling.

Appendix G

Thermobarometry

This appendix contains the mineral chemistry data and thermobarometry results presented in Chapter 3.

Table G1–3: Spectrometer set-up.
Table G4: Amphibole – plagioclase thermobarometry.
Table G5: Two-pyroxene thermometry.
Table G6: Zircon saturation thermometry.
Table G7: Apatite saturation thermometry.

EPMA Spectrometer Set-Up

Elements are listed in order of analyses and were peaked up on their assigned standards. Upper and lower backgrounds were counted for 50% of the analysis time. The elements were peaked up on:
Na, Si – albite
K, Al – sanidine
Mg – olivine
Ca – wollastonite
Ti, Fe – ilmenite
Sr – $SrTiO_3$
Cr – Cr_2O_3
Mn – Mn-metal

Matrix-matched secondary standards for the analyses were:
KK1 – Ti-rich hornblende
BCR2 – basaltic glass
SPH – labradorite
Diopside
Chromite

Plagioclase

Table G1: Spectrometer set-up for plagioclase analyses.

Spectrometer 1 LPET	Spectrometer 2 TAP	Spectrometer 3 LPET	Spectrometer 4 TAP	Spectrometer 5 LLIF
		20 kV 10 nA 5 μm beam diameter		
K (20 s)	Na (10s)	Ca (20 s)	Si (10 s)	
			Al (10 s)	
		20 kV 100 nA 5 μm beam diameter		
Sr (30 s)	Mg (30 s)	Sr (30 s)	Mg (30 s)	Fe (30 s)

Amphibole

Table G2: Spectrometer set-up for amphibole analyses.

Spectrometer 1 LPET	Spectrometer 2 TAP	Spectrometer 3 LPET	Spectrometer 4 TAP	Spectrometer 5 LLIF
		20 kV 10 nA 5 μm beam diameter		
K (10 s)	Na (10 s)	Ca (30 s)	Si (10 s)	Fe (30 s)
Cl (100 s)	F (100 s)	Ti (40 s)	Al (30 s)	Mn (60 s)
		Cr (40 s)	Mg (30 s)	

Pyroxene

Table G3: Spectrometer set-up for pyroxene analyses.

Spectrometer 1	Spectrometer 2	Spectrometer 3	Spectrometer 4	Spectrometer 5
LPET	TAP	LPET	TAP	LLIF
		20 kV 10 nA 5 μm beam diameter		
K (10 s)	Na (10 s)	Ti (30 s)	Si (10 s)	Fe (30 s)
Ca (30 s)	Mg (30 s)	Cr (40 s)	Al (30 s)	Mn (40 s)

Results

See overleaf...

Table G4: Amphibole – plagioclase thermobarometry results using calibrations of Holland and Blundy (1994) (*T*) and Mutch et al. (2016) (*P*). All elemental oxides are given in wt %.

Amphibole Analyses													Plagioclase Analyses								
SiO_2	TiO_2	Al_2O_3	Cr_2O_3	FeO	MgO	CaO	MnO	Na_2O	K_2O	F	Cl	TOTAL	SiO_2	Al_2O_3	FeO	SrO	BaO	CaO	Na_2O	K_2O	TOTAL
Kassiteres																					
KA15_013																					
51.20	1.04	4.18	0.00	9.02	17.74	12.18	0.31	0.98	0.34	0.36	0.17	97.52	60.38	24.57	0.43	0.06	0.00	6.69	7.22	0.49	99.82
52.33	0.70	3.02	0.00	8.35	18.49	12.19	0.36	0.78	0.25	0.36	0.14	96.96	60.38	24.57	0.43	0.06	0.00	6.69	7.22	0.49	99.82
51.60	0.90	4.34	0.00	10.09	17.68	11.73	0.29	1.07	0.34	0.22	0.16	98.40	60.82	24.31	0.45	0.04	0.00	6.35	7.37	0.48	99.82
KA15_016																					
53.71	0.46	2.32	0.00	9.64	18.27	11.88	0.24	0.73	0.25	0.53	0.13	98.17	64.30	22.09	0.18	0.06	0.00	3.27	9.82	0.11	99.84
51.75	0.93	3.78	0.00	8.30	18.64	11.97	0.21	1.05	0.42	0.73	0.14	97.92	56.88	26.43	0.45	0.07	0.00	9.03	6.26	0.33	99.44
52.88	0.76	3.19	0.02	7.96	19.35	12.06	0.23	0.96	0.32	0.69	0.13	98.53	56.11	27.12	0.49	0.09	0.00	9.86	5.67	0.38	99.73
KA15_017																					
54.39	0.63	2.19	0.02	7.84	19.63	11.81	0.27	0.78	0.18	0.33	0.11	98.19	64.33	22.16	0.22	0.03	0.00	3.62	9.06	0.55	99.98
53.33	0.80	2.89	0.05	9.18	18.50	11.66	0.23	0.78	0.22	0.25	0.11	98.01	64.82	21.39	0.22	0.05	0.00	2.91	9.42	0.39	99.18
KS16_006A																					
44.50	2.58	9.36	0.14	12.34	13.72	11.81	0.12	2.16	0.86	0.66	0.58	98.82	54.18	28.20	0.46	0.08	0.00	11.30	4.72	0.39	99.32
RT14_027																					
53.69	0.29	2.48	0.01	10.58	17.58	12.80	0.15	0.66	0.14	-0.23	0.08	98.22	54.55	28.13	0.41	0.00	0.00	10.73	6.06	0.21	100.08
53.20	0.48	2.67	0.08	10.47	17.72	12.60	0.19	0.68	0.20	0.26	0.08	98.65	54.55	28.13	0.41	0.00	0.00	10.73	6.06	0.21	100.08
53.88	0.34	2.25	0.04	10.34	17.81	12.75	0.18	0.60	0.18	0.87	0.07	99.30	54.55	28.13	0.41	0.00	0.00	10.73	6.06	0.21	100.08
RT14_028																					
51.14	0.73	3.78	0.05	11.23	16.46	12.05	0.21	0.84	0.31	0.30	0.15	97.25	65.37	21.45	0.14	0.00	0.00	2.33	10.32	0.12	99.73
50.12	0.82	4.68	0.02	11.91	15.92	11.82	0.24	0.98	0.42	0.06	0.20	97.20	57.64	25.68	0.41	0.00	0.00	7.96	6.90	0.51	99.10
50.84	0.77	3.94	0.06	11.89	16.67	11.39	0.23	1.00	0.31	0.21	0.15	97.47	57.63	25.76	0.48	0.00	0.00	7.97	7.02	0.40	99.26
50.29	0.81	4.84	0.01	12.25	16.08	11.81	0.21	1.21	0.43	0.43	0.19	98.55	59.88	25.07	0.33	0.00	0.00	6.92	8.44	0.41	101.05
50.57	0.81	4.27	0.03	12.06	16.38	11.54	0.22	0.98	0.38	-0.28	0.16	97.11	58.16	25.54	0.40	0.00	0.00	7.75	6.64	0.78	99.25
50.54	0.82	4.67	0.07	12.47	16.33	11.57	0.25	1.32	0.43	0.17	0.16	98.78	59.88	25.07	0.33	0.00	0.00	6.92	8.44	0.41	101.05
49.84	0.81	4.73	0.03	12.34	15.93	11.51	0.26	1.08	0.45	0.00	0.19	97.16	58.62	25.60	0.45	0.00	0.00	7.88	6.96	0.40	99.91
49.57	1.04	5.11	0.06	12.67	15.70	11.50	0.21	1.17	0.46	-0.05	0.17	97.60	58.89	25.59	0.39	0.00	0.00	7.54	7.32	0.40	100.13
50.84	0.80	4.30	0.07	12.20	16.51	11.45	0.23	1.23	0.37	1.51	0.16	99.65	56.53	27.07	0.45	0.00	0.00	9.33	6.65	0.59	100.62
50.86	1.00	4.51	0.02	12.05	16.35	11.85	0.23	1.04	0.38	0.44	0.13	98.86	56.90	27.16	0.45	0.00	0.00	9.64	6.11	0.37	100.64
48.79	0.99	5.46	0.08	12.85	15.31	11.54	0.25	1.33	0.54	0.23	0.21	97.58	59.96	24.30	0.35	0.00	0.00	6.42	7.84	0.73	99.59
48.85	1.00	5.30	0.06	12.68	15.54	11.58	0.22	1.32	0.48	0.44	0.18	97.66	58.21	25.54	0.38	0.00	0.00	7.71	6.94	0.46	99.24
Leptokaria																					
RT14_009																					
53.85	0.28	2.24	0.00	10.51	17.41	12.21	0.59	0.48	0.15	0.00	0.04	97.77	67.97	20.11	0.08	0.06	0.00	0.80	11.08	0.14	100.25
RT14_010																					
53.42	0.27	2.67	0.00	10.98	16.96	12.34	0.62	0.50	0.16	0.00	0.03	97.95	64.14	22.08	0.30	0.07	0.00	2.63	9.93	0.40	99.65
53.15	0.29	2.80	0.00	10.78	16.87	12.19	0.61	0.64	0.15	0.25	0.04	97.75	65.23	21.59	0.33	0.00	0.00	2.91	9.90	0.37	100.32
51.17	0.79	4.61	0.00	13.30	14.92	11.17	0.98	1.00	0.34	0.47	0.07	98.81	64.34	22.35	0.35	0.02	0.00	3.49	9.50	0.46	100.56
52.55	0.40	3.15	0.00	11.31	16.70	12.16	0.63	0.70	0.17	0.24	0.05	98.03	61.59	23.75	0.24	0.01	0.00	5.69	8.16	0.32	99.76
50.32	0.94	4.81	0.00	12.27	15.46	11.47	0.86	1.03	0.34	0.52	0.08	98.11	65.49	21.70	0.28	0.00	0.00	2.76	9.76	0.41	100.38
50.54	0.81	4.52	0.00	13.57	14.95	11.28	1.05	0.97	0.37	0.00	0.08	98.12	64.34	22.11	0.32	0.00	0.00	3.47	9.53	0.28	100.04
50.55	0.85	4.52	0.00	13.53	15.02	11.18	1.01	1.19	0.36	0.00	0.13	98.32	66.08	21.20	0.20	0.06	0.00	2.12	10.55	0.09	100.30
49.77	0.74	5.80	0.00	13.61	14.79	11.38	0.79	1.05	0.44	0.00	0.05	98.43	61.33	23.97	0.21	0.07	0.00	5.84	8.01	0.36	99.79
48.19	0.93	6.87	0.00	13.92	14.13	10.94	0.78	1.40	0.36	0.00	0.08	97.60	64.41	21.96	0.12	0.00	0.00	3.30	9.62	0.35	99.77
47.20	1.19	8.00	0.00	13.68	14.19	11.54	0.46	1.33	0.58	0.19	0.08	98.43	64.72	21.99	0.17	0.08	0.00	2.84	9.92	0.30	100.00
47.35	1.29	7.93	0.00	14.02	13.92	11.26	0.58	1.58	0.52	0.46	0.06	98.98	62.45	23.63	0.21	0.03	0.00	5.06	8.46	0.37	100.21

Table G4: continued...

Amphibole Analyses													Plagioclase Analyses								
SiO_2	TiO_2	Al_2O_3	Cr_2O_3	FeO	MgO	CaO	MnO	Na_2O	K_2O	F	Cl	TOTAL	SiO_2	Al_2O_3	FeO	SrO	BaO	CaO	Na_2O	K_2O	TOTAL
RT14_010																					
47.52	1.27	7.46	0.00	14.01	14.14	11.09	0.60	1.45	0.51	0.00	0.07	98.10	61.09	23.61	0.25	0.06	0.00	5.52	8.40	0.31	99.23
47.46	1.54	7.66	0.00	13.89	13.73	11.25	0.74	1.73	0.49	0.37	0.06	98.92	61.43	24.06	0.18	0.04	0.00	5.53	8.43	0.30	99.97
46.55	1.44	8.73	0.02	13.19	14.69	11.18	0.39	1.53	0.50	0.41	0.05	98.68	65.48	22.04	0.23	0.01	0.00	2.88	9.84	0.38	100.86
45.49	2.28	9.15	0.00	12.93	14.12	11.31	0.28	1.90	0.63	0.52	0.06	98.67	67.41	20.74	0.12	0.10	0.00	1.37	11.08	0.15	100.97
48.13	1.16	6.68	0.00	13.46	14.39	11.47	0.66	1.45	0.44	0.00	0.06	97.90	58.17	26.08	0.35	0.09	0.00	8.02	6.87	0.39	100.01
47.11	1.22	7.93	0.00	14.16	14.11	11.35	0.55	1.27	0.51	0.27	0.08	98.57	55.31	28.21	0.27	0.10	0.00	10.37	5.74	0.26	100.27
45.48	2.27	9.23	0.00	12.95	14.27	11.30	0.30	1.76	0.65	0.00	0.06	98.25	54.20	29.27	0.40	0.10	0.00	11.52	4.85	0.15	100.50
RT14_015																					
48.93	0.78	5.79	0.00	14.86	13.80	11.26	0.53	0.95	0.48	0.00	0.17	97.54	60.63	24.48	0.30	0.07	0.00	6.37	7.69	0.58	100.13
48.31	1.01	5.82	0.00	14.78	13.69	11.44	0.52	0.82	0.50	0.36	0.18	97.42	59.41	25.29	0.34	0.09	0.00	7.11	7.02	0.47	99.72
48.16	1.03	6.12	0.00	15.19	13.45	11.46	0.51	0.93	0.52	0.33	0.21	97.89	60.12	24.49	0.27	0.09	0.00	6.71	7.31	0.60	99.59
47.09	1.51	6.63	0.00	15.30	12.74	11.40	0.51	1.14	0.63	0.00	0.20	97.16	58.93	25.57	0.36	0.10	0.00	7.97	7.03	0.35	100.31
RT14_017																					
47.90	1.06	6.99	0.00	15.01	13.20	11.52	0.46	0.94	0.46	0.00	0.06	97.58	58.51	26.11	0.23	0.05	0.00	7.99	6.76	0.24	99.91
47.27	1.57	8.61	0.00	12.96	14.36	11.05	0.34	1.33	0.48	0.44	0.05	98.44	58.95	25.46	0.25	0.11	0.00	7.41	7.25	0.39	99.83
46.64	1.49	8.50	0.00	14.07	13.56	11.20	0.39	1.63	0.40	0.00	0.04	97.91	60.82	24.49	0.20	0.12	0.00	6.24	7.81	0.31	99.98
45.26	1.79	9.29	0.00	14.23	13.40	11.16	0.37	1.69	0.47	0.00	0.04	97.69	61.79	23.66	0.18	0.07	0.00	5.22	8.35	0.23	99.51
47.11	1.49	8.29	0.00	14.12	13.72	11.22	0.64	1.68	0.50	0.19	0.06	99.02	57.91	26.22	0.21	0.11	0.00	8.41	6.54	0.31	99.70
45.97	1.51	8.77	0.00	13.79	13.63	11.08	0.42	1.51	0.40	0.35	0.04	97.47	56.48	26.88	0.26	0.10	0.00	9.29	6.18	0.30	99.50
46.01	1.55	8.75	0.00	14.19	13.65	11.21	0.42	1.33	0.42	0.00	0.05	97.57	55.40	27.95	0.37	0.08	0.00	10.67	5.56	0.14	100.15
45.35	1.69	9.18	0.00	14.27	13.47	11.17	0.41	1.82	0.45	0.00	0.04	97.84	57.03	26.84	0.27	0.08	0.00	9.10	6.08	0.40	99.82
47.54	1.23	7.62	0.00	14.01	13.57	11.89	0.46	0.99	0.43	0.00	0.08	97.80	46.84	33.42	0.59	0.11	0.00	17.02	1.87	0.04	99.89
47.57	1.15	7.68	0.00	14.41	13.33	11.48	0.53	1.04	0.36	0.00	0.05	97.58	46.61	33.71	0.69	0.10	0.00	17.45	1.68	0.03	100.29
46.95	1.66	8.19	0.00	13.35	14.04	11.17	0.46	1.86	0.50	0.50	0.07	98.76	54.77	28.48	0.32	0.08	0.00	11.04	5.12	0.25	100.08
47.61	1.00	7.63	0.00	13.76	14.02	11.40	0.49	1.04	0.33	0.00	0.05	97.34	46.30	33.63	0.54	0.12	0.00	17.28	1.79	0.03	99.68
46.11	2.18	9.05	0.00	13.18	14.64	11.24	0.28	1.69	0.65	0.00	0.06	99.07	54.45	28.75	0.37	0.09	0.00	11.16	5.11	0.20	100.15
46.24	1.60	8.93	0.00	14.23	13.34	11.07	0.43	1.37	0.44	0.00	0.04	97.71	47.03	33.20	0.68	0.11	0.00	16.92	1.90	0.04	99.90
45.68	1.54	8.80	0.00	15.19	12.61	11.11	0.49	1.40	0.42	0.28	0.04	97.58	46.56	33.53	0.37	0.10	0.00	17.18	1.81	0.02	99.58
45.38	1.72	9.20	0.00	13.99	13.49	11.34	0.40	1.48	0.44	0.00	0.04	97.49	47.25	33.24	0.48	0.08	0.00	16.79	1.99	0.15	99.99
45.76	1.74	8.92	0.00	14.01	13.42	11.17	0.41	1.30	0.42	0.22	0.04	97.41	46.46	33.57	0.46	0.11	0.00	17.43	1.67	0.02	99.72
45.70	1.59	8.80	0.00	14.11	13.31	11.35	0.46	1.30	0.43	0.00	0.04	97.08	46.55	33.55	0.51	0.09	0.00	17.27	1.55	0.27	99.80
45.56	1.67	9.07	0.00	14.52	13.12	11.18	0.43	1.39	0.45	0.00	0.04	97.42	46.03	33.61	0.49	0.11	0.00	17.23	1.73	0.03	99.23
45.96	1.50	8.83	0.00	14.24	13.28	11.20	0.46	1.36	0.42	0.00	0.04	97.30	45.69	33.54	0.48	0.08	0.00	17.62	1.50	0.03	98.94
46.58	1.38	8.29	0.00	15.42	12.97	11.09	0.54	1.25	0.40	0.00	0.06	97.99	45.91	33.95	0.63	0.10	0.00	17.91	1.44	0.03	99.99
46.32	1.50	8.53	0.00	13.91	13.69	11.11	0.44	1.59	0.41	0.00	0.05	97.53	46.02	33.50	0.41	0.09	0.00	17.29	1.75	0.03	99.10
46.72	1.31	8.30	0.00	14.60	13.66	10.96	0.45	1.34	0.37	0.00	0.05	97.76	46.01	34.17	0.53	0.09	0.00	17.64	1.51	0.02	99.97
46.00	1.54	8.63	0.00	15.56	12.68	11.13	0.47	1.29	0.36	0.36	0.04	98.05	45.99	34.05	0.59	0.09	0.00	17.80	1.42	0.03	99.97
45.20	1.72	9.07	0.00	15.11	12.45	11.14	0.41	1.53	0.43	0.38	0.05	97.50	45.98	33.93	0.46	0.10	0.00	17.72	1.39	0.03	99.62
46.38	1.48	8.58	0.00	14.02	13.88	11.10	0.39	1.42	0.39	0.39	0.04	98.09	46.20	33.82	0.65	0.10	0.00	17.45	1.63	0.04	99.90
45.39	1.80	9.38	0.00	14.63	13.19	11.07	0.41	1.37	0.46	0.20	0.04	97.95	46.06	34.07	0.70	0.12	0.00	17.34	1.57	0.07	99.93
45.21	1.85	9.34	0.00	14.23	13.22	11.25	0.38	1.60	0.45	0.29	0.04	97.87	46.18	33.68	0.55	0.10	0.00	17.33	1.61	0.04	99.50
46.25	1.45	8.50	0.00	13.94	13.93	11.12	0.41	1.42	0.41	0.38	0.03	97.85	46.31	33.67	0.59	0.09	0.00	17.33	1.66	0.03	99.68
45.83	1.73	9.09	0.00	14.26	13.58	11.24	0.38	1.51	0.45	0.00	0.05	98.11	46.61	33.34	0.58	0.10	0.00	17.31	1.65	0.05	99.65
45.99	1.60	8.71	0.00	14.48	13.43	11.14	0.44	1.47	0.40	0.00	0.05	97.69	45.81	33.90	0.69	0.09	0.00	17.72	1.60	0.04	99.84
47.98	1.45	7.35	0.00	12.70	15.03	11.21	0.44	1.63	0.46	0.35	0.07	98.67	46.81	33.51	0.82	0.10	0.00	17.17	1.75	0.03	100.19

Table G4: continued...

Amphibole Analyses													Plagioclase Analyses							
SiO_2	TiO_2	Al_2O_3	Cr_2O_3	FeO	MgO	CaO	MnO	Na_2O	K_2O	F	Cl	TOTAL	SiO_2	Al_2O_3	FeO	SrO	BaO	CaO	Na_2O	K_2O	TOTAL
RT14_017																					
46.12	1.60	8.82	0.00	14.13	13.60	11.15	0.38	1.39	0.41	0.36	0.04	97.98	45.36	33.81	0.75	0.10	0.00	17.78	1.35	0.03	99.20
45.89	1.52	8.76	0.00	14.82	13.18	11.17	0.39	1.44	0.40	0.00	0.04	97.62	45.79	33.85	0.74	0.10	0.00	17.81	1.43	0.02	99.74
44.00	2.37	10.90	0.00	12.83	13.70	11.26	0.27	1.92	0.53	0.00	0.03	97.80	45.94	33.64	0.67	0.10	0.00	17.57	1.59	0.02	99.54
43.62	2.18	10.40	0.00	13.22	13.28	11.34	0.30	1.85	0.51	0.00	0.03	96.73	45.46	33.94	0.64	0.11	0.00	17.69	1.44	0.03	99.32
43.74	2.07	10.31	0.00	14.44	12.85	11.12	0.37	1.90	0.53	0.00	0.04	97.36	46.75	33.16	0.54	0.10	0.00	17.01	1.62	0.12	99.31
44.38	2.14	10.19	0.00	13.70	13.49	11.22	0.32	1.76	0.47	0.00	0.03	97.69	45.77	34.12	0.60	0.11	0.00	17.71	1.54	0.00	99.84
44.10	2.18	10.54	0.00	13.80	13.36	11.28	0.31	1.82	0.52	0.35	0.03	98.28	45.92	33.73	0.66	0.09	0.00	17.75	1.38	0.00	99.52
44.38	1.91	9.97	0.00	14.02	13.34	11.15	0.35	1.86	0.51	0.24	0.04	97.77	45.80	33.52	0.63	0.09	0.00	17.70	1.39	0.03	99.18
47.43	0.97	7.10	0.00	15.07	13.35	11.70	0.45	0.88	0.47	0.00	0.09	97.51	58.92	25.51	0.33	0.08	0.00	7.66	7.19	0.16	99.84
RT14_023																					
50.83	0.61	4.43	0.02	12.87	15.50	11.71	0.30	0.91	0.33	0.00	0.17	97.69	65.43	22.14	0.11	0.05	0.00	3.23	10.01	0.12	101.09
50.13	0.79	4.84	0.00	13.55	15.25	11.39	0.32	0.99	0.47	0.00	0.16	97.91	66.02	21.70	0.15	0.05	0.00	2.52	10.03	0.27	100.76
49.86	1.02	5.08	0.04	13.51	14.98	11.51	0.31	1.08	0.46	0.41	0.16	98.42	66.42	21.56	0.18	0.06	0.00	2.11	10.53	0.25	101.10
49.66	0.84	4.74	0.03	13.81	14.86	11.38	0.30	1.01	0.41	0.00	0.15	97.18	61.26	24.02	0.39	0.04	0.00	5.79	8.18	0.48	100.16
50.18	0.93	4.49	0.00	13.44	15.10	11.81	0.30	0.93	0.38	0.45	0.21	98.23	60.15	24.85	0.36	0.04	0.00	6.59	7.67	0.42	100.11
49.96	0.85	4.95	0.05	13.46	15.23	11.51	0.29	1.12	0.42	0.35	0.16	98.35	61.37	23.96	0.25	0.04	0.00	5.68	8.02	0.57	99.89
48.66	1.05	5.74	0.11	14.10	14.23	11.32	0.33	1.25	0.55	0.27	0.20	97.80	61.09	23.95	0.26	0.02	0.00	5.90	8.08	0.49	99.80
48.62	1.07	5.79	0.10	14.26	14.26	11.30	0.30	1.26	0.60	0.00	0.20	97.76	61.97	23.15	0.35	0.03	0.00	5.08	8.37	0.61	99.57

Table G4: continued...

Amphibole A.P.F.U											Plagioclase A.P.F.U							
SiO_2	TiO_2	Al_2O_3	Cr_2O_3	FeO	Fe2O3	MgO	CaO	MnO	Na_2O	K_2O	SiO_2	Al_2O_3	FeO	SrO	BaO	CaO	Na_2O	K_2O
Kassiteres																		
KA15_013																		
7.33	0.11	0.71	0.00	0.22	0.86	3.79	1.87	0.04	0.27	0.06	2.70	1.29	0.02	0.00	0.00	0.32	0.63	0.03
7.51	0.08	0.51	0.00	0.13	0.87	3.95	1.87	0.04	0.22	0.05	2.70	1.29	0.02	0.00	0.00	0.32	0.63	0.03
7.32	0.10	0.73	0.00	0.28	0.92	3.74	1.78	0.03	0.29	0.06	2.71	1.28	0.02	0.00	0.00	0.30	0.64	0.03
KA15_016																		
7.63	0.05	0.39	0.00	0.14	1.01	3.87	1.81	0.03	0.20	0.05	2.84	1.15	0.01	0.00	0.00	0.16	0.84	0.01
7.39	0.10	0.64	0.00	0.14	0.85	3.97	1.83	0.03	0.29	0.08	2.57	1.41	0.02	0.00	0.00	0.44	0.55	0.02
7.48	0.08	0.53	0.00	0.07	0.87	4.08	1.83	0.03	0.26	0.06	2.54	1.45	0.02	0.00	0.00	0.48	0.50	0.02
KA15_017																		
7.65	0.07	0.36	0.00	0.08	0.84	4.12	1.78	0.03	0.21	0.03	2.84	1.15	0.01	0.00	0.00	0.17	0.78	0.03
7.55	0.09	0.48	0.01	0.18	0.91	3.90	1.77	0.03	0.21	0.04	2.88	1.12	0.01	0.00	0.00	0.14	0.81	0.02
KS16_006A																		
6.53	0.29	1.62	0.02	0.28	1.23	3.00	1.86	0.02	0.61	0.16	2.47	1.51	0.02	0.00	0.00	0.55	0.42	0.02
RT14_027																		
7.60	0.03	0.41	0.00	0.17	1.08	3.71	1.94	0.02	0.18	0.03	2.47	1.50	0.02	0.00	0.00	0.52	0.53	0.01
7.55	0.05	0.45	0.01	0.11	1.13	3.75	1.92	0.02	0.19	0.04	2.47	1.50	0.02	0.00	0.00	0.52	0.53	0.01
7.63	0.04	0.38	0.00	0.11	1.11	3.76	1.93	0.02	0.16	0.03	2.47	1.50	0.02	0.00	0.00	0.52	0.53	0.01
RT14_028																		
7.40	0.08	0.64	0.01	0.26	1.10	3.55	1.87	0.03	0.23	0.06	2.88	1.12	0.01	0.00	0.00	0.11	0.88	0.01
7.26	0.09	0.80	0.00	0.36	1.08	3.44	1.83	0.03	0.28	0.08	2.61	1.37	0.02	0.00	0.00	0.39	0.61	0.03
7.36	0.08	0.67	0.01	0.21	1.23	3.59	1.77	0.03	0.28	0.06	2.61	1.37	0.02	0.00	0.00	0.39	0.62	0.02
7.23	0.09	0.82	0.00	0.32	1.15	3.44	1.82	0.03	0.34	0.08	2.66	1.31	0.01	0.00	0.00	0.33	0.73	0.02
7.31	0.09	0.73	0.00	0.27	1.19	3.53	1.79	0.03	0.27	0.07	2.63	1.36	0.01	0.00	0.00	0.38	0.58	0.04
7.25	0.09	0.79	0.01	0.23	1.27	3.49	1.78	0.03	0.37	0.08	2.66	1.31	0.01	0.00	0.00	0.33	0.73	0.02
7.24	0.09	0.81	0.00	0.32	1.17	3.45	1.79	0.03	0.30	0.08	2.63	1.35	0.02	0.00	0.00	0.38	0.61	0.02
7.18	0.11	0.87	0.01	0.31	1.22	3.39	1.79	0.03	0.33	0.08	2.63	1.35	0.01	0.00	0.00	0.36	0.64	0.02
7.31	0.09	0.73	0.01	0.21	1.26	3.54	1.76	0.03	0.34	0.07	2.54	1.43	0.02	0.00	0.00	0.45	0.58	0.03
7.28	0.11	0.76	0.00	0.25	1.19	3.49	1.82	0.03	0.29	0.07	2.55	1.43	0.02	0.00	0.00	0.46	0.53	0.02
7.11	0.11	0.94	0.01	0.33	1.24	3.33	1.80	0.03	0.38	0.10	2.69	1.29	0.01	0.00	0.00	0.31	0.68	0.04
7.13	0.11	0.91	0.01	0.29	1.26	3.38	1.81	0.03	0.37	0.09	2.63	1.36	0.01	0.00	0.00	0.37	0.61	0.03
Leptokaria																		
RT14_009																		
7.66	0.03	0.38	0.00	0.22	1.03	3.69	1.86	0.07	0.13	0.03	2.97	1.03	0.00	0.00	0.00	0.04	0.94	0.01
RT14_010																		
7.60	0.03	0.45	0.00	0.27	1.04	3.59	1.88	0.07	0.14	0.03	2.85	1.15	0.01	0.00	0.00	0.13	0.85	0.02
7.59	0.03	0.47	0.00	0.26	1.03	3.59	1.86	0.07	0.18	0.03	2.87	1.12	0.01	0.00	0.00	0.14	0.84	0.02
7.35	0.09	0.78	0.00	0.35	1.25	3.19	1.72	0.12	0.28	0.06	2.83	1.16	0.01	0.00	0.00	0.16	0.81	0.03
7.51	0.04	0.53	0.00	0.29	1.06	3.56	1.86	0.08	0.19	0.03	2.74	1.25	0.01	0.00	0.00	0.27	0.70	0.02
7.25	0.10	0.82	0.00	0.41	1.07	3.32	1.77	0.10	0.29	0.06	2.87	1.12	0.01	0.00	0.00	0.13	0.83	0.02
7.30	0.09	0.77	0.00	0.37	1.27	3.22	1.74	0.13	0.27	0.07	2.84	1.15	0.01	0.00	0.00	0.16	0.82	0.02
7.29	0.09	0.77	0.00	0.34	1.29	3.23	1.73	0.12	0.33	0.07	2.90	1.10	0.01	0.00	0.00	0.10	0.90	0.01
7.15	0.08	0.98	0.00	0.48	1.15	3.17	1.75	0.10	0.29	0.08	2.73	1.26	0.01	0.00	0.00	0.28	0.69	0.02
6.99	0.10	1.17	0.00	0.58	1.10	3.05	1.70	0.10	0.39	0.07	2.85	1.15	0.00	0.00	0.00	0.16	0.83	0.02
6.81	0.13	1.36	0.00	0.63	1.02	3.05	1.78	0.06	0.37	0.11	2.85	1.14	0.01	0.00	0.00	0.13	0.85	0.02
6.83	0.14	1.35	0.00	0.57	1.12	2.99	1.74	0.07	0.44	0.10	2.76	1.23	0.01	0.00	0.00	0.24	0.73	0.02

Table G4: continued...

Amphibole A.P.F.U											Plagioclase A.P.F.U							
SiO_2	TiO_2	Al_2O_3	Cr_2O_3	FeO	Fe2O3	MgO	CaO	MnO	Na_2O	K_2O	SiO_2	Al_2O_3	FeO	SrO	BaO	CaO	Na_2O	K_2O
RT14_010																		
6.87	0.14	1.27	0.00	0.62	1.07	3.04	1.72	0.07	0.40	0.09	2.74	1.25	0.01	0.00	0.00	0.27	0.73	0.02
6.85	0.17	1.30	0.00	0.51	1.17	2.96	1.74	0.09	0.48	0.09	2.73	1.26	0.01	0.00	0.00	0.26	0.73	0.02
6.68	0.15	1.48	0.00	0.75	0.83	3.14	1.72	0.05	0.43	0.09	2.86	1.14	0.01	0.00	0.00	0.14	0.83	0.02
6.59	0.25	1.56	0.00	0.51	1.05	3.05	1.75	0.03	0.53	0.12	2.93	1.06	0.00	0.00	0.00	0.06	0.93	0.01
6.97	0.13	1.14	0.00	0.52	1.11	3.10	1.78	0.08	0.41	0.08	2.61	1.38	0.01	0.00	0.00	0.39	0.60	0.02
6.79	0.13	1.35	0.00	0.71	0.99	3.03	1.75	0.07	0.35	0.09	2.49	1.50	0.01	0.00	0.00	0.50	0.50	0.02
6.57	0.25	1.57	0.00	0.56	1.00	3.07	1.75	0.04	0.49	0.12	2.44	1.55	0.02	0.00	0.00	0.56	0.42	0.01
RT14_015																		
7.14	0.09	1.00	0.00	0.46	1.36	3.00	1.76	0.06	0.27	0.09	2.70	1.29	0.01	0.00	0.00	0.30	0.66	0.03
7.09	0.11	1.01	0.00	0.49	1.32	3.00	1.80	0.07	0.23	0.09	2.66	1.34	0.01	0.00	0.00	0.34	0.61	0.03
7.05	0.11	1.06	0.00	0.52	1.34	2.93	1.80	0.06	0.26	0.10	2.69	1.29	0.01	0.00	0.00	0.32	0.64	0.03
6.95	0.17	1.16	0.00	0.47	1.42	2.81	1.80	0.06	0.33	0.12	2.63	1.35	0.01	0.00	0.00	0.38	0.61	0.02
RT14_017																		
6.99	0.12	1.20	0.00	0.50	1.33	2.87	1.80	0.06	0.27	0.09	2.62	1.38	0.01	0.00	0.00	0.38	0.59	0.01
6.80	0.17	1.46	0.00	0.53	1.03	3.08	1.70	0.04	0.37	0.09	2.64	1.35	0.01	0.00	0.00	0.36	0.63	0.02
6.76	0.16	1.45	0.00	0.56	1.14	2.93	1.74	0.05	0.46	0.07	2.71	1.29	0.01	0.00	0.00	0.30	0.67	0.02
6.59	0.20	1.60	0.00	0.65	1.08	2.91	1.74	0.05	0.48	0.09	2.75	1.24	0.01	0.00	0.00	0.25	0.72	0.01
6.78	0.16	1.41	0.00	0.57	1.13	2.94	1.73	0.08	0.47	0.09	2.60	1.39	0.01	0.00	0.00	0.41	0.57	0.02
6.70	0.17	1.51	0.00	0.64	1.04	2.96	1.73	0.05	0.43	0.07	2.55	1.43	0.01	0.00	0.00	0.45	0.54	0.02
6.68	0.17	1.50	0.00	0.72	1.00	2.95	1.74	0.05	0.37	0.08	2.50	1.49	0.01	0.00	0.00	0.52	0.49	0.01
6.60	0.18	1.58	0.00	0.64	1.10	2.92	1.74	0.05	0.51	0.08	2.57	1.42	0.01	0.00	0.00	0.44	0.53	0.02
6.89	0.13	1.30	0.00	0.55	1.14	2.93	1.85	0.06	0.28	0.08	2.16	1.82	0.02	0.00	0.00	0.84	0.17	0.00
6.92	0.13	1.32	0.00	0.53	1.23	2.89	1.79	0.06	0.29	0.07	2.15	1.83	0.03	0.00	0.00	0.86	0.15	0.00
6.78	0.18	1.39	0.00	0.51	1.10	3.02	1.73	0.06	0.52	0.09	2.47	1.52	0.01	0.00	0.00	0.53	0.45	0.01
6.91	0.11	1.31	0.00	0.60	1.07	3.03	1.77	0.06	0.29	0.06	2.14	1.84	0.02	0.00	0.00	0.86	0.16	0.00
6.59	0.23	1.52	0.00	0.64	0.93	3.12	1.72	0.03	0.47	0.12	2.46	1.53	0.01	0.00	0.00	0.54	0.45	0.01
6.71	0.18	1.53	0.00	0.61	1.12	2.89	1.72	0.05	0.39	0.08	2.17	1.81	0.03	0.00	0.00	0.84	0.17	0.00
6.70	0.17	1.52	0.00	0.64	1.22	2.76	1.75	0.06	0.40	0.08	2.15	1.83	0.01	0.00	0.00	0.85	0.16	0.00
6.61	0.19	1.58	0.00	0.68	1.02	2.93	1.77	0.05	0.42	0.08	2.18	1.80	0.02	0.00	0.00	0.83	0.18	0.01
6.67	0.19	1.53	0.00	0.66	1.05	2.92	1.75	0.05	0.37	0.08	2.15	1.83	0.02	0.00	0.00	0.86	0.15	0.00
6.68	0.18	1.52	0.00	0.67	1.05	2.90	1.78	0.06	0.37	0.08	2.15	1.83	0.02	0.00	0.00	0.86	0.14	0.02
6.65	0.18	1.56	0.00	0.68	1.09	2.85	1.75	0.05	0.39	0.08	2.14	1.84	0.02	0.00	0.00	0.86	0.16	0.00
6.70	0.16	1.52	0.00	0.66	1.08	2.89	1.75	0.06	0.39	0.08	2.13	1.84	0.02	0.00	0.00	0.88	0.14	0.00
6.77	0.15	1.42	0.00	0.65	1.22	2.81	1.73	0.07	0.35	0.07	2.12	1.85	0.02	0.00	0.00	0.89	0.13	0.00
6.74	0.16	1.46	0.00	0.61	1.09	2.97	1.73	0.05	0.45	0.08	2.14	1.84	0.02	0.00	0.00	0.86	0.16	0.00
6.77	0.14	1.42	0.00	0.68	1.09	2.95	1.70	0.06	0.38	0.07	2.12	1.86	0.02	0.00	0.00	0.87	0.13	0.00
6.71	0.17	1.49	0.00	0.68	1.22	2.76	1.74	0.06	0.36	0.07	2.12	1.85	0.02	0.00	0.00	0.88	0.13	0.00
6.65	0.19	1.57	0.00	0.59	1.27	2.73	1.76	0.05	0.44	0.08	2.13	1.85	0.02	0.00	0.00	0.88	0.13	0.00
6.72	0.16	1.46	0.00	0.70	0.99	3.00	1.72	0.05	0.40	0.07	2.14	1.84	0.03	0.00	0.00	0.86	0.15	0.00
6.60	0.20	1.61	0.00	0.72	1.06	2.86	1.72	0.05	0.38	0.09	2.13	1.86	0.03	0.00	0.00	0.86	0.14	0.00
6.59	0.20	1.61	0.00	0.62	1.11	2.87	1.76	0.05	0.45	0.08	2.14	1.84	0.02	0.00	0.00	0.86	0.14	0.00
6.71	0.16	1.45	0.00	0.73	0.96	3.01	1.73	0.05	0.40	0.08	2.14	1.84	0.02	0.00	0.00	0.86	0.15	0.00
6.63	0.19	1.55	0.00	0.69	1.04	2.93	1.74	0.05	0.42	0.08	2.16	1.82	0.02	0.00	0.00	0.86	0.15	0.00
6.68	0.17	1.49	0.00	0.69	1.07	2.91	1.73	0.05	0.41	0.07	2.12	1.85	0.03	0.00	0.00	0.88	0.14	0.00
6.88	0.16	1.24	0.00	0.58	0.95	3.21	1.72	0.05	0.45	0.08	2.16	1.82	0.03	0.00	0.00	0.85	0.16	0.00

Table G4: continued...

Amphibole A.P.F.U											Plagioclase A.P.F.U							
SiO_2	TiO_2	Al_2O_3	Cr_2O_3	FeO	Fe2O3	MgO	CaO	MnO	Na_2O	K_2O	SiO_2	Al_2O_3	FeO	SrO	BaO	CaO	Na_2O	K_2O
RT14_017																		
6.69	0.17	1.51	0.00	0.68	1.03	2.94	1.73	0.05	0.39	0.08	2.11	1.86	0.03	0.00	0.00	0.89	0.12	0.00
6.68	0.17	1.50	0.00	0.69	1.11	2.86	1.74	0.05	0.41	0.08	2.12	1.85	0.03	0.00	0.00	0.88	0.13	0.00
6.39	0.26	1.86	0.00	0.58	0.98	2.96	1.75	0.03	0.54	0.10	2.13	1.84	0.03	0.00	0.00	0.87	0.14	0.00
6.42	0.24	1.81	0.00	0.58	1.05	2.91	1.79	0.04	0.53	0.10	2.12	1.86	0.02	0.00	0.00	0.88	0.13	0.00
6.42	0.23	1.78	0.00	0.65	1.12	2.81	1.75	0.05	0.54	0.10	2.17	1.81	0.02	0.00	0.00	0.85	0.15	0.01
6.45	0.23	1.75	0.00	0.67	1.00	2.92	1.75	0.04	0.50	0.09	2.12	1.86	0.02	0.00	0.00	0.88	0.14	0.00
6.41	0.24	1.81	0.00	0.66	1.02	2.89	1.76	0.04	0.51	0.10	2.13	1.84	0.03	0.00	0.00	0.88	0.12	0.00
6.48	0.21	1.72	0.00	0.66	1.06	2.90	1.75	0.04	0.53	0.10	2.13	1.84	0.02	0.00	0.00	0.88	0.13	0.00
6.92	0.11	1.22	0.00	0.63	1.21	2.90	1.83	0.06	0.25	0.09	2.64	1.35	0.01	0.00	0.00	0.37	0.62	0.01
RT14_023																		
7.33	0.07	0.75	0.00	0.40	1.16	3.33	1.81	0.04	0.25	0.06	2.85	1.14	0.00	0.00	0.00	0.15	0.85	0.01
7.24	0.09	0.82	0.00	0.40	1.24	3.28	1.76	0.04	0.28	0.09	2.88	1.12	0.01	0.00	0.00	0.12	0.85	0.02
7.20	0.11	0.87	0.00	0.39	1.24	3.23	1.78	0.04	0.30	0.08	2.89	1.11	0.01	0.00	0.00	0.10	0.89	0.01
7.25	0.09	0.81	0.00	0.37	1.32	3.23	1.78	0.04	0.29	0.08	2.73	1.26	0.01	0.00	0.00	0.28	0.71	0.03
7.28	0.10	0.77	0.00	0.31	1.32	3.26	1.84	0.04	0.26	0.07	2.68	1.31	0.01	0.00	0.00	0.31	0.66	0.02
7.22	0.09	0.84	0.01	0.37	1.26	3.28	1.78	0.04	0.31	0.08	2.73	1.26	0.01	0.00	0.00	0.27	0.69	0.03
7.10	0.12	0.99	0.01	0.46	1.26	3.09	1.77	0.04	0.35	0.10	2.73	1.26	0.01	0.00	0.00	0.28	0.70	0.03
7.08	0.12	1.00	0.01	0.44	1.30	3.10	1.76	0.04	0.36	0.11	2.77	1.22	0.01	0.00	0.00	0.24	0.73	0.03

Table G4: continued...

XT1Si	XT1Al	XM2Al	XAK	Xares	XANa	XM4Na	XM4Ca	AN Content	T^{A}_{plag}	T^{B}_{plag}	T^{A}_{plag} OR T^{B}_{plag}	*P* (kbar)	Depth (km)
Kassiteres													
KA15_013													
0.83	0.17	0.02	0.06	0.74	0.20	0.04	0.93	0.33	988	957	TA	1.23	4.56
0.88	0.12	0.01	0.05	0.77	0.18	0.02	0.94	0.33	953	899	TA	0.93	3.44
0.83	0.17	0.02	0.06	0.75	0.19	0.05	0.89	0.31	984	970	TA	1.26	4.68
KA15_016													
0.91	0.09	0.01	0.05	0.82	0.13	0.04	0.91	0.15	877	869	TB		
0.85	0.15	0.01	0.08	0.69	0.23	0.03	0.92	0.44	1004	985	TB		
0.87	0.13	0.01	0.06	0.71	0.23	0.01	0.91	0.48	997	948	TB		
KA15_017													
0.91	0.09	0.01	0.03	0.82	0.14	0.03	0.89	0.17	887	885	TB		
0.89	0.11	0.02	0.04	0.84	0.12	0.05	0.88	0.14	893	880	TB		
KS16_006A													
0.63	0.37	0.07	0.16	0.40	0.43	0.09	0.93	0.56	1198	1140			
RT14_027													
0.90	0.10	0.01	0.03	0.82	0.15	0.02	0.97	0.49	950	937	TB		
0.89	0.11	0.00	0.04	0.79	0.17	0.01	0.96	0.49	973	884	TB		
0.91	0.09	0.00	0.03	0.82	0.15	0.01	0.97	0.49	942	898	TB		
RT14_028													
0.85	0.15	0.02	0.06	0.79	0.15	0.04	0.93	0.11	929	850	TA	1.13	4.17
0.81	0.19	0.03	0.08	0.76	0.17	0.06	0.92	0.38	998	997	TA	1.40	5.19
0.84	0.16	0.01	0.06	0.72	0.22	0.03	0.88	0.38	1000	966	TA	1.17	4.34
0.81	0.19	0.03	0.08	0.68	0.24	0.05	0.91	0.31	1005	972	TA	1.44	5.34
0.83	0.17	0.02	0.07	0.73	0.20	0.04	0.89	0.37	1006	979	TA	1.27	4.70
0.81	0.19	0.02	0.08	0.63	0.29	0.04	0.89	0.31	1009	969	TA	1.38	5.12
0.81	0.19	0.02	0.08	0.71	0.21	0.05	0.90	0.38	1014	994	TA	1.42	5.26
0.79	0.21	0.03	0.08	0.69	0.23	0.05	0.89	0.35	1024	998	TA	1.54	5.72
0.83	0.17	0.02	0.07	0.67	0.26	0.04	0.88	0.42	1025	1009	TA	1.27	4.70
0.82	0.18	0.02	0.07	0.72	0.21	0.04	0.91	0.46	1028	1010	TA	1.33	4.92
0.78	0.22	0.03	0.10	0.63	0.27	0.05	0.90	0.30	1031	990	TA	1.69	6.25
0.78	0.22	0.02	0.09	0.62	0.29	0.04	0.91	0.37	1049	1002	TA	1.63	6.03
Leptokaria													
RT14_009													
0.91	0.09	0.02	0.03	0.90	0.07	0.03	0.93	0.04	829	758	TB		
RT14_010													
0.90	0.10	0.02	0.03	0.90	0.07	0.03	0.94	0.12	850	835	TA	0.85	3.14
0.90	0.10	0.03	0.03	0.89	0.09	0.04	0.93	0.14	862	855	TA	0.88	3.25
0.84	0.16	0.06	0.06	0.82	0.11	0.08	0.86	0.16	910	900	TA	1.36	5.05
0.88	0.12	0.02	0.03	0.85	0.12	0.04	0.93	0.27	921	917	TA	0.95	3.54
0.81	0.19	0.04	0.06	0.80	0.14	0.07	0.89	0.13	948	898	TA	1.44	5.32
0.82	0.18	0.03	0.07	0.78	0.15	0.06	0.87	0.16	948	908	TA	1.34	4.98
0.82	0.18	0.03	0.07	0.74	0.20	0.07	0.86	0.10	951	878	TA	1.34	4.97
0.79	0.21	0.06	0.08	0.77	0.15	0.07	0.88	0.28	973	962	TB	1.78	6.61
0.75	0.25	0.08	0.07	0.74	0.20	0.10	0.85	0.16	986	928	TB	2.26	8.37
0.70	0.30	0.08	0.11	0.69	0.20	0.08	0.89	0.13	1006	921	TB	2.79	10.34
0.71	0.29	0.09	0.10	0.66	0.25	0.10	0.87	0.24	1030	986	TB	2.75	10.20

Table G4: continued...

XT1Si	XT1Al	XM2Al	XAK	Xares	XANa	XM4Na	XM4Ca	AN Content	T^{A}_{plag}	T^{B}_{plag}	T^{A}_{plag} OR T^{B}_{plag}	*P* (kbar)	Depth (km)
RT14_010													
0.71	0.28	0.07	0.09	0.70	0.21	0.10	0.86	0.26	1030	1001	TB	2.53	9.36
0.71	0.29	0.08	0.09	0.64	0.27	0.11	0.87	0.26	1037	1004	TB	2.62	9.72
0.67	0.33	0.08	0.09	0.69	0.22	0.10	0.86	0.14	1038	953	TB	3.15	11.69
0.65	0.35	0.08	0.12	0.55	0.33	0.10	0.88	0.06	1048	908	TB	3.44	12.76
0.74	0.26	0.05	0.08	0.68	0.24	0.09	0.89	0.38	1056	1043	TB	2.17	8.04
0.70	0.30	0.07	0.09	0.73	0.18	0.09	0.88	0.49	1090	1087	TB		
0.64	0.36	0.07	0.12	0.58	0.30	0.09	0.87	0.56	1169	1136	TB		
RT14_015													
0.79	0.21	0.07	0.09	0.78	0.14	0.07	0.88	0.30	970	963	TB		
0.77	0.23	0.05	0.09	0.79	0.12	0.06	0.90	0.35	988	985	TB		
0.76	0.24	0.05	0.10	0.77	0.13	0.07	0.90	0.32	997	987	TB		
0.74	0.26	0.05	0.12	0.71	0.17	0.08	0.90	0.38	1032	1028	TB		
RT14_017													
0.75	0.25	0.10	0.09	0.78	0.13	0.07	0.90	0.39	994	986	TB		
0.70	0.30	0.13	0.09	0.73	0.18	0.10	0.85	0.35	1016	1002	TB		
0.69	0.31	0.11	0.07	0.67	0.26	0.10	0.87	0.30	1043	1005	TB		
0.65	0.35	0.09	0.09	0.63	0.29	0.10	0.87	0.25	1073	1012	TB		
0.69	0.31	0.09	0.09	0.65	0.26	0.10	0.86	0.41	1076	1060	TB		
0.68	0.32	0.11	0.07	0.69	0.23	0.10	0.87	0.45	1087	1067	TB		
0.67	0.33	0.09	0.08	0.73	0.19	0.09	0.87	0.51	1104	1092	TB		
0.65	0.35	0.09	0.08	0.59	0.32	0.10	0.87	0.44	1134	1096	TB		
0.72	0.28	0.10	0.08	0.78	0.14	0.07	0.92	0.83	1116	1104	TB		
0.73	0.27	0.12	0.07	0.79	0.15	0.07	0.89	0.85	1115	1107	TB		
0.70	0.30	0.09	0.09	0.61	0.30	0.11	0.86	0.54	1112	1109	TB		
0.73	0.27	0.11	0.06	0.79	0.15	0.07	0.89	0.84	1119	1112	TB		
0.65	0.35	0.06	0.12	0.61	0.27	0.10	0.86	0.54	1165	1141	TB		
0.68	0.32	0.12	0.08	0.72	0.20	0.10	0.86	0.83	1166	1147	TB		
0.67	0.33	0.11	0.08	0.71	0.21	0.09	0.87	0.84	1195	1164	TB		
0.65	0.35	0.09	0.08	0.68	0.24	0.09	0.88	0.82	1229	1172	TB		
0.67	0.33	0.10	0.08	0.74	0.19	0.09	0.87	0.85	1204	1173	TB		
0.67	0.33	0.10	0.08	0.72	0.20	0.09	0.89	0.85	1224	1176	TB		
0.66	0.34	0.10	0.08	0.71	0.21	0.09	0.87	0.84	1216	1177	TB		
0.68	0.32	0.11	0.08	0.72	0.20	0.09	0.87	0.86	1215	1178	TB		
0.69	0.31	0.10	0.07	0.75	0.18	0.09	0.86	0.87	1204	1180	TB		
0.68	0.32	0.10	0.08	0.67	0.25	0.10	0.87	0.84	1216	1180	TB		
0.69	0.31	0.10	0.07	0.74	0.19	0.09	0.85	0.87	1205	1184	TB		
0.68	0.32	0.10	0.07	0.75	0.18	0.09	0.87	0.87	1223	1188	TB		
0.66	0.34	0.11	0.08	0.66	0.25	0.09	0.88	0.87	1262	1192	TB		
0.68	0.32	0.09	0.07	0.73	0.20	0.10	0.86	0.85	1219	1193	TB		
0.65	0.35	0.10	0.09	0.72	0.19	0.09	0.86	0.86	1236	1194	TB		
0.65	0.35	0.10	0.08	0.64	0.27	0.09	0.88	0.85	1270	1196	TB		
0.68	0.32	0.08	0.08	0.72	0.20	0.10	0.86	0.85	1222	1197	TB		
0.66	0.34	0.09	0.08	0.68	0.23	0.09	0.87	0.85	1249	1198	TB		
0.67	0.33	0.09	0.07	0.71	0.22	0.10	0.87	0.86	1240	1200	TB		
0.72	0.28	0.06	0.08	0.68	0.24	0.11	0.86	0.84	1204	1203	TB		

Table G4: continued...

XT1Si	XT1Al	XM2Al	XAK	Xares	XANa	XM4Na	XM4Ca	AN Content	T^{A}_{plag}	T^{B}_{plag}	T^{A}_{plag} OR T^{B}_{plag}	*P* (kbar)	Depth (km)
RT14_017													
0.67	0.33	0.10	0.08	0.73	0.20	0.10	0.87	0.88	1243	1204	TB		
0.67	0.33	0.09	0.08	0.71	0.22	0.09	0.87	0.87	1252	1204	TB		
0.60	0.40	0.12	0.10	0.55	0.35	0.09	0.88	0.86	1338	1214	TB		
0.61	0.39	0.11	0.10	0.54	0.36	0.08	0.89	0.87	1364	1218	TB		
0.61	0.39	0.10	0.10	0.55	0.35	0.09	0.87	0.85	1342	1224	TB		
0.61	0.39	0.10	0.09	0.60	0.31	0.09	0.87	0.86	1334	1226	TB		
0.60	0.40	0.11	0.10	0.57	0.33	0.09	0.88	0.88	1372	1236	TB		
0.62	0.38	0.10	0.10	0.57	0.34	0.09	0.87	0.87	1357	1238	TB		
0.73	0.27	0.07	0.09	0.79	0.13	0.06	0.91	0.37	1009	993	TB		
RT14_023													
0.83	0.17	0.04	0.06	0.81	0.13	0.06	0.90	0.15	927	891	TA	1.31	4.87
0.81	0.19	0.03	0.09	0.76	0.15	0.06	0.88	0.12	950	885	TA	1.45	5.37
0.80	0.20	0.03	0.08	0.76	0.16	0.07	0.89	0.10	955	878	TA	1.53	5.68
0.81	0.19	0.03	0.08	0.75	0.17	0.06	0.89	0.27	982	962	TA	1.43	5.30
0.82	0.18	0.02	0.07	0.75	0.18	0.04	0.92	0.31	989	959	TA	1.34	4.97
0.80	0.20	0.03	0.08	0.73	0.19	0.06	0.89	0.27	993	968	TA	1.49	5.51
0.77	0.23	0.04	0.10	0.73	0.17	0.09	0.88	0.28	1001	996	TA	1.80	6.65
0.77	0.23	0.04	0.11	0.70	0.19	0.09	0.88	0.24	1001	980	TA	1.81	6.72

Table G5: Two-pyroxene analyses and thermometry results using calibrations of Brey and Köhler (1990) and Andersen et al. (1993).

Orthopyroxene Analysis											Clinopyroxene Analysis										
SiO2	TiO2	Al2O3	FeO	MgO	CaO	MnO	Cr2O3	Na2O	K2O	TOTAL	SiO2	TiO2	Al2O3	FeO	MgO	CaO	MnO	Cr2O3	Na2O	K2O	TOTAL
Maronia																					
MA15_011																					
53.28	0.15	0.58	23.73	20.57	1.13	0.81	0.00	0.00	0.00	100.24	53.07	0.35	2.63	9.49	12.76	20.52	0.37	0.00	0.25	0.02	99.47
53.70	0.21	0.68	23.93	20.17	1.29	0.86	0.00	0.00	0.00	100.84	53.07	0.35	2.63	9.49	12.76	20.52	0.37	0.00	0.25	0.02	99.47
MA15_010																					
52.38	0.19	0.69	23.69	21.42	1.43	0.80	0.00	0.00	0.01	100.62	52.25	0.25	0.98	10.52	14.09	21.25	0.45	0.00	0.25	0.01	100.06
52.32	0.22	0.60	24.24	21.51	1.03	0.85	0.00	0.00	0.00	100.77	52.67	0.14	0.67	9.87	14.33	22.12	0.34	0.00	0.18	0.00	100.33
52.51	0.22	0.74	24.77	20.64	1.37	0.92	0.00	0.00	0.01	101.19	52.35	0.29	1.03	9.47	14.46	22.14	0.41	0.00	0.24	0.00	100.38
49.66	0.25	0.70	24.05	22.93	1.37	0.80	0.00	0.00	0.02	99.78	51.02	0.30	1.16	10.43	14.60	21.18	0.42	0.00	0.29	0.01	99.42
50.86	0.17	0.69	22.74	22.68	1.89	0.81	0.00	0.00	0.00	99.84	50.43	0.61	2.31	10.65	14.32	20.65	0.41	0.00	0.36	0.01	99.75
51.97	0.16	0.81	23.59	21.99	1.33	0.75	0.00	0.00	0.00	100.60	51.66	0.46	1.60	10.70	14.97	19.88	0.39	0.00	0.33	0.00	100.00
51.17	0.20	0.74	23.04	22.77	1.41	0.80	0.00	0.00	0.00	100.13	50.57	0.29	1.21	9.92	14.91	21.58	0.39	0.00	0.25	0.01	99.12
51.84	0.22	0.79	22.61	22.43	1.43	0.76	0.00	0.00	0.00	100.09	50.74	0.29	1.27	10.12	14.68	21.52	0.41	0.00	0.27	0.03	99.33
51.89	0.21	0.74	24.34	21.60	1.37	0.80	0.00	0.00	0.01	100.96	51.06	0.41	1.51	9.84	14.43	21.55	0.41	0.00	0.32	0.00	99.53
RT14_003																					
53.50	0.18	0.57	22.90	22.18	1.26	0.82	0.00	0.00	0.00	101.42	53.00	0.28	1.12	10.10	14.54	21.34	0.40	0.00	0.29	0.00	101.08
51.98	0.23	0.72	22.87	21.37	1.64	0.81	0.00	0.00	0.00	99.63	52.18	0.27	1.03	9.69	14.33	21.17	0.43	0.00	0.30	0.00	99.41
52.91	0.23	0.81	22.22	22.33	1.55	0.78	0.00	0.00	0.00	100.83	53.28	0.29	1.04	9.83	14.70	21.78	0.41	0.00	0.28	0.00	101.60
53.16	0.23	0.80	23.10	21.80	1.49	0.82	0.00	0.00	0.01	101.40	52.93	0.19	0.75	9.65	14.71	22.09	0.42	0.00	0.24	0.00	100.99
53.69	0.26	0.85	21.87	22.69	1.61	0.74	0.00	0.00	0.01	101.71	51.73	0.38	1.54	9.89	14.29	21.35	0.43	0.00	0.30	0.00	99.92
53.69	0.25	0.82	21.86	22.80	1.35	0.72	0.00	0.00	0.00	101.49	52.39	0.54	2.00	9.95	14.34	21.38	0.42	0.00	0.36	0.00	101.36
53.34	0.20	0.76	22.24	22.50	1.48	0.76	0.00	0.00	0.00	101.29	51.73	0.38	1.54	9.89	14.29	21.35	0.43	0.00	0.30	0.00	99.92
52.32	0.26	0.91	21.54	22.38	1.18	0.74	0.00	0.00	0.00	99.33	52.39	0.54	2.00	9.95	14.34	21.38	0.42	0.00	0.36	0.00	101.36
52.58	0.24	0.63	22.35	21.97	1.19	0.74	0.00	0.00	0.00	99.72	52.19	0.48	1.66	9.63	14.61	21.43	0.40	0.00	0.32	0.00	100.73
52.62	0.26	0.67	22.31	22.14	1.28	0.79	0.00	0.00	0.00	100.07	52.60	0.45	1.69	10.66	15.01	20.33	0.40	0.00	0.30	0.00	101.43
53.49	0.26	0.79	22.15	22.47	1.38	0.70	0.00	0.00	0.02	101.26	52.19	0.41	1.66	9.88	14.32	21.49	0.42	0.00	0.31	0.03	100.72
52.11	0.20	0.70	21.98	22.08	1.18	0.76	0.00	0.00	0.00	99.02	52.75	0.31	1.30	9.99	14.37	21.70	0.43	0.00	0.29	0.00	101.14
53.17	0.21	0.79	22.41	22.17	1.39	0.80	0.00	0.00	0.00	100.94	51.83	0.35	1.46	10.44	14.67	20.19	0.43	0.00	0.28	0.00	99.66
52.26	0.20	0.74	22.19	21.95	1.31	0.80	0.00	0.00	0.00	99.46	52.18	0.46	1.72	9.88	14.67	21.33	0.40	0.00	0.32	0.01	100.97
53.41	0.26	0.85	22.08	22.42	1.61	0.78	0.00	0.00	0.01	101.41	51.19	0.47	1.69	9.43	13.00	21.86	0.46	0.00	0.29	0.01	98.41
53.41	0.26	0.85	22.08	22.42	1.61	0.78	0.00	0.00	0.01	101.41	51.40	0.47	1.74	9.60	14.16	21.06	0.38	0.00	0.34	0.03	99.18
53.41	0.26	0.85	22.08	22.42	1.61	0.78	0.00	0.00	0.01	101.41	52.35	0.45	1.72	10.00	14.28	21.31	0.40	0.00	0.34	0.01	100.86
52.33	0.23	0.75	22.15	21.98	1.31	0.75	0.00	0.00	0.00	99.49	51.60	0.29	1.45	9.70	14.64	21.11	0.42	0.00	0.33	0.03	99.57
52.37	0.25	0.79	22.30	21.68	1.39	0.76	0.00	0.00	0.02	99.56	52.45	0.49	1.73	10.52	14.52	20.42	0.40	0.00	0.32	0.00	100.84
53.19	0.21	0.78	22.31	22.10	1.40	0.85	0.00	0.00	0.00	100.84	51.18	0.45	1.79	9.05	14.07	21.49	0.35	0.00	0.32	0.00	98.69
53.52	0.22	0.84	22.20	22.37	1.52	0.78	0.00	0.00	0.01	101.46	52.01	0.31	1.30	9.49	14.31	21.29	0.37	0.00	0.28	0.04	99.39
52.19	0.23	0.74	22.37	21.56	1.58	0.81	0.00	0.00	0.01	99.48	52.37	0.27	1.01	9.60	14.49	21.29	0.43	0.00	0.28	0.06	99.80
52.62	0.21	0.71	23.32	23.02	1.32	0.82	0.00	0.00	0.00	102.02	52.57	0.21	0.80	9.43	14.34	21.90	0.42	0.00	0.26	0.00	99.93
53.51	0.21	0.74	22.35	22.17	1.20	0.77	0.00	0.00	0.01	100.97	52.37	0.27	1.01	9.60	14.49	21.29	0.43	0.00	0.28	0.06	99.80
53.25	0.22	0.77	22.55	21.77	1.51	0.82	0.00	0.00	0.01	100.89	52.57	0.21	0.80	9.43	14.34	21.90	0.42	0.00	0.26	0.00	99.93
52.49	0.20	0.77	22.37	21.59	1.53	0.74	0.01	0.00	0.00	99.71	52.52	0.29	1.30	10.20	14.35	21.28	0.45	0.00	0.30	0.04	100.75

Table G5: continued...

Orthopyroxene Analysis											Clinopyroxene Analysis										
SiO2	TiO2	Al2O3	FeO	MgO	CaO	MnO	Cr2O3	Na2O	K2O	TOTAL	SiO2	TiO2	Al2O3	FeO	MgO	CaO	MnO	Cr2O3	Na2O	K2O	TOTAL
RT14_003																					
52.03	0.19	0.69	23.09	21.35	1.36	0.83	0.00	0.00	0.00	99.54	52.52	0.29	1.30	10.20	14.35	21.28	0.45	0.00	0.30	0.04	100.75
52.40	0.17	0.54	22.24	21.82	1.20	0.79	0.00	0.00	0.00	99.17	52.12	0.27	1.04	9.84	14.21	21.28	0.38	0.01	0.28	0.00	99.42
52.40	0.20	0.77	22.09	21.65	1.49	0.81	0.00	0.00	0.00	99.42	52.04	0.27	1.21	10.13	14.31	20.91	0.43	0.01	0.31	0.00	99.61
53.52	0.23	0.79	22.32	22.00	1.70	0.74	0.00	0.00	0.00	101.29	52.04	0.27	1.21	10.13	14.31	20.91	0.43	0.01	0.31	0.00	99.61
52.15	0.20	0.67	22.67	21.49	1.32	0.83	0.01	0.00	0.00	99.35	52.53	0.19	0.77	9.46	14.19	21.77	0.39	0.00	0.27	0.00	99.57
52.94	0.16	0.53	22.67	21.71	1.14	0.83	0.00	0.00	0.00	99.97	52.70	0.19	0.77	9.51	14.23	21.84	0.37	0.00	0.25	0.00	99.87
52.69	0.17	0.53	23.04	21.46	1.15	0.79	0.01	0.00	0.00	99.84	52.02	0.26	1.11	9.50	14.05	21.36	0.38	0.00	0.27	0.00	98.94
52.94	0.16	0.53	22.67	21.71	1.14	0.83	0.00	0.00	0.00	99.97	52.28	0.27	1.08	9.76	14.01	21.25	0.40	0.00	0.27	0.06	99.39
52.69	0.17	0.53	23.04	21.46	1.15	0.79	0.01	0.00	0.00	99.84	52.64	0.20	0.86	9.16	14.29	21.64	0.36	0.00	0.26	0.18	99.59

Table G5: continued...

T_{BKN}°C	X_{En}^{OPX}	X_{Wo}^{OPX}	X_{Fs}^{OPX}	X_{En}^{CPX}	X_{Wo}^{CPX}	X_{Fs}^{CPX}	T_{QUILF}°C	Uncertainty (2 σ)
MA15_011								
856	0.59	0.02	0.38	0.42	0.39	0.18	899	22
853	0.58	0.03	0.39	0.42	0.39	0.18	923	32
MA15_010								
818	0.68	0.03	0.29	0.43	0.42	0.15	994	20
764	0.62	0.02	0.36	0.42	0.43	0.15	874	11
752	0.59	0.03	0.38	0.45	0.42	0.13	894	106
812	0.70	0.03	0.28	0.50	0.38	0.12	1006	80
855	0.67	0.04	0.29	0.49	0.38	0.13	1064	100
888	0.64	0.03	0.34	0.48	0.38	0.14	959	82
787	0.67	0.03	0.30	0.53	0.37	0.10	968	180
792	0.65	0.03	0.32	0.51	0.38	0.11	959	162
777	0.63	0.03	0.35	0.49	0.40	0.12	930	134
RT14_003								
834	0.62	0.03	0.35	0.44	0.42	0.15	915	41
820	0.62	0.04	0.35	0.44	0.42	0.14	963	71
823	0.64	0.03	0.33	0.44	0.42	0.14	960	59
784	0.62	0.03	0.35	0.45	0.42	0.13	931	92
826	0.64	0.03	0.33	0.45	0.41	0.13	969	77
840	0.64	0.03	0.34	0.45	0.41	0.14	940	48
821	0.63	0.03	0.34	0.45	0.41	0.13	953	72
838	0.64	0.03	0.33	0.45	0.41	0.14	922	39
823	0.63	0.03	0.35	0.44	0.42	0.14	905	50
893	0.63	0.03	0.34	0.46	0.39	0.15	943	60
824	0.63	0.03	0.34	0.45	0.42	0.14	935	60
815	0.64	0.03	0.34	0.44	0.42	0.14	913	36
884	0.63	0.03	0.34	0.46	0.39	0.15	954	64
834	0.62	0.03	0.35	0.46	0.41	0.13	919	89
754	0.63	0.03	0.34	0.41	0.44	0.15	950	52
830	0.63	0.03	0.34	0.45	0.42	0.14	967	72
837	0.63	0.03	0.34	0.44	0.41	0.14	973	58
828	0.63	0.03	0.34	0.47	0.40	0.13	928	102
880	0.62	0.03	0.35	0.44	0.40	0.16	955	45
790	0.63	0.03	0.35	0.35	0.46	0.20	905	129
824	0.63	0.03	0.34	0.44	0.42	0.14	950	59
825	0.62	0.03	0.35	0.44	0.42	0.14	955	72
785	0.66	0.03	0.31	0.44	0.43	0.13	937	34
825	0.62	0.03	0.35	0.44	0.42	0.14	897	51
784	0.62	0.03	0.35	0.44	0.43	0.13	925	71
832	0.62	0.03	0.35	0.44	0.41	0.14	956	64

Table G5: continued...

T_{BKN}°C	X_{En}^{OPX}	X_{Wo}^{OPX}	X_{Fs}^{OPX}	X_{En}^{CPX}	X_{Wo}^{CPX}	X_{Fs}^{CPX}	T_{QUILF}°C	Uncertainty (2 σ)
RT14_003								
825	0.62	0.03	0.35	0.44	0.41	0.14	934	58
817	0.63	0.03	0.35	0.44	0.42	0.14	906	37
843	0.62	0.03	0.35	0.44	0.41	0.14	955	62
845	0.62	0.04	0.35	0.44	0.41	0.14	974	73
783	0.62	0.03	0.35	0.43	0.44	0.14	908	48
785	0.62	0.02	0.36	0.43	0.44	0.14	876	35
800	0.61	0.02	0.36	0.43	0.43	0.14	883	37
816	0.62	0.02	0.36	0.42	0.43	0.15	888	21
793	0.61	0.02	0.36	0.43	0.44	0.14	875	38

Table G6: Zircon saturation thermometry results using calibration of Boehnke et al. (2013)

	SiO_2	TiO_2	Al_2O_3	Cr_2O_3	FeO^T	MgO	CaO	MnO	Na_2O	K_2O	Zr (ppm)	M	$D_{Zr}^{Z/M}$	T (°C)
Kassiteres														
KA15_013	61.11	0.65	15.99	0	5.4798	3.1	5.22	0.06	3.18	2.78	104	1.91	4713	647
KA15_016	59.1	0.65	16.09	0	6.0017	3.77	5.32	0.11	3.01	3.07	110	1.98	4456	645
Leptokaria														
LB15_004	67.63	0.36	15.63	0	3.2213	1.45	3.87	0.08	3.49	2.83	157	1.58	3122	718
LB15_006	62.38	0.62	17.63	0	3.4912	2.58	5.61	0.11	4.89	0.68	55	1.84	8913	602
LC15_002	60.38	0.73	17.37	0	5.9837	2.73	5.05	0.17	3.12	2.3	71	1.68	6904	637
LC15_003	64.73	0.5	15.97	0	4.643	2.19	4.3	0.12	3.28	2.85	152	1.67	3225	705
RT14_010	67.34	0.4	15.37	0	3.7342	1.55	2.86	0.1	2.99	3.21	117	1.37	4190	713
RT14_010	67.1	0.4	15.39	0	3.6442	1.54	2.85	0.09	2.99	3.21	131	1.37	3742	725

Table G7: Apatite saturation thermometry results using calibration of Harrison and Watson (1984)

	SiO_2	P_2O_5	T (C)
Maronia			
MA15_006	50.41	0.64	887
MA15_007	51.1	0.59	886
MA15_015	51.16	0.61	892
MA15_008	52.11	0.57	897
MA15_022	52.91	0.47	880
MA15_010	53	0.52	896
MA15_016	53.32	0.46	883
MA15_012	53.43	0.6	924
MA15_020	54.71	0.42	891
MA15_011	55.25	0.5	923
MA15_017	55.27	0.5	924
MA15_014	55.57	0.56	945
RT14_006	52.93	0.43	868
RT14_006	52.83	0.43	866

Appendix H

Phase Relations

This appendix contains the phase relations of each of the thin sections described and was used to put together the crystallisation sequence (Fig. 3.9) in Chapter 3. The following abbrevations are using the appendix: CPX – clinopyroxene; OPX – orthopyroxene; PLAG – plagioclase; KFSP – K-feldspar; QTZ – quartz; APA – apatite; ZIR – zircon; Fe-OX – Fe-Ti oxides; TREM – hydrothermal amphiboles (tremolite in composition); HBL – magmatic hornblende

Maronia

RT14_003

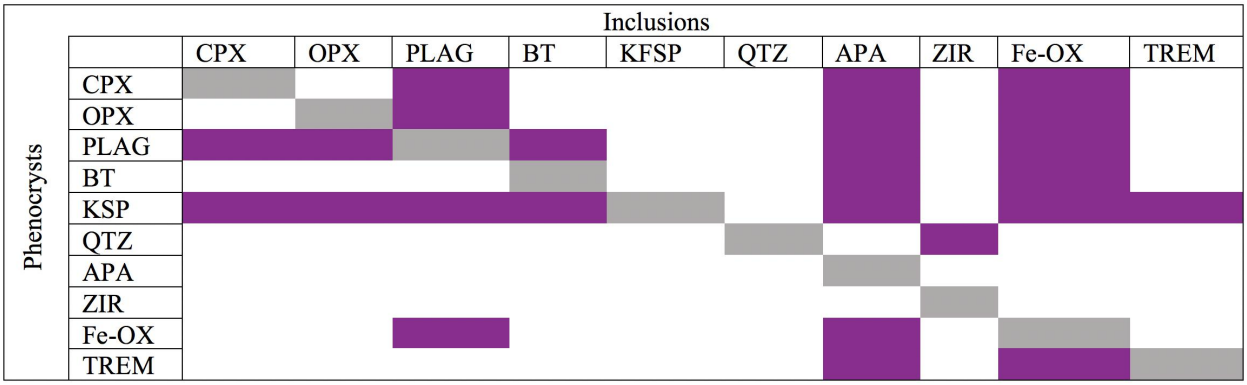

RT14_006

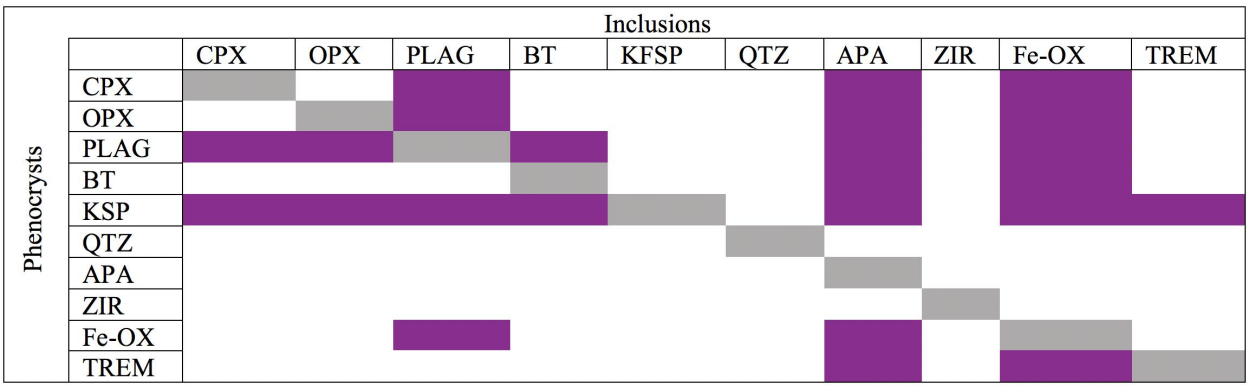

Kassiteres

RT14_027

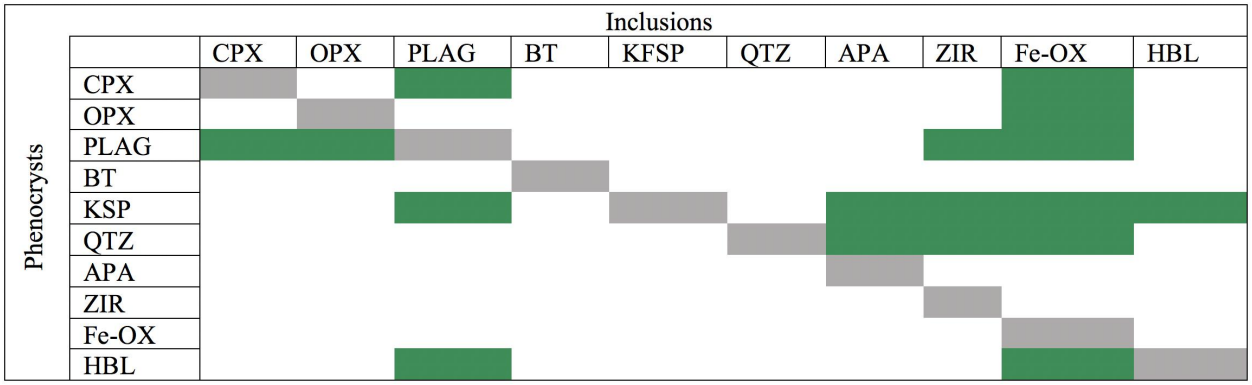

RT14_028

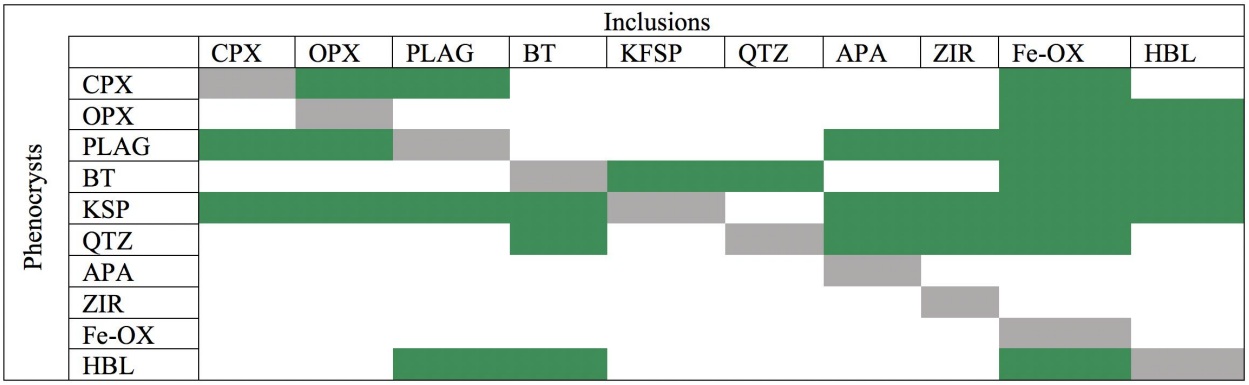

Leptokaria

RT14_009

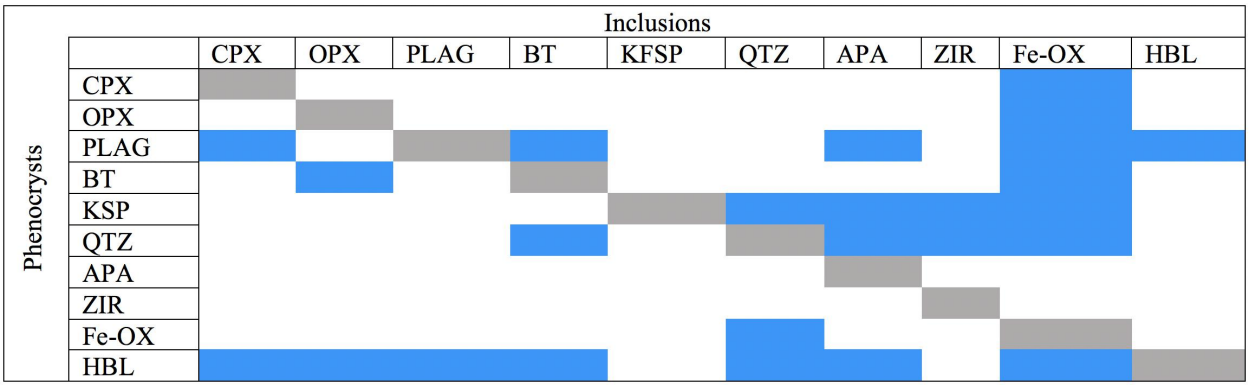

RT14_010

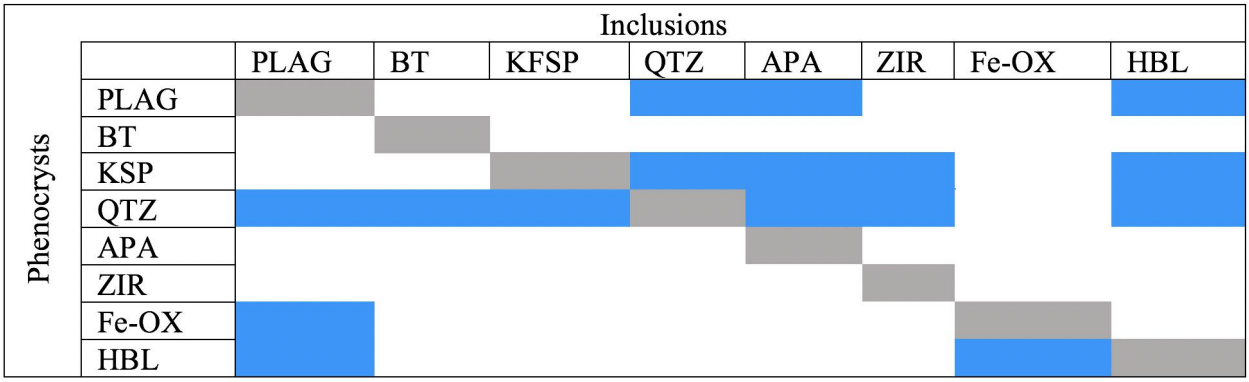

RT14_015

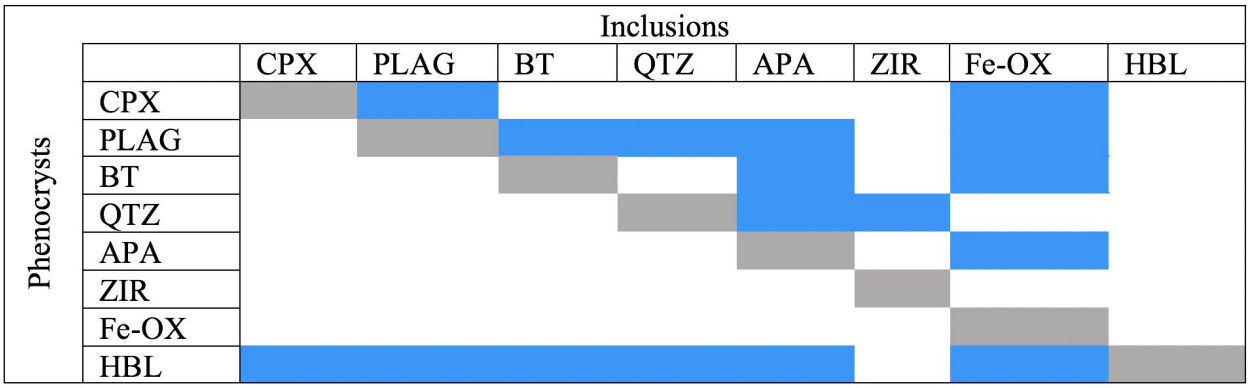

RT14_017

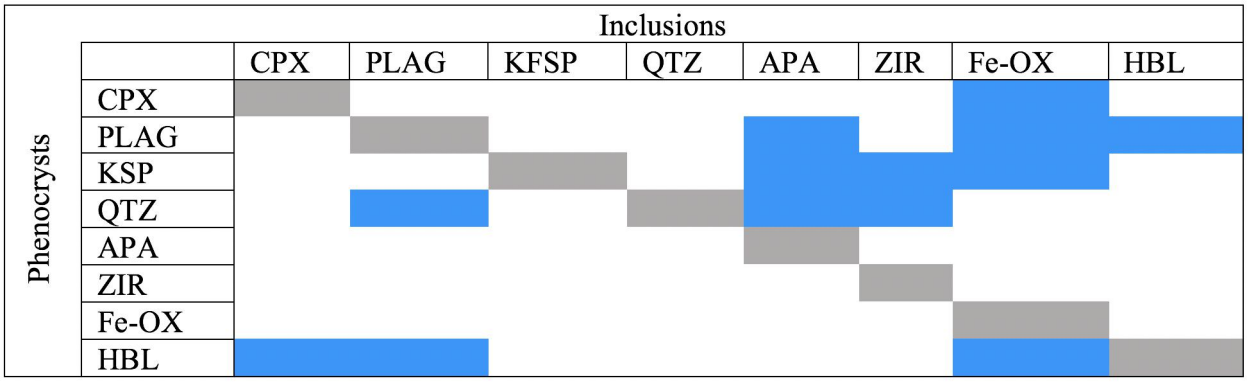

RT14_023

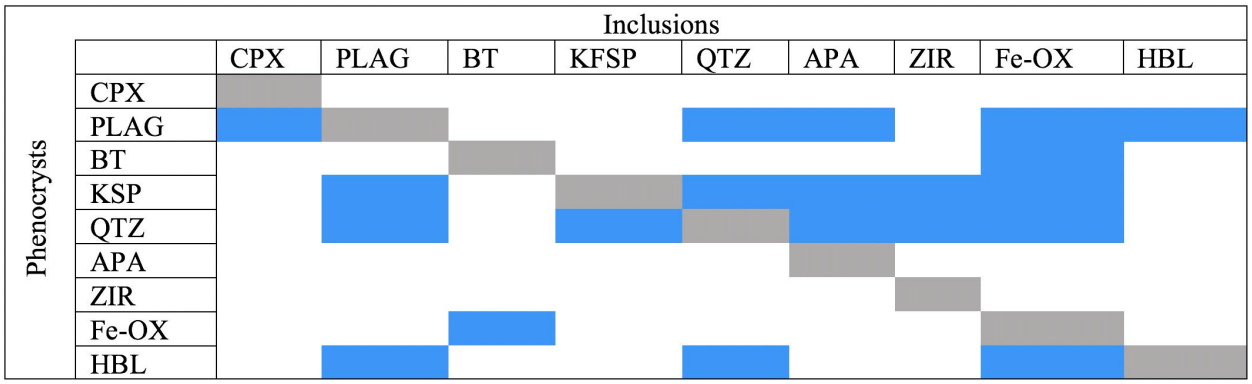

RT14_024

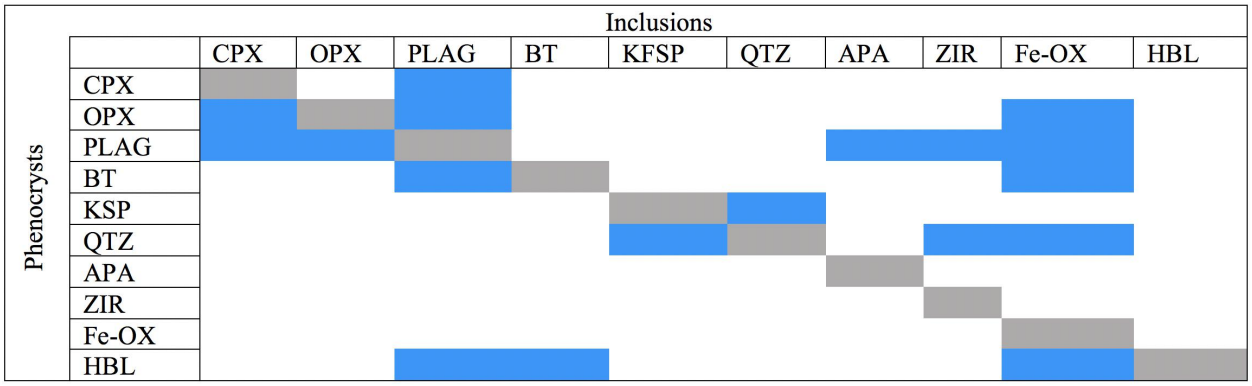

Appendix I

U-Pb Zircon LA-ICP-MS Geochronology

This appendix contains the high-spatial resolution U-Pb zircon LA-ICP-MS geochronology results of the Kassiteres, Essimi and Leptokaria porphyry zircon presented in Chapter 4.

Published values for the reference materials ($^{206}Pb/^{238}U$ ages from Horstwood et al. 2016):
91500: 1063.51 $\pm$ 0.39
GJ1: 601.86 $\pm$ 0.37
MudTank: 731 $\pm$ 0.49

Table I1: U-Pb in zircon LA-ICP-MS metadata.
Table I2: U-Pb in zircon LA-ICP-MS results.

Table 11: Reporting template for U-Pb zircon LA-ICP-MA U-Th-Pb metadata from Horstwood et al. (2016).

Laboratory and Sample Preparation	
Laboratory Name	NERC Isotope Geosciences Laboratory
Sample type	Zircon
Sample preparation	Conventional mineral separation, 1 inch mount, 1 μm polish to finish
Imaging	Centaurus cathodoluminescence detector on a Hitachi S3500N scanning electron microscope
Laser Ablation System	
Make, model type	ESI/New Wave Research, 193FX excimer
Ablation cell and volume	In-house built low volume cell, volume c.4cm^3
Laser wavelength (nm)	193
Pulse width (ns)	4
Fluence (J/cm2)	1.4–1.6
Repetition rate (Hz)	10
Ablation duration (s)	30
Ablation pit depth/ablation rate	16 μm pit depth, measured using an optical microscope, SEM and interferometry, equivalent to 0.08 μm/pulse
Spot size nominal (μm)	20
Sampling mode/pattern	Static spot ablation
Carrier gas	100% He in the cell, Ar make-up gas combined using a Y-piece 50% along the sample transport line to the torch.
Cell carrier gas flow (1/min)	0.8
ICP-MS Instrument	
Make, model type	Nu Intrusments, Nu Plasm HR, MC-ICP-MS
Sample introduction	Ablation aerosol combined with co-aspiration of desolvated
RF power (W)	1300
Make-up glas flow (1/min)	Sourced from Nu Instruments DSN-100 desolvating nebulizer. Neb pressure 24psi (estimated at 0.7l/min) Ar.
Detection system	Mixed Faraday-multiple ion counting array
Masses measured	202-207 Pb, 235 235 U
Integration time per peak/dwell times (ms)	200 for each isotope
Total integration time per output data point (ms)	?
'sensitivity' as useful yield (%, element)	0.4 % U
IC Dead time (ns)	6,9,7 on IC0, IC1 and IC2 respectively
Data Processing	
Gas blank	30 second on-peak zero subtracted
Calibration Strategy	91500 used as primary reference material, MudTank used as secondary
Reference material info	91500 (Wiedenbeck et al 1995) GJ1 (Horstwood et al., 2016) MudTank (732.3 Ma, in house ID-TIMS data)
Data processing package used	Iolite
Mass discrimination	^{207}Pb/^{206}Pb and ^{206}Pb/^{238}U additionally normalised to reference material. Otherwise standard sample bracketing only
Common-Pb correction, composition and uncertainty	No common-Pb correction applied to the data for plotting and calculation of ratiosand ages, additional ^{207}Pb method based correction (assumes concordance) provided for samples.
Uncertainty level and propagation	Ages are quoted at 2σ absolute, propagation is by quadratic addition. Reproducibility and age uncertainty of reference materialand common-Pb composition uncertainty are propagated where appropriate.
Quality control/validation	Primary reference material ^{206}Pb/^{238}Uage = 1062.2 $\pm$ 4.1, MSWD = 0.58, n = 87 Secondary reference materials GJ1 ^{206}Pb/^{238}U AGE = 601.5 $\pm$ 2.4 MSWD = 0.65, n = 87 Mudtank ^{206}Pb/^{238}U AGE = 725.0 $\pm$ 3.0 MSWD = 0.73, n = 87 Uncertainty for propogation is 1.5 % (2 σ)

Table I2: Zircon U-Pb LA-ICP-MS geochronology data.

Zircon Number	Spot Number	Core' or rim	$^{207}Pb/^{206}Pb$	2σ abs.	$^{207}Pb/^{235}U$	2σ abs.	$^{206}Pb/^{238}U$	2σ abs.	$^{206}Pb/^{238}U$ AGE (Ma)	2σ abs.	C
Leptokaria – LA15_008											
2	29	Core	0.0478	0.0017	0.0318	0.0014	0.0048	0.0001	31.04	0.83	0.98
2	30	Rim	0.0465	0.0022	0.0310	0.0017	0.0048	0.0001	31.09	0.88	1.00
4	31	Core	0.0488	0.0030	0.0329	0.0023	0.0049	0.0002	31.44	1.10	0.96
4	32	Rim	0.0471	0.0018	0.0324	0.0017	0.0050	0.0002	32.07	1.10	0.99
5	33	Core	0.0483	0.0020	0.0318	0.0016	0.0048	0.0001	30.74	0.91	0.97
5	34	Rim	0.0469	0.0022	0.0313	0.0018	0.0048	0.0002	31.12	1.00	1.00
6	35	Core	0.0471	0.0011	0.0321	0.0013	0.0050	0.0002	31.83	1.10	0.99
6	36	Rim	0.0462	0.0018	0.0318	0.0017	0.0050	0.0002	32.11	1.10	1.01
7	37	Core	0.0592	0.0026	0.0401	0.0022	0.0049	0.0002	31.66	1.10	0.79
7	38	Rim	0.0826	0.0046	0.0606	0.0040	0.0053	0.0002	34.17	1.20	0.57
8	39	Core	0.0494	0.0017	0.0336	0.0016	0.0049	0.0002	31.73	1.00	0.94
8	40	Rim	0.0477	0.0024	0.0327	0.0020	0.0050	0.0002	31.97	1.10	0.98
9	41	Core	0.0524	0.0033	0.0358	0.0025	0.0050	0.0001	31.86	0.92	0.89
9	42	Rim	0.0570	0.0042	0.0401	0.0032	0.0051	0.0002	32.83	1.10	0.82
10	43	Core	0.0472	0.0011	0.0320	0.0011	0.0049	0.0001	31.65	0.85	0.99
10	44	Rim	0.0465	0.0009	0.0307	0.0010	0.0048	0.0001	30.82	0.81	1.00
13	54	Core	0.0541	0.0049	0.0363	0.0034	0.0049	0.0001	31.30	0.77	0.86
13	55	Rim	0.0493	0.0025	0.0330	0.0019	0.0049	0.0001	31.22	0.79	0.95
14	56	Core	0.0472	0.0011	0.0314	0.0011	0.0048	0.0001	31.06	0.75	0.99
14	57	Rim	0.0474	0.0009	0.0317	0.0010	0.0049	0.0001	31.21	0.78	0.98
15	58	Core	0.0447	0.0029	0.0297	0.0022	0.0048	0.0002	30.97	1.00	1.04
15	59	Rim	0.0455	0.0013	0.0304	0.0014	0.0049	0.0002	31.21	1.10	1.03
16	60	Core	0.1775	0.0081	0.1407	0.0082	0.0058	0.0002	37.00	1.30	0.28
16	61	Rim	0.0431	0.0019	0.0287	0.0016	0.0048	0.0002	31.11	1.00	1.08
17	62	Core	0.0461	0.0013	0.0308	0.0013	0.0049	0.0002	31.20	1.00	1.01
17	63	Rim	0.0488	0.0012	0.0325	0.0014	0.0048	0.0002	31.15	1.10	0.96
18	64	Core	0.0436	0.0022	0.0291	0.0018	0.0049	0.0002	31.17	1.00	1.07
18	65	Rim	0.0560	0.0025	0.0381	0.0021	0.0049	0.0002	31.75	0.96	0.84
19	66	Core	0.0471	0.0013	0.0314	0.0014	0.0048	0.0002	31.05	1.10	0.99
19	67	Rim	0.0501	0.0014	0.0338	0.0015	0.0049	0.0002	31.48	0.99	0.93
20	68	Core	0.0482	0.0013	0.0312	0.0013	0.0047	0.0002	30.18	0.98	0.97
20	69	Rim	0.0837	0.0040	0.0587	0.0034	0.0051	0.0002	32.73	1.00	0.57
22	70	Core	0.0435	0.0015	0.0289	0.0014	0.0048	0.0002	30.98	1.10	1.07
22	71	Rim	0.0754	0.0029	0.0524	0.0025	0.0050	0.0001	32.45	0.92	0.63
23	72	Core	0.0533	0.0038	0.0361	0.0028	0.0049	0.0002	31.59	0.96	0.88
23	73	Rim	0.0435	0.0017	0.0287	0.0014	0.0048	0.0002	30.75	0.96	1.07
25	83	Core	0.0586	0.0013	0.0403	0.0013	0.0050	0.0001	32.07	0.75	0.80
25	84	Rim	0.0533	0.0013	0.0359	0.0012	0.0049	0.0001	31.46	0.76	0.88
26	85	Core	0.0493	0.0008	0.0328	0.0009	0.0048	0.0001	31.05	0.73	0.95
26	86	Rim	0.0594	0.0015	0.0403	0.0014	0.0049	0.0001	31.65	0.76	0.79
27	87	Core	0.0537	0.0012	0.0358	0.0012	0.0048	0.0001	31.08	0.75	0.87
27	88	Rim	0.0549	0.0012	0.0368	0.0012	0.0049	0.0001	31.28	0.74	0.85
30	89	Core	0.0677	0.0033	0.0457	0.0026	0.0049	0.0001	31.48	0.89	0.69

Table I2: Continued...

Zircon Number	Spot Number	Core' or rim	$^{207}Pb/^{206}Pb$	2σ abs.	$^{207}Pb/^{235}U$	2σ abs.	$^{206}Pb/^{238}U$	2σ abs.	$^{206}Pb/^{238}U$ AGE (Ma)	2σ abs.	C
					Leptokaria – LA15_008						
30	90	Rim	0.0812	0.0023	0.0573	0.0027	0.0051	0.0002	32.90	1.20	0.58
31	91	Core	0.0498	0.0009	0.0331	0.0013	0.0048	0.0002	31.00	1.10	0.94
31	92	Rim	0.0517	0.0010	0.0350	0.0014	0.0049	0.0002	31.62	1.10	0.90
31b	93	Core	0.0570	0.0018	0.0386	0.0019	0.0049	0.0002	31.59	1.10	0.82
31b	94	Rim	0.0657	0.0021	0.0457	0.0021	0.0051	0.0002	32.45	1.00	0.71
33	95	Core	0.0503	0.0009	0.0334	0.0012	0.0048	0.0002	31.01	0.96	0.93
33	96	Rim	0.0557	0.0016	0.0373	0.0016	0.0049	0.0002	31.27	0.95	0.84
35	97	Core	0.0861	0.0037	0.0605	0.0033	0.0051	0.0002	32.77	1.10	0.55
35	98	Rim	0.0747	0.0032	0.0535	0.0028	0.0052	0.0002	33.41	1.00	0.63
39	99	Core	0.0521	0.0012	0.0349	0.0015	0.0049	0.0002	31.28	1.10	0.90
39	100	Rim	0.0506	0.0010	0.0349	0.0014	0.0050	0.0002	32.17	1.10	0.92
16	101	Core	0.0966	0.0099	0.0686	0.0075	0.0052	0.0002	33.10	1.30	0.49
16	102	Rim	0.0593	0.0026	0.0396	0.0021	0.0048	0.0002	31.13	0.99	0.79
					Essimi – LK16_016						
1	30	Core	0.0460	0.0011	0.0314	0.0013	0.0050	0.0002	31.88	1.00	1.01
1	31	Rim	0.0456	0.0013	0.0321	0.0015	0.0051	0.0002	32.82	1.20	1.02
2	32	Core	0.0469	0.0014	0.0325	0.0015	0.0050	0.0002	32.37	1.10	1.00
2	33	Rim	0.0506	0.0011	0.0413	0.0016	0.0059	0.0002	38.02	1.20	0.93
3	34	Core	0.0457	0.0010	0.0320	0.0014	0.0051	0.0002	32.68	1.20	1.02
3	35	Rim	0.0451	0.0013	0.0311	0.0014	0.0050	0.0002	32.19	1.20	1.03
4	36	Core	0.0470	0.0007	0.0320	0.0013	0.0049	0.0002	31.75	1.20	0.99
4	37	Rim	0.0452	0.0010	0.0309	0.0013	0.0050	0.0002	31.99	1.20	1.03
5	38	Core	0.0732	0.0009	1.6370	0.0695	0.1622	0.0066	967.00	36.00	0.98
5	39	Rim	0.0460	0.0011	0.0319	0.0014	0.0050	0.0002	32.32	1.20	1.01
6	40	Core	0.0486	0.0010	0.0336	0.0014	0.0050	0.0002	32.25	1.20	0.96
6	41	Rim	0.0462	0.0015	0.0324	0.0016	0.0051	0.0002	32.76	1.20	1.01
8	42	Core	0.0653	0.0019	0.1998	0.0241	0.0222	0.0026	141.00	16.00	0.76
8	43	Rim	0.0459	0.0010	0.0336	0.0015	0.0053	0.0002	34.13	1.30	1.02
9	44	Core	0.0592	0.0007	0.5982	0.0238	0.0733	0.0028	455.00	17.00	0.96
9	45	Rim	0.0581	0.0007	0.5415	0.0225	0.0676	0.0027	421.00	16.00	0.96
10	46	Core	0.0465	0.0009	0.0327	0.0014	0.0051	0.0002	32.80	1.20	1.00
10	47	Rim	0.0494	0.0013	0.0346	0.0015	0.0051	0.0002	32.64	1.10	0.95
11	48	Core	0.0471	0.0012	0.0332	0.0016	0.0051	0.0002	32.86	1.30	0.99
11	49	Rim	0.0489	0.0016	0.0346	0.0018	0.0051	0.0002	33.07	1.30	0.96
13	59	Core	0.0601	0.0007	0.7721	0.0257	0.0933	0.0029	574.90	17.00	0.99
13	60	Rim	0.0479	0.0014	0.0332	0.0015	0.0050	0.0002	32.33	1.10	0.97
14	61	Core	0.0577	0.0018	0.0402	0.0018	0.0051	0.0002	32.48	1.10	0.81
14	62	Rim	0.0473	0.0012	0.0323	0.0014	0.0050	0.0002	31.89	1.10	0.99
15	63	Core	0.0464	0.0013	0.0323	0.0014	0.0051	0.0002	32.52	1.10	1.01
15	64	Rim	0.0481	0.0017	0.0329	0.0016	0.0050	0.0002	31.96	1.10	0.97
16	65	Core	0.0450	0.0018	0.0302	0.0016	0.0049	0.0002	31.28	1.00	1.04
16	66	Rim	0.0776	0.0058	0.0558	0.0046	0.0052	0.0002	33.57	1.10	0.61
17	67	Core	0.0461	0.0010	0.0319	0.0013	0.0050	0.0002	32.25	1.10	1.01
17	68	Rim	0.0467	0.0007	0.0317	0.0012	0.0049	0.0002	31.67	1.10	1.00

Table I2: Continued...

Zircon Number	Spot Number	Core' or rim	$^{207}Pb/^{206}Pb$	2σ abs.	$^{207}Pb/^{235}U$	2σ abs.	$^{206}Pb/^{238}U$	2σ abs.	$^{206}Pb/^{238}U$ AGE (Ma)	2σ abs.	C
Essimi – LK16_016											
18	69	Core	0.0456	0.0013	0.0317	0.0014	0.0051	0.0002	32.44	1.10	1.02
18	70	Rim	0.0498	0.0009	0.0389	0.0015	0.0057	0.0002	36.44	1.20	0.94
20	71	Core	0.0479	0.0015	0.0337	0.0015	0.0051	0.0002	32.78	1.10	0.98
20	72	Rim	0.0469	0.0009	0.0321	0.0012	0.0050	0.0002	31.95	1.10	1.00
21	73	Core	0.0456	0.0009	0.0309	0.0012	0.0049	0.0002	31.61	1.10	1.02
21	74	Rim	0.0461	0.0011	0.0318	0.0013	0.0050	0.0002	32.12	1.10	1.01
22	75	Core	0.0797	0.0019	0.0561	0.0023	0.0051	0.0002	32.84	1.10	0.59
22	76	Rim	0.0458	0.0011	0.0318	0.0014	0.0051	0.0002	32.45	1.10	1.02
23	77	Core	0.0467	0.0016	0.0324	0.0016	0.0050	0.0002	32.37	1.20	1.00
23	78	Rim	0.0458	0.0016	0.0322	0.0016	0.0051	0.0002	32.79	1.10	1.02
24	79	Core	0.0456	0.0012	0.0328	0.0018	0.0052	0.0003	33.60	1.70	1.03
24	80	Rim	0.0463	0.0014	0.0325	0.0019	0.0051	0.0003	32.70	1.60	1.01
26	81	Core	0.0503	0.0014	0.0348	0.0020	0.0050	0.0003	32.30	1.70	0.93
26	82	Rim	0.0455	0.0011	0.0309	0.0016	0.0049	0.0002	31.70	1.40	1.03
27	83	Core	0.0498	0.0013	0.0340	0.0016	0.0050	0.0002	31.91	1.20	0.94
27	84	Rim	0.0452	0.0016	0.0311	0.0018	0.0050	0.0002	32.10	1.50	1.03
28	85	Core	0.0464	0.0013	0.0317	0.0018	0.0050	0.0002	31.90	1.50	1.01
28	86	Rim	0.0453	0.0017	0.0314	0.0019	0.0050	0.0002	32.40	1.60	1.03
29	87	Core	0.0475	0.0013	0.0327	0.0016	0.0050	0.0002	32.10	1.30	0.98
29	88	Rim	0.0452	0.0012	0.0317	0.0018	0.0051	0.0003	32.70	1.70	1.03
31	98	Core	0.0465	0.0015	0.0311	0.0014	0.0048	0.0002	31.18	1.10	1.00
31	99	Rim	0.0472	0.0012	0.0322	0.0013	0.0049	0.0002	31.79	1.10	0.99
33	100	Core	0.0472	0.0007	0.0327	0.0012	0.0050	0.0002	32.28	1.10	0.99
33	101	Rim	0.0472	0.0015	0.0324	0.0016	0.0050	0.0002	31.99	1.10	0.99
35	102	Core	0.0462	0.0015	0.0312	0.0014	0.0049	0.0002	31.49	1.00	1.01
35	103	Rim	0.0464	0.0012	0.0318	0.0014	0.0050	0.0002	31.98	1.10	1.01
36	104	Core	0.0462	0.0015	0.0318	0.0015	0.0050	0.0002	32.12	1.10	1.01
36	105	Rim	0.5490	0.0340	1.4603	0.1763	0.0193	0.0020	123.00	12.00	0.13
37	106	Core	0.0455	0.0015	0.0309	0.0015	0.0049	0.0002	31.71	1.10	1.03
37	107	Rim	0.0479	0.0015	0.0330	0.0015	0.0050	0.0002	32.12	1.10	0.98
39	108	Core	0.0465	0.0013	0.0315	0.0014	0.0049	0.0002	31.63	1.10	1.00
39	109	Rim	0.0493	0.0016	0.0338	0.0016	0.0050	0.0002	32.04	1.10	0.95
40	110	Core	0.0472	0.0017	0.0325	0.0017	0.0050	0.0002	32.10	1.10	0.99
40	111	Rim	0.0478	0.0013	0.0333	0.0015	0.0051	0.0002	32.54	1.10	0.98
42	112	Core	0.0458	0.0014	0.0312	0.0015	0.0049	0.0002	31.76	1.10	1.02
42	113	Rim	0.0452	0.0014	0.0308	0.0015	0.0049	0.0002	31.78	1.20	1.03
44	114	Core	0.0442	0.0026	0.0308	0.0022	0.0051	0.0002	32.50	1.30	1.06
44	115	Rim	0.0449	0.0020	0.0313	0.0019	0.0051	0.0002	32.56	1.30	1.04
45	116	Core	0.0473	0.0014	0.0337	0.0017	0.0052	0.0002	33.20	1.40	0.99
45	117	Rim	0.0471	0.0011	0.0326	0.0014	0.0050	0.0002	32.26	1.20	0.99
46	118	Core	0.0471	0.0015	0.0327	0.0016	0.0050	0.0002	32.43	1.20	0.99
46	119	Rim	0.0459	0.0013	0.0315	0.0015	0.0050	0.0002	31.99	1.20	1.02
47	120	Core	0.0465	0.0013	0.0315	0.0014	0.0049	0.0002	31.64	1.10	1.00
47	121	Rim	0.0467	0.0011	0.0315	0.0013	0.0049	0.0002	31.44	1.10	1.00

Table I2: Continued...

Zircon Number	Spot Number	Core' or rim	$^{207}Pb/^{206}Pb$	2σ abs.	$^{207}Pb/^{235}U$	2σ abs.	$^{206}Pb/^{238}U$	2σ abs.	$^{206}Pb/^{238}U$ AGE (Ma)	2σ abs.	C
Essimi – LK16_016											
48	122	Core	0.0473	0.0011	0.0324	0.0014	0.0050	0.0002	31.95	1.20	0.99
48	123	Rim	0.0549	0.0020	0.0381	0.0019	0.0050	0.0002	32.34	1.10	0.85
50	124	Core	0.0598	0.0022	0.0412	0.0021	0.0050	0.0002	32.17	1.20	0.78
50	125	Rim	0.0479	0.0013	0.0329	0.0015	0.0050	0.0002	32.12	1.20	0.98
51	126	Core	0.0503	0.0014	0.0352	0.0016	0.0051	0.0002	32.66	1.20	0.93
51	127	Rim	0.0468	0.0009	0.0318	0.0013	0.0049	0.0002	31.65	1.10	1.00
52	137	Core	0.0475	0.0013	0.0327	0.0015	0.0050	0.0002	32.17	1.10	0.98
52	138	Rim	0.0469	0.0011	0.0320	0.0014	0.0050	0.0002	31.82	1.20	1.00
54	139	Core	0.0477	0.0034	0.0325	0.0026	0.0049	0.0002	31.73	1.20	0.98
54	140	Rim	0.0458	0.0015	0.0312	0.0016	0.0050	0.0002	31.84	1.30	1.02
55	141	Core	0.0599	0.0008	0.6696	0.0279	0.0811	0.0032	502.00	19.00	0.96
55	142	Rim	0.0546	0.0008	0.2564	0.0118	0.0341	0.0015	216.00	9.10	0.93
56	143	Core	0.0462	0.0016	0.0318	0.0016	0.0050	0.0002	32.15	1.20	1.01
56	144	Rim	0.0464	0.0014	0.0319	0.0016	0.0050	0.0002	32.05	1.20	1.01
57	145	Core	0.0448	0.0015	0.0304	0.0016	0.0049	0.0002	31.62	1.20	1.04
57	146	Rim	0.0474	0.0010	0.0328	0.0015	0.0050	0.0002	32.30	1.40	0.99
58	147	Core	0.0522	0.0014	0.0360	0.0017	0.0050	0.0002	32.22	1.30	0.90
58	148	Rim	0.0464	0.0015	0.0316	0.0017	0.0049	0.0002	31.70	1.30	1.00
60	149	Core	0.0471	0.0022	0.0322	0.0019	0.0050	0.0002	31.91	1.20	0.99
60	150	Rim	0.0461	0.0012	0.0317	0.0015	0.0050	0.0002	32.10	1.20	1.01
61	151	Core	0.0450	0.0019	0.0314	0.0021	0.0051	0.0003	32.50	1.70	1.04
61	152	Rim	0.0461	0.0014	0.0316	0.0018	0.0050	0.0002	32.00	1.60	1.01
62	153	Core	0.0464	0.0012	0.0325	0.0018	0.0051	0.0002	32.70	1.50	1.01
62	154	Rim	0.0441	0.0032	0.0303	0.0026	0.0050	0.0002	32.10	1.50	1.06
63	155	Core	0.0472	0.0009	0.0326	0.0016	0.0050	0.0002	32.20	1.50	0.99
63	156	Rim	0.0477	0.0013	0.0327	0.0017	0.0050	0.0002	31.90	1.40	0.98
65	157	Core	0.0467	0.0012	0.0332	0.0018	0.0052	0.0002	33.20	1.60	1.00
65	158	Rim	0.0452	0.0014	0.0311	0.0017	0.0050	0.0002	32.10	1.40	1.03
66	159	Core	0.0463	0.0009	0.0321	0.0016	0.0050	0.0002	32.30	1.50	1.01
66	160	Rim	0.0470	0.0014	0.0326	0.0019	0.0050	0.0003	32.40	1.60	0.99
67	161	Core	0.0719	0.0018	0.0512	0.0029	0.0052	0.0003	33.30	1.70	0.66
67	162	Rim	0.0473	0.0017	0.0329	0.0021	0.0051	0.0003	32.40	1.70	0.99
68	163	Core	0.0472	0.0019	0.0335	0.0021	0.0052	0.0003	33.10	1.60	0.99
68	164	Rim	0.0470	0.0009	0.0334	0.0016	0.0052	0.0002	33.10	1.50	0.99
69	165	Core	0.0496	0.0009	0.0331	0.0017	0.0048	0.0002	31.10	1.50	0.94
69	166	Rim	0.0893	0.0033	0.0634	0.0040	0.0052	0.0003	33.10	1.70	0.53
71	176	Core	0.0489	0.0016	0.0336	0.0016	0.0050	0.0002	32.03	1.10	0.96
71	177	Rim	0.0481	0.0014	0.0331	0.0016	0.0050	0.0002	32.12	1.20	0.97
72	178	Core	0.0480	0.0012	0.0333	0.0015	0.0050	0.0002	32.35	1.20	0.97
72	179	Rim	0.0473	0.0009	0.0331	0.0014	0.0051	0.0002	32.57	1.20	0.99
74	180	Core	0.0476	0.0012	0.0333	0.0015	0.0051	0.0002	32.66	1.20	0.98
74	181	Rim	0.0464	0.0015	0.0322	0.0016	0.0050	0.0002	32.40	1.30	1.01
75	182	Core	0.0471	0.0016	0.0332	0.0018	0.0051	0.0002	32.90	1.40	0.99
75	183	Rim	0.0468	0.0014	0.0322	0.0017	0.0050	0.0002	32.10	1.40	1.00

Table I2: Continued...

Zircon Number	Spot Number	Core' or rim	$^{207}Pb/^{206}Pb$	2σ abs.	$^{207}Pb/^{235}U$	2σ abs.	$^{206}Pb/^{238}U$	2σ abs.	$^{206}Pb/^{238}U$ AGE (Ma)	2σ abs.	C
Essimi – LK16_016											
76	184	Core	0.0469	0.0015	0.0332	0.0018	0.0051	0.0002	33.00	1.50	1.00
76	185	Rim	0.0470	0.0008	0.0333	0.0015	0.0051	0.0002	33.02	1.30	0.99
78	186	Core	0.0479	0.0018	0.0337	0.0018	0.0051	0.0002	32.81	1.30	0.98
78	187	Rim	0.0483	0.0011	0.0340	0.0017	0.0051	0.0002	32.90	1.40	0.97
79	188	Core	0.0528	0.0016	0.0373	0.0018	0.0051	0.0002	32.89	1.30	0.89
79	189	Rim	0.0462	0.0014	0.0323	0.0017	0.0051	0.0002	32.60	1.40	1.01
80	190	Core	0.0524	0.0008	0.2484	0.0142	0.0344	0.0019	218.00	12.00	0.97
80	191	Rim	0.0476	0.0012	0.0323	0.0015	0.0049	0.0002	31.72	1.20	0.98
81	192	Core	0.0468	0.0012	0.0322	0.0015	0.0050	0.0002	32.12	1.30	1.00
81	193	Rim	0.0469	0.0015	0.0322	0.0016	0.0050	0.0002	32.02	1.30	1.00
82	194	Core	0.0536	0.0007	0.3105	0.0132	0.0420	0.0017	265.30	10.00	0.97
82	195	Rim	0.0493	0.0014	0.0342	0.0017	0.0050	0.0002	32.35	1.30	0.95
83	196	Core	0.0480	0.0014	0.0333	0.0018	0.0050	0.0002	32.40	1.40	0.97
83	197	Rim	0.0475	0.0012	0.0329	0.0016	0.0050	0.0002	32.28	1.30	0.98
84	198	Core	0.0501	0.0009	0.0348	0.0016	0.0050	0.0002	32.43	1.30	0.93
84	199	Rim	0.0452	0.0018	0.0311	0.0018	0.0050	0.0002	32.20	1.40	1.03
85	200	Core	0.0519	0.0013	0.2461	0.0124	0.0344	0.0015	217.80	9.30	0.98
85	201	Rim	0.0512	0.0006	0.2617	0.0124	0.0371	0.0017	234.90	11.00	1.00
87	202	Core	0.0476	0.0011	0.0331	0.0015	0.0050	0.0002	32.40	1.20	0.98
87	203	Rim	0.0482	0.0014	0.0336	0.0017	0.0051	0.0002	32.50	1.30	0.97
88	204	Core	0.0490	0.0013	0.0365	0.0017	0.0054	0.0002	34.69	1.30	0.95
88	205	Rim	0.0484	0.0014	0.0345	0.0022	0.0052	0.0003	33.30	1.80	0.97
89	215	Core	0.0499	0.0010	0.0336	0.0013	0.0049	0.0002	31.38	1.10	0.94
89	216	Rim	0.0485	0.0012	0.0332	0.0015	0.0050	0.0002	31.95	1.10	0.96
90	217	Core	0.0490	0.0019	0.0345	0.0019	0.0051	0.0002	32.84	1.20	0.95
90	218	Rim	0.0475	0.0013	0.0339	0.0016	0.0052	0.0002	33.30	1.20	0.98
91	219	Core	0.0480	0.0011	0.0333	0.0014	0.0050	0.0002	32.37	1.20	0.97
91	220	Rim	0.0477	0.0016	0.0332	0.0017	0.0051	0.0002	32.44	1.20	0.98
92	221	Core	0.0483	0.0025	0.0337	0.0022	0.0051	0.0002	32.53	1.20	0.97
92	222	Rim	0.0473	0.0017	0.0329	0.0017	0.0051	0.0002	32.47	1.20	0.99
93	223	Core	0.0481	0.0012	0.0337	0.0015	0.0051	0.0002	32.74	1.20	0.97
93	224	Rim	0.0480	0.0014	0.0337	0.0015	0.0051	0.0002	32.81	1.20	0.97
94	225	Core	0.0492	0.0013	0.0348	0.0016	0.0051	0.0002	33.00	1.30	0.95
94	226	Rim	0.0510	0.0019	0.0358	0.0018	0.0051	0.0002	32.78	1.10	0.92
95	227	Core	0.0501	0.0016	0.0360	0.0017	0.0052	0.0002	33.49	1.20	0.93
95	228	Rim	0.0493	0.0014	0.0357	0.0018	0.0053	0.0002	33.80	1.40	0.95
96	229	Core	0.0551	0.0014	0.0482	0.0024	0.0064	0.0003	40.80	1.70	0.85
96	230	Rim	0.0476	0.0009	0.0331	0.0013	0.0051	0.0002	32.46	1.20	0.98
97	231	Core	0.0473	0.0017	0.0335	0.0021	0.0051	0.0003	33.10	1.70	0.99
97	232	Rim	0.0484	0.0014	0.0345	0.0020	0.0052	0.0003	33.30	1.70	0.97
98	233	Core	0.0480	0.0011	0.0346	0.0017	0.0052	0.0002	33.60	1.50	0.97
98	234	Rim	0.0484	0.0013	0.0342	0.0017	0.0051	0.0002	32.90	1.40	0.96
100	235	Core	0.0514	0.0033	0.0369	0.0028	0.0052	0.0002	33.50	1.40	0.91
100	236	Rim	0.0486	0.0014	0.0341	0.0016	0.0051	0.0002	32.76	1.20	0.96

Table I2: Continued...

Zircon Number	Spot Number	Core' or rim	$^{207}Pb/^{206}Pb$	2σ abs.	$^{207}Pb/^{235}U$	2σ abs.	$^{206}Pb/^{238}U$	2σ abs.	$^{206}Pb/^{238}U$ AGE (Ma)	2σ abs.	C
Essimi – LK16_016											
5	237		0.0494	0.0011	0.0351	0.0021	0.0052	0.0003	33.10	1.80	0.95
5	238		0.0554	0.0007	0.3145	0.0187	0.0412	0.0024	260.00	15.00	0.94
9	239		0.0602	0.0007	0.7038	0.0390	0.0849	0.0046	524.00	27.00	0.97
9	240		0.0494	0.0013	0.0364	0.0019	0.0054	0.0002	34.40	1.50	0.95
8	241		0.0522	0.0008	0.1784	0.0218	0.0248	0.0030	157.00	19.00	0.94
8	242		0.0497	0.0010	0.0369	0.0020	0.0054	0.0003	34.60	1.80	0.94
13	243		0.0590	0.0008	0.7474	0.0379	0.0920	0.0045	566.00	27.00	1.00
13	244		0.0546	0.0006	0.3475	0.0156	0.0462	0.0020	290.80	13.00	0.96
37	245		0.0477	0.0018	0.0343	0.0020	0.0052	0.0002	33.50	1.60	0.98
37	246		0.0488	0.0013	0.0346	0.0019	0.0052	0.0003	33.10	1.60	0.96
55	247		0.0866	0.0025	0.6588	0.0374	0.0552	0.0027	346.00	17.00	0.67
55	248		0.0514	0.0007	0.0680	0.0037	0.0096	0.0005	61.50	3.20	0.92
85	258		0.0522	0.0011	0.2863	0.0124	0.0398	0.0015	251.50	9.20	0.98
85	259		0.0567	0.0013	0.2712	0.0140	0.0347	0.0016	219.70	9.80	0.90
85	260		0.0526	0.0009	0.2437	0.0129	0.0336	0.0017	212.70	11.00	0.96
82	261		0.0546	0.0011	0.0836	0.0060	0.0111	0.0008	71.30	4.90	0.87
82	262		0.0494	0.0011	0.0353	0.0017	0.0052	0.0002	33.30	1.40	0.95
82	263		0.0523	0.0019	0.0373	0.0021	0.0052	0.0002	33.30	1.40	0.89
80	264		0.0548	0.0007	0.3233	0.0142	0.0428	0.0018	270.10	11.00	0.95
80	265		0.0535	0.0007	0.3583	0.0155	0.0486	0.0020	305.70	12.00	0.98
80	266		0.0500	0.0011	0.0358	0.0016	0.0052	0.0002	33.40	1.40	0.93
Kassiteres – KA15_018											
1	122	Core	0.0462	0.0009	0.0331	0.0020	0.0052	0.0003	33.40	2.00	1.01
1	123	Rim	0.0454	0.0010	0.0331	0.0025	0.0053	0.0004	33.90	2.50	1.03
2	124	Core	0.0411	0.0020	0.0289	0.0028	0.0051	0.0004	32.80	2.80	1.13
2	125	Rim	0.0455	0.0009	0.0328	0.0025	0.0052	0.0004	33.60	2.50	1.03
4	126	Core	0.0443	0.0012	0.0330	0.0026	0.0054	0.0004	34.80	2.50	1.05
4	127	Rim	0.0439	0.0013	0.0319	0.0023	0.0053	0.0003	33.90	2.20	1.06
5	128	Core	0.0473	0.0007	0.0349	0.0027	0.0054	0.0004	34.40	2.60	0.99
5	129	Rim	0.0469	0.0008	0.0360	0.0030	0.0056	0.0005	35.80	3.00	1.00
6	130	Core	0.0618	0.0023	0.1346	0.0153	0.0158	0.0017	101.00	11.00	0.79
6	131	Rim	0.0455	0.0009	0.0349	0.0032	0.0056	0.0005	35.70	3.20	1.03
7	132	Core	0.0447	0.0014	0.0327	0.0028	0.0053	0.0004	34.10	2.70	1.04
7	133	Rim	0.0450	0.0009	0.0330	0.0029	0.0053	0.0005	34.20	2.90	1.04
8	134	Core	0.0441	0.0010	0.0324	0.0029	0.0053	0.0005	34.30	2.90	1.06
8	135	Rim	0.0464	0.0008	0.0362	0.0034	0.0057	0.0005	36.30	3.40	1.01
10	136	Core	0.0455	0.0009	0.0352	0.0035	0.0056	0.0005	36.00	3.50	1.02
10	137	Rim	0.0471	0.0009	0.0366	0.0032	0.0056	0.0005	36.20	3.10	0.99
21	147	Core	0.0569	0.0014	0.0484	0.0038	0.0062	0.0005	39.60	3.00	0.83
21	148	Rim	0.0557	0.0014	0.0388	0.0018	0.0051	0.0002	32.55	1.20	0.84
18	149	Core	0.0755	0.0032	0.0532	0.0031	0.0051	0.0002	32.90	1.30	0.63
18	150	Rim	0.0495	0.0008	0.0339	0.0015	0.0050	0.0002	31.90	1.30	0.94
16	151	Core	0.0480	0.0008	0.0336	0.0012	0.0051	0.0002	32.68	1.10	0.97

Table I2: Continued...

Zircon Number	Spot Number	Core' or rim	$^{207}Pb/^{206}Pb$	2σ abs.	$^{207}Pb/^{235}U$	2σ abs.	$^{206}Pb/^{238}U$	2σ abs.	$^{206}Pb/^{238}U$ AGE (Ma)	2σ abs.	C
Kassiteres – KA15_018											
16	152	Rim	0.0539	0.0013	0.0387	0.0018	0.0052	0.0002	33.50	1.30	0.87
14	153	Core	0.0531	0.0013	0.0369	0.0017	0.0050	0.0002	32.40	1.20	0.88
14	154	Rim	0.0531	0.0012	0.0373	0.0016	0.0051	0.0002	32.79	1.20	0.88
13	155	Core	0.0487	0.0008	0.0334	0.0015	0.0050	0.0002	32.00	1.30	0.96
13	156	Rim	0.0507	0.0009	0.0353	0.0014	0.0051	0.0002	32.50	1.10	0.92
30	157	Core	0.0550	0.0008	0.2895	0.0115	0.0382	0.0014	241.40	8.70	0.94
30	158	Rim	0.0495	0.0009	0.0341	0.0015	0.0050	0.0002	32.20	1.30	0.94
29	159	Core	0.0558	0.0016	0.0387	0.0018	0.0050	0.0002	32.36	1.20	0.84
29	160	Rim	0.0493	0.0010	0.0348	0.0016	0.0051	0.0002	32.90	1.30	0.95
28	161	Core	0.0540	0.0011	0.1123	0.0064	0.0151	0.0008	96.50	5.10	0.89
28	162	Rim	0.0503	0.0010	0.0356	0.0015	0.0051	0.0002	33.01	1.20	0.93
27	163	Core	0.0514	0.0012	0.0356	0.0015	0.0050	0.0002	32.32	1.20	0.91
27	164	Rim	0.0490	0.0009	0.0340	0.0015	0.0050	0.0002	32.40	1.30	0.95
26	165	Core	0.0579	0.0021	0.0400	0.0021	0.0050	0.0002	32.20	1.20	0.81
26	166	Rim	0.0490	0.0009	0.0340	0.0014	0.0050	0.0002	32.32	1.20	0.95
25	167	Core	0.0561	0.0020	0.0394	0.0021	0.0051	0.0002	32.80	1.30	0.84
25	168	Rim	0.0506	0.0013	0.0349	0.0016	0.0050	0.0002	32.20	1.20	0.92
23	28	Core	0.0485	0.0007	0.0334	0.0014	0.0050	0.0002	32.10	1.20	0.96
23	29	Rim	0.0473	0.0006	0.0330	0.0015	0.0051	0.0002	32.60	1.40	0.99
43	30	Core	0.0472	0.0006	0.0322	0.0013	0.0050	0.0002	31.80	1.20	0.99
43	31	Rim	0.0476	0.0007	0.0336	0.0015	0.0051	0.0002	32.90	1.40	0.98
41	32	Core	0.0530	0.0004	0.2768	0.0105	0.0379	0.0014	239.50	8.80	0.97
41	33	Rim	0.0470	0.0008	0.0330	0.0016	0.0051	0.0002	32.70	1.50	0.99
40	34	Core	0.0475	0.0008	0.0331	0.0017	0.0051	0.0002	32.50	1.60	0.98
40	35	Rim	0.0476	0.0005	0.0336	0.0017	0.0051	0.0003	32.90	1.60	0.98
39	36	Core	0.0535	0.0010	0.0374	0.0017	0.0051	0.0002	32.70	1.40	0.88
39	37	Rim	0.0482	0.0009	0.0339	0.0015	0.0051	0.0002	32.80	1.30	0.97
38	38	Core	0.0486	0.0008	0.0341	0.0015	0.0051	0.0002	32.70	1.40	0.96
38	39	Rim	0.0492	0.0006	0.0338	0.0014	0.0050	0.0002	32.10	1.30	0.95
36	40	Core	0.0481	0.0006	0.0341	0.0016	0.0052	0.0002	33.10	1.50	0.97
36	41	Rim	0.0474	0.0008	0.0326	0.0015	0.0050	0.0002	32.10	1.40	0.99
52	42	Core	0.0485	0.0008	0.0340	0.0018	0.0051	0.0003	32.60	1.60	0.96
52	43	Rim	0.0471	0.0008	0.0336	0.0019	0.0052	0.0003	33.30	1.80	0.99
50	44	Core	0.0484	0.0010	0.0343	0.0017	0.0052	0.0002	33.10	1.60	0.97
50	45	Rim	0.0475	0.0004	0.0331	0.0014	0.0051	0.0002	32.50	1.40	0.98
49	46	Core	0.0494	0.0006	0.0341	0.0016	0.0050	0.0002	32.10	1.50	0.94
49	47	Rim	0.0481	0.0006	0.0339	0.0016	0.0051	0.0002	32.80	1.50	0.97
53	57	Core	0.0478	0.0008	0.0320	0.0008	0.0049	0.0001	31.28	0.56	0.98
53	58	Rim	0.0476	0.0008	0.0317	0.0008	0.0048	0.0001	31.05	0.56	0.98
54	59	Core	0.0531	0.0005	0.2150	0.0097	0.0294	0.0013	186.70	8.20	0.94
54	60	Rim	0.0475	0.0006	0.0317	0.0008	0.0049	0.0001	31.17	0.65	0.98
56	61	Core	0.0477	0.0008	0.0318	0.0009	0.0048	0.0001	31.08	0.63	0.98
56	62	Rim	0.0474	0.0009	0.0317	0.0009	0.0048	0.0001	31.16	0.62	0.99
57	63	Core	0.0478	0.0009	0.0319	0.0008	0.0048	0.0001	31.18	0.55	0.98

Table I2: Continued...

Zircon Number	Spot Number	Core' or rim	$^{207}Pb/^{206}Pb$	2σ abs.	$^{207}Pb/^{235}U$	2σ abs.	$^{206}Pb/^{238}U$	2σ abs.	$^{206}Pb/^{238}U$ AGE (Ma)	2σ abs.	C
Kassiteres – KA15_018											
57	64	Rim	0.0485	0.0010	0.0330	0.0016	0.0049	0.0002	31.70	1.40	0.96
58	65	Core	0.0480	0.0005	0.0334	0.0022	0.0051	0.0003	32.50	2.10	0.97
58	66	Rim	0.0476	0.0007	0.0325	0.0020	0.0050	0.0003	31.90	1.90	0.98
59	67	Core	0.1030	0.0120	0.0798	0.0109	0.0056	0.0004	36.10	2.60	0.46
59	68	Rim	0.0475	0.0008	0.0336	0.0020	0.0051	0.0003	33.00	1.90	0.98
60	69	Core	0.0465	0.0011	0.0322	0.0019	0.0050	0.0003	32.30	1.80	1.00
60	70	Rim	0.0498	0.0008	0.0337	0.0018	0.0049	0.0003	31.60	1.60	0.94
63	71	Core	0.0518	0.0009	0.0430	0.0028	0.0060	0.0004	38.70	2.40	0.91
63	72	Rim	0.0493	0.0006	0.0384	0.0020	0.0057	0.0003	36.30	1.80	0.95
45	73	Core	0.0666	0.0008	0.7750	0.0641	0.0844	0.0069	518.00	41.00	0.89
45	74	Rim	0.0471	0.0009	0.0336	0.0028	0.0052	0.0004	33.20	2.70	0.99
64	75	Core	0.0508	0.0007	0.1618	0.0101	0.0231	0.0014	147.10	8.60	0.97
64	76	Rim	0.0484	0.0005	0.0343	0.0025	0.0051	0.0004	33.00	2.40	0.96
66	86	Core	0.0495	0.0011	0.0336	0.0017	0.0049	0.0002	31.70	1.40	0.94
66	87	Rim	0.0481	0.0007	0.0324	0.0014	0.0049	0.0002	31.50	1.30	0.97
67	88	Core	0.0480	0.0007	0.0331	0.0017	0.0050	0.0003	32.20	1.60	0.97
67	89	Rim	0.0479	0.0006	0.0328	0.0017	0.0050	0.0003	31.90	1.60	0.97
68	90	Core	0.0479	0.0005	0.0334	0.0020	0.0051	0.0003	32.50	1.90	0.98
68	91	Rim	0.0479	0.0005	0.0324	0.0017	0.0049	0.0003	31.60	1.60	0.97
69	92	Core	0.0518	0.0006	0.1384	0.0069	0.0194	0.0009	123.60	6.00	0.94
69	93	Rim	0.0477	0.0007	0.0333	0.0017	0.0051	0.0003	32.60	1.60	0.98
71	94	Core	0.0483	0.0012	0.0335	0.0019	0.0050	0.0003	32.30	1.70	0.97
71	95	Rim	0.0478	0.0007	0.0326	0.0017	0.0049	0.0003	31.80	1.60	0.98
72	96	Core	0.0483	0.0008	0.0335	0.0019	0.0050	0.0003	32.40	1.80	0.97
72	97	Rim	0.0476	0.0006	0.0331	0.0018	0.0050	0.0003	32.40	1.60	0.98
74	98	Core	0.0578	0.0005	0.4105	0.0234	0.0515	0.0029	323.00	17.00	0.92
74	99	Rim	0.0526	0.0007	0.0414	0.0016	0.0057	0.0002	36.70	1.40	0.89
76	100	Core	0.0490	0.0009	0.0343	0.0019	0.0051	0.0003	32.60	1.70	0.95
76	101	Rim	0.0474	0.0005	0.0326	0.0017	0.0050	0.0003	32.10	1.60	0.99
77	102	Core	0.0481	0.0013	0.0346	0.0022	0.0052	0.0003	33.60	1.90	0.97
77	103	Rim	0.0482	0.0008	0.0337	0.0018	0.0051	0.0003	32.70	1.60	0.97
78	104	Core	0.1151	0.0009	1.1743	0.0673	0.0740	0.0042	459.00	25.00	0.58
78	105	Rim	0.0471	0.0005	0.0334	0.0020	0.0051	0.0003	33.00	1.90	0.99
79	115	Core	0.0483	0.0009	0.0332	0.0010	0.0050	0.0001	32.09	0.73	0.97
79	116	Rim	0.0506	0.0011	0.0352	0.0012	0.0051	0.0001	32.45	0.93	0.92
80	117	Core	0.0484	0.0009	0.0326	0.0011	0.0049	0.0001	31.43	0.87	0.96
80	118	Rim	0.0490	0.0008	0.0335	0.0011	0.0050	0.0001	31.92	0.91	0.95
81	119	Core	0.0487	0.0014	0.0338	0.0014	0.0050	0.0002	32.35	0.94	0.96
81	120	Rim	0.0483	0.0006	0.0331	0.0010	0.0050	0.0001	31.99	0.93	0.97
82	121	Core	0.0495	0.0008	0.0342	0.0010	0.0050	0.0001	32.20	0.78	0.94
82	122	Rim	0.0478	0.0005	0.0332	0.0009	0.0050	0.0001	32.39	0.86	0.98
83	123	Core	0.0857	0.0031	0.0619	0.0027	0.0052	0.0001	33.69	0.87	0.55
83	124	Rim	0.0477	0.0005	0.0334	0.0009	0.0051	0.0001	32.65	0.75	0.98
85	125	Core	0.0757	0.0035	0.0540	0.0028	0.0052	0.0001	33.28	0.83	0.62

Table I2: Continued...

Zircon Number	Spot Number	Core' or rim	$^{207}Pb/^{206}Pb$	2σ abs.	$^{207}Pb/^{235}U$	2σ abs.	$^{206}Pb/^{238}U$	2σ abs.	$^{206}Pb/^{238}U$ AGE (Ma)	2σ abs.	C
Kassiteres – KA15_018											
85	126	Rim	0.0540	0.0018	0.0392	0.0017	0.0053	0.0002	33.89	0.96	0.87
88	127	Core	0.0484	0.0009	0.0335	0.0011	0.0050	0.0001	32.35	0.91	0.97
88	128	Rim	0.0470	0.0007	0.0325	0.0011	0.0050	0.0002	32.30	0.94	0.99
89	129	Core	0.0566	0.0005	0.4554	0.0117	0.0584	0.0014	365.50	8.70	0.96
89	130	Rim	0.0513	0.0009	0.0372	0.0012	0.0053	0.0001	33.82	0.92	0.91
90	131	Core	0.0481	0.0010	0.0335	0.0011	0.0051	0.0001	32.48	0.85	0.97
90	132	Rim	0.0482	0.0008	0.0332	0.0011	0.0050	0.0001	32.16	0.90	0.97
91	133	Core	0.1025	0.0039	0.0752	0.0036	0.0053	0.0002	34.22	0.93	0.47
91	134	Rim	0.0476	0.0006	0.0329	0.0010	0.0050	0.0001	32.24	0.85	0.98
92	135	Core	0.0472	0.0005	0.0328	0.0008	0.0050	0.0001	32.41	0.78	0.99
92	136	Rim	0.0548	0.0013	0.0385	0.0014	0.0051	0.0001	32.80	0.92	0.85
93	137	Core	0.0470	0.0007	0.0327	0.0009	0.0050	0.0001	32.43	0.80	0.99
93	138	Rim	0.0481	0.0007	0.0334	0.0010	0.0050	0.0001	32.36	0.81	0.97
94	139	Core	0.0631	0.0022	0.4009	0.0185	0.0461	0.0014	290.30	8.90	0.85
94	140	Rim	0.0473	0.0007	0.0326	0.0011	0.0050	0.0002	32.18	0.96	0.99
98	141	Core	0.0489	0.0008	0.0337	0.0010	0.0050	0.0001	32.17	0.85	0.96
98	142	Rim	0.0481	0.0007	0.0333	0.0011	0.0050	0.0001	32.26	0.89	0.97
99	143	Core	0.0492	0.0009	0.0341	0.0011	0.0050	0.0001	32.26	0.86	0.95
99	144	Rim	0.0476	0.0009	0.0331	0.0011	0.0051	0.0001	32.48	0.90	0.98
100	154	Core	0.0473	0.0005	0.0331	0.0019	0.0051	0.0003	32.70	1.80	0.99
100	155	Rim	0.0477	0.0006	0.0327	0.0019	0.0050	0.0003	32.00	1.80	0.98
101	156	Core	0.0519	0.0010	0.0365	0.0021	0.0051	0.0003	32.80	1.80	0.90
101	157	Rim	0.0485	0.0006	0.0354	0.0023	0.0053	0.0003	34.00	2.10	0.96
102	158	Core	0.0572	0.0008	0.1090	0.0076	0.0138	0.0009	88.40	6.00	0.84
102	159	Rim	0.0470	0.0008	0.0329	0.0018	0.0051	0.0003	32.70	1.70	0.99
103	160	Core	0.0533	0.0005	0.1821	0.0119	0.0248	0.0016	157.50	9.90	0.93
103	161	Rim	0.0498	0.0011	0.0353	0.0025	0.0051	0.0004	33.00	2.20	0.94
105	162	Core	0.0485	0.0011	0.0344	0.0024	0.0052	0.0003	33.10	2.20	0.96
105	163	Rim	0.0484	0.0009	0.0348	0.0024	0.0052	0.0003	33.50	2.10	0.97
106	164	Core	0.0513	0.0005	0.2812	0.0178	0.0398	0.0025	251.00	16.00	1.00
106	165	Rim	0.0475	0.0011	0.0339	0.0022	0.0052	0.0003	33.30	2.00	0.98
107	166	Core	0.0476	0.0006	0.0334	0.0019	0.0051	0.0003	32.70	1.90	0.98
107	167	Rim	0.0471	0.0005	0.0330	0.0020	0.0051	0.0003	32.70	1.90	0.99
108	168	Core	0.0483	0.0006	0.0337	0.0022	0.0051	0.0003	32.50	2.00	0.97
108	169	Rim	0.0476	0.0008	0.0332	0.0019	0.0051	0.0003	32.50	1.80	0.98
109	170	Core	0.0517	0.0006	0.2214	0.0117	0.0311	0.0016	197.00	10.00	0.97
109	171	Rim	0.0478	0.0008	0.0339	0.0022	0.0052	0.0003	33.10	2.10	0.98
110	172	Core	0.0471	0.0014	0.0330	0.0022	0.0051	0.0003	32.60	1.90	0.99
110	173	Rim	0.0473	0.0008	0.0328	0.0020	0.0050	0.0003	32.30	1.90	0.99
112	174	Core	0.0570	0.0006	0.2122	0.0151	0.0270	0.0019	171.00	12.00	0.88
112	175	Rim	0.0495	0.0006	0.0354	0.0020	0.0052	0.0003	33.40	1.80	0.94
114	176	Core	0.0514	0.0005	0.2877	0.0193	0.0406	0.0027	256.00	16.00	1.00
114	177	Rim	0.0475	0.0005	0.0328	0.0017	0.0050	0.0003	32.20	1.60	0.98
115	178	Core	0.0472	0.0006	0.0326	0.0021	0.0050	0.0003	32.20	2.00	0.99

Table I2: Continued...

Zircon Number	Spot Number	Core' or rim	$^{207}Pb/^{206}Pb$	2σ abs.	$^{207}Pb/^{235}U$	2σ abs.	$^{206}Pb/^{238}U$	2σ abs.	$^{206}Pb/^{238}U$ AGE (Ma)	2σ abs.	C
					Kassiteres – KA15_018						
115	179	Rim	0.0470	0.0007	0.0333	0.0021	0.0052	0.0003	33.10	2.00	0.99
118	180	Core	0.0524	0.0007	0.0360	0.0022	0.0050	0.0003	32.10	1.90	0.89
118	181	Rim	0.0472	0.0007	0.0326	0.0019	0.0050	0.0003	32.20	1.80	0.99
120	182	Core	0.0471	0.0010	0.0324	0.0020	0.0050	0.0003	32.10	1.90	0.99
120	183	Rim	0.0480	0.0007	0.0338	0.0022	0.0051	0.0003	32.80	2.00	0.97
6	193		0.0566	0.0005	0.4240	0.0275	0.0544	0.0035	340.00	21.00	0.95
6	194		0.0528	0.0012	0.0606	0.0047	0.0083	0.0006	53.40	4.00	0.89
6	195		0.0477	0.0007	0.0338	0.0022	0.0051	0.0003	33.00	2.10	0.98
28	196		0.0528	0.0010	0.0768	0.0071	0.0106	0.0010	67.60	6.10	0.90
28	197		0.0475	0.0008	0.0333	0.0023	0.0051	0.0003	32.70	2.20	0.98
28	198		0.0483	0.0009	0.0341	0.0024	0.0051	0.0004	32.90	2.20	0.97
30	199		0.0538	0.0004	0.2314	0.0150	0.0312	0.0020	198.00	12.00	0.94
30	200		0.0556	0.0006	0.0997	0.0076	0.0130	0.0010	83.30	6.30	0.86
30	201		0.0481	0.0007	0.0337	0.0022	0.0051	0.0003	32.70	2.10	0.97
41	202		0.0474	0.0008	0.0330	0.0022	0.0051	0.0003	32.50	2.10	0.99
41	203		0.0513	0.0008	0.0785	0.0056	0.0111	0.0008	71.20	4.90	0.93
41	204		0.0476	0.0009	0.0334	0.0027	0.0051	0.0004	32.70	2.60	0.98
41	205		0.0476	0.0008	0.0326	0.0020	0.0050	0.0003	32.00	1.90	0.98
45	206		0.0594	0.0006	0.6691	0.0472	0.0817	0.0057	508.00	35.00	0.98
45	207		0.0563	0.0007	0.2500	0.0204	0.0322	0.0026	204.00	16.00	0.90
45	208		0.0486	0.0010	0.0349	0.0025	0.0052	0.0004	33.60	2.20	0.96
54	209		0.0595	0.0020	0.0447	0.0039	0.0055	0.0004	35.00	2.80	0.79
54	210		0.0512	0.0012	0.0366	0.0030	0.0052	0.0004	33.30	2.60	0.91
54	211		0.0516	0.0011	0.0373	0.0031	0.0053	0.0004	33.80	2.70	0.91
64	212		0.0507	0.0009	0.0593	0.0040	0.0085	0.0006	54.40	3.50	0.93
64	213		0.0474	0.0008	0.0330	0.0024	0.0051	0.0004	32.40	2.20	0.98
64	214		0.0476	0.0010	0.0335	0.0026	0.0051	0.0004	32.80	2.40	0.98
69	215		0.0500	0.0006	0.0698	0.0050	0.0101	0.0007	65.00	4.50	0.95
69	216		0.0691	0.0015	0.3400	0.0249	0.0357	0.0025	226.00	16.00	0.76
69	217		0.0475	0.0006	0.0338	0.0027	0.0052	0.0004	33.20	2.60	0.98
74	218		0.0560	0.0006	0.1736	0.0125	0.0225	0.0016	143.00	10.00	0.88
74	219		0.0477	0.0014	0.0361	0.0032	0.0055	0.0005	35.30	3.00	0.98
74	220		0.0478	0.0008	0.0334	0.0022	0.0051	0.0003	32.60	2.10	0.98
78	230		0.1104	0.0010	0.4685	0.0247	0.0308	0.0016	195.40	9.70	0.50
78	231		0.0488	0.0010	0.0332	0.0017	0.0049	0.0002	31.70	1.50	0.96
78	232		0.0482	0.0007	0.0326	0.0017	0.0049	0.0002	31.60	1.60	0.97
89	233		0.0567	0.0005	0.5036	0.0308	0.0644	0.0039	401.00	23.00	0.97
89	234		0.0470	0.0009	0.0339	0.0027	0.0052	0.0004	33.60	2.60	0.99
89	235		0.0516	0.0006	0.1002	0.0086	0.0141	0.0012	90.40	7.90	0.93
94	236		0.0553	0.0011	0.0522	0.0042	0.0069	0.0005	44.00	3.40	0.85
94	237		0.0472	0.0006	0.0319	0.0022	0.0049	0.0003	31.50	2.10	0.99
94	238		0.0505	0.0007	0.0391	0.0041	0.0056	0.0006	36.20	3.70	0.93
102	239		0.0594	0.0005	0.5652	0.0477	0.0691	0.0058	427.00	35.00	0.94
102	240		0.0468	0.0007	0.0326	0.0019	0.0051	0.0003	32.50	1.80	1.00

Table I2: Continued...

Zircon Number	Spot Number	Core' or rim	$^{207}Pb/^{206}Pb$	2σ abs.	$^{207}Pb/^{235}U$	2σ abs.	$^{206}Pb/^{238}U$	2σ abs.	$^{206}Pb/^{238}U$ AGE (Ma)	2σ abs.	C
					Kassiteres – KA15_018						
102	241		0.0481	0.0009	0.0325	0.0023	0.0049	0.0003	31.50	2.20	0.97
102	242		0.0952	0.0026	0.0729	0.0064	0.0056	0.0005	35.80	2.90	0.50
103	243		0.0528	0.0006	0.1484	0.0110	0.0204	0.0015	130.20	9.70	0.93
103	244		0.0520	0.0005	0.0768	0.0069	0.0107	0.0010	68.60	6.10	0.91
103	245		0.0482	0.0008	0.0351	0.0030	0.0053	0.0004	33.90	2.80	0.97
103	246		0.1215	0.0054	0.0948	0.0088	0.0057	0.0005	36.30	2.90	0.39
106	247		0.0510	0.0005	0.2894	0.0233	0.0412	0.0033	259.00	21.00	1.00
106	248		0.0526	0.0005	0.2612	0.0219	0.0360	0.0030	227.00	19.00	0.96
106	249		0.0517	0.0005	0.2847	0.0243	0.0400	0.0034	252.00	21.00	0.99
109	250		0.0512	0.0007	0.1673	0.0150	0.0237	0.0021	150.00	13.00	0.96
109	251		0.0515	0.0005	0.2496	0.0207	0.0352	0.0029	222.00	18.00	0.98
109	252		0.0486	0.0013	0.0360	0.0032	0.0054	0.0005	34.50	2.90	0.96
109	253		0.0482	0.0009	0.0341	0.0029	0.0051	0.0004	33.00	2.80	0.97
112	254		0.0487	0.0016	0.0350	0.0032	0.0052	0.0004	33.50	2.80	0.96
112	255		0.0484	0.0008	0.0352	0.0032	0.0053	0.0005	33.90	3.00	0.97
112	256		0.0478	0.0011	0.0348	0.0033	0.0053	0.0005	33.90	3.20	0.98
114	257		0.0516	0.0005	0.2843	0.0250	0.0400	0.0035	252.00	21.00	0.99
114	258		0.0513	0.0005	0.1901	0.0164	0.0269	0.0023	170.00	15.00	0.96
114	259		0.0478	0.0008	0.0350	0.0036	0.0053	0.0005	34.10	3.40	0.98

Appendix J

Zircon-Hosted Melt Inclusion Analysis

This appendix contains the supplementary information and data pertaining to the zircon-hosted melt inclusions presented in Chapter 4.

Table J1: Spectrometer set-up.
Table J2: Secondary standard data.
Table J3: Average analytical uncertainty.
Table J4: Full EPMA results from the zircon-hosted melt inclusions.
Table J5: Full EPMA results from the clay-altered zircon-hosted melt inclusions.

Zircon Analysis Workflow

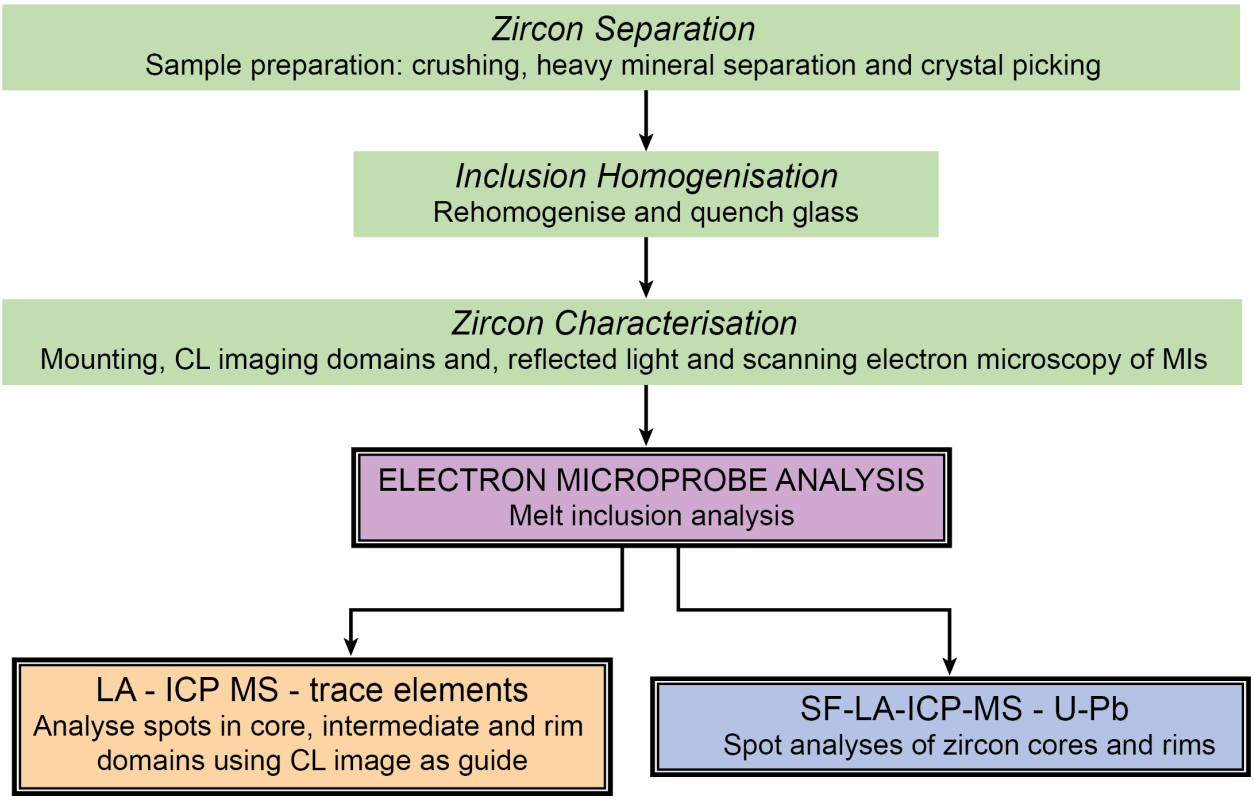

Figure J1: The zircon workflow developed and followed in this study.

EPMA Spectrometer Set-Up

All MI major element chemistry was conducted by EPMA using a 15 kV accelerating voltage, 10 nA beam current and a 1 μm beam diameter. H_2O was included in the matrix correction and calculated using the H_2O-by-difference technique. Elements are listed in order of analyses and were peaked up on their assigned standards. Upper and lower backgrounds were counted for 50 % of the analysis time. The elements were peaked up on:
Na, Si – albite
K, Al – sanidine
Mg – olivine
Ca – wollastonite
Ti, Fe – ilmenite
Zr – zircon

The matrix-matched secondary standards for the analyses was:
KN18 – rhyolite glass

Table J1: Spectrometer set-up. * indicates elements that are unstable during EPMA and thus were count times were estimated using a time dependent intensity (TDI) correction.

Spectrometer 1 TAP	Spectrometer 2 TAP	Spectrometer 3 TAPH	Spectrometer 4 PETH	Spectrometer 5 LIFL
Al (20 s) *	Si (20 s) *	Na (20 s) * Mg (20 s)	K (20 s) * Ca (10 s) Cl (100 s) Zr (10 s)	Fe (30 s) Mn (30 s) Ti (30 s)

Secondary Standard Data

KN18 (in-house Bristol) was used as a secondary standard and all EPMA data is reported with the 2σ standard deviation in KN18 as the uncertainty as the scatter in the secondary standard data is greater than the counting statistics and thus includes reproducibility in the uncertainty on the EPMA results.

Table J2: Secondary standard data collected over three analytical sessions from KN18.

	SiO_2	TiO_2	Al_2O_3	FeO	MgO	MnO	CaO	Na_2O	K_2O	Cl	ZrO_2	H_2O	TOTAL
Mean	74.51	0.18	10.37	3.58	0.02	0.06	0.13	4.67	4.49	0.32	0.25	1.48	99.97
2 σ (abs.)	1.98	0.06	0.38	0.21	0.09	0.03	0.53	1.55	0.24	0.02	0.20	1.26	0.07
2 σ (rel.)	2.66	34.92	3.71	5.84	499.62	49.40	402.24	33.22	5.32	5.13	81.53	85.04	0.07

Analytical uncertainty

Table J3: Average relative 2σ uncertainty from microprobe counting statistics.

	SiO_2	TiO_2	Al_2O_3	FeO	MgO	MnO	CaO	Na_2O	K_2O	Cl	ZrO_2	H_2O	TOTAL
Mean	74.51	0.18	10.37	3.58	0.02	0.06	0.13	4.67	4.49	0.32	0.25	1.48	99.97
2 σ (rel.)	0.26	61.53	3.05	47.06	44.48	0.03	5.03	1.76	0.75	24.17	24.50	–	–

Full EPMA results

See opposite...

Table J4: Full EPMA results for the zircon-hosted rhyolite melt inclusions.

Zircon ID	SiO_2	TiO_2	Al_2O_3	FeO	MgO	MnO	CaO	Na_2O	K_2O	Cl	ZrO_2	H_2O
						KA15_018						
KA18_z10_a	72.25	0.06	13.02	4.55	0.63	0.09	1.05	3.34	4.69	0.12	0.20	1.28
KA18_z12_a	72.58	0.12	14.29	2.34	0.36	0.04	1.47	3.74	4.65	0.12	0.30	1.94
KA18_z13_a	75.89	0.08	12.50	2.48	0.24	0.00	0.86	2.98	4.59	0.09	0.30	5.54
KA18_z14_a	75.57	0.00	12.14	3.13	0.29	0.09	0.65	2.84	4.95	0.05	0.29	1.46
KA18_z16_a	75.94	0.15	13.64	1.29	0.10	0.08	1.01	2.82	4.45	0.11	0.40	7.85
KA18_z21_a	73.01	0.00	13.73	2.61	0.51	0.00	0.99	3.33	5.00	0.12	0.71	2.79
KA18_z23_a	75.77	0.08	12.66	2.57	0.27	0.00	0.77	2.63	4.95	0.09	0.22	5.56
KA18_z31_a	72.30	0.09	13.80	3.58	0.57	0.08	1.24	3.43	4.55	0.11	0.23	2.60
KA18_z35_a	75.94	0.09	12.41	2.20	0.26	0.00	0.79	2.84	4.76	0.08	0.63	6.14
KA18_z37_a	75.95	0.08	12.36	2.03	0.26	0.07	0.70	3.04	5.21	0.09	0.20	1.70
KA18_z5_a	74.63	0.00	12.06	3.24	0.31	0.05	0.71	2.95	4.96	0.10	1.00	2.34
KA18_z8_a	77.11	0.09	9.95	2.59	0.11	0.00	0.10	1.94	7.24	0.03	0.83	1.73
KA18_z9_a	75.58	0.09	12.12	2.66	0.16	0.00	0.71	2.82	4.89	0.10	0.87	6.48
						KA15_019						
KA19_z15_a	74.04	0.08	11.94	3.73	1.14	0.08	0.67	3.20	4.68	0.08	0.35	1.56
KA19_z19_a	73.20	0.06	13.03	3.54	0.78	0.04	0.79	3.38	4.86	0.11	0.23	0.67
KA19_z19_b	71.51	0.00	12.37	6.06	0.64	0.10	0.91	2.94	4.96	0.07	0.46	0.26
KA19_z19_c	71.69	0.16	13.53	3.65	1.13	0.07	1.03	3.74	4.52	0.10	0.38	2.97
KA19_z22_a	73.33	0.09	12.95	3.64	0.52	0.04	0.96	2.92	5.13	0.11	0.30	1.21
KA19_z34_a	71.48	0.00	11.55	6.31	2.08	0.05	0.73	2.77	4.66	0.09	0.27	1.28
KA19_z9_a	69.58	0.00	14.64	5.02	0.22	0.04	1.15	3.79	5.26	0.09	0.22	0.24
						LA15_008						
LA08_z1_a	74.74	0.20	13.50	1.15	0.24	0.06	1.10	3.07	5.18	0.15	0.62	3.15
LA08_z12_a	76.26	0.22	12.68	0.95	0.11	0.00	0.82	3.07	5.52	0.17	0.21	3.43
LA08_z12_b	81.94	0.00	11.03	0.36	0.21	0.00	1.42	4.22	0.59	0.00	0.22	0.00
LA08_z2_a	74.49	0.25	13.17	1.19	0.21	0.00	1.50	3.23	5.18	0.16	0.63	5.78
LA08_z5_c	75.41	0.27	12.72	0.71	0.08	0.00	0.79	2.86	6.02	0.17	0.97	3.38
LA08_z5_e	70.91	0.00	19.84	2.41	1.79	0.00	0.22	3.60	1.20	0.04	0.00	2.17
LA08_z6_a	77.19	0.06	12.01	0.90	0.25	0.07	0.78	3.21	5.05	0.07	0.41	0.45
LA08_z8_c	75.10	0.23	14.42	1.23	0.50	0.09	2.02	3.03	2.17	0.19	1.03	8.55
LA08z1a	73.34	0.44	11.39	4.12	0.62	0.11	0.85	3.06	5.22	0.17	0.69	1.32

Table J4: Continued...

Zircon ID	SiO_2	TiO_2	Al_2O_3	FeO	MgO	MnO	CaO	Na_2O	K_2O	Cl	ZrO_2	H_2O
						LK16_016						
LK16_z1_a	82.75	0.07	9.33	0.15	0.08	0.00	0.40	2.29	4.73	0.0657	0.14	2.15
LK16_z1_b	85.22	0.12	7.22	0.21	0.06	0.00	1.18	2.08	3.46	0.0683	0.39	3.53
LK16_z10_a	77.05	0.11	12.79	0.98	0.17	0.00	1.33	6.09	1.02	0.1269	0.34	1.89
LK16_z12_a	78.54	0.14	12.37	0.66	0.14	0.08	1.33	5.12	0.92	0.1356	0.57	2.40
LK16_z12_b	78.38	0.07	12.51	0.69	0.13	0.07	1.46	5.23	0.94	0.0932	0.43	3.62
LK16_z14_b	77.73	0.13	13.16	0.53	0.15	0.06	1.37	5.50	0.98	0.1480	0.24	2.05
LK16_z15_a	79.33	0.00	12.82	0.08	0.05	0.00	1.79	5.71	0.11	0.0000	0.12	0.00
LK16_z2_b	82.71	0.00	10.81	0.07	0.04	0.04	0.94	4.31	0.81	0.0614	0.20	0.00
LK16_z20_a	75.81	0.09	13.46	0.00	0.08	0.00	1.20	3.15	5.86	0.1372	0.21	0.92
LK16_z20_a	78.52	0.08	12.01	0.07	0.00	0.00	0.82	2.61	5.64	0.1154	0.14	0.15
LK16_z20_b	82.33	0.00	11.47	0.09	0.15	0.08	0.98	4.17	0.61	0.0000	0.13	0.00
LK16_z22_a	78.46	0.12	12.45	0.66	0.20	0.07	1.72	4.96	0.90	0.0864	0.37	1.20
LK16_z22_b	77.36	0.09	12.66	0.40	0.09	0.00	1.10	3.11	4.24	0.1436	0.80	1.99
LK16_z23_b	82.67	0.00	10.86	0.00	0.05	0.00	1.54	4.42	0.28	0.0093	0.17	0.00
LK16_z24_a	77.50	0.04	13.03	0.11	0.28	0.04	1.24	5.16	2.34	0.1230	0.15	0.25
LK16_z26_a	84.43	0.00	9.25	0.17	0.11	0.04	1.03	3.87	1.04	0.0683	0.00	0.00
LK16_z26_c	78.30	0.00	13.26	0.07	0.17	0.08	1.51	4.98	1.54	0.0960	0.00	1.28
LK16_z27_a	77.01	0.13	12.75	0.73	0.14	0.05	1.04	2.88	4.75	0.1444	0.37	0.60
LK16_z29_a	77.48	0.14	12.57	0.98	0.14	0.10	1.34	5.61	1.08	0.1375	0.42	2.94
LK16_z30_a	77.40	0.12	12.54	0.90	0.12	0.08	1.23	3.15	4.15	0.1075	0.20	2.42
LK16_z33_a	76.81	0.10	12.65	0.77	0.09	0.05	1.12	2.80	4.45	0.1308	1.02	2.39
LK16_z4_a	80.34	0.00	12.54	0.22	0.18	0.06	1.03	4.59	0.64	0.1187	0.27	1.03
LK16_z7_a	78.08	0.10	11.86	0.63	0.18	0.05	0.98	6.24	0.93	0.1166	0.82	1.89
LK16z18a	77.06	0.10	12.40	1.42	0.15	0.06	1.06	2.91	4.60	0.07	0.16	0.21
LK16z23a	77.21	0.10	12.17	1.02	0.11	0.05	0.95	3.12	4.74	0.14	0.38	6.98
LK16z24a	72.68	0.15	11.61	3.48	0.27	0.10	1.64	5.42	4.16	0.01	0.48	0.00
LK16z26a	71.31	0.19	13.73	5.03	0.75	0.11	2.47	1.74	4.22	0.11	0.35	3.75
LK16z29a	75.03	0.11	12.10	3.68	0.25	0.06	1.15	2.78	4.11	0.13	0.59	2.77
LK16z32	77.45	0.16	12.45	0.99	0.14	0.04	1.05	2.92	4.40	0.13	0.28	7.16
LK16z32	77.14	0.14	12.71	0.76	0.11	0.05	1.12	3.34	4.33	0.13	0.17	5.56
LK16z41	73.51	0.23	13.38	2.70	0.24	0.04	1.11	3.74	4.88	0.03	0.12	1.45
LK16z47	78.42	0.03	11.76	0.59	0.04	0.04	1.27	3.93	3.63	0.01	0.28	0.00
LK16z54a	76.63	0.13	12.25	2.37	0.34	0.06	1.09	2.52	4.24	0.13	0.24	5.76
LK16z55a	77.74	0.11	11.85	1.38	0.12	0.05	0.97	3.20	4.20	0.12	0.27	4.72
LK16z58a	76.66	0.13	11.98	1.39	0.14	0.04	1.02	3.01	4.58	0.13	0.93	3.94
LK16z59a	77.73	0.14	12.13	1.47	0.11	0.04	1.06	2.46	4.49	0.14	0.23	4.95
LK16z5a	76.52	0.11	12.47	1.52	0.15	0.06	1.08	3.53	4.16	0.14	0.24	1.71
LK16z60a	78.69	0.16	12.02	0.86	0.14	0.06	0.99	2.59	4.13	0.11	0.22	5.34
LK16z60c	76.75	0.08	11.92	2.08	0.52	0.06	0.92	2.98	4.25	0.11	0.34	4.36

Table J5: Full EPMA results for the zircon-hosted, clay-altered melt inclusions

SiO_2	TiO_2	Al_2O_3	FeO	MgO	MnO	CaO	Na_2O	K_2O	Cl	ZrO_2
					KA15_018					
54.74	0.09	33.72	5.18	1.77	0.08	0.33	2.13	1.97	0.00	0.00
54.28	0.06	35.54	2.94	1.72	0.04	0.16	2.51	2.17	0.00	0.57
53.43	0.13	34.64	0.22	1.91	0.01	0.00	2.61	6.59	0.00	0.44
57.98	0.05	31.54	0.81	2.16	0.00	0.17	2.74	4.40	0.00	0.14
54.45	0.06	32.86	5.12	1.95	0.07	0.23	2.53	2.31	0.00	0.41
61.59	0.14	24.72	0.66	0.16	0.00	4.42	5.63	2.54	0.00	0.14
54.51	0.08	32.78	6.14	1.92	0.09	0.15	2.05	2.14	0.00	0.13
56.01	0.10	33.25	2.78	1.60	0.07	0.11	3.14	2.37	0.00	0.58
53.59	0.12	33.67	5.01	1.79	0.08	0.34	2.77	2.38	0.01	0.24
54.31	0.24	34.31	2.74	1.99	0.00	0.22	2.94	2.45	0.00	0.80
55.52	0.08	34.45	1.86	2.16	0.00	0.15	2.98	2.65	0.00	0.16
56.08	0.12	34.71	0.73	1.96	0.00	0.10	3.59	2.70	0.00	0.00
53.99	0.00	35.36	5.04	1.14	0.00	0.42	2.16	1.74	0.00	0.14
54.66	0.06	33.47	0.21	2.07	0.02	0.11	0.92	8.43	0.02	0.00
					KA15_019					
60.84	0.00	29.31	0.89	2.20	0.09	0.39	3.43	2.55	0.04	0.26
62.29	0.00	26.18	2.17	1.54	0.08	0.30	4.15	2.91	0.03	0.34
58.74	0.12	33.07	0.60	1.18	0.04	0.79	3.06	2.20	0.04	0.16
65.86	0.00	25.11	0.98	0.85	0.05	0.72	3.21	2.46	0.01	0.75
57.82	0.00	34.24	1.04	1.57	0.04	0.13	2.80	2.21	0.01	0.14
53.71	0.17	33.31	1.89	3.88	0.10	0.17	3.45	2.61	0.02	0.69
55.26	0.00	38.43	0.50	1.14	0.04	0.26	2.56	1.80	0.01	0.00
55.51	0.12	30.52	1.89	5.77	0.06	1.22	2.78	1.93	0.02	0.18
63.75	0.00	28.50	0.61	1.25	0.05	0.53	2.62	2.15	0.01	0.51
58.89	0.00	34.17	0.53	1.00	0.00	1.71	1.95	1.50	0.03	0.22
63.54	0.07	25.71	1.42	1.74	0.09	0.73	3.49	2.63	0.01	0.56
55.28	0.14	31.24	3.78	3.17	0.12	0.40	3.23	2.41	0.01	0.21
55.95	0.07	32.77	3.70	3.16	0.11	0.42	1.02	2.47	0.01	0.33
57.53	0.13	30.01	1.22	2.54	0.04	0.22	5.70	2.43	0.02	0.16
54.64	0.11	34.22	1.22	2.97	0.08	0.50	3.48	2.61	0.02	0.16
54.18	0.12	34.31	2.02	3.85	0.05	0.25	2.82	2.39	0.02	0.00
					LA15_008					
62.11	0.00	20.14	2.62	3.25	0.00	0.22	6.33	5.11	0.02	0.18
54.25	0.00	33.34	3.98	0.58	0.00	0.12	5.67	1.49	0.03	0.55
51.76	0.00	42.33	1.66	0.54	0.04	0.10	2.60	0.83	0.00	0.13

Appendix K

Zircon Trace Element Geochemistry

This appendix contains the full results of the zircon trace element geochemistry presented in Chapter 4.

Table K1: Zircon trace element LA-ICP-MS data.
Table K2: Standard reference material data.
Table K3: Average 2σ counting stats error.
Table K4: Average limit of detection (LOD) from each session.

Table K1: Full zircon trace element results. Uncertainties presented are the average 2σ internal error (relative %) on the measurements for each sample (N.B. each sample was analysed in a single analytical session). Domain characterised by CL image: R – rim; Z – intermediate zone; C – core. All results reported in ppm.

Domain	Sc	Ti	Cu	Y	Nb	Sn	La	Ce	Nd	Sm	Eu	Gd	Tb	Dy	Er	Yb	Lu	Hf	Ta	W	Pb	Th	U
Mass number	45	49	63	89	93	120	139	140	146	149	153	157	159	163	166	172	175	177	181	182	206	232	238
KA15_018																							
R	361	0	0	1026	0.0	0	0	26	0	2	0	15	0	82	163	344	67	11400	2.1	6.5	15	371	711
R	430	0	0	2090	8.8	0	0	38	5	15	3	58	0	173	289	583	117	11750	4.0	24.3	25	580	1254
Z	606	0	0	3140	23.1	0	0	55	1	3	0	39	0	238	543	1160	233	12000	6.5	21.6	33	565	1870
Z	474	0	0	2380	10.2	0	0	55	1	6	1	36	0	184	378	768	147	12600	4.9	0.0	37	960	2000
Z	451	0	0	1580	0.0	0	0	24	0	2	1	22	0	125	264	562	123	11120	1.4	0.0	16	347	837
Z	469	0	0	1650	5.0	0	0	25	0	3	1	23	0	122	273	577	117	10960	1.5	0.0	17	355	837
R	411	0	0	1570	14.7	1	0	49	2	5	1	32	0	153	330	630	124	14900	3.7	0.0	25	870	1380
Z	490	0	0	1810	5.4	0	0	31	1	3	1	28	0	140	288	607	122	10720	1.1	0.0	14	428	760
R	489	0	0	2740	0.0	0	0	42	6	12	6	75	0	269	396	793	155	9820	1.9	69.0	21	555	1030
Z	479	25	0	1430	4.8	0	0	25	0	3	0	17	0	115	241	530	109	11200	1.3	0.0	13	346	684
Z	519	0	0	2390	13.2	0	0	49	1	3	1	33	0	191	404	846	173	12370	4.8	33.0	32	793	1830
Z	497	0	0	2000	10.8	0	0	46	1	5	1	27	0	159	333	699	144	11100	3.5	0.0	21	464	1050
Z	480	18	0	1850	6.9	1	0	33	1	4	1	28	0	150	308	635	133	10280	1.5	0.0	15	395	787
C	585	0	0	3570	11.1	0	0	41	3	9	2	58	0	281	577	1126	217	10450	3.0	5.9	33	869	1770
R	522	0	0	2980	24.2	1	0	56	1	3	1	38	0	227	498	1039	204	11720	6.6	1.1	34	787	1880
R	510	0	0	2290	16.2	0	0	60	0	3	0	33	0	174	370	820	160	11400	4.3	0.0	29	664	1350
R	0	0	0	2010	16.4	1	0	40	0	2	1	26	0	149	323	660	143	10690	4.5	1.0	33	641	1570
Z	0	26	0	2200	7.0	1	0	24	0	4	1	28	0	158	338	766	160	10000	2.2	26.4	28	481	1400
R	0	0	0	1290	6.7	0	0	36	1	1	0	16	0	87	184	370	90	9200	2.2	225.0	21	506	970
C	0	0	0	3030	10.9	1	0	63	3	5	3	43	0	223	435	952	198	7480	2.6	0.0	21	628	906
R	0	0	0	2200	13.1	1	0	52	1	4	0	29	0	161	348	755	159	10850	4.8	0.0	30	656	1487
Z	0	0	0	211	0.0	0	0	0	0	0	0	5	0	21	23	44	9	12070	0.3	0.0	25	9	837
C	0	0	0	2250	0.0	0	0	1	2	5	0	36	0	194	317	605	113	10970	0.3	0.0	63	48	219
C	0	0	0	2460	0.0	0	0	1	2	6	0	46	0	221	366	671	123	10650	0.3	0.0	74	65	248
R	0	0	0	1574	7.8	1	0	41	1	2	1	23	0	114	230	499	99	9790	3.0	0.0	24	573	1085
R	0	0	0	1615	10.5	0	0	37	0	3	1	20	0	120	247	553	120	9600	3.0	0.0	19	365	843
C	518	0	0	2000	6.8	0	0	41	1	4	1	30	0	160	318	710	141	10600	1.7	0.0	16	540	970
R	0	0	0	3690	23.4	1	0	59	0	3	1	42	0	230	550	1260	220	11400	6.2	0.0	44	840	2070
R	0	0	0	1621	5.9	0	0	46	1	3	1	24	0	131	246	516	106	10290	2.8	11.1	28	804	1332
Z	0	0	0	1970	5.3	0	0	34	2	6	2	27	0	145	277	622	126	7980	1.5	4.0	18	403	718
R	0	29	0	1453	10.2	0	0	30	1	2	0	19	0	113	219	478	96	9360	3.3	0.0	27	572	1241
C	0	0	0	2950	0.0	1	0	56	7	13	4	61	0	237	398	821	156	8750	1.4	0.0	14	657	713
C	490	0	0	2200	5.6	1	0	57	2	7	2	38	0	190	363	751	154	9250	1.5	0.0	24	990	1240

Table K1: Continued...

Domain	Sc	Ti	Cu	Y	Nb	Sn	La	Ce	Nd	Sm	Eu	Gd	Tb	Dy	Er	Yb	Lu	Hf	Ta	W	Pb	Th	U
Mass number	45	49	63	89	93	120	139	140	146	149	153	157	159	163	166	172	175	177	181	182	206	232	238
KA15_018																							
R	0	0	0	2760	20.9	1	0	60	2	5	1	40	0	206	411	849	168	10660	6.2	0.0	60	1330	2810
R	0	0	0	2120	14.4	0	0	49	1	4	1	35	0	166	321	655	132	10780	4.3	99.0	47	1411	2235
R	0	0	0	1433	9.0	0	0	39	1	3	1	24	0	104	223	508	109	9960	2.4	0.0	16	364	699
R	0	0	0	947	6.0	0	0	26	1	2	0	10	0	73	145	323	71	9430	1.7	0.0	12	229	465
C	0	0	0	1530	6.8	1	0	29	0	3	1	25	0	108	240	504	107	9600	1.2	5.2	12	343	610
R	0	0	0	3520	26.7	0	0	94	2	6	1	54	0	272	517	1015	213	9730	6.3	17.2	69	2060	3300
R	0	0	0	3150	25.1	1	0	83	0	7	1	42	0	249	465	939	195	10930	6.5	13.0	63	1710	3100
Z	0	0	0	2690	9.7	0	0	45	2	7	1	43	0	204	383	842	170	9700	2.4	0.0	26	606	920
R	415	0	0	1690	12.7	0	0	40	0	2	0	24	0	139	258	554	113	11900	3.9	0.0	25	712	1340
Av. 2σ Error (rel.)			*0*	*9*	*34.8*	*104*	*60*	*12*	*114*	*80*	*39*	*53*	*17*	*11*	*10*	*10*	*10*	*9*	*19.9*	*23.2*	*12*	*11*	*9*
KA15_019																							
R	0	0	0	2050	17.9	1	0	55	1	4	1	29	0	154	315	625	127	11640	4.1	0.6	33	1060	1640
C	0	0	0	2320	7.2	1	0	66	1	6	1	38	0	168	340	700	151	9670	2.0	0.0	20	794	1035
C	0	0	0	1710	5.5	1	0	38	1	4	1	24	0	140	259	587	125	10120	2.3	0.0	18	464	794
R	0	0	0	2280	17.3	1	0	48	1	3	1	31	0	176	370	841	176	11300	4.6	0.0	29	547	1344
R	0	0	0	1903	13.5	1	0	53	2	4	1	27	0	154	291	621	129	10380	4.3	12.0	31	815	1553
C	0	0	0	1660	3.4	0	0	28	1	3	1	28	0	135	258	539	109	9930	1.3	1.2	16	396	763
R	0	0	0	1170	6.3	0	0	33	0	2	1	17	0	86	184	383	82	10740	1.9	4.7	18	420	838
R	0	0	0	3500	3.5	0	0	5	6	15	0	86	0	313	498	847	160	10210	0.7	0.1	74	146	495
C	0	0	0	4930	0.0	0	0	4	9	19	0	122	0	468	670	1120	224	10870	0.6	0.0	102	171	345
R	0	16	0	3990	33.8	3	0	83	4	7	1	58	0	314	580	1172	233	11180	9.1	1590.0	94	2290	4280
Z	0	0	0	2410	5.0	0	0	42	4	8	2	50	0	197	349	706	143	9650	1.5	0.0	18	605	873
Z	0	0	0	2420	6.3	0	0	60	2	6	1	44	0	188	342	724	152	9700	2.5	0.8	24	790	1090
R	0	0	0	1545	9.7	1	0	41	0	2	1	26	0	116	241	569	125	9890	2.8	0.0	16	326	749
R	0	0	0	1384	7.7	1	0	36	1	3	0	23	0	112	209	454	94	10650	2.8	0.4	24	674	1191
Z	0	0	0	1650	0.0	0	0	37	1	6	2	33	0	150	267	620	117	12700	1.2	0.0	12	406	660
Z	0	0	0	1994	4.3	0	0	38	2	7	2	39	0	168	293	618	127	10120	1.0	0.0	15	461	742
R	0	0	0	1470	7.9	0	0	38	0	2	1	21	0	101	240	509	102	12100	2.7	1.8	24	604	1120
Z	0	0	0	2960	6.4	1	0	40	3	7	2	46	0	243	458	895	183	9710	2.3	0.0	26	634	1260
Z	0	0	0	1820	5.1	0	0	30	1	4	1	27	0	141	270	595	123	11190	1.8	0.0	15	398	822
R	0	0	0	1541	4.5	0	0	30	1	4	1	26	0	121	238	515	106	9240	1.5	0.0	12	309	576
R	0	0	0	1982	10.9	1	0	49	1	6	1	33	0	151	298	607	129	10020	3.5	4.3	31	961	1590
Z	0	0	0	1165	0.0	0	0	18	0	2	1	15	0	93	173	393	82	8570	0.9	0.0	9	218	424
Z	0	0	0	1348	0.0	0	0	21	1	2	1	19	0	95	199	427	97	8630	0.8	0.0	10	240	476
R	0	0	0	1906	10.9	1	0	47	1	3	1	29	0	149	284	614	125	10570	4.2	0.0	38	1100	1820

Table K1: Continued...

Domain	Sc	Ti	Cu	Y	Nb	Sn	La	Ce	Nd	Sm	Eu	Gd	Tb	Dy	Er	Yb	Lu	Hf	Ta	W	Pb	Th	U
Mass number	45	49	63	89	93	120	139	140	146	149	153	157	159	163	166	172	175	177	181	182	206	232	238
KA15_019																							
Z	0	0	0	2190	12.8	1	0	60	1	5	1	35	0	174	333	706	141	9970	4.7	104.0	41	1317	2010
R	0	0	0	1714	12.0	1	0	42	0	3	1	26	0	130	258	568	115	10810	3.7	1.0	31	844	1473
R	0	0	0	2570	19.8	1	0	49	1	3	1	30	0	181	388	839	189	10310	5.7	24.0	32	669	1580
Z	0	0	0	1270	4.6	0	0	25	0	2	0	17	0	98	180	422	91	11100	1.4	2.6	11	233	552
Z	0	0	0	2100	5.0	1	0	47	1	5	1	31	0	170	329	656	137	9460	2.2	4.9	26	880	1220
R	0	26	0	2270	15.2	1	0	47	1	3	0	26	0	176	370	840	173	12000	5.6	380.0	26	590	1480
R	0	0	0	1600	8.1	0	0	39	1	4	1	23	0	125	246	563	119	10700	2.9	610.0	25	563	1169
R	0	0	0	1617	10.3	1	0	41	1	3	1	21	0	125	249	552	115	11150	3.0	68.0	20	494	1005
C	0	0	0	1960	4.0	0	0	34	2	5	2	33	0	142	291	660	125	8940	1.4	0.0	14	412	704
C	0	20	0	1588	3.3	0	0	23	2	5	2	29	0	134	244	518	104	8780	0.9	0.0	11	308	539
C	0	0	0	3040	6.1	0	0	49	4	7	2	46	0	246	458	938	197	8100	2.0	117.0	45	1013	1680
C	0	12	0	1930	8.1	0	0	52	2	4	1	31	0	146	269	585	114	10000	2.5	0.0	26	1020	1230
R	0	0	0	2460	18.2	1	0	57	1	5	1	38	0	196	375	753	153	10780	5.7	18.2	59	1500	2460
R	0	0	0	1550	5.2	0	0	22	0	2	0	20	0	116	242	567	123	11100	1.8	12.3	18	326	845
R	0	0	0	2870	23.9	1	0	79	4	8	2	50	0	246	406	854	164	9900	5.0	800.0	42	1560	2000
R	0	0	0	1990	15.0	1	0	49	1	3	1	29	0	156	300	670	132	11900	4.2	340.0	29	789	1480
Z	0	0	0	1920	5.0	0	0	33	1	4	1	31	0	138	298	627	136	9520	0.9	0.0	14	371	728
Z	0	0	0	1930	6.2	0	0	31	1	3	1	32	0	152	286	646	138	9710	1.3	0.0	15	434	793
R	0	0	0	1030	6.8	0	0	26	1	2	1	14	0	82	155	353	70	10600	2.0	0.0	15	319	720
R	0	0	0	1710	11.8	1	0	37	1	2	0	24	0	135	250	559	113	11800	4.2	1090.0	33	769	1660
C	0	0	0	1780	3.0	0	0	27	1	3	1	30	0	147	285	628	126	10510	1.5	0.4	20	372	914
R	0	0	0	1475	8.3	0	0	40	1	3	0	23	0	123	237	502	103	11530	3.2	0.0	24	590	1096
C	0	0	0	4040	13.6	1	0	39	2	10	2	61	0	318	618	1254	255	10660	3.6	10.2	49	945	2260
R	0	0	0	1580	7.6	0	0	57	1	5	1	31	0	143	259	603	106	11100	3.1	0.0	24	811	1160
R	0	0	0	1960	12.8	0	0	46	0	7	1	24	0	153	265	660	119	12900	4.4	1040.0	37	800	1660
Av. 2σ Error (rel.)			*0*	*8*	*34.8*	*58*	*103*	*10*	*90*	*53*	*32*	*36*	*15*	*11*	*10*	*10*	*9*	*8*	*18.4*	*42.3*	*11*	*10*	*9*
LA15_008																							
R	0	6	0	1680	2.4	0	0	14	4	7	2	35	12	147	243	743	105	8950	1.1	0.9	10	371	549
R	0	9	0	1423	3.1	0	0	20	2	5	1	26	9	117	212	638	93	9270	1.3	0.0	15	622	741
R	0	4	0	1550	9.7	1	0	38	1	4	1	27	10	134	234	800	86	10300	5.6	0.1	28	740	1420
R	0	6	0	2120	8.2	1	0	45	2	6	2	39	14	186	317	964	123	10220	3.0	0.0	21	557	985
C	0	14	0	2180	3.7	0	0	23	4	9	2	47	16	194	311	776	106	9150	1.7	0.0	14	689	680
C	0	8	0	1247	5.8	0	0	36	2	4	1	24	9	117	197	529	74	9790	2.4	0.1	15	542	712
R	0	6	0	1890	14.6	1	0	34	1	5	1	27	11	153	301	900	116	11410	6.6	0.4	27	610	1440

Table K1: Continued...

Domain	Sc	Ti	Cu	Y	Nb	Sn	La	Ce	Nd	Sm	Eu	Gd	Tb	Dy	Er	Yb	Lu	Hf	Ta	W	Pb	Th	U
Mass number	45	49	63	89	93	120	139	140	146	149	153	157	159	163	166	172	175	177	181	182	206	232	238
LA15_008																							
R	0	11	0	1800	6.1	0	0	21	2	4	1	29	11	142	274	772	107	9630	2.4	1.3	12	297	562
R	0	10	0	1142	1.5	0	0	10	2	5	1	28	9	115	174	441	57	8530	0.6	0.7	5	157	224
R	0	9	0	1480	2.1	0	0	14	3	7	2	37	12	145	216	535	71	8670	0.8	0.0	7	279	316
C	0	8	0	3640	3.9	0	0	30	9	19	4	90	29	342	502	1192	158	9090	1.8	0.2	16	751	802
R	0	13	0	1441	3.8	0	0	16	2	4	1	23	9	121	216	608	86	8900	1.6	0.4	9	283	457
C	0	9	0	1612	5.3	0	0	20	1	4	1	24	9	125	251	773	110	9360	2.2	0.0	13	364	659
C	0	8	1	1072	3.3	0	0	18	2	3	1	19	7	90	168	491	65	9840	1.6	7.3	12	406	578
R	0	20	0	2530	6.2	1	0	33	4	9	2	48	17	219	366	985	135	10320	2.8	8.2	16	665	848
R	0	6	0	1833	8.4	0	0	32	2	5	1	31	12	151	277	803	107	10040	3.6	0.0	18	534	868
R	0	10	0	2160	6.4	0	0	49	2	6	3	40	15	178	326	1070	158	8480	2.7	0.0	25	1170	1370
R	0	4	0	948	1.7	0	0	15	1	3	1	18	6	81	148	481	74	9660	1.1	0.0	10	311	467
R	0	13	0	1850	2.7	0	0	13	4	8	2	41	14	169	282	699	92	8330	1.1	0.0	7	287	381
R	0	10	0	1473	1.9	0	0	11	3	6	1	34	11	139	217	533	73	9490	0.9	0.0	5	202	269
Av. 2σ Error (rel.)			*242*	*7*	*7.9*	*32*	*60*	*8*	*28*	*15*	*12*	*12*	*10*	*8*	*7*	*8*	*7*	*7*	*10.9*	*59.3*	*10*	*8*	*8*
LK16_016																							
C	0	6	0	1106	3.9	0	0	23	1	3	1	18	0	87	172	609	91	9490	1.8	0.4	16	336	539
R	0	7	1	1045	3.4	0	0	21	1	3	1	17	6	81	155	483	72	8620	1.5	0.0	13	516	669
R	0	4	0	713	3.2	0	0	16	1	1	0	9	0	49	117	438	69	10080	1.5	0.0	7	156	334
R	0	4	0	1280	4.6	0	0	29	1	3	1	17	7	94	206	734	114	10460	2.3	0.0	17	418	827
R	0	5	0	781	3.0	0	0	17	1	2	1	11	0	57	121	419	66	11020	1.5	3.6	7	180	350
R	0	5	1	678	2.8	0	0	17	1	2	1	10	4	50	103	375	56	10060	1.5	0.0	9	272	470
C	0	4	3	1090	3.1	0	0	19	2	3	2	18	0	84	162	522	84	9440	1.6	2.1	12	397	643
R	0	4	0	905	3.9	0	0	20	1	2	1	11	5	66	141	547	82	10480	1.8	0.0	9	222	483
C	0	6	0	1210	3.8	0	0	20	1	3	1	19	0	93	179	589	95	9490	1.8	3.1	14	429	689
C	0	4	0	1430	4.9	0	0	33	2	6	2	26	10	120	232	830	123	10400	2.1	17.0	14	520	730
R	0	3	0	722	1.6	0	0	13	1	2	1	13	0	58	108	358	55	10760	0.9	0.0	6	182	301
R	0	4	0	805	3.3	0	0	22	1	2	1	12	5	67	123	409	60	10610	1.7	0.0	11	346	564
R	0	5	0	930	3.8	0	0	18	1	2	1	14	0	72	140	474	72	9120	1.6	0.0	9	309	461
R	0	5	0	616	1.6	0	0	9	1	1	1	8	0	45	97	335	55	8890	0.7	0.0	3	101	189
R	0	5	0	969	2.4	0	0	14	1	3	1	14	0	70	152	557	85	8450	0.9	0.0	6	197	306
R	0	8	0	3420	6.2	0	0	60	9	16	6	71	0	269	479	1470	222	9070	2.7	0.1	26	1490	1450
R	0	5	0	547	2.6	0	0	18	1	2	1	8	0	43	89	322	47	9970	1.4	0.0	9	289	483
R	0	6	1	830	2.4	0	0	10	1	2	1	14	5	68	126	419	64	9910	1.4	0.0	30	143	382
C	0	7	0	1630	9.0	0	0	64	3	6	2	31	0	130	240	836	115	9050	3.3	0.1	23	1450	1260

Table K1: Continued...

Domain	Sc	Ti	Cu	Y	Nb	Sn	La	Ce	Nd	Sm	Eu	Gd	Tb	Dy	Er	Yb	Lu	Hf	Ta	W	Pb	Th	U
Mass number	45	49	63	89	93	120	139	140	146	149	153	157	159	163	166	172	175	177	181	182	206	232	238
LK16_016																							
R	0	4	0	673	2.5	0	0	18	1	2	1	11	0	55	104	347	52	9520	1.4	0.0	10	328	518
C	0	8	0	2730	9.2	0	0	94	8	14	5	65	0	237	388	1097	162	9280	3.4	0.0	32	3060	1782
R	0	4	0	875	4.0	0	0	26	1	2	1	12	0	70	149	531	82	11470	2.2	0.2	12	321	599
R	0	4	0	677	3.1	0	0	21	1	2	1	11	0	57	115	405	61	10860	1.6	0.0	11	367	592
Z	0	6	0	1085	5.7	0	0	36	1	3	1	19	0	89	166	572	83	10750	2.5	0.0	20	895	936
Z	0	5	0	1182	3.0	0	0	19	2	4	1	18	0	95	181	645	93	11680	1.6	0.6	11	322	592
R	0	5	0	1190	2.6	0	0	22	3	6	2	24	0	102	179	542	86	9720	1.0	0.0	7	402	396
R	0	3	0	568	2.9	0	0	21	1	1	0	9	0	46	92	324	49	10410	1.6	0.0	11	383	585
R	0	4	0	1023	3.9	0	0	24	1	2	1	14	5	73	158	595	84	9810	1.8	0.0	10	284	516
R	0	3	0	411	1.9	0	0	11	0	1	0	5	0	30	70	254	40	12200	1.1	0.5	4	94	239
R	0	5	0	1190	6.0	0	0	34	1	2	1	16	0	89	188	642	98	10580	2.7	0.0	13	427	677
Z	0	5	0	1350	3.1	0	0	25	2	5	2	24	0	105	194	637	97	11100	1.6	0.0	11	408	562
C	0	5	0	1305	6.6	0	0	35	1	3	1	19	0	96	194	640	96	10880	3.9	6.0	19	734	956
R	0	4	0	696	3.0	0	0	18	1	2	1	11	0	53	105	371	58	9660	1.5	0.0	10	328	509
R	0	5	0	917	4.1	0	0	24	1	2	1	13	5	66	153	547	86	10490	2.0	5.2	11	311	559
Z	0	5	0	666	2.1	0	0	12	1	1	1	10	4	53	107	374	57	10170	0.9	0.0	5	130	252
R	0	4	0	574	2.6	0	0	19	1	1	0	8	0	43	87	299	49	11350	1.3	0.2	8	245	448
Z	0	6	0	938	3.0	0	0	15	1	3	1	16	6	79	146	467	69	8900	1.1	0.0	5	169	263
R	0	4	0	622	2.7	0	0	19	1	2	0	9	0	45	97	336	52	11540	1.6	0.5	9	287	476
R	0	7	0	3750	8.7	0	0	76	4	9	4	56	21	275	547	1748	245	8130	2.9	42.3	30	1259	1489
Z	0	5	0	893	1.9	0	0	14	2	3	1	18	0	69	132	407	63	10600	0.8	0.0	6	213	330
R	0	4	0	883	4.4	0	0	22	1	2	1	12	4	66	149	552	81	10500	2.2	0.0	9	211	465
Av. 2σ Error (rel.)			*310*	*7*	*8.9*	*30*	*59*	*8*	*32*	*18*	*15*	*13*	*11*	*8*	*8*	*8*	*7*	*7*	*10.4*	*60.0*	*10*	*9*	*8*

Table K2: Primary and secondary reference material data; all data reported in ppm.

	Sc	Ti	Cu	Y	Nb	Sn	La	Ce	Nd	Sm	Eu	Gd	Tb	Dy	Er	Yb	Lu
NIST610																	
								April Session									
Mean (ppm)	452.31	440.77		457.44	438.23	410.33	451.86	451.40	432.51	452.98	458.30	446.86		432.26	438.65	447.49	438.14
2 sigma (abs)	46.69	55.14		33.69	57.19	44.44	35.66	32.22	33.01	33.97	34.46	29.96		34.83	41.09	36.87	28.70
2 sigma (rel)	10.32	12.51		7.36	13.05	10.83	7.89	7.14	7.63	7.50	7.52	6.71		8.06	9.37	8.24	6.55
								July Session									
Mean (ppm)		435.06	431.59	450.65	418.86	394.82	456.94	447.71	429.24	450.53	458.53	442.76	442.22	425.47	424.29	445.00	435.12
2 sigma (abs)		16.01	20.13	11.47	13.52	14.39	13.55	14.07	15.90	14.80	17.34	13.67	14.38	16.76	18.57	21.47	14.88
2 sigma (rel)		3.68	4.66	2.54	3.23	3.64	2.97	3.14	3.70	3.29	3.78	3.09	3.25	3.94	4.38	4.82	3.42
NIST612																	
								April Session									
Mean (ppm)	43.96	42.63		41.21	38.61	38.31	38.27	39.84	36.64	38.19	38.18	39.81		37.13	39.40	40.24	38.12
2 sigma (abs)	23.83	55.46		29.02	22.27	24.41	20.84	20.32	25.97	19.12	26.76	24.19		25.59	28.01	19.86	20.55
2 sigma (rel)	54.21	130.10		70.43	57.68	63.72	54.45	51.00	70.88	50.07	70.09	60.75		68.90	71.09	49.36	53.92
								July Session									
Mean (ppm)		37.97	46.25	35.53	34.27	34.74	36.37	37.24	35.17	36.40	35.57	36.08	35.46	33.23	33.81	35.96	34.49
2 sigma (abs)		2.74	2.93	1.65	2.14	2.00	1.38	1.36	1.67	2.20	1.91	2.37	1.56	1.92	2.20	2.25	1.82
2 sigma (rel)		7.22	6.34	4.65	6.25	5.76	3.80	3.65	4.74	6.05	5.36	6.56	4.40	5.77	6.50	6.26	5.27
91500																	
								April Session									
Mean (ppm)	352.50	4.28		56.73	1.22	0.10	0.00	1.89	0.00	0.01	0.02	0.44		4.04	10.10	26.77	5.12
2 sigma (abs)	323.91	20.69		66.38	2.86	0.28	0.00	2.01	0.01	0.08	0.08	1.72		5.16	12.56	26.76	6.00
2 sigma (rel)	91.89	483.33		117.00	235.09	266.36	1311.66	106.44	1311.49	667.54	410.65	390.20		127.61	124.39	99.97	117.22
								July Session									
Mean (ppm)		5.27	0.03	152.39	1.36	0.07	0.00	2.48	0.24	0.53	0.29	2.74	1.01	13.10	27.02	96.75	12.76
2 sigma (abs)		0.80	0.12	10.04	0.19	0.05	0.00	0.23	0.08	0.15	0.06	0.69	0.08	1.36	2.16	7.56	1.10
2 sigma (rel)		15.20	400.13	6.59	14.17	72.22	351.84	9.26	31.90	27.54	19.54	25.15	7.66	10.36	8.01	7.81	8.59
GJ1																	
								April Session									
Mean (ppm)	327.75	4.63		240.86	1.60	0.07	0.00	15.84	0.31	1.12	0.85	6.44		18.62	26.88	56.74	11.71
2 sigma (abs)	131.65	20.80		134.59	3.60	0.37	0.00	4.29	0.45	1.04	0.57	3.66		11.69	13.98	21.46	4.89
2 sigma (rel)	40.17	449.10		55.88	224.19	495.13	-405.29	27.06	146.35	92.83	67.06	56.76		62.78	52.02	37.82	41.72
								July Session									
Mean (ppm)		3.87	0.01	256.11	2.20	0.06	0.00	15.49	0.76	1.81	1.20	7.88	2.22	23.18	30.82	84.61	11.58
2 sigma (abs)		0.48	0.14	16.77	0.22	0.06	0.01	1.05	0.10	0.32	0.14	0.98	0.18	1.68	2.57	6.59	0.60
2 sigma (rel)		12.33	1321.19	6.55	9.92	103.19	286.41	6.75	13.35	17.79	11.37	12.40	8.00	7.26	8.35	7.78	5.21

Table K2: continued...

Hf	Ta	W	Pb	Th	U
NIST610					
		April Session			
434.58	450.53	446.51	427.40	458.86	463.33
27.23	27.18	28.96	26.04	24.72	25.64
6.27	6.03	6.49	6.09	5.39	5.53
		July Session			
434.53	452.18	444.47	426.29	456.35	461.94
44.56	21.66	23.07	21.41	13.75	20.54
10.25	4.79	5.19	5.02	3.01	4.45
NIST612					
		April Session			
38.53	39.73	39.04	40.40	39.95	39.21
15.30	26.98	23.77	26.17	25.19	19.73
39.69	67.92	60.90	64.78	63.06	50.33
		July Session			
32.94	36.55	37.85	38.28	36.48	36.55
14.12	2.04	3.65	3.46	2.15	2.20
42.88	5.57	9.63	9.03	5.90	6.02
91500					
		April Session			
-1543.95	0.52	0.00	42.56	16.32	58.69
125837.60	0.31	0.04	29.65	13.05	49.59
-8150.35	60.30	1311.52	69.65	80.00	84.49
		July Session			
5657.06	0.64	0.01	56.19	28.70	79.86
516.32	0.08	0.02	6.41	2.50	5.62
9.13	13.15	191.24	11.41	8.69	7.03
GJ1					
		April Session			
6767.75	0.35	0.00	112.06	10.21	277.98
3238.33	0.20	0.04	50.95	2.73	102.65
47.85	56.26	1026.91	45.47	26.71	36.93
		July Session			
6721.18	0.53	0.02	109.96	11.12	291.00
531.74	0.07	0.03	14.82	0.70	27.08
7.91	12.59	185.88	13.48	6.25	9.31

Table K3: Average relative 2σ error from the ICP-MS counting stats.

	Sc	Ti	Cu	Y	Nb	Sn	La	Ce	Nd	Sm	Eu	Gd	Tb	Dy	Er	Yb	Lu	Hf	Ta	W	Pb	Th	U
KA15_018	6.61	151.51	0.00	8.84	34.78	104.26	60.02	11.65	114.33	79.82	39.12	52.92	16.99	10.56	10.06	9.66	9.51	8.59	19.93	23.23	11.58	10.81	9.32
KA15_019		643.35	0.00	8.33	34.84	58.08	103.09	10.32	90.29	52.68	31.97	36.01	14.70	10.69	9.89	9.60	9.35	8.40	18.39	42.34	11.43	10.49	9.27
LA15_008		17.06	242.22	6.65	7.87	32.04	60.15	7.57	28.05	15.49	12.36	11.97	9.55	7.57	7.02	8.31	7.43	6.68	10.91	59.32	10.27	8.02	8.33
LK16_016		16.81	309.92	7.10	8.93	29.72	59.20	8.12	31.90	17.93	15.05	13.36	10.71	7.77	7.60	7.75	7.16	7.07	10.40	60.00	9.91	8.63	8.03

Table K4: Average limit of detection (LOD) from the ICP-MS counting stats.

	Sc	Ti	Cu	Y	Nb	Sn	La	Ce	Nd	Sm	Eu	Gd	Tb	Dy	Er	Yb	Lu	Hf	Ta	W	Pb	Th	U
April Session																							
Average	2.48	17.34		4.05	3.56	0.50	0.05	0.02	0.08	0.14	0.03	0.22		0.06	0.05	0.03	0.06	0.39	0.08	0.11	0.23	0.01	0.01
2 σ (abs)	1.97	14.81		3.56	3.14	0.44	0.14	0.08	0.38	0.72	0.13	0.67		0.29	0.20	0.20	0.12	4.04	0.15	0.44	0.29	0.05	0.03
July Session																							
Average		0.91	0.21	0.31	0.19	0.10	0.01	0.01	0.03	0.04	0.06	0.74	0.01	0.02	0.02	0.01	0.01	0.00	0.01	0.02	0.04	0.00	0.00
2 σ (abs)		0.52	0.11	0.17	0.10	0.05	0.01	0.01	0.05	0.06	0.09	1.11	0.01	0.04	0.03	0.03	0.01	0.00	0.01	0.03	0.04	0.00	0.00

Appendix L

Short-wave Infrared Spectroscopy of the Highly Altered Samples from Kassiteres

This appendix contains the short-wave infrared (SWIR) spectroscopy data from the highly altered samples from Kassiteres presented in Chapter 5. Analyses of powdered samples were made using a portable infra-red mineral analyser (PIMA) machine at the British Geological Survey (BGS, Keyworth) and data is recorded below for every 100 nm.

Table L1: SWIR spectra from the Kassiteres system.

Table L1: Short-wave infra-red (SWIR) absorption spectra of the highly altered samples from the Kassiteres system

Sample Number	KA15_001	KA15_003	KA15_005	KA15_006	KA15_007	KA15_010	KA15_012	KA15_014	KA15_015	KA15_018	KA15_019
Host Lithology	Volcaniclastic Deposit	Volcaniclastic Deposit	Volcaniclastic Deposit	Volcaniclastic Deposit	Diorite	Volcaniclastic Deposit	Diorite	Diorite	Volcaniclastic Deposit	Quartz-Feldspar Porphyry	Quartz-Feldspar Porphyry
Wavelength_(nm)	*Absorption (1.0 - 0.0)*										
1300	0.9148	0.6018	0.7304	0.8038	0.6315	0.6712	0.6179	0.61	0.6085	0.7287	0.679
1350	0.8783	0.5787	0.7151	0.7228	0.5834	0.6689	0.55	0.5396	0.5842	0.72	0.672
1400	0.7233	0.4911	0.6226	0.4933	0.4371	0.6402	0.3663	0.3374	0.4177	0.6555	0.6196
1450	0.7462	0.4993	0.6539	0.4766	0.5829	0.6558	0.478	0.479	0.4414	0.7016	0.6459
1500	0.7781	0.5179	0.6906	0.5236	0.6009	0.6711	0.5127	0.5159	0.4859	0.7086	0.6633
1550	0.8099	0.5302	0.7158	0.5766	0.6129	0.683	0.5475	0.5542	0.5221	0.7117	0.6765
1600	0.8265	0.5341	0.7289	0.6053	0.6176	0.6898	0.5667	0.5744	0.5409	0.7121	0.6832
1650	0.8296	0.5314	0.7327	0.6113	0.613	0.6932	0.5721	0.5771	0.5479	0.7101	0.6852
1700	0.8249	0.5267	0.7314	0.6018	0.6077	0.694	0.5695	0.5689	0.5462	0.7083	0.6844
1750	0.8067	0.5149	0.7203	0.5706	0.5934	0.6901	0.551	0.5443	0.5267	0.7036	0.6786
1800	0.784	0.5019	0.7047	0.5407	0.5703	0.6855	0.5211	0.5082	0.5019	0.6978	0.6724
1850	0.7659	0.4911	0.694	0.5133	0.5662	0.6791	0.5105	0.4948	0.4766	0.6899	0.6649
1900	0.5204	0.3492	0.5373	0.2621	0.4671	0.5954	0.3233	0.3196	0.2366	0.6299	0.5692
1950	0.5219	0.3409	0.5306	0.2555	0.437	0.5996	0.3032	0.2902	0.2437	0.6383	0.568
2000	0.5787	0.3741	0.5728	0.3	0.4607	0.6247	0.3427	0.3256	0.2821	0.6511	0.5963
2050	0.6227	0.4058	0.6086	0.3507	0.4801	0.6428	0.3729	0.3565	0.3382	0.6584	0.6179
2100	0.6412	0.4175	0.6185	0.38	0.4574	0.6476	0.3718	0.3485	0.3577	0.6512	0.6229
2150	0.6111	0.4001	0.5828	0.3807	0.3527	0.6417	0.2885	0.2591	0.356	0.6353	0.6106
2200	0.5193	0.3409	0.4959	0.3237	0.3051	0.585	0.2434	0.2155	0.2695	0.5273	0.541
2250	0.5833	0.3856	0.5603	0.367	0.3842	0.6134	0.312	0.2858	0.3214	0.5974	0.5828
2300	0.5509	0.3655	0.547	0.3456	0.3446	0.616	0.2775	0.2482	0.2947	0.595	0.5828
2350	0.5091	0.336	0.5149	0.3079	0.3125	0.5935	0.2569	0.246	0.2675	0.5558	0.5489
2400	0.4812	0.3222	0.487	0.2763	0.2996	0.5743	0.2435	0.236	0.2427	0.55	0.5407
2450	0.4316	0.2954	0.4476	0.2412	0.2638	0.5423	0.2139	0.2087	0.2165	0.5173	0.5054
2500	0.4005	0.2781	0.4168	0.2214	0.2477	0.5206	0.2006	0.2007	0.2096	0.516	0.4911

Appendix M

Estimating the Exhumation Rate of the Kassiteres System

This appendix contains details of the Monte Carlo simulation of the exhumation rate of the Kassiteres system.

Figure M1: Histograms of the randomly generated time and space arrays.
Figure M2: Calibration of the Al-in-hornblende geobarometer.
Figure M3: Histogram of the Monte Carlo simulation results.

Monte Carlo Error Propagation Protocol

In Chapter 5, the exhumation rate of the Kassiteres system is calculated using the depth of emplacement of the Kassiteres host pluton and the time window between crystallisation of the pluton and mineralisation. This provides a minimum estimate of the exhumation rate using a maximum time window. A Monte Carlo error propogation protocol was used with 10^6 simulations in order to account for uncertainties in the exhumation time window and the depth of emplacement.

A normal distribution was assigned to each variable and can be described by μ, the mean value of the distribution, and σ, the standard deviation of the distribution. A random array of 10^6 values was generated for each variable. The time window between crystallisation of the host pluton and near-surface mineralisation is described by $\mu = 0.9$ Ma and $\sigma = 0.2$ Ma and the random array is shown in the histogram in Figure *M1* A. The depth of emplacement is more complex. The pressure of final crystallisation, or emplacement depth, was calculated using the calibration of Mutch et al. (2016) and is limited by amphibole instability below 0.5 kbar or 1.9 km, see Figure *M2*. As a result, a truncated normal distribution was used to generate the random array where values were limited to above 1.9 km. The truncated normal distribution of the depth of emplacement can be described by $\mu = 4.4$ km and $\sigma = 1.9$ km within the limits of $1.9 <$ depth (km) $<$ inf; the random array is shown in the histogram in Figure *M1* B.

The results of the Monte Carlo simulation are shown in Figure *M3*. The results are fitted to a log-normal distribution and the estimated mean exhumation rate of the Kassiteres system is 5.2 ± 3.0 km/Myr.

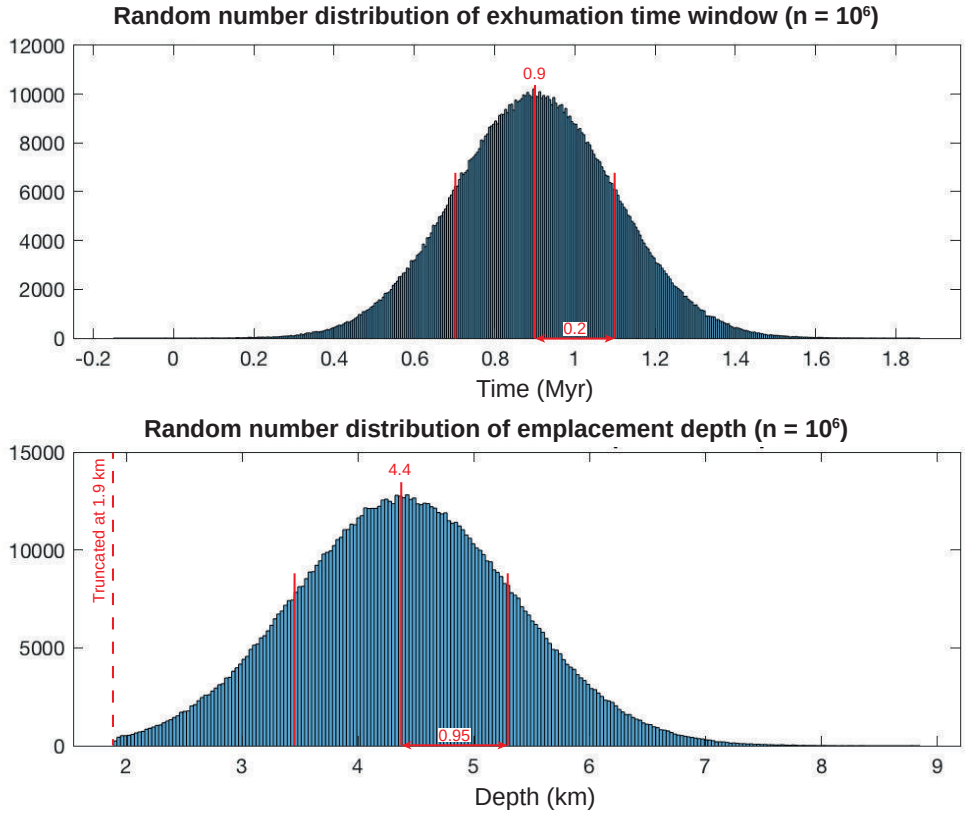

Figure M1: Histograms of the normally distributed random arrays of *A*: the exhumation time window, and *B*: the emplacement depth used in the Monte Carlo Error Propagation.

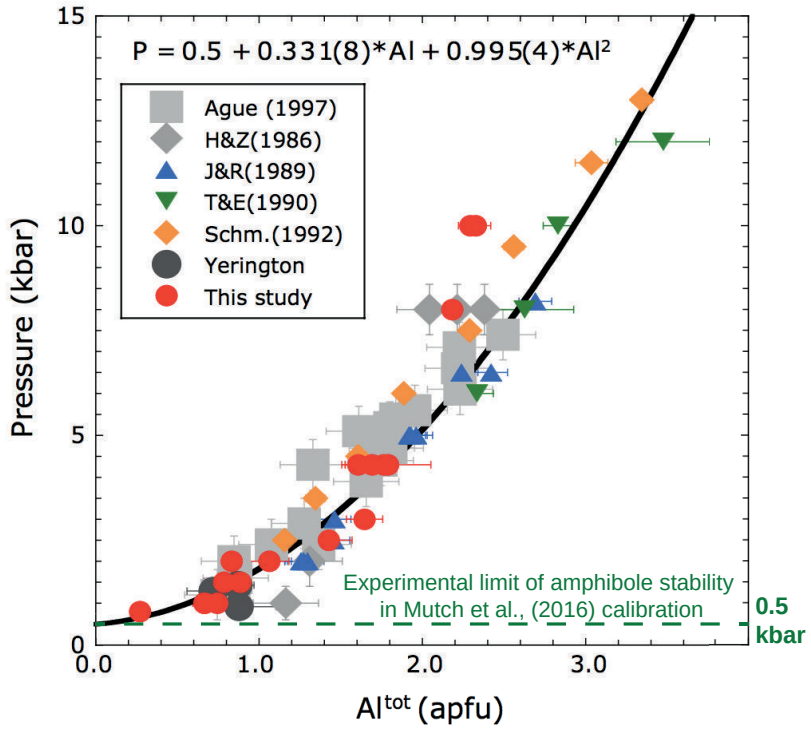

Figure M2: The calibration of the Al-in-hornblende geobarometer is limited by amphibole instability below 0.5 kbar (1.9 km); Figure 11 from Mutch et al. (2016). As a result the normal distribution was truncated at 1.9 km in the emplacement depth random number array (Figure *M1* B).

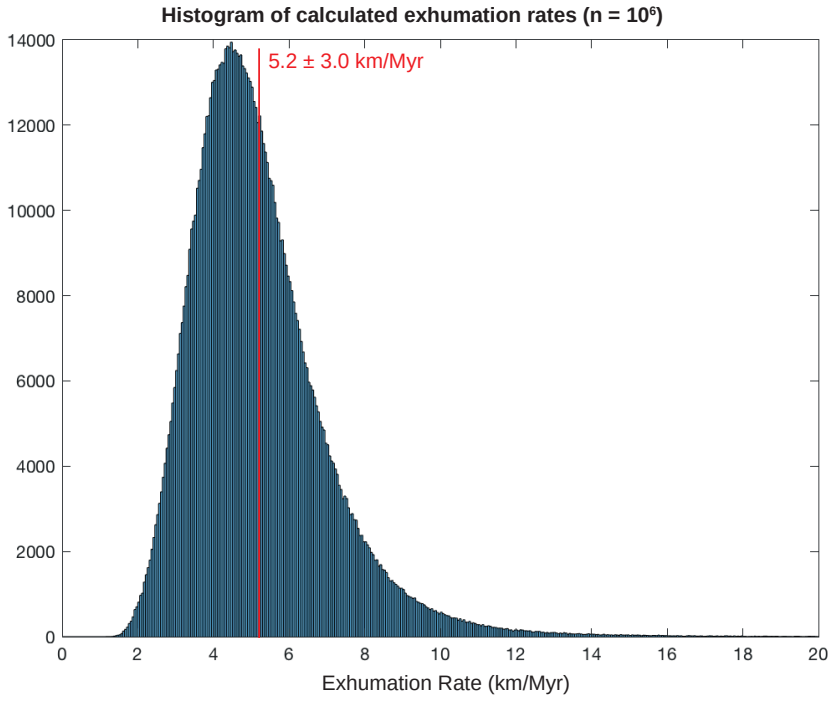

Figure M3: A histogram of the Monte Carlo simulation of the exhumation rate. The data are fitted to a log-normal distribution with $\mu = 1.59$ and $\sigma = 0.33$ and a mean value of the exhumation rate of 5.2 ± 3.0 km/Myr is calculated.

MATLAB code used for Monte Carlo Error Propagation

```
%time window
T = makedist('Normal', 0.9, 0.2);
t = random(T, 1, 10^6);

%depth of emplacement
Z = makedist('Normal',4.4,0.95);
ZT = truncate(Z, 1.9, inf);
z = random(ZT, 1, 10^6);

%calculate random exhumation rate
for i = 1:10^6
    E(i) = z(i)/t(i);
end

figure
subplot(2,1,1)
histogram(t)
title('Random number distribution of exhumation time window')

subplot(2,1,2)
histogram(z)
title('Random number distribution of emplacement depth')

E = E';
[mu, sigma] = lognfit(E);
[m, v] = lognstat(mu(1), mu(2))

figure
histogram(E)
xlim([0 20])
```

Appendix N

Field Observations from Kassiteres

This appendix contains a summary of the key field observations from the Kassiteres system made over the three field seasons conducted.

Insert N1: Full geological map of Kassiteres with cross-section and schematic diagrams.
Insert N2: Field outcrop map of Kassiteres indicating observed localities of outcrops.
Insert N3: Google Earth map of Kassiteres identifying the aerial extent of the intrusion and the lack of outcropping rock.

Figures N1–5: Annotated field photographs of key relationships observed.

Field Photographs

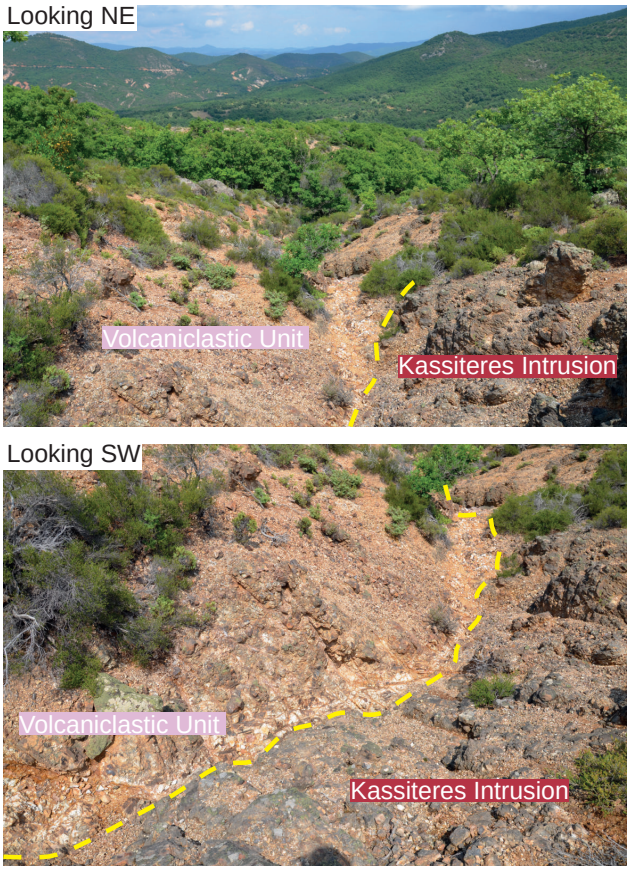

Figure N1: Field photo locality 1, the erosive contact between the Kassiteres intrusion and the overlying volcaniclastic unit.

Figure N2: Field photo locality 2, the erosive contact between the Kassiteres intrusion, outcropping predominantly in the track and the overlying volcaniclastic unit in the gully.

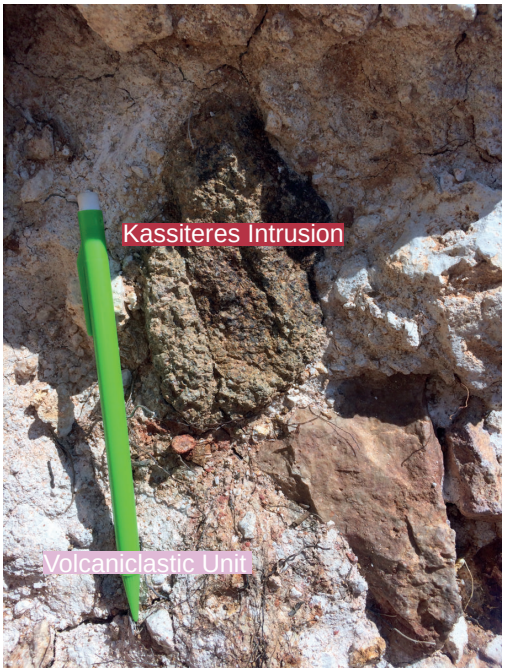

Figure N3: Field photo locality 2, a clast of the Kassiteres intrusion in the volcaniclastic unit.

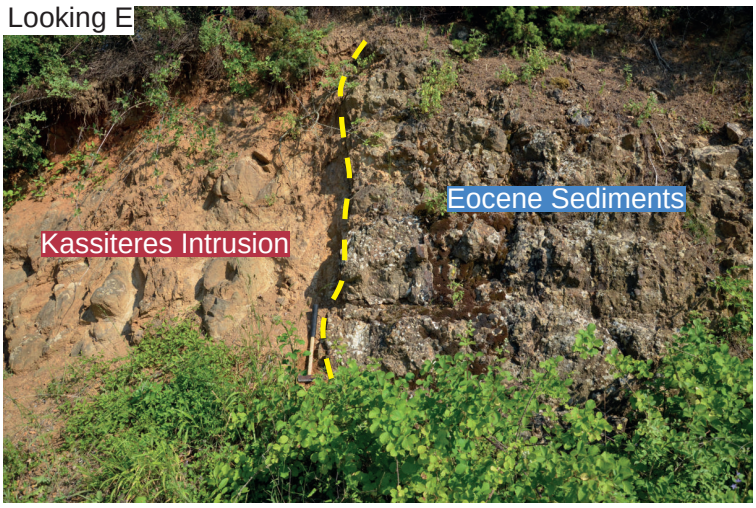

Figure N4: Field photo locality 3, vertical contact between the Kassiteres host intrusion and the Eocene sedimentary sequence.

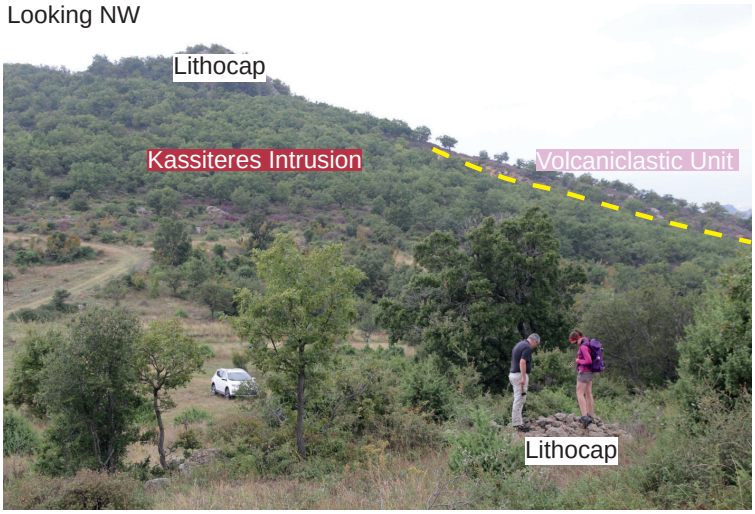

Figure N5: Field photo locality 4, showing the dense vegetation cover over the area, looking W towards a lithocap which forms a topographic high.

Appendix O

Exhumation of the Maronia Magmatic Corridor

This appendix contains the (U-Th)/He thermochronology data collected from along the Maronia Magmatic Corridor with preliminary interpretation of cooling rates. A short discussion of the future direction of thermal modelling needed to consider the cooling ages in terms of exhumation through the crust is also included.

Table O1: (U-Th)/He thermochronology results.

Figure O1: (U-Th)/He thermochronology results and geological map.

Thermochronometers record cooling of a system through time. (U-Th)/He thermochronology uses the radioactive decay of ^{238}U, ^{235}U, and ^{232}Th and the daughter ^{4}He nuclei (alpha particles) produced, to date cooling of minerals through the He-closure temperature, the temperature below which the ^{4}He nuclei can no longer diffuse out of the crystal. (U-Th)/He thermochronology is only valid for systems than have experienced monotonic cooling from high to low temperatures. Rather than considering absolute values of closure temperature, a partial retention zone, a transitional range of temperatures above which ^{4}He can readily diffuse out of the mineral and below which ^{4}He is retained, is defined (e.g. Harrison and Zeitler 2005). The partial retention zone is a function of the T-dependence of He diffusion rates, first noted by Dodson (1973), and can be described by Dodson's equation where the closure temperatre is a function of cooling rate, grain size and the diffusivity of He through the host crystal lattice. As the absolute range of the partial retention zone is a function of the cooling rate, systems that cool quickly will have a smaller partial retention zone than slowly cooled systems. For simplification, a range of effective closure temperatures can be defined for each mineral system (e.g. Ehlers et al. 2005).

The closure temperature and partial retention zone of a system can be translated into depth with knowledge of the geothermal gradient (e.g. Ehlers et al. 2005). The geothermal gradient of a system is a function of heat flux into and out of the crust and is thus dependent upon exhumation rate of a system (e.g. Carslaw and Jaeger 1959; Braun 2005; Ehlers 2005); in rapidly exhuming terranes, heat is advected towards the surface generating elevated geothermal gradients. Magmatism, a source of external heat in the crust, also affects the geothermal gradient driving advection of heat from the mantle to the surface and generating elevated geothermal gradients (e.g. Ehlers et al. 2005; McInnes and Fu 2006; Fu et al. 2010).

The exhumation study of the MMC uses the zircon and apatite (U-Th)/He thermochronometers, with effective closure temperatures of 150–200 °C and 40–80 °C respectively (Ehlers et al., 2005). Eight samples were selected from the MMC sample set, five from Leptokaria, two from Maronia and one from the Kechros dome gneisses. The Kassiteres system was specifically avoided as monotonic cooling cannot be assumed in any part of the intrusion given the pervasive nature of hydrothermal alteration. Five apatites and zircons were picked from each sample, avoiding fractured crystals or those with inclusions, measured and loaded into Pt tubes at the University of Bristol by R. Perkins. Analyses were conducted by M. van Soest at Arizona State University.

The (U-Th)/He thermochronology results can be described separately from Maronia and Leptokaria (Fig. O1; Table O1). I use approximate closure temperatures of 180 °C for zircon (U-Th)/He and 60 °C for apatite

Table O1: (U-Th)/He thermochronology results. All errors are reported at the 2σ confidence level.

Sample	*Apatite*				*Zircon*			
	age	±	% error	*n*	age	±	% error	*n*
MA15_015	20.7	2.8	13	3/3				
MN16_005	18.4	0.4	2	2/3	22.4	4.0	18	3/4
RT14_023	14.7	2	2	5/5	27.9	1.7	6	5/5
LA15_011	14.7	2.4	16	4/5	29.1	0.8	3	4/5
LB15_004	23.0	0.7	3	3/4	26.6	0.8	3	5/5
RT14_010	21.8	3.5	16	3/4	28.5	7.9	28	5/5
LK16_016	20.0	2.5	12	4/4	42	12	28	3/5
RT14_030					31.8	1.3	4	3/5

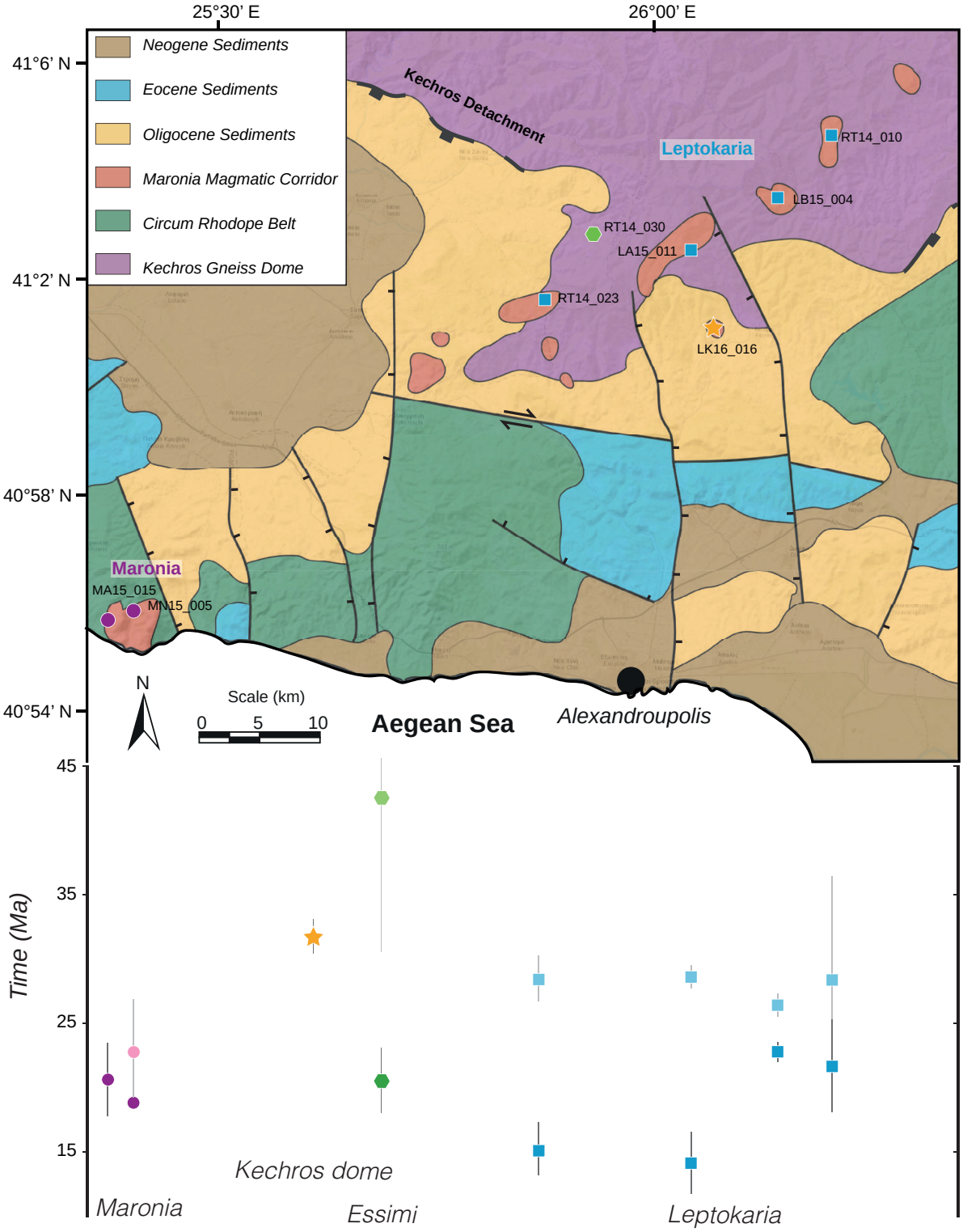

Figure O1: (U-Th)/He thermochronology data are overlain on the geological map of the Maronia Magmatic Corridor first presented in *Chapter 2*. The light colour symbols indicate a zircon (U-Th)/He age and the darker symbol an apatite (U-Th)/He age. The Maronia and Leptokaria samples are aligned with their location along the Maronia Magmatic Corridor whilst the Essimi and Kechros dome samples are not located spatially for ease of presentation. Whilst the zircon (U-Th)/He ages give consistent results across the Leptokaria intrusions in the footwall of the Kechros dome, there is a clear split in the apatite (U-Th)/He ages with the intrusions from the centre of the Kechros dome passing through the apatite closure temperature earlier than the intrusions close to the Kechros detachment.

(U-Th)/He in the following discussion. At Maronia, following emplacement of the shoshonitic magma at $\sim$ 850 °C and an unknown depth (Chapter 3), the pluton cooled through the zircon and apatite closure temperatures between 26 and 17 Ma indicating a minimum cooling rate of $\sim$ 65 °C/Myr. At Leptokaria, the results are more complex. Following magma emplacement at 32 Ma, $\sim$ 700 °C and $\sim$ 5 km (Chapter 3), all of the intrusions had cooled through zircon closure by 25 Ma, estimating a cooling rate of $\sim$ 70 °C/Myr, similar to that proposed for Maronia. Two stages of subsequent cooling are recorded. Towards the centre of the Kechros dome, samples RT14_010 and LB15_004 record cooling through apatite closure before 20 Ma, giving a cooling rate of $\sim$ 24 °C/Myr. In the intrusions at the edge of the Kechros dome, close to the detachment, the intrusions cooled more slowly, with apatite (U-Th)/He ages of 14–18 Ma and a cooling rate of $\sim$ 13 °C/Myr. In the hanging wall of the Kechros dome, the Essimi porphyry sample LK16_016, documents apatite cooling at $\sim$ 20 Ma. In the footwall of the Kechros dome, gneiss sample RT14_030, records cooling through zircon closure at $\sim$ 32 Ma, within error the same time as emplacement of the Kassiteres–Leptokaria intrusive complex.

Key to interpretation of an exhumation rate from thermochronology data is knowledge of the geothermal gradient, and how it evolves through time (e.g. Braun 2005; Ehlers 2005). Consequently, multiple numerical models have been developed which integrate thermochronology data and predicted geothermal gradients to simulate exhumation paths (e.g. 4DTHERM, McInnes and Fu 2006; Fu et al. 2010; PECUBE, Braun 2003). However, these models are not appropriate for modelling synchronous pluton cooling and exhumation, as each model attributes cooling to either emplacement and crystallisation (4DTHERM) or advection of heat to the surface during exhumation (PECUBE). Thermal modelling is ongoing, in conjuction with Byron Adams and Simon Dahlström at the University of Bristol and Todd Ehlers and Willi Kappler at the University of Tübingen, in order to combine the effects of intrusion cooling and exhumation on the geothermal gradient. Once complete, the thermal modelling will be used to reconstruct the evolution of the Leptokaria complex and Maronia pluton through the crust, exploring the link between exhumation and mineralisation.

25.73° E
25.735° E
25.74° E
25.745° E
25.75° E
25.755° E
25.76° E

41.005° N
41° N
40.995° N
40.99° N

KA15_018
KA15_019
KA15_005
RT14_028
RT14_027
KA15_008
KS16_006
KA15_017
KA15_013
KA15_010
KA15_016
X
X'

N
100 m

Stratigraphy

- Quartz - alunite lithocap
- Oligocene volcaniclastic - pyroclastic deposits
- Oligocene quartz-feldspar porphyry
- Oligocene diorite - granodiorite intrusion
- Eocene transgressive sedimentary sequence
- Circum Rhodope Belt - schists and marbles
- Normal fault

Samples

- Pyroclastic sample
- Porphyry sample
- Pluton sample
- KA15 Petrology sample
- KA15 Geochronology sample

Schematic cross-sections at time intervals through the Oligocene

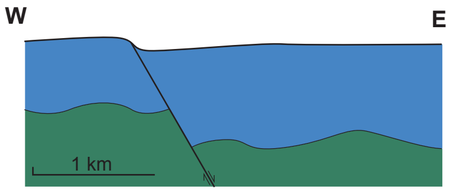

Eocene to Oligocene (> 33 Ma)
E-dipping normal faulting of the Eocene Sedimentary Sequence and CRB basement during regional extension.

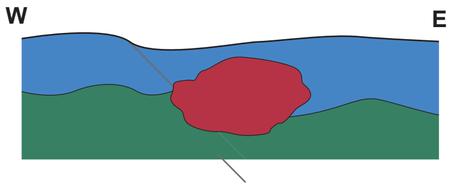

Oligocene (~ 32 Ma)
Intrusion of the Kassiteres host intrusion; exploitation of pre-existing fault structures is hypothesised.

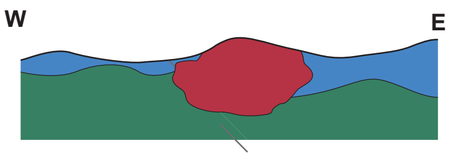

Oligocene (32.04 - 31.2 Ma)
Exhumation of the Kassiteres intrusion from emplacement at 4.4 km depth to the surface.

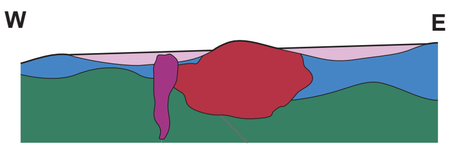

Oligocene (32.04 - 31.2 Ma)
Burial of the region by volcaniclastic material and intrusion of the mineralising porphyry intrusion must occur prior to mineralisation at 31.2 ± 0.4 Ma.

An E-W Cross-Section through Kassiteres from X to X'

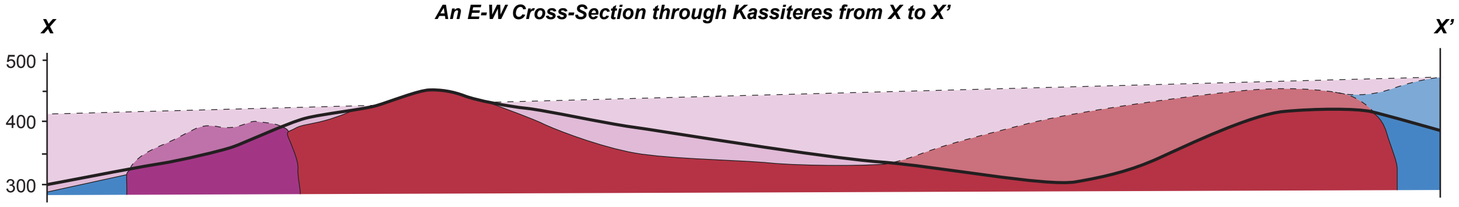

Cross section drawn to same scale as the map without vertical exaggeration.

The volcaniclastic deposit onlaps onto the Kassiteres host intrusion and Eocene sedimentary sequence as observed by erosive contacts in the field. The field relationship between the porphyry intrusion and the volcaniclastic deposit is unclear; it is envisaged that the porphyry intrusion was contemporaneous with volcanism and this crosscuts the lower half of the volcaniclastic unit but is further buried by later material.

25.725° E
25.73° E
25.735° E
25.74° E
25.745° E
25.75° E
25.755° E
25.76° E

41.005° N
41° N
40.995° N
40.99° N

KA15-001
KA15-002
KA15-003
KA15-018
KA15-019
KA15-005
RT14_029
RT14_028
KA15-004
KA15-020
KS16_018
KA15-006
KS16_011
KS16_014/15/19
KS16_013
KA16-008
KS16_002
KA15-007
KS16_012
KS16_021
KS16_020
KS16_00
KS16_006
KS16_005
KA15-01
KS16_004
KS16_007/8
KA15-013
KA15-014
KS16_016
KA15-012
KA15-009
KA15-010
KA15-011
KA15-016
KA15-017

Oligocene pyroclastic/ volcaniclastic deposits
Oligocene quartz - feldspar porphyry
Oligocene diorite - granodiorite intrusion
Eocene transgressive sedimentary sequence
Circum Rhodope Belt - schists and marbles
Lithocap
Known contact
Interpreted contact
Observed Fault
Pluton outline

N
100 m

25.725° E
25.73° E
25.735° E
25.74° E
25.745° E
25.75° E
25.755° E
25.76° E

41.005° N
41° N
40.995° N
40.99° N

1
2
3
4

Kassiteres Village

N

100 m

Pluton Outline
Lithocap
Field Photo Locality